Department of Chemical and Environmental Engineering

NOVEL MATERIALS FOR CO_2 ADSORPTION AND REDUCTION TO METHANOL VIA HYDROGENATION

By

EZEH COLLINS IZUCHUKWU

Thesis submitted to the University of Nottingham for the degree of

Doctor of Philosophy

AUGUST 2017

Dedicated To Mr. Fred Ezeagwuna

(R.I.P… Love you loads)

Synopsis

Sorption-enhanced catalysts are highly favored to improve the synthesis of methanol by hydrogenation process. This requires the development of selective catalysts and CO_2 adsorbents that are sufficiently stable to tolerate cyclic regeneration during operation. The present work focuses on the assessment of the adsorption performance of novel layered double hydroxides acting as supports for copper based catalysts in the reduction of CO_2 to methanol. Emphasis is placed on the stability and capacity of hybrids prepared using various preparation routes in order to optimize the CO_2 uptake and conversion to methanol per mass of the catalyst. This parameter is crucial in the industrial implementation of the technology as it dictates the size of the adsorption units and reactors required.

The co-precipitation of Cu^{2+}, Zn^{2+} and Zr^{4+} species onto well-dispersed layered double hydroxides is shown to be an effective preparation method that ensures adequate interaction between the catalysts and the support. Prior to the synthesis of the material, individual enhancement of the catalyst and the LDH template were carried out respectively. The catalysts were prepared via various facile methods. Calcination of the catalysts facilitated the mixture of the Cu catalyst with the respective support bolstering the formation of intermolecular oxo-bridges which resulted to the thermal stability of the catalysts. The thermal performance of the catalysts was directly related to the increase in calcination temperature. However, this temperature was capped at 673K beyond which denaturing of the catalyst occurs. For all given preparation method, comparing the different catalysts based on the Cu-loading, the performance trend is as follows: CP>DP>IM. Other factors experimented to affect the thermal properties of the catalysts include the Cu-loading and heating rate.

To improve CO_2 adsorption, amine modified Layered double hydroxide (LDHs) were prepared via the conventional, ultrasonic and hydrothermal routes, followed by MEA extraction. A comparative study was conducted with consideration of the effect of functionalization route on the adsorption capacity, regeneration and lifetime of the adsorbent. It is revealed that increase in amount of SDS has an adverse effect on the CO_2 adsorption performance by protonating considerable amount of active amino groups. This performance trend was observed across all experimented temperature with the CO_2 adsorption capacity decreasing with increase in temperature. After amine modification, adsorption capacity increased by ca. 75-90% and *ca.*10-30% at 55 ^oC and 80 ^oC, respectively. However, by sonochemical modification, the adsorption capacity showed an increase from 12-108% depending on sonic intensity. This is attributed to

the enhanced deprotonation of activated amino functional groups via the sonochemical process. Subsequently, this improved the effective amine efficiency by 60% of the conventional. In addition, the sonochemical process improved the thermal stability of the adsorbent as well as reducing the irreversible CO_2 uptake, CU_{irrev}, from 0.18 mmol/g to 0.03 mmol/g; hence improving the lifetime and ease of regenerating the adsorbent. This is presented by subjecting the prepared adsorbents to series of thermal swing adsorption (TSA) cycles until its adsorption capacity goes below 60% of the original CO_2 uptake. While the conventional adsorbent underwent a 10 TSA cycles before breaking down, the sonochemically functionalized LDH went further than 30 TSA cycles. However, adsorbents prepared via hydrothermal route showed a better CO_2 uptake capacity than sonochemical and conventional adsorbents. This is attributed to the decrease in weak basic sites (OH^- groups) and moderate basic sites (M-O) and subsequent increase in number of strong basic sites (O^{2-}). Therefore, the sonochemical-assisted hydrothermal treatment promoted the adsorption capacity of the adsorbent. However, the cyclic adsorption efficiency of the hydrothermally prepared sample was lowest ca. 53% compared to 76% and 60% for the sonochemical and conventional process respectively.

Adopting the obtained factors for optimum synthesis and operation of both $CuO/ZnO/ZrO_2$ catalyst and Mg-Al LDH adsorbent, a composite catalyst consisting of $CuO/ZnO/ZrO_2$ catalyst on LDH template was synthesised and analysed for CO_2 uptake capacity and catalytic activity with variation in Al^{3+} and Zr^{4+} compositions. The deposition of the catalyst on the LDH support was found not to alter significantly the CO_2 uptake of the hydrotalcites but helps to maintain the surface heterogeneity. Characterization tests shows an improvement in structural modification. However, this is subject to the proportion of the considered varied metals. In addition, despite the high thermal stability of Zr^{4+}, the composite material was observed to weaken in stability with increase in Zr^{4+} content. Nonetheless, the CO_2 uptake capacity was observed to increase. A thorough kinetic analysis demonstrates that the adsorption mechanism is attributed to the chemical nature of the metals which promoted chemisorption as the dominating adsorption mechanism with little contribution from physisorption. CO_2 conversion and methanol yield were also dependent on the nature and composition of the cations as well as the operating temperature. Al^{3+}:(Al^{3+}+Zr^{4+}) ratio of 0.4 was obtained as the best cation mix to attain maximum methanol yield. A preliminary catalyst screening shows that $Cu/ZnO/ZrO_2$/Mg-Al LDH is a promising candidate to catalyze simultaneous adsorption and reduction of CO_2 for methanol synthesis.

List of Publications

Published

C. I. Ezeh, X. Huang, X. Yang, C. Sun, J. Wang. Sonochemical Surface Functionalization of Exfoliated LDH: Effect on Textural Properties, CO_2 Adsorption, Cyclic Regeneration Capacities and Subsequent Gas Uptake for Simultaneous Methanol Synthesis, Ultrasonics Sonochemistry, 39 (2017), 330-343. (IF: 4.218).

C. I. Ezeh, M. Tomatis, X. Yang, J. He, C. Sun. Ultrasonic and Hydrothermal Mediated Synthesis Routes for Functionalized Mg-Al LDH: Comparison Study on Surface Morphology, Basic Site Strength, Cyclic Sorption Efficiency and Effectiveness, Ultrasonics Sonochemistry, 40 (2018), 341-352 (IF: 4.218).

C. I. Ezeh, X. Yang, J. He, C. Snape, X. M. Cheng. Correlating Ultrasonic Impulse and Addition of ZnO Promoter with CO_2 Conversion and Methanol Selectivity of CuO/ZrO_2 Catalysts. Ultrasonics Sonochemistry, (2017) DOI https://doi.org/10.1016/j.ultsonch.2017.11.013 (IF: 4.218).

Under Review

C. I. Ezeh, B. Dong, X. Yang, C. Sun, J. Wang, C. Snape. Facile Synthetic Route, Calcination Temperature and Heating Rate: Study on Optimum Thermal Performance of CuO/ZrO_2 Catalysts for Methanol Synthesis. Applied Catalysis A, Ms. No. APCATA-D-17-01539 (27th July, 2017) (IF: 4.339)

C. I. Ezeh, U. H. Richter, J. H. Seufert and C. Peng. Operational-based CO_2 Mitigation Strategy of Chinese Ports: Case Study of Ningbo Zhoushan Port. Journal of Cleaner Production, Ms. Ref. No.: JCLEPRO-D-17-03301 (2nd May, 2017). (IF: 4.959)

C. I. Ezeh, T. Marco, X. Yang, C.Sun, J. Wang, C. Snape. Synthesis and Investigation of Novel Mg-Al LDH Nano spheres. Microporous and Mesoporous Materials Ms. Ref. No.: MicMat-17-0583 (20th July, 2017) (IF: 3.615)

X. Huang, X. Yang, G. Li, C. I. Ezeh, C. Sun, C. Snape. Hybrid Two-step Preparation of Nano-sized Mg-Al Layered Double Hydroxides for CO_2 Adsorption, ACS Omega, Manuscript ID: ao-2017-001829 (16-Feb-2017).

Conferences and Symposiums

C. I. Ezeh, X. Yang, C. Sun. Enhancement of LDH Adsorbent Performance for CO_2 Adsorption. UK-Sino Clean Energy and Environmental Engineering Technology Forum, China (30th Dec. 2015).

C. I. Ezeh, U. H. Richter, J. H. Seufert, C. Peng. GREENING OF CHINESE PORTS: Case Study of Ningbo Zhoushan Port, 6th Workshop on EU-China Relations, Taiwan (28th Feb 2017).

C. I. Ezeh, U. H. Richter, J. H. Seufert, C. Peng. Operational-based CO_2 Mitigation Strategy of Chinese Ports: Rate of Efficiency Change, IAPS-Contemporary Challenges of China Symposium, China (26th May, 2017).

C. I. Ezeh, X. Yang, C. Sun. Novel Materials for CO_2 Adsorption and Reduction to Methanol via Hydrogenation. 2017 Energy Engineering (EERG) & Natural Resources & Environment (NRE) Joint Research Conference, Ningbo, China (18-19th September, 2017).

Acknowledgement

My first gratitude goes to the Almighty God for His Mercy and Compassion, for He was the source of my strength.

My heartfelt gratitude goes to my parents, Mr & Mrs Fred Ezeagwuna for their love, inspiration and support. Without their support and those of my wonderful sisters (Freda, Vivian, Cynthia, Sarah and Prisca), I will not be this inspired.

A much greater appreciation goes to Mr Uche Obiakor. Without him, this feat will not be attained and to him. In addition, i also appreciate Mrs Anastasia Akpebe, Chief Francis Ezeagwuna, Mr. Joseph Anene Okpala, Mr. Afam Nwakuche, Mr Victor Mbamalu, Mr Raymond Mbamalu, Dr. Okwi Mbamalu, Mr. Daniel Osuji and Mr. Richard Emeka for their unending support and contribution to my career up growth.

The possibility of embarking on this research study would not have been feasible without the aid of Professor Xiaogang Yang, Dr. Jun He, Dr. Jiawei Wang, Professor Colin Snape and Dr. Cheng-gong Sun. They groomed me into my present engineering status within the confines of this research. Profound thanks to Professor Yang for his immense technical expertise and wisdom, patience and assistance during the course of this study. I also appreciate Dr. Anup Patel for his numerous advice and guide during the entire program.

The laboratory technical crew were undoubtedly superb. They attended to all my requirements within schedule and with great expertise. They all acted within their capacity to make my laboratory experience hitch-free. This includes in alphabetical order Mrs. Carey Tao, Mrs. Helen Xu, Mrs. Jane Zhang, Mr. John Zhu and Mr. Julian Zhu. To this team, I offer great appreciation. I also wish to appreciate the Procurement Office (Mrs. Nancy Zhang and Mrs. Jane Li) for the relentless support in the acquisition of facilities required for the purpose of this study.

My sincere thanks also goes to the funding institutions: International Doctoral Innovation Centre (IDIC), National Natural Science Foundation of China (NSFC) (Grant No. 21576141), Zhejiang Provincial Natural Science Foundation (Grant No. LY15B060001), Ningbo Key Research Project ‘Absorption/catalytic technologies for the simultaneous removal of multi-pollutants from flue gas at power stations’ (Grant No. 1012B10042), EPSRC (Grant no. EP/G037345/1), Ningbo Science and Technology Bureau, University of Nottingham and Ningbo Education Bureau and China's MoST.

Last but not the least, I appreciate all members of the Chemical and Environmental Engineering Department, friends (most especially Mrs. Rui Gaoqiong, Mr. Felix Osebor, Mrs. Lulu Huang, Mrs. Victoria Grishina, Mr. Ayotunde Dawodu, Mr. Ashak Parvez, Mrs. Sannia Mareta, Mrs. Jumoke Oladejo, Mr. Oluleke Bamodu, Mr. Bamidele Akinwolemiwa) and Lecturers for their unfathomable supports and advice.

Table of Content

CHAPTER TWO

LITERATURE REVIEW

CHAPTER THREE

METHODS AND EXPERIMENTALS

CHAPTER FOUR

CATALYSTS FOR METHANOL SYNTHESIS: STUDY OF SYNTHETIC ROUTES, CALCINATION TEMPERATURE AND HEATING RATE ON SYNTHESIS OF CuO/ZrO_2

CHAPTER FIVE

ENHANCEMENT OF Cu/ZrO_2 CATALYST VIA ULTRASONIC IRRADIATION AND INTRODUCTION OF Zn^{2+} PROMOTERS

CHAPTER SIX

ENHANCEMENT OF CO_2 ADSORPTION BY AMINE MODIFIED LAYERED DOUBLE HYDROXIDE SYNTHESIZED VIA ULTRASONIC FACILITATED SDS/APTES INTERCALATION

CHAPTER EIGHT

ULTRASONIC AND HYDROTHERMAL MEDIATED SYNTHESIS ROUTES FOR FUNCTIONALIZED Mg-Al LDH

CHAPTER NINE

DEVELOPMENT OF NOVEL COMPOSITE CATALYST: CuO/ZnO/ZrO_2 CATALYST SUPPORTED ON Mg-Al LDH

List of Figures

CHAPTER ONE

CHAPTER TWO

CHAPTER THREE

CHAPTER FOUR

CHAPTER FIVE

CHAPTER SIX

CHAPTER SEVEN

CHAPTER EIGHT

CHAPTER NINE

Appendix

List of Tables

CHAPTER ONE

CHAPTER THREE

CHAPTER FOUR

CHAPTER FIVE

CHAPTER SIX

CHAPTER SEVEN

CHAPTER EIGHT

CHAPTER NINE

Appendix

List of Equations

CHAPTER THREE

CHAPTER FOUR

CHAPTER FIVE

CHAPTER SIX

CHAPTER SEVEN

CHAPTER EIGHT

CHAPTER NINE

List of Abbreviation

AMS	Anionic Surfactant-Mediated Mesoporous Silica
APTES	3-Aminopropyl-Triethoxysilane
APTMS	3-aminopropyl-Trimethoxysilane
BET	Brunauer-Emmett-Teller
BJH	Barrett, Joyner and Halenda
CCS	Carbon Capture and Storage
CCSU	Carbon Capture, Storage and Utilisation
CFC	Chlorofluoro Carbon
Conv	Conventional
CP	Co-precipitation
DP	Deposition Precipitation
DFT	Density Functional Theory
DSC	Differential Scanning Calorimetry
DTG	Differential Thermal Gravimetric Analysis
EDX	Energy Dispersive X-ray
EOR	Enhanced Oil Recovery
FID	Flame Ionization Detector
FTIR	Fourier Transform Infrared spectroscopy
GC-FID	Gas-Chromatograph with Flames Ionization Detector
GHSV	Gas Hourly Space Velocity
HPH	High Pressure Hydrothermal
IEA	International Energy Agency
IGCC	Integrated Gasification Combined Cycle
IM	Impregnation
LDH	Layered Doubled Hydroxides
LDO	Layered Doubled Oxides
MEA	Monoethanolamine

MFC	Mass Flow Controllers
M-O	Metal Oxides
MOFs	Metal-Organic Frameworks
PCV	Pressure Control Valves
PET	Polyethylene Terephthalate
PFO	Pseudo First Order
PSO	Pseudo Second Order
RFG	Recycled Flue Gas
RWGS	Reverse Water Gas Shift
SDS	Sodium Dodecyl Sulphate
SEM	Scanning Electron Microscopy
SSV	Steady State Value
US	Ultra-Sonication
TCD	Thermal Conductivity Detector
TPD	Temperature Programmed Desorption
TPR	Temperature Programmed Reduction
TEA	Triethylamine
TGA	Thermogravimetric Analyser
TSA	Thermal Swing Adsorption
UB	Ultrasonic Bath
UH	Ultrasonic Horn
XPS	X-ray Photoelectron Spectroscopy
XRD	X-ray Diffraction

CHAPTER ONE

INTRODUCTION

1.1 BACKGROUND

A key alternative for sustainable development is the reuse or recycling of unwanted products to useful ones. This can be attained via transformation or conversion of the end products to feedstock for another process. In this research, expanding on the concept of carbon capture and storage (CCS), the captured carbon dioxide can equally be utilized industrially rather than sequestering them away. Carbon dioxide is quite useful as a chemical reagent and can be used industrially in the manufacture of chemicals (see Figure 1.1). However, industries rarely use this chemically stable compound as source of carbon. This is ascribed to its low energy level given it is a fully oxidized state of carbon [1]. Hence, for any chemical reaction to be possible, a large energy input is required. This can be attained in various ways:

1. Supply of physical energy,
2. Controlled equilibrium shift to favour product production (forward reaction),
3. Production of selected low energy products such as oxidized products (carbonates),
4. The use of high-energy reactants alongside CO_2 such as unsaturated compounds and hydrogen.

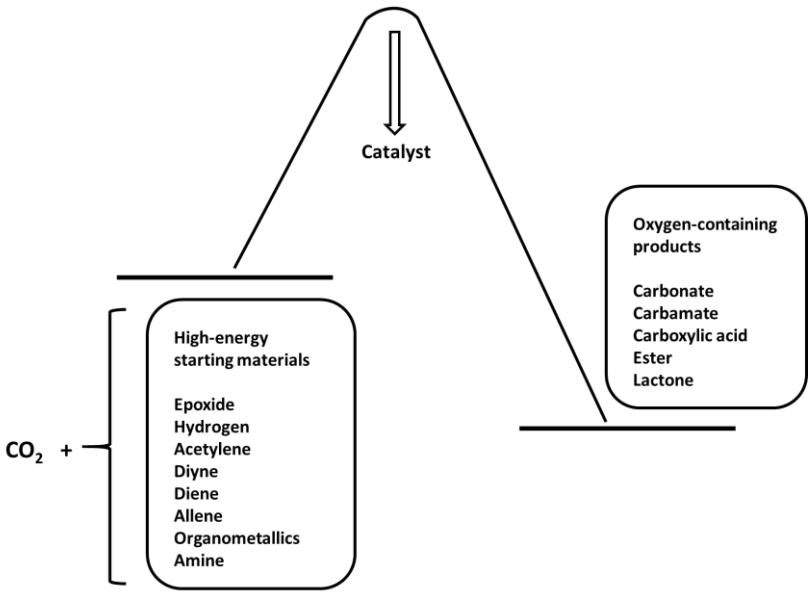

Figure 1.1: Various means of using CO2 as sources of chemical production

With regards to Figure 1.1 and the aforementioned means of conducting CO_2 transformation, many studies have been conducted to best define each reaction mechanisms and the favourable conditions supporting the reactions. Carbon dioxide is categorized as an anhydrous carbonic acid because of its affinity for electron donors and nucleophiles. However, partly due to its thermodynamic properties, this compound is not considered suitable as a carbon source for chemical reactions, both in industries and laboratories [2]. Hence, suitable materials are required to promote these thermodynamic properties both in the capturing and utilization processes.

1.1.1 Overview of Carbon Capture

There are three major sources of CO_2 emissions: (a) electricity generation (29% of global CO_2 emission), (b) 23% CO_2 emission is caused by industrial processes from cement, iron, glass and chemical industries, (c) the fuel production sector rates third [3]. An incorporation of carbon capture technologies to these sources will aid circumvent CO_2 emission. Carbon capture is a decarbonizing technology aimed at mitigating CO_2 emission by capturing and subsequently sequestrating or utilizing CO_2 for other better courses. Carbon capture process is categorised into four main technologies [4-6]. Figure 1.2 illustrates a simplified version of the post-, pre- and oxy-combustion technique. The fourth technique is the nascent processes recently researched upon.

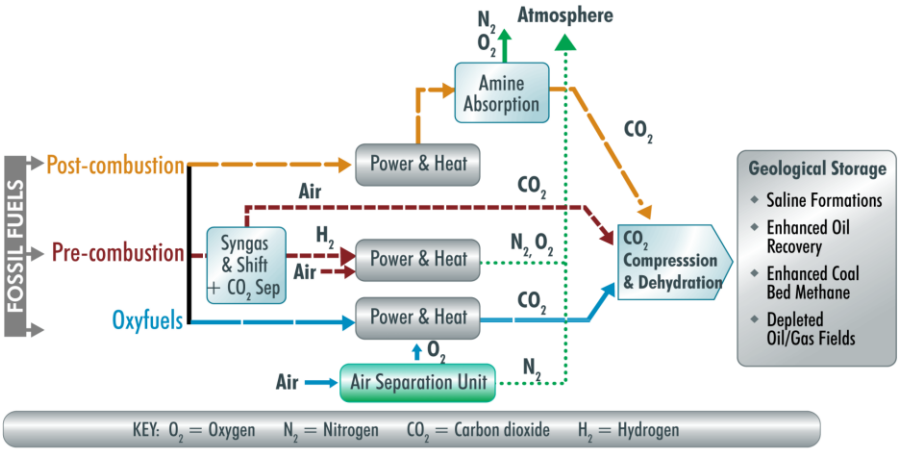

Figure 1.2: Summarized flow sheet for various CCS technology

1.1.1.1 Pre-combustion Capture

This is a capture process that involves the gasification of coal into CO, CO_2 and H_2. Subsequently, CO is converted to CO_2 using a water-gas shift reactor. The CO_2 is separated and sequestered before hydrogen is combusted in a gas turbine [7]. Alternatively, CO can be combusted after the removal of hydrogen from the syngas. A practical application of this technology is the Integrated Gasification Combined Cycle (IGCC).

1.1.1.2 Post-combustion Capture

As the name implies, this technology captures the CO_2 after the combustion process. It involves the use of amine scrubbers to separate CO_2 from the flue gas before being compressed and stored [8]. The energy requirement for the amine regeneration reduces the efficiency of the power plant [9]. According to research findings, the suspected drop in efficiency varied from 10-14% points [10]. Lots of studies have been undertaken to reduce the energy requirement concomitant with this technology. Post-combustion capture is notable for its retrofit ability downstream an existing power plants [11]. However, the high reactivity of the impurities, SO_2 and NO_2, with the absorbents necessitates flue gas cleansing prior CO_2 capturing. SO_2 and NO_2 undergoes an irreversibly reaction with the absorbent making it unrecyclable [9].

1.1.1.3 Oxy-fuel Combustion

In this technology, air is substituted with an O_2/CO_2 mix. The oxygen is obtained from air through air separating units and CO_2 is obtained from the recycled flue gas (RFG). RFG is basically used to regulate boiler temperature. The gas product contains mainly water vapour and CO_2. This stream is condensed and compressed yielding a high purity CO_2 stream [12, 13]. Incorporating this technology to existing plants will demand a significant change in plant footprint. Nonetheless, the process is evaluated to be the most economical of the CCS technologies [14]. The basic shortcoming of oxy-fuel combustion is the energy penalty incurred in air separation. This reduces the net efficiency by 7-11% point [10], corresponding to a 21-35% rise in fuel consumed [15].

1.1.1.4 New and Emerging Capture Processes

Based on plant efficiency development, operation flexibility, cost effectiveness, utility preference and retrofit tendency, new processes have emerged to cushion the demerits of CCS.

Among others includes membrane separation, chemical looping combustion, and cryogenic separation [16].

1.1.1.4.1 Membrane Separation

This is categorised into the gas separation membrane and the gas absorption membrane. The gas separation membrane is governed by the differences in physico-chemical interaction between constituents of a gaseous mixture with the membrane material. This difference causes one of the constituents to infuse through the membrane and retains the others. An augmenting factor is the permeability and selectivity of the membrane and the pressure difference across the membrane. The selectivity of the membrane is the ability of one gas to permeate faster than the other. The ideal option would be the separation of CO_2 from a concentrated CO_2 waste stream. However, in practical terms, source streams generally have low pressures, low CO_2 concentrations with many component gases. This creates an impediment towards membrane selection. For high stream purity, membranes with high selectivity are prerequisite. Nonetheless, these are hard to produce; hence, multistage processes are required which implies additional compression and costs. Examples of gas separation membranes are polymer, palladium, ceramic membranes and molecular sieves [17, 18]. Gas absorption membranes are membranes that enable gas-solvent stripping. They create a larger contact surface area for the liquid absorbents and the flue gases, thereby increasing absorption efficiency and reducing cost. Unlike the gas separation membrane, the selectivity of the gas absorption membrane process depends on the absorbing liquid. These membranes are porous hydrophobic in nature and act as contact surface but separate the liquid and gas flows [19]. The limitation of these membranes is that both the flue gas and absorption liquid must have similar pressure levels. The difference between these membranes is shown in Figure 1.3.

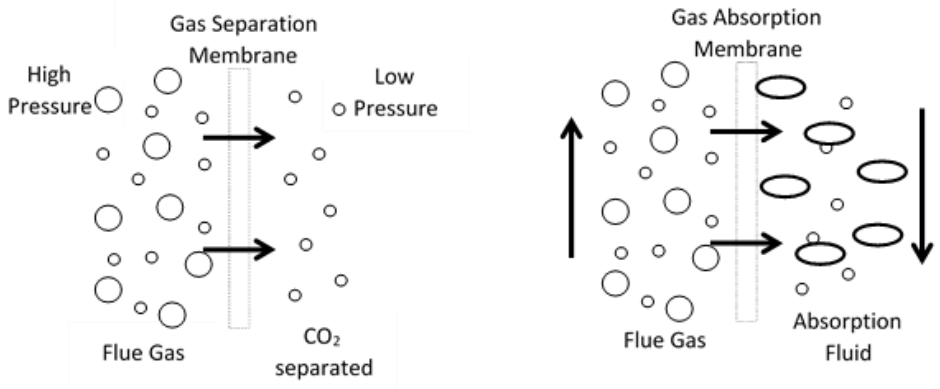

Figure 1.3: Absorption mechanism for gas separation and gas absorption membrane

1.1.1.4.2 Cryogenic Separation

This involves the separation of gases based on their differences in boiling points. It consists of series of compression and cooling of the flue gas resulting in the phase change of CO_2 to the liquid state which can be separated [20]. This is commonly used for concentrated CO_2 streams with compositions greater than 90%. In practical terms, the concentration of CO_2 is low due to the presence of water and some contaminants (SO_2 and NO_x). The presence of water poses difficulty in the separation process. Removing the water via condensation can circumvent this. Cryogenic separation is quite expensive owing to the multi-stage compression and cooling, which is energy intensive. However, the technology is advantageous in processes producing high CO_2 concentration streams like in pre-combustion and oxy-combustion processes [3].

1.1.1.4.3 Chemical looping Combustion

In this technology, oxygen is fed to the gaseous fuel through an oxygen carrier like metal oxides (Me_xO_y). This prevents direct contact between the fuel and air [21]. After combustion, the flue gas primarily contains CO_2 and water. The water is removed by condensation leaving a CO_2 concentrated stream. The reduced metal oxide is recycled in an air reactor where it is re-oxidized. The combustion is governed by the following chemical reaction [22]:

$$(2n+m)Me_xO_y + C_nH_{2m} \rightarrow (2n+m)Me_xO_{y-1} + mH_2O + nCO_2$$

$$Me_xO_{y-1} + {}^1/_2\, O_2 \rightarrow Me_xO_y$$

Reaction Scheme 1.1: Reaction equation for chemical looping combustion

The only setback of this technology is the energy requirement. Nonetheless, the absence of N_2 in the combustion air cushions the effect of the aforementioned setback in comparison to conventional combustion. International Energy Agency (IEA) [18] proposes that the metal oxide material must be resistant to corrosion, cost effective and withstand chemical recycling.

Other notable novel technologies are carbonation-calcination cycles, enzyme facilitated processes and mineralization. These methods are well reviewed by [23, 24]

1.1.2 Carbon Dioxide Utilisation

Despite the amount of anthropogenic carbon dioxide produced, a little amount of this quantity is being re-used in the industry. It is estimated that 0.5% approx. of the emitted CO_2 (24

Gtonnes annually) is being used industrially, excluding its purpose for enhanced oil recovery (EOR). This is shown in Figure 1.4.

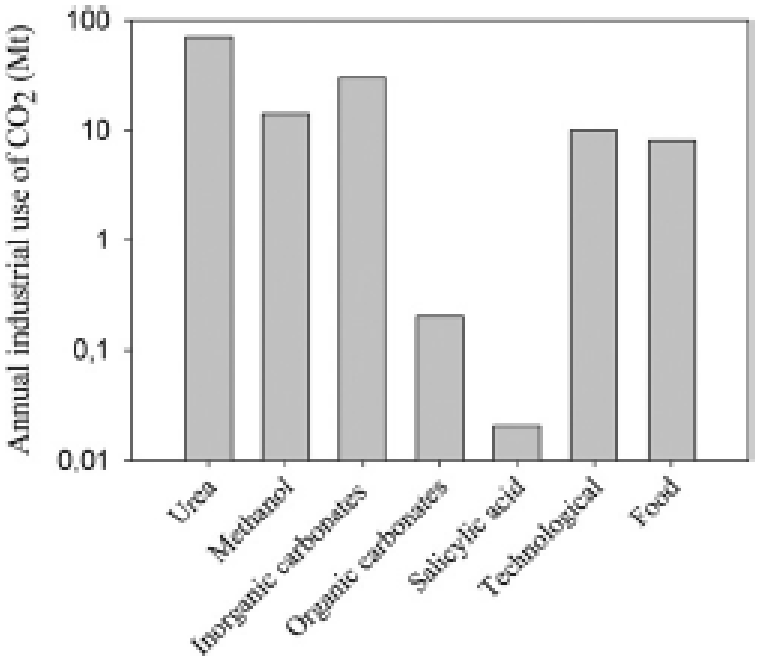

Figure 1.4: Annual Usage of CO_2 [25]

Based on its properties, carbon dioxide has been used diversely. Owning to its chemical properties as an inert and safe gas, it is used as a protective gas for welding, and food preservatives. It is also used as feed in the production of chemicals like carbonates, both inorganic and cyclic organic, urea, pigments and methanol. In its solid state, it is used as a substitute for chlorofluorocarbon (CFC) as a refrigerant. However, given its physical properties, CO_2 is used for enhanced oil recovery, preservatives in beverages and while in its supercritical state, used in the production of composites. These utilizations of CO_2 in the chemical industry are very limited compared to the amount emitted annually. A summary of its usage is shown in Reaction Scheme 1.2. One common utilization of CO_2 is the production of methanol (CH_3OH) through the hydrogenation process.

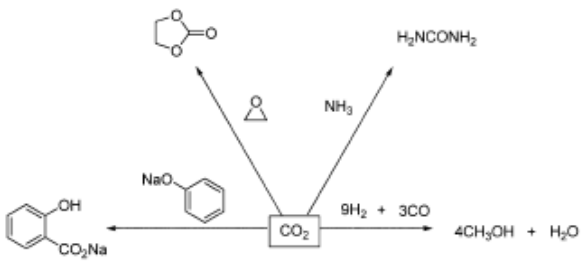

Reaction Scheme 1.2: CO_2 Utilization [2]

Other notable utilization of CO_2 are summarized in Table 1.1. This shows both recent and forecasted estimated usage as at the year of publication.

Table 1.1: Estimated recent and future usage of carbon dioxide [26]

Chemical product or application	Industrial volume (Mt/yr)	Industrial CO_2 use (Mt/yr)	Future expectations in the use of CO_2	Endothermic or exothermic reaction
Urea	100	70	100 Mt	Exothermic
Methanol (additive to CO)	40	14	Gt	Exothermic
Inorganic carbonates	80	30	-	Exothermic
Organic carbonates	2.6	0.2	100 Mt	Exothermic
Salicylic acid	0.06	0.02	100kt	Exothermic
Technological	10	10		
Food	8	8		

1.1.2.1 Methanol

Methanol is commercially used in the production of numerous chemicals including acetic acids and formaldehyde. It is also used as fuel for vehicles. Naturally, the compound is produced via anaerobic metabolism using characteristic bacteria. However commercially, the compound is produced from synthesis gas and CO_2 (as shown in Reaction Scheme 1.3).

$$3\,CO + 9\,H_2 + CO_2 \rightarrow 4\,CH_3OH + H_2O$$

Reaction Scheme 1.3: Synthesis of methanol from CO_2 and synthesis gas

This reaction is bolstered through the use of copper or zinc oxide catalysts due to its high selectivity and reactivity.

1.1.2.2 Reductive Hydrogenation

Hydrogenation is a chemical reaction purported to reduce a compound or saturate it by the introduction of hydrogen. This is basically conducted in the presence of catalysts. Hydrogenation of carbon dioxide is another means of using the compound to produce value added products. This has been greatly investigated. The process can be catalysed by either heterogeneous and/or homogeneous catalysts. In this process, carbon dioxide can be reduced to form methanol, alcohols and formic acids [27].

1.1.2.2.1 Synthesis of Methanol

This is one of the most investigated fields of hydrogenation. It involves the catalytic reduction of carbon dioxide to methanol and water as by-product. This reaction is similar to the industrial

production of methanol via syngas (CO + H_2) but with the demerit that about 30% of the hydrogen is converted to H_2O. This is quite unlikely in the syngas reaction. By comparison, it is also noteworthy that the yield of methanol in both processes differs greatly with a higher yield from syngas generation. At 200°C, the yield from syngas is about 80% whereas that from carbon dioxide is slightly below 40% [28]. This has been attributed to the unfavourable thermodynamics of the reaction between carbon dioxide and H_2 as against carbon monoxide and H_2. In this reaction, the most commonly used catalysts are a blend of Cu, Al_2O_3 and ZnO as shown in Reaction Scheme 1.4 [29].

$$\boldsymbol{CO_2 + 3H_2 \underset{Cu/ZnO/Al_2O_3}{\Longleftrightarrow} CH_3OH + H_2O}$$

Reaction Scheme 1.4: Synthesis of methanol by catalytic hydrogenation of CO_2

This technology is highly challenged by the availability of H_2. Hydrogen has often been produced from sources of fossil fuels or electrolysis [30]. However, it can also be generated thermally or via using solar energy. This process is highly energy intensive and imposes a great cost challenge in methanol production. This has resulted in the development of various means of synthesizing methanol while bypassing the production of hydrogen. Of the notable processes, the Carnol Process is another well-accepted means. In this process, the basic feeds are CH_4 and CO_2 and it comprises of a two-step reaction. The first step involves the production of H_2 via the thermal decomposition of CH_4, which is then used for CO_2 hydrogenation in the second stage. The primary by-product of this reaction is carbon, which can be used for other purposes. The reaction mechanism of this process is shown in Reaction 1.5 below.

Methane thermal decomposition: $CH_4 \longrightarrow C + 2H_2$

Methanol synthesis: $CO_2 + 3H_2 \longrightarrow CH_3OH + H_2O$

Overall Carnol process: $3CH_4 + 2CO_2 \longrightarrow 2CH_3OH + 2H_2O + 3C$

Reaction Scheme 1.5: Reaction mechanism for Carnol process (29)

Methanol has grown in its application as a source of energy. In the automobile industry, the compound can be used as a liquid energy carrier and can serve as alternative fuels for powering engines. It has been accepted as an environmentally friendly fuel given its low emission of NO_x

and SO_x when compared to other fossil fuels [27]. Conversely, its usage as fuel recommends a large burner, a strict control mechanism for formaldehyde formations and device corrosion [31]

1.1.2.3 Reaction with Transition Metals

As elaborated earlier with regards to unfavourable thermodynamics for CO_2 reactions, CO_2 conversion generally requires additional inputs to favour its reaction. This amongst all includes the use of suitable catalysts. In most cases, these catalysts are transition metal complexes. Attached to these complexes, CO_2 displays various reaction pathways [32]. These CO_2 ligand complexes are the basis of the reaction bonding with other compounds to produce value added hydrocarbons. They are nonetheless the intermediates necessary for CO_2 transformations.

Carbon dioxide bonds with the transition metals in three modes. The first involves the straight-on bonding of the metal with the central carbon atom of the CO_2 molecule [33, 34]. The other modes are the bonding of the metal to a C-O bond [35, 36], or with the oxygen atom of the CO_2 molecule [37-39]. Examples of these complexes and their structures are shown in Table 1.2.

Table 1.2: Bonding structure of transitional metals to CO_2 [32]

Mode of bonding	Structural features of the adduct	M [ref.]	ν_{asym}	ν_{sym}	C–O bond length/Å
η^1-O η^1-C	M–O–C=O 	U[20] Rh,[21] Ir[22]	2188 1610	 1210	1.122(4), 1.277(4) 1.20(2), 1.25(2)
η^2-C,O		Ni,[23] Rh,[24] Fe,[25] Pd[26]	1740	1140–1094	1.17, 1.22
μ_2-η^2	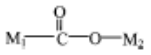	Pt[27] Ir/Zr,[28] Ir/Os,[29] Rh,[30] Ru[31]	1495	1290–1190	1.229/12), 1.306(12)
μ_2-η^3 (class I)	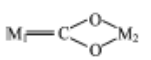	Re/Zr,[32] Ru/Zr,[33] Ru/Ti, Fe/Zr, Fe/Ti[33]	1348 1348	1288 1290	1.285(5), 1.281(5)
μ_2-η^3 (class II)	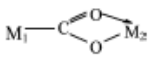	Re/Sn[34] Fe/Sn[35]	1395 1450	1188 1152	1.269(11), 2.257(7) 1.252(3), 2.394(2)
μ_3-η^3	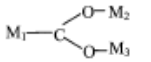	Os[36] Re[37]			1.276(5), 1.322(5) 1.28, 1.25
μ_3-η^4	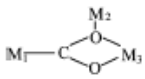	Co[38]			1.20(2), 1.24(2)
μ_4-η^4	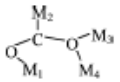	Ru[39]			1.283(15), 1.245(16)
μ_4-η^5	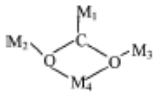	Rh/Zn[40]			1.29(14), 1.322(14)

Where the number of CO_2 ligand-metal bond is denoted by η^n and the number of metals attached to the coordinated CO_2 is designated by μ_n.

1.2 RESEARCH MOTIVATION

The commercial immaturity of the CCS technology has indiscriminately culminated to the adoption of renewables as alternative energy sources. Pending the implementation of these nascent technologies, researches are being conducted towards the utilization of the generated CO_2 in the production of value added chemicals. This involves its conversion to value-added products like urea, organic carbonates, carboxylic acids and methanol; hence transforming waste to extra income, as well as reducing CO_2 build-ups.

Due to its atmospheric presence, the ecological environment and human life are exposed to unfavourable climatic conditions and global warming. To mitigate this, CO_2 can be converted to useful chemicals and fuels through the HYDROGENATION process. However, this process is challenged by the availability of suitable catalysts with synergetic high CO_2 conversion and methanol yield capacity. Nonetheless, this is subject to the presence of captured CO_2. Thus, the development of a bi-functional material for CO_2 capture and as a catalyst for its subsequent conversion will be critical for this green chemistry. Over the years, the capture of CO_2 has been limited to four technologies. This includes adsorption and absorption. Other means include cryogenic distillation and membrane separation. The latter are challenged by the low concentration of CO_2 in the flue gases resulting to a low CO_2 partial pressure [40]. Consequently, this results to an inefficient separation of CO_2, hence requesting additional energy/cost input. On the other hand, absorption has been proposed to be the most researched and suitable technology for the removal of CO_2 [41]. Using suitable aqueous solutions, the CO_2 absorption capacity is highly efficient. However, it is posed with some operating limitations. This among all includes energy intensity desorption process, required large volume of absorbent and high corrosion capacity of operation units [9, 41, 42]. Some of these issues are addressed with the aid of solid adsorbents. Adsorption, unlike absorption, is a surface phenomenon process where the adsorbate forms a film on the adsorbent surface either via chemisorption or physisorption interface. A good adsorbent must be thermodynamically stable, have high adsorption and desorption capacity and kinetics and possess a wide operating window.

Hence, based on review of recent development, this research aims at first, re-design and synthesis of novel catalysts for methanol synthesis via simultaneous CO_2 adsorption and

conversion. Second, characterization of produced catalysts for evaluation of catalytic performance and reactivity. Finally, simulating the kinetic and internal transport mechanism.

1.3 RESEARCH AIMS AND OBJECTIVES

1.2.1 Aims

The present work is aimed at the synthesis of new materials for the production of methanol via hydrogenation. This material will simultaneously act as an adsorbent for the capture of CO_2 and a catalyst for the hydrogenation process. In particular, the study will focus on the hybrid of layered doubled hydroxides (LDH) as a support for copper (Cu)-based catalysts. First, Cu-based catalysts with suitable thermal stability and Cu dispersion are synthesized adopting improved synthetic methods to enhance its catalytic performance. Afterwards, the research concentrates on the study of LDH and strategies to improve its adsorption capacity. Emphasis is placed on the evaluation of the performance of the adsorbent with regards to CO_2 capacity and surface chemistry.

1.2.2 Objectives

In order to achieve the above set aims, series of experimentation alongside behavioural study of the dynamics and kinetics of the process will be conducted. This is divided into three sub-sections: (1) methanol synthesis, (2) CO_2 adsorption, and (3) hybrid of the two processes. The established objectives for each of the sub-sections are as follows:

1.2.2.1 Methanol Synthesis

- Evaluation of various synthetic routes and characterisation of methanol producing catalysts.
- Design and fabrication of catalyst performance evaluation rig for use in methanol synthesis via CO_2 hydrogenation.
- Modification of synthesised catalysts to enhance amount of active sites, thermal stability and catalytic performance by:
    - Metal doping
    - Sonochemistry application

- Thermal pre-treatment

❖ Investigate the impacts of the aforementioned modifications on surface texture and chemistry; as well as catalytic performance for methanol synthesis.

1.2.2.2 CO_2 Adsorption

❖ Synthesis and characterization of LDH templates.

❖ Evaluation of CO_2 uptake of the template on a pilot scale test rig.

❖ Modification of synthesized template to improve the adsorption capacity by:

- Amine surface functionalization
- Sonochemistry application
- Hydrothermal application

❖ Investigate the impact of the modifications on surface texture, chemistry, gas uptake capacity and cyclic efficiencies and effectiveness.

❖ Investigate surface reaction dynamics and kinetics for comprehensive understanding of the process.

1.2.2.2 Hybrid

❖ Synthesis and characterization of catalyst-LDH hybrid

❖ Evaluate catalytic performance for methanol synthesis.

❖ Correlate catalytic activity with dynamic and kinetic reaction mechanisms.

1.4 THESIS STRUCTURE

This thesis consists of nine chapters with the following scope:

Chapter One introduces the concept of CO_2 mitigation via carbon capture, storage and utilization (CCSU). It also conveys the aims and objective of this study.

Chapter Two covers the review of essential literatures for the present study discussing the characteristics of CCSU towards methanol synthesis and various performance enhancement strategies. Furthermore, the CO_2 uptake of LDHs and their derivatives were also addressed in details with special highlights on performance improvement measures.

Chapter Three describes the standard experimental procedures adopted in this study for the synthesis and characterization of materials. In addition, detailed description of the catalytic performance rig fabricated during the course of this study is also included. This chapter also presents the mathematic principles underlying each analysis.

Chapter Four and **Five** are concerned with the study of catalysts for methanol synthesis. The former addresses the most favourable synthetic route for the catalytic preparation considering Cu-loading, calcination temperature and heating rate. Subsequently the physicochemical properties of the catalyst are examined with the range of characterization procedures listed above. Finally, the impact of these pre-determinants on the thermal stability and catalytic performance of the catalyst is evaluated. Chapter five is an additional section to the former and it studies the effect of promoters and sonochemistry on the enhancement of the catalyst performance.

Chapter Six, Seven and **Eight** are concerned with the second phase of this study, CO_2 adsorption. The adsorbent of interest, LDH was studied in detail with regards to impact of chemical content, preparation routes and operating conditions on the adsorption capacity of the adsorbent. Characterization was conducted using the characterization techniques listed above. Furthermore, the catalyst performance evaluation rig was modified into a pilot test rig to evaluate the uptake capacity effectiveness and efficiencies of the adsorbent. Finally, the adsorption kinetics and dynamics were also studied.

Chapter Nine covers the synthesis and characterisation of the composite catalyst composing of the catalyst and adsorbent. Based on the experimental and mathematical findings from the previous chapters, the performance of the composite catalyst was benchmarked against the individual performance of the catalyst and the adsorbent respectively.

Chapter Nine presents the overall conclusions, contribution of the research and relevant recommendations for further work.

Reference

[1] T. Sakakura, J.-C. Choi, H. Yasuda, Transformation of Carbon Dioxide, Chemical Reviews, 107 (2007) 2365-2387.

[2] R.P.A. Sneeden, Reactions of Carbon Dioxide, Pergamon Press, Oxford, 1982.

[3] J. Klemes, T. Cockerill, I. Bulatov, S. Shackley, C. Gough, Engineering Feasibility of Carbon Dioxide Capture and Storage, in: S. Shackley, C. Gough (Eds.) Carbon Capture

and its Storage. An Integrated Assessment, Ashgate Publishing Company, Hampshire, 2006, pp. 42 - 85.

[4] T.F. Wall, Combustion Processes for Carbon Capture, Proceedings of the Combustion Institute, 31 (2007) 1208-1214.

[5] P.H.M. Feron, C.A. Hendricks, CO2 Capture Process Principles and Costs, Oil & Gas Science and Technology, 60 (2005) 451-459.

[6] J. Gibbins, H. Chalmers, Carbon Capture and Storage, Energy Policy, 36 (2008) 4317-4322.

[7] C. Descamps, C. Bouallou, M. Kanniche, Efficiency of an Integrated Gasification Combined Cycle (IGCC) Power Plant Including CO2 Removal, Energy, 33 (2008) 874-881.

[8] R.M. Davidson, Post-Combustion Carbon Capture from Coal-fired Plants – Solvent Scrubbing, IEA GHG R&D Programme, 2007.

[9] G.T. Rochelle, Amine Scrubbing for CO2 Capture, Science, 325 (2009) 1652–1654.

[10] International Energy Agency (IEA), Cost and Performance of Carbon Dioxide Capture from Power Generation, IEA Publication, Paris, France, 2011.

[11] J. Davison, Performance and costs of power plants with capture and storage of CO2, Energy, 32 (2007) 1163-1176.

[12] H. Li, J. Yan, J. Yan, M. Anheden, Impurity impacts on the purification process in oxy-fuel combustion based CO2 capture and storage system, Applied Energy, 86 (2009) 202-213.

[13] R.M. Davidson, S.O. Santos, Oxyfuel Combustion of Pulverised Coal, IEA GHG R&D Programme, Paris, France, 2010.

[14] T. Wall, Y. Liu, C. Spero, L. Elliott, S. Khare, R. Rathnam, F. Zeenathal, B. Moghtaderi, B. Buhre, C. Sheng, R. Gupta, T. Yamada, K. Makino, J. Yu, An overview on oxyfuel coal combustion—State of the art research and technology development, Chemical Engineering Research and Design, 87 (2009) 1003-1016.

[15] G. Scheffknecht, L. Al-Makhadmeh, U. Schnell, J. Maier, Oxy-fuel coal combustion—A review of the current state-of-the-art, International Journal of Greenhouse Gas Control, 5 (2011) S16-S35.

[16] P.H.M. Feron, C.A. Hendriks, CO2 Capture Process Principles and Costs, Oil & Gas Science and Technology - Rev. IFP, 60 (2005) 451-459.

[17] C.E. Powell, G.G. Qiao, Polymeric CO2/N2 gas separation membranes for the capture of carbon dioxide from power plant flue gases, Journal of Membrane Science, 279 (2006) 1-49.

[18] International Energy Agency (IEA), Prospects for CO2 Capture and Storage, IEA publication, Paris, France, 2004.

[19] R. Bounaceur, C. Castel, S. Rode, D. Roizard, E. Favre, Membrane contactors for intensified post combustion carbon dioxide capture by gas–liquid absorption in MEA: A parametric study, Chemical Engineering Research and Design, 90 (2012) 2325-2337.

[20] R.J. Allam, C.G. Spilsbury, A study of the extraction of CO2 from the flue gas of a 500 MW pulverised coal fired boiler, Energy Conversion and Management, 33 (1992) 373-378.

[21] H. Leion, T. Mattisson, A. Lyngfelt, CO2 capture from Direct Combustion of Solid Fuels with Chemical-Looping Combustion, The 33rd International Technical Conference on Coal Utilization & Fuel Systems, Coal for the Future, Clearwater, Florida, 2008.

[22] C. Saha, S. Bhattacharya, Chemical looping combustion of low-ash and high-ash low rank coals using different metal oxides – A thermogravimetric analyser study, Fuel, 97 (2012) 137-150.

[23] J.D. Figueroa, T. Fout, S. Plasynski, H. McIlvried, R.D. Srivastava, Advances in CO2 capture technology—The U.S. Department of Energy's Carbon Sequestration Program, International Journal of Greenhouse Gas Control, 2 (2008) 9-20.

[24] L.I. Eide, M. Anheden, A. Lyngfelt, C. Abanades, M. Younes, D. Clodic, A.A. Bill, P.H.M. Feron, A. Rojey, F. Giroudière, Novel Capture Processes, Oil & Gas Science and Technology - Rev. IFP, 60 (2005) 497-508.

[25] Intergovernmental Panel on Climate Change (IPCC), Carbon Dioxide Capture and Storage, in: B. Metz, O. Davidson, H.C. DeConinck, M. Loos, L.A. Meyer (Eds.), Cambridge University Press, UK and New York, NY, USA 2005.

[26] A. Vatani, M. Mehrpooya, F. Gharagheizi, Prediction of Standard Enthalpy of Formation by a QSPR Model, International Journal of Molecular Sciences, 8 (2007) 407.

[27] M. Mikkelsen, M. Jørgensen, F.C. Krebs, The teraton challenge. A review of fixation and transformation of carbon dioxide, Energy & Environmental Science, 3 (2010) 43.

[28] H. Arakawa, Research and development on new synthetic routes for basic chemicals by catalytic hydrogenation of CO_2, in: M.A.K.I.S.Y. T. Inui, T. Yamaguchi (Eds.) Studies in Surface Science and Catalysis, Elsevier1998, pp. 19-30.

[29] X. An, J. Li, Y. Zuo, Q. Zhang, D. Wang, J. Wang, A Cu/Zn/Al/Zr Fibrous Catalyst that is an Improved CO2 Hydrogenation to Methanol Catalyst, Catalysis Letters, 118 (2007) 264-269.

[30] G.A. Olah, A. Goeppert, G.K.S. Prakash, Chemical Recycling of Carbon Dioxide to Methanol and Dimethyl Ether: From Greenhouse Gas to Renewable, Environmentally Carbon Neutral Fuels and Synthetic Hydrocarbons, The Journal of Organic Chemistry, 74 (2009) 487-498.

[31] X. Xiaoding, J.A. Moulijn, Mitigation of CO2 by Chemical Conversion: Plausible Chemical Reactions and Promising Products, Energy & Fuels, 10 (1996) 305-325.

[32] M. Aresta, A. Dibenedetto, Utilisation of CO2 as a chemical feedstock: opportunities and challenges, Dalton Transactions, DOI 10.1039/B700658F(2007) 2975-2992.

[33] J.C. Calabrese, T. Herskovitz, J.B. Kinney, Carbon dioxide coordination chemistry. 5. The preparation and structure of the rhodium complex Rh(.eta.1-CO2)(Cl)(diars)2, Journal of the American Chemical Society, 105 (1983) 5914-5915.

[34] T. Herskovitz, Carbon dioxide coordination chemistry. 3. Adducts of carbon dioxide with iridium(I) complexes, Journal of the American Chemical Society, 99 (1977) 2391-2392.

[35] M.G. Mason, J.A. Ibers, Reactivity of some transition-metal systems toward liquid carbon dioxide, Journal of the American Chemical Society, 104 (1982) 5153-5157.

[36] M. Sakamoto, I. Shimizu, A. Yamamoto, Synthesis of the first carbon dioxide coordinated palladium(0) complex, Pd(η2-CO2)(PMePh2)2, Organometallics, 13 (1994) 407-409.

[37] D.R. Senn, K. Emerson, R.D. Larsen, J.A. Gladysz, Synthesis, structure, and reactivity of transition metal/main group metal bridging carboxylate complexes of the formula (.eta.5-C5H5)Re(NO)(PPh3)(CO2MLn) (M = Li, K, Ge, Sn, Pb), Inorganic Chemistry, 26 (1987) 2737-2739.

[38] C.C. Tso, A.R. Cutler, Heterobimetallic .mu.(.eta.1-C:.eta.2-O,O') carbon dioxide and .mu.(.eta.1-C,O) formaldehyde complexes Cp(NO)(CO)Re[C(O)O]Zr(Cl)Cp2 and Cp(NO)(CO)Re[CH2O]Zr(Cl)Cp2, Journal of the American Chemical Society, 108 (1986) 6069-6071.

[39] I. Castro-Rodriguez, K. Meyer, Carbon Dioxide Reduction and Carbon Monoxide Activation Employing a Reactive Uranium(III) Complex, Journal of the American Chemical Society, 127 (2005) 11242-11243.

[40] S. Choi, J.H. Drese, C.W. Jones, Adsorbent materials for carbon dioxide capture from large anthropogenic point sources, ChemSusChem, 2 (2009) 796-854.

[41] C.-H. Yu, C.-H. Huang, C.-S. Tan, A Review of CO2 Capture by Absorption and Adsorption, Aerosol and Air Quality Research, 12 (2012) 745-769.

[42] T.C. Drage, C.E. Snape, L.A. Stevens, J. Wood, J. Wang, A.I. Cooper, R. Dawson, X. Guo, C. Satterley, R. Irons, Materials challenges for the development of solid sorbents for post-combustion carbon capture, Journal of Materials Chemistry, 22 (2012) 2815.

CHAPTER TWO

LITERATURE REVIEW

2.1 INTRODUCTION

Despite its numerous commercial uses, the amount of CO_2 produced annually is enormous. Without any corrective measures put in place, this will result to the breakdown of the environment via greenhouse gas attacks. To this effect, carbon capture is proposed; however, its storage risk is yet undefined [1]. Nonetheless, an integration of the carbon capture process and its industrial utilization will aid in producing a value added product rather than the capture and subsequent sequestration of the carbon. Value added products like methanol are commercially used in chemical synthesis and automobile fuels. This can be produced by the controlled hydrogenation of CO_2 with the aid of catalysts [2-5].

This chapter will be split into two parts. First, it will review literatures on carbon capture addressing the various means of attaining this. Emphasis will be directed towards adsorbents before being narrowed down to the specific adsorbent for this study, layered double hydroxides (LDH).

2.2 MATERIALS FOR CO_2 ADSORPTION

2.2.1 Introduction

Over the years, the separation of CO_2 from combustion product gases has been limited to four technologies. This includes adsorption and absorption. Other means include cryogenic distillation and membrane separation. The latter are challenged by the low concentration of CO_2 in the flue gases resulting to a low CO_2 partial pressure [6]. Consequently, this results to an inefficient separation of CO_2, hence requesting additional energy/cost input. On the other hand, absorption has been proposed to be the most researched and suitable technology for the removal of CO_2 [7]. Using suitable aqueous solutions, the CO_2 absorption capacity is highly efficient. However, it is posed with some operating limitations. This among all includes energy intensity desorption process, required large volume of absorbent and high corrosion capacity of operation units [7-9]. Some of these issues are addressed with the aid of solid adsorbents.

Adsorption, unlike absorption, is a surface phenomenon process where the adsorbate forms a film on the adsorbent surface either via chemisorption or physisorption interface. A good adsorbent must be thermodynamically stable, have high adsorption and desorption capacity and kinetics and possess a wide operating window. Based on the interaction mechanism, adsorption materials are divided into two: physisorbents and chemisorbents.

2.2.2 Physisorbents

As the name implies, these are sorbent materials that supports the sorption of fluids primarily due to their physical characteristics.

2.2.2.1 Zeolites

These are porous, hydrophilic and polar crystalline structured aluminosilicates. They are either synthetic or natural with molecular sieving ability which enables its usage in separation techniques [10]. The molecular sieving ability is induced as a result of the structural configuration of Al in the Si-based framework. In addition, this framework tends to support gas adsorption due to the presence of exchangeable cations located within the pore space of the framework. The cations are favoured adsorption sites and depending on their type, can alter the properties of the zeolite [11]. This has resulted in the study of the variable properties of zeolites especially with regards to adsorption. In its capacity, adsorption is by both physisorption and chemisorption. But this is primarily dominated by physisorption as a result of the electric field generated between the cation and the hydrogen bonds within the lattice [6, 12]. Another factor that affects zeolites adsorption capability is the porous nature of its framework. Despite the presence of the cations occupying the pore space, the volume and diameter of the pore plays a key role in the adsorption capability of the material [6, 13, 14]. Zeolites with higher the pore size demonstrated greater adsorption capacity. The impact of the operating conditions was also examined by various researchers using generated adsorption isotherms [10, 13, 15]. From the obtained results, it was concluded that at a given temperature, the adsorption capacity of zeolites increases with increase in pressure. This is unlike the trend experienced with increase in temperature at constant pressure. Cavenati, Grande and Rodrigues [15] showed that CO_2 adsorption by 13X zeolite at a given pressure reduces with increase in temperature from 293-323 K and can be defined using the Toth and Langmuir model. Moreover, the presence of moisture also limits the performance of the zeolite.

One other factor notable of affecting the adsorption capacity of zeolites is the moisture content of the flue gas. The presence of water in a flue gas is common and this tends to affect the selective adsorption of CO_2. However, depending on the concentration of CO_2, the presence of moisture can either improve or deter its adsorption. It is reported that Na-X zeolites attained adsorption equilibrium much faster in the presence of moisture [16]. The water molecules served as catalysts improving the chemisorption of CO_2 in the zeolite or facilitating hydrogen bonding to stabilize the carbonate species. Moreover, this was proposed to be the case for low concentration of CO_2, < 300 ppm. However, as CO_2 concentration increases beyond 1000 ppm, the zeolite adsorption capacity reduces in the presence of moisture [17]. This was explained by Brandani and Ruthven [18] to be due to the competition between the strongly adsorbed water molecule and the less strongly adsorbed CO_2 molecule on the adsorption sites. The interaction of the water molecule with the exchangeable cations reduces the electric field gradient. Consequently, this affects the adsorption of CO_2 on the active site.

One basic advantage of the zeolite material is its relative ease of regeneration. The adsorbed CO_2 can be desorbed either via pressure or temperature swing, regenerating the zeolite for another adsorption cycle [1]. While studying the adsorption-desorption cycle of CO_2 in natural zeolites, it was observed that despite the high regenerating capacity of the zeolite, some amount of CO_2 were isothermally irreversible [19]. This was attributed to chemisorption forming stable carboxylates or carbonates entrapping the CO_2. More also, this is further bolstered by the occurrence of hydrogen bonds provided by the presence of moisture [20]. Nonetheless, at elevated temperatures, the residual/total adsorbed CO_2 ratio was seen to be negligible [18]. This implies that for CO_2 to be completely recovered, desorption has to be conducted at relatively higher temperatures as shown by various researchers [19, 21]. This was supported by the study of Siriwardane, Shen and Fisher [14] in the effect of temperature on regeneration. To this regard, it was emphasised that a large amount of energy preferably via temperature swings is required to recover negligible amount of residual CO_2 in zeolites.

Based on its numerous merits, zeolites are being subjected to various modifications to correct its limitations in usage for CO_2 adsorption. In most cases, the modifications are based on altering the physisorption properties of the zeolite. This is achieved by substituting the exchangeable cations with other metal species to improve the strength of the electric field created by these cations, which supports physisorption [6]. Recent works done in this regard was the modification of zeolites with alkali metals and their respective study towards CO_2 adsorption. In this study, it is observed that the CO_2 adsorption capacity of the alkali metal-

modified NaX and NaY zeolites increased with decrease in ionic radii [10]. This trend was also observed down the group for alkali earth metals based on the infrared spectra of adsorbed CO_2 on the modified X zeolites. However, the alkali metals showed more potential than the alkali earth metals [12]. Other studies showed that the treatment of zeolites (Y in particular) with alkaline solutions (NaOH or $NaCO_3$) prevented the detrimental effect of moisture present in an adsorbed stream. In this experimental study, the adsorbent was pre-adsorbed with water prior being tested for adsorption. When compared with the untreated zeolites, the absorption capacity of the alkaline treated zeolites remained intact after a cycle of adsorption and desorption of the adsorbent [22].

2.3.2 Carbonaceous Materials

These are micro and meso-porous carbon based materials with good adsorption properties. Common among these materials is activated carbon. Activated carbon are good adsorbents owing to their surface functional group, modifiable pore structures and readily available at low costs. However, its adsorption is more preferable at lower temperatures, < 200 ^oC, but at temperature range of 50-120 ^oC, its adsorption capacity tends to reduce [23]. More also, adsorption in this adsorbent is weak and has low CO_2 selectivity; hence, recent researches are aimed to enhance the functionality of these adsorbents in this regard. This has resulted in altering the adsorbents physical properties like pore structure and surface area [24, 25], structural configuration [26-28] or surface functional modification [29-31]. In most cases as illustrated in the aforementioned literatures, the activated carbon is impregnated with various chemical precursors to improve its functionality. However, it is argued to impose diffusion challenges as a result of the pores being blocked by these additives; hence, reducing the adsorption capacity of the adsorbents [32]. Nonetheless, it has been observed that the doping of carbonaceous adsorbents with N-containing compounds like ammonia [32] or amines [9, 28] improved the adsorption capacity and in some cases, CO_2 selectivity. However, issues associated to cost of the adsorbent are yet to be addressed. In this regard, studies are being carried out to investigate the adsorption performance of other carbon sources like fly ash [30], almond shell [33] and recyclable materials like polyethylene terephthalate (PET) [31].

Activated carbon is mostly prepared through two steps: carbonization and activation. The first stage consist of initial heating and pyrolysis in an inert atmosphere, devolatilizing the raw material to produce char. The activation stage is the treatment of the generated chars, both

physically and chemically modifying it to improve porosity, surface area and adsorption active sites [34]. Chemical treatments include the use of $ZnCl_2$ or KOH for pore enhancement and restructuration [35], whereas physical treatments include partial gasification with steam, CO_2 and/or air at temperature range of 830-980 ^oC [36]. Based on its preparation, these set of adsorbents have a large variation of textural properties when compared to zeolites. However, at low temperature and pressure, zeolites are observed to be better adsorbents than activated carbon [37]. Nonetheless, both adsorbent share similar adsorption capacity trend with elevation in temperature. As temperature increases, CO_2 adsorption reduces drastically in both adsorbents as shown in Figure 2.1 below [38, 39].

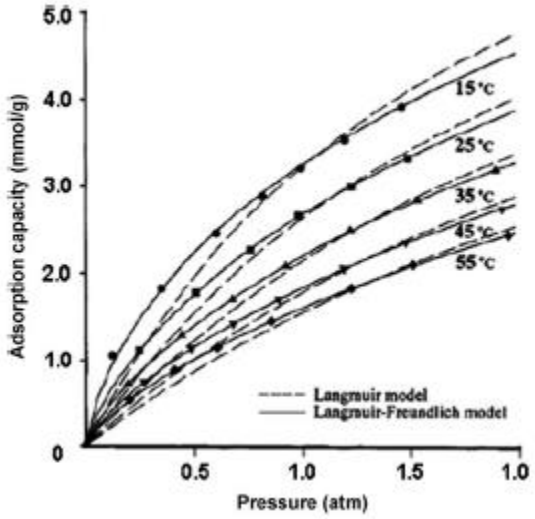

Figure 2.1: Variation of adsorption isotherm with temperature for activated carbon [38]

However, at high pressure, adsorption capacity of activated carbon was observed to be higher than zeolites. This performance comparative study was depicted in the works of Siriwardane, Shen, Fisher and Poston [20] with zeolites 13X and 4A and activated carbon G-32H at 25 ^oC and 300 psi. In this report, it was validated that zeolites are preferable adsorbents at lower pressure; however as the pressure increases beyond 25 psi, the reverse was obtained (see Figure 2.2). Given the Brunauer-Emmett-Teller (BET) surface area of both adsorbents, the high adsorption capacity of activated carbon was attributed to its high surface area of 879 m^2/g as against 506 m^2/g of the zeolite. The reverse trend at low pressure was explained by the low surface affinity of the activated carbon compared to that of the zeolite.

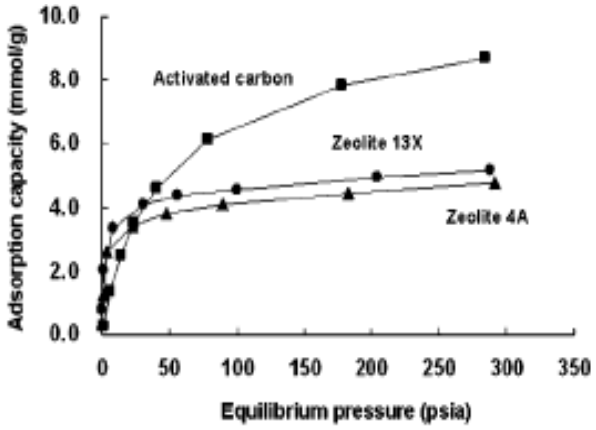

Figure 2.2: Variation of Adsorption Isotherm at High Pressure for Zeolites 13X & 4A and Activated Carbon [20]

Owing to its low surface affinity at low pressure, activated carbon can easily be regenerated than the zeolites. Its lower physical interaction with CO_2 renders it having a lower heat of adsorption; hence making the desorption process less energy demanding [37, 40]. Also, for this same reason, activated carbon adsorption performance is less affected by the presence of moisture when compared to zeolites [38]. This also works in its favour in the desorption process. Subjecting zeolites and activated carbon to series of adsorption-desorption cycles via pressure swing, Siriwardane and co-researchers showed that the generated isotherms for both desorption and adsorption were closely similar with no significant difference in trend profile for the activated carbon. Conversely, this was not the case for the zeolite materials where the desorption isotherm slightly deviated from the adsorption isotherm [20]. Similar to the adverse effect of water to the adsorption capacity of zeolite, CO_2 uptake in activated carbon is also affected by the presence of moisture. At low pressures, the adsorption capacity decreases with the presence of water. This was more pronounced in micro-porous carbon adsorbents than meso-porous ones. However, at high pressures, the amount of CO_2 adsorbed increases drastically when compared to the dry adsorbents (see Figure 2.3) [41].

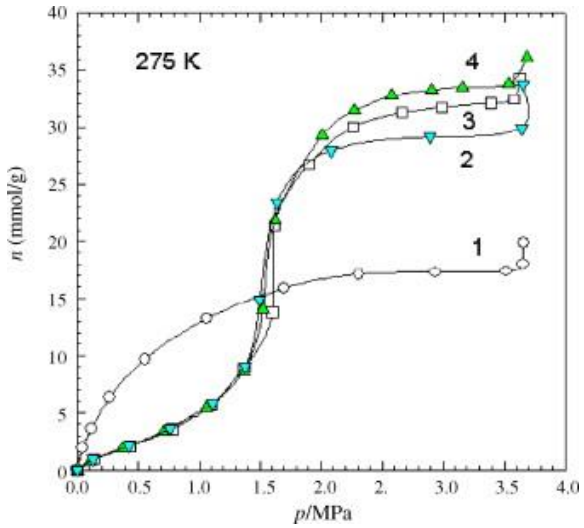

Figure 2.3: Variation of Adsorption Isotherms of CO2 in Coconut Shell-derived Activated Carbon at various Moisture/Dry Carbon Weight Ratios: (1) 0, (2) 1.74, (3) 1.32, (4) 1.65 [41]

Presently, with regards to its adsorption kinetics, it is argued that the adsorption mechanism of activated carbon can best be described by either the isothermal or non-isothermal model. On one hand, the isothermal model defines the bi-disperse pore structure of the carbon involving diffusional flow mechanisms [42]; while on the other hand, the non-isothermal model best suited the dynamics of the activated carbon in describing the simultaneous high rate of adsorption and its relative slow dissipation of head of adsorption. To this regard, it is argued that the isothemal model cannot define such behaviours [43, 44]. An extension to the adsorption kinetics study reveals that a supplementary transport flux occurred concurrently with the diffusional flow mechanism. More also, it was distinguished that the flow mechanism on the surface is slower than in the pores. Nonetheless, the surface flow mechanism accounted for about 50% of the total mass flux. This was attributed to the higher concentration of the adsorbate on the surface [45]. Considering all these factors, Gray and Do [46] proffered a single model that related all these factors with temperature. However, it was assumed that the adsorbent particles varied in temperature with adsorption and has a bi-disperse pore distribution. This proposed model supported the non-isothermal dynamics of Sircar [44], but it was noticeably argued that the model was isothermal given that the temperature range considered was less than 2 ^{o}C as considered by Andrieu and Smith [42]. In general, it is stated that activated carbon, unlike zeolites has a bi-disperse pore size distribution, but displays similar adsorption kinetics as zeolites.

2.3.3 Metal-Organic Frameworks (MOFs)

These are highly porous materials consisting of coordinated organic ligands and metal ions. Depending on the metal and ligands, the properties of the MOFs material can be varied. This includes the shape and size of the pores, structural configuration and chemical functionality [47]. These materials have shown great potential for CO_2 capture despite its weak interaction with CO_2 and poor performance at high temperatures. In the same trend, its CO_2 adsorption capacity is reduced at low pressure regimes (about atmospheric pressure) and presence of other gases. However, at high pressure, results have shown that its CO_2 capture capacity is quite high. A capturing capacity of 35 mmol/g and 40 mmol/g were reported at 3.5 MPa [48] and 5 MPa [49] respectively. Other desirable properties of MOFs are high corrosion resistance, high CO_2 selectivity and thermal stability among others [23]. In order to meet with these requirements, some modification studies have been carried out on various MOFs by either altering the metal ions, the ligands or a mix of both.

Depending on the metal ion, vacant coordination sites are made more available for adsorption active sites; thus, improving CO_2 capture. This improvement as reported in the study of Yang, Cho, Kim, Yang and Ahn [45] also included high CO_2 selectivity over a Mg-based MOF (Mg-MOF-74, see Figure 2.4) with no structural deterioration after ten adsorption-desorption cycles. Reported CO_2 uptake varied from 450 mg/g at 273 K to 350 mg/g at 293 K at a relative pressure (P/P_o) of 1. For further improvement, the metal nodes can be impregnated with amine groups to enhance adsorption [45, 50]. Arstad and co-researchers investigated the impact of uncoordinated amines impregnated in MOFs. In this study, it was reported that amine functionalized MOFs exhibited the highest CO_2 adsorption capacity when compared to MOFs without amine functionalities. The adsorption capacity however increased with increase in CO_2 pressure. At a temperature of 25 ^oC, CO_2 uptake increased from ~14% at 1 atm to ~60% at 25 atm. In addition, the adsorption capacity of this material depicted a linear relationship with its physical property (pore volume and surface area) [50]. Incorporating the amine functionality into the Mg-MOF-74 material, Yang, Cho, Kim, Yang and Ahn [45] showed that the binding of triethylamine (TEA) to the MOF resulted in the increase of the particle size from ~0.6 – 14 µm with the formation of mesopores. This was suggested to have contributed to the increased performance of the MOF by about 10 mg CO_2/g at same operating condition. It is also reported that the selectivity of CO_2 can be improved by the modification of the MOFs cavity with the introduction of highly polar -CF_3 ligands. This as a result, altered the surface area and pore sizes of the MOFs and was suggested to have made the pores more constricted and less likely

to adsorb N_2 at 77 K and 18 bar with an ~83% increase in CO_2/N_2 (Figure 2.5a) and ~33% increase in CO_2/CH_4 (Figure 2.5b) selectivities when compared to the uncoordinated MOF at low pressures. In addition, the difference in CH_4 and N_2 polarizability also contributed to the selective adsorption of CH_4 over N_2 after the strong adsorption of CO_2 in the highly-polar modified MOF [51].

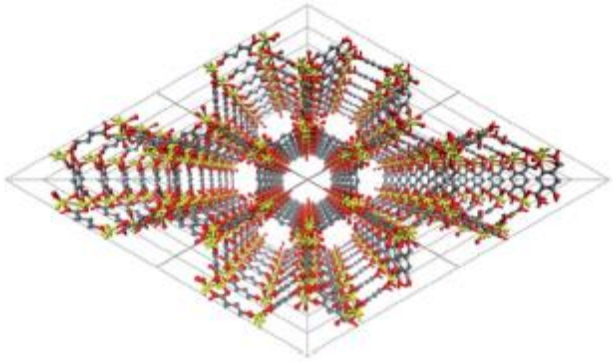

Figure 2.4: Crystal Structure of Mg-based MOF (Mg-MOF-74) [45]

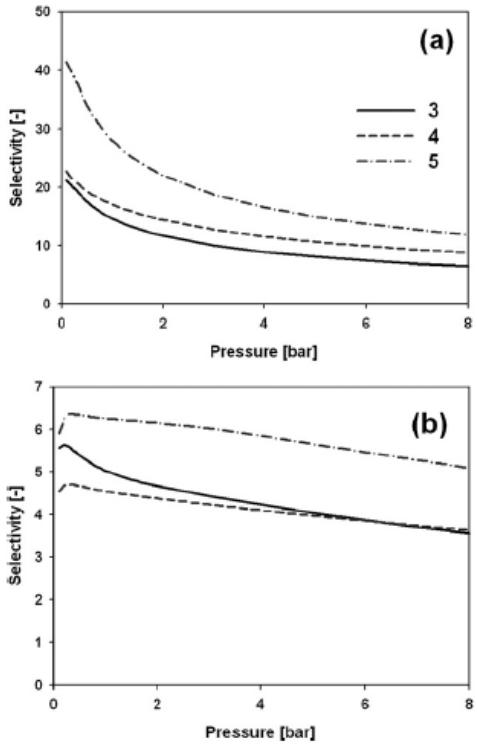

Figure 2.5: Selectivities of CO2 over (a) N2 and (b) CH4 in yCO2= 0.5 mixtures respectively (3 = Zn-DMF (dimethylformamide) coordinated MOF (4,4',4'',4'''-benzene-1,2,4,5-tetrayltetrabenzoic acid), 4 = uncoordinated MOF, 5 = highly polar –CF3 coordinated MOF) [51]

2.2.3 Chemisorbents

Unlike physisorbents, these type of sorbent materials depend on their surface chemical nature for the sorption of fluids. Owing to the acidic nature of CO_2, most chemical sorbents tend to have basic sites for easy interaction between CO_2 molecule and sorbent sites. Examples of these are metal-based adsorbents like alkali metal oxides (K_2O and Na_2O) and alkali earth metal oxides (CaO and MgO) [6], Lithium zirconates [52, 53] and hydrotalcite-like compounds [54] and its composite with physisorbents like graphene [55, 56]. All aforementioned sorbent materials perform optimally at given set of operation conditions. This is illustrated in Figure 2.6. From the figure, it is observed that the physisorbents operate optimally at low temperatures but have relative high adsorption capacity. However, the chemisorbents operate more at high temperatures. For the purpose of adsorption CO_2 from industrial effluent gases, sorbent materials with high sorption capacity at medium to high temperatures should be considered. This is logically defined given that the effluent gases are at temperatures beyond 300 ^oC. Based on this consideration, the adsorbent of wider operable temperature range was selected for this study. This is highlighted by the green area in Figure 2.6. However, the adsorption capacity of this sorbents are relatively low when compared to other chemisorbents. Hence, the following section will emphasis on an in-depth review of the hydrotalcite-like compounds also known as Layered double hydroxides.

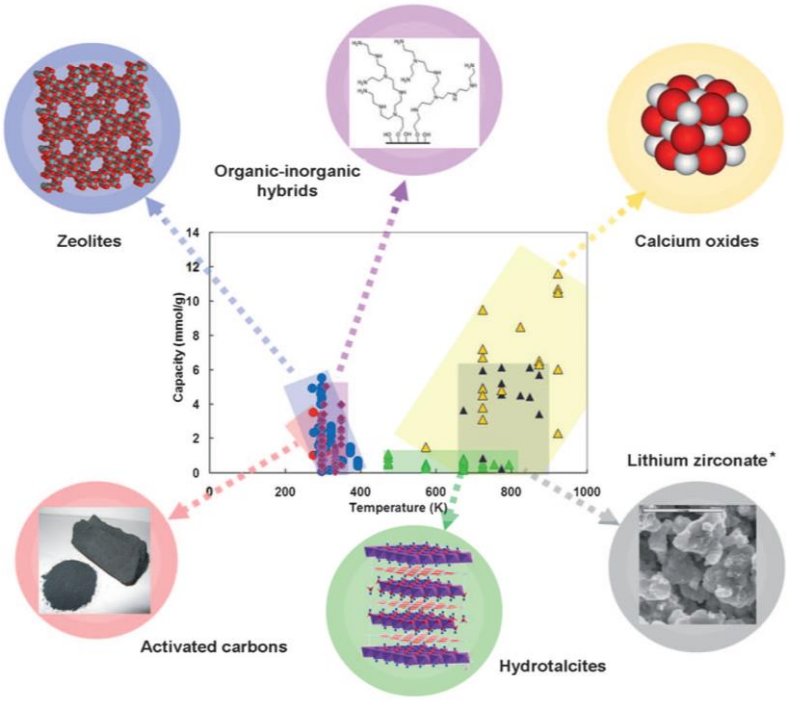

Figure 2.6: Optimal operating conditions of sorbent materials [52]

2.3 LAYERED DOUBLE HYDROXIDES

Layered double hydroxides (LDH) are anionic clay minerals also known as mixed-metal layered hydroxides or hydrotalcite-like compounds. They possess two dimensional structure of layers shaped by trivalent and divalent cations parted by water and anions molecules (see Figure 2.) with a general formula:

$$(M_{1-x}^{2+}M_x^{3+}(OH)_2)^{x+}\left(A_{x/m}^{m-}.nH_2O\right)^{x-}$$

where M^{2+} and M^{3+} are divalent and trivalent cations respectively, A^{m-} is a compensating anionic charge, x is the partial substitution of M^{2+} and M^{3+}, usually within a M^{2+}/M^{3+} ratio of 2 and 5 [57-59].

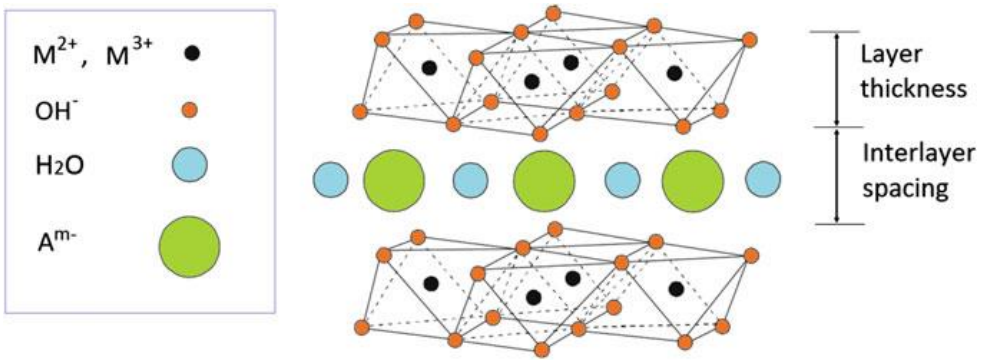

Figure 2.7: Structural configuration of layered double hydroxides [58]

This compound exists naturally as $Mg_6Al_2(OH)_{16}CO_3.4H_2O$ with Al^{3+} and Mg^{2+} being the trivalent and divalent metals respectively and CO_3^{2-} is the compensating anion. Varying the trivalent and divalent metals, a range of LDH are obtained [57, 58, 60]. These are basically synthesized by co-precipitation of the solution of the metal mix with that of the compensating anion. This must be prepared at a given pH value which regulates the adequate precipitation of the hydroxides [61]. Most LDH are usually prepared within a pH range of 8-10 [62]. The preparation method can be conducted at high or low supersaturation environments. In low supersaturation condition, the metal solutions are added concurrently to the solution containing the alkali; whereas the metal (at a given M^{2+}/M^{3+} ratio) mixture is added to the alkali and anion precursor solution for high supersaturation conditions. The former tends to produce more crystalline structures because of the increased rate of nucleation over crystallization [59]. The rate of nucleation is greater than the crystal growth rate [61]. Besides this method, other means of synthesizing LDH are sol-gel and urea techniques [63, 64]. Additionally, the thermal treatment of LDH aids in improving the intimate contacting of the metallic components. This

subsequently promotes the use of this compound as precursors for various catalysts for dehydrogenation and hydrogenation reactions [65].

2.3.1 Fundamental Properties

2.3.1.1 Chemical Stability

One of the key properties of LDH towards its industrial applicability is its chemical stability. Asides CO_2 adsorption, this characteristic is considered paramount for its usage in other applications. For instance, in the treatment of nuclear wastes, the stability of LDH is a major factor [66]. Similarly, in its application towards drug targeting and control, this property is as well considered to be key [67]. Various studies investigated the impact of the metal component of LDH on its chemical stability, it was seen that stability decreased in the following sequence: $Fe^{3+}>Al^{3+}>Zn^{2+}>Ni^{2+}\approx Co^{2+}>Mn^{2+}>Mg^{2+}$ [68-71]. It was also found that this trend corresponds to the solubility product of the hydroxides of these metals. Due to this, the metals are well dispersed and tend to produce a basic product [72]. Additionally, the impact of the intercalating anion was also investigated. It was discerned that these anions also affect the aqueous solubility of LDH [66]. In terms of solubility, nitrates and sulphates showed the highest solubility followed by carbonates and then silicates and borates.

2.3.1.2 Thermal Stability

As a catalyst, the thermal strength of this material is also important. However, most LDH displayed similar thermal decomposition despite the nature or composition of the anions or cations. At a temperature of about 250 ^oC, LDH releases interlayer water. This is followed by the dehydroxylation process with the loss of hydroxide layers. Subsequently, at higher temperatures, the decomposition of interlayer anions occur. This is suggested to occur between 250-450 ^oC for CO_3^{2-} and OH^- anions. This mostly occurs with two decomposition peaks. The first peak relates to the loss of interlayer OH^- group on Al^{3+} and the second peak is associated with the loss of OH^- group bound to Mg^{2+} together with the degradation of CO_3^{2-} [73]. Nonetheless, it is reported that the layer structure was unaffected with the loss of interlayer water using x-ray diffraction analysis. In terms of thermal stability, it was discerned that Mg-Cr$\approx$Mg-Al > Ni-Al$\approx$Mg-Fe > Cu-Al$\approx$Zn-Al >Co-Al. Mg-Al LDH showed the highest decomposition temperature of about 400 ^oC whereas Co-Al exhibited the least at a temperature of 220 ^oC [74].

It is worth noting that at a particular temperature, the formation of spinels occur. This is detrimental to the activity of the material. This was investigated to vary with the type of metallic ions [73, 75-77]. LDH with tetravalent metal ions generated metal ions which were evenly dispersed during calcination [78]. Comparing to Mg-based LDH, Ni-based LDH were observed to be less thermally stable [79]. This is followed by Zn-based LDH and then Co-based LDH [80].

2.3.2 Layered Double Hydroxides with Specific Morphology

Presently, increasing attempt has been made to improve the morphologies of LDH, which as a result could increase the performance of the adsorbent [81]. The use of additives or mixed solvents like biopolymers has influenced the morphology of LDH during co-precipitation process [82]. Another examples was the use of nickel glycinate complex as an additive to improve Ni-Al LDH nanoparticles [83]. Due to the flexible morphology of LDH, the material can be deposited on various supports to obtain nano-structured particles. In some cases, these supports act as templates for the formation of porous LDH particles.

2.3.3 Calcination/Thermal Reconstruction of LDH

LDH is commonly categorised to be limited in activity at temperatures or most catalytic reactions. This has been attributed to the low basic strength of the compound [84]. The presence of adsorbed water is reported to be the cause of this phenomenon. The adsorbed water molecule on the basic sites restricts access of the reacting gas to these sites. Hence, hindering reactions on the surface and interlayer region [65]. As a result of this, the need of thermal treatment is required. This is mostly done in N_2 or air atmosphere at temperatures ranging from 673-823 K depending on the nature of the LDH. The desired temperature is based and should not exceed the decomposition temperature of the LDH. This is then held isothermally for at least 4 hours [41, 85-87]. As a result of this treatment, the morphology of the compound is altered resulting to a higher surface area. This is facilitated from the formation of significant porosity with the transformation of LDH to layered double oxides (LDO) [88]. Despite this benefits, the process is challenged by some limitations. One disadvantage of this treatment technique is the formation of spinels, cubic crystal systems of $MgAl_2O_4$. This spinel phase relatively affects the adsorption/reactive capacity of the compound. Therefore, an adequate calcination temperature should be selected for optimum balance between the morphology and surface basic sites. This

has been recommended to be 673 K for maximum CO_2 uptake beyond 473 K. additionally, in the presence of H_2O, LDO is hydrolysed to meixnerite, $MgAl_2(OH)_{18}.4H_2O$, a hydrated LDH as shown in Reaction Scheme 2.1.

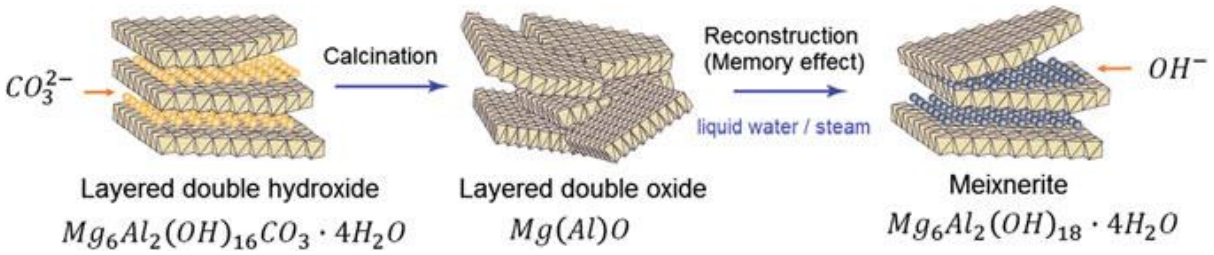

Reaction Scheme 2.1: Reconstruction of thermally activated LDH [89]

Owing to the mild basic strength of this compound, it is commonly used as a catalyst for self- and aldol-condensation reactions [89-92]. Furthermore, series of studies have examined the structural modifications associated with calcination of these compounds [87, 88, 93-95]. It is reported that below 473 K, no significant modification was observed. However, partial dehydration and structural changes occurred at this temperature with the migration of Al^{3+} cations from the octahedral layer to the tetrahedral interlayer sites. This led to the reduction in interlayer spacing and was observed to increase with temperature [95]. Beyond this temperature and less than 623 K, dehydroxylation on Al^{3+} metal occurs leading to the destruction of the layered structure. Further than 623 K, structural modification is associated with loss of CO_2 and CO_3^{2-}. This culminates to the formation of spinels resulting from the migration of Al^{3+} to MgO.

2.3.4 Factors Affecting LDH Basicity

LDH are well known to behave as basic solids and depending of the synthetic method, these basic strengths can be varied. This is attributed to the layered structure produced by the mix of cations, which are isolated by molecules of the intercalating anions and water. Based on the nature of the intercalating anions and moisture content, LDH exists as weak Bronsted basics. But with calcination, the moisture compensating ions are lost resulting to high Lewis basics [84]. This is validated by reported findings that basicity of LDH increases with calcination temperature. However, this is capped at 923 K due to spinel formation and phase segregation [65]. Aside temperature, the nature of the trivalent and divalent cations also affect the basic strength of the compound. This is related to the ratio of cationic charge to radius. A low ratio produces high negative charge densities which is situated on the coordinated O^{2-}. This acts as

a strong basic site. Acting alone, the individual metal oxides have varying basic strengths. However, the synergetic improvement in basic strength when these oxides are mixed can be partially described by the crystallite size reduction [89].

Applying this adsorbent to CO_2 adsorption, it is observed that CO_2 weakly bonds with surface OH^- group to produce HCO_3^- ions. This is related to the acidity of CO_2 to be high enough to coordinate weakly with weak basic sites. At intermediate basic sites, CO_2 is found to bond with metal oxides forming bidentate carbonates, whereas the formation of monodentate CO_3^{2-} is synthesised on defective surface with low O^{2-} coordination (see Figure 2.8) [65, 96]. Hence, to improve the strength of the basic sites, methods that promotes the formation of monodentate and bidentate CO_3^{2-} is encouraged. An example of this is the introduction or doping with alkali metals especially monovalent alkali metals [65]

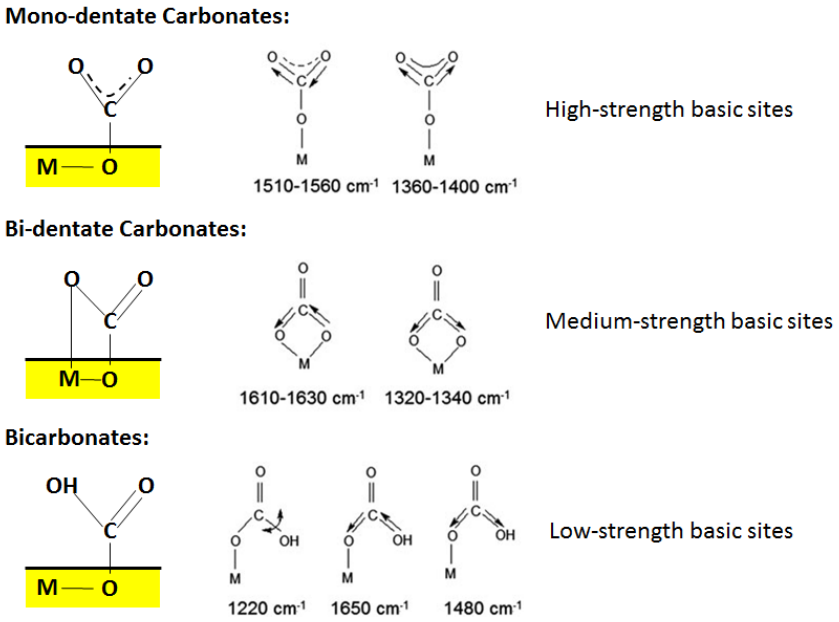

Figure 2.8: *Infrared bands of adsorbed CO_2 on LDH surface [97]*

2.3.5 Means of Improving LDH Adsorption Capacity

A good adsorbent must have fast adsorption kinetics and ease of regeneration. Within the same temperature range, LDH is most effective for CO_2 adsorptions when compared to other adsorbents. This is due to its outstanding adsorption kinetics. However, their stability and adsorption capacity need to be improved. In this regard, different means has been established.

This includes substitution of various metal frameworks metal, use of promoters and supported framework for the LDH.

2.3.5.1 Use of Support Framework

The use of supports with high surface area has been investigated to boost the adsorption capacity of LDH. This will promote high dispersion of more stable and defective LDH crystals. Owing to this, there is an enhanced accessibility of CO_2 to the adsorption sites. CO_2 adsorption is highly promoted with the presence of basic sites, most especially strong basic sites. Moreover, these sites are dependent on the size characteristics of the LDH adsorbent. The strong basic sites are mostly situated at the corners of the crystallites. Hence, to effectively adsorb CO_2 at these corners, the crystallite size must be optimized and properly dispersed. Additionally, it is recommended that the adequate support must not promote sintering during the adsorption process.

The adsorption capacity of LDH was observed to double the adoption of zeolite as the support within 303-573 K [64]. However, it was unable to ascertain the contributive impact of the supports on CO_2 adsorption of the LDH since the support is equally a good adsorbent of CO_2. Other investigated supports include carbon nanofibers [96], boehmite alumina [98], and graphite [84]. In all cases the use of support proves to improve the intrinsic sorption capacity of LDH. However, this strategy is faced with some challenges. One of which is the relative reduction of CO_2 uptake with respect to the total weight of the adsorbent, which includes the weight of both LDH and support. It is explained that for high CO_2 uptake, LDH must be highly dispersed. In order to achieve this, high amount of the support is required. Consequently, this increases the total volume of the adsorbent. Cost evaluation of this can be assumed to affect the industrial applicability of this strategy. In conclusion, an adequate support will be one to boost CO_2 uptake capacity of the LDH while optimizing the stability at low support loading.

2.3.5.2 Use of Promoters

Doping LDH with alkaline promoters is a common means of improving CO_2 uptake capacity. Most common alkali ions used are Cs^+, Na^+ and K^+. These ions increase the amount and strength of basic sites, proportionately increasing CO_2 uptake. The doping of these metals is mostly achieved by conventional impregnation and co-precipitation [85, 99, 100]. Most commonly used promoter is potassium and has been reported to also improve sorption-assisted reactions alongside CO_2 uptake improvement [100-107]. However, this is dependent on the K^+ species introduced into the LDH [104]. A combination of K^+ and Cs^+ dopants has also shown

to improve CO_2 uptake capacity [105]. In this work, it was found that the surface area of the resultant LDH reduced when compared to the non-promoted LDH. Hence, the increase in CO_2 uptake was attributed to the additional interactions supported by the presence of the alkali cations. With special consideration to Mg-Al LDH, it was discovered that the presence of K^+ interacted with Al^{3+} generating reversible basic sites. These basic sites adsorbed CO_2 at 673 K [106].

2.3.5.3 Substitution of Metal Framework

One of the adopted method for improving the performance of LDH is the substitution of the structural ions. Varying the cations of the LDH, it was observed that CO_2 uptake was also varied [108]. Similarly, a variation in the compensating anions also resulted to difference in CO_2 adsorption. The amount of CO_2 adsorbed doubled when CO_3^{2-} was compared to OH^- [93]. It was also reported that anions with close proximity to the natural formula of mineral hydrotalcites exhibited high adsorption capacity and fast kinetics [58]. In general, it was stipulated that a change in any of the divalent, trivalent cations or compensating anions will affect the structure of the LDH especially during thermal treatment, subsequently, affecting the CO_2 uptake

2.3.5.4 Microwave, Ultrasound, and Hydrothermal Treatments

Another means of improving the adsorption capacity of LDH is by the modification of the synthetic method or the post-synthesis treatment. This is achieved by varying the structural and textural properties [6]. One of the notable synthetic method for controlling the texture and structure of LDH is the microwave method [109, 110]. In this method, it was reported that the surface area and porosity of the material increased with longer microwave exposure. Another experimented means of improving the structure of the material is via sonochemical method [54]. In this case, the crystallinity of the material was reported to vary with sonic irradiation. The higher the ultrasonic intensity, the larger the particle size [111]. Additionally, crystallinity and crystallite size was also observed to vary under hydrothermal reactions by tuning the temperature, pressure, residence time and even the hydrothermal ageing process [112-115]. A combination of these processes were also reported to affect the structural properties of the material [115, 116].

2.4 METHANOL SYNTHESIS

Methanol is a widely used chemical especially as a primary reactant for the synthesis of other hydrocarbons. Conventionally, its production is from synthesis gas and CO_2. However, recent development shows that it can also be synthesised from the hydrogenation of CO_2 [2] as shown in Reaction Scheme 2.2. However, the yield of methanol production is lower when compared to that via syngas production [117].

$$CO_2 + 3H_2 \rightarrow CH_3OH + H_2O, \Delta H_{298\,K} = -49.5\ KJmol^{-1}$$

Reaction Scheme 2.2: Methanol synthesis from hydrogenation of CO_2

As shown in the reaction above, methanol production, designated by the forward reaction, can be favoured by the decrease and/or increase in reaction temperature and/or pressure respectively. Despite this, the formation of other hydrocarbons is also likely. Consequently, the need for a controlled reaction is indispensable. This is facilitated with the use of selected promoters and catalysts with suitable thermal stability. Studies are being carried out to this effect to best describe the most effective catalysts [3, 5, 117-122].

2.4.1 Catalysts

Commonly used catalysts for CO_2 hydrogenation to methanol are the same adopted in methanol formation from synthesis gas. These are Cu-based catalysts and have aided various investigations in developing novel catalysts for CO_2 hydrogenation process [3, 5, 118, 123, 124]. Cu is treated with several modifiers, which help to facilitate the formation and stabilization of the catalyst. Yoshihara and co-authors demonstrated the stabilization of Cu-based catalysts by impregnating it with ZnO [125]. The stability was attributed to the dispersion of Cu catalyst due to the free electron pair oxygen lattice present in the modifier. This theory was buttressed using a proposed dynamic micro-kinetic model to kinetically study the morphological changes and its effect on a Cu-ZnO catalyst during CO_2 hydrogenation [126]. Aside supporting the purported theory, the study also posited that the interfacial presence of vacant oxygen lattice was affected by the morphological change in the catalyst. This was considered to be one of the reasons for the poor dispersion of Cu in methanol formation using wet Pd impregnation. In this case, the catalyst preparation resulted in the crystalline lattice restructuring which in turn had an effect on the catalyst performance [127, 128].

Among other studied promoters and stabilizers is Si/Ga-doped Cu-catalysts. The hydrophobic silica acted as a stabilizer at high temperature while the Ga helped in promoting the catalyst by improving Cu dispersion. This is ascribed to the formation of Cu^{+} intermediates favoured by the size distribution of the promoter. As a result, stabilizing the catalyst while also attaining a high methanol selectivity [119]. Moreover, it is also discerned that hydrogen spill over on the surface active site bolstered the hydrogenation process. This was investigated by the introduction of noble metal like palladium. This metal reduced the active site of the Cu catalyst resulting to the spill over of hydrogen to the support; hence, resulting to increased hydrogen consumption and higher yield of methanol production [127, 128]. In conclusion, it is posited that the reduction of the catalysts active site favoured the hydrogenation process.

Another promoter commonly studied for methanol synthesis via CO_2 hydrogenation is zirconium. The element in the form of ZrO_2 also improves the catalytic activity and methanol selectivity [129]. This was also explained by the enhanced dispersion of Cu supported by the adsorbed hydrogen spill-over mechanism as shown in Figure 2.9. However, the rate of water adsorption was reduced in the presence of other elements like aluminium and gallium. Comparing Cu with other elements like Ag and Au using the ZrO_2 promoter, an improved methanol selectivity was observed according to the following series Au > Ag > Cu with the metallic dispersion following the trend Cu ≅ Au > Ag. This was related to the nature and content of the metal [130].

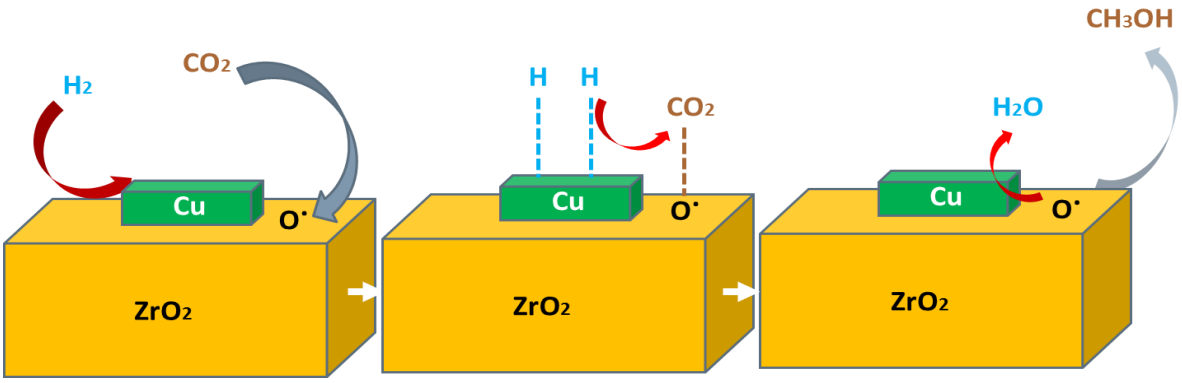

Figure 2.9: Hydrogen spill-over mechanism in CO_2 hydrogenation for methanol synthesis using Cu/ZrO_2 catalyst

Another notable catalyst aside Cu-based catalyst is the Pd catalyst. This catalyst has high catalytic and methanol selectivity. When doped with Ga in the form of Ga_2O_3, new active sites for methanol formation are generated [131]. The reaction dynamics is also defined by the

hydrogen spill-over mechanism as shown in Figure 2.9. On the active site, the hydrogen molecule is dissociated on the catalyst, subsequently spilling over to the Ga-based support to react with CO_2 attached to the vacant oxygen lattice. This reaction produces intermediates, formate species, which results to methanol formation on further hydrogenation [132].

2.4.2 Theoretical Studies

Within the past century, CO_2 hydrogenation process dynamics and kinetics have been difficult to comprehend given the undefined reaction mechanism, especially the activation of CO_2 over the surface sites of the catalyst and its relationship with the Cu nature of the of the catalyst [133]. Regarding this, Borodko and Somorjai suggested that CO_2 activation occurred at the copper-oxide interface [134]. As proposed by the hydrogen spill-over theory, the adsorbed CO_2 on the vacant lattice of the oxide is reduced by the supply of Cu-dissociated hydrogen [132, 135]. However, the nature of the Cu species is yet to be defined, which is key factor for catalyst activity. Through the use of XRD, Cu was observed to exist as a metal in Cu/ZrO_2 catalyst [136]; but with the $Cu/ZnO/SiO_2$, Cu primarily existed as Cu^+ while using the static ion scattering analyser [137]. While the Cu phase nature changes with various supports and promoters, the spatial and electronic configuration definition of the active sites in methanol synthesis via hydrogenation of CO_2 will aid in defining the best suitable catalyst in terms of selectivity and activity [138].

The hydrogenation of CO_2 to produce methanol has been proposed to occur in either two reaction pathways: Reverse Water Gas Shift (RWGS) [139] or formate [140] mechanism. These mechanisms involve the formation of formate functional group, HCOO- and CO intermediates respectively which are hydrogenated to produce methanol. In the formate mechanism, the intermediates formed on the catalyst and support surfaces are bi-dentates and mono-dentates respectively, with the bi-dentate being the most stable [141]. However, both mechanisms transpires with the emission of CO as by-product, supporting the results of Inui and Takeguchi [142] and Nitta et al. [143]. In the RWGS reaction route, CO results as a by-product of the synthesis reaction, while in formate mechanism, it results from the decomposition of methanol.

Using an in-situ FITR spectroscopy, the formate mechanism was investigated on a $Pd/\beta\text{-}Ga_2O_3$ catalyst [132]. In this study, formates are formed on the metal oxide from the absorption of CO_2 on the vacant oxygen lattice. This is further reduced to dioxomethylene by the spilled-

over palladium-dissociated hydrogen. Subsequent hydrogenation results in the formation of methoxy functional group prior the formation and discharge of methanol and water molecules. The spill-over mechanism is a key determinant for the reaction efficiency.

This mechanism was supported by the study of methanol synthesis on Cu (111) and Cu nanoparticles using density functional theory calculation (DFT) by Yang et al. [144]. Despite the higher catalytic activity of the nanoparticles over the Cu (111) active surfaces as a result of its fluxionality and configuration, methanol synthesis proceeds via the formate mechanism; and its rate of reaction is limited by the hydrogenation of formate and dioxomethylene process. However, the RWGS reaction route was also observed in this investigation, but it was estimated to occur at a faster magnitude than the former owing to the presence of unstable formyl intermediates which continuously dissociates to CO and H atom on Cu catalyst. Negating the essence of the RWGS reaction mechanism on methanol synthesis, it was proposed that this mechanism could be favoured by the addition of promoters or dopants for formyl species stabilization. Nonetheless, RWGS mechanism was claimed to be the predominant reaction route in the formation of methanol in the study of Liu et al. [133]. In this review, CO_2 is reduced to CO, which is further reduced by hydrogenation to form HCO radical intermediates before forming methanol. The radical formation reaction was identified to be the rate determining reaction. This observation was also validated using the DFT calculations.

In other findings, it was detected that both mechanisms contributed in the hydrogenation mechanism on a Cu/ZrO_2 catalyst. However, the catalytic activity and selectivity was dependent on the atomic oxygen bond-strength. As a result, to vary the activity and selectivity, the oxygen affinity on the active site can be manipulated. Regarding this, another parameter was identified as a key factor for improving catalytic performance. In the work of Chan and Radom [145], while studying the three stage hydrogenation of CO_2 using a catalysed zeolite, the authors stipulated that the hydrogenation process is base sensitive. It was shown that the catalytic activity of the zeolites increases as the zeolite becomes more basic. In other words, for an improved catalytic activity, the pH of the adjacent group of the catalyst should be tuned up.

2.4.3 Reactor Design and Optimization

Considerable studies have been made to analyse methanol selectivity and yield in various reactors. Unlike the conventional fixed bed tubular reactors, a two stage catalyst bed has been

proposed for methanol synthesis via CO_2 conversion. This is due to the enhanced catalyst life and activity [146]. Among investigated reactors is also the membrane reactor. This was suggested to improve reactions restrained by kinetics, overcome thermodynamic limitations and better regulate stoichiometric feed [147]. Due to the results obtainable from an equilibrium reaction, more research has been channelled towards the use of membrane reactors in methanol synthesis. From studies, it is shown that under the same experimental operation, a kinetic model analysis shows that a membrane reactors exhibit more CO_2 conversion than the conventional reactor [148]. However, its usage has a major setback as the membrane reactor cannot withstand high temperatures necessary for most catalytic activity.

Apart from the palladium-silver membrane reactor studied, other studied membranes include zeolite [149] and ceramic zeolite [150]. In all cases, a higher CO_2 conversion was attained. In the case of zeolite membrane reactors, high yield of methanol was achievable at low pressure and high temperature. However, the later limited the functionality of the membranes. At given operating conditions, the methanol-water permeate ratio also directly affected the yield and selectivity of methanol. Consolidating the performance of the membrane reactors over the conventional reactors, the composite membrane reactors exhibited an increased CO_2 conversion to the degree of 22%. This was attributed to the membrane permeation rate which facilitated reaction.

In addition to the membrane reactors with regards to its advantage of overcoming thermodynamic limitations, a semi-batch autoclave reactor was also suggested for the synthesis of methanol [151]. In this study, the production of methanol via a Cu catalyst was conducted through a novel low-temperature mechanism. The mechanism at a low temperature of 170^{o}C attained approx. 73% selectivity of methanol and approx. 26% conversion of CO_2 at a pressure of 5 MPa. Other low temperature methanol production mechanism was studied in a liquid media. Here, despite the increased efficiency of heat transfer resulting to lower operating costs, the process experiences a high CO_2 conversion [152]. This was explained by the effect of the calcination process on the structure of CuO in the catalyst, which subsequently affects the catalyst's activity in a liquid media. In the same liquid phase, copper-boride catalyst doped with Chromium, Zirconium and Thorium was seen to enhance methanol formation by increased stability and dispersion of the catalyst [123].

2.5 CONCLUDING REMARKS

With the exponential population growing rate, it is envisaged that the amount of the CO_2 emission will surge relative to the growth in population if no mitigating measures are adopted. As the demand for energy increases, there will also be a commensurate increase in the amount of CO_2 produced without any corrective measures put in place. As a result, the global community will be challenged with an environmental breakdown via greenhouse gas attack. Despite the increase in research for other energy sources like renewable energies, they are primarily being challenged with integrating them into the energy mix. Pending when these and other energy sources contribute a large share in the energy grid, carbon capture and storage is still suggested to be the most prominent CO_2 mitigation alternative. However, its storage risk is yet undefined. Hence, it is proposed that rather sequestering this gas underground, their subsequent utilization for industrial application was suggested.

Among one of these application is the conversion of the captured CO_2 into value added products like methanol, ethanol, formaldehydes and other valuable hydrocarbons. Value added products like methanol is the foundation block for other hydrocarbons. They are commercially used in chemical synthesis and automobile fuels. This can be produced by the controlled hydrogenation of CO_2 with the aid of suitable catalysts. Thus far, different catalysts have been studied for the synthesis of methanol from the reduction of CO_2 via hydrogenation. These research studies have based their research strongly on the catalytic performance of the catalysts without further effort on the adsorption capacity. Improving the adsorption capacity alongside with other parameters affecting catalytic performance will improve the accessibility of CO_2 to the catalyst active site for subsequent conversion to methanol. Hence, a sorption-enhanced catalyst is proposed in this study.

Among the different means of enhancing the sorption capacity of the catalyst is by using a support framework, one with high CO_2 uptake capacity. The catalysts will be dispersed on the surface of the support forming a novel composite material with both good sorption and catalytic performance. The aim of the present work hence is to develop and assess a stable, both chemical and thermal, sorption-enhanced catalyst with an adequate sorption and catalytic activity. This will involve the modification of both physical and chemical properties of the materials. To achieve this, the study is split into two sections consisting of the individual development of suitable catalysts and adsorbents with good physicochemical properties to support and optimise their individual purpose. Within the limited time frame, various preparation methods together

with the use of promoters were texted. In addition, favourable synthetic conditions were also investigated. Finally, in some relevant samples, thermodynamic and kinetic studies suitable for the description of the process were studied.

Reference

[1] S.D. Kenarsari, D. Yang, G. Jiang, S. Zhang, J. Wang, A.G. Russell, Q. Wei, M. Fan, Review of recent advances in carbon dioxide separation and capture, RSC Advances, 3 (2013) 22739.

[2] M. Mikkelsen, M. Jørgensen, F.C. Krebs, The teraton challenge. A review of fixation and transformation of carbon dioxide, Energy & Environmental Science, 3 (2010) 43.

[3] A. Baiker, Utilization of carbon dioxide in heterogeneous catalytic synthesis., Applied Organometallic Chemistry, 14 (2000) 751-762.

[4] I. Omae, Aspects of carbon dioxide utilization, Catalysis Today, 115 (2006) 33-52.

[5] W. Wang, S. Wang, X. Ma, J. Gong, Recent advances in catalytic hydrogenation of carbon dioxide, Chemical Society reviews, 40 (2011) 3703-3727.

[6] S. Choi, J.H. Drese, C.W. Jones, Adsorbent materials for carbon dioxide capture from large anthropogenic point sources, ChemSusChem, 2 (2009) 796-854.

[7] C.-H. Yu, C.-H. Huang, C.-S. Tan, A Review of CO2 Capture by Absorption and Adsorption, Aerosol and Air Quality Research, 12 (2012) 745-769.

[8] G.T. Rochelle, Amine Scrubbing for CO2 Capture, Science, 325 (2009) 1652–1654.

[9] T.C. Drage, C.E. Snape, L.A. Stevens, J. Wood, J. Wang, A.I. Cooper, R. Dawson, X. Guo, C. Satterley, R. Irons, Materials challenges for the development of solid sorbents for post-combustion carbon capture, Journal of Materials Chemistry, 22 (2012) 2815.

[10] K.S. Walton, M.B. Abney, M. Douglas LeVan, CO2 adsorption in Y and X zeolites modified by alkali metal cation exchange, Microporous and Mesoporous Materials, 91 (2006) 78-84.

[11] O. Talu, S.Y. Zhang, D.T. Hayhurst, Effect of Cations on Methane Adsorption by NaY, MgY, CaY, SrY, and BaY Zeolites, Journal of Physical Chemistry, 97 (1993) 12894-12898.

[12] J.W. Ward, H.W. Habgood, The Infrared Spectra of Carbon Dioxide Adsorbed on Zeolite X, Journal of Physical Chemistry, 70 (1966) 1178-1182.

[13] R.V. Siriwardane, M.-S. Shen, E.P. Fisher, Adsorption of CO2, N2, and O2 on Natural Zeolites, Energy & Fuels, 17 (2003) 571-576.

[14] R.V. Siriwardane, M.-S. Shen, E.P. Fisher, Adsorption of CO_2 on Zeolites at Moderate Temperatures, Energy & Fuels, 19 (2005) 1153-1159.

[15] S. Cavenati, C.A. Grande, A.E. Rodrigues, Adsorption Equilibrium of Methane, Carbon Dioxide, and Nitrogen on Zeolite 13X at High Pressures, Journal of Chemical & Engineering Data, 49 (2004) 1095-1101.

[16] L. Bertsch, H.W. Habgood, AN INFRARED SPECTROSCOPIC STUDY OF THE ADSORPTION OF WATER AND CARBON DIOXIDE BY LINDE MOLECULAR SIEVE X1, The Journal of Physical Chemistry, 67 (1963) 1621-1628.

[17] S.U. Rege, R.T. Yang, A novel FTIR method for studying mixed gas adsorption at low concentrations: H2O and CO2 on NaX zeolite and γ-alumina, Chemical Engineering Science, 56 (2001) 3781-3796.

[18] F. Brandani, D.M. Ruthven, The Effect of Water on the Adsorption of CO2 and C3H8 on Type X Zeolites, Industrial & Engineering Chemistry Research, 43 (2004) 8339-8344.

[19] R. Hernández-Huesca, L. Díaz, G. Aguilar-Armenta, Adsorption equilibria and kinetics of CO2, CH4 and N2 in natural zeolites, Separation and Purification Technology, 15 (1999) 163-173.

[20] R.V. Siriwardane, M.-S. Shen, E.P. Fisher, J.A. Poston, Adsorption of CO_2 on Molecular Sieves and Activated Carbon, Energy & Fuels, 15 (2001) 279-284.

[21] P.J.E. Harlick, F.H. Tezel, An experimental adsorbent screening study for CO2 removal from N2, Microporous and Mesoporous Materials, 76 (2004) 71-79.

[22] E. Díaz, E. Muñoz, A. Vega, S. Ordóñez, Enhancement of the CO2 Retention Capacity of Y Zeolites by Na and Cs Treatments: Effect of Adsorption Temperature and Water Treatment, Industrial & Engineering Chemistry Research, 47 (2008) 412-418.

[23] Q. Wang, J. Luo, Z. Zhong, A. Borgna, CO2 Capture by Solid Adsorbents and their Applications: Current Status and New Trends, Energy & Environmental Science, 4 (2011) 42.

[24] V.Y. Yakovlev, A.A. Fomkin, A.V. Tvardovski, Adsorption and deformation phenomena at the interaction of CO2 and a microporous carbon adsorbent, Journal of colloid and interface science, 268 (2003) 33-36.

[25] D. Saha, S. Deng, Adsorption equilibrium and kinetics of CO2, CH4, N2O, and NH3 on ordered mesoporous carbon, Journal of colloid and interface science, 345 (2010) 402-409.

[26] M. Cinke, J. Li, C.W. Bauschlicher, A. Ricca, M. Meyyappan, CO2 adsorption in single-walled carbon nanotubes, Chemical Physics Letters, 376 (2003) 761-766.

[27] C. Lu, H. Bai, B. Wu, F. Su, J.F. Hwang, Comparative Study of CO2 Capture by Carbon Nanotubes, Activated Carbons, and Zeolites, Energy & Fuels, 22 (2008) 3050-3056.

[28] N. Sun, C. Sun, H. Liu, J. Liu, L. Stevens, T. Drage, C.E. Snape, K. Li, W. Wei, Y. Sun, Synthesis, characterization and evaluation of activated spherical carbon materials for CO2 capture, Fuel, 113 (2013) 854-862.

[29] P.J.M. Carrott, J.M.V. Nabais, M.M.L. Ribeiro Carrott, J.A. Pajares, Preparation of activated carbon fibres from acrylic textile fibres, Carbon, 39 (2001) 1543-1555.

[30] A. Arenillas, K.M. Smith, T.C. Drage, C.E. Snape, CO2 capture using some fly ash-derived carbon materials, Fuel, 84 (2005) 2204-2210.

[31] A. Arenillas, F. Rubiera, J.B. Parra, C.O. Ania, J.J. Pis, Surface modification of low cost carbons for their application in the environmental protection, Applied Surface Science, 252 (2005) 619-624.

[32] C. Pevida, M.G. Plaza, B. Arias, J. Fermoso, F. Rubiera, J.J. Pis, Surface modification of activated carbons for CO2 capture, Applied Surface Science, 254 (2008) 7165-7172.

[33] M.G. Plaza, C. Pevida, C.F. Martín, J. Fermoso, J.J. Pis, F. Rubiera, Developing almond shell-derived activated carbons as CO2 adsorbents, Separation and Purification Technology, 71 (2010) 102-106.

[34] P. Davini, Flue gas treatment by activated carbon obtained from oil-fired fly ash, Carbon, 40 (2002) 1973-1979.

[35] A. Ahmadpour, D.D. Do, The preparation of active carbons from coal by chemical and physical activation, Carbon, 34 (1996) 471-479.

[36] E. Utrera-Hidalgo, C. Moreno-Castilla, J. Rivera-Utrilla, M.A. Ferro-García, F. Carrasco-Marín, Activated carbon columns as adsorbents of gallic acid from aqueous solutions: Effect of the presence of different electrolytes, Carbon, 30 (1992) 107-111.

[37] K.T. Chue, J.N. Kim, Y.J. Yoo, S.H. Cho, R.T. Yang, Comparison of Activated Carbon and Zeolite 13X for CO2 Recovery from Flue Gas by Pressure Swing Adsorption, Industrial & Engineering Chemistry Research, 34 (1995) 591-598.

[38] B.-K. Na, K.-K. Koo, H.-M. Eum, H. Lee, H.K. Song, CO2 recovery from flue gas by PSA process using activated carbon, Korean Journal of Chemical Engineering, 18 (2001) 220-227.

[39] D.D. Do, K. Wang, A new model for the description of adsorption kinetics in heterogeneous activated carbon, Carbon, 36 (1998) 1539-1554.

[40] E.S. Kikkinides, R.T. Yang, S.H. Cho, Concentration and recovery of carbon dioxide from flue gas by pressure swing adsorption, Industrial & Engineering Chemistry Research, 32 (1993) 2714-2720.

[41] X.P. Wang, J.J. Yu, J. Cheng, Z.P. Hao, Z.P. Xu, High-temperature adsorption of carbon dioxide on mixed oxides derived from hydrotalcite-like compounds, Environmental science & technology, 42 (2008) 614-618.

[42] J. Andrieu, J.M. Smith, Rate Parameters for Adsorption of CO2 in Beds of Carbon Particles, American Institute of Chemical Engineers Journal, 26 (1980) 944–948.

[43] D.M. Ruthven, L.-K. Lee, H. Yucel, Kinetics of non-isothermal sorption in molecular sieve crystals, AIChE Journal, 26 (1980) 16-23.

[44] S. Sircar, Sorption of carbon dioxide on activated carbons: Effect of the heat of sorption during kinetic measurements, Carbon, 19 (1981) 153-160.

[45] D.-A. Yang, H.-Y. Cho, J. Kim, S.-T. Yang, W.-S. Ahn, CO2 capture and conversion using Mg-MOF-74 prepared by a sonochemical method, Energy & Environmental Science, 5 (2012) 6465-6473.

[46] P.G. Gray, D.D. Do, Dynamics of carbon dioxide sorption on activated-carbon particles, AIChE Journal, 37 (1991) 1027-1034.

[47] A. Torrisi, R.G. Bell, C. Mellot-Draznieks, Predicting the impact of functionalized ligands on CO2 adsorption in MOFs: A combined DFT and Grand Canonical Monte Carlo study, Microporous and Mesoporous Materials, 168 (2013) 225-238.

[48] A.R. Millward, O.M. Yaghi, Metal−Organic Frameworks with Exceptionally High Capacity for Storage of Carbon Dioxide at Room Temperature, Journal of the American Chemical Society, 127 (2005) 17998-17999.

[49] P.L. Llewellyn, S. Bourrelly, C. Serre, A. Vimont, M. Daturi, L. Hamon, G. De Weireld, J.S. Chang, D.Y. Hong, Y. Kyu Hwang, S. Hwa Jhung, G. Ferey, High uptakes of CO2 and CH4 in mesoporous metal-organic frameworks MIL-100 and MIL-101, Langmuir, 24 (2008) 7245-7250.

[50] B. Arstad, H. Fjellvåg, K.O. Kongshaug, O. Swang, R. Blom, Amine functionalised metal organic frameworks (MOFs) as adsorbents for carbon dioxide, Adsorption, 14 (2008) 755-762.

[51] Y.-S. Bae, O.K. Farha, J.T. Hupp, R.Q. Snurr, Enhancement of CO2/N2 selectivity in a metal-organic framework by cavity modification, Journal of Materials Chemistry, 19 (2009) 2131.

[52] R. Xiong, J. Ida, Y.S. Lin, Kinetics of carbon dioxide sorption on potassium-doped lithium zirconate, Chemical Engineering Science, 58 (2003) 4377-4385.

[53] J.-I. Ida, R. Xiong, Y.S. Lin, Synthesis and CO2 sorption properties of pure and modified lithium zirconate, Separation and Purification Technology, 36 (2004) 41-51.

[54] C.I. Ezeh, X. Huang, X. Yang, C.-g. Sun, J. Wang, Sonochemical surface functionalization of exfoliated LDH: Effect on textural properties, CO2 adsorption, cyclic regeneration

capacities and subsequent gas uptake for simultaneous methanol synthesis, Ultrasonics Sonochemistry, 39 (2017) 330-343.

[55] D. Iruretagoyena, M.S.P. Shaffer, D. Chadwick, Layered Double Oxides Supported on Graphene Oxide for CO2 Adsorption: Effect of Support and Residual Sodium, Industrial & Engineering Chemistry Research, 54 (2015) 6781-6792.

[56] A. Garcia-Gallastegui, D. Iruretagoyena, V. Gouvea, M. Mokhtar, A.M. Asiri, S.N. Basahel, S.A. Al-Thabaiti, A.O. Alyoubi, D. Chadwick, M.S.P. Shaffer, Graphene Oxide as Support for Layered Double Hydroxides: Enhancing the CO2 Adsorption Capacity, Chemistry of Materials, 24 (2012) 4531-4539.

[57] F. Cavani, F. Trifirò, A. Vaccari, Hydrotalcite-type anionic clays: Preparation, properties and applications, Catalysis Today, 11 (1991) 173-301.

[58] N.D. Hutson, B.C. Attwood, High temperature adsorption of CO2 on various hydrotalcite-like compounds, Adsorption, 14 (2008) 781-789.

[59] D.I. Ferrer, Supported Layered Double Hydroxides as CO2 Adsorbents for Sorption-enhanced H2 Production, Chemical Engineering, Imperial College, London, United Kingdom, Springer International Publishing Switzerland, 2016, pp. 209.

[60] I. Rousselot, C. Taviot-Guého, F. Leroux, P. Léone, P. Palvadeau, J.-P. Besse, Insights on the Structural Chemistry of Hydrocalumite and Hydrotalcite-like Materials: Investigation of the Series Ca2M3+(OH)6Cl·2H2O (M3+: Al3+, Ga3+, Fe3+, and Sc3+) by X-Ray Powder Diffraction, Journal of Solid State Chemistry, 167 (2002) 137-144.

[61] J. He, M. Wei, B. Li, Y. Kang, D.G. Evans, X. Duan, Layered Double Hydroxides, Springer, Berlin Heidelberg, 2006.

[62] M.R. Othman, Z. Helwani, Martunus, W.J.N. Fernando, Synthetic hydrotalcites from different routes and their application as catalysts and gas adsorbents: a review, Applied Organometallic Chemistry, 23 (2009) 335-378.

[63] L.H. Chagas, G.S.G. De Carvalho, W.R. Do Carmo, R.A.S. San Gil, S.S.X. Chiaro, A.A. Leitão, R. Diniz, L.A. De Sena, C.A. Achete, MgCoAl and NiCoAl LDHs synthesized by the hydrothermal urea hydrolysis method: Structural characterization and thermal decomposition, Materials Research Bulletin, 64 (2015) 207-215.

[64] Y. Gao, Z. Zhang, J. Wu, X. Yi, A. Zheng, A. Umar, D. O'Hare, Q. Wang, Comprehensive investigation of CO2 adsorption on Mg-Al-CO3 LDH-derived mixed metal oxides, Journal of Materials Chemistry A, 1 (2013) 12782-12790.

[65] D.P. Debecker, E.M. Gaigneaux, G. Busca, Exploring, tuning, and exploiting the basicity of hydrotalcites for applications in heterogeneous catalysis, Chemistry (Weinheim an der Bergstrasse, Germany), 15 (2009) 3920-3935.

[66] R. Allada, A. Navrotsky, H.T. Berbeco, W.H. Casey, Thermochemistry and aqueous solubilities of hydrotalcite-like solids, Science, 296 (2002) 721-723.

[67] J.-M. Oh, C.-B. Park, J.-H. Choy, Intracellular Drug Delivery of Layered Double Hydroxide Nanoparticles, Journal of Nanoscience and Nanotechnology, 11 (2011) 1632-1635.

[68] J.W. Boclair, P.S. Braterman, Layered double hydroxide stability. 1. Relative stabilities of layered double hydroxides and their simple counterparts, Chemistry of materials : a publication of the American Chemical Society, 11 (1999) 298-302.

[69] J.W. Boclair, P.S. Braterman, J. Jiang, S. Lou, F. Yarberry, Layered Double Hydroxide Stability. 2. Formation of Cr(III)-Containing Layered Double Hydroxides Directly from Solution, Chemistry of Materials, 11 (1999) 303-307.

[70] J.J. Bravo-Suárez, E.A. Páez-Mozo, S.T. Oyama, Review of the synthesis of layered double hydroxides: a thermodynamic approach, Química Nova, 27 (2004) 601-614.

[71] R.K. Allada, J.D. Pless, T.M. Nenoff, A. Navrotsky, Thermochemistry of Hydrotalcite-like Phases Intercalated with CO32-, NO3-, Cl-, I-, and ReO4, Chemistry of Materials, 17 (2005) 2455-2459.

[72] B.R. Shaw, Y. Deng, F.E. Strillacci, K.A. Carrado, M.G. Fessehaie, Electrochemical Surface Analysis of Nonconducting Solids: Ferricyanide and Phenol as Electrochemical Probes of the Surfaces of Layered Double Hydroxide Anion-Exchanging Clays, Journal of The Electrochemical Society, 137 (1990) 3136-3143.

[73] S. Miyata, Physico-chemical properties of synthetic hydrotalcites in relation to composition, Clays and Clay Minerals, 28 (1980) 50-56.

[74] J.S. Valente, F. Figueras, M. Gravelle, P. Kumbhar, J. Lopez, J.P. Besse, Basic Properties of the Mixed Oxides Obtained by Thermal Decomposition of Hydrotalcites Containing Different Metallic Compositions, Journal of Catalysis, 189 (2000) 370-381.

[75] E. LÓPez-Salinas, E. Torres-GarcÍA, M. GarcÍA-SÁNchez, THERMAL BEHAVIOR OF HYDROTALCITE-LIKE [Mg1−xGax(OH)2](CO3)x/2·mH2O AS A FUNCTION OF GALLIUM CONTENT, Journal of Physics and Chemistry of Solids, 58 (1997) 919-925.

[76] J. Maria Fernandez, M. Angeles Ulibarri, F. M. Labajos, V. Rives, The effect of iron on the crystalline phases formed upon thermal decomposition of Mg-Al-Fe hydrotalcites, Journal of Materials Chemistry, 8 (1998) 2507-2514.

[77] T. Hibino, A. Tsunashima, Calcination and rehydration behavior of Mg-Fe-CO3 hydrotalcite-like compounds, Journal of Materials Science Letters, 19 (2000) 1403-1405.

[78] S. Velu, V. Ramaswamy, S. Sivasanker, New hydrotalcite-like anionic clays containing Zr4+ in the layers, Chemical Communications, DOI 10.1039/A704752E(1997) 2107-2108.

[79] M. del Arco, P. Malet, R. Trujillano, V. Rives, Synthesis and Characterization of Hydrotalcites Containing Ni(II) and Fe(III) and Their Calcination Products, Chemistry of Materials, 11 (1999) 624-633.

[80] V. Rives, Layered Double Hydroxides: Present and Future, Nova Science, New York, 2001.

[81] Q. Wang, D. O'Hare, Recent Advances in the Synthesis and Application of Layered Double Hydroxide (LDH) Nanosheets, Chemical Reviews, 112 (2012) 4124-4155.

[82] H. Wang, G. Fan, C. Zheng, X. Xiang, F. Li, Facile Sodium Alginate Assisted Assembly of Ni−Al Layered Double Hydroxide Nanostructures, Industrial & Engineering Chemistry Research, 49 (2010) 2759-2767.

[83] V. Prevot, N. Caperaa, C. Taviot-Guého, C. Forano, Glycine-Assisted Hydrothermal Synthesis of NiAl-Layered Double Hydroxide Nanostructures, Crystal Growth & Design, 9 (2009) 3646-3654.

[84] F.D. Iruretagoyena, Supported Layered Double Hydroxides as CO2 Adsorbents for Sorption-enhanced H2 Production, Springer International Publishing, London, UK, 2016.

[85] M. León, E. Díaz, S. Bennici, A. Vega, S. Ordóñez, A. Auroux, Adsorption of CO2 on Hydrotalcite-Derived Mixed Oxides: Sorption Mechanisms and Consequences for Adsorption Irreversibility, Industrial & Engineering Chemistry Research, 49 (2010) 3663-3671.

[86] A.D. Ebner, S.P. Reynolds, J.A. Ritter, Understanding the Adsorption and Desorption Behavior of CO2 on a K-Promoted Hydrotalcite-like Compound (HTlc) through Nonequilibrium Dynamic Isotherms, Industrial & Engineering Chemistry Research, 45 (2006) 6387-6392.

[87] M.K. Ram Reddy, Z.P. Xu, G.Q. Lu, J.C. Diniz da Costa, Layered Double Hydroxides for CO2 Capture: Structure Evolution and Regeneration, Industrial & Engineering Chemistry Research, 45 (2006) 7504-7509.

[88] N.D. Hutson, S.A. Speakman, E.A. Payzant, Structural Effects on the High Temperature Adsorption of CO2 on a Synthetic Hydrotalcite, Chemistry of Materials, 16 (2004) 4135-4143.

[89] D. Tichit, B. Coq, Catalysis by Hydrotalcites and Related Materials, CATTECH, 7 (2003) 206-217.

[90] J.I. Di Cosimo, V.K. Díez, C.R. Apesteguía, Base catalysis for the synthesis of α,β-unsaturated ketones from the vapor-phase aldol condensation of acetone, Applied Catalysis A: General, 137 (1996) 149-166.

[91] S. Abello, F. Medina, D. Tichit, J. Perez-Ramirez, J.C. Groen, J.E. Sueiras, P. Salagre, Y. Cesteros, Aldol condensations over reconstructed Mg-Al hydrotalcites: structure-activity relationships related to the rehydration method, Chemistry (Weinheim an der Bergstrasse, Germany), 11 (2005) 728-739.

[92] M.J. Climent, A. Corma, S. Iborra, K. Epping, A. Velty, Increasing the basicity and catalytic activity of hydrotalcites by different synthesis procedures, Journal of Catalysis, 225 (2004) 316-326.

[93] Z. Yong, Mata, A.E. Rodrigues, Adsorption of Carbon Dioxide onto Hydrotalcite-like Compounds (HTlcs) at High Temperatures, Industrial & Engineering Chemistry Research, 40 (2001) 204-209.

[94] W. Yang, Y. Kim, P.K.T. Liu, M. Sahimi, T.T. Tsotsis, A study by in situ techniques of the thermal evolution of the structure of a Mg–Al–CO3 layered double hydroxide, Chemical Engineering Science, 57 (2002) 2945-2953.

[95] T. Hibino, Y. Yamashita, K. Kosuge, A. Tsunashima, Decarbonation behavior of Mg-Al-CO3 hydrotalcite-like compounds during heat treatment., Clays and Clay Minerals, 43 (1995) 427-432.

[96] N.N.A.H. Meis, J.H. Bitter, K.P. de Jong, Support and Size Effects of Activated Hydrotalcites for Precombustion CO2 Capture, Industrial & Engineering Chemistry Research, 49 (2010) 1229-1235.

[97] J.I. Di Cosimo, V.K. Díez, M. Xu, E. Iglesia, C.R. Apesteguía, Structure and Surface and Catalytic Properties of Mg-Al Basic Oxides, Journal of Catalysis, 178 (1998) 499-510.

[98] O. Aschenbrenner, P. McGuire, S. Alsamaq, J. Wang, S. Supasitmongkol, B. Al-Duri, P. Styring, J. Wood, Adsorption of carbon dioxide on hydrotalcite-like compounds of different compositions, Chemical Engineering Research and Design, 89 (2011) 1711-1721.

[99] S. Abelló, F. Medina, D. Tichit, J. Pérez-Ramírez, X. Rodríguez, J.E. Sueiras, P. Salagre, Y. Cesteros, Study of alkaline-doping agents on the performance of reconstructed Mg–Al hydrotalcites in aldol condensations, Applied Catalysis A: General, 281 (2005) 191-198.

[100] A.D. Ebner, S.P. Reynolds, J.A. Ritter, Nonequilibrium Kinetic Model That Describes the Reversible Adsorption and Desorption Behavior of CO2 in a K-Promoted Hydrotalcite-like Compound, Industrial & Engineering Chemistry Research, 46 (2007) 1737-1744.

[101] K.B. Lee, A. Verdooren, H.S. Caram, S. Sircar, Chemisorption of carbon dioxide on potassium-carbonate-promoted hydrotalcite, Journal of colloid and interface science, 308 (2007) 30-39.

[102] Y. Ding, E. Alpay, Adsorption-enhanced steam–methane reforming, Chemical Engineering Science, 55 (2000) 3929-3940.

[103] E.R. van Selow, P.D. Cobden, P.A. Verbraeken, J.R. Hufton, R.W. van den Brink, Carbon Capture by Sorption-Enhanced Water−Gas Shift Reaction Process using

Hydrotalcite-Based Material, Industrial & Engineering Chemistry Research, 48 (2009) 4184-4193.

[104] H.T.J. Reijers, S.E.A. Valster-Schiermeier, P.D. Cobden, R.W. van den Brink, Hydrotalcite as CO2 Sorbent for Sorption-Enhanced Steam Reforming of Methane, Industrial & Engineering Chemistry Research, 45 (2006) 2522-2530.

[105] E.L.G. Oliveira, C.A. Grande, A.E. Rodrigues, CO2 sorption on hydrotalcite and alkali-modified (K and Cs) hydrotalcites at high temperatures, Separation and Purification Technology, 62 (2008) 137-147.

[106] S. Walspurger, L. Boels, P.D. Cobden, G.D. Elzinga, W.G. Haije, R.W. van den Brink, The crucial role of the K+-aluminium oxide interaction in K+-promoted alumina- and hydrotalcite-based materials for CO2 sorption at high temperatures, ChemSusChem, 1 (2008) 643-650.

[107] Y.J. Wu, P. Li, J.G. Yu, A.F. Cunha, A.E. Rodrigues, K-Promoted hydrotalcites for CO2 capture in sorption enhanced reactions., Chemical Engineering and Technology, 36 (2013) 567-574.

[108] M. Tsuji, G. Mao, T. Yoshida, Y. Tamaura, Hydrotalcites with an extended Al3+-substitution: Synthesis, simultaneous TG-DTA-MS study, and their CO2 adsorption behaviors, Journal of Materials Research, 8 (2011) 1137-1142.

[109] P. Benito, F.M. Labajos, V. Rives, Uniform Fast Growth of Hydrotalcite-like Compounds, Crystal Growth & Design, 6 (2006) 1961-1966.

[110] P. Benito, M. Herrero, C. Barriga, F.M. Labajos, V. Rives, Microwave-Assisted Homogeneous Precipitation of Hydrotalcites by Urea Hydrolysis, Inorganic Chemistry, 47 (2008) 5453-5463.

[111] X. Xie, X. Ren, J. Li, X. Hu, Z. Wang, Preparation of Small Particle Sized ZnAl-Hydrotalcite-Like Compounds by Ultrasonic Crystallization, Journal of Natural Gas Chemistry, 15 (2006) 100-104.

[112] J.-M. Oh, S.-H. Hwang, J.-H. Choy, The effect of synthetic conditions on tailoring the size of hydrotalcite particles, Solid State Ionics, 151 (2002) 285-291.

[113] H. Hayashi, Y. Hakuta, Hydrothermal Synthesis of Metal Oxide Nanoparticles in Supercritical Water, Materials, 3 (2010) 3794-3817.

[114] S.K. Sharma, P.K. Kushwaha, V.K. Srivastava, S.D. Bhatt, R.V. Jasra, Effect of hydrothermal conditions on structural and textural properties of synthetic hydrotalcites of varying Mg/Al ratio, Industrial & Engineering Chemistry Research, 46 (2007) 4856–4865.

[115] C.I. Ezeh, M. Tomatis, X. Yang, J. He, C.-g. Sun, Ultrasonic and Hydrothermal Mediated Synthesis Routes for Functionalized Mg-Al LDH: Comparison Study on Surface Morphology, Basic Site Strength, Cyclic Sorption Efficiency and Effectiveness, Ultrasonics Sonochemistry, DOI https://doi.org/10.1016/j.ultsonch.2017.07.013.

[116] Z.P. Xu, G. Stevenson, C.Q. Lu, G.Q. Lu, Dispersion and size control of layered double hydroxide nanoparticles in aqueous solutions, The journal of physical chemistry. B, 110 (2006) 16923-16929.

[117] H. Arakawa, Research and development on new synthetic routes for basic chemicals by catalytic hydrogenation of CO_2, in: M.A.K.I.S.Y. T. Inui, T. Yamaguchi (Eds.) Studies in Surface Science and Catalysis, Elsevier1998, pp. 19-30.

[118] X. An, J. Li, Y. Zuo, Q. Zhang, D. Wang, J. Wang, A Cu/Zn/Al/Zr Fibrous Catalyst that is an Improved CO2 Hydrogenation to Methanol Catalyst, Catalysis Letters, 118 (2007) 264-269.

[119] J. Toyir, P. Ramirez de la Piscina, J. L. G. Fierro, N. Homs, Catalytic Performace for CO_2 Conversion to Methanol of Gallium Promoted Copper based Catalysts: Influence of Metallic Precursors, Applied Catalysis B, 34 (2001) 255-266.

[120] X. Guo, D. Mao, G. Lu, S. Wang, G. Wu, CO_2 hydrogenation to methanol over Cu/ZnO/ZrO_2 catalysts prepared via a route of solid-state reaction, Catalysis Communications, 12 (2011) 1095-1098.

[121] C. Li, X. Yuan, K. Fujimoto, Development of highly stable catalyst for methanol synthesis from carbon dioxide, Applied Catalysis A: General, 469 (2014) 306-311.

[122] F. Arena, K. Barbera, G. Italiano, G. Bonura, L. Spadaro, F. Frusteri, Synthesis, characterization and activity pattern of Cu–ZnO/ZrO_2 catalysts in the hydrogenation of carbon dioxide to methanol, Journal of Catalysis, 249 (2007) 185-194.

[123] B.J. Liaw, Y.Z. Chen, Liquid-phase synthesis of methanol from CO2/H2 over ultrafine CuB catalysts, Applied Catalysis A: General, 206 (2001) 245-256.

[124] Y.-F. Zhao, Y. Yang, C. Mims, C.H.F. Peden, J. Li, D. Mei, Insight into methanol synthesis from CO2 hydrogenation on Cu(111): Complex reaction network and the effects of H2O, Journal of Catalysis, 281 (2011) 199-211.

[125] J. Yoshihara, C.T. Campbell, Methanol Synthesis and Reverse Water–Gas Shift Kinetics over Cu(110) Model Catalysts: Structural Sensitivity, Journal of Catalysis, 161 (1996) 776-782.

[126] C.B.S. Ovesen C.V., Schiøtz J., Stoltze P., Topsøe H. and Nørskov J.K., Kinetic Implications of Dynamical Changes in Catalyst Morphology during Methanol Synthesis over Cu/ZnO Catalyst, Journal of Catalysis, 168 (1997) 133-142.

[127] I. Melián-Cabrera, M. López Granados, J.L.G. Fierro, Reverse Topotactic Transformation of a Cu–Zn–Al Catalyst during Wet Pd Impregnation: Relevance for the Performance in Methanol Synthesis from CO_2/H_2 Mixtures, Journal of Catalysis, 210 (2002) 273-284.

[128] I. Melián-Cabrera, M.L. Granados, J.L.G. Fierro, Pd-Modified Cu–Zn Catalysts for Methanol Synthesis from CO_2/H_2 Mixtures: Catalytic Structures and Performance, Journal of Catalysis, 210 (2002) 285-294.

[129] K. T. Jung, A. T. Bell, Effects of Zirconia Phase on the Synthesis of Methanol over Zirconia-Supported Copper, Catalysis Letters, 80 (2002) 63-68.

[130] J. Słoczyński, R. Grabowski, A. Kozłowska, P. Olszewski, J. Stoch, J. Skrzypek, M. Lachowska, Catalytic activity of the M/(3ZnO·ZrO2) system (M = Cu, Ag, Au) in the hydrogenation of CO2 to methanol, Applied Catalysis A: General, 278 (2004) 11-23.

[131] S.E. Collins, M.A. Baltanás, J.L. Garcia Fierro, A.L. Bonivardi, Gallium–Hydrogen Bond Formation on Gallium and Gallium–Palladium Silica-Supported Catalysts, Journal of Catalysis, 211 (2002) 252-264.

[132] S.E. Collins, D.L. Chiavassa, A.L. Bonivardi, M.A. Baltanás, Hydrogen Spillover in Ga_2O_3–Pd/SiO_2 Catalysts for Methanol Synthesis from CO_2/H_2, Catalysis Letters, 103 (2005) 83-88.

[133] X. M. Liu, G. Q. Lu, Z. F.Yan, J. Beltramini, Recent Advances in Catalysts for Methanol Synthesis via Hydrogenation of CO and CO_2, Industrial and Engineering Chemistry Research, 42 (2003) 6518-6530.

[134] Y. Borodko, G.A. Somorjai, Catalytic hydrogenation of carbon oxides – a 10-year perspective, Applied Catalysis A: General, 186 (1999) 355-362.

[135] I.A. Fisher, A. T. Bell, In-Situ Infrared Study of Methanol Synthesis from H2/CO_2 over Cu/SiO_2 and $Cu/ZrO_2/SiO_2$, Journal of Catalysis, 172 (1997) 222-237.

[136] R.A. Koeppel, A. Baiker, A. Wokaun, Copper/zirconia catalysts for the synthesis of methanol from carbon dioxide: Influence of preparation variables on structural and catalytic properties of catalysts, Applied Catalysis A: General, 84 (1992) 77-102.

[137] W. Jansen, Dynamic Behavior of the Surface Structure of Cu/ZnO/SiO2 Catalysts, Journal of Catalysis, 210 (2002) 229-236.

[138] Q.-L. Tang, Q.-J. Hong, Z.-P. Liu, CO2 fixation into methanol at Cu/ZrO2 interface from first principles kinetic Monte Carlo, Journal of Catalysis, 263 (2009) 114-122.

[139] K.R.A. Weigel J., Baiker A. and Wokaun A., Surface Species in CO and CO2 Hydrogenation over Copper/Zirconia: On the Methanol Synthesis Mechanism, Langmuir, 12 (1996) 5319-5329.

[140] D.L. Chiavassa, S.E. Collins, A.L. Bonivardi, M.A. Baltanás, Methanol synthesis from CO2/H2 using Ga2O3–Pd/silica catalysts: Kinetic modeling, Chemical Engineering Journal, 150 (2009) 204-212.

[141] J. Tabatabaei, B.H. Sakakini, K.C. Waugh, On the mechanism of methanol synthesis and the water-gas shift reaction on ZnO, Catalysis Letters, 110 (2006) 77-84.

[142] T. Inui, T. Takeguchi, Effective Conversion of Carbon Dioxide and Hydrogen to Hydrocarbons, Catalysis Today, 10 (1991) 95-106.

[143] S.O. Nitta Y., Ikeda Y., Okamoto Y. and Imanaka T. , Copper-Zirconia Catalysts for Methanol Synthesis from Carbon Dioxide: Effect of ZnO Addition to Cu-ZrO2 Catalysts, Catalysis Letters, 26 (1994) 345-354.

[144] Y. Yang, J. Evans, J.A. Rodriguez, M.G. White, P. Liu, Fundamental studies of methanol synthesis from CO2 hydrogenation on Cu(111), Cu clusters, and Cu/ZnO(000$\bar{1}$), Physical Chemistry Chemical Physics, 12 (2010) 9909.

[145] B. Chan, L. Radom, Zeolite-Catalyzed Hydrogenation of Carbon Dioxide and Ethene., Journal of American Chemical Society, 130 (2008) 9790-9799.

[146] M.R. Rahimpour, A two-stage catalyst bed concept for conversion of carbon dioxide into methanol, Fuel Processing Technology, 89 (2008) 556-566.

[147] M.R. Rahimpour, S. Ghader, Enhancement of CO conversion in a novel Pd–Ag membrane reactor for methanol synthesis, Chemical Engineering and Processing: Process Intensification, 43 (2004) 1181-1188.

[148] R.P.W.J. Struis, S. Stucki, Verification of the membrane reactor concept for the methanol synthesis, Applied Catalysis A: General, 216 (2001) 117-129.

[149] G. Barbieri, G. Marigliano, G. Golemme, E. Drioli, Simulation of CO2 hydrogenation with CH3OH removal in a zeolite membrane reactor, Chemical Engineering Journal, 85 (2002) 53-59.

[150] F. Gallucci, A. Basile, A theoretical analysis of methanol synthesis from CO2 and H2 in a ceramic membrane reactor, International Journal of Hydrogen Energy, 32 (2007) 5050-5058.

[151] L. Yong, Z. Yi, W. Tiejun, T. Noritatsu, Efficient Conversion of Carbon Dioxide to Methanol Using Copper Catalyst by a New Low-temperature Hydrogenation Process, Chemistry Letters, 36 (2007) 1182-1183.

[152] X. Zhang, L. Zhong, Q. Guo, H. Fan, H. Zheng, K. Xie, Influence of the calcination on the activity and stability of the Cu/ZnO/Al2O3 catalyst in liquid phase methanol synthesis, Fuel, 89 (2010) 1348-1352.

CHAPTER THREE

METHODS AND EXPERIMENTALS

3.1 INTRODUCTION

This chapter introduces the standard experimental techniques and instruments used for the purpose of this research study. Descriptions of the various synthetic methods adopted for the preparation of both catalysts and adsorbents are explained in Section 3.2. Section 3.3 and 3.4 describes the standard experimental techniques for measuring CO_2 uptake and catalytic performance respectively. Characterization equipment and procedures are enlisted in Section 3.5. These are used to measure the physicochemical properties of the prepared samples. Finally, Section 3.6 covers the adopted experimental principles used in analysing the obtained results.

3.2 SYNTHESIS OF CATALYSTS AND ADSORBENTS

Within the course of this study, various synthetic routes were adopted in the preparation of both catalysts and adsorbents. However, in this section, the conventional preparation route is described. Any modifications in this route are specified in subsequent chapters. All reagents used for material synthesis were purchased from SinoPharm Chemical Reagents Co. Ltd. The CO_2, H_2 and N_2 gases used for characterization and adsorption measurements are 99.99% pure and were supplied by Linde Group, China.

3.2.1 Catalyst Synthesis

In this study, the catalyst of interest was limited to Cu/Zn/Zr composite.

3.2.1.1 Cu/ZrO_2

In the preparation of this catalyst, the zirconia aerogel was first synthesized. This was carried out by adding 0.17M $ZrOCl_2 \cdot 8H_2O$ solution and 0.2M NH_4OH solution dropwise respectively in a beaker containing 100ml of deionized water while sustaining the pH at 8.25. The

precipitate was then filtered and washed with deionised water before being washed by ethanol to inhibit further reaction [1]. Formed aerogels were then calcined at desired temperatures depending on the purpose of the study. In cases of calcination, the purported samples are labelled as ZrO_2-n, where n is the calcination temperature (K). The Zirconia aerogel was then used to synthesis the catalysts via deposition precipitation (DP) and impregnation (IM) methods at various CuO/ZrO_2 ratios.

3.2.1.1.1 Deposition Precipitation

This was synthesized by the direct precipitation of 0.1M NaOH solution and 0.1M $Cu(NO_3)_2$ solution in the zirconia aerogel suspended solution. This reaction was sustained at a pH of 7.0; after which, the precipitates were filtered, washed with distilled water, dried at 383 K (overnight) and calcined at 623 K for 4 hours. This sample is labelled as CZr-DP.

3.2.1.1.2 Impregnation

The zirconia aerogel was impregnated with 0.1M $Cu(NO_3)_2$ solution with a volume 10% more than the impregnating volume before being filtered, dried and calcined as in above. This sample is labelled as CZr-IM.

3.2.1.1.3 Co-precipitation

Unlike the other methods, without the use of the aerogel, the CP catalyst was prepared by a reaction of 0.17M mixed reaction of $ZrOCl_2$ and $Cu(NO_3)_2$ and 0.1M NaOH solution while sustaining the pH at 7.0. After which, the precipitates were filtered, washed, dried and calcined as in above. This sample is labelled as CZr-CP.

3.2.1.2 Cu/Zn/ZrO_2

A mix of $Cu(NO_3)_2{\cdot}3H_2O$, $Zn(NO_3)_2{\cdot}6H_2O$ and $Zr(NO_3)_4{\cdot}5H_2O$ were blended in a Cu^{2+}:Zn^{2+}:Zr^{4+} at varying molar ratio depending on the purpose of the study. This mix was further blended with citric acid ligand, $C_6H_8O_7{\cdot}H_2O$ in a molar ratio of 1:1.3. This was carried out for 30 minutes at room temperature until the reactants were transformed to a homogeneous muddy precursor [3]. Afterwards, the catalyst was dried at 383 K overnight before being calcined at a temperature of 623 K for 4 hours.

3.2.2 Synthesis of Layered Double Hydroxides (LDH) Adsorbents

3.2.2.1 Mg-Al LDH

200 ml solution containing APTES (≥98%) and SDS (≥86%) (molar ratio: 5:1) respectively dissolved in a mixture of 50 ml C_2H_5OH (≥99.7%) and 150 ml distilled water was stirred for about 30 min at a temperature of 333 K until the pH stabilized at about 10.3. This solution was then reacted with $Mg(NO_3)_2 \cdot 6H_2O$ (≥98%) and $Al(NO_3)_3 \cdot 9H_2O$ (≥99%) (molar ratio: 3:1, dissolved in 100 ml of distilled water) solution by adding the latter dropwise while maintaining the temperature of the former at 333 K. The mixture pH was regulated towards 10 using 4 M NaOH (≥96%) solution. The substrate (molar ratio of Mg:Al:APTES:SDS = 3:1:5:1) was then aged for 20 hr with the constant stirring at the maintained temperature. The filtered precipitates were then washed with ionised water before being vacuum dried (500 mbar at 343 K) overnight [4]. This sample is labelled as Conv-LDH. Using the same chemical composition and process, a set of new samples were prepared using sonicated mixing by ultrasonic horns. The sonication intensity was varied based on the purpose of the study. This sample is labelled as US-LDH.

For ultrasonic-assisted hydrothermal synthesized samples, HPH-LDH, 32 ml solution containing APTES (≥ 98%) and SDS (≥ 86%) (APTES:SDS molar ratio: 5) was reacted with $Mg(NO_3)_2.6H_2O$ (≥ 98%) and $Al(NO_3)_3.9H_2O$ (≥ 99%) (Mg:Al molar ratio: 3, dissolved in 16 ml of distilled water) solution. The latter was added dropwise while maintaining the temperature of the former at 333 K and sonicating with ultrasonic horn. The substrate (molar ratio of Mg:Al:APTES:SDS = 3:1:5:1) was moved to the hydrothermal reactor. After being vented with pure N_2 gas (99.99%) for 15 mins in order to remove all of the oxygen before the reaction, the reactor was sealed and heated to a temperature of 723 K with a ramp of 2 °C/min and then held for 15 mins. After reaction, the solution was aged for 12 hr. The precipitates were filtered, washed with distilled water and then dried in a vacuum oven (500 mbar at 343 K) overnight.

3.2.2.2 Mg-Al LDH-MEA

The prepared LDHs were functionalised via MEA extraction. 0.5 g of LDH sample was dispersed in a solution of 100 ml C_2H_5OH (≥99.7%) containing 20 g MEA (≥99%). The mixture was then refluxed for 20 hr at a temperature of 363 K. After which the samples were

filtered, washed with ethanol and dried in a vacuum oven overnight [5]. These samples are labelled Conv-MEA. Using an ultrasonic horn, the procedure was repeated for the synthesised US-LDHn samples. The obtained samples are labelled US-MEA. Similarly, this was repeated for the HPH-LDH samples and labelled as HPH-MEA.

3.3 EXPERIMENTAL TECHNIQUES FOR MEASURING ADSORPTION CAPACITY

Within the course of this study, the adsorption capacity of the adsorbents was determined using the thermogravimetric analyser [6, 7] and a fixed bed test rig.

3.3.1 Thermogravimetric Analyser

Netzsch STA 449 F3 Jupiter thermogravimetric analyser (TGA) with a Proteus Autosampler and Proteus Kinetic 3 Analysis software were used for the purpose of this analysis. The TGA was used to analyse the weight changes of the prepared sample with respect to temperature in a controlled atmosphere. Effects of the change in gas density and viscosity were corrected by measuring the response to an empty alumina crucible using the same method. The Netzsch STA 449 F3 TGA operates within the temperature range of 298-1273 K with a temperature precision of ± 0.1 ^{o}C, weighing capacity of 25 mg and sensitivity of 0.1 μg. Using this instrument, the thermal stability, CO_2 uptake capacity and regeneration efficiency were measured.

3.3.1.1 CO_2 Uptake Measurement

Approximately 5-10 mg of each sample was heated from 278-378 K at 20 K/min under N_2. The sample was held at 378 K for 30 min and then cooled to the desired adsorption temperature at a rate of 10 K/min. The gas input was switched from N_2 to CO_2 and held isothermally for 90 min. The experimented adsorption temperatures were 328 K and 353 K (reported optimum adsorption temperature for most amine functionalised adsorbents [8]). The CO_2 adsorption capacity was determined from the weight change of the samples in CO_2 atmosphere.

3.3.1.2 Adsorbent Regeneration via Thermal Swing Adsorption Cycles

A thermal swing adsorption-desorption programme in the presence of N_2 was conducted using this equipment to measure the regeneration capacity of the adsorbents. This is to determine the lifetime adsorption capacity of the adsorbent. After the CO_2 uptake measurement, the adsorbent was heated to 378 K at a rate of 20 K/min in a N_2 atmosphere with a constant flow rate of 20 ml/min and held isothermally for 30 mins. After desorption, the adsorption cycle was repeated several times. The experimented adsorption temperature is 328 K. Adsorption capacities were computed based on the mass of the adsorbent.

3.3.1.3 Thermal Stability Measurement

The stability of the as synthesised LDH samples in air was determined by first loading about 5-10 mg of sample into an alumina crucible, and the decomposition was monitored by increasing temperature from 298-1273 K with a heating rate of 10 K/min and under a flow of air (50 ml/min).

3.3.2 Fixed Bed Adsorption Rig

Owing to limited resources, the catalyst performance evaluation rig was used for this purpose. This was slightly modified to conduct adsorption measurements, Figure 3.1. The adsorption column was made of stainless steel with diameter, D = 7.5 mm and length, L = 200 mm) heated by a Blooming furnace with maximum design temperature of 700 ^oC (working temperature restriction = 600 ^oC). The column is divided into three sections: preheater (silicon carbide furnace), main heater and post-heater with individual WATLOW K-type thermocouples (0-600 ^oC). The adsorption bed was posited within the main heating section and the temperature of this section was recorded as the temperature of the adsorbent bed.

Prior to the adsorption column, a helix curled Blooming preheater (silicon carbide) with stainless steel shell was installed to prevent adverse effects of thermal gradient on the adsorption process within the adsorption column. The maximum design temperature of the preheater is 400 ^oC (but with working temperature restriction = 350 ^oC). Feed streams were introduced via independent feeding lines for N_2, H_2 and CO_2 respectively. Flowrates of these streams were monitored with electrical actuated Brooks mass flow controllers (MFC) with 0-100 mL/min flowrate range and accuracy of ± 1% and SWAGELOK control valves (PCV). Connectors and pipelines are made of 316SS and 316L materials respectively with dimensions

¼” and 1/8” card sets. Installed mixers and separators are 316L with 25 MPa design pressure, but restricted to 20 MPa working pressure.

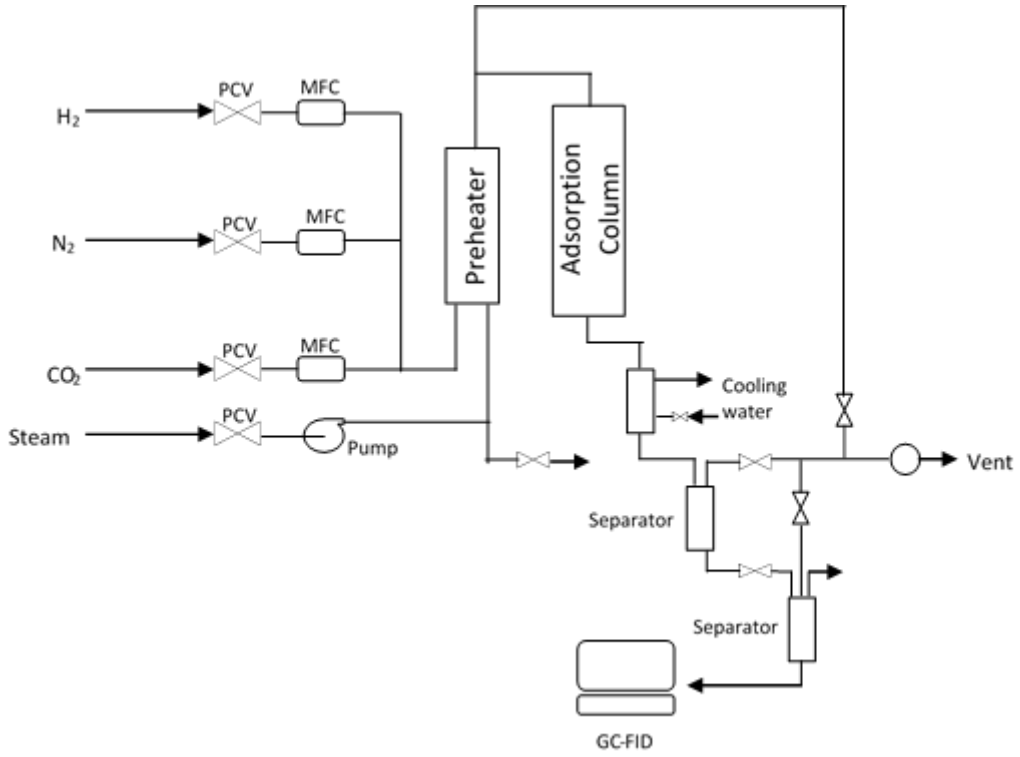

Figure 3.1: Brief schematic diagram of the adsorption column

3.3.2.1 Experimental Procedure

A sample of the adsorbent *ca.* 0.5 g was loaded in a stainless steel column with inner diameter. For each run, the adsorbent was activated in situ at 423 K for 2 hr under the flow of N_2 at 20 mL/min. The temperature was then cooled to room temperature before switching the gas to the desired composition of CO_2 gas mixture (adsorptive gas). Additionally, the pressures of the gases were maintained to be equal by use of metering valve posited at the vent of the cylinders. The process was then sustained isothermally for a particular period of time depending on the purpose of the study (0.5 – 1 hr) and at desired pressures. After which the adsorbent was regenerated by purging it with N_2 at the same conditions as the activation process and the adsorption process repeated for a particular number of cycles. The effluent stream was constantly monitored with the aid of a gas-chromatograph with flames ionization detector (GC-FID). The breakthrough curves were obtained from the GC-FID results. After the experiment, the regenerated adsorbent was collected and reweighed to determine the exact mass of

adsorbent. Prior to the running of the experiment, a blank run was carried out to measure the dead volume of the system. This is a corrective measure to ensure accurate data computation.

3.4 EXPERIMENTAL TECHNIQUES FOR CATALYST TESTING

The synthesised catalysts were tested using the catalyst performance evaluation rig connected to a GC-FID as illustrated above in Section 3.3.2.

3.4.1 Catalyst Performance Evaluation Rig

The rig used for this study is the same as that described in Section 3.3.2. In addition to the rig set up, the effluent transfer connector to the GC-FID (316SS, ¼" set card) was connected to a taped electric heater. This was used to heat up the effluent gas to avoid condensation of the product stream. The temperature was maintained at 413 K using a K-type thermocouple attached externally to the transfer line.

3.4.2 Catalyst Performance Standard Procedure [9]

First, 0.5g of the catalyst was reduced at 623 K in H_2/N_2 (10/90 vol%) environment for 3 hr at atmospheric pressure before being cooled to room temperature. The reactant gas H_2/CO_2 (molar ratio = 3:1) under operating conditions of 3 MPa, 623 K and GHSV = 3100 hr^{-1}. The effluent was analysed online using an Agilent gas chromatograph (GC) 7890A with the transfer line from the reactor to the GC preheated at 373 K to avoid condensation of effluent products. TCD was used to measure N_2, CO and CO_2 gases while organic compounds were studied using the flame ionization detector (FID). From this test, catalytic conversion and selectivity were computed using mass balance and resulting steady-state values (SSV). SSV was computed as an average of three tests over a period of 3 hr of continuous operation.

3.4.3 Product Analysis

Table 3.1: Composition of standard gas mixture used for GC calibration

Cylinder	Gas Mixture (%)						
	CH_3OH	CO_2	H_2	N_2	CO	CH_4	C_6H_6
1	0.3	22	66	11.7	-	-	-
2	0.2	23	69	7.8	-	-	-
3	0.1	24	72	3.8	-	-	0.1
4	3	50	15	20	10	2	-

The results of catalytic reactions was obtained from the area of the peaks obtained from the GC spectra. To quantify the products, standard gas mixtures as illustrated in Table 3.1 were used to calibrate the GC signals. This was repeated for three runs and the average documented. Comparing the area of the peaks to the composition of the standard gas mixtures (Figures 3.2 and 3.3), the corresponding proportionality factors for methanol and carbon dioxide were estimated as 3×10^{-5} mmol/L/pA.s and 1.5×10^{-4} mmol/L/μV.s respectively with a R-squared value of 0.9419 and 0.9823 respectively.

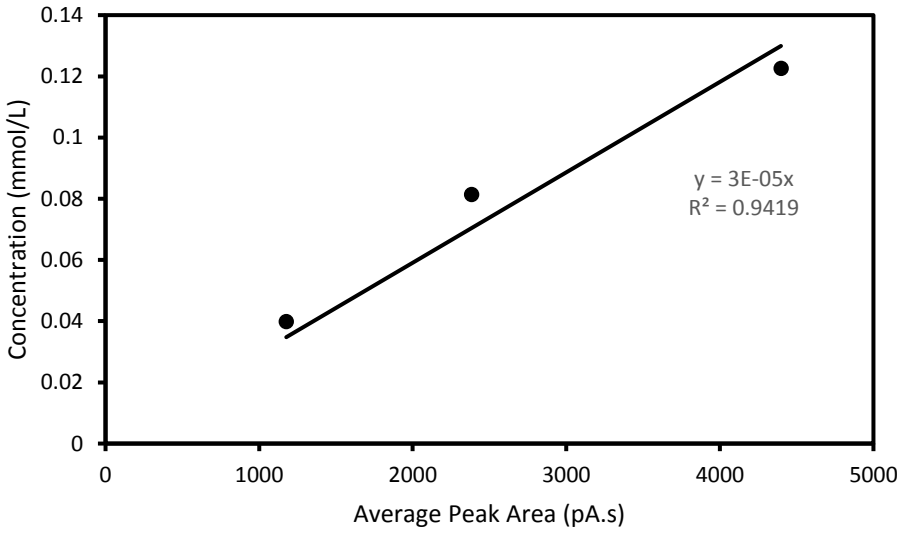

Figure 3.2: GC calibration curve for methanol

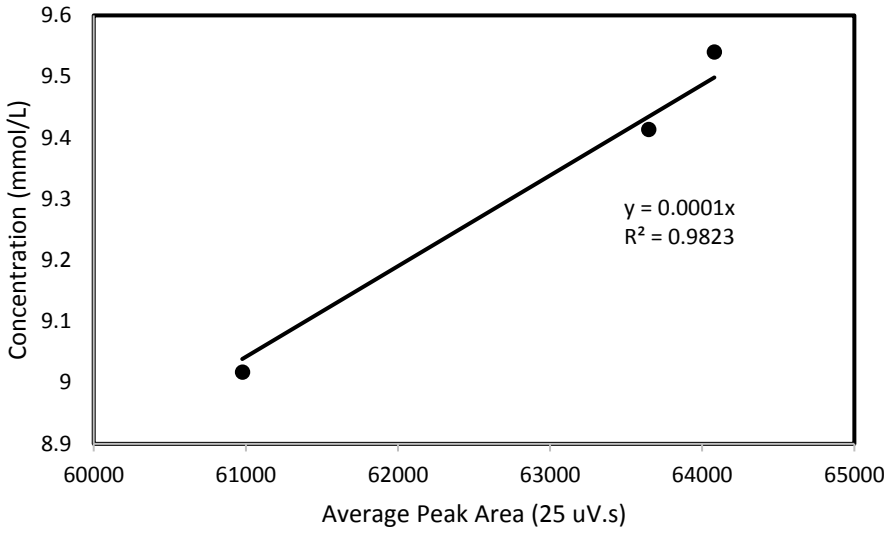

Figure 3.3: GC calibration curve for CO_2

3.5 CHARACTERISATION OF CATALYSTS AND ADSORBENTS

Physicochemical properties of the synthesised catalysts and adsorbents were studied using the following characterisation equipment:

3.5.1 Scanning Electron Microscopy (SEM) – Energy Dispersive X-ray Spectroscopy (EDX) Analysis.

The surface morphology of the prepared materials were studied with a Zeiss ΣIGMA™ Field Emission SEM. With the aid of an Oxford Instrument INCAx-act PentaFET® Precision EDX, the EDX spectra for the LDHs were obtained. This was also used to compute the amine content present in the adsorbents.

3.5.2 X-ray Diffraction (XRD)

XRD patterns were studied using a Bruker-AXS D8 advance powder diffractometer with a scanning range of $10^o \leq 2\theta \leq 90^o$ at a step size of 0.010216^o. The basal spacing was calculated with Bragg's Law using the d_{003} peak from the diffraction pattern. Average crystallite size was estimated using the Scherrer's formula:

Equation 3.1: Scherrer's Formula

$$d = \frac{0.9\lambda}{\beta \cos \theta}$$

where d is the crystallite size (nm), λ is the radiation wavelength (nm) = 1.5406 nm in this case, β is the full width at half maximum (radians) and θ is the Bragg's angle of the maximum intense peak (degrees) [10].

3.5.3 X-ray Photoelectron Spectroscopy (XPS) Analysis.

X-ray Photoelectron Spectroscopy (XPS) data of the adsorbent was obtained using Kratos X-ray Photoelectron Spectrometer – Axis Ultra DLD with a 96 W monochromatic Al Kα X-ray source (1486.69 eV) at a photoelectron take-off angle of 45°. Wide scans were performed from 1100 eV to 0 eV with a dwell time of 150 ms and steps of 1 eV. Narrow scans were performed with steps of 0.05 eV with dwell time of 600 ms. The binding energy (BE) was calibrated by using the C 1s peak at 284.6 eV as a reference.

3.5.4 Nitrogen Adsorption-Desorption Measurement.

The textural properties of the prepared adsorbents were studied by Nitrogen physisorption analysis at -196 ^{o}C using the Micrometrics ASAP 2020 Surface Area and Porosity Analyser. Prior to this analysis, samples were degassed at a temperature of 105 ^{o}C for 4hr. The BET (Brunauer, Emmett and Teller) model was used to determine the surface area (S_{BET}) of the samples. The total pore volumes (V_{Total}) were computed from the amount of nitrogen adsorbed at relative pressure (P/P_o) of 0.99 and the average pore volumes from $4V_{Total}/S_{BET}$. The pore size distribution was calculated using the BJH (Barrett, Joyner and Halenda) model. The t-plot method was used to calculate the micopore volume (V_{micro}).

3.5.5 Temperature-Programmed Desorption (TPD)

3.5.5.1 CO_2-TPD

This was conducted using AutoChem II 2920 to assess the basicity of the catalysts. First, the 0.1 g of the catalyst was reduced at 573 K for 1 hr in a flow of H_2 at 30 ml/min. Subsequently, the catalyst was cooled to 323 K before being flushed with He for 0.5 hr at same temperature at 40 ml/min. The catalyst was then exposed to pure CO_2 for 1 hr at a flow rate of 30 ml/min before being flushed with He at 40 ml/min to remove all physisorbed molecules. TPD

measurement was conducted at temperature range of 323-1073 K with a heating rate of 10 K/min under the flow of He at 40 ml/min, and the CO_2 desorption monitored using a thermal conductivity detector (TCD).

3.5.5.2 H_2-TPD

Experiment was performed in the same equipment as CO_2-TPD. 0.1 g of the catalyst was first reduced in situ at 573 K for 2 hr in mixed flow of H_2/He (10:90 vol%). After which, the catalyst was cooled down to 323 K and then saturated in 10% H_2/He for 1 hr, followed by purging with N_2 for 0.5 hr to remove any physisorbed molecules. H_2-TPD measurement was then performed to 1073 K with a heating rate of 5 K/min under N_2 atmosphere.

3.6 ADOPTED EXPERIMENTAL PRINCIPLES

3.6.1 Conversion, Selectivity and Yield

Conversion and selectivity were computed using mass balance and obtained SSV. These are based on the carbon amount in the molecules. CO_2 conversion (X_{CO2}), selectivity (S_i) and yield (Y_i) (where i is the molecule of interest) were computed as follows:

Equation 3.2: CO_2 conversion computation

$$x_{CO_2} = \frac{n_{CH_3OH} + n_{CO}}{n^0_{CO_2}}$$

Equation 3.3: Methanol and carbon monoxide selectivity computation

$$s_{CH_3OH} = \frac{n_{CH_3OH}}{n_{CH_3OH} + n_{CO}}$$

$$s_{CO} = \frac{n_{CO}}{n_{CH_3OH} + n_{CO}}$$

Equation 3.4: Computation of yield for methanol

$$y_{CH_3OH} = \frac{s_{CH_3OH} \times x_{CO_2}}{100}$$

where n_i is the amount of molecule i after a particular time. n_i^0 is the initial amount of molecule i in the feed.

3.6.2 Adsorption Isotherms

The equilibrium state of an adsorbent is best described by the adsorption isotherm. Adsorption isotherm describes useful information pertaining to the adsorption process. From this information, properties of the adsorbent can be ascertained. This includes the total pore volume, (v_p), heat of adsorption, pore size distribution, surface area and so on. Adsorption isotherms are obtained by volumetric studies of the adsorbent during the adsorption process. In this regard, changes in mass of the adsorbent with respect to change in pressure at constant temperature are being measured. This analysis is usually conducted in a vacuumed environment. Hence, the change in adsorbent mass is related to the amount of adsorbate adsorbed. The obtained adsorption isotherm is the plot of the amount adsorbed with the relative pressure.

3.6.2.1 Classes of Isotherms

In describing the adsorption isotherm, there are basically five types of isotherms [11]. These are based on the BET parameters, relative pressure and BET constant. The relationship of these parameters is shown below:

Equation 3.5: BET equation [11]

$$\frac{1}{X\left[\left(\frac{P_0}{P}\right)-1\right]} = \frac{1}{X_m C} + \frac{C-1}{X_m C}\left(\frac{P}{P_0}\right)$$

where C is the BET constant, X_m is the monolayer capacity [volume of adsorbate at STP = standard temperature (273 K) and pressure (1 atm)] and P/P_0 is the relative pressure.

3.6.2.1.1 Type I Isotherm

This is a pseudo-Langmuir isotherm. It describes the adsorption process in monolayer (see Figure 3.4). It is a characteristic of microporous materials with 2 nm pore size. It is mostly obtained when the relative pressure is less than 1 and the BET constant is greater than 1.

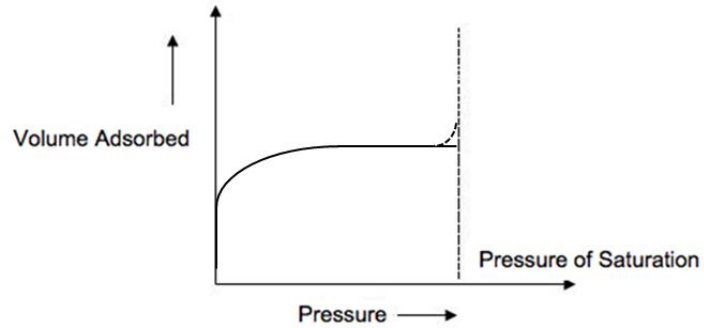

Figure 3.4: Type I adsorption isotherm [12]

3.6.2.1.2 Type II Isotherm

Unlike the Type I isotherm, this is the most common type of isotherm. It also occurs when the BET constant is greater than 1. The plot as shown in Figure 3.5 indicates the filling of adsorbate within the micropores at low pressure, the formation of monolayers at mid-pressures and occurrence of capillary condensation at high pressure.

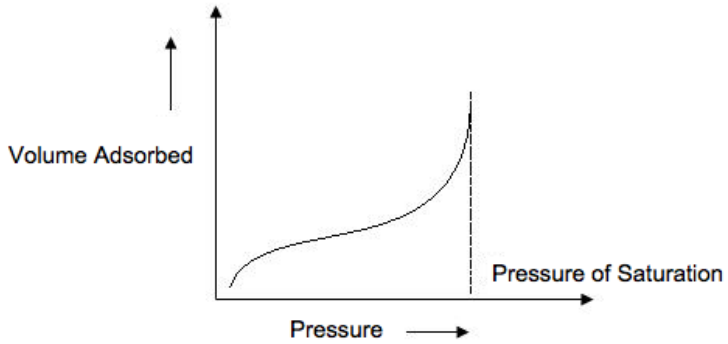

Figure 3.5: Type II adsorption isotherm [12]

3.6.2.1.3 Type III Isotherm

Unlike the Type I and II isotherms, type III isotherm (Figure 3.6) is obtained when BET constant is less than 1. It depicts the formation of multilayers with no signs of monolayers being formed.

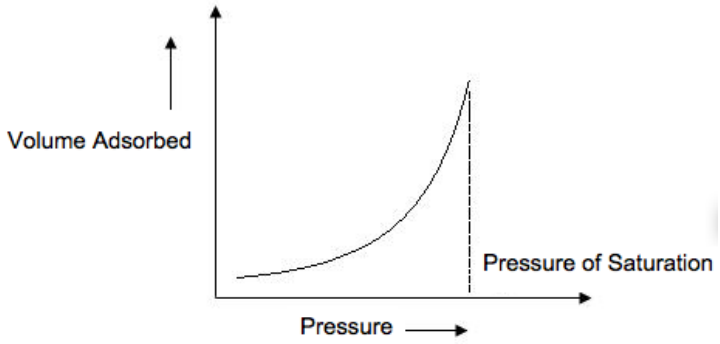

Figure 3.6: Type III adsorption isotherm [12]

3.6.2.1.4 Type IV Isotherm

This is a peculiar type of isotherm that basically occurs during capillary condensation (Figure 3.7). Below the saturation pressure of the adsorbate, the adsorbate condenses in the adsorbent pores. These are characteristics of mesoporic materials. Monolayers are formed at low pressures before the formation of multilayers

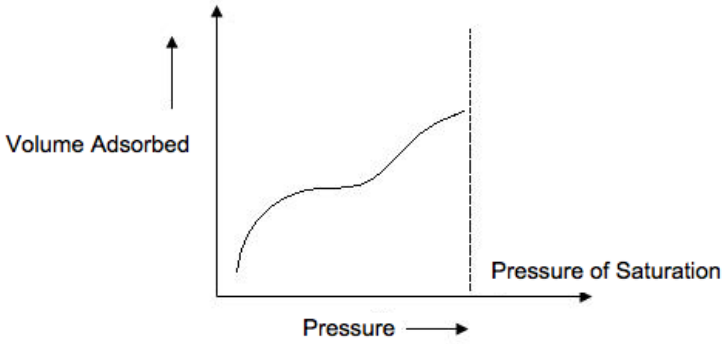

Figure 3.7: Type IV adsorption isotherm [12]

3.6.2.1.5 Type V Isotherm

This isotherm is similar to type IV but are not applicable to BET analysis (See Figure 3.8).

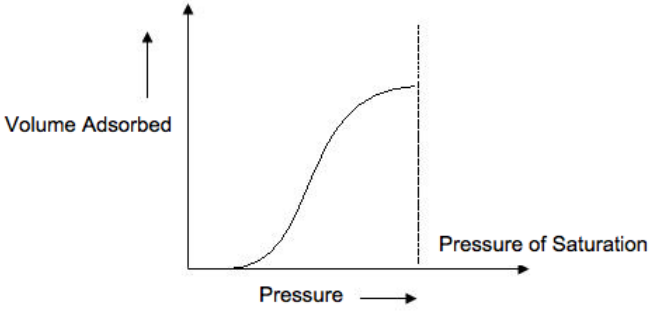

Figure 3.8: Type V adsorption isotherm

3.6.2.2 Adsorption Hysteresis

This is a phenomenon whereby the adsorption trend does not coincide with the desorption trend. As a result a hysteresis loop is formed. This is attributed to capillary condensation in the multilayer region. This is common with type IV and V isotherms, which are notable in mesoporic materials.

3.6.3 Adsorption Models

Adsorption models are mathematical expressions that describe the adsorption isotherms. There are series of formulated models to interpret the various adsorption isotherm types. This includes Langmuir, Freundlich, BET as described earlier and Toth. In this study, the models will be limited to Langmuir, Freundlich and Toth models.

3.6.3.1 Langmuir Model

This is the first theoretical adsorption model and is based on the gas kinetic theory. It describes chemisorption at the monolayer region. It is governed by four basic assumptions [13, 14]:

- all sites are homogeneous with equal energy,
- adsorbates are adsorbed on localised sites,
- only one adsorbate molecule is adsorbed on each site, and
- no interaction occurs between neighbouring adsorbate molecules.

Using chemical reaction equilibrium approach, the model can be thus derived:

$$A_{(g)} + S_{(s)} \leftrightarrow A.S_{(s)}$$

Forward reaction is adsorption process with rate = $k_{ads}p_A(1-\theta_A)$, and backward reaction is desorption process with rate = $k_{des}\theta_A$, where $\theta_A = \frac{q_A}{m}$. A is the adsorbate, S is the adsorption site, θ_A is fractional coverage, p_A is the partial pressure of A, m is the amount of adsorbate needed to thoroughly cover the adsorbent surface, q_A is the amount of adsorbate adsorbed at a given temperature and p_A, $k_{ads,\ des}$ are the adsorption and desorption rate constants.

At equilibrium the rate of desorption is equal to the rate of adsorption. Hence

$$k_{ads}p_A(1-\theta_A) = k_{des}\theta_A$$

Equation 3.6: Langmuir adsorption model

$$\therefore \qquad \theta_A = \frac{q_A}{m} = \frac{Kp_A}{1 + Kp_A}$$

Where K is the adsorption equilibrium constant = $\frac{k_{ads}}{k_{des}}$. It depends on temperature defined by the von't Hoff equation:

$$-RTln\ K = \Delta G_{ads} = \Delta H_{ads} - T\Delta S_{ads}$$

$$\therefore K = K_0 \exp\left(\frac{-\Delta H_{ads}}{RT}\right)$$

Where $K_0 = \exp\left(\frac{\Delta S_{ads}}{R}\right)$ and $-\Delta H_{ads}$ is the enthalpy change during adsorption, which is also defined as the heat of adsorption (Q_{ads}) and does not depend on coverage. K is also known as the affinity constant which describes the extent of adsorption on the surface of the adsorbent. von't Hoff's equation shows that it depends on temperature. The extent of adsorption decreases with increase in temperature. This is because as temperature increase, it provides adequate energy to favour desorption rather than adsorption.

3.6.3.2 Freundlich Model

Langmuir model was based on ideal cases. However, this model does not adequately define real cases of adsorption. Therefore, various empirical models were established to rectify the assumptions on which Langmuir model was based. One of such models is the Freundlich model:

$$\theta_A = kp_A^{\frac{1}{n}}$$

Where n and k are inversely dependent on temperature [15]. Freundlich equation is more accurate for moderate coverage since the model does not adequately account for low and high pressure adsorption as can be ascertained in Langmuir model. In Langmuir model, θ_A approaches Kp_A and 1 as p_A tends towards zero and infinity respectively. The theoretical implication of Freundlich model is that the adsorbent has heterogeneous surface with different sites having equal adsorption energies. Each site, i, is described using the Langmuir equation (Equation 3.6):

Equation 3.7: Freundlich adsorption model

$$\theta_i = \frac{K_i p_A}{1 + K_i p_A}$$

$$\theta_A = \sum_{i}^{n} \alpha_i \, \theta_i$$

Where α_i is the fraction of each site i.

3.6.3.3 Toth Model

The Toth model is an extension of the Freundlich model. It broadens the model by accounting for both low and high pressure adsorption. The equation is defined as [16]:

Equation 3.8: Toth adsorption model

$$\theta_A = \frac{q_A}{m} = \frac{Kp_A}{[1 + (Kp_A)^n]^{1/n}}$$

K and n are temperature dependent and are particular for each adsorbent-adsorbate pair [14]. n is a parameter that defines the heterogeneity of the adsorbent and is usually less than 1. When it is 1, it means the system is homogeneous as assumed by Langmuir model and Equation 3.8 returns to Equation 3.6. The greater the deviation of value of n from 1, the more heterogeneous the adsorption process is. This can partly be due to either the nature of the adsorbate and or adsorbent.

3.6.4 Adsorption Kinetic Models

One of the expected characteristics of a good adsorbent is a fast adsorption kinetics. This is because the efficiency and capacity of its adsorption in a high adsorbate flow stream is dependent on its adsorption rate. Establishing the kinetic behaviour of the adsorbents makes it possible to understand the interactions between the adsorbent and adsorbate. Series of kinetic models have been proposed for this purpose and are validated by finding the most suitable model that best fits with experimental data. To predict the kinetic behaviour of this adsorbent, the experimental results were simulated assuming pseudo first order (PFO), pseudo second order (PSO) [17], double-exponential [18] and Avrami kinetic models [19]. Although both PFO and PSO are related to surface reaction system, PFO model better explains low surface coverage adsorption [19] whereas PSO model best describes chemisorption or adsorption at high adsorbate loadings [20]. The double exponential model was considered because of its feasibility to explain the surface heterogeneity of the adsorbent accounting for two different

adsorption sites [9]. Additionally, it can partially elaborate the kinetic mechanisms associated with both pseudo-first and second order reactions. This mechanism can be categorised into a controlled slow phase intra-particle diffusion and a controlled fast phase surface reaction [17]. However, unlike the double exponential model, the Avrami model takes into account a fractional order kinetics, n [19]. This was adequately used for the description of adsorption processes on some adsorbents [21, 22], hence the reason for adopting the model for this study.

Equation 3.9: PFO model

$$x = x_e\left(1 - e^{-k_f t}\right)$$

Equation 3.10: PSO model

$$x = \frac{x_e^2 k_s t}{1 + x_e k_s t}$$

Equation 3.11: Avrami kinetic model

$$x = x_e\left(1 - e^{-k_A t^n}\right)$$

Equation 3.12: Double exponential kinetic model

$$x = x_e - \left(A_1 e^{-k_1 t} + A_2 e^{-k_2 t}\right)$$

where x and x_e represents the CO_2 uptake at a given time and equilibrium respectively, k_A, k_f and k_s are Avrami, PFO and PSO kinetic rate constants respectively, A_i and k_i, i=1,2 are pre-exponential factors and rate constants for the two adsorption sites respectively for double exponential kinetic model, and t is the time of adsorption. The obtained experimental data are fitted to the models and selecting the one with the best fit.

3.6.4.1 Error function and correlation coefficient

To determine the suitability of each model, an error function (Err) and correlation coefficient (R^2) defined by Equation 3.13 and 3.14 were applied:

Equation 3.13: Error function equation

$$Err(\%) = \sqrt{\frac{\sum_{j=1}^{N}\left[\frac{x_{j,\exp} - x_{j,\mathrm{mod}}}{x_{j,\exp}}\right]^2}{N-1}} \times 100$$

Equation 3.14: Correlation coefficient equation

$$R^2 = 1 - \left(\frac{\sum_{j=1}^{N}\left(x_{j,exp} - x_{j,mod}\right)^2}{\sum_{j=1}^{N}\left(x_{j,exp} - \overline{x_{J,mod}}\right)^2}\right) \times \left(\frac{N-1}{N-p}\right)$$

where x_{exp} and x_{mod} are CO_2 uptake determined experimentally and computed using the model respectively, $\overline{x_{mod}}$ is the mean experimental data, p is the number of model parameters and N is the total number of experimental points. The most suitable model to describe the experimental data is one with the least Err and highest R^2 value.

3.6.5 Adsorption Capacity

CO_2 uptake capacity of the LDH samples was calculated by a mass balance over the sorption column using the stoichiometric time as shown in Equation 3.15 [19]

Equation 3.15: Evaluation of adsorption capacity

$$Q_{ad} = \frac{FC_i t_s}{M_{ad}}$$

where Q_{ad} is the amount of CO_2 adsorbed, F is the total molar flow rate, C_i is the concentration of the adsorbate in the inlet stream, M_{ad} is the mass of adsorbent in the packed column, and t_s is the stoichiometric time computed using Equation 3.163.16

Equation 3.16: Estimating the stoichiometric time

$$t_s = \int_0^{\infty}\left(1 - \frac{C_o}{C_i}\right)dt$$

where C_o and C_i are the concentrations of the adsorbate at the inlet and outlet stream respectively.

Reference

[1] S.O. Nitta Y., Ikeda Y., Okamoto Y. and Imanaka T. , Copper-Zirconia Catalysts for Methanol Synthesis from Carbon Dioxide: Effect of ZnO Addition to Cu-ZrO2 Catalysts, Catalysis Letters, 26 (1994) 345-354.

[2] S.-I. Fujita, Y. Kanamori, A.M. Satriyo, N. Takezawa, Methanol synthesis from CO2 over Cu/ZnO catalysts prepared from various coprecipitated precursors, Catalysis Today, 45 (1998) 241-244.

[3] G. J. Millar, H.I. Holm, P.J. R. Uwins, J. Drennan, Characterization of Precursors to Methanol Synthesis Catalysts Cu/ZnO System, J. Chem. Soc., Faraday Trans., 94 (1998) 593-600.

[4] C.I. Ezeh, X. Huang, X. Yang, C.-g. Sun, J. Wang, Sonochemical surface functionalization of exfoliated LDH: Effect on textural properties, CO2 adsorption, cyclic regeneration capacities and subsequent gas uptake for simultaneous methanol synthesis, Ultrasonics Sonochemistry, 39 (2017) 330-343.

[5] J. Wang, L.A. Stevens, T.C. Drage, C.E. Snape, J. Wood, Preparation and CO2 adsorption of amine modified layered double hydroxide via anionic surfactant-mediated route, Chemical Engineering Journal, 181-182 (2012) 267-275.

[6] N.D. Hutson, B.C. Attwood, High temperature adsorption of CO2 on various hydrotalcite-like compounds, Adsorption, 14 (2008) 781-789.

[7] C.P. Ogbuka, Development of solid adsorbent materials for CO2 capture, Chemical Engineering, University of Nottingham, Nottingham, UK, 2012.

[8] X. Zhao, X. Hu, G. Hu, R. Bai, W. Dai, M. Fan, M. Luo, Enhancement of CO2 adsorption and amine efficiency of titania modified by moderate loading of diethylenetriamine, Journal of Material Chemistry A, 1 (2013) 6208-6215.

[9] C.I. Ezeh, M. Tomatis, X. Yang, J. He, C.-g. Sun, Ultrasonic and Hydrothermal Mediated Synthesis Routes for Functionalized Mg-Al LDH: Comparison Study on Surface Morphology, Basic Site Strength, Cyclic Sorption Efficiency and Effectiveness, Ultrasonics Sonochemistry, DOI https://doi.org/10.1016/j.ultsonch.2017.07.013.

[10] A. Fathy, O. Elkady, A. Abu-Oqail, Synthesis and characterization of Cu–ZrO2 nanocomposite produced by thermochemical process, Journal of Alloys and Compounds, 719 (2017) 411-419.

[11] H. Nina, A.R. Barron, BET Surface Area Analysis of Nanoparticles, Rice University, Houston TX, 2011.

[12] S. Brunauer, L.S. Deming, W.E. Deming, E. Teller, On a Theory of the van der Waals Adsorption of Gases, Journal of the American Chemical Society, 62 (1940) 1723-1732.

[13] D.M. Ruthven, Principles of adsorption and adsorption processes, Wiley, NY, USA, 1984.

[14] D.D. Do, Adsorption analysis: Equilibria and Kinetics, Imperial College Press, London, UK, 1998.

[15] T.-C. Huang, L.-T. Cho, RELATIONSHIPS BETWEEN CONSTANTS OF THE FREUNDLICH EQUATION AND TEMPERATURE FOR GASEOUS ADSORPTION, Chemical Engineering Communications, 75 (1989) 181-194.

[16] F.D. Iruretagoyena, Supported Layered Double Hydroxides as CO2 Adsorbents for Sorption-enhanced H2 Production, Springer International Publishing, London, UK, 2016.

[17] K.L. Tan, B.H. Hameed, Insight into the adsorption kinetics models for the removal of contaminants from aqueous solutions, Journal of the Taiwan Institute of Chemical Engineers, 74 (2017) 25-48.

[18] S. Loganathan, M. Tikmani, A. Mishra, A.K. Ghoshal, Amine tethered pore-expanded MCM-41 for CO2 capture: Experimental, isotherm and kinetic modeling studies, Chemical Engineering Journal, 303 (2016) 89-99.

[19] R. Serna-Guerrero, A. Sayari, Modeling adsorption of CO2 on amine-functionalized mesoporous silica. 2: Kinetics and breakthrough curves, Chemical Engineering Journal, 161 (2010) 182-190.

[20] J.M. Borah, J. Sarma, S. Mahiuddin, Adsorption comparison at the α-alumina/water interface: 3,4-Dihydroxybenzoic acid vs. catechol, Colloids and Surfaces A: Physicochemical and Engineering Aspects, 387 (2011) 50-56.

[21] E.C.N. Lopes, F.S.C. dos Anjos, E.F.S. Vieira, A.R. Cestari, An alternative Avrami equation to evaluate kinetic parameters of the interaction of Hg(II) with thin chitosan membranes, Journal of colloid and interface science, 263 (2003) 542-547.

[22] A.R. Cestari, E.F.S. Vieira, G.S. Vieira, L.E. Almeida, The removal of anionic dyes from aqueous solutions in the presence of anionic surfactant using aminopropylsilica—A kinetic study, Journal of Hazardous Materials, 138 (2006) 133-141.

CHAPTER FOUR

CATALYSTS FOR METHANOL SYNTHESIS: STUDY OF SYNTHETIC ROUTES, CALCINATION TEMPERATURE AND HEATING RATE ON SYNTHESIS OF CuO/ZrO_2

Abstract

The thermal characteristics of Cu-based catalysts for CO_2 utilization towards the synthesis of methanol were analysed and discussed in this study. The catalysts were prepared by various methods including impregnation (IM), co-precipitation (CP) and deposition precipitation (DP), characterised using SEM, BET and TG-DTG-DSC. Calcination of the catalysts facilitated the mixture of the Cu catalyst with the respective support bolsters the formation of intermolecular oxo-bridges due to the thermal stability of the catalysts. The characterisation analysis clearly reveals that the thermal performance of the catalysts was directly related to the increase in calcination temperature but this temperature was capped at 673K with denaturing of the catalyst occurring above the temperature. For all the given preparation methods, comparisons of different synthesised catalysts based on the Cu-loading indicate that the performance trend can be described by: CP>DP>IM. The Cu-loading and heating rate were found to affect the thermal characteristics of the catalysts.

Keywords: *Carbon dioxide, Hydrogenation, Catalysts, Methanol synthesis.*

4.1 INTRODUCTION

Methanol, a widely used chemical, can be synthesised from the hydrogenation of CO_2 as shown in Reaction Scheme 4.1 [1,2]. However, the yield of methanol production is lower when compared to that via syngas production [2].

$$CO_2 + 3H_2 \rightarrow CH_3OH + H_2O, \Delta H_{298\,K} = -49.5\ KJmol^{-1}$$

Reaction Scheme 4.1: Methanol synthesis from hydrogenation of CO_2

As shown in the reaction above, methanol production can be favoured by the decrease and/or increase in reaction temperature and/or pressure respectively. Despite this, formation of other hydrocarbons is also likely. Consequently, the need for a controlled reaction is indispensable. This is facilitated with the use of selected promoters and catalysts with suitable thermal stability [2-9]. Commonly used catalysts for CO_2 hydrogenation to methanol are Cu-based catalysts and have aided various investigations in developing novel catalysts for CO_2 hydrogenation process [3-5, 10, 11]. Cu is treated with several modifiers, which help to facilitate the formation and stabilization of the catalyst. Yoshihara and Campbell [12] demonstrated the stabilization of Cu-based catalysts by impregnating it with ZnO. The stability was attributed to the dispersion of Cu catalyst due to the free electron pair oxygen lattice present in the modifier. This theory was buttressed using a proposed dynamic micro-kinetic model to kinetically study the morphological changes and its effect on a Cu-ZnO catalyst during CO_2 hydrogenation [13]. Aside supporting the purported theory, the study also posited that the interfacial presence of vacant oxygen lattice was affected by the morphological change in the catalyst. This was considered to be one of the reasons for the poor dispersion of Cu in methanol formation using wet Pd impregnation [14, 15]. In conclusion, it is posited that the reduction of the catalysts active site favoured the hydrogenation process as a result of the increased hydrogen spill over on the surface active site.

Another promoter commonly studied for methanol synthesis via CO_2 hydrogenation is zirconium. The element in the form of ZrO_2 also improves the catalytic activity and methanol selectivity [16, 17]. This was also explained by the enhanced dispersion of Cu supported by the adsorbed hydrogen spill-over mechanism as shown in Figure 4.1. However, the rate of water adsorption was reduced in the presence of other elements like aluminium and gallium.

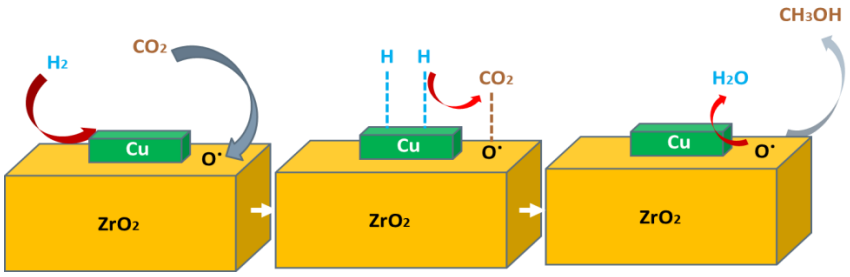

Figure 4.1: Hydrogen spill-over mechanism in CO2 hydrogenation for methanol synthesis using Cu/ZrO_2 catalyst.

Another notable catalyst aside Cu-based is the Pd catalyst [18]. The reaction dynamics is also defined by the hydrogen spill-over mechanism as shown in Figure 4.1. This reaction produces intermediates, formate species, which results to methanol formation on further hydrogenation [19]. CO_2 hydrogenation process dynamics and kinetics have been difficult to comprehend especially the activation of CO_2 over the surface sites of the catalyst and its relationship with the Cu nature of the of the catalyst [20]. Borodko and Somorjai suggested that CO_2 activation occurred at the copper-oxide interface [21], as also supported by the hydrogen spill-over mechanism [19, 22]. However, this is dependent on nature of the Cu species which was observed to exist as Cu metal [23] and Cu^+ [24]. While the Cu phase nature changes with various supports and promoters, the spatial and electronic configuration definition of the active sites will aid in defining the best suitable catalyst in terms of selectivity and activity [25].

The hydrogenation of CO_2 to produce methanol has been proposed to occur in either two reaction pathways: Reverse Water Gas Shift (RWGS) [26] or formate [27] mechanism. Both mechanisms transpires with the emission of CO as by-product, supporting the results of previous studies [28]. In RWGS reaction route, CO results as a by-product of the synthesis reaction, while in formate mechanism, it results from the decomposition of methanol [29]. This mechanism was supported by Yang et al. [30] and the limiting reaction is the hydrogenation of formate and dioxomethylene. However, the RWGS reaction route was also observed in this investigation, but it was estimated to occur at a faster magnitude than the formate mechanism owing to the presence of unstable formyl intermediates which continuously dissociates to CO and H atom on Cu catalyst. In other findings, it was detected that both mechanisms contributed in the hydrogenation mechanism on a Cu/ZrO_2 catalyst. Nonetheless, other factors like thermal and oxygen bond-strength [30] and pH of the adjacent group of the catalysts [31] contributed to the catalyst performance.

This paper aims to analyse the thermal characteristics of Cu-based catalysts for CO_2 utilization towards the synthesis of methanol. Catalysts were synthesised via various routes: impregnation (IM), co- (CP) and deposition (DP) precipitation. Characterization of prepared catalysts was conducted using XRD, TPD (CO_2 and H_2), SEM, BET and TG-DTG-DSC and the effects of these synthetic routes and Cu-loading on thermal stability, surface morphology and chemistry, copper dispersion and structure on the support, methanol synthesis were investigated. In addition, to further improve the thermal strength of the catalyst by bolstering the formation of intermolecular oxo-bridges, the catalysts were calcined and the impact of calcination temperature on the thermal performance of the catalyst was also studied. Furthermore, the impact of heating rate on the thermal characteristics of the catalysts was measured.

4.2 EXPERIMENTAL

4.2.1 Preparation of catalyst - Cu/ZrO_2

In the preparation of this catalyst, the zirconia aerogel was first synthesized. This was carried out by adding 0.17M $ZrOCl_2 \cdot 8H_2O$ solution and 0.2M NH_4OH solution dropwise respectively in a beaker containing 100ml of deionized water while sustaining the pH at 8.25. The precipitate was then filtered and washed with deionised water before being washed by ethanol to inhibit further reaction [32]. Afterwards, the formed aerogel is calcined at 523 K, 573 K and 623 K for 4 hours to examine the impact of calcination temperature on the support. The prepared aerogels at different calcination temperatures are labelled as ZrO_2-523, ZrO_2-573 and ZrO_2-623 respectively. The Zirconia aerogel was then used to synthesis the catalysts via deposition precipitation (DP) and impregnation (IM) methods in the CuO/ZrO_2 ratio of 10/90, 30/70, 40/60 and 90/10 as follows:

4.2.1.1 Deposition Precipitation: This was synthesized by the direct precipitation of 0.1M NaOH solution and 0.1M $Cu(NO_3)_2$ solution in the zirconia aerogel suspended solution. This reaction was sustained at a pH of 7.0; after which, the precipitates were filtered, washed with distilled water, dried at 383K (overnight) and calcined at 623K for 4 hours. This sample is labelled as CZr-DP.

4.2.1.2 Impregnation: The zirconia aerogel was impregnated with 0.1M $Cu(NO_3)_2$ solution with a volume 10% more than the impregnating volume before being filtered, dried and calcined as in (a) above. This sample is labelled as CZr-IM.

4.2.1.3 Co-precipitation: Unlike the other methods, without the use of the aerogel, the CP catalyst was prepared by a reaction of 0.17M mixed reaction of $ZrOCl_2$ and $Cu(NO_3)_2$ and 0.1M NaOH solution while sustaining the pH at 7.0. After which, the precipitates were filtered, washed, dried and calcined as in (a) above. This sample is labelled as CZr-CP.

4.2.2 Catalyst Characterization

The support and supported catalysts in the as-synthesised and calcinated form were characterised using a range of physicochemical techniques: Scanning Electron Microscope (SEM), Brunauer-Emmett-Teller (BET), Temperature-Programmed Desorption (TPD), X-ray Diffraction (XRD), Thermal Gravimetric Analysis (TGA), Differential Scanning Calorimetry (DSC) and Differential Thermal Analysis (DTA). Detailed description of the characterisation techniques are explained in section 3.5. TGA, DSC and DTA details are provided in section 3.3. Average crystallite size was estimated using the Scherrer's formula:

Equation 4.1: Scherrer's Formula

$$d = \frac{0.9\lambda}{\beta \cos\theta}$$

where d is the crystallite size (nm), λ is the radiation wavelength (nm) = 1.5406 nm in this case, β is the full width at half maximum (radians) and θ is the Bragg's angle of the maximum intense peak (degrees) [33].

4.2.3 In-situ GC-FID Analysis

The performance of the catalysts towards methanol synthesis was assessed in a continuous flow fixed bed reactor. First, 0.5g of the catalyst was reduced at 623 K in H_2/N_2 (10/90 vol%) environment for 3 hr at atmospheric pressure before being cooled to room temperature. The reactant gas H_2/CO_2 (molar ratio = 3:1) under operating conditions of 3 MPa, 623 K and GHSV = 3100 hr^{-1}. The effluent was analysed online using an Agilent gas chromatograph (GC) 7890A with the transfer line from the reactor to the GC preheated at 373 K to avoid condensation of effluent products. TCD was used to measure N_2, CO and CO_2 gases while organic compounds were studied using the flame ionization detector (FID). From this test, catalytic conversion and selectivity were computed using mass balance and resulting steady-state values (SSV). SSV was computed as an average of three tests over a period of 3 hr of continuous operation. CO_2

conversion (x_{CO_2}), selectivity (s_i) and yield (y_i) (where i is the molecule of interest) were computed as follows:

Equation 4.2: CO_2 conversion computation

$$x_{CO_2} = \frac{n_{CH_3OH} + n_{CO}}{n^0_{CO_2}}$$

Equation 4.3: Methanol and carbon monoxide selectivity computation

$$s_{CH_3OH} = \frac{n_{CH_3OH}}{n_{CH_3OH} + n_{CO}}$$

$$s_{CO} = \frac{n_{CO}}{n_{CH_3OH} + n_{CO}}$$

Equation 4.4: Computation of yield for methanol

$$y_{CH_3OH} = s_{CH_3OH} \times x_{CO_2}$$

4.3 RESULTS AND DISCUSSIONS

4.3.1 Variation of Support's Particle size and Porosity on Calcination Temperature

The ZrO_2 support prepared via normal precipitation and different calcination temperatures are compared in Table 4.1. The obtained result shows the effect of calcination temperature on the physicochemical properties of the support. A reductive change in the surface area and volume was witnessed with an increase in the calcination temperature. The pore size also exhibited same trend although it witnessed an increase at 623K calcination temperature compared to that at 573K. A contrary trend was observed for the particle size as the temperature increased [34, 35]. This tends to bolster the results of the SEM analysis (Section 4.3.2) and is attributed to the formation of intermolecular oxo-bridges leading to molecular catenation and increase in particle sizes [36]. Zirconium exists as metal hydrates in solution and is hydrolyzed by NH_4OH to form oxides or hydroxides depending on the pH of the precipitant. When dried and calcined, intermolecular hydroxyl bonds are broken resulting to agglomeration/aggregation. However, as the calcination temperature is increased, heat transfer to the support bulk is buttressed

culminating to improved intermolecular dehydration and subsequent agglomeration (Reaction Scheme 4.2). This tends to result to the increased density of larger agglomerates and particle size observed in the SEM and BET analysis respectively.

$$2ZrOCl_2 + 3NH_4OH \rightarrow 3NH_4Cl + ZrO(OH)Cl + ZrO(OH)_2$$

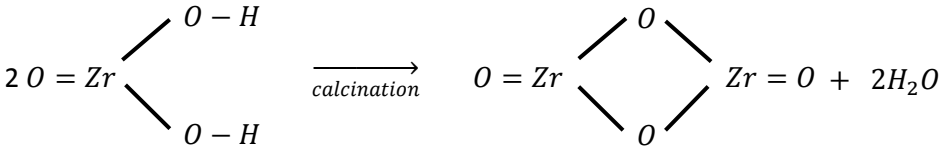

Reaction Scheme 4.2: Synthesis of Zirconia support using ammonia solution

The adsorption/desorption isotherms (Figure 4.2) of the calcined zirconia support at different calcination temperatures all showed a similar trend with an initial formation of monolayer at relative pressure < 0.2 before forming a multilayer resulting from capillary condensation, a typical characteristics of mesopore materials. A decreased adsorption capacity of the support with rise in calcination temperature was also detected with hysteresis effect spanning over a wider pressure range at low temperatures compared to the higher temperatures. From Figure 4.2, at a calcination temperature of 523K, the peak of hysteresis occurs ~0.5 relative pressure and spans across $0.4<\frac{p}{p^o}<0.65$ when compared to ~0.45 (span = $0.4<\frac{p}{p^o}<0.55$) for the other temperatures (573 and 623K). This effect can be explained by the pore distribution result of the support species. At 523K, pore size of 2-4nm accounted for 71% of the distribution against 84% and 85% at 573K and 623K respectively (see Table S4.1, Appendix A). In conclusion, at a lower calcination temperature, the surface area and adsorption capacity of the support is high compared to higher calcination temperatures. However, the hysteresis effect is large owing to the wider spread pore distribution.

Table 4.1: BET results of ZrO_2 aerogel at different calcination temperatures

Sample (ZrO_2)	**T_c (K)**	**S_{BET} (m^2/g)**	**V_p (cm^3/g)**	**d_p (nm)**	**Adsorption average pore width (nm)**
ZrO_2-523	523	251.84	0.17	23.82	2.65
ZrO_2-573	573	229.26	0.14	26.17	2.36
ZrO_2-623	623	193.12	0.12	31.07	2.49

T_c = Calcination Temperature

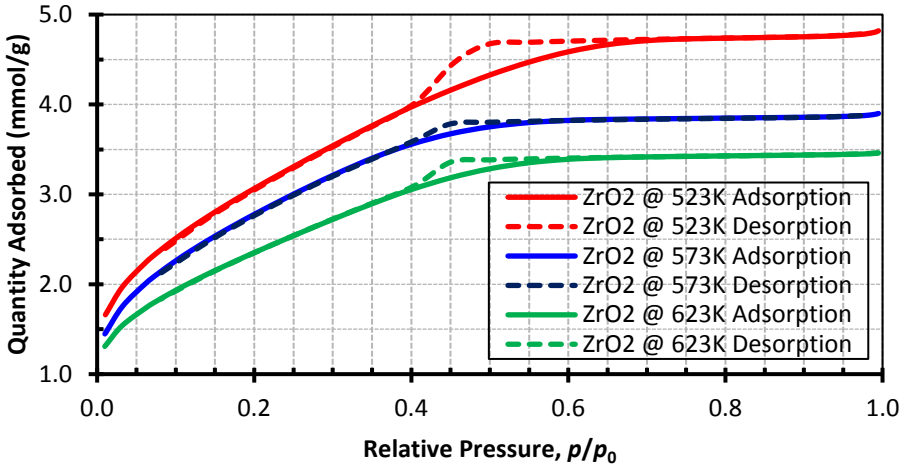

Figure 4.2: BET Isotherm plot of Zirconia support from different calcination temperatures.

4.3.2 Surface Morphology

4.3.2.1 Dependence on Preparation Method

Doping the support with Cu via the considered different preparation method resulted to a change in the surface composition of the initial zirconium support. Although, the impregnated support showed similar semblance to the original support, it however showed that the agglomerated particles are more adhered or embedded to the support than in the undoped support (Figure 4.3a and b). This can be attributed to the surface reaction between the Cu and ZrO_2 support, which is subject to further investigation. With regards to the surface reaction between these compounds, the SEM images also depicts that this is affected by the preparation method as shown in the surface structure of the catalyst. From a series of SEM images, the support surface of the CP and DP catalysts were more densely agglomerated with particles. On the DP catalyst, a cluster of spongy particles with average pore size ranging from ~10-50 nm dominated the deposited particles on the surface of the support (Figure 4.3d). On the contrary, the CP catalysts showed a combination of different sized particles on the supports surface. This included sparsely distributed spongy-shaped particles (similar to that in DP), irregular shaped particles (similar to that in IM and the support) and some block-structured/tetragonal shaped particles with 1-4μm equivalent diameters (Figure 4.3c). This explains that the texture quality of the catalyst is basically associated with the preparation method. While the adoption of NaOH as a precursor promotes the deposition of CuO on the surface of ZrO_2 in the DP synthetic method, the IM method embeds the particles.

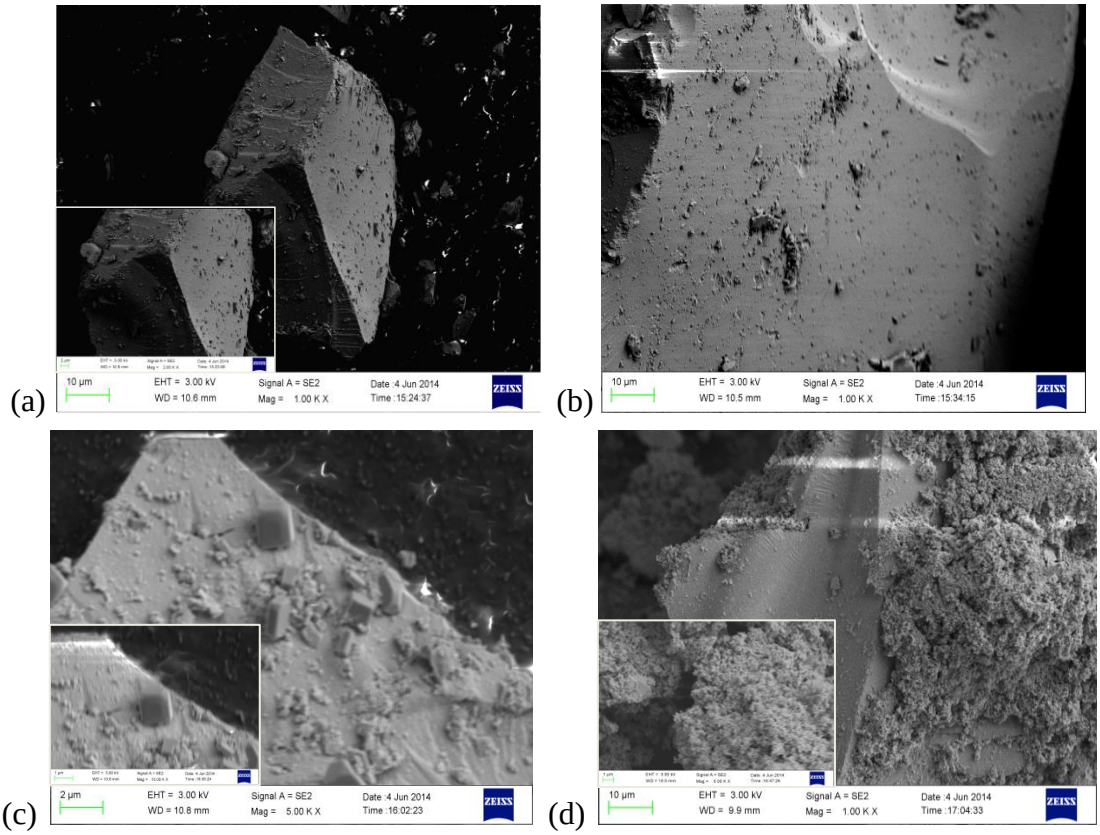

Figure 4.3: SEM image of the surface of the ZrO2 support doped with Cu at calcination temperatures of 623K prepared via (a) undoped ZrO2 support, (b) IM method, (c) CP method and (d) DP method.

4.3.2.2 Dependence on Calcination Temperature

The zirconium oxide is observed to be a mesoporous spongy material with few macropores (Figure C4.1, Appendix C). As seen in the image, this structure is covered by a smooth layered surface with particle agglomeration. The particles adhered to the surface of the support varied with size at the various calcination temperatures considered. Several SEM images were taken of all zirconia specimens and no significant differences in grain size or grain size distribution were observed. Although, similar in structure at the various temperatures, however a distinct difference is observed with respect to the particles. It is found that the agglomerated particles are predominated by small sized particles (< 20 nm) and are fewer at lower temperature of 523 K. But as the temperature increases, the number of particles attached to the parent support increases (Figure 4.4a) with the formation or presence of larger particles (> 20 nm) on the surface. At a further increased temperature of 623 K (Figure 4.4b), more larger particles were situated on the surface of the support but with the smaller particles still dominating. This

phenomenon can be attributed to the sintering effect caused by increase in calcination temperature which promotes particle agglomeration.

(a) 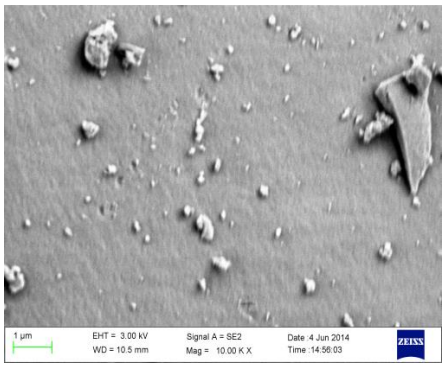

(b) 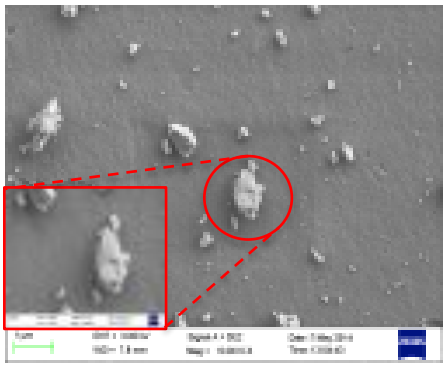

Figure 4.4: SEM image of agglomerated particles on the surface of the Zirconium support at various calcination temperatures: (a) 573K and (b) 623K.

4.3.3 Thermal Characteristics

4.3.3.1 Particle Agglomeration of the Calcined Support from loss of Physisorbed Moisture

The synthesized supports were also characterized via TG-DTG analysis and its moisture composition determined (Table C4.2, Appendix C). From the thermogravimetric results shown in Figure 4.5, it is observed that all support specimen showed a one-step decomposition indicating the weight loss due to interstitial moisture dehydration but with the moisture content increasing with decrease in calcination temperature. This varied from ~13% at 573K and 623K to ~20% at 523K. However, the 573K-calcined support showed an insignificant second step at temperature of 773 K. Although unclear from the TG plot, it is quite obvious from the DTG plot. However, this can be overlooked as a second step as it is attributed to the presence of interstitial residual contamination like nitrates.

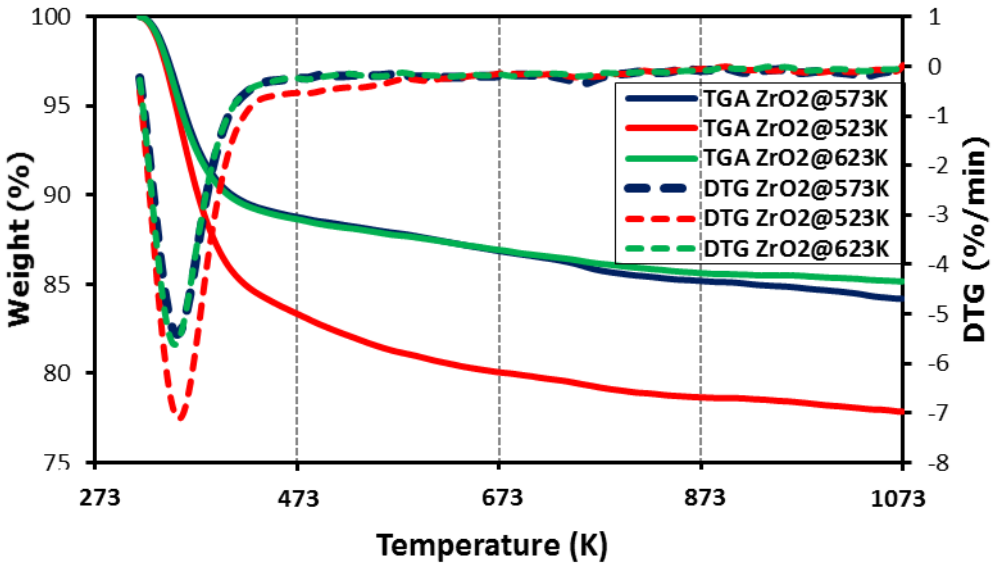

Figure 4.5: TG-DTG analysis of zirconia support from different calcination temperature.

The DTG results displayed the rate of weight loss within the tested decomposition temperature. In addition, it also portrays how loosely bound the water molecules are to the support. From the results, it shows that the support from 523 K-calcination temperature continued to lose moisture till a temperature of 643 K. Prior to this, it lost moisture at a highest rate from 303 – 423 K but slowly lost moisture from 423 – 643 K. The former depicts the loss of physisorbed moisture and the latter ascribed to the initialization of phase transformation resulting from the breakage of the Zr-OH bond forming intermolecular oxo-bridges as explained earlier [36]. However, the attained intermolecular dehydration temperature (T_{ID}) differ from that obtained in literature but corresponds to the 623 K suggested by Silva et al. [37]. Intermolecular dehydration temperature is considered to be the maximum temperature for complete loss of water molecules from the sample. Using this temperature, the interstitial moisture composition of the support was computed using the TGA result within a temperature range of 313 – 673 K (see Equation 4.5). This was computed using the stoichiometric ratio of moisture content to the dried residual support based on the formula $ZrO_2.xH_2O$ and assuming complete dehydration of the specimen (see Table C4.2).

Equation 4.5: Computation of interstitial moisture content

$$\frac{18x}{RMW_{ZrO_2}} = \frac{100 - RW_{TGA}}{RW_{TGA}}$$

where *x* denotes the number of moles of interstitial water molecule, RMW_{ZrO_2} is the relative molecular weight of zirconia aerogel and RW_{TGA} stands for the residual weight at 673 K. Calculating the values of *x* at the different residual weights obtained for the each ZrO_2 specimen, it is shown that *ca.* 2 moles of water molecule is attached to the zirconia support at 523 K-calcination temperature compared to approx. 1 mole H_2O molecule at 573 and 623 K. This quantifies the explanation relating the absence of water molecules to the initiation of particle agglomeration; hence, the increase in particle size and lower surface area.

4.3.3.2 Dependence on Preparation Method and Cu-loading

Using the 623 K-calcined ZrO_2 support as the foundation of the catalyst preparation, the catalysts were synthesized at different Cu loading and characterized. Surface chemical property depends on Cu loading and thermal pre-treatment. Having ascertained the effect of thermal pre-treatment on the support and hence its effect on the catalyst the results from the preparation methods will discern the effect of Cu loading on the catalyst. Using the impregnation, co-precipitation and deposition precipitation method as means of preparation, the impact of Cu loading and heating rate on the thermal stability of the catalyst is studied.

From the results from the IM catalyst, no significant effect was observed as all plot of the catalysts followed a similar trend with at different Cu loading. However, traceable amount of moisture was lost during dehydration step (300-378 K) as the Cu loading increased (see Figure 4.6). This trend is contrary to that obtained in the CP and DP preparation method (Figure 4.7 and 4.8 respectively) where the moisture content directly decreased with increase in Cu loading. One can suggest that the difference in trend with IM method is associated with selective adsorption of water molecules by the ZrO_2 support unlike the incorporation of Cu into the support via co-precipitation or deposition in CP and DP respectively. Hence, as the Cu loading increased, it can be fortuitously stated that the amount of water adsorbed increased which explains the continuous dehydration of CuO/ZrO_2 catalyst with Cu loading of 40% till a temperature of 673 K. Similarly, the DSC profile showed similar results for all composition. However, IM catalyst with 30% CuO showed the least energy flow across all temperature indicating a more thermally stable catalyst composition. Comparing the energy change at phase transformation, it is observed that its magnitude decreases with increase in Cu loading with change in peak phase transformation temperature ΔT_{TB}^{*} of about 15-17 K greater than that for the ZrO_2 support (see Table 4.2).

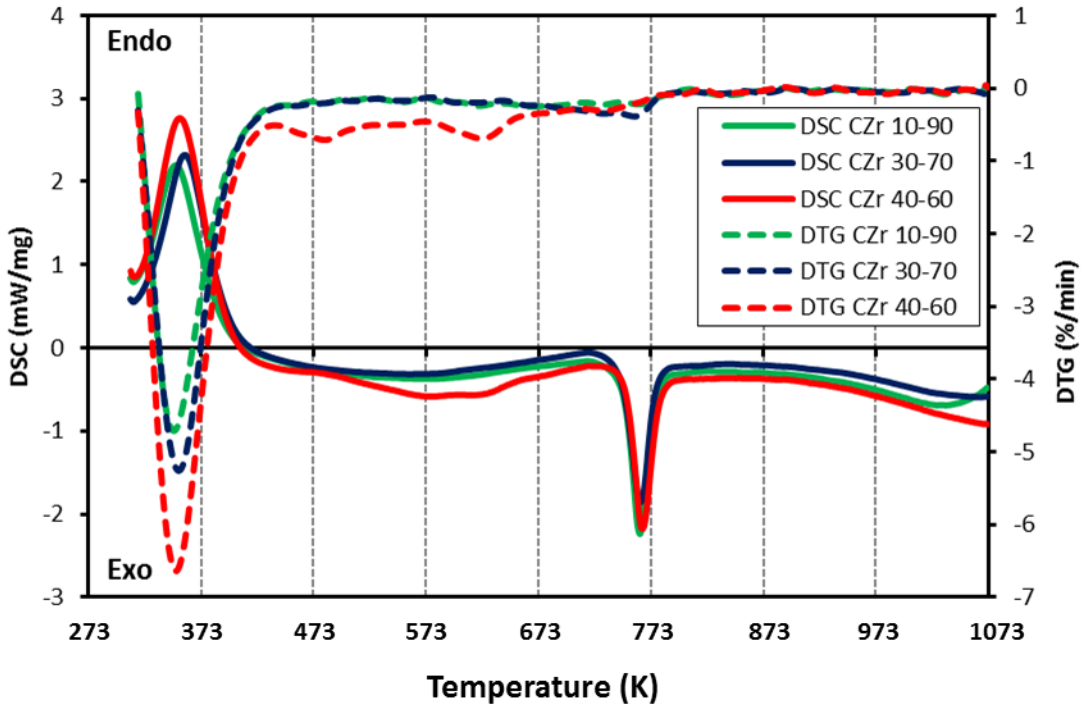

Figure 4.6: Thermal Characterization of IM Catalysts CuO/ZrO_2 at different Cu-loading.

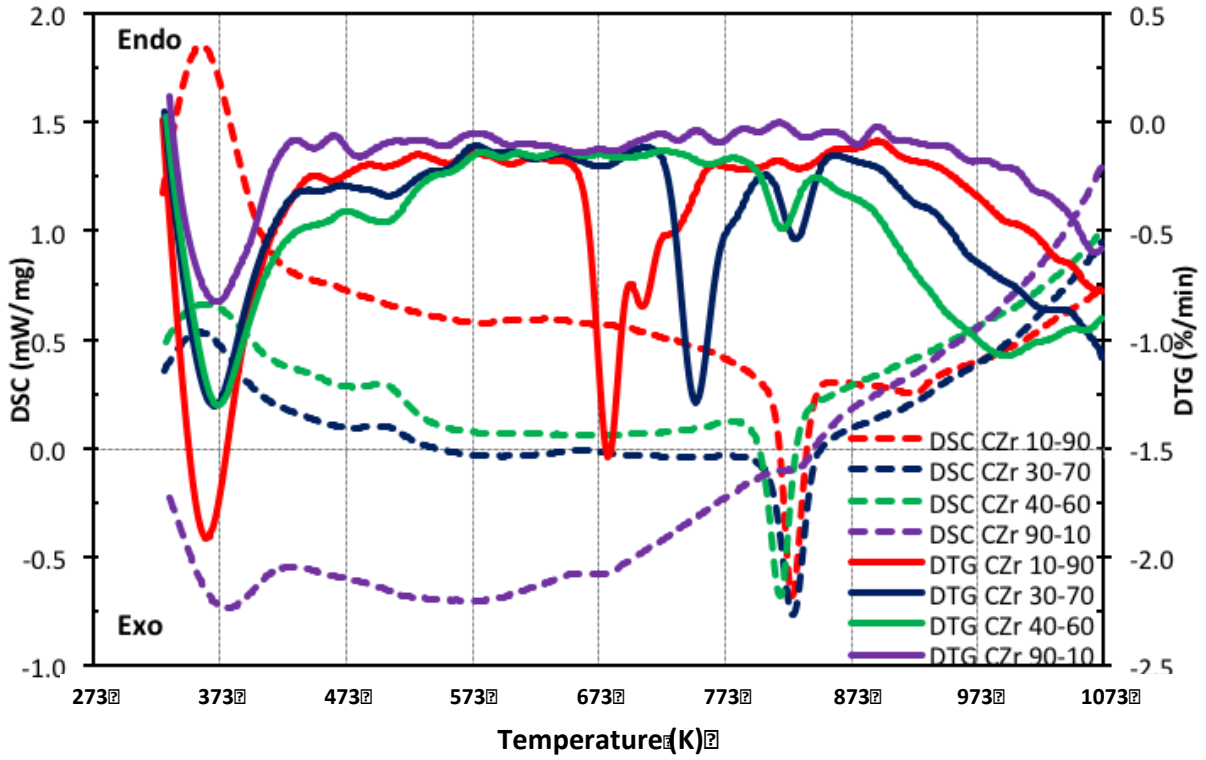

Figure 4.7: Thermal Characterization of CP Catalysts CuO/ZrO_2 at different Cu-loading.

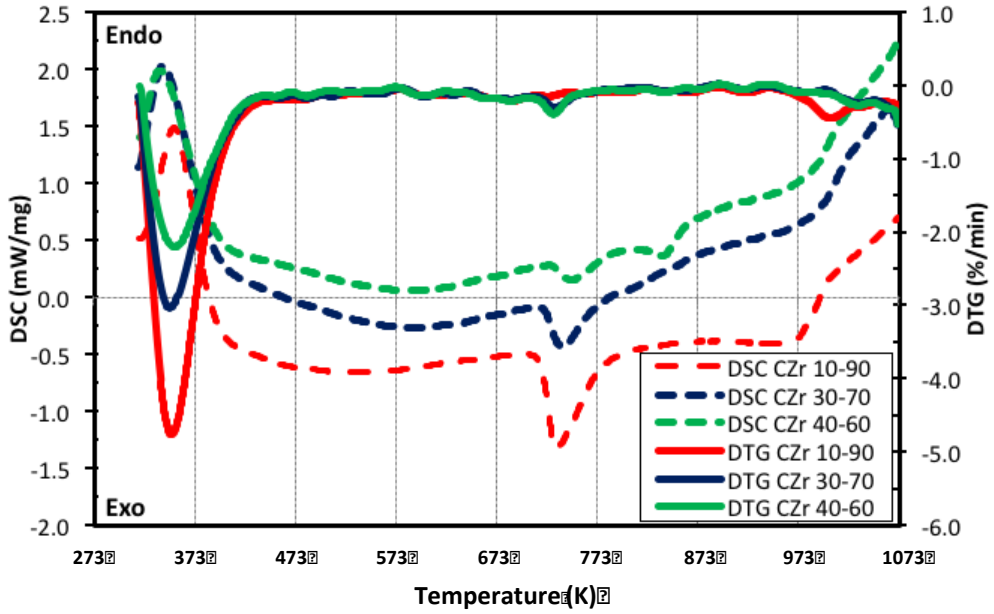

Figure 4.8: Thermal Characterization of DP Catalysts CuO/ZrO₂ at different Cu-loading.

Table 4.2: DSC results for ZrO_2 supports prepared at different calcination temperatures and CuO/ZrO_2 catalyst prepared via different methods

Sample	Wt_{Cu} (%)	T_c (K)	Heating Rate (K/min)	T_{TB} (K)		T_{TB}^* (K)	ΔT_{TB}^* (K)	ΔE (J/g)
				Range	Span			
ZrO_2	-	523	20	718 - 778	60	747.1	-	98.47
	-	573	20	738 - 780	42	753.8	-	106.40
	-	623	20	725 - 773	48	748.4	-	119.50
CZr-IM	10	623	20	738 - 783	45	763.1	14.7	116.20
	30	623	20	739 - 780	41	763.6	15.2	114.10
	40	623	20	739 - 782	43	765.1	16.7	110.30
CZr-CP	10	623	20	787 - 847	60	827.1	78.7	55.64
	30	623	20	783 - 726	57	827.8	79.4	48.66
	30	623	10	789 - 747	42	818.5	70.1	57.30
	40	623	20	780 - 833	53	827.3	78.9	52.25
	90	623	20	-	-	836.0	87.6	6.33
CZr-DP	10	623	20	700 - 781	81	732.9	-15.5	69.68
	30	623	20	707 - 765	58	739.2	-9.2	37.61
	40	623	20	713 - 777	64	752.4	4.0	14.93
				796 - 855	59	842.4	94.0	10.77

T_{TB}^* = Peak Transformation Base Temperature

ΔT_{TB}^* = based on T_{TB}^* of the support computed as the difference between T_{TB}^* of the catalyst and T_{TB}^* of ZrO_2 at 623 K

ΔE = Enthalpy change using Bezier baseline approximation from the TGA

Unlike the thermal characteristics results of the IM catalysts, a significant effect of Cu-loading was spotted in the CP catalysts. In these catalysts, two-step decomposition was observed for all Cu composition except for the 30% Cu loading where a three-step decomposition was seen (Figure 4.7). These decomposition steps can be attributed to the presence of moisture and interstitial impurities contaminating the catalyst like Cl^- and N-based compounds. The first step is attributed to moisture dehydration while subsequent steps are associated with Cl^- and NO_3^- decomposition respectively. The Cl^- was introduced from the precursor $ZrOCl.8H_2O$. As the ZrO_2 content reduces, the amount of Cl^- reduces as shown in the reduction of the DTG second decomposition step when the ZrO_2 content reduced from 90% to 70%. However, this is compensated with the introduction of NO_3^-, obtained from the precursor $Cu(NO_3)_2$. As the Cu loading increases, the NO_3^- also increases resulting to the initiation of the DTG third decomposition step witnessed in the 30% Cu-loading at a temperature of 823 K. Also noticed in the curves is the shifting of the second decomposition step peak temperature from 683 K at 10% Cu-loading to 753 K at 30% Cu-loading. This suggests that the Cl^- species strongly bonds on the surface of the catalyst as the Cu-loading increases. However, it was observed that the Cl^- decomposition peak decreases as the Cu-loading increases until it diminishes while the N-based compounds continue to gradually decompose all through the rest of the decomposition temperature. This trend was also reported by Prasad et al [36]. However, unlike the results of Prasad et al., this phenomenon commenced from the temperature range of 853 – 893 K depending on the Cu-loading compared to 773 K reported. The DSC results also correspond to those of IM catalysts with the 30% Cu-loading catalyst exhibiting the lowest heat flow all through the decomposition process. However, like the IM catalysts, the Cu-loading variation has no effect on the T_{TB}^*. Nonetheless, the CP preparation method shifted T_{TB}^* to the right by ~80% when compared to that of the support. This indicates that the preparation method boosts the transformation temperature of the catalyst when compared to the support.

The DP catalyst on the other hand showed a one-step thermal decomposition across all Cu-composition with an insignificant peak of the DTG curve at 723 K for 30 and 40% Cu loading and at 973 K for 10% Cu-loading. As explained earlier, this can be attributed to the presence of interstitial contaminations. With regards to the DSC curves, the 30 and 40% Cu based catalysts showed a lower heat flow with the 40% Cu catalyst predominating at low temperatures till 673 K. Beyond this temperature is a phase transformation for both specimens.

However, the 30% Cu catalyst showed a lower heat flow and displayed a more thermal stability than that of 40% Cu catalyst, which exhibited a second phase transformation peak at 842 K. In general, in all preparation routes, catalysts with Cu-loading of 30% displayed the lowest heat flow indicating a high thermal stability of this catalyst.

4.3.3.3 Dependence on Calcination of ZrO_2 Support

The DSC plot shows the amount of heat per unit mass of the support required to increase the temperature of the support. This plot is shown in Figure 4.9 below and shows a similar trend profile for the three ZrO_2 specimens. The first peak exhibits the endothermic desorption of moisture from 223 – 413 K with a peak temperature at 353 K. The second peak, similar to all three specimens, shows an exothermic phase transformation of the supports with the 523 K-calcined support having a broader transformation base temperature (T_{TB}) spanning over 60 K when compared to 40-50 K span of the higher temperatures (see Table 4.2). In addition, this points out the thermal threshold (718 K) of the supports before their degradation. The plot also shows the continuous exothermic transformation of the 523 K-calcined support beyond 773 K illustrating its thermal instability when compared to the latter. The 623 K-calcined support showed a more promising thermal stability in comparison to the 573 K-calcined support owing to its ~0 mW/mg heat requirement both before and after the phase transformation. Using the Bezier baseline approximation and a width of 37%, the enthalpy change at the phase transformation was obtained (Table 4.2). Despite the close proximity of the peak temperatures, the exothermic change in enthalpy increased with increase in calcination temperature. The enthalpy change reduced from -98.47 J/g for the 523 K-calcined support to -119.50 J/g for the 623 K-calcined support. This portrays that the formation of oxo-bridged zirconia intermolecules are associated with high energy density facilitating the supports thermal stability.

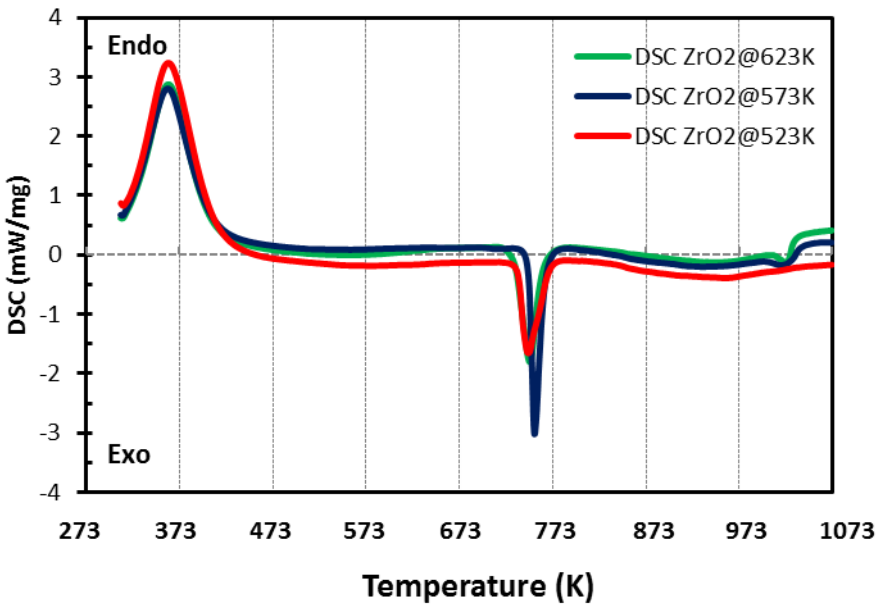

Figure 4.9: DSC analysis of zirconia support from different calcination temperature.

4.3.3.4 Dependence on Heating Rate

In all catalyst preparation method, the 30% Cu loading on ZrO_2 support showed better synergic characteristics in terms of energy density, thermal stability and structural composition. Based on this composition, the thermal properties of the three preparation methods are compared (Figure C4.2, Appendix C). The CP catalysts displayed the lowest moisture content but had the highest impurity present. However, the DSC curve shows that the catalyst is more stable than that of IM and DP catalysts given the low heat flow and T_{TB}^{*} of 827.9 K compared to 739.4 K and 763.8 K of DP and IM catalysts respectively. Considering the effect of heating rate on this catalyst, the 30% Cu-based catalyst via CP preparation method was subjected to a heating rate of 10 K/min TGA analysis and the results compared to the initial heating rate, 20 K/min. Comparing both heating rates, it can be observed that at a high heating rate, there is an accelerated decomposition of the catalyst as shown by the red-continuous lines in Figure 4.10. This is discerned by the magnitude of the DTG all through the temperature range when compared to the blue lines (10 K/min). However, in terms of thermal stability, it is seen that the catalyst exhibited a more thermally unwavering decomposition at 10 K/min than at higher rate. This was the case at low temperatures till about 673 K. Beyond this temperature, the 20 K/min heating rate showed a more thermally stable catalyst than at lower heating rate. Nevertheless, this was momentary given the phase transformation of the catalysts at 783 K for

20 K/min but at 789 K for 10 K/min with the former having a larger phase transformation window of ~80 degrees as when compared to the ~40 degrees temperature window of the latter.

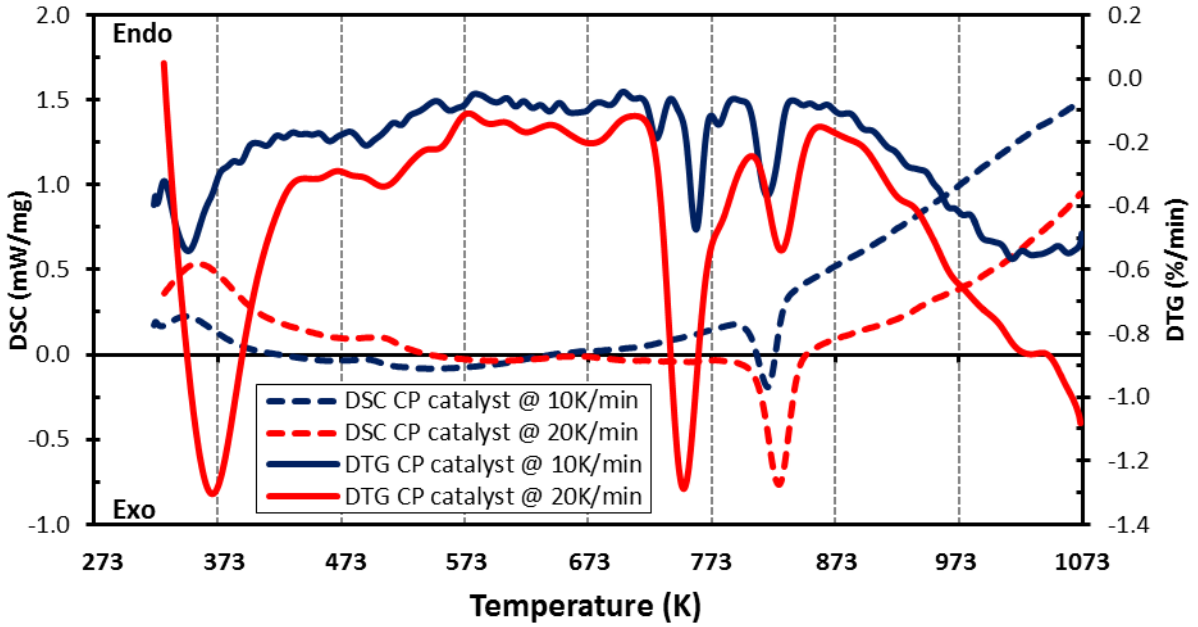

Figure 4.10: Effect of heating rate on CuO/ZrO_2 thermal characteristics

4.3.4 H_2 Desorption of Calcined Catalysts

4.3.4.1 Dependence on Preparation Method

Using the 623K-calcined ZrO_2 support with Cu-loading of 30%, the H_2-TPD pattern for the catalysts was studied based on the synthetic method (see Figure 4.11a). The desorption profile spanned across a temperature range 50 – 800 ^oC and displayed several adsorption states of H-species on the catalysts. These peaks are classed into two categories, low (130 – 300 ^oC) and high (400 – 500 ^oC) temperature peaks [38-40]. Desorption at low and high temperature region is ascribed to the release of H-species adsorbed on surface Cu sites and on surface ZrO_2 respectively. It is observed from Figure 4.a that the low temperature peak reduced in the following trend: DP > CP > IM. This is quantified in Table 4.3 and explains that the amount of Cu sites reduces in the same trend. However, CZr-CP showed the highest desorbed H_2 with a smaller temperature range at high temperature region indicating that the co-precipitation method is more suitable for promoting hydrogen-spillover mechanism. In addition, a mid-temperature adsorption region was also observed in the profile for CZr-CP. This can be partly explained to be a hybrid complex between CuO-ZrO_2 and H-species. Liu *et al.* [35] reported that CuO and ZrO_2 does not only undergo physical mixing but also involves chemical reaction

with an alteration in electron distribution, hence facilitating the reaction between the $CuO\text{-}ZrO_2$ and H-species.

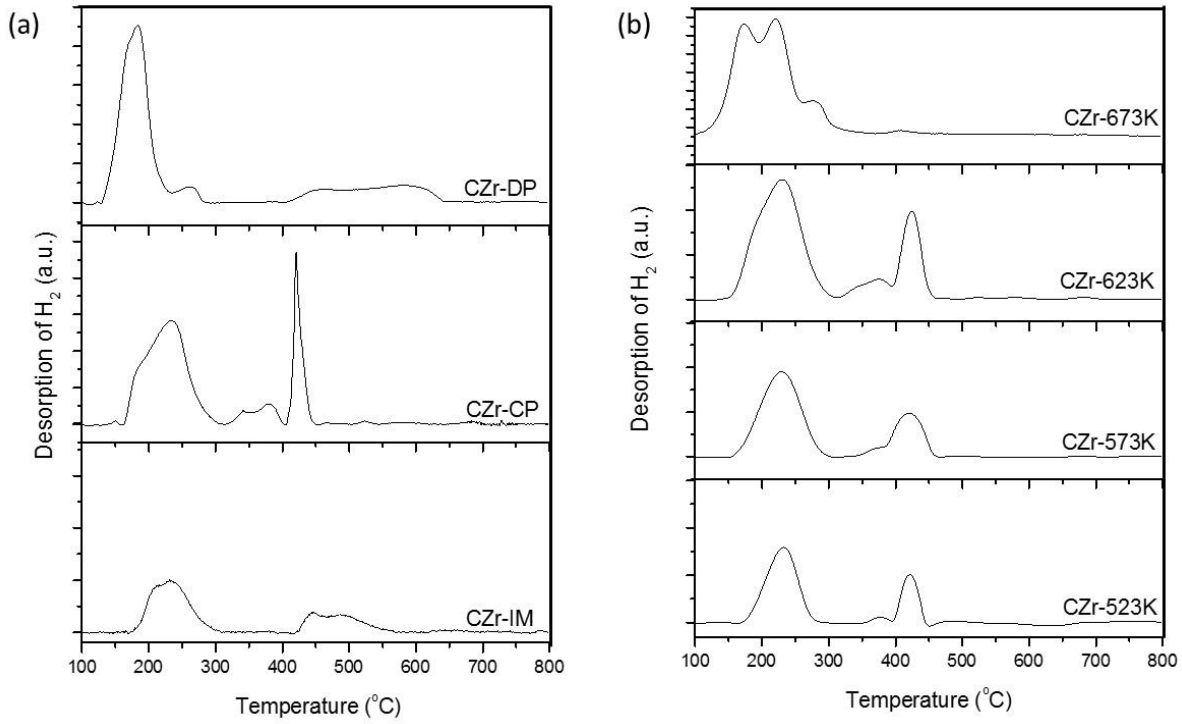

Figure 4.11: H_2-TPD pattern of (a) CZr catalysts prepared by different method. Catalyst composition: CuO/ZrO_2 = 30/70 (wt.%), (b) CZr catalysts prepared via co-precipitation method at different calcination temperatures compared to CZr catalyst calcined at 673 K (capped phase transformation temperature)

Table 4.3: Peak temperature and quantity of desorbed H_2 over calcined CZr catalysts at 623 K prepared by different methods

Sample	Low Region Desorption		Mid Region Desorption		High Region Desorption	
	Mid-Range Temp. (°C)	H_2 Desorbed (cm^3/g STP)	Mid-Range Temp. (°C)	H_2 Desorbed (cm^3/g STP)	Mid-Range Temp. (°C)	H_2 Desorbed (cm^3/g STP)
CZr-IM	231.93	7.27	-	-	445.27	4.37
CZr-CP	231.89	32.95	379.35	3.00	420.47	89.28
CZr-DP	224.34	76.36	-	-	525.27	10.29

4.3.4.2 Dependence on Calcined Temperature

Figure 4.11b shows the impact of calcination temperature on desorption of H_2 considering the co-precipitation synthetic method. It is observed that the calcination temperature affects the catalysts surface chemical properties. Therefore, this was studied at calcination temperatures of 523, 573 and 623 K. An increase in calcination temperature resulted to a corresponding

increase in area of the peaks obtained across the three desorption regions. From this finding, it can be suggested that increased calcination temperature increases the amount of Cu active sites. Result data are tabulated in Table 4.4. This is similar to reported results [35] and is ascribed to the formation of large CuO particles. The severity of particle aggregation as well as enlargement of crystallite sizes are characteristics of increase in calcination temperature. This is as a result of particle sintering during calcination, consequently leading to the increase in the number of Cu-species [34]. Additionally, an increase in calcination temperature led to a positive shift in temperature range for the low temperature region. Similar to results produced in literature, this phenomenon reveals the interaction between CuO and ZrO_2 [35]. This tends to elucidate the increase of H-species desorbed with increase in calcination temperature as a result of the enhanced CuO-ZrO_2 interaction. However, comparing these patterns with the suggested capped calcination temperature (673 K), it is noticed that low desorption region was highest at 673 K with little or no mid and high region desorption. This can be partly attributed to the limited interaction between CuO and ZrO_2.

Table 4.4: Peak temperature and quantity of desorbed H_2 over CZr catalysts with different calcination temperature

Sample	Low Region Desorption		Mid Region Desorption		High Region Desorption	
	Mid-Range Temp. (°C)	H_2 Desorbed (cm^3/g STP)	Mid-Range Temp. (°C)	H_2 Desorbed (cm^3/g STP)	Mid-Range Temp. (°C)	H_2 Desorbed (cm^3/g STP)
CZr-523K	222.15	20.92	378.99	0.72	420.45	45.23
CZr-573K	226.78	24.76	379.34	1.06	420.47	56.72
CZr-623K	231.89	32.95	379.35	3.00	420.47	89.28

4.3.5 Surface Basicity of Catalysts

4.3.5.1 Dependence on Preparation Method

The surface basicity of the catalysts were studied using the CO_2-TPD technique. The desorption profiles and data are shown in Figure 4.12a and Table 4.5 respectively. Generally, the basicity of metal oxides are categorized into three: weak, medium (or moderate) and strong basic strengths. In this study, these three zones are depicted at their corresponding temperature peaks ranging from 100-160 °C, 160-300 °C and > 300 °C respectively. Weak basic sites are associated with the surface hydroxyl (OH^-) group; whereas the moderate basic sites are related to metal-oxygen (M^{n+}-O^{2-}, where n+ is the valence of the metal) pair. The strong basic sites are attributed to the low coordination unsaturated oxygen (O^{2-}) and electronegative anions [40].

Figure 4.12a shows the deconvolution of the TPD profile into four or five Gaussian peaks. From the obtained results, it was observed that the weak and medium basic sites varied in the following trend: CZr-IM > CZr-DP > CZr-CP; while the strong basic sites varied in the opposite trend accordingly. This suggests that the preferential formation of these basic sites is dependent on the preparation method. Whereas the impregnation and deposition precipitation methods promotes formation of weak and medium basic sites, co-precipitation method facilitates the formation of basic sites with strong sites. This can be explained from Reaction Scheme 4.2 shown above which is the characteristic reaction mechanism for the impregnation and deposition precipitation method. Due to the prior preparation of ZrO_2 support, more hydroxyl groups and metal-oxygen (Zr^{4+}-O^{2-}) pair are alleged to be present before the impregnation of CuO into the support [41]. Hence, increasing the amount of weak and moderate basic sites in CZr-IM and CZr-DP respectively. However, the strong basic sites was observed to be highest in CZr-CP. Furthermore, these basic site is observed to have a wider temperature span with three desorption profiles suggesting an increase in the strength of the basic sites. This is the effect of complex overlapping of several CO_2 desorption profiles from basic sites with different strengths [41]. This can be suggested to be associated with the presence of attached Cl^- species connected with the preparation method (see Reaction Scheme 4.3). Unlike the DP and IM synthetic methods, the lack of using ammonium solution in the synthesis of the catalyst can be suggested to deposit more Cl^- species on the catalyst surface. Subsequently, the electron density of basic sites tends to increase due to aggregates of unsaturated Cl^- and O^{2-} [40].

$$2\ ZrOCl_2 + Cu(NO_3)_2 \rightarrow 2\ ZrO(NO_3)Cl + CuCl_2$$

Reaction Scheme 4.3: Proposed chemical reaction over co-precipitation synthetic method

To quantify and evaluate the contribution of each basic sites on the total basicity of the catalyst, the amount of each single site was estimated by evaluating the integral of each region, and the data shown in Table 4.5. It is estimated that the medium basic sites contributed most of the basicity for CZr-IM (59.44%) and CZr-DP (52.22%) catalysts, while the strong basic sites contributed more for the CZr-CP (41.28%) catalyst of the total basicity amount of 43.33, 32.08 and 19.93 cm^3/g STP for CZr-IM, CZr-DP and CZr-CP respectively. This is followed by the weak basic sites for both CZr-IM and CZr-DP with a contribution of 29.88% and 24.39% respectively; and the medium basic sites (39.15%) for CZr-CP catalyst.

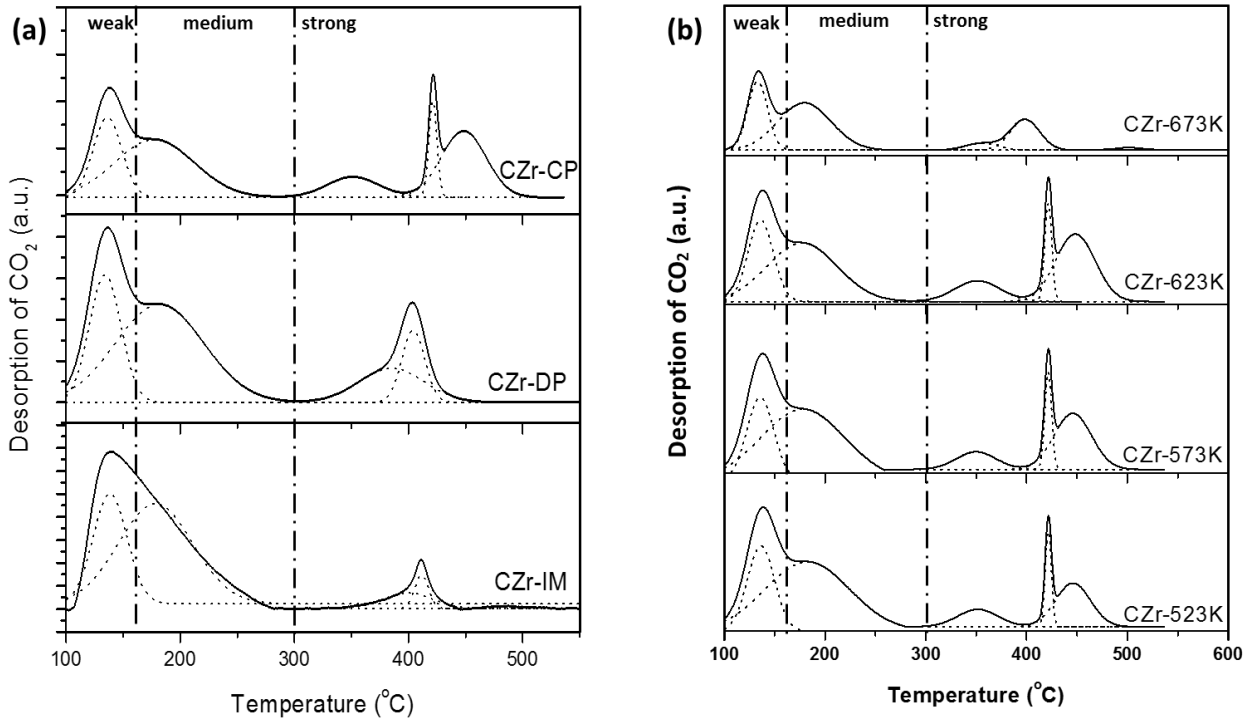

Figure 4.12: CO_2-TPD pattern of (a) CZr catalysts prepared by different method. Catalyst composition: CuO/ZrO_2 = 30/70 (wt.%), (b) CZr catalysts prepared via co-precipitation method at different calcination temperatures

Table 4.5 Surface basicity and distribution of basic sites over CZr catalysts calcined at 623 K with different preparation method

Sample	Weak Basic Site (100-160 °C)		Medium Basic Sites (160-300 °C)		Strong Basic Sites					
					(300-400 °C)		(400-430 °C)		(430-500 °C)	
	cm^3/g STP	%	cm^3/g STP	%	cm^3/g STP	%	cm^3/g STP	%	cm^3/g STP	%
CZr-IM	12.95	29.88	25.76	59.44	2.70	6.22	1.62	3.74	0.31	0.71
CZr-DP	7.82	24.39	16.75	52.22	4.31	13.42	3.20	9.97	-	-
CZr-CP	3.90	19.57	7.80	39.15	1.82	9.12	1.33	6.68	5.08	25.49

4.3.5.2 Dependence on Calcined Temperature

Table 4.6: Surface basicity and distribution of basic sites over CZr-CP catalysts calcined at different temperatures

Sample	Weak Basic Site (100-160 °C)		Medium Basic Sites (160-300 °C)		Strong Basic Sites					
					(300-400 °C)		(400-430 °C)		(430-500 °C)	
	cm^3/g STP	%	cm^3/g STP	%	cm^3/g STP	%	cm^3/g STP	%	cm^3/g STP	%
CZr-523	6.05	37.05	8.67	53.10	0.71	4.35	0.59	3.61	0.31	1.89
CZr-573	4.83	27.51	8.21	46.75	1.19	6.78	0.81	4.61	2.52	14.35
CZr-623	3.90	19.57	7.80	39.15	1.82	9.12	1.33	6.68	5.08	25.49
CZr-673	2.58	26.22	4.74	48.20	0.49	4.98	1.92	19.54	0.10	1.07

Figure 4.12b and Table 4.6 show the graphical and quantitative data respectively of the effect of calcination temperature on the surface basicity of the catalysts prepared via co-precipitation method. As elucidated in the previous section, the TPD profile consisted of three basic sites: weak (OH^- groups), medium or moderate (Zr^{4+}-Cl^- and Zr^{4+}-O^{2-} pairs) and strong (coordinative unsaturated Cl^- and O^{2-} ions). From the obtained results, the weak basic sites were observed to decrease considerably with increase in calcination temperature. Similarly, moderate basic sites were also detected to decrease but insignificantly with increase in temperature from 523-623 K. However, above this temperature, the medium basic sites decreased substantially. This occurrence can be explained to be partly due to the decomposition of hydroxyl group and metal-oxygen pairs associated with temperature increase. This indicates that these basic sites are partly transformed to strong basic sites with residual metal-chlorine and lesser amount of metal-oxygen pair [42]. However, on further increase of calcination temperature to 673 K, the breakage of Zr^{4+}-Cl^- linkages commences, which is reported in literature to dissociate at *ca.* 700 K [43, 44] and 673 K for other metal-chloride pairs [42]. This clarifies the sudden decrease in medium basic sites at calcination temperature of 673 K. Furthermore, it can be logically deduced that the medium basic sites mostly comprises of metal-chlorine pairs given the approximately constant amount of medium basic sites before 673 K.

Contrary to the weak and medium basic sites, the strong basic sites showed a considerable increase in amount with increase in calcination temperature from 523-623 K but decreased after this temperature. The strong basic sites can be attributed to the aggregate of both metal-chlorine (Zr^{4+}-Cl^-) and metal-oxygen pairs (Zr^{4+}-O^{2-}) producing unsaturated coordinated Cl^- and O^{2-} ions [40, 42]. As calcination temperature increases, more weak and moderate sites are transformed to strong basic results resulting to the increase in amount of strong basic sites.

However, this is quickly decomposed at temperatures at the neighbourhood of 700 K required for breaking Zr^{4+}-Cl^{-} linkages. Reaction scheme 4.4 shows the probable schematic reaction mechanism during thermal decomposition of the catalyst transforming the weak basic sites to strong basic sites through medium basic sites.

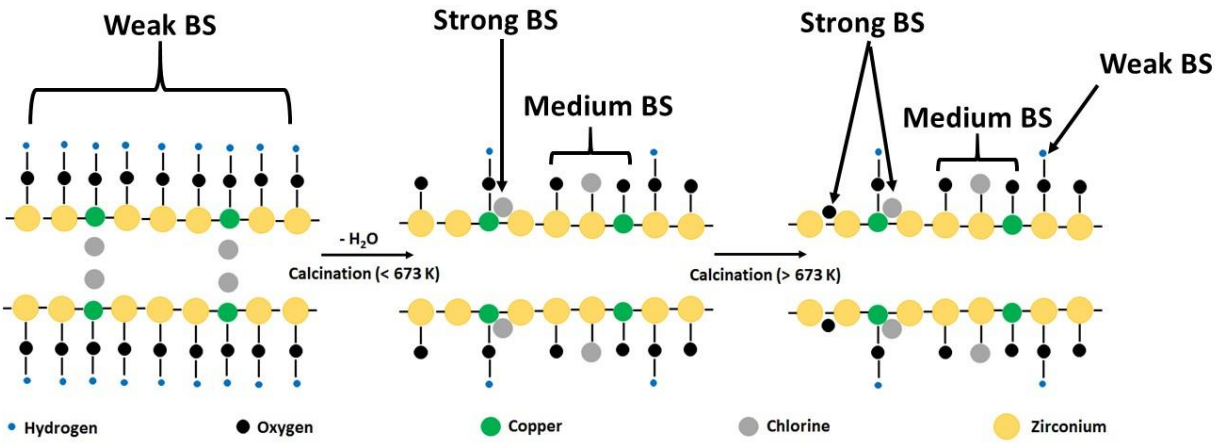

Reaction Scheme 4.4: Proposed decomposition stages for generation of basic sites for calcined CZr catalysts (BS = Basic Sites)

Considering the total basicity of each calcined catalysts, it can been seen that the total basicity increased from 16.33-19.93 cm^3/g STP with increase in calcination temperature from 523-623 K. However, beyond this temperature, the total amount of basic sites decreased sharply to 9.84 cm^3/g STP. This corresponds to reported findings with similar catalyst and was described to be linked with the steady breakdown of porous structure due to increased calcination temperature resulting a sudden reduction in the quantity of accessible basic sites [42].

4.3.6 Structure of Supported CuO and Dispersion Capacity

4.3.6.1 Dependence on Preparation Method

The X-ray diffraction pattern of the catalysts with different synthetic methods are shown in Figure 4.13a. The obtained patterns showed common peaks at $2\theta = 30^o$ and 32^o which are characteristics of tetragonal and monoclinic ZrO_2 respectively regardless of the preparation method. Peaks for tetragonal ZrO_2 (t-ZrO_2) were more distinct in CZr-CP and CZr-DP when compared to CZr-IM. This suggests the structural configuration of the catalyst support to vary with method of preparation. Due to the intensity of the peaks, CZr-IM is perceived to contain more monoclinic ZrO_2 (m-ZrO_2) while CZr-CP consists more of t-ZrO_2. Additionally, the CuO peak at $2\theta = 35.5^o$ and 38.7^o were also observed to be common in the three patterns. However,

the intensity of the peaks was observed to vary in the following trend: CZr-CP> CZr-DP> CZr-IM. This proposes that Cu loading in least in CZr-IM and more bulky deposited in CZr-CP. In other words, it can be stipulated that CuO exists as a highly dispersed surface species in CZr-IM while existing as bulk crystals for CZr-CP and CZr-DP catalysts [45]. Comparing the later catalysts, the co-precipitation method was seen to promote more deposition of Cu on the ZrO_2 support. This is ascertained by the increased intensity of the peaks of CZr-CP when compared to CZr-DP. This supports the results obtained from the SEM images.

4.3.6.2 Dependence on Calcined Temperature

Figure 4.13b shows the variation of XRD pattern with calcination temperatures from 523-623 K. Upon thermal treatment, most of the detectable peaks disappeared. This suggests that the undetected metal oxides tend to exist in amorphous state. Furthermore, the ZrO_2 peaks were observed to display a lower intensity than that of CuO. This can be partly due to the ZrO_2 particles existing in a less ordered structure [34] or the smaller size of the ZrO_2 particles are embedded within the bulk CuO particles [33]. Other effects of increasing the calcination temperature were the decrease in peak intensity for m-ZrO_2 ($2\theta = 23^o$) and subsequent increase for t-ZrO_2 ($2\theta = 62^o$). In addition, other m-ZrO_2 peaks obvious at 523 K were also perceived to have disappeared. This can be explained to be as a result of the thermal transition of m-ZrO_2 to t-ZrO_2. ZrO_2 is reported to adopt a monoclinic crystallite structure at room temperature but however, transforms to tetragonal structure at high temperature. Moreover, as the calcination temperature increased, it was observed that CuO diffraction peaks ($2\theta = 35.5^o$ and 38.7^o) also increased in intensity indicating an increase in particle size [34, 46].

To evaluate the crystallite size of the particles, Scherrer's formula was adopted. With this formula, the crystallite sizes of CuO, t-ZrO_2 and m-ZrO_2 were estimated and tabulated in Table 4.7. The estimated results stipulate that CuO and t-ZrO_2 crystals are almost of equal sizes across all preparation methods. However m-ZrO_2 showed an increasing in size in the following trend: CZr-IM < CZr-DP < CZr-CP. Increase in the calcination temperature resulted to increase in sizes of CuO and t-ZrO_2 and reduction in m-ZrO_2 sizes. This is in agreement with findings established earlier and can be attributed to sintering effect caused by calcination; hence, resulting in increase in particle size. However, the reduction of m-ZrO_2 can be related to its thermal transition to t-ZrO_2. Hence, increase in t-ZrO_2 crystal size can be partly due to calcination sintering and or transformation of m-ZrO_2. Furthermore, a linear relationship was

established between the calcination temperature from 523-623 K and crystallite sizes of the particles. This is shown in Figure 4.14.

Table 4.7: Crystallite sizes of prepared catalysts from XRD data

Variation of Crystallite Sizes with Preparation Method			
Sample	**CuO (nm)**	**t-ZrO_2 (nm)**	**m-ZrO_2 (nm)**
CZr-DP	21.22	25.45	10.88
CZr-CP	22.44	21.34	17.11
CZr-IM	23.50	24.65	4.50

Variation of Crystallite Sizes with Calcination Temperature			
Sample	**CuO (nm)**	**t-ZrO_2 (nm)**	**m-ZrO_2 (nm)**
CZr-523 K	22.75	22.15	11.41
CZr-573 K	30.68	26.19	8.57
CZr-623 K	32.66	28.20	7.86

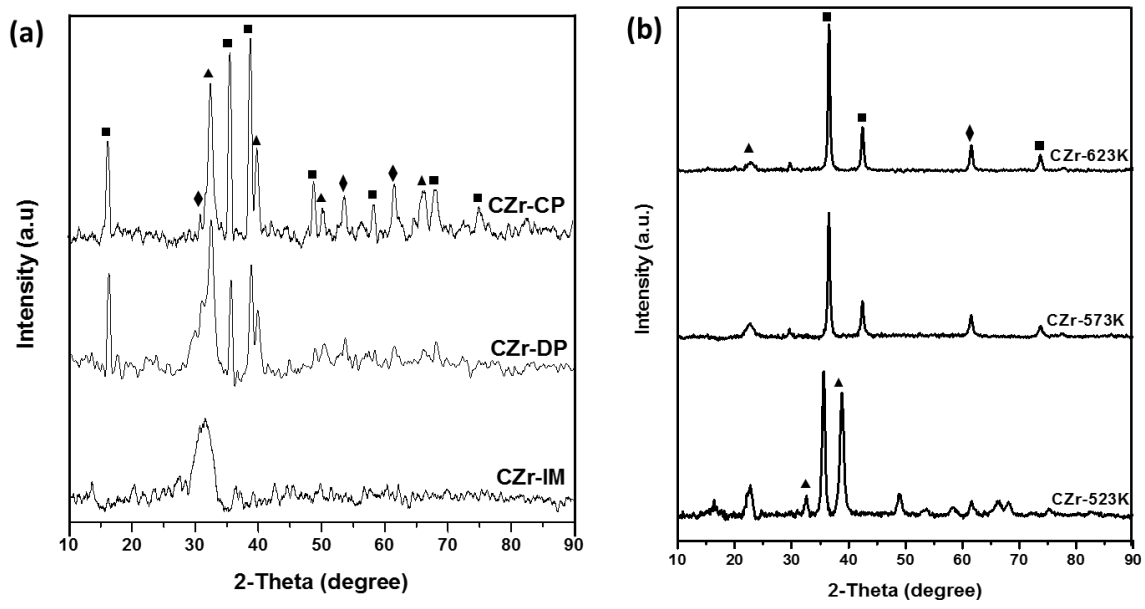

Figure 4.13: XRD pattern of (a) CZr catalysts prepared by different method. Catalyst composition: CuO/ZrO_2 = 30/70 (wt.%), (b) CZr catalysts prepared via co-precipitation method at different calcination temperatures

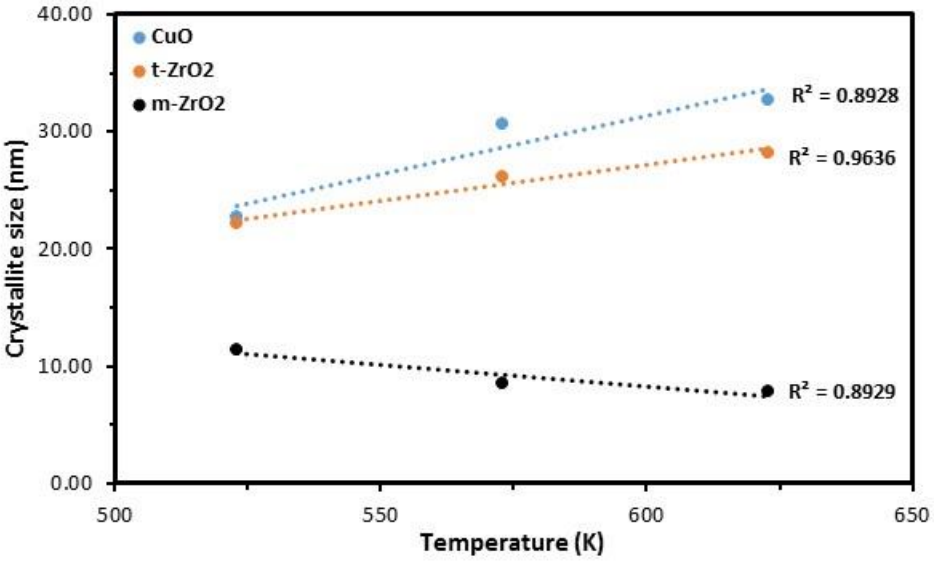

Figure 4.14: Variation of crystallite sizes of CuO, t-ZrO_2 and m-ZrO_2 with calcination temperature

4.3.7 Catalytic Performance for Methanol Synthesis

4.3.7.1 Dependence on Preparation Method

In this study, the catalytic performance was evaluated based on the catalytic selectivity and activity for CO_2 hydrogenation. The results are shown in Table 4.8. CO_2 hydrogenation process involves two simultaneous primary reactions: reverse water gas shift (RWGS) and methanol synthesis defined by the chemical reactions stipulated in Reaction scheme 4.5 and 4.1 respectively. The key products of this process are CH_3OH, CO and H_2O with CH_4 being detected in trace amount.

$$CO_2 + H_2 \leftrightarrow CO + H_2O \qquad \Delta H_{298\,K,\ 5\,MPa} = 40.9\ KJ/mol$$

Reaction Scheme 4.5: Chemical reaction for reverse water gas shift

From the obtained results, it is observed that CO_2 conversion is least in CZr-IM and highest with CZr-DP. This can be explained using the H_2-TPD data within the neighbourhood of the reaction temperature. The principle of H_2-TPD discloses the ease of hydrogen adsorption on Cu-sites. This is assumed to reflect the reducibility of the catalyst, hence providing active Cu-sites readily available to facilitate CO_2 conversion. Hence, the high CO_2 conversion capacity of CZr-DP can be related tentatively to its high adsorption of hydrogen within the reaction temperature of 623 K (350 ^oC). The following proposition also applies for the other catalysts.

The hydrogen adsorbed by CZr-IM and CZr-CP are 7.27 and 32.95 cm^3/g STP respectively. This corresponds to a 2.85 and 5.87% CO_2 conversion respectively.

Furthermore, it was observed that methanol selectively was highest in CZr-DP (63.82%) and least in CZr-CP (48.83%). This can be attributed to various factors [6, 41]. Recent studies proposed that the surface basicity of the catalyst plays a key role in the catalytic selectivity. It is promulgated that CO_2 adsorbed at the strong basic sites favourably promotes methanol synthesis over RWGS [38, 40]. The results from CO_2-TPD shows that both intensity and contribution of strong basic sites is highest with the deposition precipitation method (4.31 cm^3/g STP) and least in CZr-CP (1.82 cm^3/g STP). With these parameters, the methanol yield was estimated and was seen to vary according to the following sequence: CZr-DP>CZr-CP>CZr-IM.

Table 4.8: Catalytic performance of CZr catalysts for methanol synthesis‡

Variation with Preparation Method				
Sample	**X_{CO2} (%)**	**S_{CH3OH} (%)**	**S_{CO} (%)**	**Y_{CH3OH} (% mol CH_3OH/mol CO_2 fed)**
CZr-DP	7.12	63.82	26.18	4.54
CZr-CP	5.87	48.83	51.17	2.87
CZr-IM	2.85	52.66	47.34	1.50

Variation with Calcination Temperature				
Sample	**X_{CO2} (%)**	**S_{CH3OH} (%)**	**S_{CO} (%)**	**Y_{CH3OH} (% mol CH_3OH/mol CO_2 fed)**
CZr-523 K	4.09	30.37	69.63	1.24
CZr-573 K	4.62	35.93	64.07	1.66
CZr-623 K	5.87	48.83	51.17	2.87

‡ Reaction conditions: P = 3.0 MPa, T = 623 K, GHSV = 3100 hr^{-1}, CO_2:H_2 = 1:3. Experimental errors = ± 4.6 %

4.3.7.2 *Dependence on Calcination Temperature*

To study the impact calcination temperature on catalytic performance, the CZr-CP catalyst (Cu-loading = 30%) was used. As explained earlier, the same principle governs the conversion of CO_2 and methanol selectivity even at varied calcination temperatures. Analysing the impact of the calcination temperature on amount of hydrogen adsorbed and surface basicity, the catalytic performance based on variation with calcination temperature can be verified. As

calcination temperature is increased from 523-623 K, the amount of adsorbed hydrogen also increased from 20.92-32.95 cm^3/g STP. This corresponds to the increase in CO_2 conversion from 4.09-5.87%. In the same sequence, increasing the calcination temperature resulted in an increase in the amount of strong basic sites from 0.71-1.82 cm^3/g STP. This is associated with the increase in methanol selectivity from 30.37-48.83% and a corresponding increase in methanol yield from 1.24-2.87%.

4.4 CONCLUSIONS

In the synthesis of methanol via hydrogenation process, one key contributor to the effectiveness of this process is the presence of a suitable catalyst. The most suitable and widely used catalyst is the Cu-based catalyst and its optimal performance is based partly on its thermal characteristics and surface morphology and chemistry. Subsequently, this is dependent on various factors including catalyst preparation, calcination temperature, Cu-loading and heating rate. The following conclusions have been reached as a result of the current study:

(1) The calcination temperature plays a major role in the structure and pore distribution of the support. Calcination is favoured at high temperatures but with a cap at 673K where the catalyst undergoes phase transformation.

(2) As calcination temperature increases, the surface area, porosity and pore size distribution reduces. However, the particle size of the support increases due to particle agglomeration.

(3) Although all supports showed a similar trend and characteristics at different calcination temperature, however, the 623 K-calcined support showed the minimal heat flow all through the temperature range.

(4) Textural quality and chemical property of the catalyst are highly dependent on the synthetic method and calcination temperature. For all given preparation method, comparing the different catalysts based on the Cu-loading, the 30% Cu-loading showed a more thermal stability. In addition, the performance trend is as follows: CP>DP>IM.

(5) The Co-precipitation method showed the best thermal characteristics and surface chemistry properties with a change in phase transformation temperature of about 78-90 K when compared to the phase transformation temperature of the support. However, the method had more impurities than other methods.

(6) At a high heating rate of 20 K/min, the catalyst undergoes an accelerated phase transformation. However, the thermal stability is significantly lower when compared to a lower heating rate of 10 K/min. This trend was reversed at a temperature of 673 K, after which the 10 K/min heating rate showed a late phase transformation 6 K after that of 20 K/min heating rate. In addition, the transformation temperature window of the lower rate is smaller than that at lower rate.

(7) Despite the high thermal characteristics of catalysts prepared via co-precipitation, the catalytic performance of deposition precipitation catalysts (Cu-loading = 30%) showed a better CO_2 conversion and methanol selectivity, which tends to decrease with decrease in calcination temperature.

ACKNOWLEDGEMENT

In addition, sincere appreciation goes to Mr. Bin Dong for all his assistance towards the completion of this study.

Reference

[1] M. Mikkelsen, M. Jørgensen, F.C. Krebs, The teraton challenge. A review of fixation and transformation of carbon dioxide, Energy & Environmental Science, 3 (2010) 43.

[2] H. Arakawa, Research and development on new synthetic routes for basic chemicals by catalytic hydrogenation of CO_2, in: M.A.K.I.S.Y. T. Inui, T. Yamaguchi (Eds.) Studies in Surface Science and Catalysis, Elsevier1998, pp. 19-30.

[3] A. Baiker, Utilization of carbon dioxide in heterogeneous catalytic synthesis., Applied Organometallic Chemistry, 14 (2000) 751-762.

[4] W. Wang, S. Wang, X. Ma, J. Gong, Recent advances in catalytic hydrogenation of carbon dioxide, Chemical Society reviews, 40 (2011) 3703-3727.

[5] X. An, J. Li, Y. Zuo, Q. Zhang, D. Wang, J. Wang, A Cu/Zn/Al/Zr Fibrous Catalyst that is an Improved CO2 Hydrogenation to Methanol Catalyst, Catalysis Letters, 118 (2007) 264-269.

[6] J. Toyir, P. Ramirez de la Piscina, J. L. G. Fierro, N. Homs, Catalytic Performace for CO_2 Conversion to Methanol of Gallium Promoted Copper based Catalysts: Influence of Metallic Precursors, Applied Catalysis B, 34 (2001) 255-266.

[7] X. Guo, D. Mao, G. Lu, S. Wang, G. Wu, CO_2 hydrogenation to methanol over Cu/ZnO/ZrO_2 catalysts prepared via a route of solid-state reaction, Catalysis Communications, 12 (2011) 1095-1098.

[8] C. Li, X. Yuan, K. Fujimoto, Development of highly stable catalyst for methanol synthesis from carbon dioxide, Applied Catalysis A: General, 469 (2014) 306-311.

[9] F. Arena, K. Barbera, G. Italiano, G. Bonura, L. Spadaro, F. Frusteri, Synthesis, characterization and activity pattern of Cu–ZnO/ZrO_2 catalysts in the hydrogenation of carbon dioxide to methanol, Journal of Catalysis, 249 (2007) 185-194.

[10] B.J. Liaw, Y.Z. Chen, Liquid-phase synthesis of methanol from CO2/H2 over ultrafine CuB catalysts, Applied Catalysis A: General, 206 (2001) 245-256.

[11] Y.-F. Zhao, Y. Yang, C. Mims, C.H.F. Peden, J. Li, D. Mei, Insight into methanol synthesis from CO2 hydrogenation on Cu(111): Complex reaction network and the effects of H2O, Journal of Catalysis, 281 (2011) 199-211.

[12] J. Yoshihara, C.T. Campbell, Methanol Synthesis and Reverse Water–Gas Shift Kinetics over Cu(110) Model Catalysts: Structural Sensitivity, Journal of Catalysis, 161 (1996) 776-782.

[13] C.B.S. Ovesen C.V., Schiøtz J., Stoltze P., Topsøe H. and Nørskov J.K., Kinetic Implications of Dynamical Changes in Catalyst Morphology during Methanol Synthesis over Cu/ZnO Catalyst, Journal of Catalysis, 168 (1997) 133-142.

[14] I. Melián-Cabrera, M. López Granados, J.L.G. Fierro, Reverse Topotactic Transformation of a Cu–Zn–Al Catalyst during Wet Pd Impregnation: Relevance for the Performance in Methanol Synthesis from CO_2/H_2 Mixtures, Journal of Catalysis, 210 (2002) 273-284.

[15] I. Melián-Cabrera, M.L. Granados, J.L.G. Fierro, Pd-Modified Cu–Zn Catalysts for Methanol Synthesis from CO_2/H_2 Mixtures: Catalytic Structures and Performance, Journal of Catalysis, 210 (2002) 285-294.

[16] K. T. Jung, A. T. Bell, Effects of Zirconia Phase on the Synthesis of Methanol over Zirconia-Supported Copper, Catalysis Letters, 80 (2002) 63-68.

[17] J. Słoczyński, R. Grabowski, A. Kozłowska, P. Olszewski, J. Stoch, J. Skrzypek, M. Lachowska, Catalytic activity of the M/(3ZnO·ZrO2) system (M = Cu, Ag, Au) in the hydrogenation of CO2 to methanol, Applied Catalysis A: General, 278 (2004) 11-23.

[18] S.E. Collins, M.A. Baltanás, J.L. Garcia Fierro, A.L. Bonivardi, Gallium–Hydrogen Bond Formation on Gallium and Gallium–Palladium Silica-Supported Catalysts, Journal of Catalysis, 211 (2002) 252-264.

[19] S.E. Collins, D.L. Chiavassa, A.L. Bonivardi, M.A. Baltanás, Hydrogen Spillover in Ga_2O_3–Pd/SiO_2 Catalysts for Methanol Synthesis from CO_2/H_2, Catalysis Letters, 103 (2005) 83-88.

[20] L.G.Q. Liu X. M., Yan Z. F. and Beltramini J. , Recent Advances in Catalysts for Methanol Synthesis via Hydrogenation of CO and CO_2, Industrial and Engineering Chemistry Research, 42 (2003) 6518-6530.

[21] Y. Borodko, G.A. Somorjai, Catalytic hydrogenation of carbon oxides – a 10-year perspective, Applied Catalysis A: General, 186 (1999) 355-362.

[22] I.A. Fisher, A. T. Bell, In-Situ Infrared Study of Methanol Synthesis from $H2/CO_2$ over Cu/SiO_2 and $Cu/ZrO_2/SiO_2$, Journal of Catalysis, 172 (1997) 222-237.

[23] R.A. Koeppel, A. Baiker, A. Wokaun, Copper/zirconia catalysts for the synthesis of methanol from carbon dioxide: Influence of preparation variables on structural and catalytic properties of catalysts, Applied Catalysis A: General, 84 (1992) 77-102.

[24] W. Jansen, Dynamic Behavior of the Surface Structure of Cu/ZnO/SiO2 Catalysts, Journal of Catalysis, 210 (2002) 229-236.

[25] Q.-L. Tang, Q.-J. Hong, Z.-P. Liu, CO2 fixation into methanol at Cu/ZrO2 interface from first principles kinetic Monte Carlo, Journal of Catalysis, 263 (2009) 114-122.

[26] K.R.A. Weigel J., Baiker A. and Wokaun A., Surface Species in CO and CO2 Hydrogenation over Copper/Zirconia: On the Methanol Synthesis Mechanism, Langmuir, 12 (1996) 5319-5329.

[27] D.L. Chiavassa, S.E. Collins, A.L. Bonivardi, M.A. Baltanás, Methanol synthesis from CO2/H2 using Ga2O3–Pd/silica catalysts: Kinetic modeling, Chemical Engineering Journal, 150 (2009) 204-212.

[28] T. Inui, T. Takeguchi, Effective Conversion of Carbon Dioxide and Hydrogen to Hydrocarbons, Catalysis Today, 10 (1991) 95-106.

[29] J. Tabatabaei, B.H. Sakakini, K.C. Waugh, On the mechanism of methanol synthesis and the water-gas shift reaction on ZnO, Catalysis Letters, 110 (2006) 77-84.

[30] Y. Yang, J. Evans, J.A. Rodriguez, M.G. White, P. Liu, Fundamental studies of methanol synthesis from CO2 hydrogenation on Cu(111), Cu clusters, and Cu/ZnO(000$\bar{1}$), Physical Chemistry Chemical Physics, 12 (2010) 9909.

[31] B. Chan, L. Radom, Zeolite-Catalyzed Hydrogenation of Carbon Dioxide and Ethene., Journal of American Chemical Society, 130 (2008) 9790-9799.

[32] G.L.J.P. Silva, M.L.C.P. Silva, T. Caetano, Preparation and Characterization of Hydrous Zirconium Oxide Formed by Homogeneous Precipitation, Materials Research, 5 (2002) 149-153.

[33] A. Fathy, O. Elkady, A. Abu-Oqail, Synthesis and characterization of Cu–ZrO2 nanocomposite produced by thermochemical process, Journal of Alloys and Compounds, 719 (2017) 411-419.

[34] L. Li, D. Mao, J. Xiao, L. Li, X. Guo, J. Yu, Facile preparation of highly efficient CuO-ZnO-ZrO2/HZSM-5 bifunctional catalyst for one-step CO2 hydrogenation to dimethyl ether: Influence of calcination temperature, Chemical Engineering Research and Design, 111 (2016) 100-108.

[35] J. Liu, J. Shi, D. He, Q. Zhang, X. Wu, Y. Liang, Q. Zhu, Surface active structure of ultra-fine Cu/ZrO2 catalysts used for the CO2+H2 to methanol reaction, Applied Catalysis A: General, 218 (2001) 113-119.

[36] K. Prasad, D.V. Pinjari, A.B. Pandit, S.T. Mhaske, Synthesis of zirconium dioxide by ultrasound assisted precipitation: Effect of calcination temperature, Ultrasonics Sonochemistry, 18 (2011) 1128-1137.

[37] G.L.J.P. Silva, M.L.C.P. Silva, T. Caetano, Preparation and Characterization of Hydrous Zirconium Oxide Formed by Homogeneous Precipitation, Materials Research, 5 (2002) 149-153.

[38] X. Guo, D. Mao, G. Lu, S. Wang, G. Wu, The influence of La doping on the catalytic behavior of Cu/ZrO2 for methanol synthesis from CO2 hydrogenation, Journal of Molecular Catalysis A: Chemical, 345 (2011) 60-68.

[39] F. Arena, G. Italiano, K. Barbera, S. Bordiga, G. Bonura, L. Spadaro, F. Frusteri, Solid-state interactions, adsorption sites and functionality of Cu-ZnO/ZrO2 catalysts in the CO2 hydrogenation to CH3OH, Applied Catalysis A: General, 350 (2008) 16-23.

[40] P. Gao, H. Yang, L. Zhang, C. Zhang, L. Zhong, H. Wang, W. Wei, Y. Sun, Fluorinated Cu/Zn/Al/Zr hydrotalcites derived nanocatalysts for CO2 hydrogenation to methanol, Journal of CO2 Utilization, 16 (2016) 32-41.

[41] C. Zhong, X. Guo, D. Mao, S. Wang, G. Wu, G. Lu, Effects of alkaline-earth oxides on the performance of a CuO-ZrO2 catalyst for methanol synthesis via CO2 hydrogenation, RSC Advances, 5 (2015) 52958-52965.

[42] G. Wu, X. Wang, W. Wei, Y. Sun, Fluorine-modified Mg–Al mixed oxides: A solid base with variable basic sites and tunable basicity, Applied Catalysis A: General, 377 (2010) 107-113.

[43] N.N. Greenwood, A. Earnshaw, Chemistry of the Elements, 2nd ed. ed., Butterworth-Heinemann, Oxford, 1997.

[44] W.S. Hummers, S.Y. Tyree, S. Yolles, F. Basolo, L. Bauer, Zirconium and Hafnium Tetrachlorides, Inorganic Syntheses, John Wiley & Sons, Inc.2007, pp. 121-126.

[45] Z. Liu, M.D. Amiridis, Y. Chen, Characterization of CuO Supported on Tetragonal ZrO2 Catalysts for N2O Decomposition to N2, The Journal of Physical Chemistry B, 109 (2005) 1251-1255.

[46] X. Guo, D. Mao, G. Lu, S. Wang, G. Wu, Glycine–nitrate combustion synthesis of CuO–ZnO–ZrO2 catalysts for methanol synthesis from CO2 hydrogenation, Journal of Catalysis, 271 (2010) 178-185.

CHAPTER FIVE

ENHANCEMENT OF Cu/ZrO_2 CATALYST VIA ULTRASONIC IRRADIATION AND INTRODUCTION OF Zn^{2+} PROMOTERS

Abstract

The thermal characteristics of Cu-based catalysts for CO_2 utilization towards the synthesis of methanol were analysed and discussed in this study. The preparation process were varied by adopting ultrasonic irradiation at various impulses for the co-precipitation route and also, by introducing ZnO promoters using the solid-state reaction route. Prepared catalysts were characterised using XRD, TPR, TPD, SEM, BET and TG-DTG-DSC. In addition, the CO_2 conversion and CH_3OH selectivity of these samples were assessed. Calcination of the catalysts facilitated the interaction of the Cu catalyst with the respective support bolstering the thermal stability of the catalysts. The characterisation analysis clearly reveals that the thermal performance of the catalysts was directly related to the sonication impulse and heating rate. Surface morphology and chemistry was enhanced with the aid of sonication and introduction of promoters. However, the impact of the promoter outweighs that of the sonication process. CO_2 conversion and methanol selectivity showed a significant improvement with a 270% increase in methanol yield.

Keywords: *Carbon dioxide, Thermal stability, Hydrogenation, Catalysts, Methanol synthesis.*

5.1 INTRODUCTION

Present research undertaking towards methanol synthesis has been aimed at developing catalysts with great catalytic activity. One notable catalyst for this purpose is the alumina (Al_2O_3) based catalyst with good yield of methanol. However, this catalyst is limited in performance due to its strong hydrophilic characteristics [1-3]. Other catalysts used are Cu-ZrO_2 based catalysts with high thermal stability and Cu dispersion. This is due to the role of ZrO_2 [3, 4]. As a result, the catalytic capacity of this material was observed to increase. Further improvement with the dispersion of Cu in this material was achieved by the use of promoters like oxides of Mg [5-7], Mn [5, 7, 8], Ga [7] and Zn [9, 10].

Despite the composition of the catalyst, other means of promoting the performance of the catalyst is the adopted synthetic method and conditions [7, 11-13]. Common synthetic methods used for the preparation of these compounds are co-precipitation [3, 4, 11, 12, 14-20], sol gel [21, 22] and citrate thermal decomposition [7, 19, 20, 23]. Recently, new synthetic methods are being proposed. This includes solid-state chemical reactions [24] and solution combustion [25, 26]. Nonetheless, this methods produce materials with low surface area, which is a demerit for catalytic activity [27-31].

In this work, CuO-ZrO_2 composite oxide was synthesised by an ultrasonic enhanced co-precipitation method. In addition, ZnO promoter was also used to study the promotional effect of ZnO on CuO-ZrO_2 catalyst. The structural and textural characteristics of these compounds was assessed by Thermo-gravimetric Analysis- Differential Scanning Calorimetry (TGA-DSC), X-ray Diffraction analysis (XRD), Temperature-Programmed Desorption (TPD: CO_2 and H_2), Scanning Electron Microscope (SEM) and Temperature-Programmed Reduction (TPR) as well as N_2 sorption analysis.

5.2 EXPERIMENTAL

5.2.1 Material Preparation

In this study, the catalysts were synthesised by the ultrasonic aided co-precipitation method. All chemicals used for experimentation were acquired from SinoPharm Chemical Reagents Co. Ltd.

5.2.2 Preparation of catalyst

5.2.2.1 Cu/ZrO_2

The catalyst was prepared by a reaction of 0.17 M mixed reaction of $Zr(NO_3)_4$ and $Cu(NO_3)_2$ (Cu-loading = 30%) and 0.1M NaOH solution while sustaining the pH at 7.0. Mixing was done with the aid of ultrasonic irradiation at different impulses (continuous, 1, 4 and 8 seconds). After which, the precipitates were filtered, washed, dried (383 K for 6 hr) and calcined (at temperature of 623 K for 4 hr). This sample is labelled as CZr.

5.2.2.2 $Cu/Zn/ZrO_2$ [24]

A mix of $Cu(NO_3)_2 \cdot 3H_2O$, $Zn(NO_3)_2 \cdot 6H_2O$ and $Zr(NO_3)_4 \cdot 5H_2O$ were blended in a Cu^{2+}:Zn^{2+}:Zr^{4+} molar ratio of 3:1:6. This mix was further blended with citric acid ligand, $C_6H_8O_7 \cdot H_2O$ in a molar ratio of 1:1.3. This was carried out for 30 minutes at room temperature until the reactants were transformed to a homogeneous muddy precursor. Afterwards, the catalyst was dried at 383 K for 6 hr before being calcined at a temperature of 623 K for 4 hr. This sample is labelled as CZZr-316. The effect of Zn^{2+} on the catalyst was studied by varying the composition of Zn^{2+} in the catalyst while keeping the composition of Cu^{2+} constant. For this purpose, the molar ratios 3:3:4 and 3:6:1 were also synthesised with the catalysts labelled as CZZr-334 and CZZr-361 respectively

5.2.3 Catalyst Characterization

The support and supported catalysts in the as-synthesised and calcinated form were characterised using a range of physicochemical techniques: Scanning Electron Microscope (SEM), Brunauer-Emmett-Teller (BET), Temperature-Programmed Desorption (TPD), X-ray Diffraction (XRD), Thermal Gravimetric Analysis (TGA), Differential Scanning Calorimetry (DSC) and Differential Thermal Analysis (DTA). Detailed description of the characterisation techniques are explained in section 3.5. TGA, DSC and DTA details are provided in section 3.3. Average crystallite size was estimated using the Scherrer's formula:

Equation 5.1: Scherrer's Formula

$$d = \frac{0.9\lambda}{\beta \cos\theta}$$

where d is the crystallite size (nm), λ is the radiation wavelength (nm) = 1.5406 nm in this case, β is the full width at half maximum (radians) and θ is the Bragg's angle of the maximum intense peak (degrees) [32].

H_2 temperature program reduction (H_2-TPR) of catalysts (50 mg) was carried out in a U-tube quartz reactor using a Micromeritics ChemiSorb 2920 with a thermal conductivity detector (TCD). Before reduction, the sample was first degassed with He flow of 40 mL min^{-1} at 473 K for 60 min to remove physically adsorbed water and cooled down to the 333 K. Then the sample was reduced at a heating rate of 10 K min^{-1} at 1023 K with 50 mL min^{-1} of 5% H_2/Ar mixture gas.

5.2.4 Catalyst Performance Evaluation

The performance of the catalysts towards methanol synthesis was assessed in a continuous flow fixed bed reactor. First, 0.5g of the catalyst was reduced at 623 K in H_2/N_2 (10/90 vol%) environment for 3 hr at atmospheric pressure before being cooled to room temperature. The reactant gas H_2/CO_2 (molar ratio = 3:1) under operating conditions of 3 MPa, 623 K and GHSV = 3100 hr^{-1}. The effluent was analysed online using an Agilent gas chromatograph (GC) 7890A with the transfer line from the reactor to the GC preheated at 373 K to avoid condensation of effluent products. TCD was used to measure N_2, CO and CO_2 gases while organic compounds were studied using the flame ionization detector (FID). From this test, catalytic conversion and selectivity were computed using mass balance and resulting steady-state values (SSV). SSV was computed as an average of three tests over a period of 3 hr of continuous operation. CO_2 conversion (x_{CO2}), selectivity (s_i) and yield (y_i) (where i is the molecule of interest) were computed as follows:

Equation 5.2: CO_2 conversion computation

$$X_{CO_2} = \frac{n_{CH_3OH} + n_{CO}}{n^0_{CO_2}}$$

Equation 5.3: Methanol and carbon monoxide selectivity computation

$$S_{CH_3OH} = \frac{n_{CH_3OH}}{n_{CH_3OH} + n_{CO}}$$

$$S_{CO} = \frac{n_{CO}}{n_{CH_3OH} + n_{CO}}$$

Equation 5.4: Computation of yield for methanol

$$Y_{CH_3OH} = s_{CH_3OH} \times x_{CO_2}$$

5.3 RESULTS AND DISCUSSIONS

5.3.1 Variation of Surface Morphology on Ultrasonic Modulation and Metal Composition

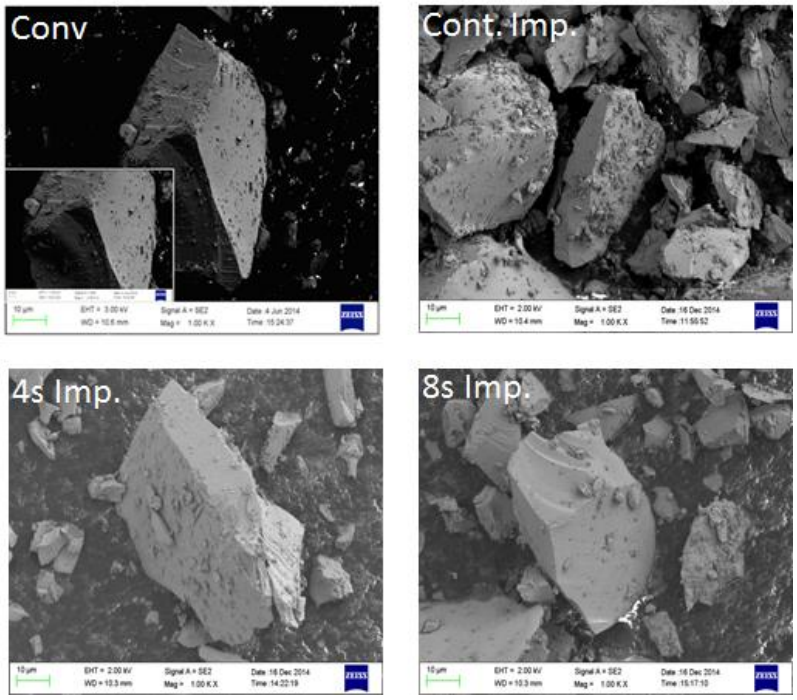

Figure 5.1: SEM Analysis of CZr prepared via Ultrasonic Modulation at different Impulse times (continuous impulse (Cont. Imp.), 4 sec and 8 sec) in comparison with conventional co-precipitation method (Conv)

The Cu/ZrO_2 catalysts prepared via normal co-precipitation and ultrasonic-assisted co-precipitation method are shown in Figure 5.1. SEM micrograph shows that the samples are of irregular shape with particle agglomeration. However, this is affected by the introduction of ultrasonic irradiation. Despite the similarity in particle boulder shape, agglomeration was observed to increase with decrease in impulse of ultrasonic irradiation. With no impulse (continuous impulse), agglomeration was attained its highest and least with 8 sec impulse, which was slightly similar to the conventional catalyst. This stresses the impact of ultrasonic

irradiation on the morphology, and probably, on the physical properties of the material [33]. Figure 5.2 shows the surface morphology of the calcined CZZr catalysts. In each sample, possible cavities were observed all over the surface of the catalyst. This is attributed to the decomposition of formed citrates with an obvious caking of the particles [10]. The cavities and compactness or caking of the catalyst was detected to increase with increase in Cu/Zn ratio. This is similar to findings reported by Huang, Chen, Fei, Liu and Zhang [10].

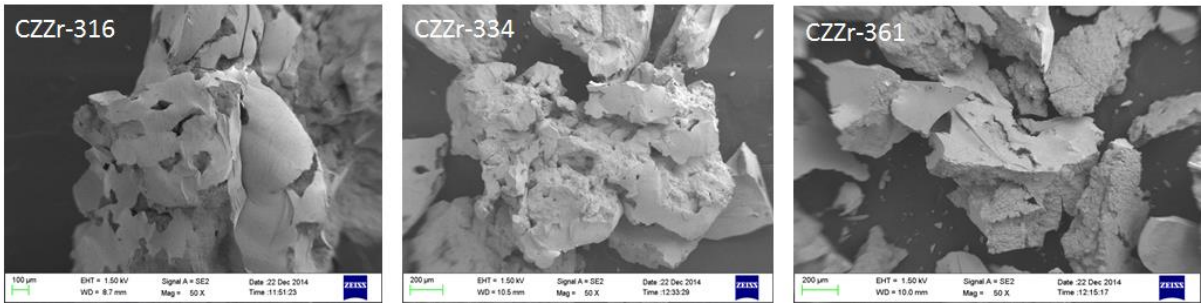

Figure 5.2: SEM images of prepared CZZr catalysts at varying compositions and continuous impulse ultrasonic irradiation

The sorption isotherm obtained from the BET analysis for samples prepared with varying impulse time of ultrasonic irradiation was used to compute the surface area (S_{BET}), pore volume (V_P), and particle size (D_P). The results are tabulated in Table 5.1. The data indicates that an increase in surface area was obtained with decrease in impulse time. Although no significant difference was achieved with respect to the pore volume, however the particle size showed an appreciable decrease with decrease in pulse modulation. This can be attributed to the enhanced interaction as a result of continuous ultrasonic irradiation. This depicts an improvement in the pore structure of the samples and is attributed to the enhancement of nucleation and precipitate growth resulting from improved dissolution and reaction process via sonication [34, 35]. When compared to the conventional samples (designated by conv), it was observed that at impulses greater than 1 s, sonication tends to have an adverse effect on the particle surface area. Nonetheless, with the introduction of Zn^{2+} metal ion into the composite oxide, the surface area and pore volume increased but varied inversely with increase in Cu^{2+}/Zn^{2+} ratio (Table 5.2). Although, not much difference was observed with pore volume. However, the particle diameter was detected to increase with Cu^{2+}/Zn^{2+} ratio. This can be associated with the additional interactions facilitated by the presence of the promoting metal ion. The observed trend corresponds with reported phenomenon and was explained that the variation in Cu/Zn ratio

affects the crystal growth and particle agglomeration of the catalyst. This in turn alters the textural properties of the catalyst [10].

Table 5.1: BET results of CZr catalysts prepared at different ultrasonic impulse time

Structural Characteristics	8s Imp	4s Imp	1s Imp	Cont imp	Conv
BET Surface Area (m^2/g)	53.84	54.31	58.33	64.36	57.03
Pore Volume (cm^3/g)	0.15	0.14	0.14	0.17	0.15
Pore size (nm)	2.70	2.63	2.46	2.60	2.62
Average Particle Size (nm)	27.86	26.49	25.72	23.31	26.30

Table 5.2: BET and metallic composition analysis of CZZr catalysts prepared at different metallic composition

Sample	Metallic Composition (wt%)[a]			Cu^{2+}:Zn^{2+}	S_{BET} (m^2/g)	V_P (cm^3/g)	D_P (nm)
	Cu^{2+}	Zn^{2+}	Zr^{4+}				
CZZr-316	30.52	15.36	54.12	3.0	64.71	0.17	23.31
CZZr-334	32.19	31.37	36.44	1.0	68.52	0.20	21.36
CZZr-361	31.45	60.82	7.73	0.5	70.38	0.21	15.82

[a] computed by atomic emission spectroscopy (AES)

XRD pattern of the prepared samples are shown in Figure 5.3. Figure 5.3a shows the pattern for CZr catalysts at different ultrasonic modulation at constant Cu-loading of 30%. The pattern shows no difference in peak position. However, peak intensity was perceived to increase with ultrasonic irradiation at continuous impulse. This suggests that ultrasonic irradiation has limited impact in improving the crystallinity of the catalyst. The notable peaks observed were the tetragonal ZrO_2 (t-ZrO_2) at peak angles $2\theta = 62^o$, monoclinic ZrO_2 (m-ZrO_2) with peak angles $2\theta = 23^o$ and 28.2^o and Cu species with peak angles $2\theta = 35.6^o$ related to CuO and $2\theta = 42.8^o$ and 72^o related to Cu metal. Incorporating the metal Zn^{2+} to the CZr composite oxide, a series of overlapping peaks were obtained. The presence of CuO was indicated with peaks at $2\theta = 32.4^o$, 35.4^o and 38.7^o. The 35.4^o peak overlapped with 36.3^o peak for ZnO. Other ZnO peaks are at $2\theta = 31.8^o$ and 34.5^o. Noticeably, as the Cu/Zn ratio decreases, the ZnO diffraction peaks increases as well relative to their individual CuO peak intensities. The diffraction peaks of ZrO_2 was also detected but as monoclinic at $2\theta = 23^o$ and 28.8^o and as tetragonal at $2\theta = 30.3^o$. It is observed that the m-ZrO_2 which was the more dominant ZrO_2 crystal increased in accordance with its normal composition in the composite oxide. The crystallite size of CuO crystal was computed using the Scherrer's equation as 16.64, 19.99 and 19.63 nm for CZZr-

316, CZZr-334 and CZZr-361 respectively. This indicates that the presence of Zn^{2+} has an impact on the crystallinity and relative dispersion of Cu. Crystallinity of the catalyst is suggested to be highest at moderate composition of Zn^{2+}.

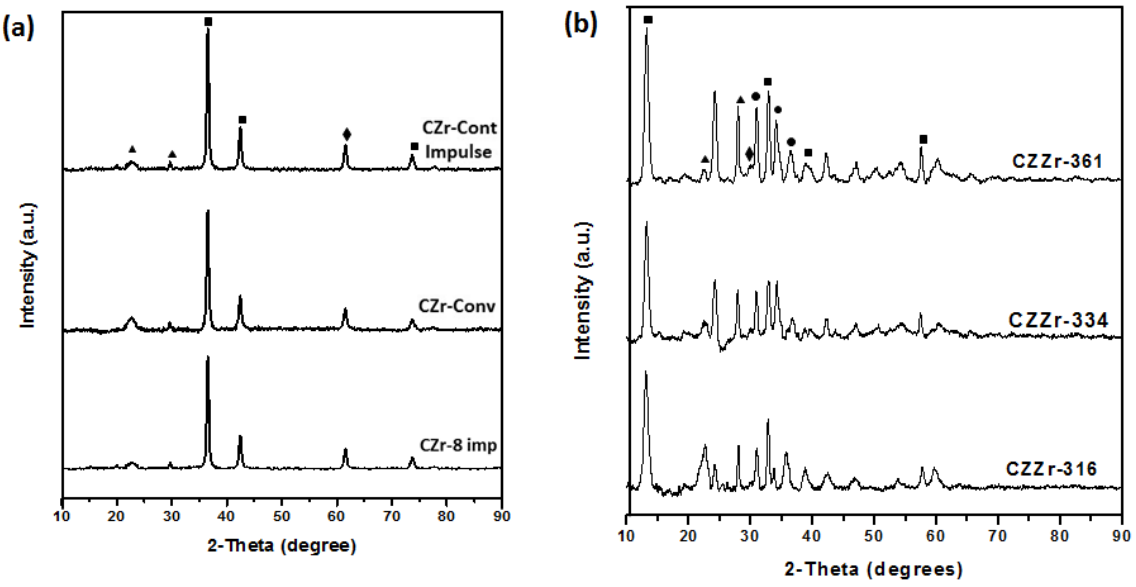

Figure 5.3: XRD pattern for (a) calcined CZr catalysts prepared with variation in ultrasonic impulse at Cu-loading of 30 wt%, and (b) CZZr catalyst prepared with difference in metallic composition. (□) CuO, (○) ZnO, (◊) t-ZrO_2 and (Δ) m- ZrO_2.

5.3.2 Thermal Characteristics

The thermal strength of the prepared catalysts with varying ultrasonic modulation is shown in Figure 5.4. It is detected that there are three decomposition steps in all cases. Although this varied with the level of ultrasonic impulse. As shown in the figure, the first decomposition step occurred at temperature less than 250 ^{o}C. This is associated with the loss of moisture. The second decomposition step as a result of interstitial moisture loss is existed between 250 and maximum temperature of *ca.* 680 ^{o}C. Maximum temperature of the second decomposition peak varied with impulse of ultrasonic irradiation with continuous and 1 s impulse having the highest. Beyond this temperature is the loss of NO_3^- attached to the surface of the catalyst. This explains that the thermal stability of the catalyst was enhanced by ultrasonic modulation. Nonetheless, this is dependent on the intensity of the irradiation. With a continuous or near-continuous impulse, a more thermal stable material is obtained. In terms of energy required for the thermal breakdown of the catalyst, Figure 5.5 was obtained. This is the DSC analysis of the prepared catalysts within a temperature range of 0-800 ^{o}C. The result validates the thermal stability of

samples prepared at continuous and 1 s impulse. This is observed from to the plot to be closest to the zero DSC line indicating a minimal energy differential per mass of the sample. In the profile, it is also noteworthy that the loss of NO_3^- was at a more extended temperature than that of the conventional and higher impulse samples.

Varying the heating rate, it is shown that a better thermal stability is achieved at 20 K/min as shown in Figure 5.6. The 20 K/min profile for both continuous and 1 sec impulse were observed to be have the minimal change in energy (closest to the zero line). In addition, it is also witnessed that at 20 K/min, the breakdown peaks of the catalysts (solid lines) occurred at higher temperatures than that of 10 K/min (broken lines). This suggests that for optimum industrial applicability, the material will be well suited at a thermal operation with heating rate at 20 K/min rather than 10 K/min.

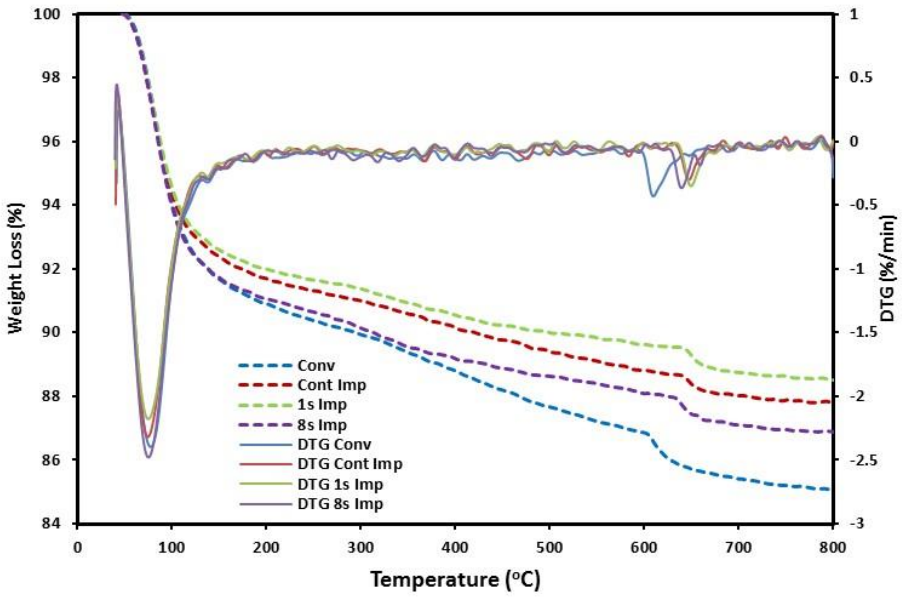

Figure 5.4: TGA-DTA profile for CZr catalysts

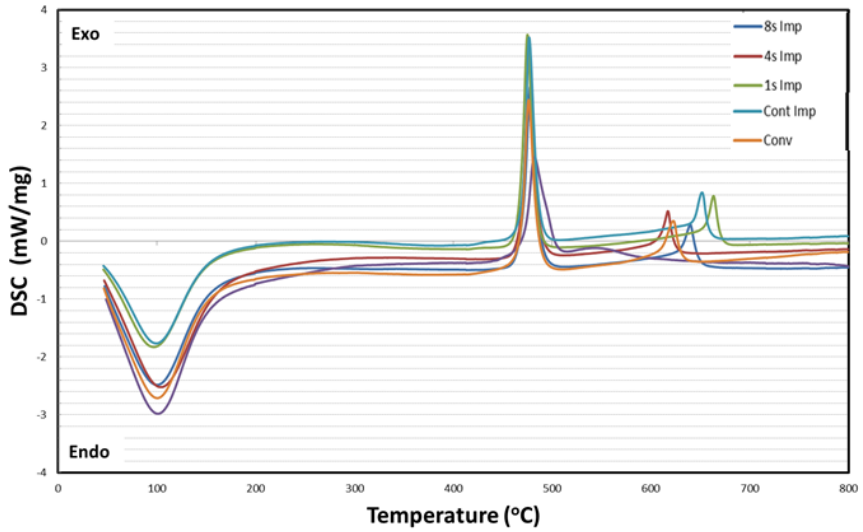

Figure 5.5: DSC profile for CZr catalysts at different ultrasonic impulse

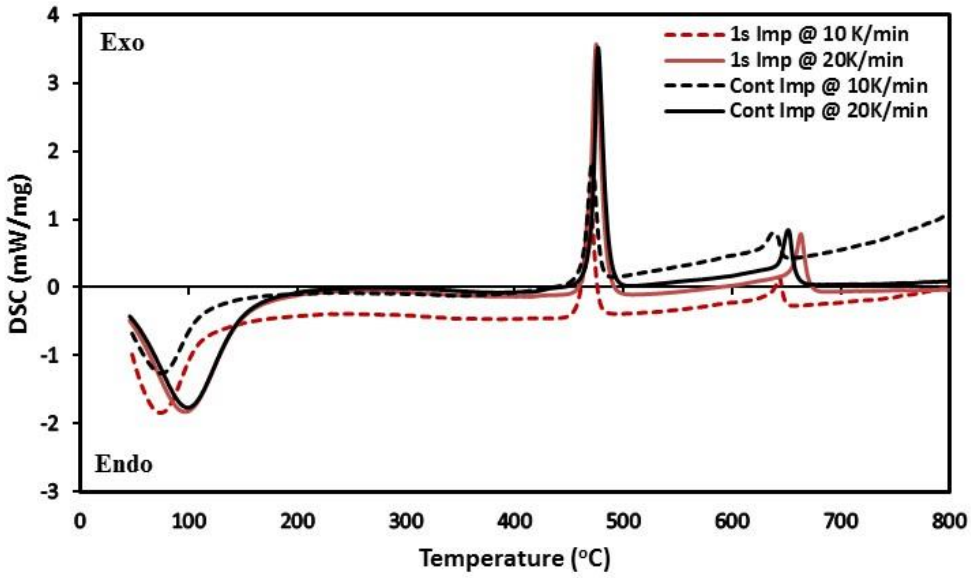

Figure 5.6: DSC analysis at different heating rate for CZr catalysts prepared with ultrasonic irradiation at 1s and continuous impulse

5.3.3 Reducibility of Catalysts

To understand the reducibility of the catalysts, H_2-TPR analysis was conducted. The results are as shown in Figure 5.7. Three classes of adsorption peaks were observed for the catalysts depending on the preparation method and composition of metal. In accordance with literature, the first peak (α) occurred at low temperature range (100-300 °C) and is attributed to the adsorption of atomic hydrogen highly dispersed Cu^{2+}. The second desorption peak (β) occurred at mid temperature range from 300-500 °C, assigned to the adsorption of hydrogen on

moderately dispersed Cu^{2+} species. The final peak (γ) situated at temperature range 500-700 ^{o}C is associated with hydrogen adsorption by bulk Cu^{2+} species [36-39]. Figure 5.7a shows the profile for CZr reduction. Reducing the radiation impulse resulted to an increase in the intensity of α-peak and decrease in β-peak. High temperature adsorption of H_2 was not witnessed in this catalysts. This suggests that the increase in ultrasonic impact (designated by reduced impulse time) will aid in high Cu dispersion. The quantitative analysis of this effect is summarised in Table 5.3. Fig 5.7b shows the profile for CZZr at varying amount of Zn^{2+} ion. At low amount of zinc (CZZr-316), the α-peak was still detected alongside with the detection of a β'-peak, which can be explained to be due to difficulties in the reduction of some dispersed Cu [38]. However, both peaks tend to fade as the composition of Zn increased. This is associated with an increase in intensity, reduction in width and shift of β-peak towards a higher temperature. A logical explanation can be given that the presence of Zn increases the dispersion of Cu species and makes it more accessible for potential dissociation of hydrogen molecule [10]. In this set of catalysts, the γ-peaks were observed and this tends to increase with increase in the amount of Zn. These results show that the amount of easily reducible well dispersed and bulk CuO increased with increase in Zn (Table 5.3). The result data also shows that the impact of introduction of Zn promoter outweighs the impact of ultrasonic modulation. For instance, comparing the total peak area of CZr at 1s impulse and CZZr-316 with that of the conventional catalyst, it is estimated that the difference between the former is a unit magnitude while the latter is of 6 fold magnitude difference.

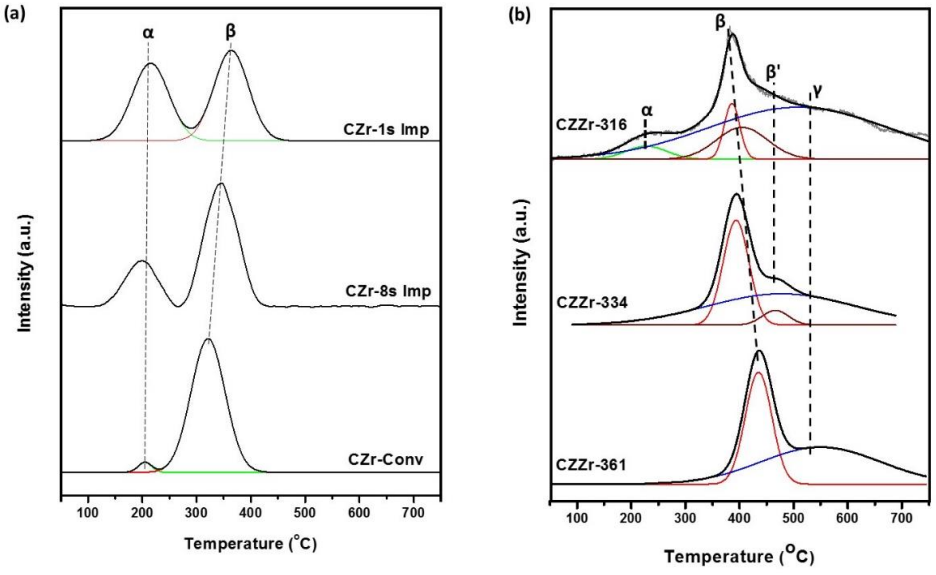

Figure 5.7: TPR profile of (a) CZr catalyst at various ultrasonic impulse, and (b) CZZr Catalyst at different metal composition

Table 5.3: Peak areas of H_2-TPD profiles of reduced CZr and CZZr catalysts

Sample	Peak Areas (a.u.)				Total Area (a.u.)
	α-peak	β-peak	β'-peak	γ-peak	
CZr-1s Impulse	2.74	3.04	-	-	5.78
CZr-8s Impulse	0.13	4.42	-	-	4.55
CZr-Conv	0.03	4.52	-	-	4.55
CZZr-316	3.32	11.61	15.89	1.84	32.66
CZZr-334	-	22.67	3.27	39.03	64.97
CZZr-361	-	28.98	-	42.39	71.37

5.3.4 H_2 Desorption

The H_2-TPD pattern for the pre-reduced catalysts was also studied (see Figure 4.5.8). The desorption profile spanned across a temperature range 50 – 800 ^oC and displayed several adsorption states of H-species on the catalysts. These peaks are classed into two categories, low (130 – 300 ^oC) and high (400 – 500 ^oC) temperature peaks designated as α and β peaks respectively [16, 38, 40]. Desorption at low and high temperature region is ascribed to the release of H-species adsorbed on surface Cu sites and on surface ZnO or ZrO_2 respectively. Figure 5.8a shows that as the impulse time reduces, the intensity of the peaks increased indicating that an increased impact in ultrasonic irradiation will boost the amount of surface Cu sites and available metal oxides. Hydrogen spillover phenomenon is suggested to facilitate the hydrogen adsorption process on ZnO and ZrO_2 sites [16, 40]. For the CZZr catalysts, two peaks were equally obtained within the reported temperature range. However, it was observed that both peaks had broader bands that the CZr catalysts. This is attributed to the presence of the Zn promoter which aids in increasing the amount of Cu active sites. CZZr-316 with the lowest composition of Zn showed the basic α and β peaks. But with an increase in Zn composition resulted to an increase in peak intensity with the detection of additional peaks, α' and β' peaks as shown in Figure 5.8b. The α'-peak can be attributed to both physical and chemical interactions between Cu and the metal oxides with an alteration in electron distribution, which will facilitate the adsorption of hydrogen [42]. The β' peak can be explained as a separated hydrogen adsorption on the individual ZnO and ZrO_2 surface sites. With further increase in Zn composition (CZZr-361), the intensity of the peaks was reduced. It may be suggested that above a specific metal composition, hydrogen adsorption will be deterred by the metals. Li, Mao, Yu and Guo [9] suggested that this interaction could be facilitated by the

sintering effect [9], which in turn will result to reduction in surface area [10]. In conclusion, the best catalyst for the purpose of methanol synthesis via hydrogenation process is one with a better H_2 adsorption strength and good desorption of the dissociated hydrogen atom [41]. Emphasis for the selection of these catalysts should be based on the α-peak desorption profile because it is the hydrogen desorbed from this peak region that will be made available for the hydrogenation process [42].

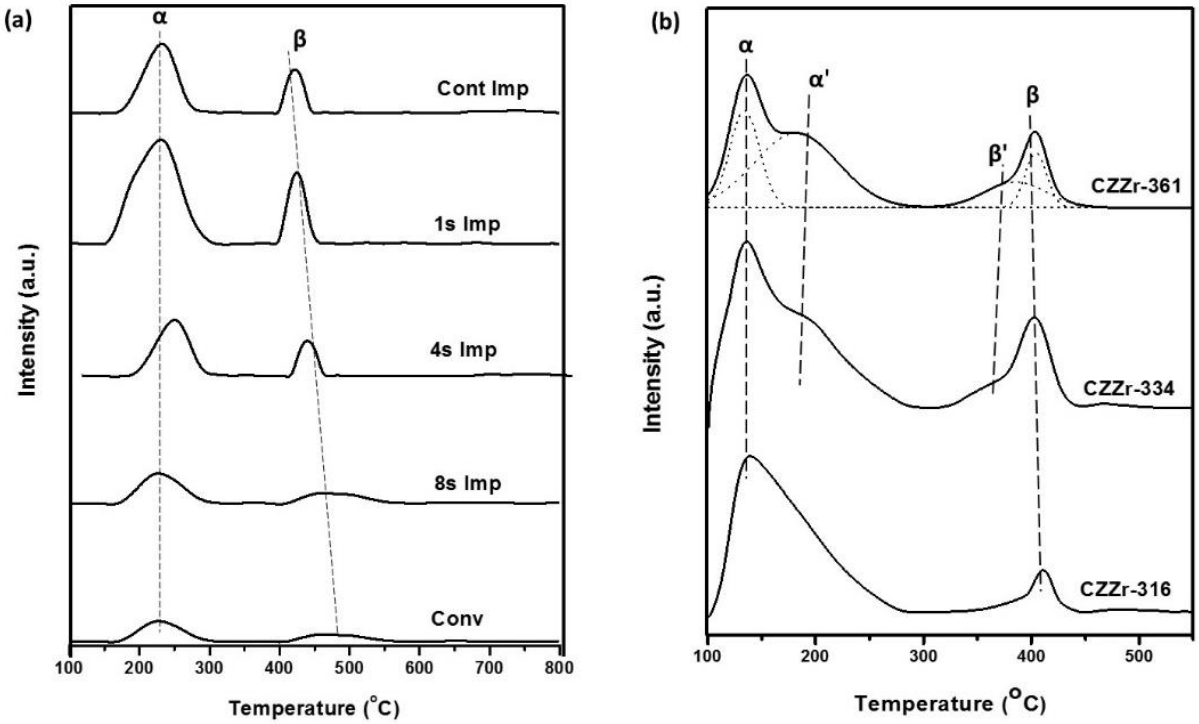

Figure 5.8: H_2-TPD profile for (a) reduced CZr at various ultrasonic impulse time, and (b) CZZr catalysts at different metal composition

5.3.5 Surface Basicity of Catalysts

The surface basicity of the catalysts were studied using the CO_2-TPD technique. The desorption profiles and data are shown in Figure 5.9 and Table 5.4 respectively. Generally, the basicity of metal oxides are categorized into three: weak, medium (or moderate) and strong basic strengths. In this study, these three zones are depicted at their corresponding temperature peaks ranging from 100-160 ^oC, 300-550 ^oC and > 600 ^oC respectively. Weak basic sites (α) are associated with the surface hydroxyl (OH^-) group; whereas the moderate basic sites (β) are related to metal-oxygen (M^{n+}-O^{2-}, where n+ is the valence of the metal) pair. The strong basic sites (γ) are attributed to the low coordination unsaturated oxygen (O^{2-}) and electronegative anions [38].

Figure 5.9a shows TPD profile for CZr catalysts at varying modulation impulse. As can be seen, peak intensities increased with increase in impact of ultrasonic modulation. Hence, ultrasonic irradiation has yet proven to improve the surface basicity of the catalyst. This can be attributed to the enhanced surface morphology of the catalyst hence making the basic sites accessible for CO_2 adsorption. Figure 5.9b portrays the CO_2 desorption profile for the CZZr catalysts prepared at different metal composition. Result data shows that a variation of metal composition has an impact on the surface basicity of the catalyst. As Cu/Zn ratio (also associated with the increase in Zr^{2+} content) increases, the intensity of α-peaks decreased but the β and γ-peaks showed an appreciable increase in intensity. The increase in moderate and strong basic sites can be attributed to the increase in Zr^{4+} content since this metal is suggested to have a great synergetic effect on CO_2 desorption at moderate and strong basic sites when compared to Zn^{2+} [10]. Additionally, the γ-peak was observed to shift towards higher temperature with increase in Cu/Zn ratio. This is suggested to be due to the increased electron density of the strong basic sites, and can be attributed to the aggregation of saturated O^{2-} ions [38].

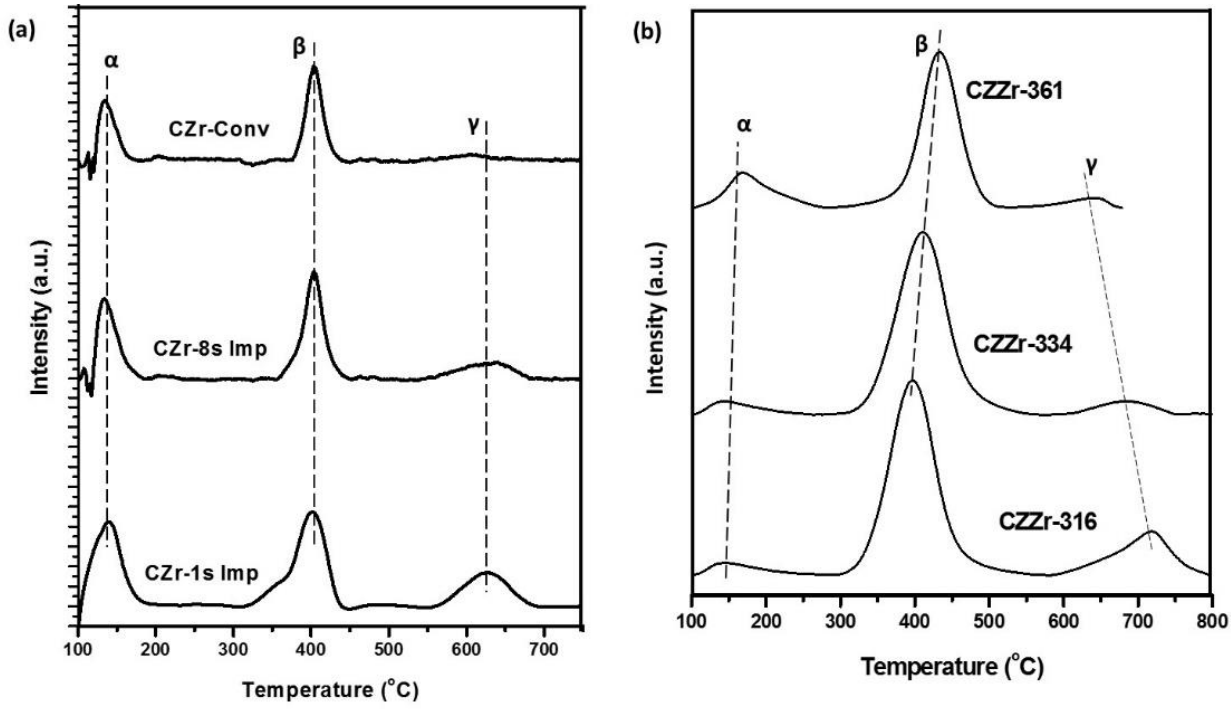

Figure 5.9: CO_2 desorption profile for (a) reduced CZr at various ultrasonic impulse time, and (b) CZZr catalysts at different metal composition

Table 5.4: Result data for CO_2 desorption profile for reduced CZr and CZZr catalysts

Sample	Weak Basic Site		Medium Basic Sites		Strong Basic Sites		Total (a.u.)
	Temp. (°C)	Peak Area (a.u.)	Temp. (°C)	Peak Area (a.u.)	Temp. (°C)	Peak Area (a.u.)	
CZr-Conv	148.00	3.53	400.00	8.67	620.00	0.06	12.26
CZr-8s Imp	147.00	4.31	399.00	9.31	632.00	1.35	14.97
CZr-4s Imp	147.00	4.99	400.00	8.48	630.00	2.49	15.96
CZr-1s Imp	148.00	5.84	400.00	11.43	625.00	5.43	22.70
CZr-Cont Imp	147.00	5.46	401.00	10.91	630.00	5.52	21.89
CZZr-361	148.00	6.53	412.00	30.23	658.00	0.86	37.62
CZZr-334	148.00	6.18	409.00	33.86	699.00	2.14	42.18
CZZr-316	160.00	5.30	400.00	39.71	717.00	10.82	55.83

5.3.6 Catalytic Performance for Methanol Synthesis

In this study, the catalytic performance was evaluated based on the catalytic selectivity and activity for CO_2 hydrogenation. The results are shown in Table 5.5. From the obtained results, it is observed that CO_2 conversion increased with increased impact of sonication. As the sonication impulse reduced from 8s to 1s, CO_2 conversion increased from 5.67% to 8.82%. This can be explained using the H_2-TPD data within the neighbourhood of the reaction temperature. The principle of H_2-TPD discloses the ease of hydrogen adsorption on Cu-sites. This is assumed to reflect the reducibility of the catalyst, hence showing readily available active Cu-sites for hydrogen dissociation. This will facilitate CO_2 conversion. Hence, the high CO_2 conversion capacity of this catalyst can be related tentatively to its high adsorption of hydrogen within the reaction temperature of 623 K (350 °C). Furthermore, it was observed that methanol selectivity was highest with the 1s impulse sample (50.72%) and least in CZr-8s impulse sample (47.83%). This can be attributed to various factors [43, 44]. Recent studies proposed that the surface basicity of the catalyst plays a key role in the catalytic selectivity. It is promulgated that CO_2 adsorbed at the strong basic sites favourably promotes methanol synthesis over RWGS [38, 40, 45]. The adsorbed CO_2 at this sites will hardly be reduced to CO. The results from CO_2-TPD shows that both intensity and contribution of strong basic sites is highest with the 1s impulse sample and least in the conventional CZr catalyst. With these parameters, the methanol yield was estimated with samples with frequent ultrasonic irradiation having the highest yields. Correlating the amount of CO_2 desorbed to the CO_2 conversion and

methanol yield, a linear relationship was obtained for the former. This suggests that the amount of CO_2 converted is directly related to the amount adsorbed. Whereas, for methanol selectivity, a minimum is attained before it begins to ascend. This is as a result of the simultaneous occurrence of reverse water gas shift reaction with the production of CO (see Figure 5.10).

The presence of Zn in the catalyst is also considered to affect the conversion of CO_2 and selectivity of methanol. As the Cu/Zn ratio decreases from 3 to 0.5, the conversion of CO_2 showed an initial increase from 17.78% to 18.68% before descending to 17.08%. This corresponds to the H_2-TPD profile of these catalysts validating the effect of dissociative desorption of hydrogen on hydrogenation of CO_2. Moreover, the increase in Cu/Zn ratio was associated with an increase in methanol selectivity. This is at par with the CO_2-TPD results for strong basic sites. Correlating the CO_2 desorption profile at this basic sites with the methanol selectivity and CO_2 conversion, it can be proposed that at a low Cu/Zn ratio (< 1), the methanol selectivity and CO_2 conversion displays a sharp reduction slope. But at higher Cu/Zn ratio (> 1), a low change gradient is observed for both selectivity and conversion of methanol and CO_2 respectively. This is diagrammatically illustrated in Figure 5.11.

Table 5.5: Catalytic performance of CZr and CZZr catalysts for methanol synthesis[‡]

Variation with ultrasonic impulse				
Sample	**X_{CO2} (%)**	**S_{CH3OH} (%)**	**S_{CO} (%)**	**Y_{CH3OH} (% mol CH_3OH/mol CO_2 fed)**
CZr-Conv	5.71	48.92	51.08	2.79
CZr-Cont Imp	8.43	50.31	49.69	4.24
CZr-1s Imp	8.82	50.72	49.28	4.47
CZr-4s Imp	6.36	49.16	50.84	3.13
CZr-8s Imp	5.67	47.83	52.17	2.71
Variation with metal composition				
Sample	**X_{CO2} (%)**	**S_{CH3OH} (%)**	**S_{CO} (%)**	**Y_{CH3OH} (% mol CH_3OH/mol CO_2 fed)**
CZZr-316	17.78	54.28	48.72	9.65
CZZr-334	18.68	53.57	46.43	10.01
CZZr-361	17.08	49.93	49.07	8.53

[‡] Reaction conditions: P = 3.0 MPa, T = 623 K, GHSV = 3100 hr^{-1}, CO_2:H_2 = 1:3. Experimental errors = ± 3.2 %

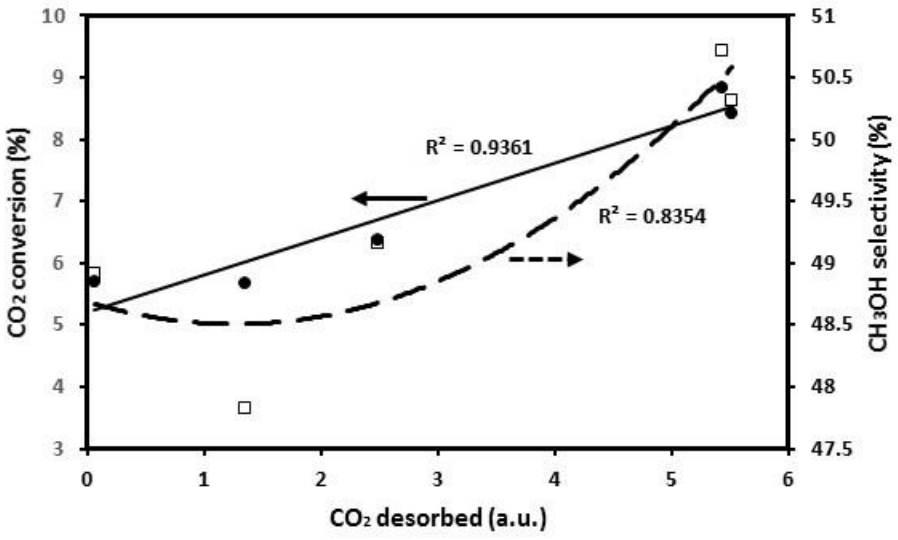

Figure 5.10: Correlation between CO_2-TPD data with CO_2 conversion and CH_3OH selectivity for CZr catalyst

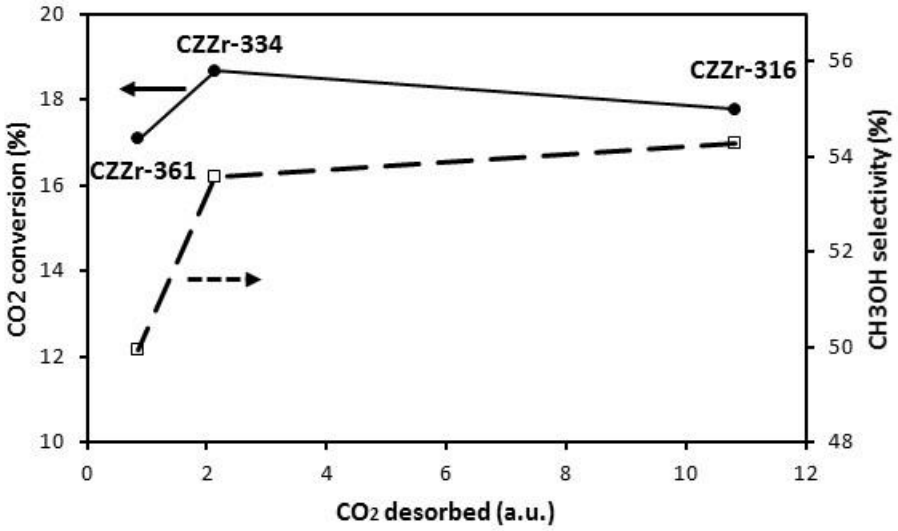

Figure 5.11: Correlation between CO_2-TPD data with CO_2 conversion and CH_3OH selectivity for CZZr catalyst

5.4 CONCLUSIONS

In the synthesis of methanol via hydrogenation process, one key contributor to the effectiveness of this process is the presence of a suitable catalyst. The most suitable and widely used catalyst is the Cu-based catalyst and its optimal performance is based partly on its thermal characteristics and surface morphology and chemistry. Subsequently, this is dependent on

various factors including catalyst synthetic method, metal content and composition. In addition, its thermal strength is also dependent on the heating rate. The effect of these factors are summarised as follows based on the results of the current study:

1. The adoption of ultrasonic irradiation at different sonication impulse affects particle agglomeration, which in turn contributes to the surface morphology and chemistry of the Cu/ZrO_2 catalysts. Low sonication impulses displayed the best properties for the catalyst with improved surface area, particle size and porosity.
2. Metal promoter, ZnO had a greater impact on these properties with an optimum performance at moderate Zn content.
3. Based on the thermal tests, this study suggests that for optimum industrial applicability, the material will be well suited at a thermal operation with heating rate at 20 K/min rather than 10 K/min.

ACKNOWLEDGEMENT

In addition, sincere appreciation goes to Mr. Bin Dong for all his assistance towards the completion of this study.

Reference

[1] K. Fujimoto, Y. Yu, Spillover effect on the stabilization of Cu-Zn catalyst for CO2 hydrogenation to methanol, Studies in Surface Science and Catalysis, 77 (1993) 393-396.

[2] F. Arena, K. Barbera, G. Italiano, G. Bonura, L. Spadaro, F. Frusteri, Synthesis, characterization and activity pattern of $Cu–ZnO/ZrO_2$ catalysts in the hydrogenation of carbon dioxide to methanol, Journal of Catalysis, 249 (2007) 185-194.

[3] C. Li, X. Yuan, K. Fujimoto, Development of highly stable catalyst for methanol synthesis from carbon dioxide, Applied Catalysis A: General, 469 (2014) 306-311.

[4] S. Natesakhawat, J.W. Lekse, J.P. Baltrus, P.R. Ohodnicki, B.H. Howard, X. Deng, C. Matranga, Active Sites and Structure–Activity Relationships of Copper-Based Catalysts for Carbon Dioxide Hydrogenation to Methanol, ACS Catalysis, 2 (2012) 1667-1676.

[5] J. Słoczyński, R. Grabowski, A. Kozłowska, P. Olszewski, M. Lachowska, J. Skrzypek, J. Stoch, Effect of Mg and Mn oxide additions on structural and adsorptive properties of Cu/ZnO/ZrO2 catalysts for the methanol synthesis from CO2, Applied Catalysis A: General, 249 (2003) 129-138.

[6] J. Słoczyński, R. Grabowski, A. Kozłowska, M. Lachowska, J. Skrzypek, Effect of additives and a preparation method on catalytic activity of Cu/ZnO/ZrO2 system in the carbon dioxide hydrogenation to methanol, Studies in Surface Science and Catalysis, 153 (2004) 161-164.

[7] J. Słoczyński, R. Grabowski, P. Olszewski, A. Kozłowska, J. Stoch, M. Lachowska, J. Skrzypek, Effect of metal oxide additives on the activity and stability of Cu/ZnO/ZrO2 catalysts in the synthesis of methanol from CO2 and H2, Applied Catalysis A: General, 310 (2006) 127-137.

[8] M. Lachowska, J. Skrzypek, Methanol synthesis from carbon dioxide and hydrogen over Mn-promoted copper/zinc/zirconia catalysts, Reaction Kinetics and Catalysis Letters, 83 (2004) 269-273.

[9] L. Li, D. Mao, J. Yu, X. Guo, Highly selective hydrogenation of CO2 to methanol over CuO–ZnO–ZrO2 catalysts prepared by a surfactant-assisted co-precipitation method, Journal of Power Sources, 279 (2015) 394-404.

[10] C. Huang, S. Chen, X. Fei, D. Liu, Y. Zhang, Catalytic Hydrogenation of CO2 to Methanol: Study of Synergistic Effect on Adsorption Properties of CO2 and H2 in CuO/ZnO/ZrO2 System, Catalysts, 5 (2015) 1846.

[11] Y. Ma, Q. Sun, D. Wu, W.-H. Fan, Y.-L. Zhang, J.-F. Deng, A practical approach for the preparation of high activity Cu/ZnO/ZrO2 catalyst for methanol synthesis from CO2 hydrogenation, Applied Catalysis A: General, 171 (1998) 45-55.

[12] R. Raudaskoski, M.V. Niemelä, R.L. Keiski, The effect of ageing time on co-precipitated Cu/ZnO/ZrO2 catalysts used in methanol synthesis from CO2 and H2, Topics in Catalysis, 45 (2007) 57-60.

[13] E. Frei, A. Schaadt, T. Ludwig, H. Hillebrecht, I. Krossing, The Influence of the Precipitation/Ageing Temperature on a Cu/ZnO/ZrO2 Catalyst for Methanol Synthesis from H2 and CO2, ChemCatChem, 6 (2014) 1721-1730.

[14] M. Saito, T. Fujitani, M. Takeuchi, T. Watanabe, Development of copper/zinc oxide-based multicomponent catalysts for methanol synthesis from carbon dioxide and hydrogen, Applied Catalysis A: General, 138 (1996) 311-318.

[15] J. Słoczyński, R. Grabowski, A. Kozłowska, P. Olszewski, J. Stoch, J. Skrzypek, M. Lachowska, Catalytic activity of the M/(3ZnO·ZrO2) system (M = Cu, Ag, Au) in the hydrogenation of CO2 to methanol, Applied Catalysis A: General, 278 (2004) 11-23.

[16] F. Arena, G. Italiano, K. Barbera, S. Bordiga, G. Bonura, L. Spadaro, F. Frusteri, Solid-state interactions, adsorption sites and functionality of Cu-ZnO/ZrO2 catalysts in the CO2 hydrogenation to CH3OH, Applied Catalysis A: General, 350 (2008) 16-23.

[17] F. Arena, G. Italiano, K. Barbera, G. Bonura, L. Spadaro, F. Frusteri, Basic evidences for methanol-synthesis catalyst design, Catalysis Today, 143 (2009) 80-85.

[18] R. Raudaskoski, E. Turpeinen, R. Lenkkeri, E. Pongrácz, R.L. Keiski, Catalytic activation of CO2: Use of secondary CO2 for the production of synthesis gas and for methanol synthesis over copper-based zirconia-containing catalysts, Catalysis Today, 144 (2009) 318-323.

[19] F. Arena, G. Mezzatesta, G. Zafarana, G. Trunfio, F. Frusteri, L. Spadaro, Effects of oxide carriers on surface functionality and process performance of the Cu–ZnO system in the synthesis of methanol via CO2 hydrogenation, Journal of Catalysis, 300 (2013) 141-151.

[20] R. Ladera, F.J. Pérez-Alonso, J.M. González-Carballo, M. Ojeda, S. Rojas, J.L.G. Fierro, Catalytic valorization of CO2 via methanol synthesis with Ga-promoted Cu–ZnO–ZrO2 catalysts, Applied Catalysis B: Environmental, 142 (2013) 241-248.

[21] X. Liu, P. Ramírez de la Piscina, J. Toyir, N. Homs, CO2 reduction over Cu-ZnGaMO (M=Al, Zr) catalysts prepared by a sol-gel method: Unique performance for the RWGS reaction, Catalysis Today, DOI http://dx.doi.org/10.1016/j.cattod.2017.04.022(2017).

[22] S. Esposito, M. Turco, G. Bagnasco, C. Cammarano, P. Pernice, New insight into the preparation of copper/zirconia catalysts by sol–gel method, Applied Catalysis A: General, 403 (2011) 128-135.

[23] G. Bonura, M. Cordaro, C. Cannilla, F. Arena, F. Frusteri, The changing nature of the active site of Cu-Zn-Zr catalysts for the CO2 hydrogenation reaction to methanol, Applied Catalysis B: Environmental, 152 (2014) 152-161.

[24] X. Guo, D. Mao, G. Lu, S. Wang, G. Wu, CO_2 hydrogenation to methanol over $Cu/ZnO/ZrO_2$ catalysts prepared via a route of solid-state reaction, Catalysis Communications, 12 (2011) 1095-1098.

[25] X. Guo, D. Mao, G. Lu, S. Wang, G. Wu, Glycine–nitrate combustion synthesis of CuO–ZnO–ZrO2 catalysts for methanol synthesis from CO2 hydrogenation, Journal of Catalysis, 271 (2010) 178-185.

[26] X. Guo, D. Mao, S. Wang, G. Wu, G. Lu, Combustion synthesis of CuO–ZnO–ZrO2 catalysts for the hydrogenation of carbon dioxide to methanol, Catalysis Communications, 10 (2009) 1661-1664.

[27] F. Liao, Y. Huang, J. Ge, W. Zheng, K. Tedsree, P. Collier, X. Hong, S.C. Tsang, Morphology-Dependent Interactions of ZnO with Cu Nanoparticles at the Materials' Interface in Selective Hydrogenation of CO2 to CH3OH, Angewandte Chemie International Edition, 50 (2011) 2162-2165.

[28] M.-F. Luo, J.-M. Ma, J.-Q. Lu, Y.-P. Song, Y.-J. Wang, High-surface area CuO–CeO2 catalysts prepared by a surfactant-templated method for low-temperature CO oxidation, Journal of Catalysis, 246 (2007) 52-59.

[29] L. Qi, Q. Yu, Y. Dai, C. Tang, L. Liu, H. Zhang, F. Gao, L. Dong, Y. Chen, Influence of cerium precursors on the structure and reducibility of mesoporous CuO-CeO2 catalysts for CO oxidation, Applied Catalysis B: Environmental, 119 (2012) 308-320.

[30] Z. Wang, Z. Qu, X. Quan, Z. Li, H. Wang, R. Fan, Selective catalytic oxidation of ammonia to nitrogen over CuO-CeO2 mixed oxides prepared by surfactant-templated method, Applied Catalysis B: Environmental, 134 (2013) 153-166.

[31] X. Ma, X. Feng, X. He, H. Guo, L. Lv, J. Guo, H. Cao, T. Zhou, Mesoporous CuO/CeO2 bimetal oxides: One-pot synthesis, characterization and their application in catalytic destruction of 1,2-dichlorobenzene, Microporous and Mesoporous Materials, 158 (2012) 214-218.

[32] A. Fathy, O. Elkady, A. Abu-Oqail, Synthesis and characterization of Cu–ZrO2 nanocomposite produced by thermochemical process, Journal of Alloys and Compounds, 719 (2017) 411-419.

[33] H. Xu, B.W. Zeiger, K.S. Suslick, Sonochemical synthesis of nanomaterials, Chemical Society reviews, 42 (2013) 2555-2567.

[34] C.I. Ezeh, M. Tomatis, X. Yang, J. He, C.-g. Sun, Ultrasonic and Hydrothermal Mediated Synthesis Routes for Functionalized Mg-Al LDH: Comparison Study on Surface Morphology, Basic Site Strength, Cyclic Sorption Efficiency and Effectiveness, Ultrasonics Sonochemistry, DOI https://doi.org/10.1016/j.ultsonch.2017.07.013.

[35] H.W. Olfs, L.O. Torres-Dorante, R. Eckelt, H. Kosslick, Comparison of different synthesis routes for Mg–Al layered double hydroxides (LDH): Characterization of the structural phases and anion exchange properties, Applied Clay Science, 43 (2009) 459-464.

[36] X. Dong, H.-B. Zhang, G.-D. Lin, Y.-Z. Yuan, K.R. Tsai, Highly Active CNT-Promoted Cu–ZnO–Al2O3 Catalyst for Methanol Synthesis from H2/CO/CO2, Catalysis Letters, 85 (2003) 237-246.

[37] J.A. Ahlers, J.A. Grasser, B.T. Loveless, D.S. Muggli, Room-temperature oxidation of reduced Cu/ZnO surfaces by lattice oxygen diffusion, Catalysis Letters, 114 (2007) 185-191.

[38] P. Gao, H. Yang, L. Zhang, C. Zhang, L. Zhong, H. Wang, W. Wei, Y. Sun, Fluorinated Cu/Zn/Al/Zr hydrotalcites derived nanocatalysts for CO2 hydrogenation to methanol, Journal of CO2 Utilization, 16 (2016) 32-41.

[39] H. Wilmer, T. Genger, O. Hinrichsen, The interaction of hydrogen with alumina-supported copper catalysts: a temperature-programmed adsorption/temperature-programmed desorption/isotopic exchange reaction study, Journal of Catalysis, 215 (2003) 188-198.

[40] X. Guo, D. Mao, G. Lu, S. Wang, G. Wu, The influence of La doping on the catalytic behavior of Cu/ZrO2 for methanol synthesis from CO2 hydrogenation, Journal of Molecular Catalysis A: Chemical, 345 (2011) 60-68.

[41] L. Zhang, Y. Zhang, S. Chen, Effect of promoter SiO2, TiO2 or SiO2-TiO2 on the performance of CuO-ZnO-Al2O3 catalyst for methanol synthesis from CO2 hydrogenation, Applied Catalysis A: General, 415–416 (2012) 118-123.

[42] H. Zhan, F. Li, P. Gao, N. Zhao, F. Xiao, W. Wei, L. Zhong, Y. Sun, Methanol synthesis from CO2 hydrogenation over La–M–Cu–Zn–O (M = Y, Ce, Mg, Zr) catalysts derived from perovskite-type precursors, Journal of Power Sources, 251 (2014) 113-121.

[43] J. Toyir, P. Ramirez de la Piscina, J. L. G. Fierro, N. Homs, Catalytic Performace for CO_2 Conversion to Methanol of Gallium Promoted Copper based Catalysts: Influence of Metallic Precursors, Applied Catalysis B, 34 (2001) 255-266.

[44] C. Zhong, X. Guo, D. Mao, S. Wang, G. Wu, G. Lu, Effects of alkaline-earth oxides on the performance of a CuO-ZrO2 catalyst for methanol synthesis via CO2 hydrogenation, RSC Advances, 5 (2015) 52958-52965.

[45] P. Gao, F. Li, H. Zhan, N. Zhao, F. Xiao, W. Wei, L. Zhong, H. Wang, Y. Sun, Influence of Zr on the performance of Cu/Zn/Al/Zr catalysts via hydrotalcite-like precursors for CO2 hydrogenation to methanol, Journal of Catalysis, 298 (2013) 51-60.

CHAPTER SIX

ENHANCEMENT OF CO_2 ADSORPTION BY AMINE MODIFIED LAYERED DOUBLE HYDROXIDE SYNTHESIZED VIA ULTRASONIC FACILITATED SDS/APTES INTERCALATION

Abstract

To improve CO_2 adsorption, amine modified Layered double hydroxide (LDHs) were prepared via a two stage process, SDS/APTES intercalation was supported by ultrasonic irradiation and then followed by MEA extraction. The prepared samples were characterised using Scanning electron microscope-Energy dispersive X-ray spectroscopy (SEM-EDX), X-ray Photoelectron Spectroscopy (XPS), X-ray diffraction (XRD), Temperature Programmed Desorption (TPD), Brunauer-Emmett-Teller (BET), and Thermogravimetric analysis (TGA), respectively. The characterisation results were compared with those obtained using the conventional preparation method with consideration to the effect of sonochemical functionalization on textural properties, adsorption capacity, regeneration and lifetime of the LDH adsorbent. It is found that LDHs prepared by sonochemical modification had improved pore structure and CO_2 adsorption capacity, depending on sonic intensity. This is attributed to the enhanced deprotonation of activated amino functional groups via the sonochemical process. Subsequently, this improved the amine loading and effective amine efficiency by 60% of the conventional. In addition, the sonochemical process improved the thermal stability of the adsorbent and also, reduced the irreversible CO_2 uptake, CUirrev, from 0.18 mmol/g to 0.03 mmol/g. Subsequently, improving the lifetime and ease of regenerating the adsorbent respectively. This is authenticated by subjecting the prepared adsorbents to series of thermal swing adsorption (TSA) cycles until its adsorption capacity goes below 60% of the original CO_2 uptake. While the conventional adsorbent underwent a 10 TSA cycles before breaking down, the sonochemically functionalized LDH went further than 30 TSA cycles.

Keywords: *CO_2 Capture, Layered Double Hydroxide, Ultrasound, Adsorption, Regeneration.*

6.1 INTRODUCTION

Carbon dioxide adsorption is viewed as one of the promising methods in Carbon Capture and Storage (CCS) technology [1, 2]. It has been widely accepted that an estimated 30-50% energy requirement reduction can be obtained when compared to absorption by amine solvents [3, 4]. However, numerous factors must be considered for achieving this optimum performance as pointed out by Drage et al. [4]. Extensive reviews on materials used for CO_2 adsorption have been done by many researchers. These materials include amine polymers [5, 6], immobilized amines [7, 8], carbonaceous materials [9-11], Layered double hydroxides (LDHs) [2, 12, 13], zeolites [14-16] and organic-inorganic hybrids [17-19]. Owing to its comparably high adsorption capacity and numerous catalytic applications [13, 20], the LDHs has been broadly investigated and considered to be one of the most promising flexible adsorbents [21]. In addition, its ionic inter-layered structural configuration provides the material with relatively high contact surface area and active basic sites to serve as a catalyst (or support) [20]. However, the material is challenged by its low CO_2 uptake, regeneration capacity and thermo-stability [21, 22].

The low adsorption capacity of LDH is partly attributed to the poor textural characteristics [23, 24] and low amine loading as reported in previous studies [2]. Adopted methods to improve these features involved the use of anionic surfactants and organoalkoxysilane amines which served the purpose of widening the interlayer gallery of the LDHs to bolster its exfoliation process [12] while simultaneously increasing the amine content [25]. Frequently used surfactants are sodium dodecyl sulphate (SDS) [2, 26] and sodium dodecyl sulphonate [27], while the organoalkoxysilanes includes N-trimethoxysilylpropyl-N,N,N-trimethylammonium chloride [28], (3-aminopropyl)-triethoxysilane (APTES) [2, 27, 29] and (3-aminopropyl)-trimethoxysilane (APTMS) [26]. Nonetheless, reported amine loading and subsequent adsorption capacity of the adsorbent is not satisfactory. This was attributed to the poor pore structure of the adsorbent.[24]. To further enhance the porosity and textural properties of the adsorbent, sonic irradiation has been applied in chemical synthesis of the adsorbent. Ultrasonic technology has been observed to rapidly promote inorganic and organic reactions without

weakening the final material properties [23]. Furthermore, this technology improves the porosity and surface area of the synthesized material in addition to increasing metallic dispersion across the material [13]. However, in its industrial applicability, the prepared adsorbent should be able to withstand the thermal atmosphere during adsorption. Review of sonochemical route reports that ultrasonic irradiation can lead to detrimental acoustic cavitation [30] which can result to breakdown of the material. This can be partly due to the sonic intensity. Another crucial feature of LDH for industrial application is the lifetime and ease of regenerating the adsorbent. The ease of regeneration will reduce the energy required for CO_2 recovery; hence, improving the overall capture efficiency. Moreover, the adsorbents lifetime will define the rate of replacing the adsorbent, consecutively affecting the process economics.

In this work, we have understudied the contribution of the sonochemical preparation of functionalized LDH to its industrial applicability with regards to its textural characteristics, thermal strength, adsorption and cyclic regeneration capacity, as well as its impact for further gaseous adsorption. The LDH adsorbents were synthesised via anionic surfactant interaction and amine extraction through ultrasonic modulation. The adopted amine used for functionalization of the LDH is monoethanolamine (MEA). The obtained LDHs were characterised using Scanning Electron Microscope (SEM), Energy Dispersion X-ray Spectroscopy (EDX), Brunauer-Emmett-Teller (BET), Thermal Gravimetric Analyzer (TGA), Temperature-Programmed Desorption (TPD), X-ray Photoelectron Spectroscopy (XPS) and X-ray Diffraction (XRD). With consideration to the energy demand for CO_2 recovery, transportation and storage, the thermal swing adsorption cycle (TSA) was favoured against the pressure swing adsorption (PSA) to study the cyclic regeneration of the adsorbent [5]. To this regard, the regeneration of the adsorbent was carried out isothermally at ambient pressure using N_2 as the stripping gas. The adsorbents lifetime was also examined over numerous TSA cycles till its CO_2 uptake is 60% of the original sorption capacity.

6.2 EXPERIMENTAL

6.2.1 Materials

The LDHs were prepared via different route: co-precipitation and ultrasonic mediated means. Subsequently, MEA extractions of these LDHs were carried out to produce the amine modified LDHs. All reagents used for material synthesis were purchased from SinoPharm Chemical Reagents Co. Ltd. The CO_2 and N_2 gases used for characterization and adsorption measurements are 99.99% pure and were supplied by Linde Group, China.

6.2.2 Sample Synthesis

For *MgAl LDH,* 200 ml solution containing APTES (≥98%) and SDS (≥86%) (molar ratio: 5:1) respectively dissolved in a mixture of 50 ml C_2H_5OH (≥99.7%) and 150 ml distilled water was stirred for about 30 min at a temperature of 60 ^oC until the pH stabilized at about 10.3. This solution was then reacted with $Mg(NO_3)_2{\cdot}6H_2O$ (≥98%) and $Al(NO_3)_3{\cdot}9H_2O$ (≥99%) (molar ratio: 3:1, dissolved in 100 ml of distilled water) solution by adding the latter dropwise while maintaining the temperature of the former at 60 ^oC. pH of the mixture was regulated towards 10 by adding 4 M NaOH (≥96%) solution. The substrate with a molar ratio of Mg:Al:APTES:SDS = 3:1:5:1 was then aged for 20hr with the temperature and stirring maintained. The precipitates were filtered, washed with distilled water and then dried in a vacuum oven (500 mbar at 70 ^oC) overnight. This sample is labelled as LDH5. Varying the amount of SDS, two other samples were produced with mole ratios of Mg:Al:APTES:SDS = 3:1:5:2.5 and 3:1:5:5 labelled as LDH2 and LDH1 respectively. Using the same chemical composition and process, a set of new samples were prepared using sonicated mixing either by ultrasonic horns (high intensity sonication, 600W) or bath (low intensity sonication, 150W). These samples are labelled as UH-LDHn and UB-LDHn respectively, n being the stoichiometric ratio of APTES to SDS.

For *MgAl LDH-MEA,* in the preparation of the amine modified LDH, the SDS surfactant were removed via MEA extraction as applied by Zheng et al. [31]. 0.5 g of LDH5 sample was

dispersed in a solution of 100ml C_2H_5OH (≥99.7%) containing 20g MEA (≥99%). The mixture was then refluxed for 20 hr at a temperature of 90 ^oC. After which the samples were filtered, washed with ethanol and dried in a vacuum oven overnight. These samples are labelled LDH-MEA5, LDH-MEA2 and LDH-MEA1 respectively. Using an ultrasonic bath, the procedure was repeated for the synthesised UB-LDHn samples. Synthesised UB-LDHn samples were similarly dispersed in a solution of C_2H_5OH and MEA; and then refluxed for 20 hr while using the ultrasonic bath filled with distilled water at a temperature of 90 ^oC. The obtained samples are labelled as UB-MEAn. In the same procedure, UH-MEAn samples were prepared. During reflux, ultrasonic horn was used rather than the bath.

6.2.3 Characterization

6.2.3.1 Scanning Electron Microscopy (SEM) – Energy Dispersive X-ray Spectroscopy (EDX) Analysis

The surface morphology of the prepared materials were studied with a Zeiss ΣIGMA™ Field Emission SEM. With the aid of an Oxford Instrument INCAx-act PentaFET® Precision EDX, the EDX spectra for the LDHs were obtained. This was also used to compute the amine content present in the adsorbents.

6.2.3.2 X-ray Diffraction (XRD and X-ray Photoelectron Spectroscopy (XPS)) Analysis

XRD patterns were studied using a Bruker-AXS D8 advance powder diffractometer with a scanning range of $10^o \leq 2\theta \leq 90^o$. The basal spacing was calculated with Bragg's Law using the d_{003} peak from the diffraction pattern. X-ray Photoelectron Spectroscopy (XPS) data of the adsorbent was obtained using Kratos X-ray Photoelectron Spectrometer – Axis Ultra DLD with a 96 W monochromatic Al Kα X-ray source (1486.69 eV) at a photoelectron take-off angle of 45°. Wide scans were performed from 1100 eV to 0 eV with a dwell time of 150 ms and steps of 1 eV. Narrow scans were performed with steps of 0.05 eV with dwell time of 600 ms. The binding energy (BE) was calibrated by using the C 1s peak at 284.6 eV as a reference.

6.2.3.3 Nitrogen Adsorption-Desorption Measurement

The textural properties of the prepared adsorbents were studied by Nitrogen physisorption analysis at -196 ^{o}C using the Micrometrics ASAP 2020 Surface Area and Porosity Analyser. Prior to this analysis, samples were degassed at a temperature of 105 ^{o}C for 4hr. The BET (Brunauer, Emmett and Teller) model was used to determine the surface area (S_{BET}) of the samples. The total pore volumes (V_{Total}) were computed from the amount of nitrogen adsorbed at relative pressure (P/P_o) of 0.99 and the average pore volumes from $4V_{Total}/S_{BET}$. The pore size distribution was calculated using the BJH (Barrett, Joyner and Halenda) model. The t-plot method was used to calculate the micopore volume (V_{micro}).

6.2.3.4 CO_2 Uptake Measurement

CO_2 adsorption was measured by a Netzsch STA 449 F3 Jupiter thermo-gravimetric analyser (TGA). Approximately 5-10 mg of each sample was heated from 25 to 105 ^{o}C at 20 ^{o}C/min under N_2. The sample was held at 105 ^{o}C for 30 min and then cooled to the desired adsorption temperature at a rate of 10 ^{o}C/min. The gas input was switched from N_2 to CO_2 and held isothermally for 90 min. The experimented adsorption temperatures were 55 ^{o}C and 80 ^{o}C (reported optimum adsorption temperature for most amine functionalised adsorbents [32]). The CO_2 adsorption capacity was determined from the weight change of the samples in CO_2 atmosphere. Effects of the change in gas density and viscosity were corrected by measuring the response to an empty alumina crucible using the same method.

6.2.3.5 Adsorbent Regeneration via Thermal Swing Adsorption Cycles

A thermal swing adsorption-desorption programme in the presence of N_2 was conducted using the Netzsch STA 449 F3 Jupiter thermo-gravimetric analyser. This is to determine the lifetime adsorption capacity of the adsorbent. After the CO_2 uptake measurement, the adsorbent was heated to 105 ^{o}C at a rate of 20 ^{o}C/min in a N_2 atmosphere with a constant flow rate of 20 ml/min and held isothermally for 30 mins. After desorption, the adsorption cycle was repeated

several times. The experimented adsorption temperature is 55 ^{o}C. Adsorption capacities were computed based on the mass of the adsorbent.

6.2.3.6 Thermal Stability Measurement

The stability of the as synthesised LDH samples in air was determined using the Netzsch STA 449 F3 Jupiter thermogavimetric analyser. About 5-10 mg of sample was loaded into an alumina crucible, and the decomposition was monitored by increasing temperature from 25 to 1000 ^{o}C with a heating rate of 10 ^{o}C/min and under a flow of air (50 ml/min).

6.2.3.7 Temperature-Programmed Desorption (TPD)

CO2-TPD analysis was conducted using AutoChem II 2920. The TPD of CO2 measurements were implemented to analyze the acidity and basicity of the catalysts. 0.1 g of the adsorbent was first placed in the reactor and treated at 350 °C for 2 hr in N2. During desorption, a thermal conductivity detector (TCD) was employed to record the TPD profiles from 100 to 800 °C with a heating rate of 10 °C/min.

6.3 RESULTS AND DISCUSSION

6.3.1 Effect of the variation of SDS and sonication on the morphology of LDHs

Figure 6.1 shows the SEM images of prepared LDHs. At low amount of SDS (Mole ratio, n = 5), the layered hydroxide exhibits irregular shapes and is highly porous and permeable with little or no agglomeration on the surface of the sample. As the addition of SDS increases, APTES/SDS mole ratio decreases, accompanied by significant changes of the surface of the adsorbent with remarkably increased particle agglomeration. It can be seen from the figure that the LDH2 sample clearly forms a flake-like shell over an irregular dense shaped core. Further increase of SDS results in the flake-like shell becoming curled up as can be seen from the sample of LDH1. This may be explained by the formation of shell-core structure caused by the sequential reduction of two different metallic ions [33], resulting from difference in the

reduction potentials of Mg^{2+} and Al^{3+} ions. It could be said that the excess Mg^{2+} ions are oxidized preferably to the Al^{3+} ions, resulting in the formation of Mg-core/Al-shell particles. The increased particle aggregation and subsequent surface restructuring was due to the physiochemical property of SDS. Due to its mean aggregation number of 62, SDS are able to form aggregates at high concentrations [34]. Comparing the inter-layer spacing between the flake-shells for different samples, LDH2 seems to be more spaced due to an irregular layering of flakes. Unlike LDH2, LDH1 was observed to have a lower interlayer spacing due to the folding of the flaky layers while undergoing intra-layer interactions. The amine modified LDHs show similar surface structures irrespective of the variation in SDS amount. However, they exhibited more surface granular agglomeration, as seen from Figure 6.2. It is interesting to note here that the flaky-shells of the LDH2 and LDH1 were no longer visible after applying MEA extraction. The samples of LDH-MEA2 and LDH-MEA1 showed some coated edges on the surface of the particles while this was not found in the sample of LDH-MEA5. Figure 6.3 shows the SEM image of LDH prepared using ultrasonic irradiation at APTES/SDS mole ratio of 5 (UH-LDH5) in comparison to the conventional method. The surface of the sonicated LDH shows an evenly distributed undulated surface sites (Figure 6.3b) when compared to that of the conventional (Figure 6.3a). This stresses the impact of the sonication on the morphology, and probably, on the physical properties of the material [33] as shown in the Table 6.1. Comparing the BET results of the conventional and sonochemically modified LDHs, it is observed that there is a significant difference in the textural properties of LDHs. S_{BET} and V_{Total} increased from 25.03 m^2/g and 0.02 cm^3/g for the conventional route to 171.20 m^2/g and 0.5528 cm^3/g respectively from the sonochemical process. However, the percentage of micropores to the total pore volume showed a decrease in value.

In order to fundamentally reveal the effect of addition of SDS on the internal structures of the LDHs and modified LDHs, the X-ray diffraction (XRD) was also used to characterise the prepared samples. The XRD pattern for LDH samples are shown in Figure 6.4. A rough look from the figure indicates that all samples exhibit similar patterns. However, a careful observation reveals that the intensity of the reflections at the peaks differs for each sample. A

notable peak appears at $2\theta = 60^{o}$. The appearance of this peak is as a result of overlapping of reflections from structural configurations of (113) and (110). It has been observed from the test that an increase in SDS (decrease in n) results in a decrease in the non-basal reflections. Reflections at (110) are common for the non-modified LDHs with large interlayer spacing [33, 35]. Hence, it can be stipulated that the increase in SDS will result in the reduction of large interlayer spacing [2], supported by the SEM images of the LDHs. Another insignificantly notable variation in peaks was observed to occur at $15^{o} \leq 2\theta \leq 25^{o}$. Within this range, the reflection is likely associated with the lattice (0018) [36]. It was also noticed that the increase in surfactant results in an increase in the reflection sharpness and intensity. This clearly indicates that the crystallinity of the sample increases for the LDH modification with SDS-APTES intercalation. However, the non-basal reflections at (012) seem to be preserved, indicating that the layered structures were unaffected by the change in surfactant amount. These trends were also observed in the sonochemically modified LDHs (Figures 6.5-6.8). Figures 6.5 and 6.6 show the XRD patterns for the sonicated LDH samples using low and high intensity sonications respectively. The patterns show similar trends to those of non-sonicated LDHn. It can be conjectured with a certain reservation that the adoption of sonication has no remarkable impact on the structure of the LDHn. However, a slight increase in the peak of (110) reflection was noticed for both ultrasonic modulated LDH. The use of MEA extraction for all prepared samples also demonstrates less influence on the structure of the adsorbents. The results of non-basal XRD peaks (0018), (012) and (110) shown in Figures 6.7 and 6.8 clearly indicates that the structure of the adsorbents is less affected by using MEA extraction.

Table 6.1: Pore structure of modified LDHs, gas uptake and recoverable adsorbed CO_2

Sample	Gas Uptake (mmol/g)		$\frac{\text{mmol } N_2}{\text{mmol } CO_2}$	CU_{rev}	CU_{irrev}	% of CU_{irrev}	S_{BET} (m^2/g)	Average Pore Width (nm)	V_{Total} (cm^3/g)	V_{micro} (cm^3/g)
	CO_2	N_2								
LDH-MEA5	1.45	0.23	0.16	1.27	0.18	12.64	25.03	2.57	0.0161	0.0008
UB-MEA5	0.54	0.14	0.25	0.51	0.03	6.39	-	-	-	-
UH-MEA5	1.37	0.43	0.31	1.33	0.03	2.43	171.20	12.92	0.5528	0.0229

Table 6.2: EDX elemental analysis and CO_2 uptake of prepared LDH and calculation results for the molecular formulas, removed SDS and effective amine efficiency

Sample	N (wt%)	C (wt%)	S (wt%)	Molecular formula (mmol/g)[a]	SDS/APTES	Amine Loading (mmol/g)	CO_2 Adsorbed (mmol/g)	SDS removed (%)	Effective amine loading (mmol/g)[b]	Effective Amine Efficiency[c]
LDH5	0.65	51.35	11.41	$[C_{12}H_{25}SO_4]_{3.57}$-.$[C_{0.01}H_{0.52}SiNO_3]_{0.46}$	7.68	0.46	0.82			
LDH-MEA5	6.60	26.60	1.05	$[C_{12}H_{25}SO_4]_{0.33}$-.$[C_{3.87}H_{10.17}SiNO_3]_{4.71}$	0.07	4.71	1.45	99.09	4.25	0.15
UB-LDH5	1.69	47.78	8.22	$[C_{12}H_{25}SO_4]_{2.57}$-.$[C_{7.45}H_{19.12}SiNO_3]_{1.21}$	2.13	1.21	0.48			
UB-MEA5	7.37	25.38	0.64	$[C_{12}H_{25}SO_4]_{0.20}$-.$[C_{3.56}H_{9.40}SiNO_3]_{5.26}$	0.04	5.26	0.54	98.21	4.06	0.02
UH-LDH5	3.11	51.16	11.08	$[C_{12}H_{25}SO_4]_{3.46}$-.$[C_{0.49}H_{1.72}SiNO_3]_{2.22}$	1.56	2.22	0.66			
UH-MEA5	7.34	30.64	0.60	$[C_{12}H_{25}SO_4]_{0.19}$-.$[C_{4.44}H_{11.60}SiNO_3]_{5.24}$	0.04	5.24	1.37	97.71	3.02	0.24

a All Nitrogen, Carbon and Sulphur elements in the grafted LDHs were attributed to come from organic compounds used for intercalation

b. Effective amine loading = Difference in amine loading before and after LDH modification

c. Effective Amine Efficiency = Difference in CO_2 adsorbed before and after LDH modification/effective amine loading

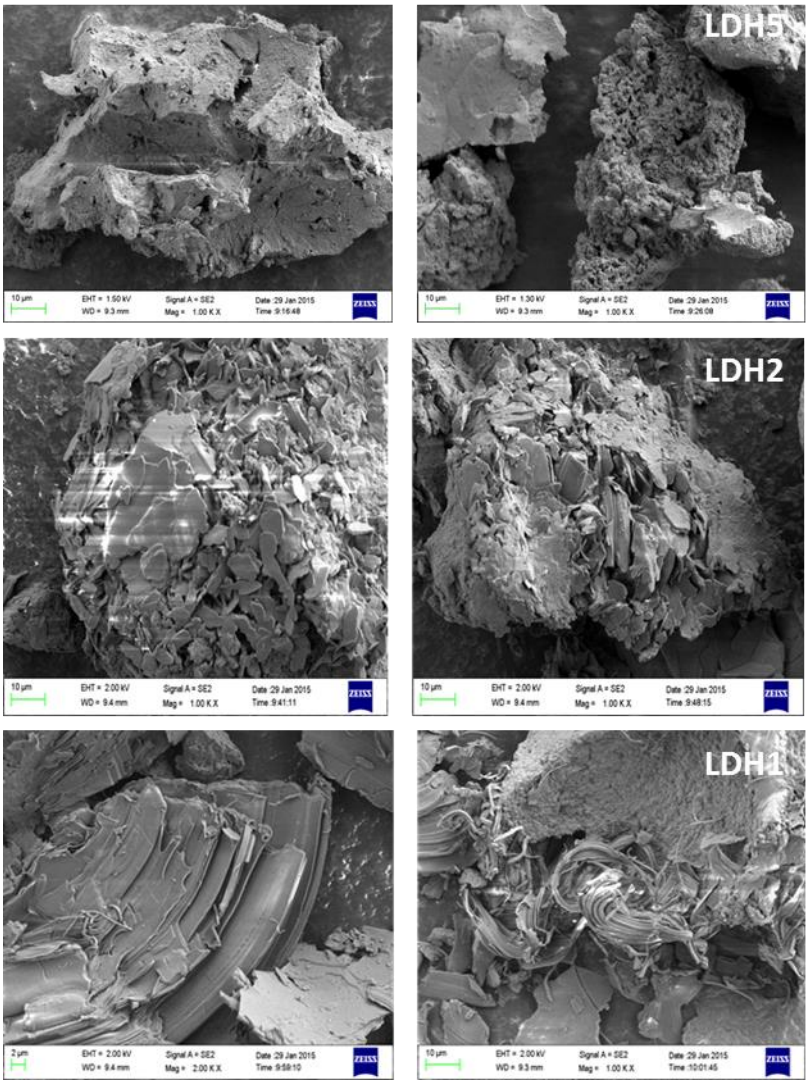

Figure 6.1: SEM Images of prepared LDHs with variation in Surfactant, SDS

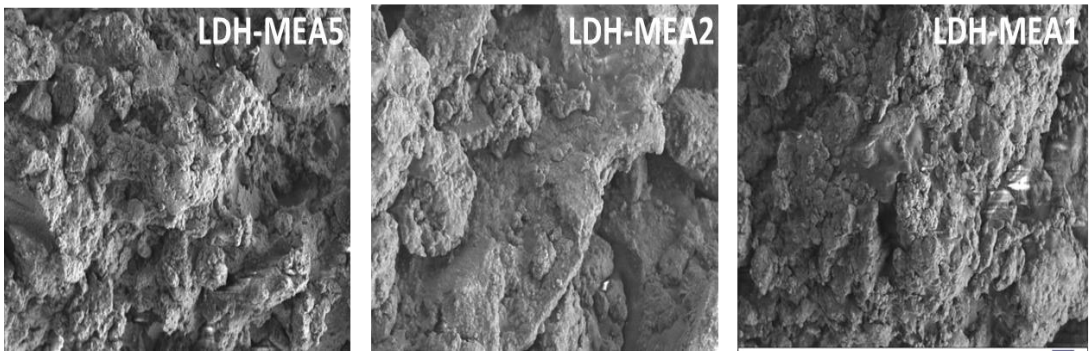

Figure 6.2: SEM images of LDH-MEAn at various APTES/SDS mole ratios (n = 5, 2 and 1)

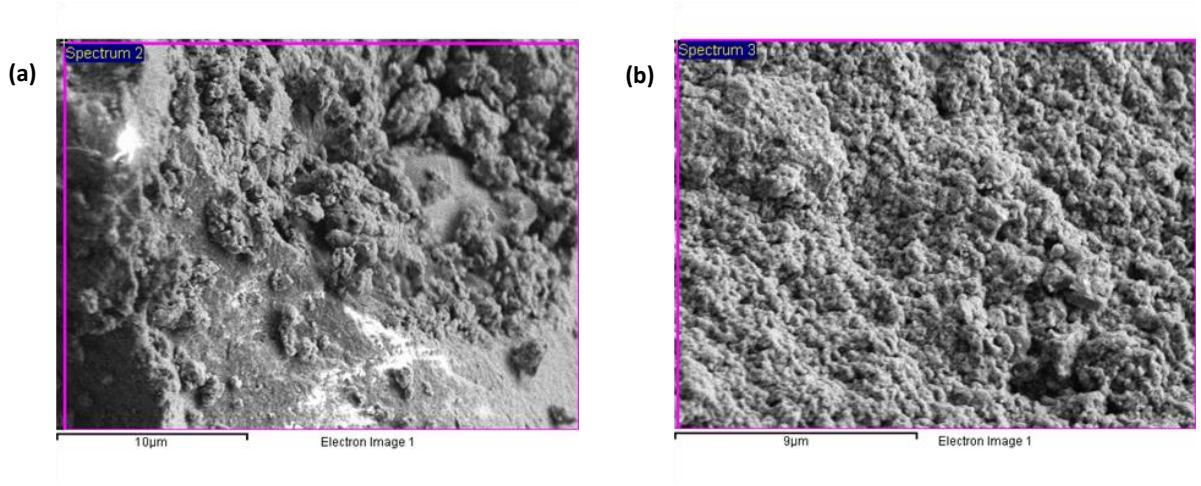

Figure 6.3: Comparison of surface texture of LDH prepared via (a) conventional, and (b) ultrasonic irradiation routes, at APTES/SDS mole ratio = 5 using ultrasonic horn (UH-LDH5)

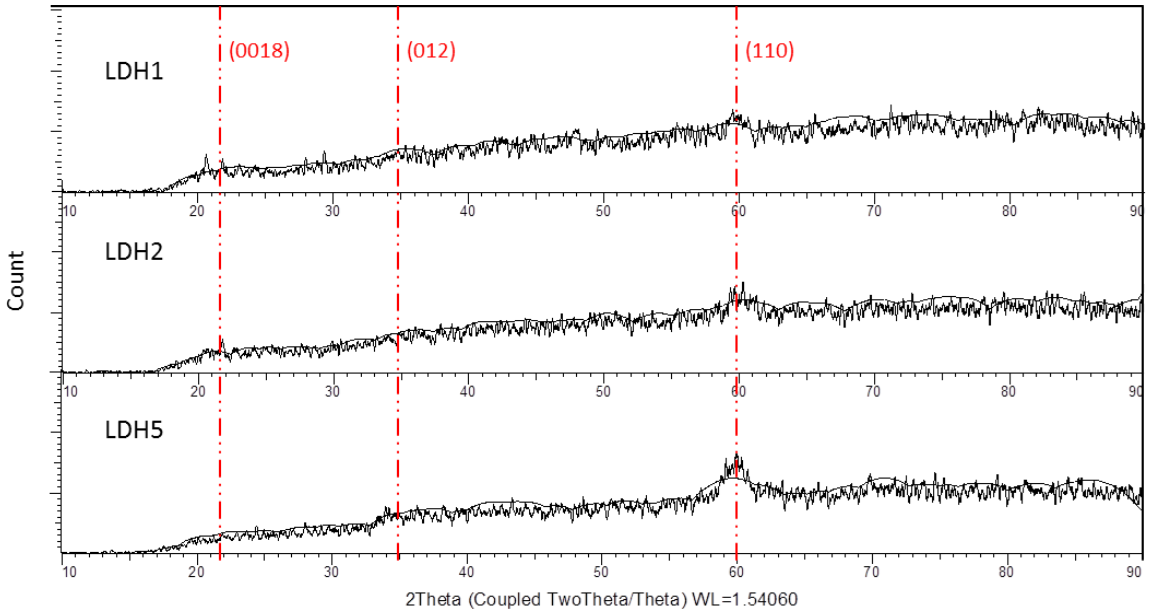

Figure 6.4: XRD patterns for LDHn (n = 1, 2 and 5) samples

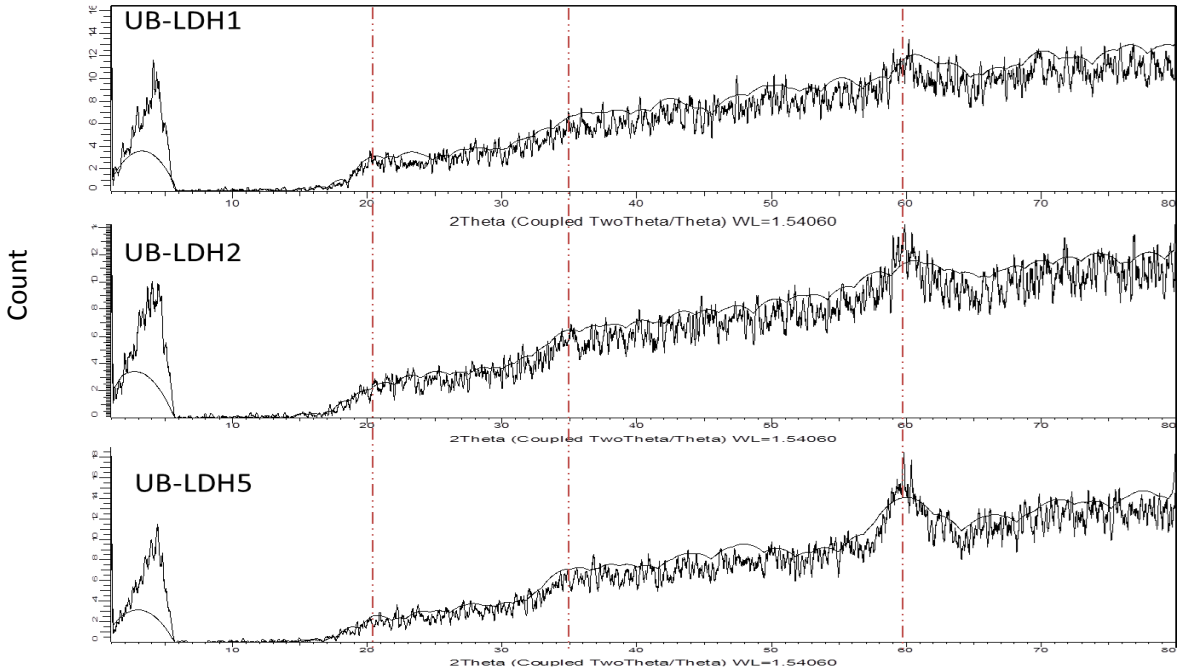

Figure 6.5: XRD patterns for UB-LDHn (n = 1, 2 and 5) samples

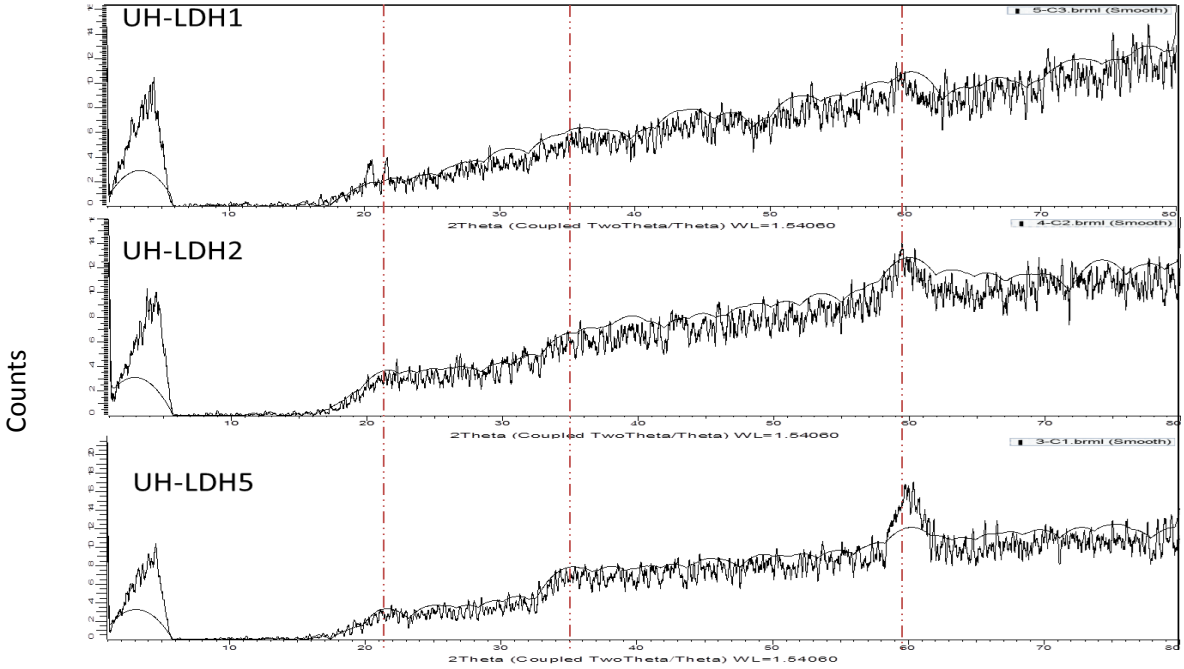

Figure 6.6: XRD patterns for UH-LDHn (n = 1, 2 and 5) samples

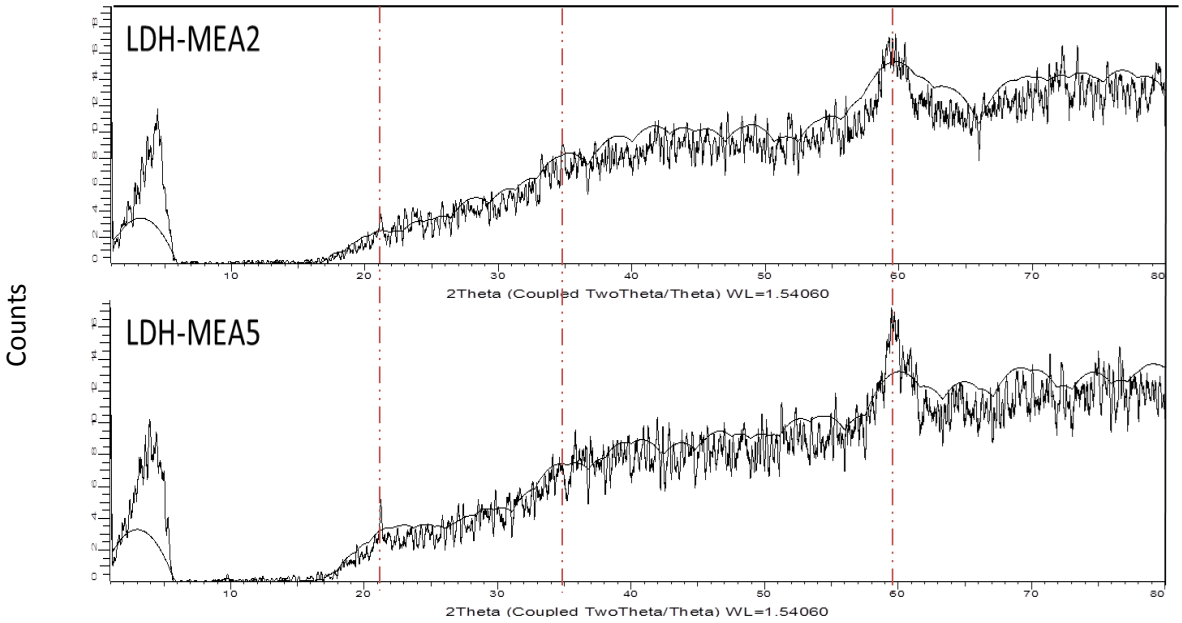

Figure 6.7: XRD patterns for LDH-MEAn (n = 2 and 5) samples

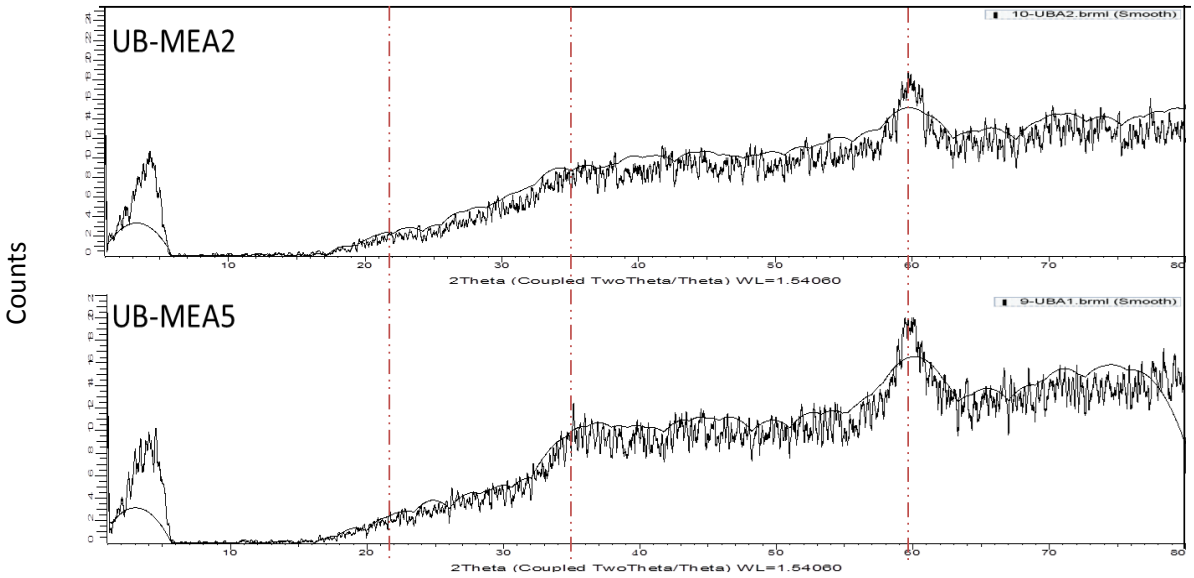

Figure 6.8: XRD patterns for UB-MEAn (n = 2 and 5) samples

6.3.2 Effect of amine modification on the prepared LDH on CO_2 adsorption capacity

For evaluating the effect of amine modification on CO_2 adsorption capacity, the characterisation of CO_2 adsorption process using the TGA is divided into three phases: (1) pre-heating of the sample from room temperature to 105 ^oC for 30 minutes under N_2 atmosphere

for the removal of absorbed water molecules; (2) under the same N_2 atmosphere, the sample was then cooled to the desired temperature for adsorption; and (3) switching the gas from N_2 to CO_2 for isothermal CO_2 adsorption. In the third phase, the CO_2 adsorbed by the sample is measured from the weight gained by the sample. An illustration of this process is shown in Figure 6.9(a).

Figure 6.10 shows the CO_2 adsorption capacities for those samples of (a) LDHn and (b) LDH-MEAn (with n being the molar ratio of APTES to SDS). The adsorption experiments were carried out twice (Appendix D, Table D6.1) and the data of the averaged weight gained from CO_2 adsorption were used in generating the figure. It was observed from the obtained data that as SDS increases (indicated by the decrease in mole ratio from 5 to 1) at 55 ^oC, the CO_2 uptake decreases from 0.82 to 0.59 mmol/g. This is consistent with finding reported in previous study but with lower CO_2 adsorption capacities 0.58 to 0.12 mmol/g [2]. The decrease in adsorption capacity is attributed to the protonation of amino groups by the surfactant's anions given the increased addition of SDS, thus preventing CO_2 adsorption on these sites. The same trend was also observed at 80 ^oC but with a decreased adsorption capacity of about 35-50% of that at 55 ^oC.

After adoption of MEA extraction, the CO_2 uptake by the LDH-MEAn samples at 55 ^oC increased by about 75-90% based on the LDHn samples. This is partly due to the increased amine loading, facilitating the extraction of the surfactant and consequently making the amino groups available for CO_2 adsorption. This trend was also found at 80^oC with an increase of about 10-30% in the CO_2 adsorption capacity of the LDH-MEAs. This significant change in adsorption performance can be explained by the CO_2 adsorption profile of APTES at varying temperature which tends to achieve the maximum in the range of the temperature of 60 to70 ^oC [2]. This trend was also observed in the sonicated LDHs. After amine modification, the adsorption capacity at 55 ^oC of the UB-LDH5 increased from 0.48 to 0.54 mmol/g, while UH-LDH increased from 0.66 – 1.37 mmol/g (Table 6.2). This increase can be attributed to the exfoliation of the surfactant and simultaneous increase in the amine loading by the MEA

extraction process. In this regard, the interacted amino groups with the negative head-groups of the surfactant are deprotonated, which are now free to react with CO_2. This can be validated by the increase in amine loading after MEA extraction as shown in Table 6.2.

Using the EDX spectroscopy, inspection tests were carried out for each LDH and the tabulated results (Table 6.2) show the average composition of the samples. The EDX results show the elemental configuration and dispersion across the internal micro structures of the prepared samples (Appendix D, Figure D6.1). From the obtained elemental analysis, the molecular formula of the grafted organic species, SDS and APTES, was computed using the general chemical formula for all amine modified LDH, $[Mg_3Al(OH)_m]_x^+.[C_{12}H_{25}SO_4]_y^-.[C_nH_{2.5n+0.5}SiNO_3]_z$ [5]. From the table, it is observed that the amount of sulphur reduced after MEA extraction resulting to a corresponding increase in nitrogen content. This shows that the extraction process was effective (c.a. 97-99% of SDS was removed) across all preparation route; hence, increasing the adsorption capacity after MEA extraction.

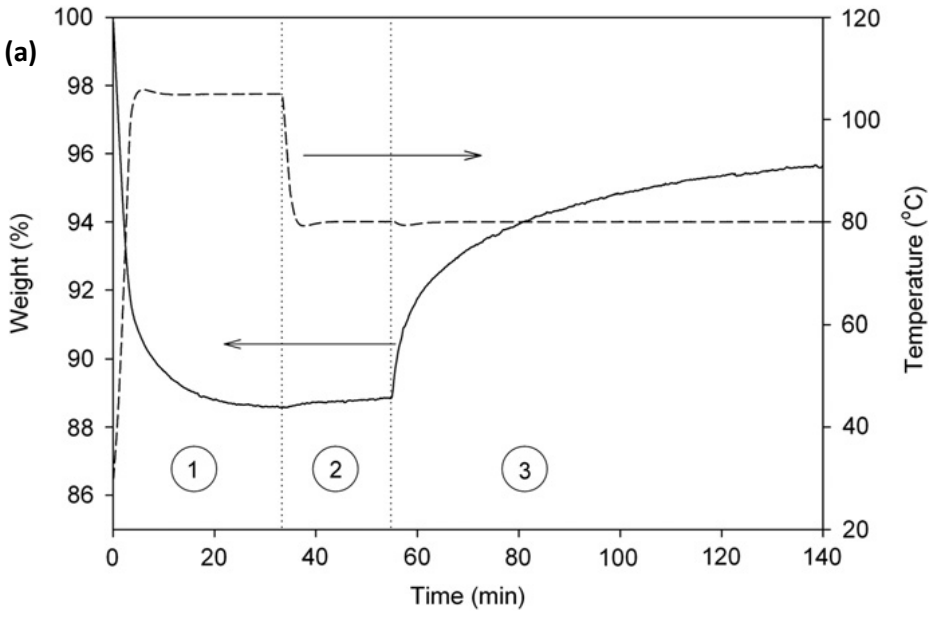

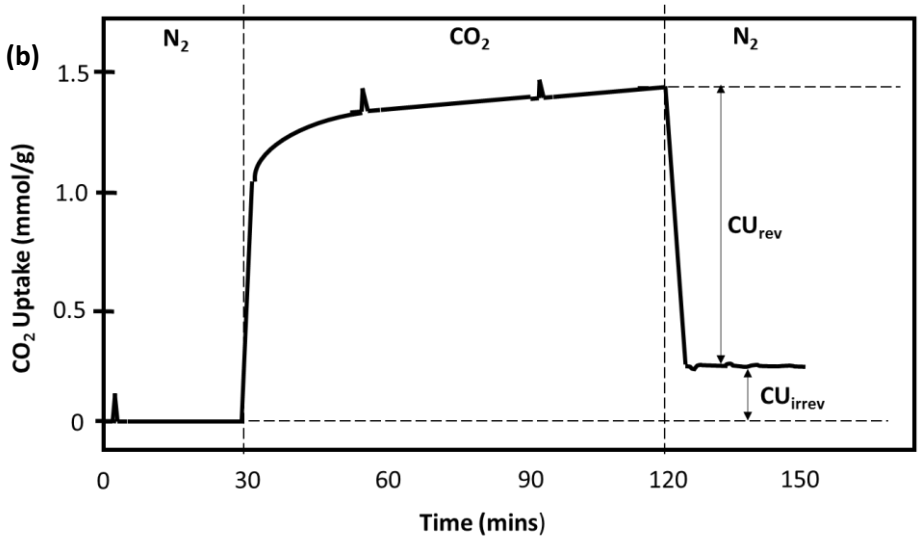

Figure 6.9: Example of (a) TGA curve for CO_2 adsorption, (b) recoverable CO_2 uptake using TSA at 105 ^oC in N_2 atmosphere.

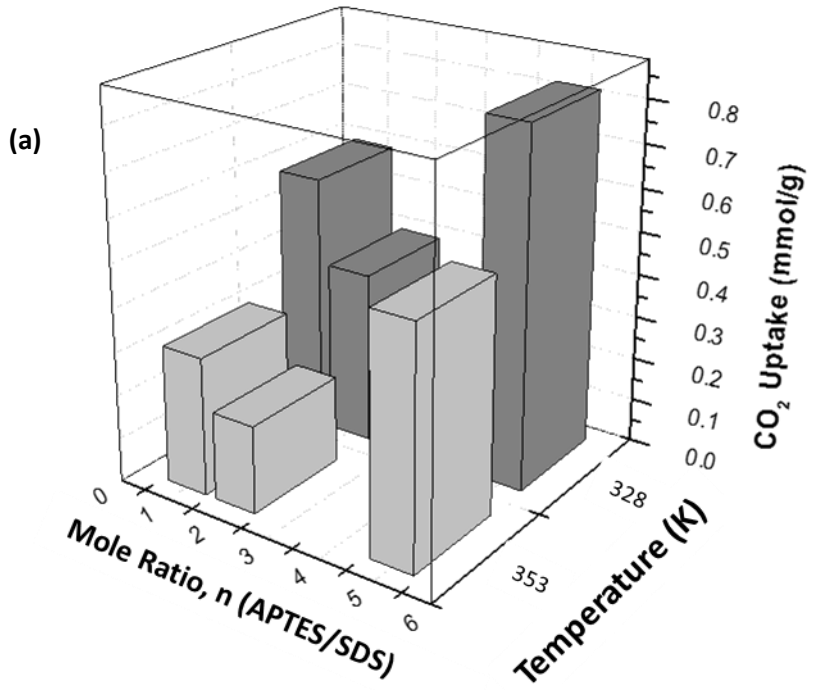

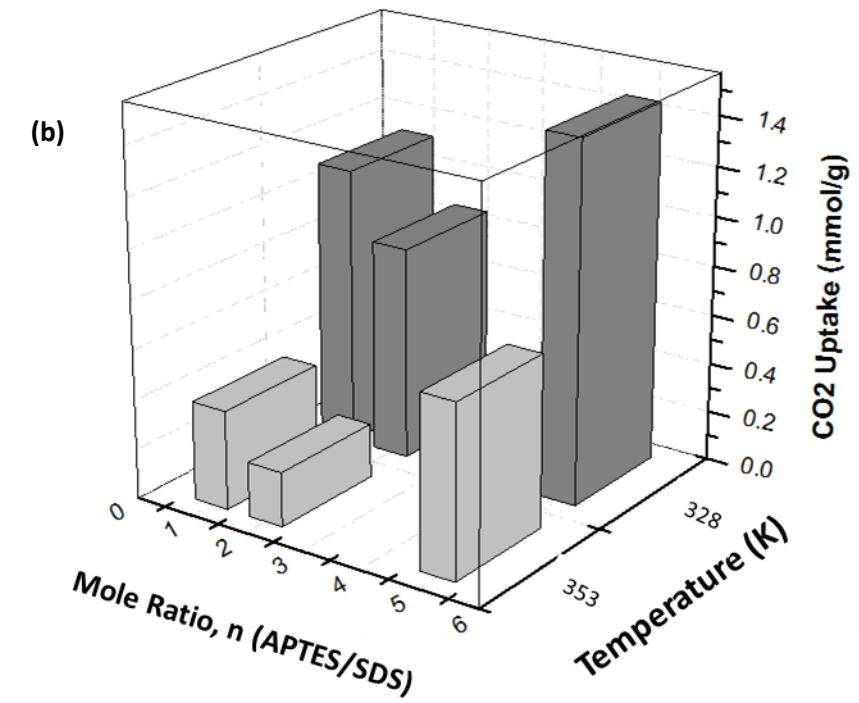

Figure 6.10: CO_2 Uptake for (a) LDHn and (b) LDH-MEAn (with n being the molar ratio of APTES to SDS)

6.3.3 Effect of ultrasonic modulation on CO_2 adsorption capacity

The effect of ultrasonic modulation was also studied in the preparation process. The stirring process was sonicated by applying either ultrasonic horn or ultrasonic bath. Table 6.3 shows the CO_2 uptake by LDHs produced using ultrasonic irradiation with ultrasonic horn and bath at temperatures of 55 ^oC and 80 ^oC. The results show a reduction in CO_2 uptake at both temperatures when compared to the conventional co-precipitation route as shown in Figure 6.11. It should be noted here that the result is yet to be validated with an optimum sonication condition for this material. This is subject to further research. However, the decrease in CO_2 adsorption by the sonicated sample can be explained by the enhanced chemical reaction facilitated by accelerated inter-particle collision within the local hot spot of the collapsing bubbles that are generated by the sonication [33]. Consequently, the available amino groups are readily bonded to the anionic surfactants, resulting to limited amino group active site for

CO_2 adsorption. Sonication aids in rearranging reactions with a bias towards reaction mechanisms that yields molecules not necessarily obtained from purely thermal or light induced reactions [35] or by adjusted physicochemical parameters [33]. Adequate studies must be carried out to discern the optimal ultrasonic power output for any preparation process. This importance can be illustrated by the use of mild sonication using ultrasonic bath rather than intense sonication from the ultrasonic horn. With the limited results obtained from the ultrasonic bath, it was observed that at a temperature of 80 ^oC, the CO_2 adsorbed at APTES/SDS mole ratio of 5, 2 and 1 are 0.74, 0.81 and 0.61 mmol/g, respectively, which is remarkably higher than that obtainable from the conventional LDHs (0.54, 0.20 and 0.315 mmol/g, respectively) and LDH-MEAs (0.695, 0.22 and 0.40 mmol/g, respectively). This clearly demonstrated that the preparation method can be optimised for favourable adsorbent synthesis using the controlled sonication.

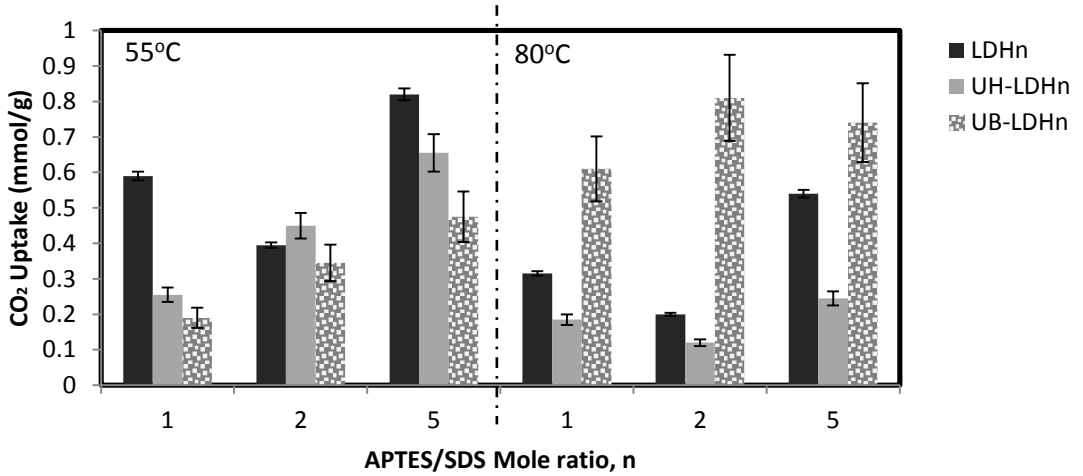

Figure 6.11: Comparison of CO_2 uptake by samples prepared via conventional (LDHn) and ultrasonic irradiation route (UH-LDHn and UB-LDHn) at 55°C and 80°C.

Table 6.3: Average CO_2 adsorption for prepared ultrasonic mediated LDHn samples

Sample		UH-LDH5	UH-LDH2	UH-LDH1	UB-LDH5	UB-LDH2	UB-LDH1
55°C	1st Trial	0.70	0.39	0.21	0.49	0.34	0.21
	2nd Trial	0.61	0.51	0.30	0.46	0.35	0.17
	Average	**0.655**	**0.45**	**0.255**	**0.475**	**0.345**	**0.19**
80°C	1st Trial	0.21	0.09	0.13	0.74	0.81	0.61
	2nd Trial	0.28	0.15	0.24	-	-	-
	Average	**0.245**	**0.12**	**0.185**	**0.74**	**0.81**	**0.61**

At the given desirable temperature of 55 ^{o}C, a comparison of the CO_2 uptake profile by the conventional and ultrasonic irradiation (both horn and bath) for APTES/SDS mole ratio of 5 is shown in Figure 6.12. In comparison to the conventional LDH5, the sonochemically prepared adsorbents, UB-LDH5 and UH-LDH5 exhibit a lower CO_2 uptake of 0.44 and 0.66 mmol/g respectively despite the high amine loading of 1.21 and 2.22 mmol/g when compared to the 0.46 mmol/g of the conventional with a CO_2 uptake of 0.82 mmol/g (see Table 6.2). This can be attributed to the enhanced protonation of the amino groups by the negative head of the surfactant caused by the ultrasonic irradiation irrespective of the high surfactant content in LDH5 (depicted by the high SDS/APTES ratio), which still possesses more active amino groups for CO_2 uptake. This is supported by the XPS result presented in Figure 6.13. XPS was conducted to investigate the content of the amino functional group on the adsorbent surface. Two bands of N 1s spectrum of LDH were observed at *ca*. 397 eV (Peak 1) and 401 eV (Peak 2) binding energies. These are assigned to free amine and protonated/H-bonded amines respectively [37, 38]. The spectrum shows the sonochemically prepared LDH to have less concentration of free amines, depicted by peak 1 (Figure 6.13b) when compared to that of the conventional (Figure 6.13a). Consequently, it reveals that there are limited amino group active sites readily available for CO_2 adsorption for UH-LDH. In addition, it is also relevant to note that the amine loading increased with sonication intensity. This is subject to further research for optimizing adsorbent performance. However, after amine modification, the amine loading of LDH-MEA5, UB-MEA5 and UH-MEA5 increased to 4.71, 5.26 and 5.24 mmol/g respectively with a corresponding increase in CO_2 uptake to 1.45, 0.54 and 1.37 mmol/g respectively. As reported by Wang et al [2], the average amine loading for monomeric amines grafted adsorbents is 3-4 mmol/g (See supporting document, Table S6.3). However, in this study, it is shown that this can be further improved via ultrasonic irradiation. The incremental change in amine loading is part due to the exfoliation of the surfactant. Nonetheless, the percentage of surfactants removed decreased insignificantly according to the trend conventional>UB>UH. Subsequently, this has an impact on the effective amine loading and effective amine efficiency. In this study, the effective amine efficiency was calculated as the amount of CO_2 uptake resulting from the additional amine loading after LDH functionalization

with MEA. UH-MEA5 showed the highest effective amine efficiency of 0.24 compared to 0.15 of LDH-MEA5. This elaborates the importance of sonication in deprotonating protonated and/or probably dispersing the amino groups during MEA extraction, making these groups available as active sites for CO_2 adsorption by about 60%.

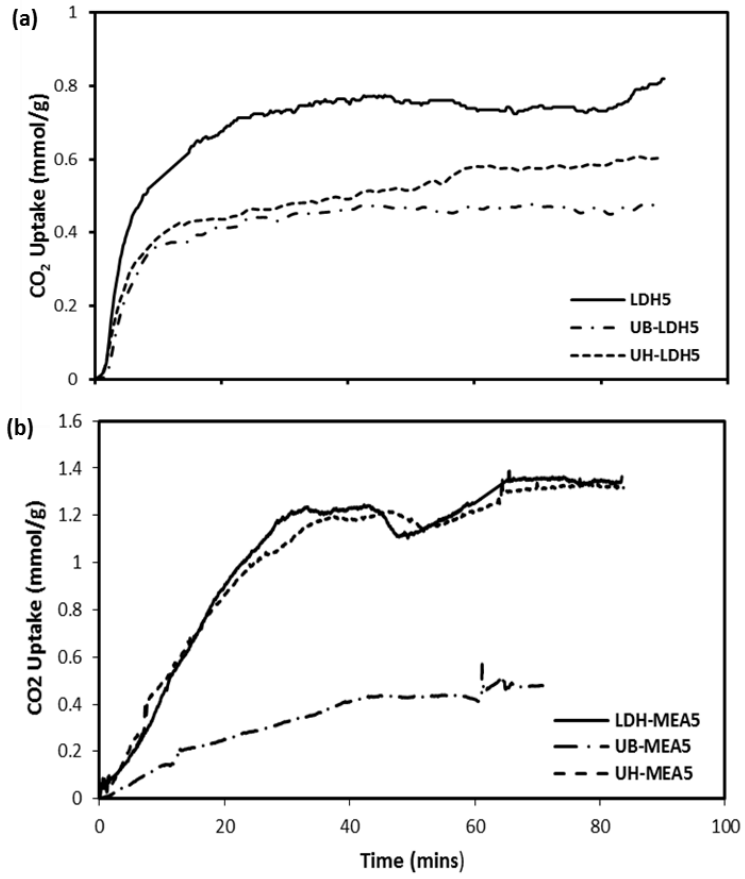

Figure 6.12: Comparison of CO_2 uptake by samples prepared via conventional (LDHn) and ultrasonic irradiation route (ultrasonic horn, UH-LDHn and ultrasonic bath, UB-LDHn) with APTES/SDS mole ratio, n = 5 at 55^oC (a) prior MEA extraction, and (b) post MEA extraction

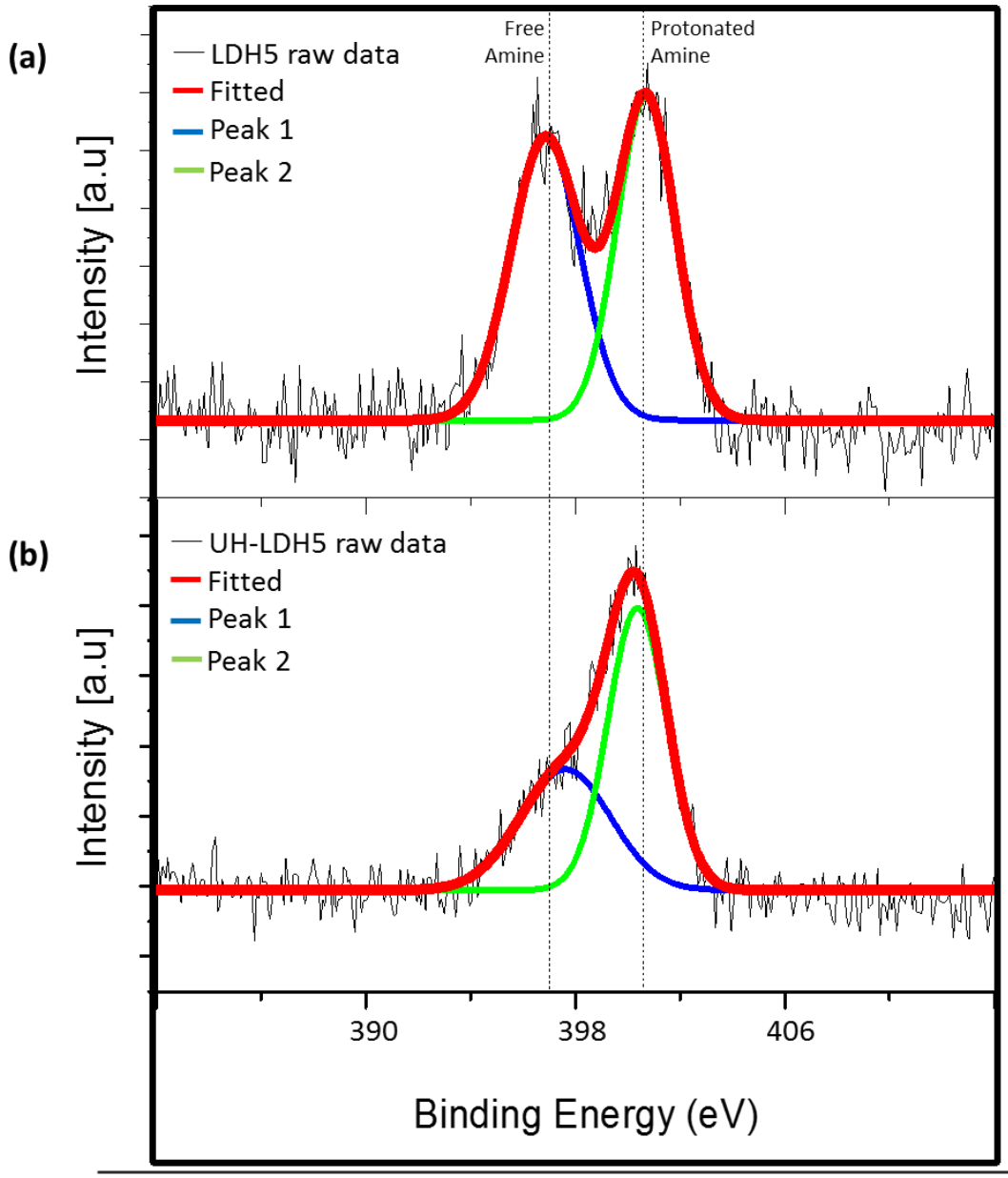

Preparation Route	Sample	Binding Energy (eV)		Area (cps eV)		Content (Free/Protonated)
		Free Amine	Protonated Amine	Free Amine	Protonated Amine	
Conventional	LDH5	396.7	400.8	660.0	606.4	1.1
Sonochemical	UH-LDH5	396.9	400.3	596.0	854.7	0.7

Figure 6.13: N 1s XPS spectra for (a) LDH5 and (b) UH-LDH5

6.3.4 Effect of the preparation routes on thermal stability of the amine modified LDHn

Using the TGA, the thermal stability of the prepared samples was determined from room temperature of about 20 ^{o}C to 1000 ^{o}C at a variation rate of 10 ^{o}C/min. The TGA profiles, as shown in Figure 6.14, indicate that the samples disintegrate within three temperature phases: T<~150 ^{o}C, ~150< T<~750 ^{o}C and ~750 ^{o}C< T. However, the second stage of disintegration for LDHn shows an uneven weight loss as compared to the regular weight loss for LDH-MEAn. The first stage of weight loss (T<~150 ^{o}C) is attributed to the loss of interstitial water molecules. While for the second phase (~150<T<~750 ^{o}C), the decomposition can be ascribed to the dehydroxylation and breakdown of the organic alkyl chain of the LDH. The observed irregular decomposition curve in this stage may implicate the occurrence of an uneven bonding structure, resulting to multi-stage dehydroxylation processes. The final weight loss (~750 ^{o}C<T) results from the decomposition of the sulphate species residuum.

Table 6.4 shows the tabulated results of the weight loss (%) of LDHn samples prepared using conventional and the ultrasonic routes. From the table, it can be seen that as the APTES/SDS mole ratio, n, reduces, the amount of interstitial moisture decreases. This has been observed in all preparation methods and could be explained by the additional presence of anionic surfactants that replace the water molecules. However, the ultrasonic route (UH) shows a less weight loss in the second and third stage (49-64%) compared with the UB-route (54-66%), which has a nearly same weight loss as that of the conventional method (54-66%). This can be further elaborated by the comparison of those curves in Figure 6.14a-c, where the decomposition curves of LDH and UB-LDH are seen to be undulated while the decomposition curve of UH-LDH seems to be regular, likely attributed to the more uniform mixing in UH-LDH so that a more even bonding structure within the material can be obtained. This indicates that the adoption of the UH-route may be beneficial to the synthesis of a more stable material than the UB and the conventional method.

After introducing amine modification of the samples, the decomposition curves clearly show different behaviour compared with that of the untreated LDHs prepared by the different methods. The curves display a well-defined three phase decomposition steps unlike the

untreated ones, as can be seen from Figure 6.14(d-f). Within the same temperature range as that of the LDHs, the MEA-treated LDHs show higher moisture content than the unprocessed ones (See Supporting document, S6.5). This can be caused by the presence of leftover MEA molecules after the extraction process. However, the weight losses in the second and third phase reduce significantly, benefitting to production of a more stable material than the pure LDH. This can be explained by the reduced presence of the surfactant after the amine extraction.

In addition, it can be discerned that the sonochemically prepared samples (UB-MEA and UH-MEA) demonstrate a more thermally stable profile than the conventional ones, showing by the total weight loss of 46-52% as compared with 53-64% of the LDH-MEA samples. This demonstrates that the adoption of ultrasonic route may contribute to an accessible distribution of the surfactant during the preparation of the LDH. As a result, the surfactants are easily extracted during the MEA extraction process, thus enhancing the stability of prepared material.

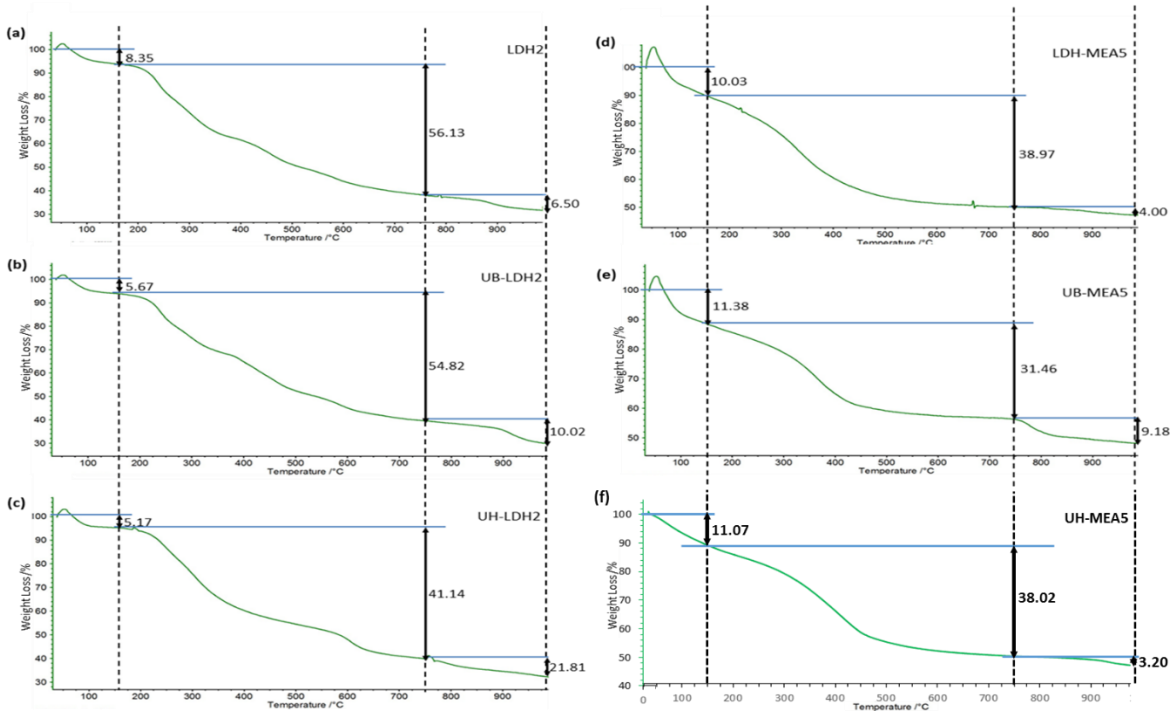

Figure 6.14: TGA curves comparing thermal stabilities of LDHs prepared via conventional and ultrasonic irradiation: (a) LDH2, (b) UB-LDH2 and (c) UH-LDH2; as well as with amine modified LDHs: (d) LDH-MEA5 and (e) UB-MEA5 (f) UH-MEA5

Table 6.4: Thermal degradation of samples prepared via conventional (LDHn) and ultrasonic irradiation route (UH-LDHn and UB-LDHn)

Preparation Route	APTES/SDS mole ratio, n	Sample Name	Weight Loss (%)			
			T<150°C	150< T<750°C	750°C< T	Total
Conventional	5	LDH5	10.43	43.63	11.24	**65.30**
	2	LDH2	8.35	56.13	6.50	**70.98**
	1	LDH1	2.73	46.02	20.30	**69.05**
Ultrasonic Bath	5	UB-LDH5	9.36	46.63	8.76	**64.75**
	2	UB-LDH2	5.67	54.82	10.02	**70.51**
	1	UB-LDH1	5.05	57.95	8.39	**71.39**
Ultrasonic Horn	5	UH-LDH5	9.04	44.74	12.39	**66.17**
	2	UH-LDH2	5.17	41.14	21.81	**68.12**
	1	UH-LDH1	3.77	36.32	13.46	**53.55**

6.3.5 Effect of the sonochemical functionalization on ease of regeneration, lifetime of the LDH adsorbent and subsequent gas uptake.

After CO_2 adsorption, the adsorbents were subjected to a desorption process at a temperature of 105 ^oC for 30 mins in N_2 atmosphere. This was used to compute the ease of recovering the adsorbed CO_2 within the given regeneration test time. The ease of regeneration will contribute to the overall capture efficiency over a period of time and will impact on the economics of the process. Figure 6.9(b) shows an example of recoverable CO_2 uptake using TSA. The recoverable CO_2 uptake was denoted as CU_{rev}, while the retained CO_2 uptake as CU_{irrev}. The results (Table 1) show that the sonochemical functionalized LDHs, UB-MEA5 and UH-MEA5 has CU_{rev} of 0.51 and 1.33 mmol/g representing c.a. 93% and 98% of the CO_2 uptake. Compared with the CU_{rev} of the conventional modified LDH-MEA5, of 1.27 mmol/g (c.a. 87% of the adsorbed CO_2), the sonochemically prepared adsorbents showed a better performance for the capture of CO_2. Analysing the CU_{rev} for UH-MEA5 and LDH-MEA5, it is observed that despite the higher CO_2 uptake of LDH-MEA5, the amount of CO_2 recovered during desorption is lower than that of UH-MEA5.

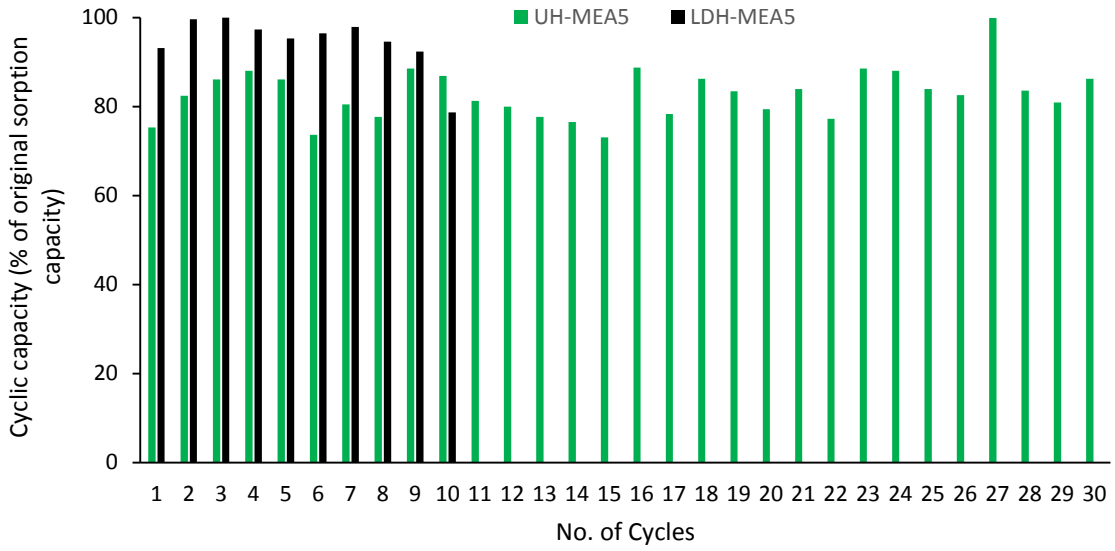

Figure 6.15: TSA Cycles of LDH-MEA5 and UH-MEA5 at 55 ^{o}C (30 mins regeneration time at 105 ^{o}C in N_2 atmosphere) based on the initial adsorption capacity of 1.45 and 1.37 mmol/g respectively

The impact of the preparation route on the cyclic sorption capacity is presented in Figure 6.15. The sorption capacity is calculated as a percentage of the original capacity of 1.45 and 1.37 mmol/g for LDH-MEA5 and UH-MEA5 respectively. These two adsorbents were considered given that they have close adsorption capacities and that UH-MEA5 was more stable than UB-MEA5. The TSA cycle was repeated several times, with a regeneration temperature of 105 ^{o}C until the sorption capacity reduced below 60% of the original capacity. For deployment of these adsorbents on a large scale, the greater the cyclic adsorption capacity, the lesser the replacement of the adsorbent and potentially more efficient the adsorbent will be. From Figure 6.15, LDH-MEA5 showed an initial high cyclic adsorption capacity greater than 90% of the initial sorption capacity. However, its lifetime did not exceed the 11th cycle before degrading to a capacity less than 60% of the original sorption uptake. Degradation in cyclic adsorption capacity can be attributed to the secondary reaction occurring between the amino group and CO_2 as observed in Figure 6.12 (b). This is shown by the second ascent in CO_2 uptake after 48, 50 and 55 mins of adsorption by LDH-MEA5, UB-MEA5 and UH-MEA5 respectively. Drage et al. [5] refuted the possibility of adsorbent volatilization or loss of reactive amino functional groups as the responsible factors for degradation in performance of amine grafted adsorbent. It was revealed

that secondary reaction resulted in the formation of stable poly urea compounds deposited on the adsorbent. This corresponds to the 12.64%, 6.39% and 2.43% of CU_{irrev} for LDH-MEA5, UB-MEA5 and UH-MEA5 respectively (Table 6.1) elaborating the potential ease of formation of urea linkages in the conventional LDH adsorbent. These linkages pose a deleterious effect on the reaction between CO_2 and the active amino functional groups. The destructive impact of this side reaction can be a contributor to the breakdown of LDH-MEA5 under numerous TSA cycles especially when the adsorption cycle is increased beyond 60 mins. Unlike the LDH-MEA5, UH-MEA5 displayed a lower initial cyclic adsorption capacity (averaging about 80%) but seemed to oscillate about this capacity for more than 30 TSA cycles (trice the lifetime of LDH-MEA5).

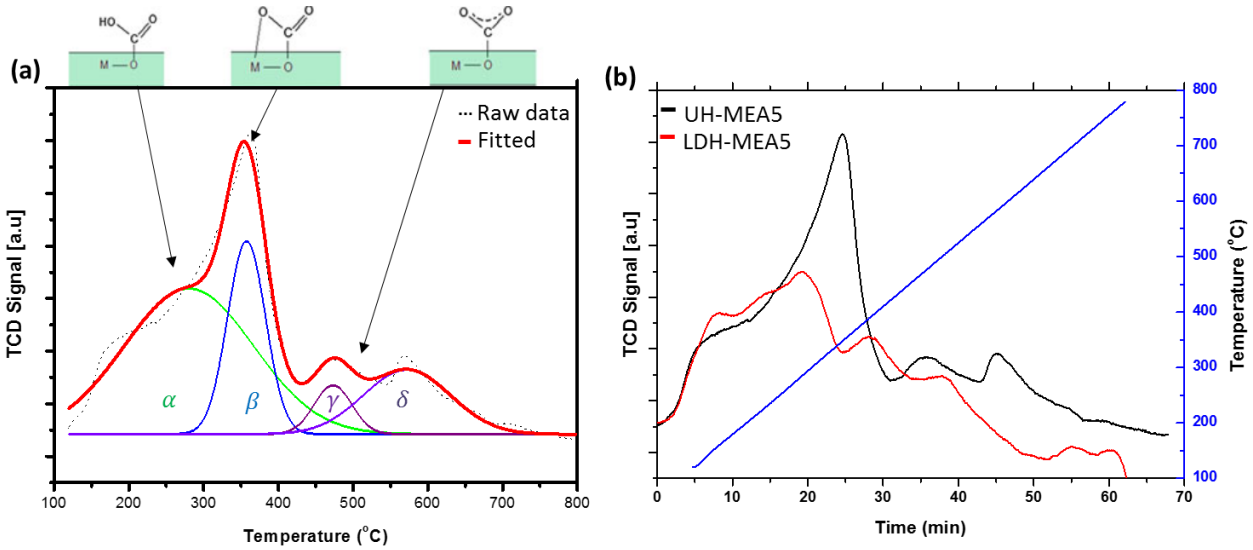

Figure 6.16: CO_2-TPD of functionalised LDH (a) Deconvolution of the CO_2-TPD of UH-MEA5 and (b) Comparison of CO_2-TPD of UH-MEA5 and LDH-MEA5.

These hypotheses can be supported by CO_2-TPD profile on the functionalised LDH is shown in Figure 6.16. The desorption of CO_2 occurs at overlapping peaks of 270 ^oC (α) and 363 ^oC (β), 474 ^oC (γ) and 569 ^oC (δ) (Figure 6.16a). The α-peak has been assigned to CO_2 desorption from bicarbonates formed on OH- groups and tends to occur at low temperatures, whereas the β-peak occurs at intermediate temperatures and is characterised by desorption of CO_2 from bidentate carbonates formed on metal-oxygen pairs. At high temperatures, desorption is attributed to monodentate carbonates produced on low-coordination oxygen anions [23]. This is designated by the γ and δ-peaks [22]. In this study, the low and intermediate energy states

are the major contributors to CO_2 uptake, predominated by the intermediate energy state. This is more pronounced in the ultrasonic irradiated adsorbents as shown in Figure 6.16b where intermediate energy desorption of UH-MEA5 outweighs that of LDH-MEA5. Nonetheless, the reverse was observed at low energy desorption with LDH-MEA5 slightly desorbing more CO_2 than UH-MEA5. However, the overall desorption by the sonochemically prepared LDH within the time analysed showed a better performance than the conventional. In other words, it can be deduced that the performance of a conventionally synthesised LDH is dependent on its basicity while sonochemically synthesised LDHs will profit from low regeneration temperature gradients, especially in temperature-swing operations.

These findings were further compared to pseudo-first and pseudo-second order kinetic models:

Equation 6.1: Pseudo first order

$$x = A_1(1 - e^{-k_1 t}) \; ; \qquad Differential\ form: \ \frac{dx}{dt} = k_1(A_1 - x)$$

Equation 6.2: Pseudo second order

$$x = \frac{{A_2}^2 k_2 t}{A_2 k_2 t + 1} \; ; \qquad Differential\ form: \ \frac{dx}{dt} = k_2(A_2 - x)^2$$

where x and $A_{i,\ i=1,\ 2}$ represents the CO_2 uptake at a given time and equilibrium respectively for an i^{th} order model, $k_{i,\ i=1,\ 2}$ is the i^{th} order rate constant and t is the time of adsorption. The obtained experimental data are fitted to the models and selecting the one with the best fit. To determine the suitability of each model, an error function (Err) defined by Equation 1 was applied:

Equation 6.3: Error function equation

$$Err\ (\%) = \sqrt{\frac{\sum \left[\frac{(x_{exp} - x_{mod})}{x_{exp}}\right]^2}{N - 1}} \times 100$$

where x_{exp} and x_{mod} are CO_2 uptake determined experimentally and computed using the model respectively and N is the total number of experimental points. It is reasonable to assume that the adsorption rate constant, k for both pseudo-first and -second order model is the same for each group of functionalized and non-functionalized adsorbents since they are both grafted

with the same amino silane. The kinetic parameters are shown in Table 6.5 with the estimated standard errors and R^2 values. From the simulation results, it is observed that pseudo-second order model displayed a comparatively good fit with the value of equilibrium CO_2 uptake close to that of experimental data for the non-functionalized adsorbents. Hence, despite the effect of sonication on the adsorption capacity and textural properties of the adsorbent, the adsorption kinetics is more favoured by the second order rate function. This model explains adsorption process involving chemical reactions or at high amine loading as compared to pseudo-first order model which explains adsorption under low surface coverage. However, after amine extraction, UH-MEA5 experimental data was best fitted by the pseudo-first order model with a standard error of 0.20%. This explains the ease of recovering the CO_2 uptake as a result of the minimal chemisorption. Figure 6.17 shows the fitting of the models with the experimental data for conventional (LDH5) and sonicated (UH-LDH5) non-functionalized adsorbents. Despite the pseudo second order being the better fit, the standard error tends to increase in the sonication route.

Table 6.5: CO_2 kinetic model parameters, R^2 and standard errors (%) for prepared LDHs and amine functionalized LDHs at 55 ^oC and APTES/SDS ratio, n of 5

Samples	Pseudo 2nd Order		Err (%)	R^2	Pseudo 1st Order		Err (%)	R^2
	A_2	k_2			A_1	k_1		
LDH5	0.83		0.22	0.9483	0.76		0.23	0.9281
UB-LDH5	0.51	0.05	0.54	0.9609	0.46	0.06	0.38	0.9292
UH-LDH5	0.63		0.84	0.9629	0.56		0.74	0.9057
LDH-MEA5	1.35		0.16	0.8306	1.38		0.20	0.8177
UB-MEA5	0.51	0.04	0.13	0.8583	0.45	0.03	0.13	0.8361
UH-MEA5	1.67		0.55	0.8909	1.32		0.20	0.9226

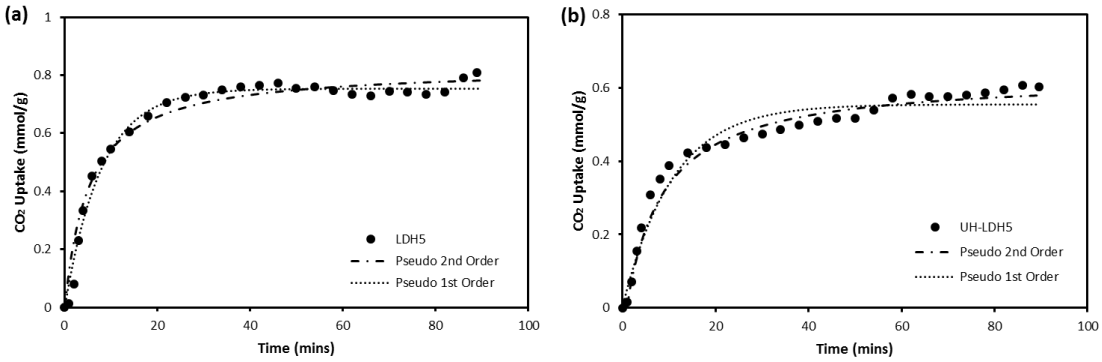

Figure 6.17: Comparison of kinetic models with experimental results for CO_2 uptake on (a) LDH5 and (b) UH-LDH5

After CO_2 adsorption by the LDH adsorbent, the adsorbents were subjected to further isothermal adsorption in N_2 atmosphere at 50 ml/min for 20 mins. This is to measure the additional gas uptake capacity of the adsorbent when considered as a catalytic support for hydrogenation of the adsorbed CO_2 to methanol. From the results (Table 6.1), it is observed that the ultrasonic mediated adsorbents (UB-MEA5 and UH-MEA5) showed a greater potential for additional gaseous uptake than the conventional LDH-MEA5. The amount of N_2 adsorbed per adsorbed CO_2 were 0.31, 0.25 and 0.16 mmol N_2/mmol CO_2 for UH-MEA5, UB-MEA5 and LDH-MEA5 respectively. This can be attributed to the high pore volume of the sonochemically produced adsorbents. Hence, proposing the sonochemical process as a viable catalyst preparation means for synthesising methanol via hydrogenation of CO_2.

6.4 CONCLUSIONS

The present study has shown that the LDHs with high CO_2 adsorption capacity can be synthesised via amine modification by means of anionic surfactant intercalation reinforced by ultrasonic irradiation. The use of sonochemical process in the synthesis step led to a more developed pore structure than that of the conventional process. However, this was dependent on sonication intensity. Despite the advancement in physical properties which is beneficial to the physical adsorption of CO_2, the further adoption of the sonochemical process for amine

functionalization of the prepared LDH led to an improved amine loading and effective amine efficiency of the adsorbent. In addition, the recoverable CO_2 uptake of the sonochemically prepared adsorbent increased to 1.33 mmol/g as against 1.27 mmol/g of the conventional. In combination with the improved thermal stability of the adsorbent as a result of this process, the sonochemically functionalized LDH exhibited a greater ease of regeneration with a longer life span than the conventional LDH. Therefore, sonochemical route can be an effective preparation method for long-lasting recyclable layered double hydroxides for CO_2 adsorption.

ACKNOWLEDGEMENT

I humbly appreciate Mrs. Xiani Huang for all her assistance towards the completion of this study.

References

[1] J.D. Figueroa, T. Fout, S. Plasynski, H. McIlvried, R.D. Srivastava, Advances in CO2 capture technology—The U.S. Department of Energy's Carbon Sequestration Program, International Journal of Greenhouse Gas Control, 2 (2008) 9-20.

[2] J. Wang, L.A. Stevens, T.C. Drage, C.E. Snape, J. Wood, Preparation and CO2 adsorption of amine modified layered double hydroxide via anionic surfactant-mediated route, Chemical Engineering Journal, 181-182 (2012) 267-275.

[3] M.L. Gray, K.J. Champagne, D. Fauth, J.P. Baltrus, H. Pennline, Performance of immobilized tertiary amine solid sorbents for the capture of carbon dioxide, International Journal of Greenhouse Gas Control, 2 (2008) 3-8.

[4] T.C. Drage, C.E. Snape, L.A. Stevens, J. Wood, J. Wang, A.I. Cooper, R. Dawson, X. Guo, C. Satterley, R. Irons, Materials challenges for the development of solid sorbents for post-combustion carbon capture, Journal of Materials Chemistry, 22 (2012) 2815.

[5] T.C. Drage, A. Arenillas, K.M. Smith, C.E. Snape, Thermal stability of polyethylenimine based carbon dioxide adsorbents and its influence on selection of regeneration strategies, Microporous and Mesoporous Materials, 116 (2008) 504-512.

[6] X. Xu, C. Song, J.M. Andrésen, B.G. Miller, A.W. Scaroni, Preparation and characterization of novel CO2 "molecular basket" adsorbents based on polymer-modified mesoporous molecular sieve MCM-41, Microporous and Mesoporous Materials, 62 (2003) 29-45.

[7] J. Tanthana, S.S. Chuang, In situ infrared study of the role of PEG in stabilizing silica-supported amines for CO(2) capture, ChemSusChem, 3 (2010) 957-964.

[8] R. Serna-Guerrero, E. Da'na, A. Sayari, New Insights into the Interactions of CO2 with Amine-Functionalized Silica, Industrial and Engineering Chemistry Research, 47 (2008) 9406-9412.

[9] D. Saha, S. Deng, Adsorption equilibrium and kinetics of CO2, CH4, N2O, and NH3 on ordered mesoporous carbon, Journal of colloid and interface science, 345 (2010) 402-409.

[10] M. Cinke, J. Li, C.W. Bauschlicher, A. Ricca, M. Meyyappan, CO2 adsorption in single-walled carbon nanotubes, Chemical Physics Letters, 376 (2003) 761-766.

[11] A. Arenillas, K.M. Smith, T.C. Drage, C.E. Snape, CO2 capture using some fly ash-derived carbon materials, Fuel, 84 (2005) 2204-2210.

[12] A.-Y. Park, H. Kwon, A.J. Woo, S.-J. Kim, Layered Double Hydroxide Surface Modified with (3-Aminopropyl)triethoxysilane by Covalent Bonding, Advanced Materials, 17 (2005) 106-109.

[13] M. Szabados, R. Mészáros, S. Erdei, Z. Kónya, Á. Kukovecz, P. Sipos, I. Pálinkó, Ultrasonically-enhanced mechanochemical synthesis of CaAl-layered double hydroxides intercalated by a variety of inorganic anions, Ultrasonics Sonochemistry, 31 (2016) 409-416.

[14] R. Hernandez-Huesca, L. Dıaz, G. Aguilar-Armenta, Adsorption Equilibria and Kinetics of CO_2, CH_4 and N_2 in Natural Zeolites, Separation and Purification Technology, 15 (1999) 163-173.

[15] R.V. Siriwardane, M.-S. Shen, E.P. Fisher, Adsorption of CO_2 on Zeolites at Moderate Temperatures, Energy & Fuels, 19 (2005) 1153-1159.

[16] K.S. Walton, M.B. Abney, M. Douglas LeVan, CO2 adsorption in Y and X zeolites modified by alkali metal cation exchange, Microporous and Mesoporous Materials, 91 (2006) 78-84.

[17] Y.-S. Bae, O.K. Farha, J.T. Hupp, R.Q. Snurr, Enhancement of CO2/N2 selectivity in a metal-organic framework by cavity modification, Journal of Materials Chemistry, 19 (2009) 2131.

[18] D.-A. Yang, H.-Y. Cho, J. Kim, S.-T. Yang, W.-S. Ahn, CO2 capture and conversion using Mg-MOF-74 prepared by a sonochemical method, Energy & Environmental Science, 5 (2012) 6465.

[19] K. Yamamoto, Y. Sakata, Y. Nohara, Y. Takahashi, T. Tatsumi, Organic-inorganic hybrid zeolites containing organic frameworks, Science, 300 (2003) 470-472.

[20] F. Cavani, F. Trifirò, A. Vaccari, Hydrotalcite-type anionic clays: Preparation, properties and applications, Catalysis Today, 11 (1991) 173-301.

[21] Q. Wang, J. Luo, Z. Zhong, A. Borgna, CO2 Capture by Solid Adsorbents and their Applications: Current Status and New Trends, Energy & Environmental Science, 4 (2011) 42.

[22] D.I. Ferrer, Supported Layered Double Hydroxides as CO2 Adsorbents for Sorption-enhanced H2 Production, Chemical Engineering, Imperial College, London, United Kingdom, Springer International Publishing Switzerland, 2016, pp. 209.

[23] S. Zhao, H. Yi, X. Tang, F. Gao, Q. Yu, Y. Zhou, J. Wang, Y. Huang, Z. Yang, Enhancement effects of ultrasound assisted in the synthesis of NiAl hydrotalcite for carbonyl sulfide removal, Ultrasonics Sonochemistry, 32 (2016) 336-342.

[24] M.P. Bernardo, F.K.V. Moreira, L.A. Colnago, C. Ribeiro, Physico-chemical assessment of [Mg-Al-PO4]-LDHs obtained by structural reconstruction in high concentration of phosphate, Colloids and Surfaces A: Physicochemical and Engineering Aspects, 497 (2016) 53-62.

[25] S.D. Kenarsari, D. Yang, G. Jiang, S. Zhang, J. Wang, A.G. Russell, Q. Wei, M. Fan, Review of recent advances in carbon dioxide separation and capture, RSC Advances, 3 (2013) 22739.

[26] K. Yao, Y. Imai, L. Shi, A. Dong, Y. Adachi, K. Nishikubo, E. Abe, H. Tateyama, The functional layered organosilica materials prepared with anion surfactant templates, Journal of colloid and interface science, 285 (2005) 259-266.

[27] Q. Tao, H. He, R.L. Frost, P. Yuan, J. Zhu, Nanomaterials based upon silylated layered double hydroxides, Applied Surface Science, 255 (2009) 4334-4340.

[28] S. Che, A.E. Garcia-Bennett, T. Yokoi, K. Sakamoto, H. Kunieda, O. Terasaki, T. Tatsumi, A novel anionic surfactant templating route for synthesizing mesoporous silica with unique structure, Nat Mater, 2 (2003) 801-805.

[29] T. Yokoi, H. Yoshitake, T. Tatsumi, Synthesis of Anionic-Surfactant-Templated Mesoporous Silica using Organoalkoxysilane-containing Amino Groups, Chemistry of Materials, 15 (2003) 4536-4538.

[30] H. Xu, B.W. Zeiger, K.S. Suslick, Sonochemical synthesis of nanomaterials, Chemical Society reviews, 42 (2013) 2555-2567.

[31] H. Zheng, C. Gao, S. Che, Amino and quaternary ammonium group functionalized mesoporous silica: An efficient ion-exchange method to remove anionic surfactant from AMS, Microporous and Mesoporous Materials, 116 (2008) 299-307.

[32] X. Zhao, X. Hu, G. Hu, R. Bai, W. Dai, M. Fan, M. Luo, Enhancement of CO2 adsorption and amine efficiency of titania modified by moderate loading of diethylenetriamine, Journal of Material Chemistry A, 1 (2013) 6208-6215.

[33] H. Xu, B.W. Zeiger, K.S. Suslick, Sonochemical synthesis of nanomaterials, Chemical Society reviews, 42 (2013) 2555-2567.

[34] C.R. Hickenboth, J.S. Moore, S.R. White, N.R. Sottos, J. Baudry, S.R. Wilson, Biasing Reaction Pathways with Mechanical Force, Nature, 446 (2007) 423.

[35] M. Herrero, F.M. Labajos, V. Rives, Size Control and Optimisation of Intercalated Layered Double Hydroxides, Applied Clay Science, 42 (2009) 510–518.

[36] F. Wypych, A. Bail, M. Halma, S. Nakagaki, Immobilization of iron(III) porphyrins on exfoliated MgAl layered double hydroxide, grafted with (3-aminopropyl)triethoxysilane, Journal of Catalysis, 234 (2005) 431-437.

[37] Y. Kong, X. Shen, S. Cui, M. Fan, Development of monolithic adsorbent via polymeric sol-gel process for low-concentration CO2 capture, Applied Energy, 147 (2015) 308-317.

[38] Y. Kong, G. Jiang, Y. Wu, S. Cui, X. Shen, Amine hybrid aerogel for high-efficiency CO2 capture: Effect of amine loading and CO2 concentration, Chemical Engineering Journal, 306 (2016) 362-368.

CHAPTER SEVEN

ENHANCEMENT OF CO_2 ADSORPTION BY AMINE MODIFIED LAYERED DOUBLE HYDROXIDE SYNTHESIZED VIA HYDROTHERMAL REACTION

Abstract

The structure and capacitive properties of layered double hydroxides (LDH) nano-spheres synthesised by supercritical hydrothermal method were investigated. Spheres of varying particle sizes and morphology were obtained by tuning the pressure of water around its critical point, 22.1 MPa. This was varied between the subcritical pressure (20 MPa) and supercritical pressure (26 MPa). The prepared adsorbent samples were characterised using X-ray diffraction (XRD), Scanning electron microscope (SEM), Brunauer-Emmett-Teller (BET), and Thermogravimetric analysis (TGA) respectively. Spherical sizes varied from 30-60 nm with surface area range of 100-180 m^2/g of adsorbent. Controlling the ageing process, spherical sizes reduced to < 20 nm with increase in surface area within 250-500 m^2/g. Varying magnitude in size is associated with the effect of pressure on the solvent strength of water around the critical point. This tends to promote simultaneous dissolution and recrystallization of crystals around the critical pressure, which may support substantial particle growth. According to the kinetic model analysis, adsorption mechanism was described using a double adsorption routes kinetic model with one adsorption route having an impact of ca. 84% on CO_2 uptake.

Keywords: *CO_2 Adsorption, Layered Double Hydroxide, Supercritical water, Hydrothermal.*

7.1 INTRODUCTION

The most common synthetic method for preparing layered double hydroxides (LDH) is the co-precipitation route [1-3] conducted at high or low supersaturation environments. The metal mixture is added to the alkali and anion precursor solution for high supersaturation conditions; whereas in low supersaturation condition, the metal solutions are added concurrently to the solution containing the alkali. The later tends to produce more crystalline structures because of the increased rate of nucleation over crystallization [2]. Besides this method, other means of synthesizing LDH are sol-gel and urea techniques [1, 4]. Despite the preparation method, product crystallinity is affected by various factors including pH, temperature, post-synthesis conditions like ageing, etc. Series of studies have examined the physicochemical properties and application of this compound, but only a few has analysed the control of particle size, a key factor for commercial application [5]. Hydrothermal treatment has been reported to improve the crystallinity of this adsorbent. In the presence of water vapour, hydrothermal crystallization is facilitated at high temperatures which do not exceed the decomposition temperature of the compound [3]. But for samples that can withstand high temperatures, supercritical hydrothermal crystallization is very beneficial.

Supercritical hydrothermal synthesis is shown to produce ultrafine particles with its morphology controlled by variation in pressure and/or temperature [6]. This has been attributed to the effective control of the enhanced transport properties of water by changes in pressure and temperature. The enhanced transport properties has contributed to the high dispersion of deposited metals. Consequently, improving the catalytic activity and selectivity of the material in structure sensitive reactions [7]. However, this is dependent on composition of reactants [8], hydrothermal ageing [9], temperature [10] and pressure. Till date, studies have limited the impact of this synthetic route to mostly temperature, neglecting the variation with pressure.

In this study, supercritical hydrothermal synthetic method has been adopted to produce novel Mg-Al LDH nano-spheres with variation in pressure. The impact of supercritical pressure on the morphology was investigated using the TGA, SEM, XRD and BET. In addition, the

adsorption capacity of amine functionalised LDH spheres was also examined given the effect of amine loading on sorption performance [11, 12].

7.2 EXPERIMENTATION

7.2.1 Material Preparation

In this study, Mg-Al LDH was synthesised by the supercritical hydrothermal aided co-precipitation method. Subsequently, MEA extractions of these LDHs were carried out to produce the amine modified LDHs. The co-precipitation and extraction method are slight modifications of methods used in previous study [13]. All chemicals used for experimentation were acquired from SinoPharm Chemical Reagents Co. Ltd.

7.2.2 Sample Synthesis

7.2.2.1 For Hydrothermal synthesized samples, HPH-LDH.

32 ml solution containing APTES (≥ 98%) and SDS (≥ 86%) (APTES:SDS molar ratio: 5) was reacted with $Mg(NO_3)_2.6H_2O$ (≥ 98%) and $Al(NO_3)_3.9H_2O$ (≥ 99%) (Mg:Al molar ratio: 3, dissolved in 16 ml of distilled water) solution. The latter was added dropwise while maintaining the temperature of the former at 333 K under constant stirring for 15 mins. The substrate (molar ratio of Mg:Al:APTES:SDS = 3:1:5:1) was moved to the hydrothermal reactor (see Figure 7.1). After being vented with pure N_2 gas (99.99%) for 15 mins in order to remove all of the oxygen before the reaction, the reactor was sealed and heated to a temperature of 723 K with a ramp of 2 K/min and then held for 15 mins. After reaction, the solution was aged for 12 hr. The precipitates were filtered, washed with distilled water and then dried in a vacuum oven (500 mbar at 343 K) overnight. Samples were prepared at constant temperature by varying the pressure between 20 and 26 MPa; increasing the pressure of 1 Mpa for each sample, in order to determine the influence of the water density on the particles physical structure. After the reaction the reactor was quickly cooled down to room temperature in an ice bath and was

compared to cooling under room temperature. The prepared samples are labelled HPH-n (n denotes the hydrothermal pressure, Mpa).

7.2.2.2 For HPH-M.

The prepared LDHs were functionalised via MEA extraction. 0.5 g of LDH sample was dispersed in a solution of 100 ml C_2H_5OH (≥99.7%) containing 20 g MEA (≥99%). The mixture was then refluxed for 20 hr at a temperature of 363 K. After which the samples were filtered, washed with ethanol and dried in a vacuum oven overnight. These samples are labelled HPH-M20. This was repeated using 10 g and 5 g MEA respectively to study the effect of amine amount on adsorption capacity.

7.2.3 Characterisation

7.2.3.1 Nitrogen sorption analysis

The textural characteristics of the prepared catalysts were studied by Nitrogen physisorption analysis at -196 ^oC using the Micrometrics ASAP 2020 Surface Area and Porosity Analyser. Prior to this analysis, samples were degassed at a temperature of 105 ^oC for 4 hr. The surface area (S_{BET}) of the samples was determined using the BET (Brunauer, Emmett and Teller) model. The total pore volumes (V_{Total}) were computed from the amount of nitrogen adsorbed at relative pressure (P/P_o) of 0.99 and the average pore volumes from $4V_{Total}/S_{BET}$. The pore size distribution was calculated using the BJH (Barrett, Joyner and Halenda) model. The t-plot method was used to calculate the micopore volume (V_{micro}).

7.2.3.2 Scanning electron microscope-Energy dispersive X-ray spectroscopy (SEM-EDX)

The surface composition and structure of the prepared materials were studied with a Zeiss ΣIGMA™ Field Emission SEM and an Oxford Instrument INCAx-act PentaFET® Precision EDX. The EDX spectra for the LDHs were obtained. This was also used to compute the amine content present in the adsorbents

7.2.3.3 X-ray Diffraction (XRD) Analysis

XRD patterns were studied using a Bruker-AXS D8 advance powder diffractometer using Cu radiation with a scanning range of $10^o \leq 2\theta \leq 90^o$ at a step size of 0.010216^o. Average crystallite size was estimated using the Scherrer's formula:

Equation 7.1: Scherrer's Formula

$$d = \frac{0.9\lambda}{\beta \cos \theta}$$

where d is the crystallite size (nm), λ is the radiation wavelength (nm) = 1.5406 nm in this case, β is the full width at half maximum (radians) and θ is the Bragg's angle of the maximum intense peak (degrees) [14].

7.2.3.4 Thermo-gravimetric analysis

CO_2 uptake measurements were conducted using the Netzsch STA 449 F3 Jupiter thermogravimetric analyser (TGA). Approximately 5-10 mg of the synthesized sample was heated from 25 to 378 K at 20 K/min under N_2 at a flow rate of 50 ml/min; and then held isothermally for 30 min before being cooled to the required adsorption temperature at a rate of 10 K/min. The gas was switched from N_2 to CO_2 and held isothermally for 60 min at a flow rate of 20 ml/min. The experimental adsorption temperature is 323 K. The CO_2 adsorption capacity was calculated from the weight difference of the samples in CO_2 atmosphere. The uptake profile was measured against an empty alumina crucible using the same method so as to correct the impact of change in gas density and viscosity.

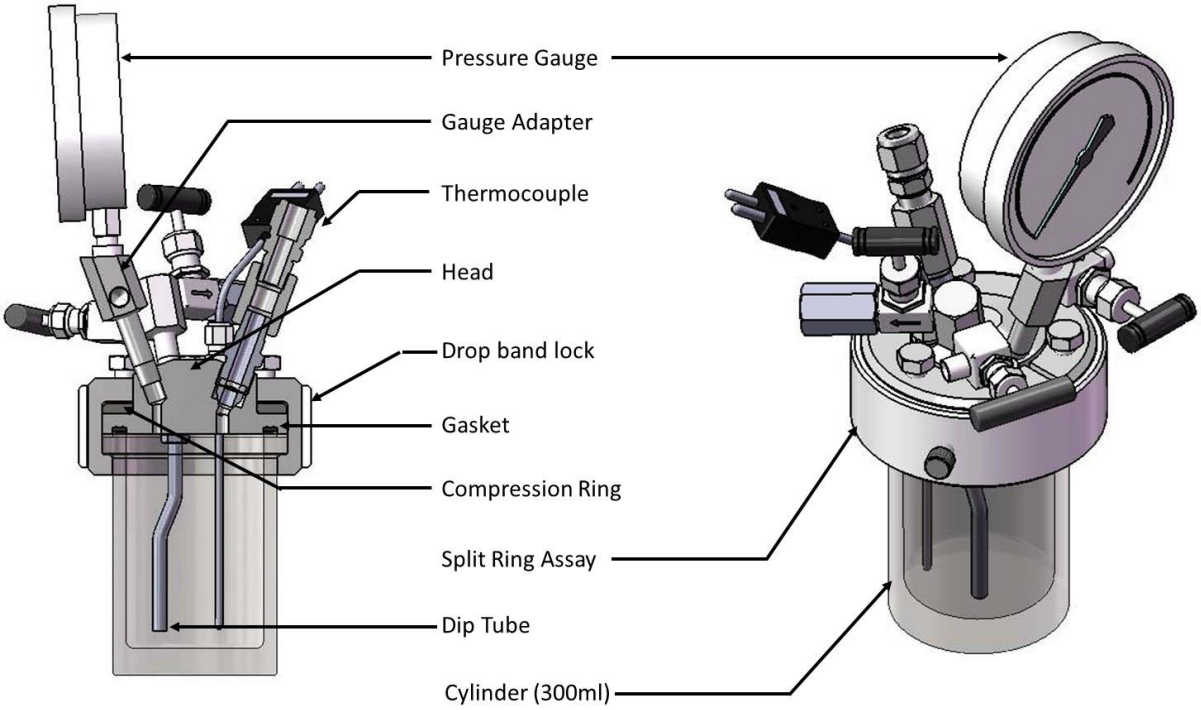

Figure 7.1: Schematic diagram of the hydrothermal reactor

7.3 THEORETICAL

One of the expected characteristics of a good adsorbent is to have fast adsorption kinetics. This is because the efficiency and capacity of its adsorption in a high adsorbate flow stream is dependent on its adsorption rate. Establishing the kinetic behaviour of the adsorbents makes it possible to understand the interactions between the adsorbent and adsorbate. Series of kinetic models have been proposed for this purpose and are validated by finding the most suitable model that best fits with experimental data. To predict the kinetic behaviour of this adsorbent, the experimental results were simulated assuming double-exponential [12] and Avrami kinetic models [15]. The double exponential model was considered because of its feasibility to explain the surface heterogeneity of the adsorbent accounting for two different adsorption sites [16]. Additionally, it can partially elaborate the kinetic mechanisms associated with both pseudo-first and second order reactions. This mechanism can be categorised into a controlled slow phase intra-particle diffusion and a controlled fast phase surface reaction [17]. However, unlike

the double exponential model, the Avrami model takes into account a fractional order kinetics, n [15]. This was adequately used for the description of adsorption processes on some adsorbents [18, 19], hence the reason for adopting the model for this study.

Equation 7.2: Avrami kinetic model

$$x = x_e\left(1 - e^{-k_A t^n}\right)$$

Equation 7.3: Double exponential kinetic model

$$x = x_e - \left(A_1 e^{-k_1 t} + A_2 e^{-k_2 t}\right)$$

where x and x_e represents the CO_2 uptake at a given time and equilibrium respectively, k_A is Avrami kinetic constant, A_i and k_i, i=1,2 are pre-exponential factors and rate constants for the two adsorption sites respectively, and t is the time of adsorption. The obtained experimental data are fitted to the models and selecting the one with the best fit.

To determine the suitability of each model, an error function (Err) defined by equation (5) was applied:

Equation 7.4: Error function equation

$$Err(\%) = \sqrt{\frac{\sum_{j=1}^{N}\left[\frac{x_{j,\exp} - x_{j,\mathrm{mod}}}{x_{j,\exp}}\right]^2}{N-1}} \times 100$$

where x_{exp} and x_{mod} are CO_2 uptake determined experimentally and computed using the model respectively and N is the total number of experimental points.

7.4 DISCUSSION OF RESULTS

7.4.1 Nitrogen sorption analysis

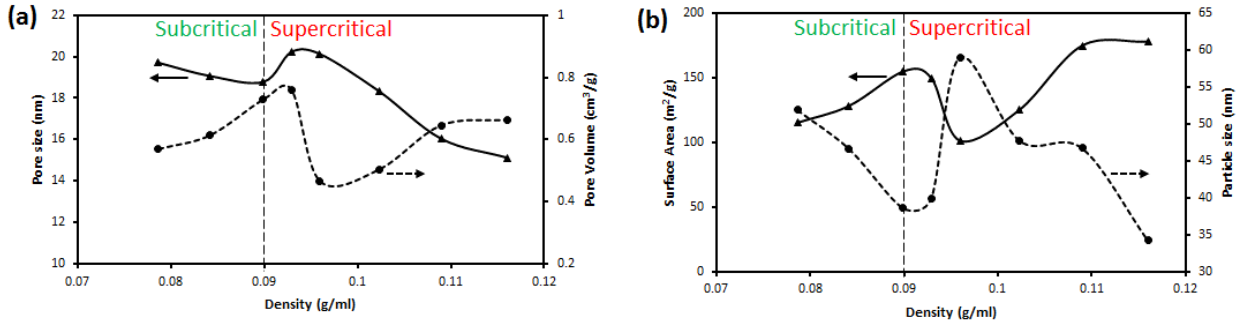

Figure 7.2: BET analysis of prepared LDH with variation in density: (a) variation of pore size and volume, and (b) variation of surface area and particle size

Table 7.1: Density of subcritical and supercritical water at temperature 723 K (Critical Pressure, Pc = 22.1 MPa)

Pressure (MPa)	Density (g/ml)
20.0	0.0786
21.0	0.0841
22.0	0.0899
22.5	0.0928
23.0	0.0959
24.0	0.1023
25.0	0.1089
26.0	0.1160

At a constant temperature, a corresponding increase in water density is obtained with increase in pressure for both subcritical and supercritical phase as shown in Table 7.1. However, at high pressures, the change in crystallite morphology is by first approximation linked to the variation in density and not pressure. This is based on the dependence of solvent power of the supercritical fluid on its density rather than pressure [20]. Hence, it is logical to compare the textural characteristics of the material to density of the supercritical fluid. Figure 7.2 shows the variation of textural properties of as-synthesised LDH with density of water. Surface area and pore volume of LDH spheres are observed to increase with density in both the subcritical and

supercritical regime of water. With a brief view, it can be estimated that the rate of increase is in both regime are similar. However an anomaly in this trend occurred at the critical density of 0.0899 g/ml, where the surface area and pore volume underwent a sudden decrease. This is due to the increased density gradient with slight increase in pressure within the vicinity of the critical pressure. In other words, the solvent power of water tends to exhibit a large gradient with slight increase in pressure. This will result to a simultaneous and competing dissolution and recrystallization of the smallest crystallites and amorphous particles based on classical nucleation theory. The dynamics of this phenomenon has caused great controversies. However, the sudden reduction in surface area and pore volume is suggested to be related to this theory within the vicinity of the critical pressure. Furthermore, the anomaly was also seen to occur with the pore and particle sizes. Within the subcritical and supercritical regime, these properties were observed to decrease at almost a similar rate. Nonetheless, around the critical density, the samples experienced a surge in pore and particle sizes. As initially elaborated, it is also suggested that the sudden change in solubility around the critical pressure may support substantial particle growth.

7.4.2 Variation of surface morphology

Figure 7.3 shows the SEM images of as-synthesised LDH at various supercritical pressures at 723 K. In all experimented pressures, Mg-Al LDH synthesised had spherical shapes with varying sizes depending on the pressure when compared to the conventional LDH with irregular shape [21]. Findings from the images suggest that spherical structure was well formed with increasing pressure. At low pressure 20 MPa, the amount of spherical LDH in comparison to the crumb-like LDH was low. This tends to increase with pressure as more spherical structures were formed. Additionally, as the pressure increased, the particle size was seen to increase. Particle agglomeration was also witnessed to increase with pressure. Notable transformation of the crumb-like LDH to spherical LDH was observed at pressure of 22 MPa. This is noted to be the critical pressure of water. Beyond this pressure, it was observed that the spheres became denser and more aggregated even without significant increase in size. It will

be important to specify that an increase in size of crystal may reflect structural reordering with or without considerable crystal growth. This elucidates the increase in density of particle as a result of structure ordering without significant crystallite size increase.

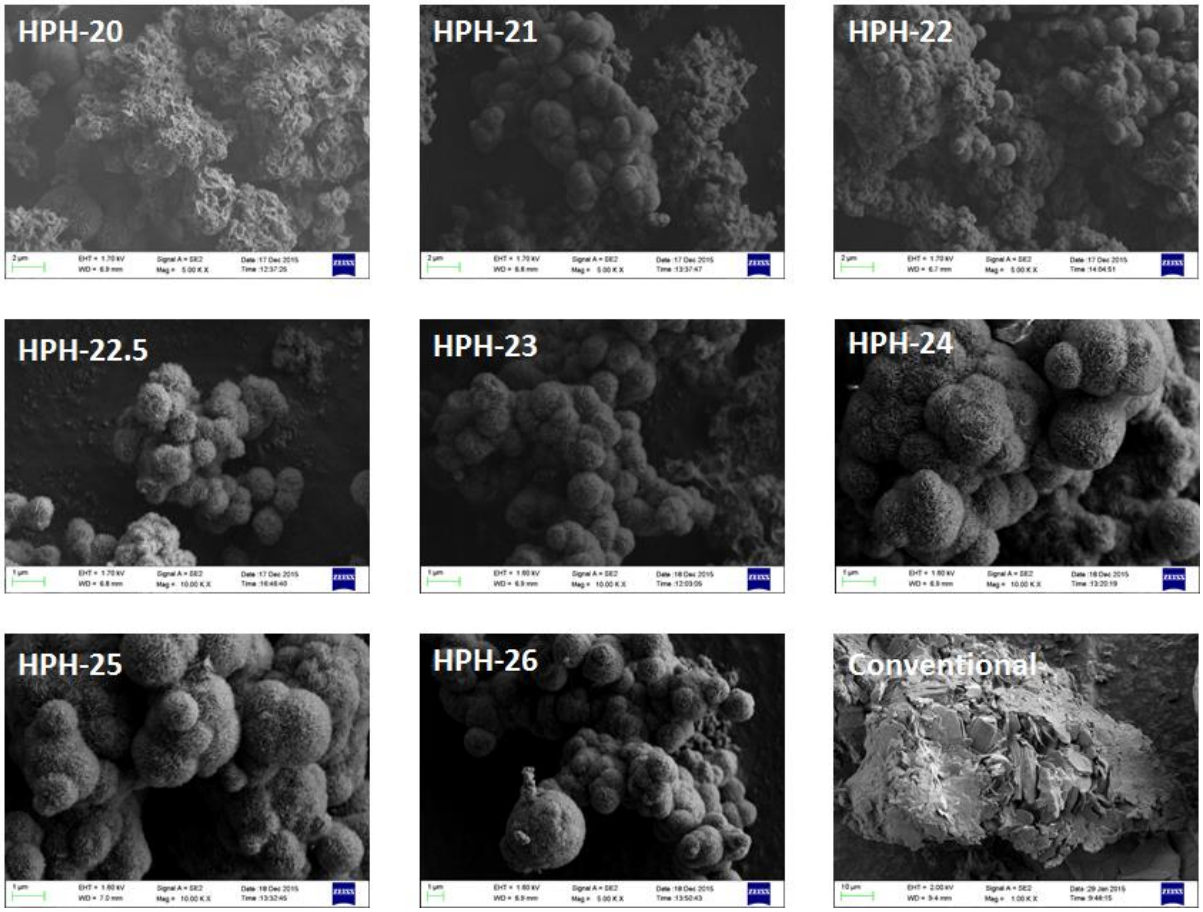

Figure 7.3: SEM images of Mg-Al LDH nano-spheres prepared at various pressures, 20-26 MPa in comparison to conventionally prepared LDH

This result demonstrates that the morphology of LDH does not only depend on pH, feed concentration and temperature [6], but is also affected by the pressure especially at the critical condition. Within the synthesised temperature of 723 K, the water phase changed from subcritical/vapour (20 MPa) to supercritical (26 MPa) phase via the critical point (22.1 MPa). An increase in pressure results in subsequent increase in density of water with a phase change anomaly existing around the critical point [22]. Subsequently, solubility increases with density which tends to affect the nucleation and particle growth [23]. Therefore, the variation in particle size with increase in pressure can be attributed to the variation in the solvent power of the supercritical water [24]. However, around the critical point, $1 < T/T_C < 1.1$ (where T and T_c are

the supercritical and critical temperatures respectively), a little change in pressure can result in a large density change [22]. This sudden change in density might have promoted the formation of spherical LDH from the irregular shaped LDH at the critical pressure, 22.1 MPa. Moreover, as a result of the change in pressure around the critical point, the equilibrium constant of the chemical reaction changes. This can also affect the crystal habit of the LDH as a result of the change in chemical species distribution. In conclusion, it can be suggested that within the sub critical and supercritical regime of water, an increase in the pressure will result in an increase in the spherical size and density of the formed LDH crystals.

7.4.3 Structural configuration of spherical crystallites

Figure 7.4 shows the XRD pattern for LDH nano-spheres at varying preparation pressures: subcritical region (20 MPa), critical region (23 MPa) and supercritical region (26 MPa). From the figure, a relatively well crystallized LDH was observed as reported in our previous study [16]. The reflections of the spectra have been indexed in accordance with the R3m hexagonal lattice with rhombohedral symmetry [25-27]. Peak reflections were categorised into three regions as discussed in previous studies. The low angle region situated at $2\theta < 30^o$ is attributed to the size of compensating anion [25]. The peaks in this region consist of 00l and h00 basal reflections. The middle angle region consists of non-basal reflections 0kl and ranges from $30^o < 2\theta < 60^o$. Reflections at this region are characteristics of structural disorder. Finally, the high angle region ($2\theta > 60^o$) are reflections of *hk0* and *hkl* and are attributed to the ordering within the metal hydroxide layers,

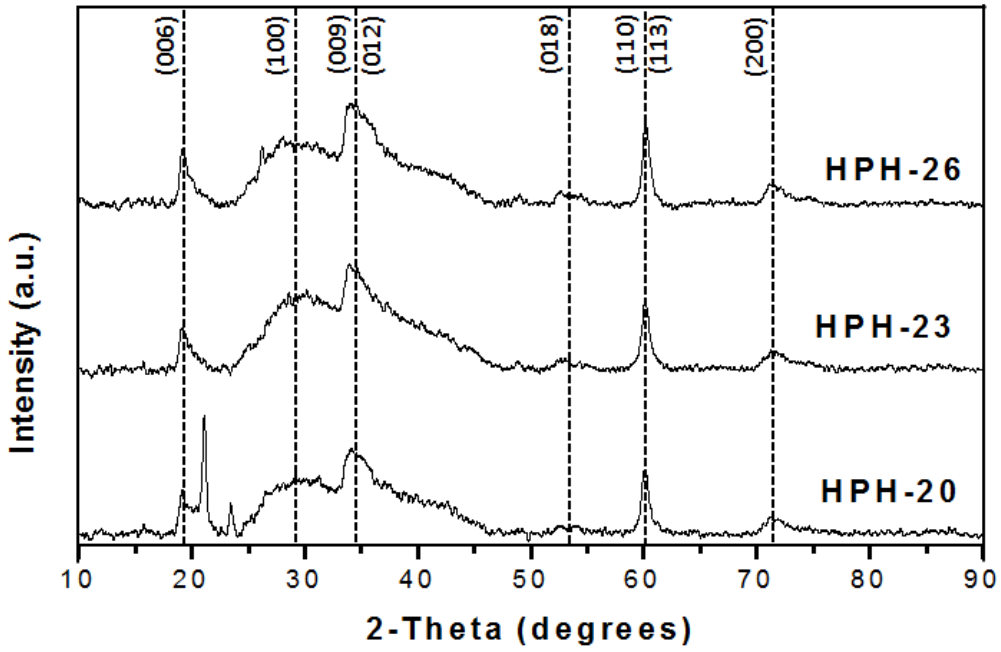

Figure 7.4: X-ray spectra for synthesised LDH nano-spheres prepared at various pressures at a temperature of 723 K

The XRD pattern shows that the intensity of the peaks increased with pressure suggesting a characteristic increase in crystallite size. Using the Scherrer's formula, this was computed to be 48.36, 48.82 and 55.11 nm for HPH-20, HPH-23 and HPH-26 respectively. This corresponds to the particle size range obtained from the nitrogen sorption analysis.

A notable peak at $2\theta = 23.5^{o}$ was witnessed for HPH-20. This was discovered to gradually disappear with increase in pressure. Based on literature, it can be suggested that this is due to the crystallization of boehmites, AlOOH [24]. During hydrothermal reaction, the formation of metal hydroxide proceeds from the hydrolysis of metal ions as shown in Reaction Scheme 7.1. This is as a result of electrostatic reaction between OH^- ions and metal ions and is boosted by the enhanced reaction rate due to the low dielectric constant of supercritical water when compared to subcritical water. This is governed by Born's theory (Equation 7.2) relating the dielectric constant to rate of chemical reaction [6, 24, 28]. A smaller dielectric constant will result to a higher reaction rate.

$$Al^{3+} + 3\,H_2O \rightarrow Al(OH)_3 + 3\,H^+ \qquad Hydrolysis\ Process$$

$$2\,Al(OH)_3 \rightarrow 2\,AlO(OH) + 2H_2O \qquad Dehydroxylation\ Process$$

Reaction Scheme 7.6: Proposed chemical equation for the formation of boehmites from aluminium hydroxide

Equation 7.5: Born's Theory

$$\ln k = \ln k_0 - \frac{\omega}{RT}\left(\frac{1}{\epsilon} - \frac{1}{\epsilon_0}\right)$$

where k and k_0 are the reaction rates at dielectric constants ϵ and ϵ_o respectively, ω is a reaction system constant, T is the absolute temperature and R is gas constant.

In the case of Al^{3+} ion, $Al(OH)_3$ is formed which precipitates through dehydroxylation to form boehmites which further dehydrates to produce alumina (Al_2O_3). However, dehydroxylation process is promoted at lower density. Moreover, supercritical water density is stipulated to be lesser than that of subcritical water. Hence, the formation beohmites is more favoured in subcritical water because dehydration reaction is stimulated by the reduction in water density, which is more likely in supercritical water.

7.4.4 Adsorption Capacity of amine functionalised LDH spheres

The impact of the preparation pressure on the adsorption performance of the adsorbents after amine modification (20 g of MEA) was investigated. The result is shown in Figure 7.5. The profile shows that an increase in preparation pressure results to adsorbents with decreasing adsorption capacity. However, this trend is overturned in the supercritical region where adsorption capacity increases with preparation pressure. Adsorption capacity of the adsorbents prepared within the vicinity of the critical pressure was slightly affected by change of pressure. However, at high supercritical pressure, there was a significant change in adsorption capacity. This can be attributed to the textural and chemical modification associated with the anomaly of water around its critical point.

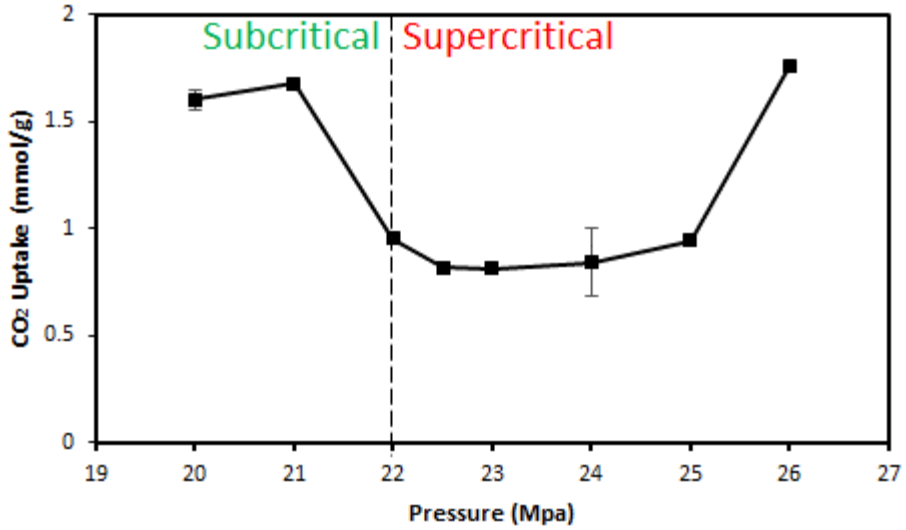

Figure 7.5: Variation of CO_2 uptake with preparation pressure for HPH-M20

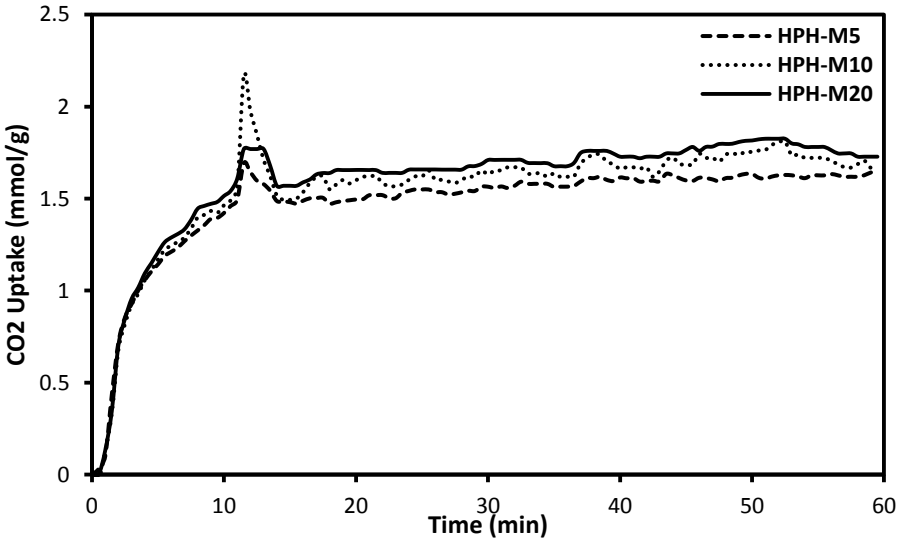

Figure 7.5: CO_2 uptake of amine modified HPH-26 at varying amine loading of 5g, 10g and 20g

Furthermore, the adsorption capacity of the modified adsorbent at varying amount of amine loading was tested. Experimented amine loadings were 5, 10 and 20 g MEA using HPH-26. The results of the CO_2 uptake are shown in Figure 7.6. The obtained results showed insignificant increase in CO_2 uptake with amine loading [11]. Estimated equilibrium CO_2 uptake are 1.83, 1.81 and 1.65 mmol/g for HPH-M20, HPH-M10 and HPH-M5 respectively. From the acquired data, it can be suggested that the adsorbent is about to attain its optimum amine uptake at amine loading of 20 g.

7.4.5 Effect of rapid cooling on spherical size

In the adopted synthesis method, the effect of cooling on the morphology of the spheres was also investigated. A comparison of the surface morphology for rapid and slow cooling is shown in Figure 7.7. Further results are summarized in Table 7.2. The results are obtained from nitrogen sorption analysis.

Table 7.2: Surface characteristics of HPH-20 and HPH-26 under rapid and slow cooling

Surface Characteristics	HPH-20		HPH-26	
	Rapid	Slow	Rapid	Slow
Surface area (m2/g)	115.47	493.96	178.27	311.18
Particle size (nm)	51.96	12.15	46.78	19.28
Pore size (nm)	19.13	14.88	20.13	18.01
Pore Volume (cm3/g)	0.57	1.84	0.66	1.40

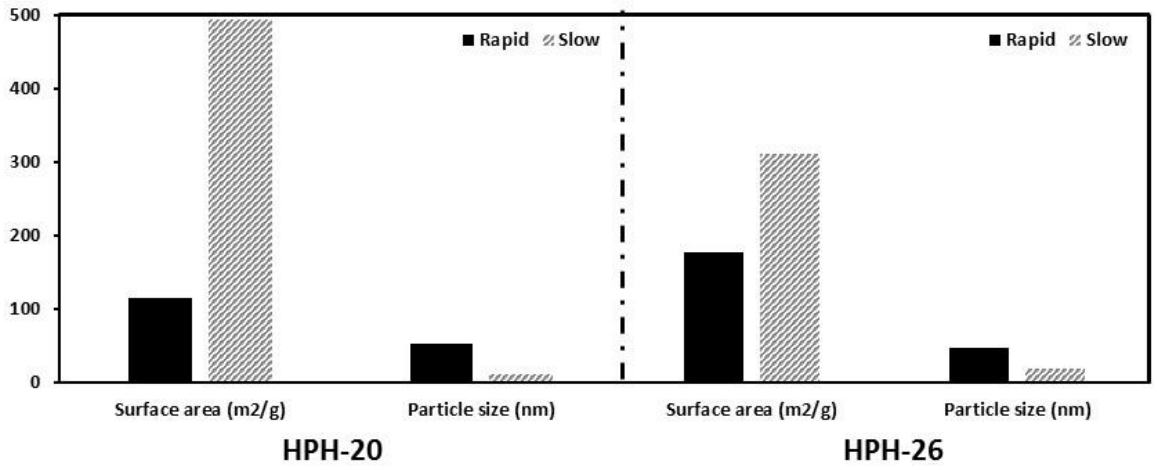

Figure 7.6: Rapid vs slow cooling effect on surface morphology of LDH spheres

It is observed that during the ageing process, the physical properties of the adsorbent were enhanced when allowed to cool under room temperature than using a cooling bath. Cooling under room temperature, the ageing process is longer and hence expedites the increase in crystallinity and crystallite size of particle [3]. This is supported by the gradual cooling temperature gradient which facilitates nucleation and growth of crystals. The dissolution and recrystallization of the smallest amorphous and crystalline particles are characteristics of this stage and is considered to aid in the improvement of particle morphology [3].

7.4.5 Kinetic Study

Comparison of experimental kinetic uptake data for HPH-M20 sample is shown in Figure 7.8 and the kinetic parameters summarised in Table 7.3. From the obtained simulation result, both models produced relatively good description of the experimental kinetic data. Nonetheless, the comparison result shows that the double exponential model best suits the obtained experimental data based on the R^2 value of 0.9746 when compared to 0.9607 for Avrami model. Similarly, the errors were 4.21% and 4.03% for Avrami and double exponential model respectively. The computed Avrami kinetic order is *ca.* 0.99. This fractional order identifies that the adsorption mechanism is complex or there exist more than one adsorption route [15]. As elaborated in previous study, double exponential model accounts for the occurrence of more than one adsorption mechanism [16]. This is described by the rate constants k_1 and k_2 with values 0.01788 and 0.30321 s^{-1}, with pre-exponential factors, A_1 and A_2 as 0.33636 and 1.72917 mmol/g. The pre-exponential factors in double exponential model suggest the share of each proposed adsorption mechanism on the total CO_2 uptake. Comparing A_1 and A_2, the adsorption mechanism described by A_2 can be stated to have a greater contribution towards CO_2 adsorption of the amine functionalised LDH spheres.

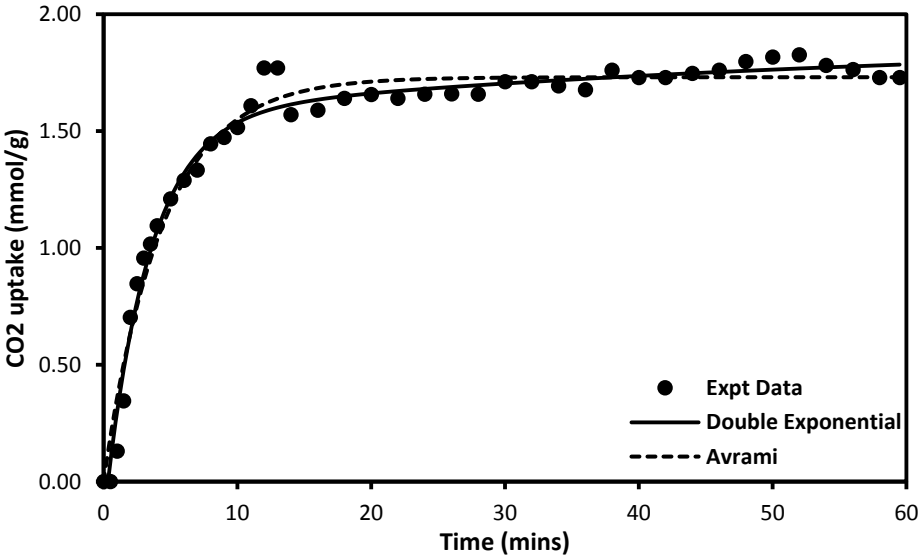

Figure 7.8: Simulation of adsorption kinetics based on experimental data of HPH-M20

Table 7.3: Kinetic parameters for Avrami and Double exponential models

Samples	Expt data (x_e)	Avrami			Err (%)	R^2	Double Exponential					Err (%)	R^2
		x_e	k_A	n			x_e	A_1	A_2	k_1	k_2		
HPH-M20	1.83	1.73	0.22	0.99	4.21	0.9607	1.90	0.34	1.73	0.02	0.30	4.03	0.9746

7.5 CONCLUSIONS

This review paper describes the synthesis of novel Mg-Al LDH spheres using supercritical hydrothermal method. A great feature of this method is the modification of particle size and morphology by tuning of water properties. The as-synthesised samples had spherical shapes ranging from 30-60 nm depending on the tuned pressure/density of water at constant temperature. However, this can be further reduced to < 20 nm depending on the cooling temperature. XRD patterns suggest the presence of boehmites in the crystal structure of spheres produced at low hydrothermal pressure. This gradually disappears with increase in pressure. CO_2 adsorption capacity dropped with samples produced around the critical pressure but surged in samples prepared within the supercritical zone.

ACKNOWLEDGEMENT

I deeply thank Mr. Marco Tomatis and Dr. Jun He for their assistance in this research study.

Reference

[1] L.H. Chagas, G.S.G. De Carvalho, W.R. Do Carmo, R.A.S. San Gil, S.S.X. Chiaro, A.A. Leitão, R. Diniz, L.A. De Sena, C.A. Achete, MgCoAl and NiCoAl LDHs synthesized by

the hydrothermal urea hydrolysis method: Structural characterization and thermal decomposition, Materials Research Bulletin, 64 (2015) 207-215.

[2] D.I. Ferrer, Supported Layered Double Hydroxides as CO2 Adsorbents for Sorption-enhanced H2 Production, Chemical Engineering, Imperial College, London, United Kingdom, Springer International Publishing Switzerland, 2016, pp. 209.

[3] F. Kovanda, D. Koloušek, Z. Cílová, V. Hulínský, Crystallization of synthetic hydrotalcite under hydrothermal conditions, Applied Clay Science, 28 (2005) 101-109.

[4] Y. Gao, Z. Zhang, J. Wu, X. Yi, A. Zheng, A. Umar, D. O'Hare, Q. Wang, Comprehensive investigation of CO2 adsorption on Mg-Al-CO3 LDH-derived mixed metal oxides, Journal of Materials Chemistry A, 1 (2013) 12782-12790.

[5] W. Lv, L. Yang, B. Fan, Y. Zhao, Y. Chen, N. Lu, R. Li, Silylated MgAl LDHs intercalated with MnO2 nanowires: Highly efficient catalysts for the solvent-free aerobic oxidation of ethylbenzene, Chemical Engineering Journal, 263 (2015) 309-316.

[6] T. Adschiri, Y. Hakuta, K. Arai, Hydrothermal Synthesis of Metal Oxide Fine Particles at Supercritical Conditions, Industrial and Engineering Chemistry Research, 39 (2000) 4901-4907.

[7] J. Otsu, Y. Oshima, New approaches to the preparation of metal or metal oxide particles on the surface of porous materials using supercritical water: Development of supercritical water impregnation method, J. of Supercritical Fluids, 33 (2005) 61-67.

[8] S. Miyata, Physico-chemical properties of synthetic hydrotalcites in relation to composition, Clays and Clay Minerals, 28 (1980) 50-56.

[9] J.-M. Oh, S.-H. Hwang, J.-H. Choy, The effect of synthetic conditions on tailoring the size of hydrotalcite particles, Solid State Ionics, 151 (2002) 285-291.

[10] F. Cavani, F. Trifirò, A. Vaccari, Hydrotalcite-type anionic clays: Preparation, properties and applications, Catalysis Today, 11 (1991) 173-301.

[11] Y. Kong, G. Jiang, Y. Wu, S. Cui, X. Shen, Amine hybrid aerogel for high-efficiency CO2 capture: Effect of amine loading and CO2 concentration, Chemical Engineering Journal, 306 (2016) 362-368.

[12] S. Loganathan, M. Tikmani, A. Mishra, A.K. Ghoshal, Amine tethered pore-expanded MCM-41 for CO2 capture: Experimental, isotherm and kinetic modeling studies, Chemical Engineering Journal, 303 (2016) 89-99.

[13] J. Wang, L.A. Stevens, T.C. Drage, C.E. Snape, J. Wood, Preparation and CO2 adsorption of amine modified layered double hydroxide via anionic surfactant-mediated route, Chemical Engineering Journal, 181-182 (2012) 267-275.

[14] A. Fathy, O. Elkady, A. Abu-Oqail, Synthesis and characterization of Cu–ZrO2 nanocomposite produced by thermochemical process, Journal of Alloys and Compounds, 719 (2017) 411-419.

[15] R. Serna-Guerrero, A. Sayari, Modeling adsorption of CO2 on amine-functionalized mesoporous silica. 2: Kinetics and breakthrough curves, Chemical Engineering Journal, 161 (2010) 182-190.

[16] C.I. Ezeh, M. Tomatis, X. Yang, J. He, C.-g. Sun, Ultrasonic and Hydrothermal Mediated Synthesis Routes for Functionalized Mg-Al LDH: Comparison Study on Surface Morphology, Basic Site Strength, Cyclic Sorption Efficiency and Effectiveness, Ultrasonics Sonochemistry, DOI https://doi.org/10.1016/j.ultsonch.2017.07.013.

[17] K.L. Tan, B.H. Hameed, Insight into the adsorption kinetics models for the removal of contaminants from aqueous solutions, Journal of the Taiwan Institute of Chemical Engineers, 74 (2017) 25-48.

[18] E.C.N. Lopes, F.S.C. dos Anjos, E.F.S. Vieira, A.R. Cestari, An alternative Avrami equation to evaluate kinetic parameters of the interaction of Hg(II) with thin chitosan membranes, Journal of colloid and interface science, 263 (2003) 542-547.

[19] A.R. Cestari, E.F.S. Vieira, G.S. Vieira, L.E. Almeida, The removal of anionic dyes from aqueous solutions in the presence of anionic surfactant using aminopropylsilica—A kinetic study, Journal of Hazardous Materials, 138 (2006) 133-141.

[20] S. Otles, SUPERCRITICAL FLUIDS AND ITS APPLICATIONS IN FOOD INDUSTRY, in: R. Askin (Ed.), ELECSUS, Turkey, 2006.

[21] C.I. Ezeh, X. Huang, X. Yang, C.-g. Sun, J. Wang, Sonochemical surface functionalization of exfoliated LDH: Effect on textural properties, CO2 adsorption, cyclic regeneration capacities and subsequent gas uptake for simultaneous methanol synthesis, Ultrasonics Sonochemistry, 39 (2017) 330-343.

[22] M. Türk, Fundamentals, Supercritical Fluid Science and Technology, 6 (2014) 13-44.

[23] J.M. Yuk, Q. Zhou, J. Chang, P. Ercius, A.P. Alivisatos, A. Zettl, Real-Time Observation of Water-Soluble Mineral Precipitation in Aqueous Solution by In Situ High-Resolution Electron Microscopy, ACS Nano, 10 (2016) 88-92.

[24] H. Hayashi, Y. Hakuta, Hydrothermal Synthesis of Metal Oxide Nanoparticles in Supercritical Water, Materials, 3 (2010) 3794-3817.

[25] N. Touisni, F. Charmantray, V. Helaine, C. Forano, L. Hecquet, C. Mousty, Optimized immobilization of transketolase from E. coli in MgAl-layered double hydroxides, Colloids and Surfaces B: Biointerfaces, 112 (2013) 452-459.

[26] S.-L. Wang, C.H. Liu, M.K. Wang, Y.H. Chuang, P.N. Chiang, Arsenate adsorption by Mg/Al–NO3 layered double hydroxides with varying the Mg/Al ratio, Applied Clay Science, 43 (2009) 79-85.

[27] M. Bellotto, B. Rebours, O. Clause, J. Lynch, D. Bazin, E. Elkaïm, A Reexamination of Hydrotalcite Crystal Chemistry, The Journal of Physical Chemistry, 100 (1996) 8527-8534.

[28] T. Adschiri, K. Kanazawa, K. Arai, Rapid and Continuous Hydrothermal Synthesis of Boehmite Particles in Subcritical and Supercritical Water, Journal of the American Ceramic Society, 75 (1992) 2615-2618.

CHAPTER EIGHT

ULTRASONIC AND HYDROTHERMAL MEDIATED SYNTHESIS ROUTES FOR FUNCTIONALIZED Mg-Al LDH

Abstract

Amine functionalized layered double hydroxide (LDHs) adsorbents prepared using three different routes: co-precipitation, sono-chemical and ultrasonic-assisted high pressure hydrothermal. The performance of the prepared adsorbents was tested under a controlled thermal-swing adsorption process to measure its adsorption capacity, regeneration and cyclic efficiencies subsequently. The characterisation results were compared with those obtained using the conventional preparation routes but taking the impact of sonochemical and hydrothermal pre-treatment on textural properties, adsorption capacity, regeneration and cyclic efficiencies into account. Textural results depict a surge in surface area of the adsorbent synthesised by hydrothermal route (311 m^2/g) from 25 and 171 m^2/g for conventional and ultrasonic routes respectively. Additionally, it has been revealed from the present study that adsorbents prepared using ultrasonic-assisted hydrothermal route exhibit a better CO_2 uptake capacity than that prepared using sonochemical and conventional routes. Thus, the ultrasonic-assisted hydrothermal treatment can effectively promote the adsorption capacity of the adsorbent. This is probably due to the decrease of moderate (M-O) and weak (OH^- groups) basic sites with subsequent surge in the number of strong basic sites (O^{2-}) resulting from the hydrothermal process. Moreover, the cyclic adsorption efficiency of the ultrasonic mediated process was found to be 76% compared with 60% for conventional and 53% for hydrothermal routes, respectively. According to the kinetic model analysis, adsorption mechanism is mostly dominated by physisorption before amine modification and chemisorption after the modification process.

Keywords: *CO_2 Adsorption, Layered Double Hydroxide, Ultrasound, Hydrothermal, Regeneration.*

8.1 INTRODUCTION

Adsorption of carbon dioxide is perceived as the most suitable method for Carbon Capture and Storage (CCS) technology [1, 2]. Extensive studies on various adsorbents used for CO_2 uptake has been carried out over the years. Layered double Hydroxides (LDHs) provided comparatively high uptake capacity with numerous catalytic applications [3, 4]. Additionally, its ionic inter-layered configuration enhances the number of basic sites and provides high contact surface area [4]. LDHs are anionic clay minerals also known as mixed-metal layered hydroxides or hydrotalcites-like compounds. They possess two dimensional structure of layers shaped by trivalent and divalent cations parted by water and anions molecules (see Figure 2.) with a general formula:

$$(M_{1-x}^{2+}M_{x}^{3+}(OH)_2)^{x+}\left(A_{x/m}^{m-}.nH_2O\right)^{x-}$$

where M^{2+} and M^{3+} are divalent and trivalent cations respectively, A^{m-} is a compensating anionic charge, x is the partial substitution of M^{2+} and M^{3+}, usually within a M^{2+}/M^{3+} ratio of 2 and 5 [4-6].

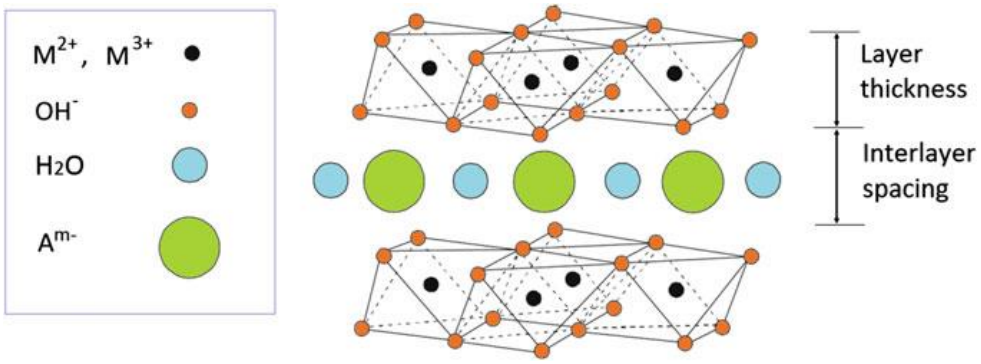

Figure 8.1: Structural configuration of layered double hydroxides [5]

LDHs are basically synthesized via co-precipitation of solutions containing M^{2+} and M^{3+} metal salts in a preferred interlayer anion [6, 7]. This synthesis method can be conducted at high or low supersaturation environments. In low supersaturation condition, the metal solutions are added concurrently to the solution containing the alkali; whereas the metal (at a given M^{2+}/M^{3+} ratio) mixture is added to the alkali and anion precursor solution for high supersaturation conditions. The former tends to produce more crystalline structures because of the increased rate of nucleation over crystallization [6]. Besides this method, other means of synthesizing LDH are sol-gel and urea techniques [7, 8].

A key property of this material for the purpose of CO_2 adsorption and other catalytic reactions is its basic property. Owing to the occurrence of interlayered anions and water molecules in the structure, LDH behave as solid bases. Wide ranges of basic strength can be obtained depending on the treatment route and metallic composition. This is primarily attributed to the nature and deposition of the divalent and trivalent cations on the material. With this property, CO_2 has enough acidic strength to bond with the weak basic sites of LDH. However, with an improved basic strength, CO_2 is chemisorbed weakly on low basic sites, surface hydroxyl groups forming bicarbonates and strongest on strong basic sites, free lattice oxygen (O^{2-}) forming mono-dentate carbonates. Adsorption on medium basic sites are on acid-base (metal-oxygen) pairs like Mg^{2+}-O^{2-} or Al^{3+}-O^{2-} forming tri-dentates or bi-dentates. The use of temperature-programmed desorption monitored by infrared spectroscopy, shown in Figure 8.2, further explains this theory [9].

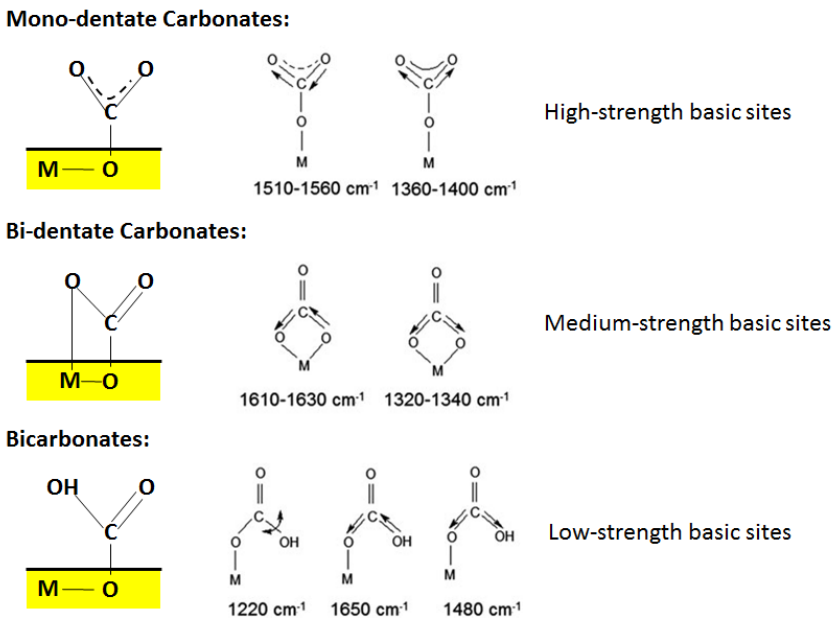

Figure 8.2: Infrared bands of adsorbed CO_2 on LDH surface [9]

The strength of these basic sites determines the adsorption and regeneration capacity of the adsorbent. Most research studies, to the best our knowledge, have emphasised the effect of metallic composition on this property. However, it is observed from this study that the preparation route plays a key role in the basic strength of this material. Subsequently, this affects the adsorption and regeneration capacities, as well as the life span of the material [10]. In addition, the intimate contact

between the metallic contents of the LDHs enhances the physico-chemical properties of these materials making it suitable precursors for the synthesis of mixed oxides for hydrogenation and dehydrogenation reactions [6, 11]. Metallic contact can be improved upon by boosting the deposition and dispersion of the cations on the adsorbent. This can be achieved by adopting several preparation routes [3, 12-14].

In this work, the impact of ultrasonic irradiation and ultrasonic-assisted hydrothermal synthesis route on the basicity, adsorption, regeneration and cyclic efficiencies were investigated. This is a follow-up study to recent work [10]. This method has shown to produce materials with well-ordered formation [15]. The prepared samples were characterized using Scanning Electron Microscope (SEM), Energy Dispersion X-ray Spectroscopy (EDX), Brunauer-Emmett-Teller (BET), Thermal Gravimetric Analyzer (TGA), Temperature-Programmed Desorption (TPD), X-ray Photoelectron Spectroscopy (XPS) and X-ray Diffraction (XRD).

8.2 EXPERIMENTAL

8.2.1 Material preparation

Different preparation methods were used in preparing the layered double hydroxides (LDHs) using the standard method from previous study [10]: conventional co-precipitation, ultrasonic mediated and ultrasonic-assisted hydrothermal. Subsequently, MEA extractions of these LDHs were carried out to produce the amine modified LDHs. All chemicals used for experimentation were acquired from SinoPharm Chemical Reagents Co. Ltd.

8.2.2 Sample Synthesis

8.2.2.1 For Mg-Al LDH

200 ml solution containing APTES (≥98%) and SDS (≥86%) (molar ratio: 5:1) respectively dissolved in a mixture of 50 ml C_2H_5OH (≥99.7%) and 150 ml distilled water was stirred for about 30 min at a temperature of 60 ^oC until the pH stabilized at about 10.3. This solution was then reacted with $Mg(NO_3)_2 \cdot 6H_2O$ (≥98%) and $Al(NO_3)_3 \cdot 9H_2O$ (≥99%) (molar ratio: 3:1, dissolved in 100 ml of distilled water) solution by adding the latter dropwise while maintaining the temperature

of the former at 60 ^{o}C. The mixture pH was regulated towards 10 using 4 M NaOH (≥96%) solution. The substrate (molar ratio of Mg:Al:APTES:SDS = 3:1:5:1) was then aged for 20hr with the constant stirring at the maintained temperature. The filtered precipitates were then washed with ionised water before being vacuum dried (500 mbar at 70 ^{o}C) overnight. This sample is labelled as Conv-LDH. Using the same chemical composition and process, a set of new samples were prepared using sonicated mixing by ultrasonic horns (high intensity sonication, 600 W) [10]. This sample is labelled as US-LDH.

For ultrasonic-assisted hydrothermal synthesized samples, HPH-LDH, 32 ml solution containing APTES (≥ 98%) and SDS (≥ 86%) (APTES:SDS molar ratio: 5) was reacted with $Mg(NO_3)_2.6H_2O$ (≥ 98%) and $Al(NO_3)_3.9H_2O$ (≥ 99%) (Mg:Al molar ratio: 3, dissolved in 16 ml of distilled water) solution. The latter was added dropwise while maintaining the temperature of the former at 60 ^{o}C and sonicating with ultrasonic horn. The substrate (molar ratio of Mg:Al:APTES:SDS = 3:1:5:1) was moved to the hydrothermal reactor. After being vented with pure N_2 gas (99.99%) for 15 mins in order to remove all of the oxygen before the reaction, the reactor was sealed and heated to a temperature of 450 °C with a ramp of 2 °C/min and then held for 15 mins. After reaction, the solution was aged for 12 hr. The precipitates were filtered, washed with distilled water and then dried in a vacuum oven (500 mbar at 70 ^{o}C) for 7 h.

8.2.2.2 For Mg-Al LDH-MEA

The prepared LDHs were functionalised via MEA extraction. 0.5 g of LDH sample was dispersed in a solution of 100 ml C_2H_5OH (≥99.7%) containing 20 g MEA (≥99%). The mixture was then refluxed for 20 hr at a temperature of 90 ^{o}C. After which the samples were filtered, washed with ethanol and dried in a vacuum oven overnight. These samples are labelled Conv-MEA. Using an ultrasonic horn, the procedure was repeated for the synthesised US-LDHn samples. The obtained samples are labelled US-MEA. Similarly, this was repeated for the HPH-LDH samples and labelled as HPH-MEA.

8.2.3 Characterisation

8.2.3.1 Nitrogen adsorption-desorption analysis

The textural characteristics of the prepared catalysts were studied by Nitrogen physisorption analysis at -196 ^{o}C using the Micrometrics ASAP 2020 Surface Area and Porosity Analyser. Prior to this analysis, samples were degassed at a temperature of 105 ^{o}C for 4 hr. The surface area (S_{BET}) of the samples was determined using the BET (Brunauer, Emmett and Teller) model. The total pore volumes (V_{Total}) were computed from the amount of nitrogen adsorbed at relative pressure (P/P_o) of 0.99 and the average pore volumes from $4V_{Total}/S_{BET}$. The pore size distribution was calculated using the BJH (Barrett, Joyner and Halenda) model. The t-plot method was used to calculate the micopore volume (V_{micro}).

8.2.3.2 Scanning electron microscope-Energy dispersive X-ray spectroscopy (SEM-EDX)

The surface composition and structure of the prepared materials were studied with a Zeiss ΣIGMA™ Field Emission SEM and an Oxford Instrument INCAx-act PentaFET® Precision EDX. The EDX spectra for the LDHs were obtained. This was also used to compute the amine content present in the adsorbents

8.2.3.3 X-ray Diffraction (XRD) and X-ray Photoelectron Spectroscopy (XPS) Analysis

XRD patterns were studied using a Bruker-AXS D8 advance powder diffractometer with a scanning range of $10^{o} \leq 2\theta \leq 90^{o}$. X-ray Photoelectron Spectroscopy (XPS) data of the adsorbent was obtained using Kratos X-ray Photoelectron Spectrometer – Axis Ultra DLD with a 96 W monochromatic Al Kα X-ray source (1486.69 eV) at a photoelectron take-off angle of 45°. Narrow scans were conducted at steps of 0.05 eV with dwell time of 600 ms whereas wide scans were conducted from 1100 eV to 0 eV with 150 ms dwell time and at 1 eV steps. The C 1s peak at 284.6 eV was used as the reference for standardizing the binding energy.

8.2.3.4 Temperature-Programmed Desorption (TPD)

CO_2-TPD analysis was conducted using AutoChem II 2920. The TPD of CO_2 measurements were conducted to evaluate the basicity of the catalysts. 0.1 g of the adsorbent was treated in the reactor

in N_2 atmosphere at a temperature of 350 ^oC for 2 hr. A thermal conductivity detector (TCD) was adopted to analyze desorption trends from 100 to 800 °C at a heating rate of 10 °C/min.

8.2.3.5 Thermo-gravimetric analysis

Thermal stability and CO_2 uptake measurements were conducted using the Netzsch STA 449 F3 Jupiter thermogravimetric analyser (TGA).

8.2.3.5.1 Thermal Stability Measurement

The stability of the as-synthesised LDH samples in air was determined. 0.4 cm^3 alumina crucible was loaded with 5-10 mg of sample and the thermal decomposition examined from 25 to 1000 ^oC , ramped 10 ^oC/min and under air flow (50 ml/min).

8.2.3.5.2 CO_2 Uptake Measurement.

Approximately 5-10 mg of the synthesized sample was heated from 25 to 105 ^oC at 20 ^oC/min under N_2 at a flow rate of 50 ml/min; and then held isothermally for 30 min before being cooled to the required adsorption temperature at a rate of 10 ^oC/min. The gas was switched from N_2 to CO_2 and held isothermally for 90 min at a flow rate of 20 ml/min. The experimental adsorption temperature is 55 ^oC. The CO_2 adsorption capacity was calculated from the weight difference of the samples in CO_2 atmosphere. The uptake profile was measured against an empty alumina crucible using the same method so as to correct the impact of change in gas density and viscosity.

8.2.3.5.3 Thermally Assisted Regeneration of Adsorbent.

Regeneration efficiency of the functionalized samples were analysed by thermal-assisted regeneration using nitrogen as a sweep gas. Two cycles of the CO_2 uptake measurement was repeated in this case. In between the cycles, the adsorbents were thermally desorbed at 105 ^oC in a stream of N_2 at a flow rate of 50 ml/min for 10 mins. The amounts adsorbed (Q_a) and desorbed (Q_d) were deduced by the change in weight of the samples. The regeneration efficiency (RE) was thus estimated based on Equation 8.1:

Equation 8.1: Regeneration efficiency equation

$$RE = \frac{Q_d}{Q_a} \times 100\%$$

8.3 THEORETICAL

To predict kinetic behaviour, the experimental results were simulated assuming pseudo-first, pseudo-second order and double-exponential kinetic models (as listed in Section 3.6.4). The double exponential model was considered because of its feasibility to explain the surface heterogeneity of the adsorbent accounting for two different adsorption sites. Additionally, it can partially elaborate the kinetic mechanisms associated with both pseudo-first and second order reactions. This mechanism can be categorised into a controlled slow phase intra-particle diffusion and a controlled fast phase surface reaction [17].

To determine the suitability of each model, error function (Err) and correlation coefficient (R^2) equations defined in Section 3.6.4.1 were applied. It is reasonable to assume that the adsorption rate constant, k for both pseudo-first and -second order model is the same for each group of functionalized and non-functionalized adsorbents since they are both grafted with the same amino silane. However, this was not assumed in this study. The effect of preparation route on the rate constant was rather studied

8.4 DISCUSSION OF RESULTS

8.4.1 Impact of preparation route on textural properties and surface morphology

Table 8.1: Texture properties of the samples

Sample	S_{BET}	Particle Size	V_{Total}	V_{micro}	Average Pore Width	%Micro*
	(m^2/g)	(nm)	(cm^3/g)	(cm^3/g)	(nm)	(%)
Conv-LDH	25.03	239.67	0.0161	0.0008	2.57	4.97
US-LDH	171.20	35.05	0.5528	0.0229	12.92	4.14
HPH-LDH	311.18	19.28	1.4005	0.0023	18.00	0.16

*$\%Micro = V_{micro}/V_{Total}$

From Table 8.1, S_{BET} of Conv-LDH is *ca.* 25 m^2/g which showed an increase to 171.20 and 311.18 m^2/g for US-LDH and HPH-LDH respectively. In the same trend, the total pore volume showed a tremendous increase indicating that the sonication and hydrothermal preparation method enhances the porosity of the sample as well as the surface area when compared to other studies (see Table 8.2). However, these methods tend to reduce the micropores in the sample with the hydrothermal route exhibiting the least microporous percentile. This depicts that the sample is a mesoporous/macroporous material with minor microporous features. The features of these pores can be seen from Figure 8.3. All three samples contained approximately the same volume ratio of mesopores to macropores. However, the Conv-LDH is observed to have a higher percentile of low range mesopores (2-10 nm) contributing to 55% of the total pore volume as compared to 10% and 15% for US-LDH and HPH-LDH respectively. The high range mesopores (10-50 nm) accounted for about 50% of the total pore volume of the US-LDH and HPH-LDH samples compared to *ca.* 7% in Conv-LDH. This can be further illustrated by the inserted image of Figure 8.3 displaying the pore size distribution in terms of total volume percentages.

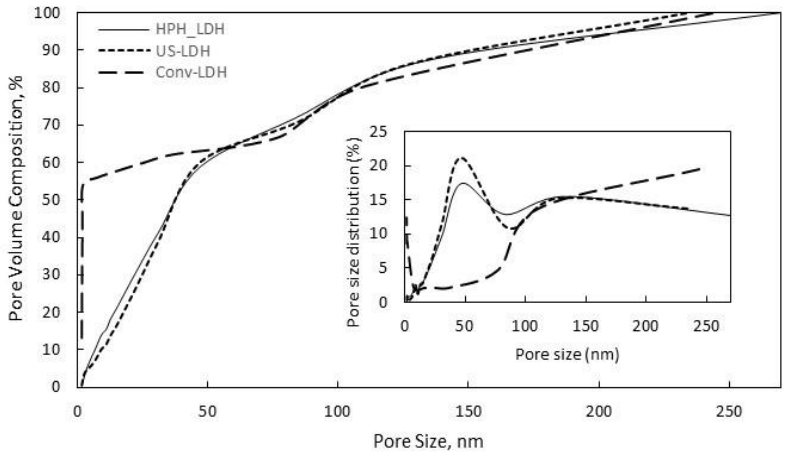

Figure 8.3: Pore size distribution of Conv-, US- and HPH-LDH samples

Figure 8.4 shows the total absolute volume of the pores at various pore size. It depicts that the high range mesopores mostly contribute to the total pore volume of the samples and comprises of a higher pore distribution.

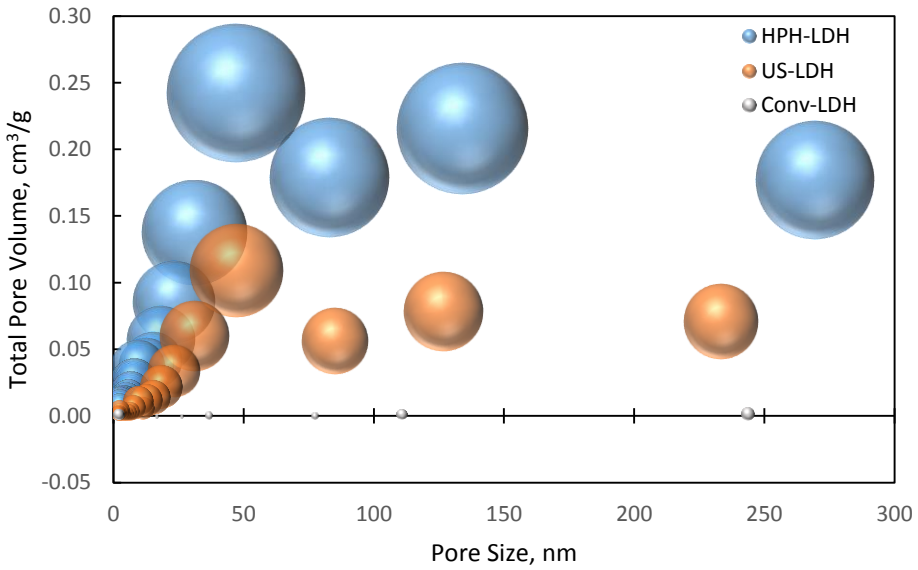

Figure 8.4: Total pore volume of various pore sizes of Conv-, US- and HPH-LDH samples (bubble size indicates relative amount of pore size)

Table 8.2: Comparison of S_{BET} for different LDH adsorbent via different preparation routes

Sample*	Preparation Method	SBET (m^2/g)	Reference
LDH	Commercial	2.90	[18]
CO_3-LDH	Commercial	18.90	[19]
Conv-LDH	Co-precipitation	10.50	[20]
Conv-LDH	Co-precipitation	44-70	[18]
Conv-LDH	Co-precipitation	69.78	[21]
Conv-LDH	Co-precipitation	25.03	Current work
c-LDH	Calcined Co-precipitation	84-123	[18]
c-CO_3-LDH	Calcined Solvothermal	165.07	[22]
US-LDH	Ultrasonic assisted	84.44	[21]
US-LDH	Ultrasonic assisted	171.20	Current work
r-LDH	Reconstructed	45-55	[18]
CO_3-LDH	Solvothermal	24.74	[22]
LDH	Silylated-Calcined	19.20	[23]
HPH-LDH	Hydrothermal	311.18	Current work

**LDH samples are Mg-Al LDH*

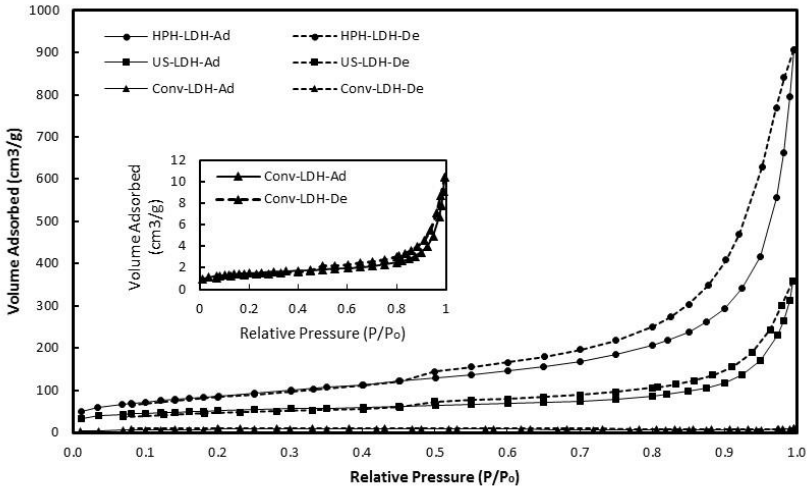

Figure 8.5: Nitrogen adsorption-desorption isotherms for Conv-LDH, US-LDH and HPH-LDH samples (inserted image shows the enlarged isotherm for Conv-LDH)

Table 8.3: Surface content and binding energy for N 1s and O 1s levels for LDH, US-LDH and HPH-LDH

Preparation Route	Sample	N 1s Spectra					O 1s Spectra				
		Binding Energy (eV)		Area (cps eV)		Content	Binding Energy (eV)		Area (cps eV)		Content
		Free Amine	Protonated Amine	Free Amine	Protonated Amine	$\left(\frac{Free}{Protonated}\right)$	Lattice Oxygen (O^{2-})	Hydroxyl Group (OH^-)	Lattice Oxygen (O^{2-})	Hydroxyl Group (OH^-)	$\left(\frac{OH^-}{O^{2-}}\right)$
Conventional	Conv-LDH	396.7	400.8	640.0	626.4	1.02	529.9	531.4	7633.2	1011.8	0.13
Ultrasonic	US-LDH	396.9	400.3	574.1	876.6	0.65	529.8	531.3	10109.2	2053.1	0.21
Hydrothermal	HPH-LDH	395.4	399.1	349.7	791.2	0.44	530.4	-	60510.2	-	-

Table 8.4: EDX elemental analysis and CO2 uptake of prepared LDH and calculation results for the molecular formulas, removed SDS and effective amine efficiency

Sample	N (wt%)	C (wt%)	S (wt%)	Molecular formula (mmol/g)[a]	SDS/APT ES	Amine Loading (mmol/g)	CO_2 Adsorbed (mmol/g)	SDS removed (%)	Effective amine loading (mmol/g)[b]	Effective Amine Efficiency[c]
Conv-LDH	0.65	51.35	11.41	$[C_{12}H_{25}SO_4]_{3.57}$-.$[C_{0.01}H_{0.52}SiNO_3]_{0.46}$	7.68	0.46	0.82			
Conv-MEA	6.60	26.60	1.05	$[C_{12}H_{25}SO_4]_{0.33}$-.$[C_{3.87}H_{10.17}SiNO_3]_{4.71}$	0.07	4.71	1.45	99.09	4.25	0.15
US-LDH	3.11	51.16	11.08	$[C_{12}H_{25}SO_4]_{3.46}$-.$[C_{0.49}H_{1.72}SiNO_3]_{2.22}$	1.56	2.22	0.66			
US-MEA	7.34	30.64	0.60	$[C_{12}H_{25}SO_4]_{0.19}$-.$[C_{4.44}H_{11.60}SiNO_3]_{5.24}$	0.04	5.24	1.37	97.71	3.02	0.24
HPH-LDH	2.55	13.68	1.50	$[C_{12}H_{25}SO_4]_{0.47}$-.$[C_{3.17}H_{8.43}SiNO_3]_{1.82}$	0.26	1.82	0.88			
HPH-MEA	7.36	9.27	0.82	$[C_{12}H_{25}SO_4]_{0.26}$-.$[C_{0.88}H_{2.71}SiNO_3]_{5.26}$	0.05	5.26	3.75	81.06	3.44	0.83

a. All Nitrogen, Carbon and Sulphur elements in the grafted LDHs were attributed to come from organic compounds used for intercalation

b. Effective amine loading = Difference in amine loading before and after LDH modification

c. Effective Amine Efficiency = Difference in CO_2 adsorbed before and after LDH modification/effective amine loading (mmol CO_2/mmol amine added during amine modification

Table 8.5: CO_2 kinetic model parameters, R^2 and standard errors (%) for prepared LDHs and amine functionalized LDHs at 55 ^oC and 1 atm

Samples	Pseudo 1st Order		Err	R^2	Pseudo 2nd Order		Err	R^2	Double Exponential					Err	R^2
	x_e	k_f	(%)		x_e	k_s	(%)		x_e	A_1	A_2	k_1	k_2	(%)	
Conv-LDH	0.75	0.12	0.07	0.9766	0.83	0.23	0.34	0.9483	0.76	0.31	0.55	0.31	0.10	3.71	0.9815
US-LDH	0.55	0.09	0.37	0.9062	0.63	0.20	0.81	0.9631	0.85	0.47	0.45	0.01	0.23	9.24	0.9897
HPH-LDH	0.89	0.05	0.14	0.9356	1.14	0.04	0.38	0.9034	0.88	0.48	0.48	0.06	0.06	0.28	0.9421
Conv-MEA	1.33	0.13	0.10	0.8786	1.46	0.14	0.08	0.9711	1.41	0.75	0.67	0.05	0.69	0.41	0.9968
US-MEA	1.32	0.05	0.10	0.9826	1.67	0.03	0.28	0.9709	1.30	0.70	0.70	0.06	0.06	0.09	0.9861
HPH-MEA	3.52	0.35	2.06	0.8733	3.72	0.17	2.34	0.9155	3.58	1.63	2.04	0.14	1.07	2.01	0.9327

Figure 8.5 shows the N_2 adsorption-desorption isotherms for Conv-LDH, US-LDH and HPH-LDH samples. The adsorbents show a type IV isotherm with H1 hysteresis loop characterized with the formation of a monolayer accompanied by multilayers occurring as a result of capillary condensation. This is a characteristic feature of mesoporous materials [24-26] validating the data represented in Table 8.1. These H1-hysteresis type materials are attributed to the formation of aggregates or compact uniform spheres as shown in the SEM images [26]. The hysteresis loop for the HPH-LDH was observed to be broader than that of US- and Conv-LDHs indicating the extent of capillary condensation in the samples. It is observed that the volume adsorbed by HPH-LDH is 3 folds that of US-LDH, which in turn is ~30 folds of the conventional LDH. This depicts an enhancement in the pore structure of the samples and is attributed to the enhancement of nucleation and precipitate growth resulting from improved dissolution and reaction process via sonication [20] and hydrothermal crystallization [27].

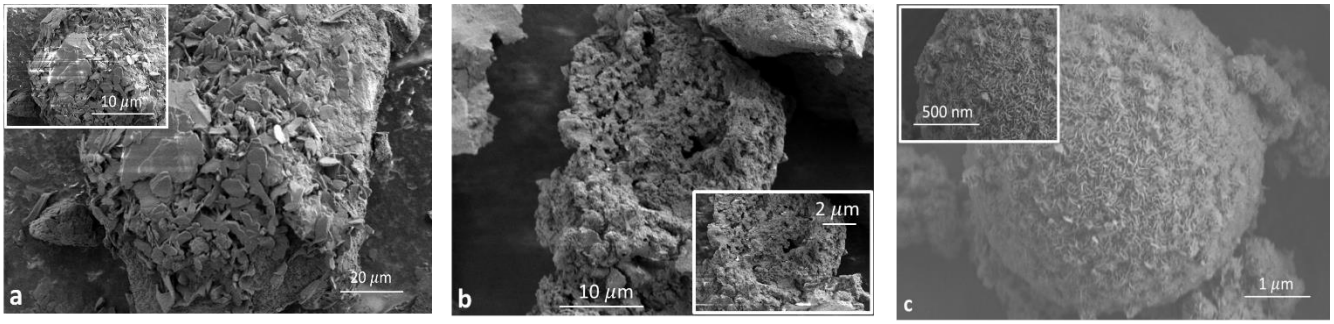

Figure 8.6: SEM images of prepared LDHs (a) Conv-LDH, (b) US-LDH, and (c) HPH-LDH

Considering the surface texture of the samples, Figure 8.6 shows images of surface morphology of the prepared LDH samples. It can be seen from the figure that Conv-LDH presents a boulder-shaped material with aggregated flaky plate-like surface. This may be explained by the formation of shell-core structure caused by the sequential reduction of two different metallic ions [10, 28] resulted from the difference in the reduction potentials of Al^{3+} and Mg^{2+} ions. This is similar to the sonication route sample but without the plate-like surface. Surface of these samples displayed more pores attributable to high-speed jets or shock waves resulting from bubble collapse [28]. Unlike the conventionally and ultrasonically prepared samples, the hydrothermal LDHs were smaller and of spherical structure, hence increasing the effective surface area for adsorption.

8.4.2 Impact of preparation route on surface chemical content

To investigate the impact of preparation route on the amine functional group and extent of oxidation on the surface of the adsorbent, XPS analysis was conducted. The N 1s and O 1s spectra are shown in Figure 8.7 and the data are summarized in Table 8.3. The deconvolution of N 1s spectra has two peaks at *ca.* 396 ($\pm$0.9) eV and 400 ($\pm$0.9) eV respectively (Figure 8.7a). These are assigned to free amine and protonated amines respectively [10, 29]. The concentration of free amino group decreased for species prepared via ultrasonic and hydrothermal mediation. This reveals that despite the enhanced physical properties of the adsorbent, ultrasonic and hydrothermal process has a reduced amount of free amino active sites on the adsorbent. This can be explained by the enhanced protonation of the free amine groups. However, the amine loading (deduced by the total concentration of N atom) is highest in species prepared via ultrasonic irradiation and least in the hydrothermal process. This can be partially attributed to the efficient ejection of hydroxyl radicals from bubbles during cavitation, which readily hydrates the anions; hence bonding the anions within the interlayers of the adsorbent [30]. This can be supported by the high content of hydroxyl group (OH^-) in samples synthesised via ultrasonic irradiation. Similar to the N 1s spectra, Figure 8.7b shows the deconvolution of the O 1s spectra into two bands at 529.1 eV and 531.6 eV respectively. However, only the former band (with a 0.75 eV chemical shift) was observed in the hydrothermally prepared sample. The first band relates to lattice oxygen (O^{2-}), while the latter relates to adsorbed surface oxygen or hydroxyl groups (OH^-) [13, 31]. The results summarised in Table 8.3 show that the ratio of hydroxyl group to lattice oxygen increased with ultrasonic irradiation but decreased with hydrothermal synthesis. This indicates that the surface concentration of the OH^- group is least for the hydrothermal process and greatest in the ultrasonic mediated process. This is consistent with findings from CO_2-TPD analysis. This can be ascribed to the boosted crystallization of the metal oxides due to enhanced transport properties of supercritical water, a characteristic of the hydrothermal process [32]. Supplementary documents (Tables E8.1 and E8.2) support this finding. This hypothesis is made visible with the aid of the EDX spectroscopy (see Appendix E, Figure E8.1), which shows the enhanced dispersion of the metals (Al^{3+} and Mg^{2+}) across the adsorbent. The high concentration of lattice oxygen in the hydrothermal route can be associated to the increased Mg content in the form of Mg-O-Mg groups or Mg^{2+}-O^{2-} ion pairs [33].

CO_2-TPD analysis was used to measure the surface basicity of the synthesised LDHs (Figure 8.8). Surface basicity increases with increase in desorption temperature [6]. As shown in Figure 8.8a, the desorption of CO_2 basically occurs at overlapping peaks of 270 ^oC (α) and 363 ^oC (β), 474 ^oC (γ) and 569 ^oC (δ). At low temperatures (< 400 ^oC), desorption of CO_2 is related to released CO_2 from bicarbonates formed on weak and medium basic sites [10]. These weak sites are characteristics of the Brønsted OH^- group which are observed to be more prominent in the conventional and ultrasonic mediated routes [6] (Figure 8.8b). This corresponds with reported literatures validating that more weak and moderate basic sites are formed with the aid of ultrasonic irradiation [13]. Nonetheless, HPH-LDH desorbed CO_2 at intermediate/high temperature states (> 400 ^oC). These are strong basic sites and relate to bi-dentate and mono-dentate carbonates adsorbed on low coordinative unsaturated lattice oxygen (O^{2-}). This tends to agree with XPS and EDX results. A practical application of the basicity of this material varies from the recovery of CO_2 from flue gases at low basic strength (low temperature level) to higher basic strength (high temperature level) processes like sorption-enhanced hydrogenation. The latter has the advantage of ease of regeneration at low temperature gradients [6].

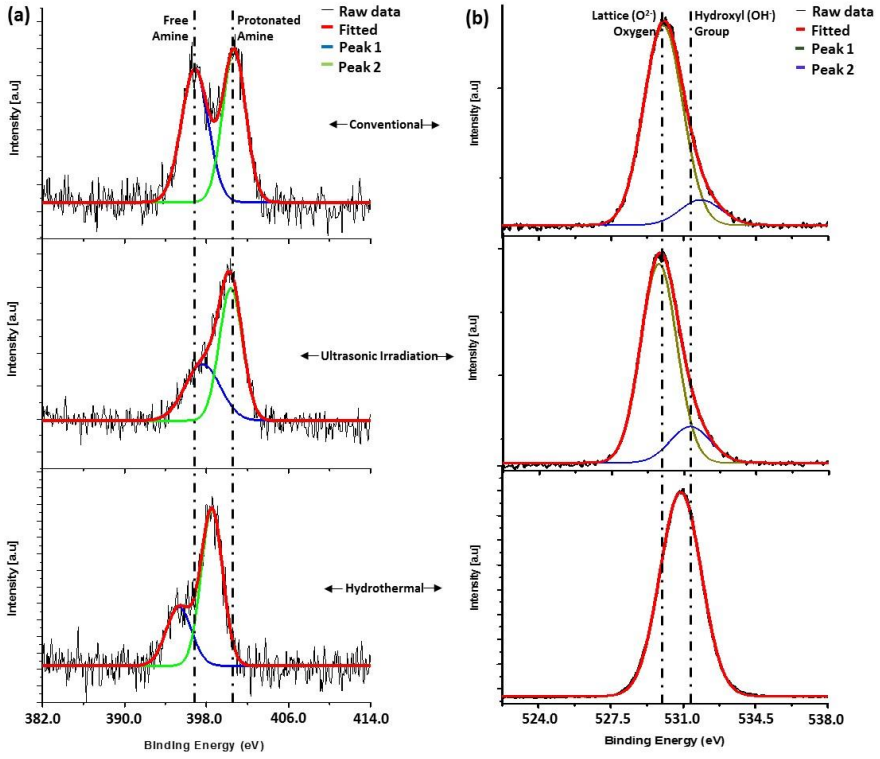

Figure 8.7: *XPS spectra of conventionally-, ultrasonically- and hydrothermally-prepared LDHs for (a) N 1s and (b) O 1s*

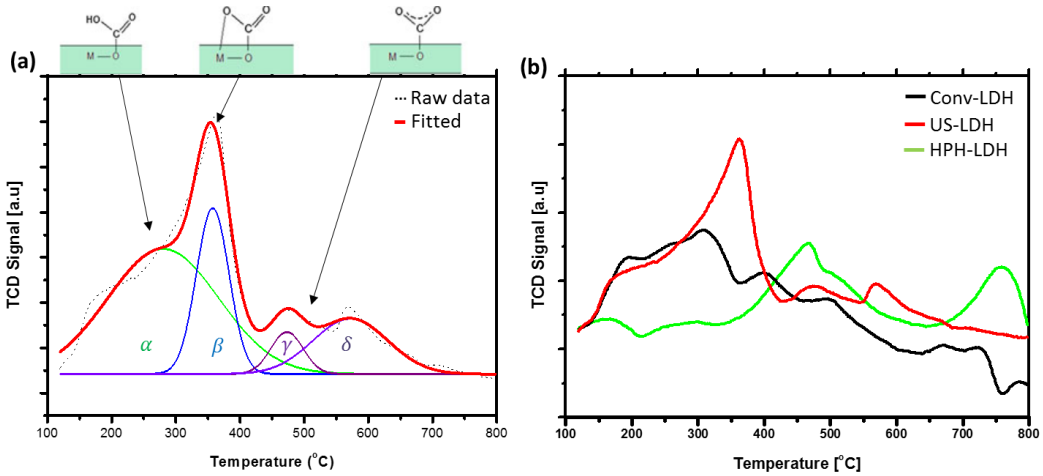

***Figure 8.8**: CO_2-TPD of synthesised LDH (a) Deconvolution of the CO_2-TPD of UH-LDH and (b) Comparison of CO_2-TPD of Conv-LDH, US-LDH and HPH-LDH.*

To further understand the surface chemical content of the adsorbent, the amino functional group necessary for adsorption of CO_2 was quantified using EDX results (See supplementary data Table E8.1, Appendix E). Table 8.4 shows the elemental analysis of each prepared sample using the EDX results from Table E8.1. As shown in Table 8.4, the amine loading was more effective using ultrasonic mediated route with 2.22 mmol/g as against 1.82 and 0.46 mmol/g for ultrasonic-assisted hydrothermal and the conventional route respectively. However, after functionalization of the adsorbent, the amine loading increased to 4.71, 5.24 and 5.26 mmol/g for conventional, ultrasonic and ultrasonic-assisted hydrothermal synthesis respectively. This is observed to be a significant improvement compared to those results reported in literatures as documented in supplementary Table E8.3.

8.4.3 Impact of preparation route on structural configuration

Figure 8.9 shows the XRD analysis of synthesised LDHs. Typical Mg-Al LDH exhibits three separate peak regions: (a) high angle region ($2\theta > 60^o$) consisting of *hk0* and *hkl* reflections attributed to the ordering within the metal hydroxide layers, (b) the mid-angle region ($30^o < 2\theta < 60^o$) attributed to non-basal reflection *0kl* whose locations are characteristic of the structural disorder and, (c) the low angle region ($2\theta < 30^o$) consisting of the *00l* and *h00* basal reflections characteristic of the size of intercalated anion [34]. These XRD reflections have been indexed according to the hexagonal lattice with rhombohedral symmetry (space group: R3m) [34-

36]. A brief look from the figure indicates that the intensity of all reflections increased with the hydrothermal process. This is associated with an increase in interlayer water molecule and partial hydroxylation of double hydroxide sheets [37]. For the high angle region, peak at $2\theta = 60^{o}$ containing overlapping reflections of (110) and (113) attributed to interlayer spacing indicates that the hydrothermal route increases interlayer spacing. This is reported to be associated with the presence of oxygen-containing functional groups [38], which is observed to be highest in the hydrothermal synthetic method due to high metallic deposition and dispersion. Hydrothermal route is considered an important synthetic method for the preparation of highly dispersed heterogeneous materials. This is due to its tendency to dissolve and recrystallize materials at high temperature and pressure [39]. The 200 lattice peak reflection explains the crystal size of the material and its intensity is dependent on chemical composition and molar (M^{2+}/M^{3+}) ratio [40]. Consequently, the strength of basic sites should vary with the peak intensity, thus validating the effect of deposition and dispersion of divalent and trivalent cations on basic strength. For the low and mid-angle region, the increase in peak intensities can be attributed to change in configuration of the interlayer nitrate from single flat-lying molecular layer to multiple layers and with different orientation [35, 41]. To this effect, using the results of X-ray diffraction and polarized attenuated total reflection FTIR spectroscopy, Wang and Wang [41] explained that the change in orientation of interlayer nitrate anions is dependent on chemical composition of LDH. This corresponds with XPS and TPD results.

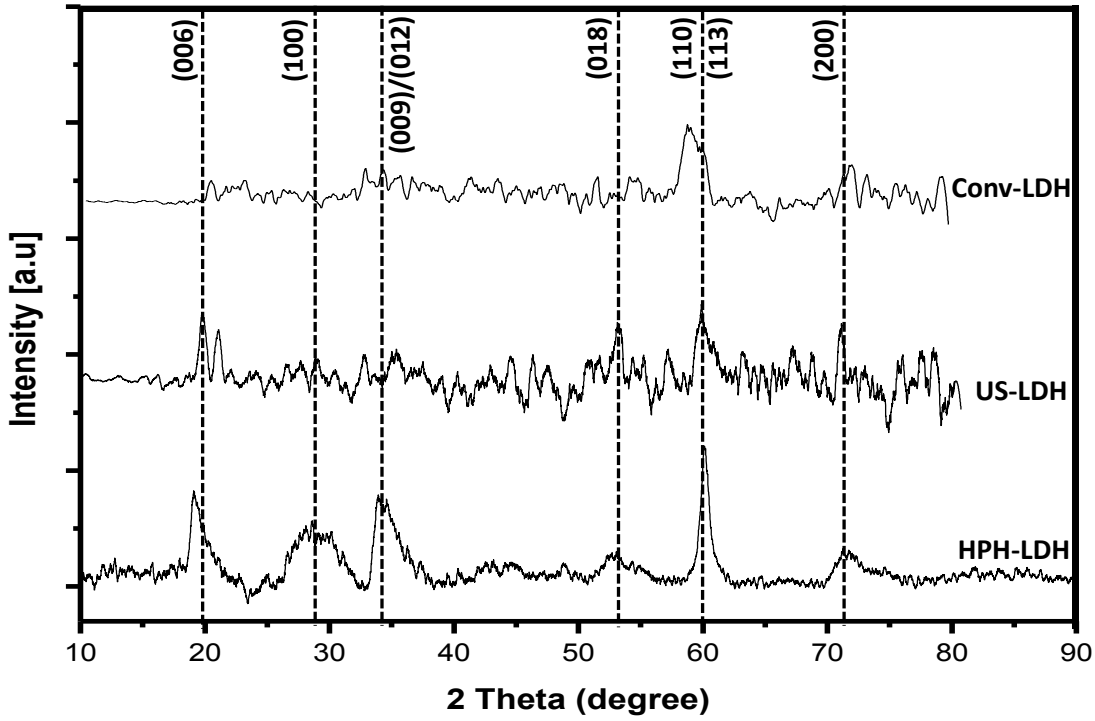

Figure 8.9: X-ray diffraction patterns of synthesised Mg/Al LDHs via conventional co-precipitation (Conv-LDH), ultrasonic irradiation (US-LDH) and sonochemical-assisted hydrothermal route (HPH-LPH)

8.4.4 Impact of preparation route on thermal stability

The thermal stability of the prepared samples were obtained using Netzsch STA 449 F3 TGA from 25 ^{o}C to 1000 ^{o}C with a 10 ^{o}C/min ramp. Figure 8.10 shows the TGA profiles for thermal disintegration of the prepared samples. Three distinct temperature phases were observed for material disintegration: T<~150 ^{o}C, ~150< T<~750 ^{o}C and ~750 ^{o}C< T. The first phase of weight loss (T<~150 ^{o}C) is attributed to the loss of interstitial water molecules. While for the second phase (~150<T<~750 ^{o}C), the decomposition can be ascribed to the dehydroxylation and breakdown of the organic alkyl chain of the LDH. The observed irregular decomposition curve in this stage may indicate the occurrence of an uneven bonding structure, resulting to multi-stage dehydroxylation processes. The final weight loss (~750 ^{o}C<T) results from the decomposition of the sulphate species residuum [10]. From Figure 8.10a-c, it can be inferred that the thermal strength of HPH-LDH is higher than that of the conventional and ultrasonically prepared samples with a total weight loss of 68.98 amd 68.12% respectively, when compared to 10.56% of HPH-LDH as tabulated in Table E8.4

(Appendix E). For the first phase, the moisture content decreased significantly from 8.35 to 3.41% as the preparation process changed from conventional to hydrothermal. A more drastic reduction was experienced with the interstitial moisture content (second phase). This can be attributed to the enhanced bonding introduced by the hydrothermal process forming multi-layers as estimated from the XRD results. The third degradation phase infers that ultrasonic process is more likely to deposit more sulphate species, while the hydrothermal process is the least to do so. This corresponds to the results obtained from XPS analysis (Table E8.2, supporting document). This indicates that the adoption of the hydrothermal-route may be beneficial to the synthesis of a more stable material than the ultrasonic and conventional method.

After introducing amine modification of the samples, the decomposition curves clearly show different behaviour compared with that of the untreated LDHs prepared by the same method. The curves display a well-defined three phase decomposition steps unlike the untreated ones, as can be seen from Figure 8.10(d-f). Within the same temperature range as that of the LDHs, the MEA-treated LDHs showed higher moisture content than the unprocessed ones except for the hydrothermal samples. This can be caused by the presence of leftover MEA molecules after the extraction process, which may have been strongly bonded to the hydrothermal samples resulting to the increase in weight loss in the second and third phase. However, for the ultrasonic and conventional route, the weight losses in the second and third phase reduced significantly, benefitting to production of a more stable material than the pure LDH. This can be explained by the reduced presence of the surfactant after the amine extraction. Showing from the total weight loss, it can be concluded that the thermal strength of the hydrothermal samples (total weight loss: 38.17%) even after amine extraction is better than that of the conventional and ultrasonically prepared samples (total weight loss: 52-53%).

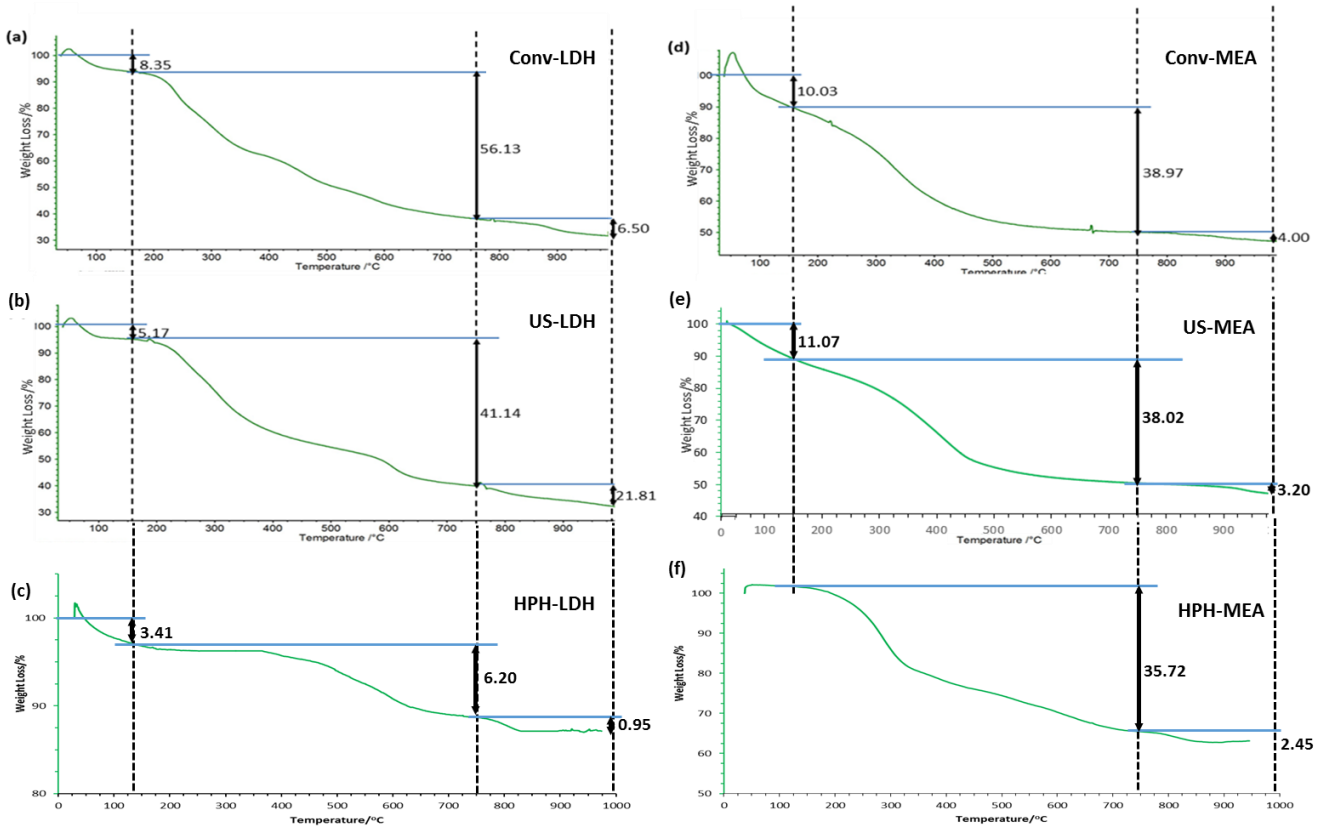

Figure 8.10: TGA curves comparing thermal stabilities of LDHs prepared via conventional and ultrasonic irradiation: (a) Conv-LDH, (b) UH-LDH and (c) HPH-LDH; as well as with amine modified LDHs: (d) Conv-MEA (e) UH-MEA and (f) HPH-MEA

8.4.5 Impact of preparation route on effective amine efficiency, CO_2 uptake, regeneration efficiency and cyclic efficiency

The average CO_2 uptake for the various synthesis route is shown in Figure 8.11. The results show a reduction in CO_2 uptake for the US-LDH when compared to the conventional, Conv-LDH. This corresponds to results from previous study [10]. However, an insignificant increase in CO_2 uptake was observed for the hydrothermally prepared sample, HPH-LDH. Despite the enhanced textural properties of HPH-LDH, the adsorption capacity of this adsorbent showed no appreciable improvement. However, after amine extraction, the amine loading of adsorbents increased for all considered routes. This is part due to the exfoliation of the surfactant (SDS) (shown in Table 8.4) which varied from *ca.* 99%, 98% and 81% in the conventional, ultrasonic and hydrothermal processes respectively. As a result, this impacted on the effective amine loading and efficiency of the adsorbent. The effective amine loading was computed as the difference in amine loading before

and after amine extraction, whereas effective amine efficiency was computed as the ratio of the difference in CO_2 adsorbed before and after amine extraction to effective amine loading. HPH-MEA showed the highest effective amine efficiency of 0.83 compared to 0.24 and 0.15 for US-MEA and Conv-MEA respectively. This can be partly related to the improved deprotonation of protonated amino groups resulting from enhanced transport properties, characteristic of the hydrothermal process [32]. This expounds the impact of sonication and hydrothermal pre-treatment in deprotonating protonated and/or probable dispersion of amino sites during LDH-amine modification. Consequently, the adsorption capacity of HPH-LDH increases from 0.88-3.75 mmol/g when compared to the increase of Conv-LDH from 0.82-1.45 mmol/g (Appendix E, Table E8.5). This indicates that CO_2 uptake was stimulated more by chemisorption rather than physisorption. This can be attributed to the difference in basic strength of the prepared adsorbents.

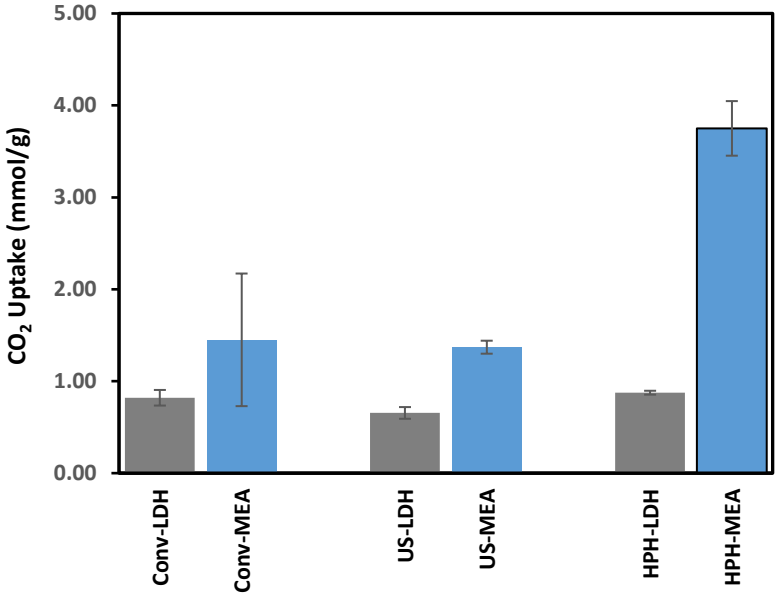

Figure 8.11: Average CO_2 Uptake of LDH and amine-modified LDH prepared via the different routes

Thermal swing regeneration in an atmosphere of N_2 was adopted for the regeneration of the amine-modified adsorbent. A typical example of the regeneration profile is shown in Figure E8.2 (Appendix E). In this figure, the effect of the preparation route on the cyclic sorption capacity of the adsorbent is presented. Amount of CO_2 desorbed was measured after the first adsorption cycle prior to the second adsorption process. Consecutively, the regeneration and cyclic efficiencies of the adsorbents were calculated (Appendix E, Table E8.5). From the tabulated results in the figure, it is observed

that HPH-MEA has the highest regeneration efficiency of 93%. This is a significant change when compared to 78% and 86% regeneration efficiencies for US-MEA and Conv-MEA respectively. However, the cyclic efficiency (computed as the percentage ratio of CO_2 uptake from 2^{nd} cycle to 1^{st} cycle) of US-MEA is 76% compared to 60% and 53% for Conv-MEA and HPH-MEA respectively. Analysing the cyclic and regenerated efficiencies, it can be projected that the ultrasonic mediated synthesis route has an effective adsorption potential than the other two processes. It is observed that of the 78% regenerated active site, approx. 76% of this active site underwent the 2^{nd} adsorption process. This is lesser in Conv-MEA and HPH-MEA respectively. The degradation in the cyclic adsorption efficiencies of these samples can be ascribed to the secondary reactions occurring between the amino group and CO_2 as elaborated in previous study [10]. This implies that the ultrasonic mediated route is more suitable for the synthesis of long term effective CO_2 LDH adsorbents. However, the hydrothermal process provides a significant change in sorption capacity of the adsorbent. Optimization of these two processes will contribute immensely to both sorption efficiency and effectiveness.

8.4.6 Comparison of kinetic models

From simulation results, the experimental kinetic uptake data for the samples synthesized from the different synthesis routes are summarized in Table 8.5. Comparative plots of these data using the kinetic models discussed in the previous section are shown in Figure 8.2. The results show that the double exponential model produced the best fit for the experimental data (considering the R^2 values). This unlike the pseudo first and second order model, is explained to account for the heterogeneity of the adsorbent's surface [16]. In other words, it describes the adsorption mechanism to comprise of two different adsorption sites. Consequently, elucidating the occurrence of more than one reaction mechanism [42]. Therefore, the double exponential model can be explained to be of best fit of the three models because it possibly accounts for both chemisorption and physisorption of CO_2. Rate constants $k_{i=1,2}$ are the reaction rate coefficients for the respective adsorption mechanisms. The simulated results showed no particular variation of these parameter with the preparation route. The pre-exponential factors, $A_{i=1,2}$, indicate the weight coefficient that reflects the share of each adsorption mechanism [17]. From the tabulated results, it is observed that the second adsorption mechanism (indicated by i = 2) contributed a greater share towards CO_2 adsorption in Conv-LDH.

This gradually reduced in US-LDH and was approximately evenly distributed between the two mechanisms in HPH-LDH.

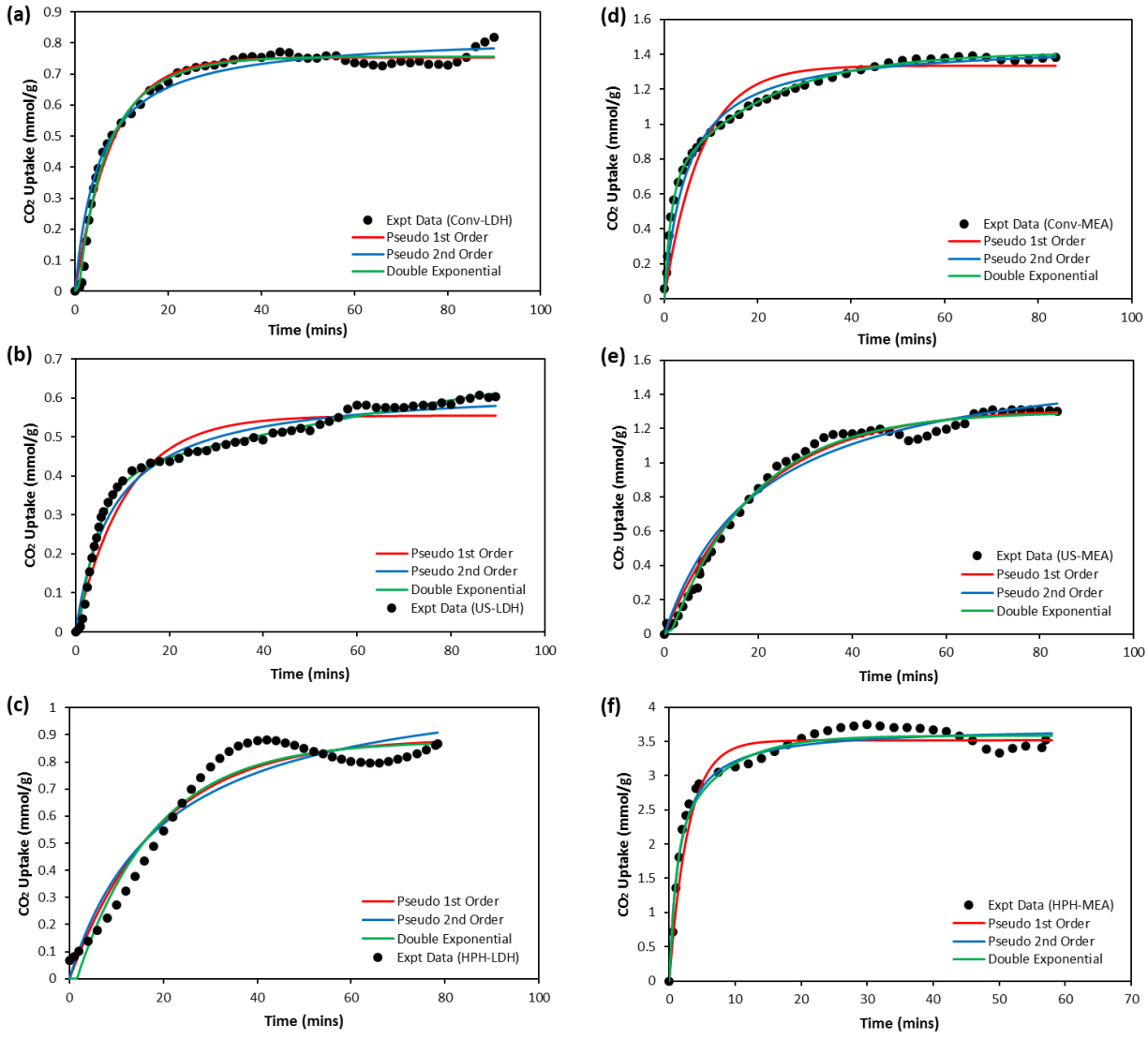

Figure 8.12: Comparison of different kinetic models with experimental data generated for adsorption kinetics of CO_2 on (a) Conv-LDH, (b) US-LDH, (c) HPH-LDH, (d) Conv-MEA, (e) US-MEA and (f) HPH-MEA under and 55^oC and 1 atm

Pseudo first and second order model also provided a relatively good fit for the experimental results. However, comparing to pseudo second order model, pseudo first order provided a better fit for both Conv-LDH and HPH-LDH experimental data. This model better explains low surface coverage

adsorption [43] whereas the pseudo second order model accounts for adsorption by chemisorption or adsorption at high adsorbate loadings [44]. Hence, it is logical to attribute the fitting of the second order model to US-LDH experimental data to the high amine loading. Considering the kinetic parameters, k_f and k_s, which depicts the time scale for the process to reach equilibrium [17]. Inverse of these parameters indicates the time required for the process to attain equilibrium. As shown in Table 8.5, the $k_{f,s}$ decreased in the following trend: conventional > ultrasonic > hydrothermal. This portrays that conventionally prepared LDH tends to attain equilibrium quicker than samples prepared from the other routes. Although pseudo first and second order models are associated with surface reaction control systems [17], the former was also derived by assuming film diffusion (FD) control [45] whereas the later simulates intra-particle diffusion (IPD)-driven kinetics of sorption for systems with both plane and spherical sorbent particles [46]. Consequently, it is likely to assume that IPD is more promoted in US-LDH.

After amine extraction, the double exponential model was also of best fit for the obtained experimental data. However, the reverse trend was observed for the share of each adsorption mechanisms. Summarised results (Table 8.5) show that both adsorption mechanism approximately contributed evenly in the adsorption process in Conv-MEA and US-MEA; but the second mechanism dominated in HPH-MEA. The nature of these mechanisms are undetermined in this study but can be seen to give an insight on the adsorption trend of each sample. Nonetheless, correlating these findings with characterization results, the first adsorption mechanism (indicated by i = 1) can be inferred to be associated with the physical textural properties of the adsorbent. Subsequently, the enhanced textural properties via ultrasonic and hydrothermal treatment resulted to the increase in the share of the first adsorption mechanism. However, after amine extraction, the second mechanism, assumed to be characterized by chemisorption, increased in share in the following trend: Conv-MEA < US-MEA < HPH-MEA. This can be attributed to the enhanced amine loading and effective amine efficiency.

8.5 CONCLUSION

A detailed comparison study of the impact of ultrasonic and hydrothermal pre-treatment on the basic strength, textural characteristics, effective amine efficiency, CO_2 adsorption and regeneration capacities of Mg-Al LDH has been conducted. In addition, the contribution of these preparation

routes to the thermal stability and reaction kinetics was discussed. The results obtained using the kinetic models clearly indicate that prior to amine extraction, the adsorption of Mg-Al LDH adsorbent is mostly facilitated by physisorption while adsorption is mainly promoted by chemisorption after amine extraction. The conclusions reached as the result of the present study can be summarised:

(1) Characterization results show that the ultrasonic-assisted hydrothermal route immensely improves the porosity and surface morphology of the adsorbent. Furthermore, the surface chemical content was characterised with improved metal-ion distribution, hence increasing the basic strength of the adsorbent. This strongly contributes to the improved adsorption and regeneration capacities, as well as the thermal stability of the adsorbent.

(2) The reason that the ultrasonic-assisted hydrothermal treatment can effectively promote the adsorption capacity of the adsorbent can be partially attributed to the ascent in the amount of strong basic sites (O^{2-}) and subsequent decrease in both moderate (M-O) and weak (OH^- groups) basic sites resulting from the hydrothermal process.

(3) The cyclic adsorption efficiency of the sonochemical process is better than that of both hydrothermal and conventional preparation routes. The sonochemical route shows the potential for enhanced amine loading and cyclic efficiency, thus providing a more suitable and economical approach for synthesis of double layered hydroxides.

ACKNOWLEDGEMENT

This study was conducted at the International Doctoral Innovation Centre (IDIC). The authors would like to acknowledge the financial support from National Natural Science Foundation of China (NSFC) (Grant No. 21576141) and Zhejiang Provincial Natural Science Foundation (Grant No. LY15B060001) and Ningbo Key Research Project ‘Absorption/catalytic technologies for the simultaneous removal of multi-pollutants from flue gas at power stations’ (Grant No. 1012B10042), and from Ningbo Science and Technology Bureau, The University of Nottingham, Ningbo Education Bureau and China's MoST . The study is also partly supported by EPSRC (Grant no. EP/G037345/1).

References

[1] J. Wang, L.A. Stevens, T.C. Drage, C.E. Snape, J. Wood, Preparation and CO2 adsorption of amine modified layered double hydroxide via anionic surfactant-mediated route, Chemical Engineering Journal, 181-182 (2012) 267-275.

[2] J.D. Figueroa, T. Fout, S. Plasynski, H. McIlvried, R.D. Srivastava, Advances in CO2 capture technology—The U.S. Department of Energy's Carbon Sequestration Program, International Journal of Greenhouse Gas Control, 2 (2008) 9-20.

[3] M. Szabados, R. Mészáros, S. Erdei, Z. Kónya, Á. Kukovecz, P. Sipos, I. Pálinkó, Ultrasonically-enhanced mechanochemical synthesis of CaAl-layered double hydroxides intercalated by a variety of inorganic anions, Ultrasonics Sonochemistry, 31 (2016) 409-416.

[4] F. Cavani, F. Trifirò, A. Vaccari, Hydrotalcite-type anionic clays: Preparation, properties and applications, Catalysis Today, 11 (1991) 173-301.

[5] N.D. Hutson, B.C. Attwood, High temperature adsorption of CO2 on various hydrotalcite-like compounds, Adsorption, 14 (2008) 781-789.

[6] D.I. Ferrer, Supported Layered Double Hydroxides as CO2 Adsorbents for Sorption-enhanced H2 Production, Chemical Engineering, Imperial College, London, United Kingdom, Springer International Publishing Switzerland, 2016, pp. 209.

[7] L.H. Chagas, G.S.G. De Carvalho, W.R. Do Carmo, R.A.S. San Gil, S.S.X. Chiaro, A.A. Leitão, R. Diniz, L.A. De Sena, C.A. Achete, MgCoAl and NiCoAl LDHs synthesized by the hydrothermal urea hydrolysis method: Structural characterization and thermal decomposition, Materials Research Bulletin, 64 (2015) 207-215.

[8] Y. Gao, Z. Zhang, J. Wu, X. Yi, A. Zheng, A. Umar, D. O'Hare, Q. Wang, Comprehensive investigation of CO2 adsorption on Mg-Al-CO3 LDH-derived mixed metal oxides, Journal of Materials Chemistry A, 1 (2013) 12782-12790.

[9] J.I. Di Cosimo, V.K. Díez, M. Xu, E. Iglesia, C.R. Apesteguía, Structure and Surface and Catalytic Properties of Mg-Al Basic Oxides, Journal of Catalysis, 178 (1998) 499-510.

[10] C.I. Ezeh, X. Huang, X. Yang, C.-g. Sun, J. Wang, Sonochemical surface functionalization of exfoliated LDH: Effect on textural properties, CO2 adsorption, cyclic regeneration capacities and subsequent gas uptake for simultaneous methanol synthesis, Ultrasonics Sonochemistry, 39 (2017) 330-343.

[11] D.P. Debecker, E.M. Gaigneaux, G. Busca, Exploring, tuning, and exploiting the basicity of hydrotalcites for applications in heterogeneous catalysis, Chemistry—A European Journal, 15 (2009) 3920-3935.

[12] Y. Mu, Y. Zhang, J. Fan, C. Guo, Effect of ultrasound pretreatment on the hydrothermal synthesis of SSZ-13 zeolite, Ultrasonics Sonochemistry, 38 (2017) 430-436.

[13] S. Zhao, H. Yi, X. Tang, F. Gao, Q. Yu, Y. Zhou, J. Wang, Y. Huang, Z. Yang, Enhancement effects of ultrasound assisted in the synthesis of NiAl hydrotalcite for carbonyl sulfide removal, Ultrasonics Sonochemistry, 32 (2016) 336-342.

[14] H.J. Jang, C.H. Lee, S. Kim, S.H. Kim, K.B. Lee, Hydrothermal Synthesis of K2CO3-Promoted Hydrotalcite from Hydroxide-Form Precursors for Novel High-Temperature CO2 Sorbent, ACS Applied Materials & Interfaces, 6 (2014) 6914-6919.

[15] I. Khan, A.A.M. Ibrahim, M. Sohail, A. Qurashi, Sonochemical assisted synthesis of RGO/ZnO nanowire arrays for photoelectrochemical water splitting, Ultrasonics Sonochemistry, 37 (2017) 669-675.

[16] S. Loganathan, M. Tikmani, A. Mishra, A.K. Ghoshal, Amine tethered pore-expanded MCM-41 for CO2 capture: Experimental, isotherm and kinetic modeling studies, Chemical Engineering Journal, 303 (2016) 89-99.

[17] K.L. Tan, B.H. Hameed, Insight into the adsorption kinetics models for the removal of contaminants from aqueous solutions, Journal of the Taiwan Institute of Chemical Engineers, 74 (2017) 25-48.

[18] M.P. Bernardo, F.K.V. Moreira, L.A. Colnago, C. Ribeiro, Physico-chemical assessment of [Mg-Al-PO4]-LDHs obtained by structural reconstruction in high concentration of phosphate, Colloids and Surfaces A: Physicochemical and Engineering Aspects, 497 (2016) 53-62.

[19] A. Laskowska, M. Zaborski, G. Boiteux, O. Gain, A. Marzec, W. Maniukiewicz, Effects of unmodified layered double hydroxides MgAl-LDHs with various structures on the properties of filled carboxylated acrylonitrile–butadiene rubber XNBR, European Polymer Journal, 60 (2014) 172-185.

[20] H.W. Olfs, L.O. Torres-Dorante, R. Eckelt, H. Kosslick, Comparison of different synthesis routes for Mg–Al layered double hydroxides (LDH): Characterization of the structural phases and anion exchange properties, Applied Clay Science, 43 (2009) 459-464.

[21] L. Dong, C. Ge, P. Qin, Y. Chen, Q. Xu, Immobilization and catalytic properties of candida lipolytic lipase on surface of organic intercalated and modified MgAl-LDHs, Solid State Sciences, 31 (2014) 8-15.

[22] B. Li, Y. Zhang, X. Zhou, Z. Liu, Q. Liu, X. Li, Different dye removal mechanisms between monodispersed and uniform hexagonal thin plate-like MgAl–CO32--LDH and its calcined product in efficient removal of Congo red from water, Journal of Alloys and Compounds, 673 (2016) 265-271.

[23] W. Lv, L. Yang, B. Fan, Y. Zhao, Y. Chen, N. Lu, R. Li, Silylated MgAl LDHs intercalated with MnO2 nanowires: Highly efficient catalysts for the solvent-free aerobic oxidation of ethylbenzene, Chemical Engineering Journal, 263 (2015) 309-316.

[24] H. Nina, A.R. Barron, BET Surface Area Analysis of Nanoparticles, Rice University, Houston TX, 2011.

[25] S. Brunauer, L.S. Deming, W.E. Deming, E. Teller, On a Theory of the van der Waals Adsorption of Gases, J. Am. Chem. Soc., 62 (1940) 1723-1732.

[26] K.S.W. Sing, D.H. Everett, R.A.W. Haul, L. Moscou, R.A. Pierotti, J. Rouquerol, S. T., Reporting Physisorption Data for Gas/Solid Systems with Special Reference to the Determination of Surface Area and Porosity, Pure & Appl. Chem., 57 (1985) 603-619.

[27] T. Adschiri, Y. Hakuta, K. Arai, Hydrothermal Synthesis of Metal Oxide Fine Particles at Supercritical Conditions, Industrial and Engineering Chemistry Research, 39 (2000) 4901-4907.

[28] H. Xu, B.W. Zeiger, K.S. Suslick, Sonochemical synthesis of nanomaterials, Chemical Society reviews, 42 (2013) 2555-2567.

[29] Y. Kong, G. Jiang, Y. Wu, S. Cui, X. Shen, Amine hybrid aerogel for high-efficiency CO2 capture: Effect of amine loading and CO2 concentration, Chemical Engineering Journal, 306 (2016) 362-368.

[30] R. Dolores, S. Raquel, G.-L. Adianez, Sonochemical synthesis of iron oxide nanoparticles loaded with folate and cisplatin: Effect of ultrasonic frequency, Ultrasonics Sonochemistry, 23 (2015) 391-398.

[31] E. Genty, J. Brunet, C. Poupin, S. Casale, S. Capelle, P. Massiani, S. Siffert, R. Cousin, Co-Al mixed oxides prepared via LDH route using microwaves or ultrasound: Application for catalytic toluene total oxidation, Catalysts, 5 (2015) 851-867.

[32] J. Otsu, Y. Oshima, New approaches to the preparation of metal or metal oxide particles on the surface of porous materials using supercritical water: Development of supercritical water impregnation method, J. of Supercritical Fluids, 33 (2005) 61-67.

[33] M. Manikandan, A.K. Venugopal, K. Prabu, R.K. Jha, R. Thirumalaiswamy, Role of surface synergistic effect on the performance of Ni-based hydrotalcite catalyst for highly efficient hydrogenation of furfural, Journal of Molecular Catalysis A: Chemical, 417 (2016) 153-162.

[34] N. Touisni, F. Charmantray, V. Helaine, C. Forano, L. Hecquet, C. Mousty, Optimized immobilization of transketolase from E. coli in MgAl-layered double hydroxides, Colloids and Surfaces B: Biointerfaces, 112 (2013) 452-459.

[35] S.-L. Wang, C.H. Liu, M.K. Wang, Y.H. Chuang, P.N. Chiang, Arsenate adsorption by Mg/Al–NO3 layered double hydroxides with varying the Mg/Al ratio, Applied Clay Science, 43 (2009) 79-85.

[36] M. Bellotto, B. Rebours, O. Clause, J. Lynch, D. Bazin, E. Elkaïm, A Reexamination of Hydrotalcite Crystal Chemistry, The Journal of Physical Chemistry, 100 (1996) 8527-8534.

[37] H. Ji, W. Wu, F. Li, X. Yu, J. Fu, L. Jia, Enhanced adsorption of bromate from aqueous solutions on ordered mesoporous Mg-Al layered double hydroxides (LDHs), Journal of Hazardous Materials, 334 (2017) 212-222.

[38] S. Zhao, X. Meng, K. Zhu, F. Du, G. Chen, Y. Wei, Y. Gogotsi, Y. Gao, Li-ion uptake and increase in interlayer spacing of Nb4C3 MXene, Energy Storage Materials, 8 (2017) 42-48.

[39] H. Emadi, M. Salavati-Niasari, A. Sobhani, Synthesis of some transition metal (M: 25Mn, 27Co, 28Ni, 29Cu, 30Zn, 47Ag, 48Cd) sulfide nanostructures by hydrothermal method, Advances in Colloid and Interface Science, DOI https://doi.org/10.1016/j.cis.2017.06.007.

[40] J.S. Valente, M. Sánchez-Cantú, E. Lima, F. Figueras, Method for Large-Scale Production of Multimetallic Layered Double Hydroxides: Formation Mechanism Discernment, Chemistry of Materials, 21 (2009) 5809-5818.

[41] S.-L. Wang, P.-C. Wang, In situ XRD and ATR-FTIR study on the molecular orientation of interlayer nitrate in Mg/Al-layered double hydroxides in water, Colloids and Surfaces A: Physicochemical and Engineering Aspects, 292 (2007) 131-138.

[42] L. Sciascia, M.L. Turco Liveri, M. Merli, Kinetic and equilibrium studies for the adsorption of acid nucleic bases onto K10 montmorillonite, Applied Clay Science, 53 (2011) 657-668.

[43] R. Serna-Guerrero, A. Sayari, Modeling adsorption of CO2 on amine-functionalized mesoporous silica. 2: Kinetics and breakthrough curves, Chemical Engineering Journal, 161 (2010) 182-190.

[44] J.M. Borah, J. Sarma, S. Mahiuddin, Adsorption comparison at the α-alumina/water interface: 3,4-Dihydroxybenzoic acid vs. catechol, Colloids and Surfaces A: Physicochemical and Engineering Aspects, 387 (2011) 50-56.

[45] W. Plazinski, Applicability of the film-diffusion model for description of the adsorption kinetics at the solid/solution interfaces, Applied Surface Science, 256 (2010) 5157-5163.

[46] W. Plazinski, J. Dziuba, W. Rudzinski, Modeling of sorption kinetics: the pseudo-second order equation and the sorbate intraparticle diffusivity, Adsorption, 19 (2013) 1055-1064.

CHAPTER NINE

DEVELOPMENT OF NOVEL COMPOSITE CATALYST: $CuO/ZnO/ZrO_2$ CATALYST SUPPORTED ON Mg-Al LDH

Abstract

Adopting the obtained factors for optimum synthesis and operation of both $CuO/ZnO/ZrO_2$ catalyst and Mg-Al LDH adsorbent, a composite catalyst consisting of $CuO/ZnO/ZrO_2$ catalyst on LDH template was synthesised and analysed for CO_2 uptake capacity and catalytic activity with variation in Al^{3+} and Zr^{4+} compositions. Characterisation of the composite catalyst was conducted using TGA, SEM, XRD and N_2 sorption analysis via the BET. Characterisation tests shows an improvement in structural modification. However, this is subject to the proportion of the considered varied metals. In addition, despite the high thermal stability of Zr^{4+}, the composite material was observed to weaken in stability with increase in Zr^{4+} content. Nonetheless, the CO_2 uptake capacity was observed to increase. Using series of isotherm models, this was attributed to the chemical nature of the metals which promoted chemisorption as the dominating adsorption mechanism with little contribution from physisorption. CO_2 conversion and methanol yield were also dependent on the nature and composition of the cations as well as the operating temperature. Al^{3+}:(Al^{3+}+Zr^{4+}) ratio of 0.4 was obtained as the best cation mix to attain maximum methanol yield.

Keywords: *Carbon dioxide, Thermal stability, Hydrogenation, Catalysts, Methanol synthesis.*

9.1 INTRODUCTION

Methanol synthesis via CO_2 hydrogenation has gained much attention over the years as a strategy for combating global emission crises. In this field, numerous research are directed towards the synthesis of adequate catalysts for the production of methanol [1-6]. The basis of these catalysts is the CuO/ZrO_2 catalyst. This is the most commonly researched catalyst for the production of methanol via hydrogenation of carbon dioxide especially at a molar ration of 3:7. This is basically due to the high thermal stability of ZrO_2 compound. In addition, the compound is known to improve Cu dispersion as well as enhance the surface basicity of the catalyst. Hence, many studies are inclined towards modifying this catalyst for optimum catalytic performance. The addition of Zn as a promoter has shown to further enhance Cu dispersion and improve the amount of strong basic sites necessary for CO_2 reduction to methanol [2, 7, 8].

Aside the nature and composition of the metal ion constituents of the catalyst, the preparation method has shown to also affect the performance of the catalyst as well as its structural configuration. As illustrated in Chapters 4 and 5, the heating rate, calcination temperature and synthetic route also plays a major role in defining the qualities of the catalyst. The co-precipitation route supported by ultrasonic irradiation with calcination temperature of 623 K and 20 K/min heating rate produced a more stable catalyst. Furthermore, it was discerned that the yield of methanol depends on the amount of CO_2 adsorbed on the surface of strong basic sites [2, 8]. Hence, to improve the amount of CO_2 adsorbed, a composite catalyst with a support framework having a high CO_2 uptake capacity is recommended. Recently, composite catalysts are synthesised using layered double hydroxides as supports [2, 7, 9-11]. This is due to the high application flexibility of this material based on its structure. Synthesised composites catalyst using LDHs has shown homogeneous metallic dispersion, high thermal stability, increased amount of basic sites and good structural morphology [12, 13]. These properties of LDH are also critically affected by metal composition, synthetic route and operating conditions. As investigated in Chapter 6-8, the preparation method also plays a key role in the modification of catalysts structure and functionality. An ultrasonic-assisted supercritical hydrothermal reaction showed a high modification of surface morphology. However, the cyclic adsorption efficiency of the sonochemical process is better than that of both hydrothermal and conventional preparation routes. Unlike the hydrothermal reaction, the ultrasonic-assisted co-precipitation route shows the potential for enhanced amine loading and cyclic efficiency, thus

providing a more suitable and economical approach for synthesis of double layered hydroxides. Despite the synthetic route, metallic ion nature and composition is also a crucial criteria for the material performance. Hence, to adopt LDH as the support for the Cu-based catalyst, whose catalytic activity also depends on the metal ion constituents, a suitable metallic configuration must be used to avoid any detrimental effect on the catalyst. Therefore, a novel composite catalyst with varying cation is investigated. However, due to time limitation, this final chapter studies the impact of Zn in the composite catalyst comprising of CuO/ZnO/ZrO_2 catalysts supported on Mg-Al LDH template. The synthesised catalyst is characterised by SEM, BET, XRD and TGA. Emphasis is directed towards CO_2 adsorption capacity and catalytic performance at varying operating conditions.

9.2 EXPERIMENTAL

9.2.1 Material preparation

Preparation of the composite material was done via co-precipitation method aided by supercritical hydrothermal route. The component of the layered double hydroxides (LDHs) are based on the standard method described in Chapter 8 [14]. Whereas, the component of the catalyst is based on the standard method as described in Chapter 5 [8]. All chemicals used for experimentation were acquired from SinoPharm Chemical Reagents Co. Ltd.

For ultrasonic-assisted hydrothermal synthesized samples, HPH-LDH, APTES (≥ 98%), SDS (≥ 86%), $Mg(NO_3)_2.6H_2O$ (≥ 98%) and $Al(NO_3)_3.9H_2O$ (≥ 99%) (molar ratio of Mg:Al:APTES:SDS = 3:1:5:1) was dissolved in 50 ml of distilled water at a temperature of 333 K and sonicating with ultrasonic horn with an impulse of 1s for 30 mins. Simultaneously, a mix of $Cu(NO_3)_2 \cdot 3H_2O$ (≥ 98%), $Zn(NO_3)_2 \cdot 6H_2O$ (≥ 99%) and $Zr(NO_3)_4 \cdot 5H_2O$ (≥ 98%) were blended in a Cu^{2+}:Zn^{2+}:Zr^{4+} molar ratio of 3:3:4. This mix was further blended with citric acid ligand, $C_6H_8O_7 \cdot H_2O$ in a molar ratio of 1:1.3. This was carried out for 30 minutes at room temperature until the reactants were transformed to a homogeneous muddy precursor. The two mixtures were moved to the hydrothermal reactor. After being vented with pure N_2 gas (99.99%) for 15 mins in order to remove all of the oxygen before the reaction, the reactor was sealed and heated to a temperature of 723 K with a ramp of 2 K/min and then held for 15 mins. After reaction, the solution was aged for 12 hr. The precipitates

were filtered, washed with distilled water and then dried in a vacuum oven (500 mbar at 343 K) for 7 h. The composite catalyst is calcined at temperature of 623 K. The sample is designated as HPH-14 where 1 is the composition of Al and 4 is the composition of Zr. These metals are chosen for the basis of understanding the individual impact of the adsorbent and catalysts respectively. Keeping the other metals at the present composition, Al and Zr composition were varied. The synthesised catalysts are HPH-23, HPH-32, HPH-41 and HPH-50.

9.2.2 Characterisation

9.2.2.1 Nitrogen adsorption-desorption analysis

The textural characteristics of the prepared catalysts were studied by Nitrogen physisorption analysis at 77 K using the Micrometrics ASAP 2020 Surface Area and Porosity Analyser. Prior to this analysis, samples were degassed at a temperature of 378 K for 4 hr. The surface area (S_{BET}) of the samples was determined using the BET (Brunauer, Emmett and Teller) model. The total pore volumes (V_{Total}) were computed from the amount of nitrogen adsorbed at relative pressure (P/P_o) of 0.99 and the average pore volumes from $4V_{Total}/S_{BET}$. The pore size distribution was calculated using the BJH (Barrett, Joyner and Halenda) model. The t-plot method was used to calculate the micopore volume (V_{micro}).

9.2.2.2 Scanning electron microscope (SEM)

The surface composition and structure of the prepared materials were studied with a Zeiss ΣIGMA™ Field Emission SEM.

9.2.2.3 X-ray Diffraction (XRD) and X-ray Photoelectron Spectroscopy (XPS) Analysis

XRD patterns were studied using a Bruker-AXS D8 advance powder diffractometer with a scanning range of $10^o \leq 2\theta \leq 90^o$. X-ray Photoelectron Spectroscopy (XPS) data of the adsorbent was obtained using Kratos X-ray Photoelectron Spectrometer – Axis Ultra DLD with a 96 W monochromatic Al Kα X-ray source (1486.69 eV) at a photoelectron take-off angle of 45°. Narrow scans were conducted at steps of 0.05 eV with dwell time of 600 ms whereas wide scans were conducted from 1100 eV to 0 eV with 150 ms dwell time and at 1 eV steps. The C 1s peak at 284.6 eV was used as the reference for standardizing the binding energy.

9.2.2.4 Thermo-gravimetric analysis

Thermal stability and CO_2 uptake measurements were conducted using the Netzsch STA 449 F3 Jupiter thermogravimetric analyser (TGA).

9.2.2.4.1 Thermal Stability Measurement

The stability of the as-synthesised LDH samples in air was determined. 0.4 cm^3 alumina crucible was loaded with 5-10 mg of sample and the thermal decomposition examined from 25 to 1273 K , ramped 20 K/min and under air flow (50 ml/min).

9.2.2.4.2 CO_2 Uptake Measurement.

Approximately 5-10 mg of the synthesized sample was heated from 298 to 378 K at 20 K/min under N_2 at a flow rate of 50 ml/min; and then held isothermally for 30 min before being cooled to the required adsorption temperature at a rate of 10 K/min. The gas was switched from N_2 to CO_2 and held isothermally for 60 min at a flow rate of 20 ml/min. The experimental adsorption temperature is 328 K. The CO_2 adsorption capacity was calculated from the weight difference of the samples in CO_2 atmosphere. The uptake profile was measured against an empty alumina crucible using the same method so as to correct the impact of change in gas density and viscosity.

9.2.3 Catalyst Performance Evaluation

The performance of the catalysts towards methanol synthesis was assessed in a continuous flow fixed bed reactor. First, 0.5g of the catalyst was reduced at 623 K in H_2/N_2 (10/90 vol%) environment for 3 hr at atmospheric pressure before being cooled to room temperature. The reactant gas H_2/CO_2 (molar ratio = 3:1) under operating conditions of 3 MPa, 623 K and GHSV = 3100 hr^{-1}. The effluent was analysed online using an Agilent gas chromatograph (GC) 7890A with the transfer line from the reactor to the GC preheated at 373 K to avoid condensation of effluent products. TCD was used to measure N_2, CO and CO_2 gases while organic compounds were studied using the flame ionization detector (FID). From this test, catalytic conversion and selectivity were computed using mass balance and resulting steady-state values (SSV). SSV was computed as an average of three tests over

a period of 3 hr of continuous operation. CO_2 conversion (x_{CO_2}), selectivity (s_i) and yield (y_i) (where i is the molecule of interest) were computed as follows:

Equation 9.1: CO_2 conversion computation

$$X_{CO_2} = \frac{n_{CH_3OH} + n_{CO}}{n^0_{CO_2}}$$

Equation 9.2: Methanol and carbon monoxide selectivity computation

$$S_{CH_3OH} = \frac{n_{CH_3OH}}{n_{CH_3OH} + n_{CO}}$$

$$S_{CO} = \frac{n_{CO}}{n_{CH_3OH} + n_{CO}}$$

Equation 9.3: Computation of yield for methanol

$$Y_{CH_3OH} = s_{CH_3OH} \times x_{CO_2}$$

9.3 MATHEMATICAL MODELS OF ADSORPTION ISOTHERMS

Within this study, four adsorption isotherm models were considered. Alongside the three listed in Chapter three (Langmuir, Freundlich and Toth), modified versions of the Langmuir and Freundlich models were also adopted. This includes the Langmuir-Freundlich and Langmuir Multi-site (LMS) models.

Equation 9.4: Langmuir Isotherm model

$$q = q_m \frac{kp}{1 + kp}$$

Equation 9.5: Langmuir-Freundlich isotherm model

$$q = q_m \frac{kp^n}{1 + kp^n}$$

Equation 9.6: Toth isotherm model

$$q = q_m \frac{kp}{(1 + kp^n)^{1/n}}$$

Equation 9.7: Langmuir Multi-Site isotherm model

$$q = \sum_{i=1}^{n} q_i \frac{k_i p}{1 + k_i p} \qquad where\ n\ is\ the\ no.\ of\ i\ sites$$

Where q and q_m are the equilibrium and maximum adsorption capacity respectively, k is the affinity constant for each of the mathematical model adopted, p is the pressure of the adsorbate. The isotherm parameters were determined by non-linear regression using iterative method with the aid of ORIGIN8. To determine the suitability of each model, an error function (Err) and correlation coefficient (R^2) defined by Equations 3.13 and 3.14 in Chapter 3.

9.4 RESULTS AND DISCUSSIONS

9.4.1 Textural and structural properties of synthesised composite material

Figure 9.1 shows the SEM images of the synthesised catalyst at varying Al/Zr ratio. From the produced images, the material is a well-developed spherically shaped crystal with thin layered plates on the surface. Alongside with the occurrence of the spheres are crumb-like particles densely connected to the spheres. The formation of layered crystal plates on the surface of the spherical particles is characteristic of layered structures [15, 16]. The formed materials are highly agglomerated exhibiting denser particle stacking than previously reported. This can be attributed to the smaller particle size when compared to SEM images in Chapters 7 and 8. In addition, the plate-like crystal formed on the surface of the material are homogeneous, well dispersed and also densely packed. This can be explained geometrically. Surface particles are more compact with one another at low particle size. The findings correlate with that reported in literature. Small crystal size of layered double hydroxides enhances particle interaction. Hence, facilitating agglomeration between particles especially with dispersed plate-like crystal surfaces [17, 18]. Apparently, with the increase in amount of Zr content, the particle size insignificantly increased. This was however spotted because of some random and distinct large particles spotted at high Zr content, HPH-14. This can be

attributed to the large ionic radius of Zr^{4+} (0.072 nm) when compared to Al^{3+} (0.053 nm). Moreover, as Zr content increases, particles are observed to be less aggregated with the gradual disappearance or breakage of the crumb-like particles. This can also be related to the ionic size of Zr.

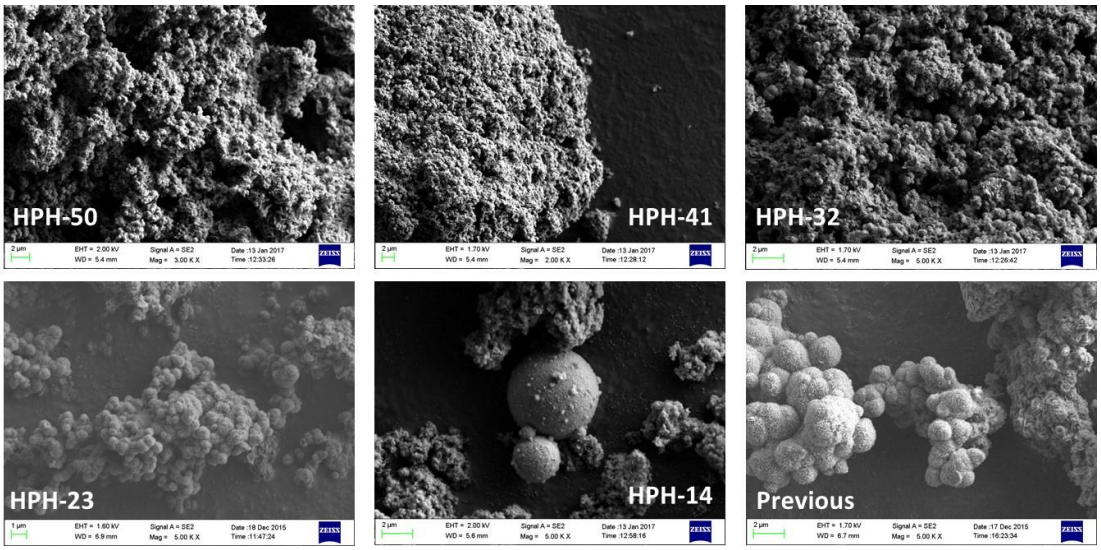

Figure 9.1: SEM images of synthesised CuO/ZnO/ZrO_2 catalyst on Mg-Al LDH support in comparison to previously prepared Mg-Al LDH adsorbent

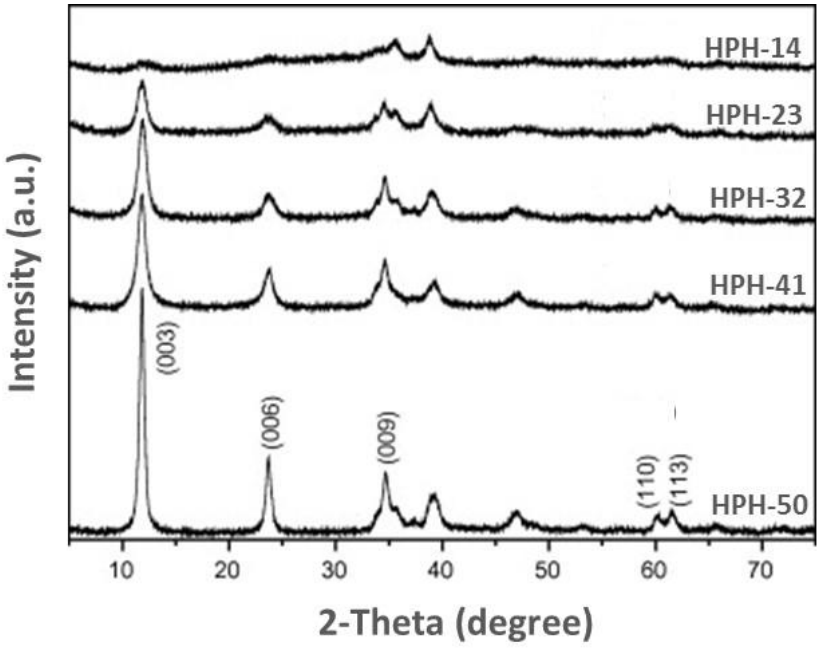

Figure 9.2: XRD pattern synthesised CuO/ZnO/ZrO_2 catalyst on Mg-Al LDH support in comparison to previously prepared Mg-Al LDH adsorbent

The XRD pattern of the prepared catalyst is shown in Figure 9.2. The profile shows pattern for a layered structure as reported in previous chapters. However, as the amount of Zr increases, the intensity of the peaks decreases. This illustrates that the presence of Zr reduces the crystallinity of the material. This supports the SEM result and further validates that the substitution of Al with a larger particle like Zr will distort the layer structure of the material as depicted in the SEM images. This agrees with reported findings of Shannon [19] who reported that a reduction in the occupancy of a cation as a result of cation displacement will increase mean distances in a predictable manner. As a result of this cationic substitution, the composite material exhibits an amorphous state [20]. It is therefore established that the presence of Al is paramount for the formation of layered structure for the composite material [21, 22]. The results from N_2 adsorption-desorption analysis agrees with the findings from XRD and SEM. It is observed that as $Al^{3+}/Al^{3+}+Zr^{4+}$ increased, the surface area of the composite increase. This was also observed for the pore volume but an opposite trend was witnessed for the particle size (see Table 9.1).

Table 9.1: N_2 sorption analysis for as-synthesised composite catalyst

Sample	$Cu^{2+}:Mg^{2+}:Zn^{2+}:Al^{3+}:Zr^{4+}$ nominal atomic ratio	$\frac{Al^{3+}}{Al^{3+}+Zr^{4+}}$	SBET (m^2/g)	Vp (cm^3/g)	Dp (nm)
HPH-14	3:3:3:1:4	0.2	204.51	0.54	28.73
HPH-23	3:3:3:2:3	0.4	190.32	0.58	32.59
HPH-32	3:3:3:3:2	0.6	215.69	0.61	26.56
HPH-41	3:3:3:4:1	0.8	226.37	0.66	24.86
HPH-50	3:3:3:5:0	1.0	243.18	0.63	21.15

9.4.2 Thermal characterization of composite material

To test the thermal strength of the composite catalyst, the material was exposed to thermal decomposition within a controlled volume using the TGA. The results obtained are shown in Figure 9.3 and summarised in Table 9.2. The decomposition profile for each of the sample showed a three stage decomposition step. The first stage is due to the loss of adsorbed surface moisture and occurred with the temperature less than 250 ^oC. However, as the $Al^{3+}/Al^{3+}+Zr^{4+}$ increased, there was a decrease in the extent of this stage indicating that less energy is required to eliminate the surface moisture. The second decomposition stage is attributed to the loss of interstitial moisture or

dehydroxylation process and occurred within 250 and 800 ^{o}C. Stage two decomposition was also assigned to the decomposition of the layered network of the LDH [7]. This is logical given the loss of interlayer OH^- group. As a result, the layered structure of the material will collapse given the loss of OH^- and the intercalating anions [23, 24]. In addition, Velu *et al.* [20] suggested that this stage is also associated with the loss of amorphous hydroxycarbonates. In total, the second stage is a combination of losses of both the amorphous phase and layered network which transforms into oxocarbonates. The oxocarbonates are then further decomposed in the third stage [22, 25]. The third stage decomposition step occurs at temperature greater than 800 ^{o}C. TGA profile shows that the commencement of the third stage was extended towards a higher temperature as the $Al^{3+}/Al^{3+}+Zr^{4+}$ ratio increases. It suggests that the thermal strength of the material decreases as the amount of Zr increases. This corresponds to the XRD and SEM results signifying that the substitution of Al^{3+} with Zr^{4+} results to the dissociation of hydrogen bonds within the interlayer structure. Therefore reducing the electrostatic interaction between the anions and the layers resulting to the weakening of the layers. This will make the material less thermally stable. In addition, as illustrated in Table 9.2, the weight loss resulting from the second stage was seen to increase with increase in Zr content with subsequent decrease in the weight loss at the third stage. This suggests that less amount of oxo-carbonates are formed from the increased decomposition at the second stage. This implies that the amount of layered network in the material is relatively small compared to the amorphous phase. Hence, it can be concluded that the presence of Zr facilitates the formation of amorphous material. In other words, the presence of Al is required for the formation of layered structure of the LDH. This further elaborates the findings obtained from the XRD analysis.

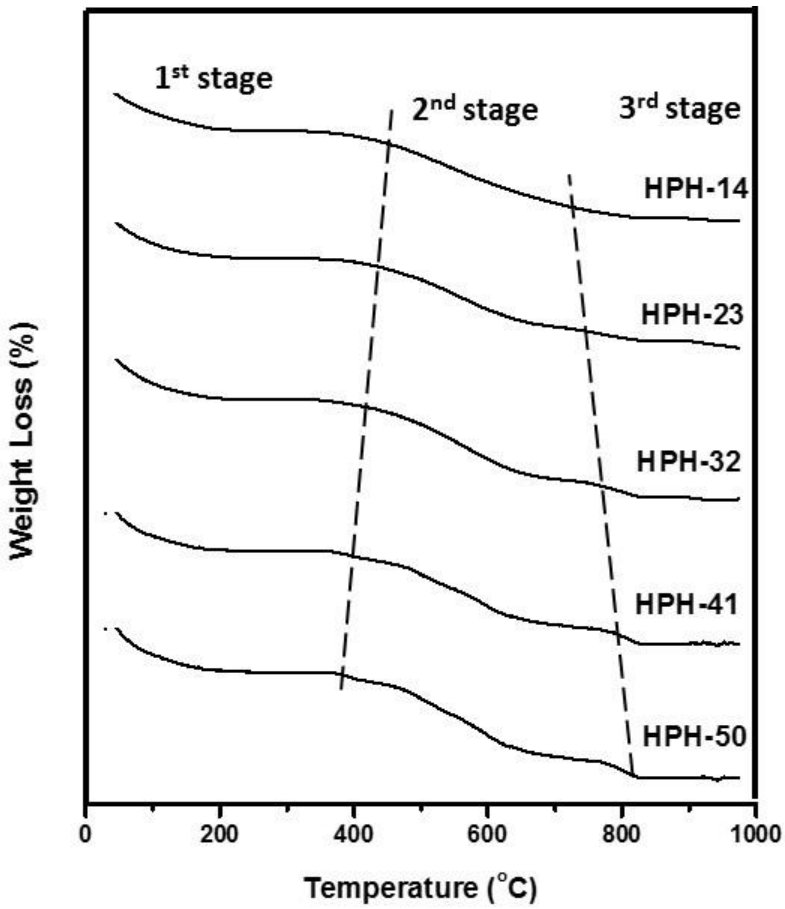

Figure 9.3: Thermogravimetric analysis of composite catalyst

Table 9.2: TGA data for material decomposition and CO_2 adsorption

Sample	Al^{3+}:(Al^{3+}+Zr^{4+}) atomic ratio	TGA Weight Loss (%)			Total (%)	CO_2 Uptake (mmol/g)
		1st stage	2nd Stage	3rd Stage		
HPH-14	0.2	3.39	5.81	0.02	9.22	1.65
HPH-23	0.4	3.41	5.69	0.61	9.71	1.61
HPH-32	0.6	3.40	5.65	1.25	10.30	1.58
HPH-41	0.8	3.43	5.32	1.58	10.33	1.46
HPH-50	1.0	3.41	5.20	1.95	10.56	0.81

9.4.3 CO_2 adsorption capacity

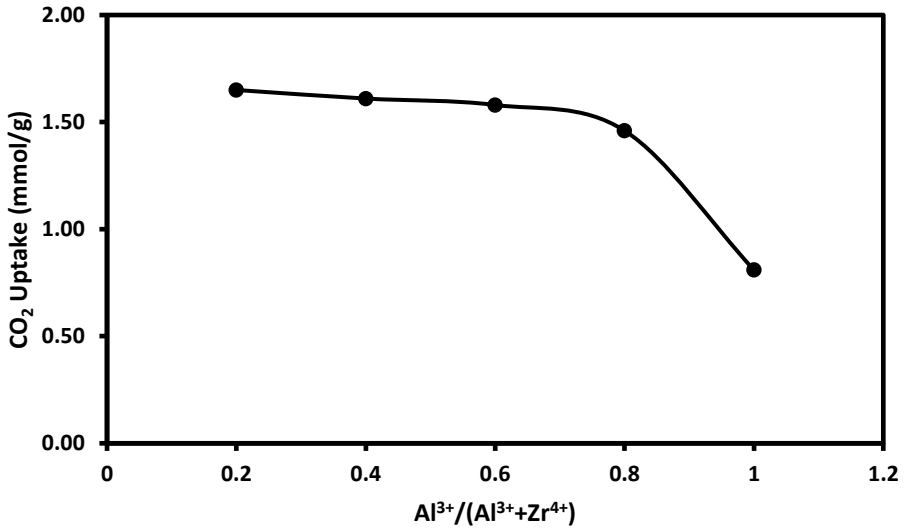

Figure 9.4: Correlation between metal composition and CO_2 uptake for composite catalyst

Figure 9.4 shows the adsorption capacity of the catalyst as $Al^{3+}/Al^{3+}+Zr^{4+}$ ratio increases from 0.2 to 1. The profile shows a descending trend with increase in Al content or in other words, the decrease in Zr content. This is quite unlikely given the increasing specific surface area of the material with increase in Al content (decrease in Zr content). It is expected that the CO_2 uptake should increase with increase in surface area and not the other way round. It can be explained that the increased presence of Zr had an impact of increasing the adsorption capacity of the material. This may be partially attributed to the Zr ability to form low coordinative unsaturated O^{2-} lattice resulting from its high net electronic charge. In addition, its interaction with Zn^{2+} can form a complex coordinated site which in turn can interact with CO_2. Hence, this goes to suggest that the physisorption mechanism was less dominant than the chemisorption mechanism immediately Zr species was introduced into the composite mix. From the figure, this is apparent giving the steep increase in CO_2 uptake from 0.81 to 1.46 mmol/g for HPH-50 and HPH-41 respectively. Immediately after this, subsequent increase in Zr content (or reduction in Al content) resulted in a gradual increase in CO_2 uptake.

To further understand the adsorption mechanism, the material was subjected to several adsorption processes at varying pressures from 0-6 bars in order to ascertain the most suitable isotherm model

that best describes the adsorption process of the material. Among the several models, the Langmuir, Langmuir-Freundlich, Langmuir Multiple site (LMS) and Toth models were used to fit the experimental data. This is as shown in Figure 9.5. The equation of the models are shown from Equation 9.4-9.7. Within the plots, the corresponding isotherm parameters are listed out with the correlation coefficient and error function based on the deviation of q_m from the experimental. A quick glance at the plots shows that each model provided a relatively good fit for the experimental. However, based on the correlation coefficient, R^2 the Langmuir-Fruendlich model was the closest to the experimental data. The theoretical implication of this model is that the adsorbent has heterogeneous surface with different sites having equal adsorption energies. This is seconded by the Toth model which was the second best fit to the experimental data. Toth model is an extension of the Freundlich model and best describes the heterogeneity of the material by the value of n. The heterogeneity of a material is defined by the absolute difference of the value of n and unity. The greater the difference, the more heterogeneous the adsorption process is. However, there is no basis for this comparison to be made upon. Nonetheless, it goes to suggest that the adsorption process is dominated by one of the adsorption mechanism as stipulated by the good fit of the Langmuir model. The dominating adsorption mechanism is simultaneously being augmented by a secondary but inconsequential adsorption pathway. Correlating the results from this study with that of material characterization, it can be concluded that the primary adsorption mechanism in this composite material is as a result of the impact of Zr^{4+} in the layer of the materials. Hence, the CO_2 adsorption is controlled by the chemisorption process with little impact of physisorption mechanism. This is also the basis behind the Langmuir dual site model (LMS) which suggests that there are two different sites that are responsible for the adsorption of CO_2. However, due to the kinetic parameters, it is observed that the parameters q_1 and k_1 for the first site is almost similar to q_2 and k_2 for the second site. This suggests that both adsorption sites adopt the same adsorption mechanisms but with a little difference in the affinity constants, k. this describes the extent of adsorption on the surface of that adsorption site.

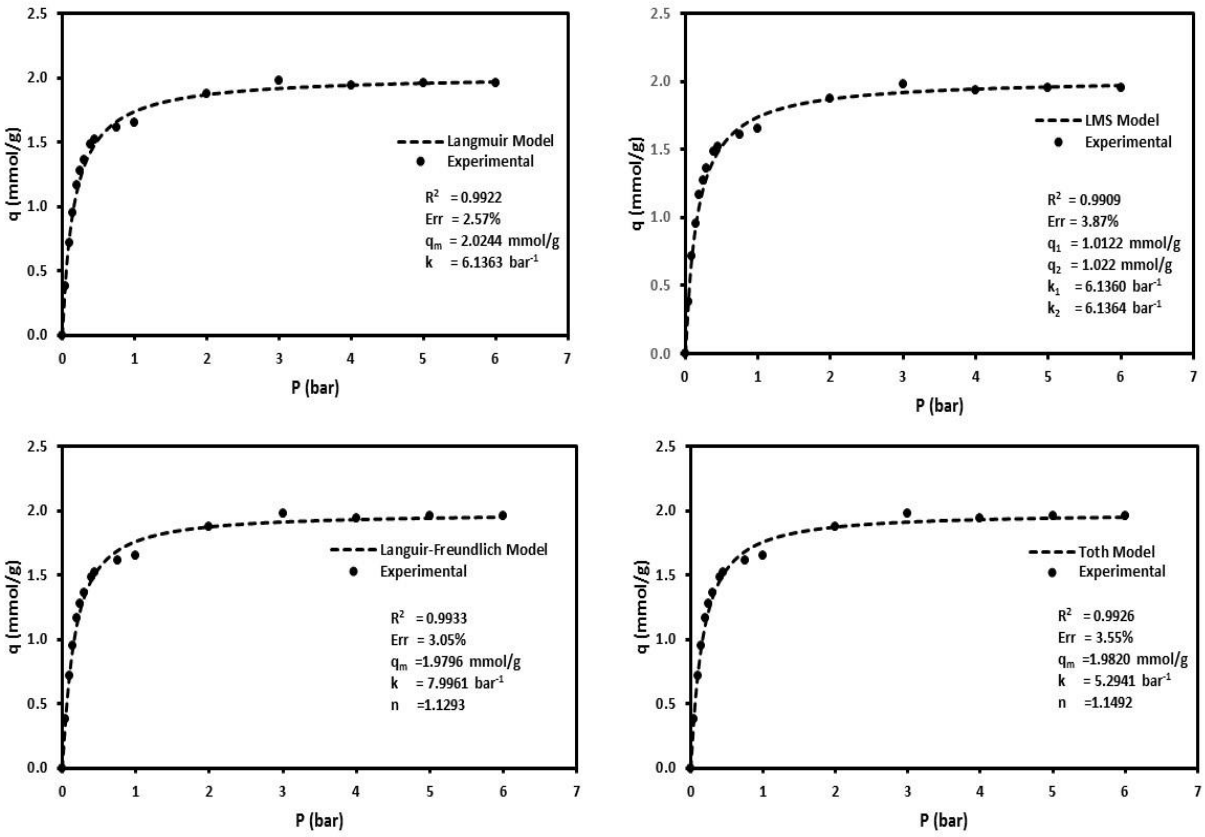

Figure 9.5: Comparison of different isotherm models with experimental data for HPH-14 at temperature of 328 K

9.4.4 Catalytic performance of the composite material

Table 9.3: Catalytic performance of composite catalysts at varying temperature‡

		Temperature 623 K			
Sample	**$Al^{3+}/(Al^{3+}+Zr^{4+})$**	**X_{CO2} (%)**	**S_{CH3OH} (%)**	**S_{CO} (%)**	**Y_{CH3OH} (% mol CH_3OH/mol CO_2 fed)**
HPH-50	1.0	14.69	42.43	57.57	6.23
HPH-41	0.8	16.27	48.62	51.38	7.91
HPH-32	0.6	19.54	49.47	50.53	9.67
HPH-23	0.4	22.73	50.55	49.45	11.49
HPH-14	0.2	19.85	51.06	48.94	10.14

Temperature 573 K					
Sample	**$Al^{3+}/(Al^{3+}+Zr^{4+})$**	**X_{CO2} (%)**	**S_{CH3OH} (%)**	**S_{CO} (%)**	**Y_{CH3OH} (% mol CH_3OH/mol CO_2 fed)**
HPH-50	1.0	12.81	34.82	65.18	4.46
HPH-41	0.8	13.37	38.59	61.41	5.16
HPH-32	0.6	15.71	40.08	59.92	6.30
HPH-23	0.4	19.03	42.79	57.21	8.14
HPH-14	0.2	17.98	43.17	56.83	7.76

‡ Reaction conditions: P = 3.0 MPa, GHSV = 3100 hr^{-1}, CO_2:H_2 = 1:3.

The catalytic performance of the prepared composite catalyst with regards to methanol synthesis and CO_2 conversion is shown in Table 9.3. Experimental result shows that CO_2 conversion tends to rise with decrease in $Al^{3+}/(Al^{3+}+Zr^{4+})$ ratio until it attains a maximum at 0.4 ratio before descending. This is similar across all experimented temperatures. However, the methanol selectivity showed a continuous ascent with increase in $Al^{3+}/(Al^{3+}+Zr^{4+})$ ratio. As illustrated in previous chapters (Chapter 4 and 5), the basic principles governing CO_2 conversion and methanol selectivity is dependent on the amount of active Cu surface sites available for dissociating hydrogen molecules and the distribution of basic sites respectively. Regarding to the conversion of CO_2, a decrease in $Al^{3+}/(Al^{3+}+Zr^{4+})$ ratio results to the increase in the amount of Zr metal. This metal is known for its high dispersion of Cu to methanol [7, 8]. Hence, it is suspected that the replacement of Al metal with Zr metal will aid in further dispersion of the Cu metal making it accessible for the adsorption and subsequent dissociation of hydrogen into its respective atoms for the hydrogenation process. However, with further increase till a $Al^{3+}/(Al^{3+}+Zr^{4+})$ ratio of 0.4, the introduction of Zr favoured the Cu dispersion and hence promoting CO_2 conversion. Beyond this composition, a decrease in conversion of CO_2 was witnessed. As elucidated earlier, this can be attributed to the detrimental effect of high proportion of Zr^{4+} situated in the lattice layer of the material. Gao *et al.* [7] suggested that the increased content of Zr may result to a decreased proportion of the Zr^{4+} ion in the crystal layer in comparison to the total Zr^{4+}. As a result, this will result to the reduction in Cu dispersion and subsequent reduction in the available Cu surface area [26].

Considering methanol selectivity, this was observed to increase with reduction of $Al^{3+}/(Al^{3+}+Zr^{4+})$ ratio. This can be attributed to the replacement of the Al metal with Zr metal resulting to the enhancement of the strong basic sites of the material. Consequently, since the selectivity of methanol

is dependent on the strong basic sites distribution, it is logical that this will increase with increasing Zr content. However, no maximum peak was ascertained unlike the case of CO_2 conversion. Nonetheless, it was observed that selectivity tends to climax at low Al content as shown in Figure 9.6. Figure 9.6 correlates the catalytic performance with the metallic composition of Al and Zr cations. Finally, despite the irregularity in trend of methanol selectivity and CO_2 conversion, the yield of methanol was observed to increase with decrease in Al^{3+} content (or increase in Zr^{4+} content) until $Al^{3+}/(Al^{3+}+Zr^{4+})$ ratio of 0.4. At a reduced temperature of 573 K, the same trend was repeated but at a reduced magnitude. This indicates that the reduction in operating temperature will bring about the reduction in catalytic performance of the composite catalyst.

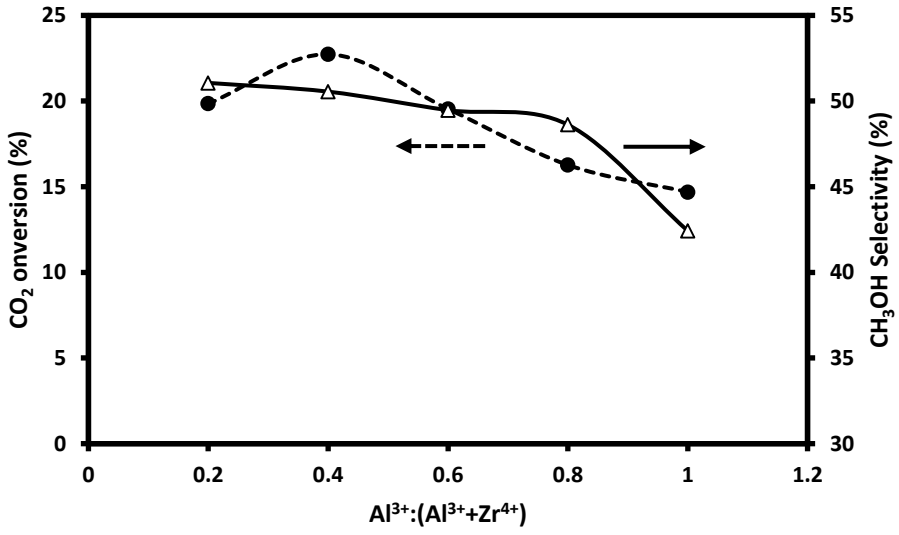

Figure 9.6: Correlation between CO_2 conversion and methanol selectivity with metal composition

9.5 CONCLUSIONS

Combining all the relevant findings from previous chapters, a composite catalyst consisting of $CuO/ZnO/ZrO_2$ catalyst on a Mg-Al LDH template was synthesised and characterised using BET, XRD, TGA and SEM. Varying the ratio of Al^{3+}:$(Al^{3+}+Zr^{4+})$, the surface morphology and thermal characteristics and catalytic activity was investigated. Findings from this shows that the surface morphology of the composite was enhanced with a greater specific surface area and pore volume. Despite being higher than the individual structures of the catalyst and adsorbent respectively, the surface area tends to decrease with increase in Zr^{2+}. Likewise, the thermal strength of the composite

was observed to follow the same trend. In addition, the CO_2 adsorption capacity of the composite was observed to decrease with increase in Al^{3+}:(Al^{3+}+Zr^{4+}). Supported by Langmuir, Toth, Langmuir multi-site and Langmuir-Freundlich isotherm models, the adsorption process on this material was dominated primarily by chemisorption with insignificant contribution from physisorption. Finally, a high methanol yield was obtained for this catalyst when compared to the unsupported catalyst reported in Chapters 4 and 5. However, a critical Al^{3+}/(Al^{3+}+Zr^{4+}) ratio of 0.4 is stipulated for a high CO_2 conversion and methanol yield. Nonetheless, challenged by time, this finding was only conducted once. Hence the result are subject for further verification.

Reference

[1] F. Arena, G. Italiano, K. Barbera, S. Bordiga, G. Bonura, L. Spadaro, F. Frusteri, Solid-state interactions, adsorption sites and functionality of Cu-ZnO/ZrO2 catalysts in the CO2 hydrogenation to CH3OH, Applied Catalysis A: General, 350 (2008) 16-23.

[2] P. Gao, H. Yang, L. Zhang, C. Zhang, L. Zhong, H. Wang, W. Wei, Y. Sun, Fluorinated Cu/Zn/Al/Zr hydrotalcites derived nanocatalysts for CO2 hydrogenation to methanol, Journal of CO2 Utilization, 16 (2016) 32-41.

[3] X. Guo, D. Mao, G. Lu, S. Wang, G. Wu, Glycine–nitrate combustion synthesis of CuO–ZnO–ZrO2 catalysts for methanol synthesis from CO2 hydrogenation, Journal of Catalysis, 271 (2010) 178-185.

[4] X. Guo, D. Mao, G. Lu, S. Wang, G. Wu, The influence of La doping on the catalytic behavior of Cu/ZrO2 for methanol synthesis from CO2 hydrogenation, Journal of Molecular Catalysis A: Chemical, 345 (2011) 60-68.

[5] W.S. Hummers, S.Y. Tyree, S. Yolles, F. Basolo, L. Bauer, Zirconium and Hafnium Tetrachlorides, Inorganic Syntheses, John Wiley & Sons, Inc.2007, pp. 121-126.

[6] J. Liu, J. Shi, D. He, Q. Zhang, X. Wu, Y. Liang, Q. Zhu, Surface active structure of ultra-fine Cu/ZrO2 catalysts used for the CO2+H2 to methanol reaction, Applied Catalysis A: General, 218 (2001) 113-119.

[7] P. Gao, F. Li, H. Zhan, N. Zhao, F. Xiao, W. Wei, L. Zhong, H. Wang, Y. Sun, Influence of Zr on the performance of Cu/Zn/Al/Zr catalysts via hydrotalcite-like precursors for CO2 hydrogenation to methanol, Journal of Catalysis, 298 (2013) 51-60.

[8] X. Guo, D. Mao, G. Lu, S. Wang, G. Wu, CO_2 hydrogenation to methanol over Cu/ZnO/ZrO_2 catalysts prepared via a route of solid-state reaction, Catalysis Communications, 12 (2011) 1095-1098.

[9] A. Garcia-Gallastegui, D. Iruretagoyena, V. Gouvea, M. Mokhtar, A.M. Asiri, S.N. Basahel, S.A. Al-Thabaiti, A.O. Alyoubi, D. Chadwick, M.S.P. Shaffer, Graphene Oxide as Support for Layered Double Hydroxides: Enhancing the CO2 Adsorption Capacity, Chemistry of Materials, 24 (2012) 4531-4539.

[10] D. Iruretagoyena, X. Huang, M.S.P. Shaffer, D. Chadwick, Influence of Alkali Metals (Na, K, and Cs) on CO2 Adsorption by Layered Double Oxides Supported on Graphene Oxide, Industrial & Engineering Chemistry Research, 54 (2015) 11610-11618.

[11] D. Iruretagoyena, M.S.P. Shaffer, D. Chadwick, Layered Double Oxides Supported on Graphene Oxide for CO2 Adsorption: Effect of Support and Residual Sodium, Industrial & Engineering Chemistry Research, 54 (2015) 6781-6792.

[12] L.H. Zhang, C. Zheng, F. Li, D.G. Evans, X. Duan, Copper-containing mixed metal oxides derived from layered precursors: control of their compositions and catalytic properties, Journal of Materials Science, 43 (2008) 237-243.

[13] G. Busca, U. Costantino, F. Marmottini, T. Montanari, P. Patrono, F. Pinzari, G. Ramis, Methanol steam reforming over ex-hydrotalcite Cu–Zn–Al catalysts, Applied Catalysis A: General, 310 (2006) 70-78.

[14] C.I. Ezeh, X. Huang, X. Yang, C.-g. Sun, J. Wang, Sonochemical surface functionalization of exfoliated LDH: Effect on textural properties, CO2 adsorption, cyclic regeneration capacities

and subsequent gas uptake for simultaneous methanol synthesis, Ultrasonics Sonochemistry, 39 (2017) 330-343.

[15] J.T. Kloprogge, L. Hickey, R.L. Frost, The effects of synthesis pH and hydrothermal treatment on the formation of zinc aluminum hydrotalcites, Journal of Solid State Chemistry, 177 (2004) 4047-4057.

[16] Z. Ni, A. Chen, C. Fang, L. Wang, W. Yu, Enhanced NOx adsorption using calcined Zn/Mg/Ni/Al hydrotalcite-like compounds, Journal of Physics and Chemistry of Solids, 70 (2009) 632-638.

[17] F. Bellezza, M. Nocchetti, T. Posati, S. Giovagnoli, A. Cipiciani, Synthesis of colloidal dispersions of NiAl, ZnAl, NiCr, ZnCr, NiFe, and MgFe hydrotalcite-like nanoparticles, Journal of colloid and interface science, 376 (2012) 20-27.

[18] L. Wang, C. Li, M. Liu, D.G. Evans, X. Duan, Large continuous, transparent and oriented self-supporting films of layered double hydroxides with tunable chemical composition, Chemical Communications, DOI 10.1039/B613687G(2007) 123-125.

[19] R. Shannon, Revised effective ionic radii and systematic studies of interatomic distances in halides and chalcogenides, Acta Crystallographica Section A, 32 (1976) 751-767.

[20] S. Velu, D.P. Sabde, N. Shah, S. Sivasanker, New Hydrotalcite-like Anionic Clays Containing Zr4+ in the Layers: Synthesis and Physicochemical Properties, Chemistry of Materials, 10 (1998) 3451-3458.

[21] K. Nishida, I. Atake, D. Li, T. Shishido, Y. Oumi, T. Sano, K. Takehira, Effects of noble metal-doping on Cu/ZnO/Al2O3 catalysts for water–gas shift reaction, Applied Catalysis A: General, 337 (2008) 48-57.

[22] M. Behrens, I. Kasatkin, S. Kühl, G. Weinberg, Phase-Pure Cu,Zn,Al Hydrotalcite-like Materials as Precursors for Copper rich Cu/ZnO/Al2O3 Catalysts, Chemistry of Materials, 22 (2010) 386-397.

[23] Z.P. Xu, H.C. Zeng, Decomposition Processes of Organic-Anion-Pillared Clays CoaMgbAl(OH)c(TA)d·nH2O, The Journal of Physical Chemistry B, 104 (2000) 10206-10214.

[24] J. Cheng, J. Yu, X. Wang, L. Li, J. Li, Z. Hao, Novel CH4 Combustion Catalysts Derived from Cu−Co/X−Al (X = Fe, Mn, La, Ce) Hydrotalcite-like Compounds, Energy & Fuels, 22 (2008) 2131-2137.

[25] R. Trujillano, M.J. Holgado, F. Pigazo, V. Rives, Preparation, physicochemical characterisation and magnetic properties of Cu–Al layered double hydroxides with CO32− and anionic surfactants with different alkyl chains in the interlayer, Physica B: Condensed Matter, 373 (2006) 267-273.

[26] D. Tichit, B. Coq, Catalysis by Hydrotalcites and Related Materials, CATTECH, 7 (2003) 206-217.

CHAPTER TEN

CONCLUSIONS

To sustain the booming global population, the demand for energy will surge. Consequently, the amount of anthropogenic CO_2 emission will equally rise without any adequate mitigation strategy put in place to arrest this. Carbon Capture, Storage and Utilization (CCSU) has received much attention over the years as a prospective technology to circumvent CO_2 emissions. This technology does not only capture CO_2 but also converts it to value-added products like methanol. Methanol can be produced by the controlled hydrogenation of CO_2 with the aid of suitable catalysts. Thus far, different catalysts have been studied for the synthesis of methanol from the reduction of CO_2 via hydrogenation. These research studies have based their research strongly on the catalytic performance of the catalysts without further effort on the adsorption capacity. Incidentally, the catalytic performance depends on the ability of the catalyst to convert CO_2 to methanol. This can only be achieved if the catalyst possesses suitably good CO_2 adsorption at its strong basic sites. Hence, improving the adsorption capacity alongside with other parameters affecting catalytic performance will improve the accessibility of CO_2 to the catalyst active site for subsequent conversion to methanol. Hence, a sorption-enhanced composite catalyst is proposed for this technology. As a result of this, numerous studies have investigated the performance of these composite catalysts. Emphasis were directed towards correlating the catalytic performance to surface morphology and chemistry. Conversely, no in depth study has been carried out to assess the rudimentary synthetic methods and its conditions favouring the formation of the desired surface morphology and chemistry. To this regard, this research is centred on investigating several synthetic methods and assessing the physicochemical effects of this synthetic routes on the performance of the composite catalyst. The adopted composite catalysts for methanol synthesis via CO_2 hydrogenation is a Cu-based catalyst supported on a layered double hydroxide (LDH) framework.

Among the different means of enhancing the sorption capacity of the catalyst is by using a support framework, one with high CO_2 uptake capacity. The catalysts will be dispersed on the surface of the support forming a novel composite material with both good sorption and catalytic performance. The aim of the present work hence is to develop and assess a stable, both chemical and thermal, sorption-

enhanced catalyst with an adequate sorption and catalytic activity. This will involve the modification of both physical and chemical properties of each individual materials. To achieve this, the study is split into two sections consisting of the individual development of suitable catalysts and adsorbents with good physicochemical properties to support and optimise their individual purpose. Within the limited time frame, various preparation methods together with the use of promoters were texted. In addition, favourable synthetic conditions were also investigated. This study is supported by kinetic studies suitable for the description of the process were studied.

The most commonly used catalyst for methanol synthesis via CO_2 hydrogenation is CuO/ZrO_2 catalyst and its optimal performance is based partly on its thermal characteristics and surface morphology and chemistry. Calcining the catalyst improved its thermal stability. In addition, despite the several preparation methods used, calcination temperature affected the surface area and porosity of the material. This results from agglomeration of particles due to sintering effects at high temperature. However, this temperature was capped at a maximum of 673 K beyond which the catalyst denatures. Another factor that affected the performance of this catalyst was the Cu composition. It was discovered across all investigated synthetic routes that catalyst with Cu-loading of 30% was more thermally stable. However, considering the preparation route, the co-precipitation method produced the most thermally stable catalyst with the impregnation method being the least. In spite of the high thermal characteristics of catalysts prepared via co-precipitation, the catalytic performance of deposition precipitation catalysts (Cu-loading = 30%) showed a better CO_2 conversion and methanol selectivity than other preparation routes. Furthermore, tuning the impact of ultrasonic irradiation by varying the sonication impulse also altered the catalyst physico-chemical properties. At low sonication impulse, the surface area and pore distribution of the catalytic material was greatly improved. This was further promoted with the introduction of ZnO additives. But this has to be at adequate Zn composition. A $Zn^{2+}/(Zn^{2+}+ Zr^{4+})$ ratio of 3/7 exhibited the best CO_2 conversion and methanol selectivity. Lastly, based on thermal tests, this study suggests that for optimum industrial applicability, the material will be well suited at a thermal operation with heating rate at 20 K/min rather than 10 K/min.

With regards to the catalyst support framework, LDHs with high CO_2 adsorption capacity was synthesised via anionic surfactant intercalation subjected to sonochemical functionalization. The use of sonochemical process in the synthesis step led to a more developed pore structure than that of the

conventional process. However, this was dependent on sonication intensity. Despite the advancement in physical properties which is beneficial to the physical adsorption of CO_2, the further adoption of the sonochemical process for amine functionalization of the prepared LDH led to an improved amine loading and effective amine efficiency of the adsorbent. In addition, the sonochemically functionalized LDH exhibited a greater ease of regeneration with a longer life span than the conventional LDH. Therefore, sonochemical route can be an effective preparation method for long-lasting recyclable layered double hydroxides for CO_2 adsorption. Likewise the ultrasonic route, the hydrothermal route also enhanced the physicochemical features of the adsorbent. In this case, novel Mg-Al LDH nano-spheres were synthesized using supercritical hydrothermal method. By tuning the density of supercritical water, the spherical shape was varied from 30-60 nm. However, this can be further reduced to < 20 nm depending on the cooling temperature. XRD patterns suggest the presence of boehmites in the crystal structure of spheres produced at low hydrothermal pressure. This gradually disappears with increase in pressure. CO_2 adsorption capacity dropped with samples produced around the critical pressure but surged in samples prepared within the supercritical zone. Comparing the impact of this method to the ultrasonic synthetic route, hydrothermal treatment was more effective in promoting the adsorption capacity of the adsorbent due to the ascent in the amount of strong basic sites (O^{2-}) and subsequent decrease in both moderate (M-O) and weak (OH^- groups) basic sites. However, the cyclic adsorption efficiency of the sonochemical process is better than that of both hydrothermal and conventional preparation routes. The sonochemical route shows the potential for enhanced amine loading and cyclic efficiency, thus providing a more suitable and economical approach for synthesis of double layered hydroxides. Results obtained from kinetic models clearly indicate that prior to amine extraction, the adsorption on Mg-Al LDH adsorbent is mostly facilitated by physisorption while adsorption is mainly promoted by chemisorption after amine extraction.

Combining all acquired knowledge in the previous chapters, a novel composite catalyst consisting of $CuO/ZnO/ZrO_2$ catalyst on Mg-Al LDH template is synthesised and analysed. With a varying ratio of Al^{3+}:(Al^{3+}+Zr^{4+}), the surface morphology, thermal characteristics and catalytic activity of the dual functional hybrid material was altered. Despite having a better structure than the individual structures of the catalyst and adsorbent respectively, the surface area of the composite tends to decrease with increase in Zr^{2+}. Likewise, the thermal strength of the composite was observed to follow the same trend. In addition, the CO_2 adsorption capacity of the composite was observed to

decrease with increase in Al^{3+}:(Al^{3+}+Zr^{4+}). Supported by Langmuir, Toth, Langmuir multi-site and Langmuir-Freundlich isotherm models, the adsorption process on this material was dominated primarily by chemisorption with insignificant contribution from physisorption. Finally, a high methanol yield was obtained for this catalyst when compared to the unsupported catalyst reported in Chapters 4 and 5. However, a critical Al^{3+}/(Al^{3+}+Zr^{4+}) ratio of 0.4 is stipulated for high CO_2 conversion and methanol yield.

In general, a novel hybrid catalyst with dual functionality, for the simultaneous adsorption and reduction of CO_2 via hydrogenation process, is synthesised. Its performance can be varied by tuning the nature and composition of its cations and intercalating anion constituents. Emphasis should be directed towards not destroying the layered network of the LDH. Tuning should be controlled to improve both inter-particle diffusion and surface reaction. With this in mind, the dual functional composite catalyst will be optimised both in production and application.

Recommended Future Work

Although this study was carried out to enhance the competitiveness of LDH as a solid adsorbent, its chemical flexibility and structural plasticity has gained it much attention as a template for supporting catalysts. In this regard, the synergy of these two materials, a catalyst and an adsorbent, is recommended for industrial applications requiring catalysts with high sorption capacity. Pertaining to methanol synthesis via CO_2 hydrogenation, these composite catalysts can simultaneously serve as a sink as well as a source for CO_2 in methanol production. Due to this, sorption-enhanced catalyst are seen as a new means of integrating adsorption and catalysis. This study sets the foundation for sorption-enhanced catalysts for methanol synthesis via CO_2 hydrogenation. A list of variable factors were considered before developing these composite catalysts. The catalysts has shown to out-perform the individualistic capacity of each material. Hence, it is paramount to identify the key factors necessary for optimizing the performance of this composite material.

First, investigating the impact of cationic and anionic exchange with various cations and anions will not only alter the structure of this composite, but will also affect its chemical functionality. This technology may not be limited to just methanol production. It can also be applied in all sectors where LDH or hydrotalcite-like compounds are utilized like in the pharmaceutical, food processing,

environmental, hydrogen production, etc. Therefore, understanding the impact of this ions will help understand the means of applying this knowledge to promote the composite material. Owing to time and resources constraints, this was not achieved within the stipulated time frame of this study. However, this is highly recommended before scaling up or industrial implementation of this material.

Aside addressing the issue of scaling up the production of these material for industrial application, further fundamental knowledge regarding the hybrid of this adsorbent and the catalyst is required. Basic understanding of the effect of water, operating conditions like pH, temperature and pressure, transport dynamics and phenomena, thermal strength and kinetics are basic criteria to enable the effective and efficient operability of the material. Likewise, this will aid in the cost evaluation of the material. In the absence of experimentation, mathematical simulation or modelling (CFD, DFT, etc) of this technology is highly recommended.

Having said and done the aforementioned, the design of a suitable reactor for the synthesis and operation of this technology is key for its scaling up and commercialization.

As a parallel study, LDH is considered an environmentally friendly material and its flexibility has extended its usage towards water treatment. This material is known to only operate at low to moderate temperatures and pressures. Therefore, in the absence of high temperatures, this technology can also be extended towards low temperature processes as a sorption material or as a template providing adequate sites for surface reaction.

Finally, I strongly recommend that research should be channelled towards understanding means of regenerating or disposing the composite catalyst. LDH might be considered environmentally friendly, but the incorporated catalysts might not. Hence, the need to develop means of disposing the material or recycling for same or further use is highly suggested.

APPENDIX

Appendix A: Experimental Equipment

Figure A3.1: Thermogravimetric Analyser

Figure A3.2: Catalyst evaluation/adsorption test rig

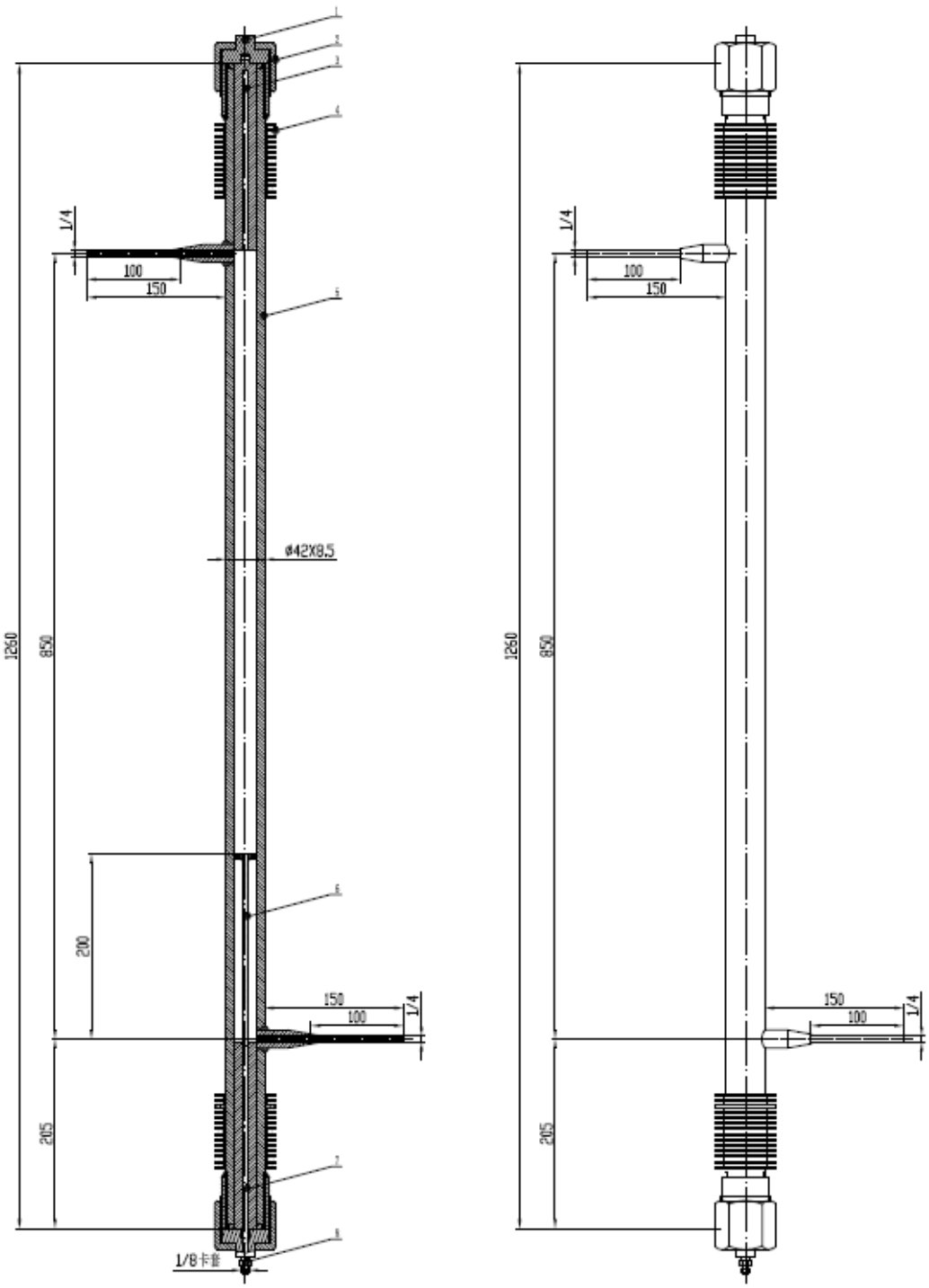

Figure A3.3: Design specification for the adsorption column (dimensions are in mm)

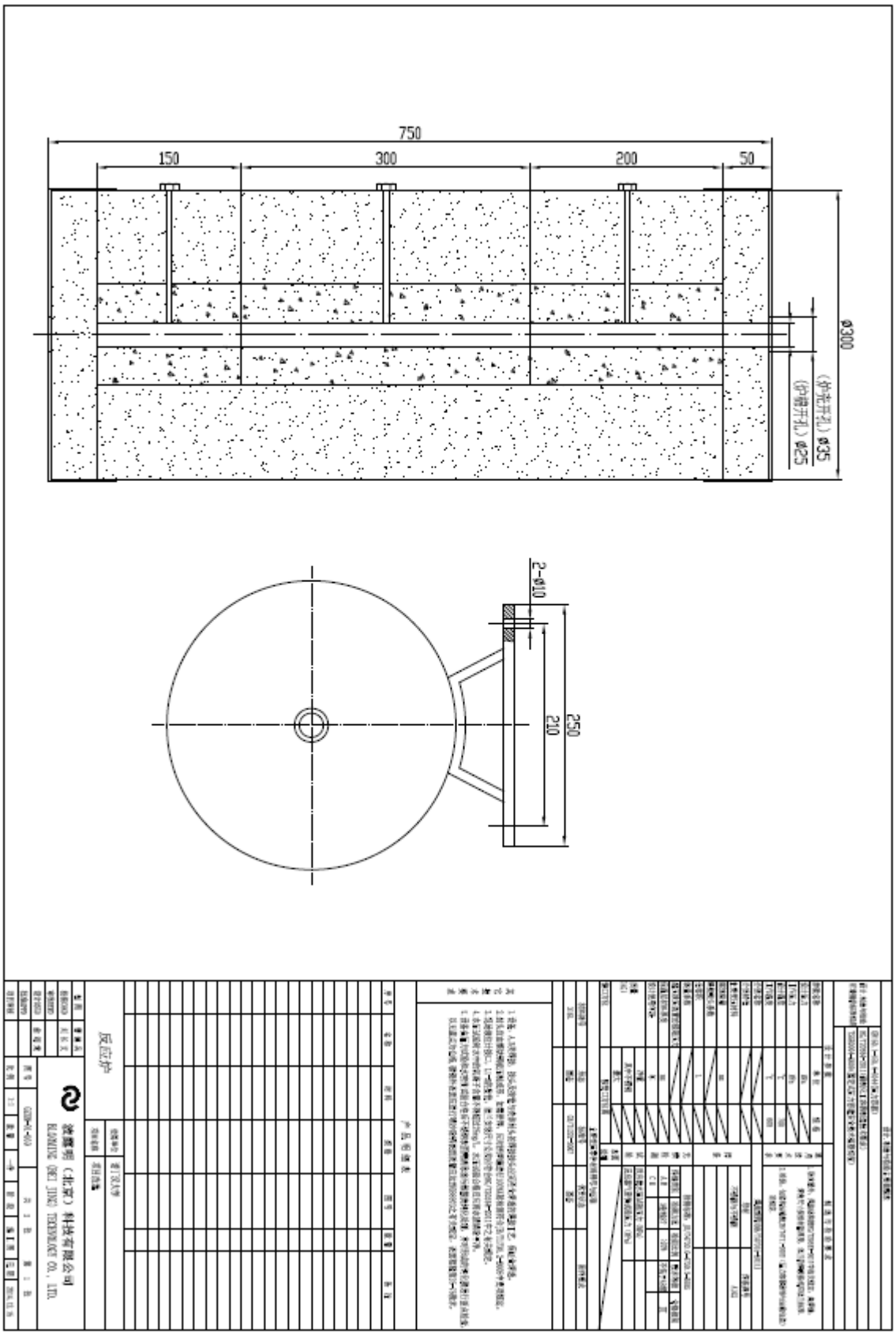

Figure A3.4: Design sheet for the reactor furnace

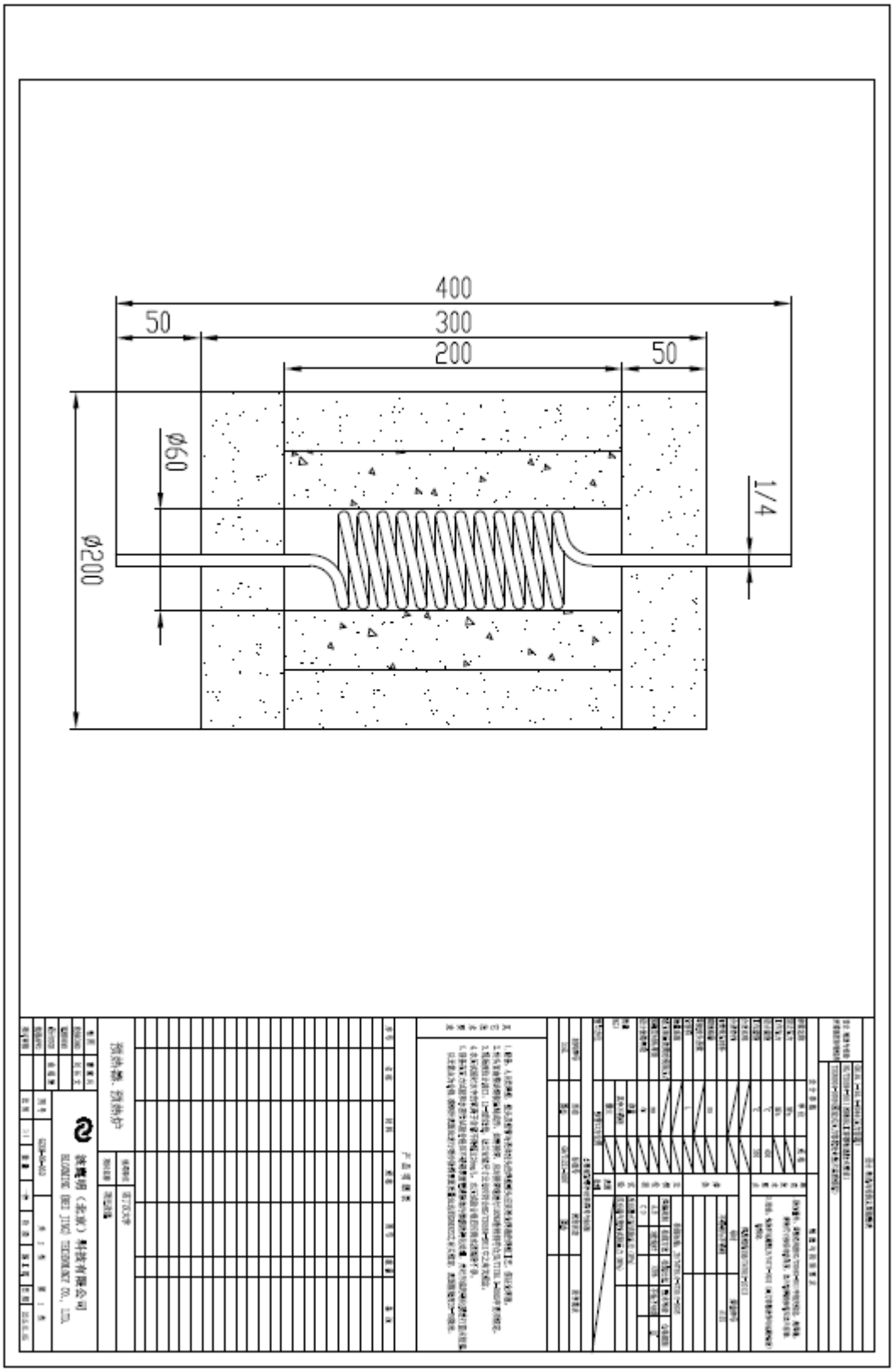

Figure A3.5: Design sheet for the preheater

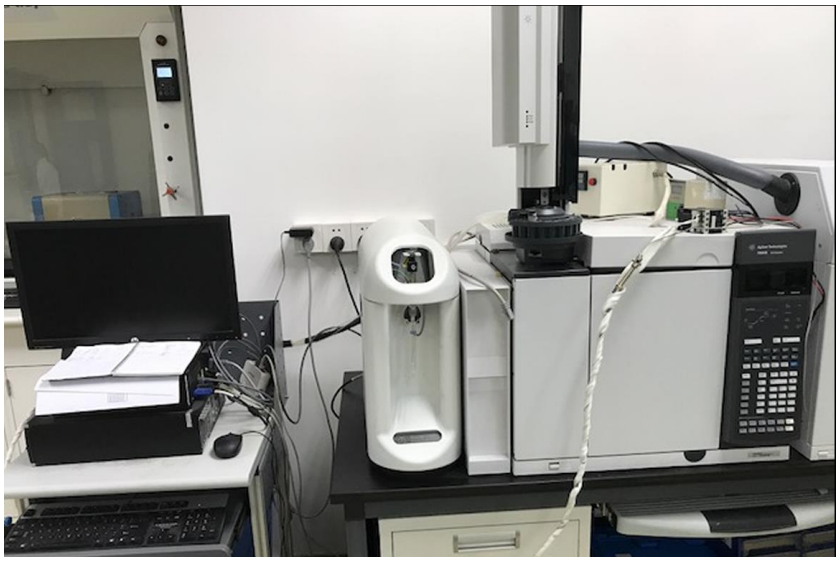

Figure A3.6: Gas Chromatograph-flame ionization detector (GC-FID)

Figure A3.7: Scanning Electron Microscopy (SEM) – Energy Dispersive X-ray Spectroscopy (EDX)

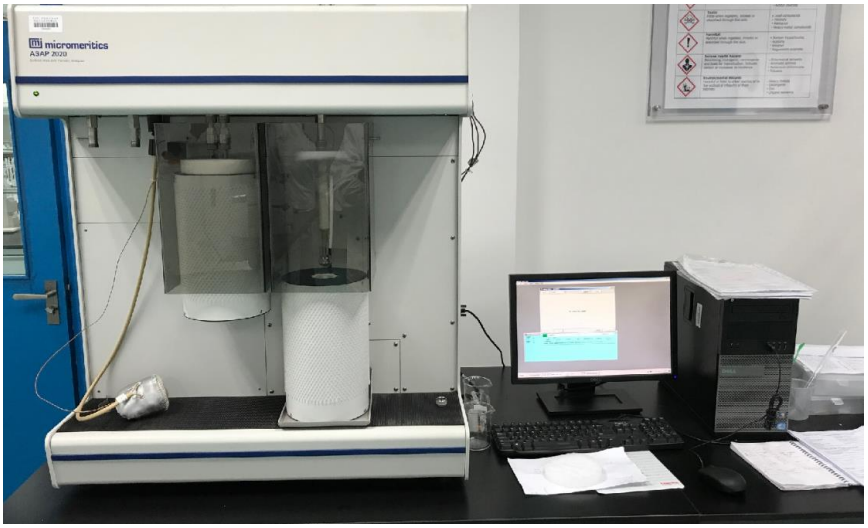

Figure A3.8: Micrometrics ASAP 2020 Surface Area and Porosity Analyser

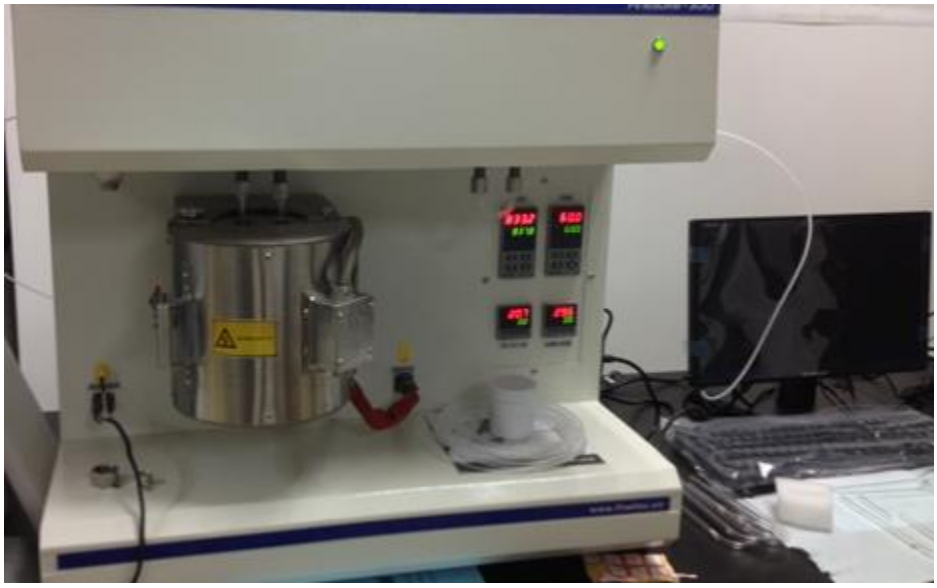

Figure A3.9: Temperature-Programmed Desorption (TPD) reactor

Figure A3.10: Hydrothermal Reactor

Figure A3.11: X-ray Diffractometer

Appendix B: Rig Design Specifications

波露明（北京）科技有限公司
BLOOMING (BEIJING) TECHNOLOGY CO., LTD.
地址：北京市朝阳区慧忠北里金科大厦432室
邮编：100012
电话：010-62680087 64808446
邮箱：blooming@bloomingtech.net
开户银行：工行六铺炕支行
账户：0200022319006834823

多功能催化剂性能评价装置配置及工艺流程

序号	名称	规格	品牌	单位	数量
1	质量流量计	介质：CO2、O2、H2、N2 、载气 操作压力：（max）6MPa or 20MPa 氢气流量：0～100ml/min 工作温度：常温 压差：≤0.3MPa 精度：±1% 输出信号：0-5V 接口：1/8″ 卡套 材质：316SS	BROOKS	台	5
2	计量泵	介质：液体原料液 工作压力：10MPa or 20MPa 流量（Max）：100mL/min 精度：±1% 接口：1/8″卡套 材质：316SS	ELDEX	台	1
3	湿式气表	防腐、带远传 气量：60L/h	国产	台	1
4	电子天平	60Kg±1g 带 RS232 通讯口	国产	台	1
5	减压阀	入口压力：25MPa 出口压力：20MPa 接口：1/4″ 卡套 材质：316SS 介质：CO2、O2、H2、N2 、载气	SWAGELOK	台	5
6	背压阀	压力控制范围：0～3500psig 温度：常温 接口：1/4″卡套 材质：316SS 介质：混合气体 进出口数量：一进一出 安装方式：面板安装	SWAGELOK	台	1
7	卸荷阀	压力范围：3000～3500psig 温度：500℃ 介质：H2、N2 等 接口：1/4″ 卡套 材质：316SS	SWAGELOK	个	2

地址：北京市朝阳区慧忠北里金利大厦432室
邮编：100012
电话：010-62680087 64808446
邮箱：blooming@bloomingtech.net
开户银行：工行六铺炕支行
账户：0200022319006834823

序号	名称	规格	品牌	单位	数量
8	压力传感器	压力：0～25MPa 接口：1/4"NPT 材质：316SS 输出： 4-20mA 电源：24DCV，不带现场显示	WIKA	个	1
9	普通压力表	量程:0～25MPa 精度：2.5级 接口：1/4"NPT（轴向带前边固定） 表盘直径：Φ63mm 检测方式：禁油检测	WIKA	个	14
10	精密压力表	量程：0～25MPa 温度：常温 精度：0.25级 接口：1/4"NPT（径向） 表盘直径：Φ150 检测方式：禁油检测	WIKA	个	1
11	针型阀	介质：CO2、O2、H2、N2 、载气等 温度：常温 接口：1/8" 卡套 材质：316SS	SWAGELOK	个	16
12	气体过滤器	介质：CO2、O2、H2、N2 、载气 压力（max）：3000psi 接口：1/8" 卡套 孔径：7μ 材质：316SS	SWAGELOK	个	6
13	液体过滤器	介质：液体原料液 温度：常温 接口：1/8" 卡套 孔径：40μ 材质：316SS	SWAGELOK	个	1
14	两通球阀	压力：3500psi 接口：1/8" 卡套 材质：316SS	SWAGELOK	个	24
15	三通球阀	压力：3500psi 接口：1/8" 卡套 材质：316SS	SWAGELOK	个	1
16	单向阀	开启压力：10psi 接口：1/8" 卡套 材质：316SS	SWAGELOK	个	6

地址：北京市朝阳区慧忠北里金科大厦432室
邮编：100012
电话：010-62680087 64808446
邮箱：blooming@bloomingtech.net
开户银行：工行六铺炕支行
账户：0200022319006834823

序号	名称	规格	品牌	单位	数量
17	各种连接件	接口：1/8″ 卡套、1/4″ 卡套 材质：316SS 耐温：常温 耐压力：3000psi	SWAGELOK	个	120
18	管线	管径:1/4″、1/8″ 卡套 材质：316L	SWAGELOK	米	100
19	预热器及预热炉	碳化硅炉瓦、等温开式炉、不锈钢外壳 温度：400℃ 材质：316L	BLOOMING	个	1
20	反应器	材质：316L 设计压力：22Mpa 设计温度：600℃ 使用压力：20Mpa 使用温度：常温~427℃ 催化剂装填量：100ml	BLOOMING	个	1
21	反应加热炉	操作温度（max）：600℃ 电炉段数：四段 电源：220VAC/50HZ	BLOOMING	个	1
22	盘管冷凝器	材质：304 设计压力：22Mpa 使用压力：20Mpa 冷却温度：40℃ 冷却方式：盘管水冷	BLOOMING	个	1
23	气液分离器	材质：316L 设计压力：25Mpa 使用压力：20Mpa 使用温度：常温 容积：3000ml	BLOOMING	个	1
24	缓存罐	材质：316L 设计压力：22Mpa 使用压力：20Mpa 使用温度：室温 容积：3000ml	BLOOMING	个	1
25	液体原料罐	50L	BLOOMING	个	1
26	工艺设备主体框架	材质：铝型材	BLOOMING	套	1
27	加热带	带保温	BRISKHEAT	批	1
28	热电偶	形式：K型热偶 测温范围：0~600℃	WATLOW	根	11
29	热偶插座	与热电偶配套	OMEGA	个	11

序号	名称	规格	品牌	单位	数量
30	补偿导线	K 型	神驰	米	90
31	固态继电器	40H	施耐德	个	6
32	流量控制	PI6100	WEST	个	5
33	温度控制	PI6100	WEST	个	6
34	流量检测	PI6100	WEST	个	5
35	温度检测	PI6100	WEST	个	5
36	液位检测	PI6100	WEST	个	1
37	电子天平检测	PI6100	WEST	个	1
38	串口服务器	RS232 或 RS485 双通道	华威创联	个	1
39	控制软件	IFIX 5.1	iFIX5.1	套	1
40	上位机计算机		DELL	台	1
41	镀锌线槽	40×40	国产	批	1
42	自控附件	施耐德空开、电源、端子、电线等	国产	批	1
43	控制柜	标准机柜	国产	个	1

波露明（北京）科技有限公司
BLOOMING (BEI JING) TECHNOLOGY CO., LTD.
地址：北京市朝阳区慧忠北里金科大厦432室
邮编：100012
电话：010-62680087 64808446
邮箱：blooming@bloomingtech.net
开户银行：工行六铺炕支行
账户：0200022319006834823

多功能催化剂性能评价装置工艺流程图

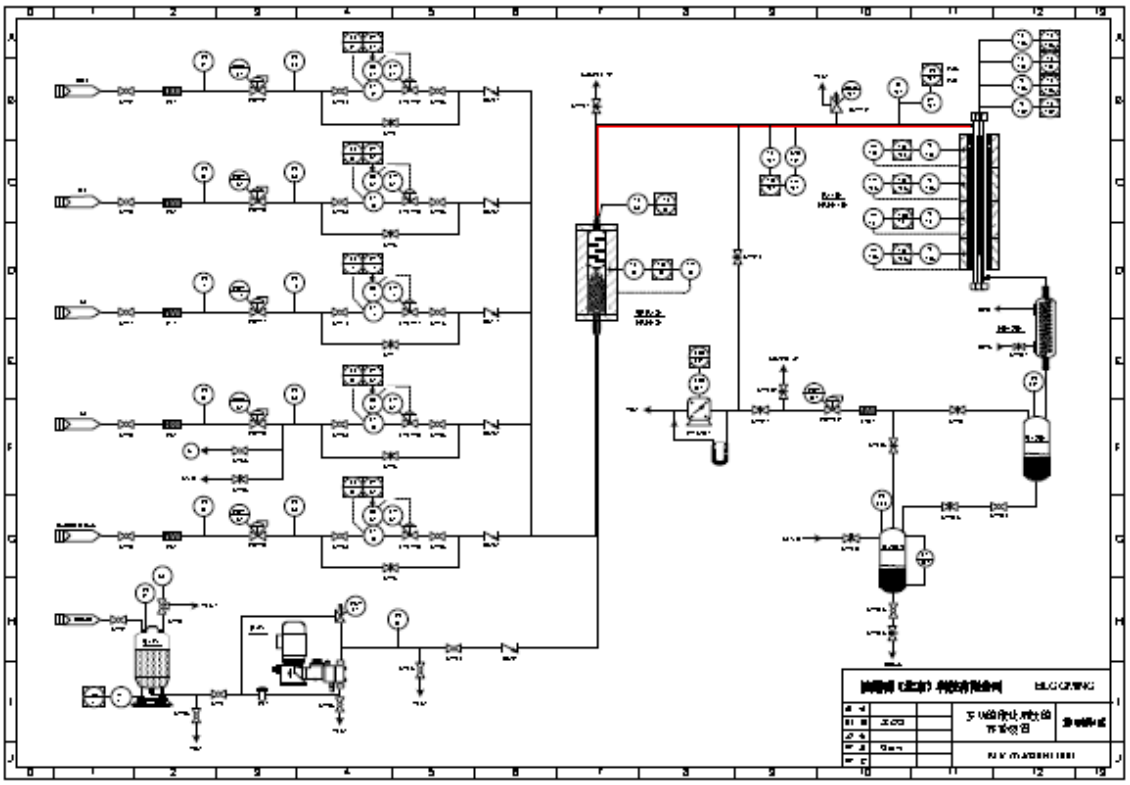

Figure B3.1: PID Flowsheet for Rig Design

Appendix C: Supporting Data for Chapter 4

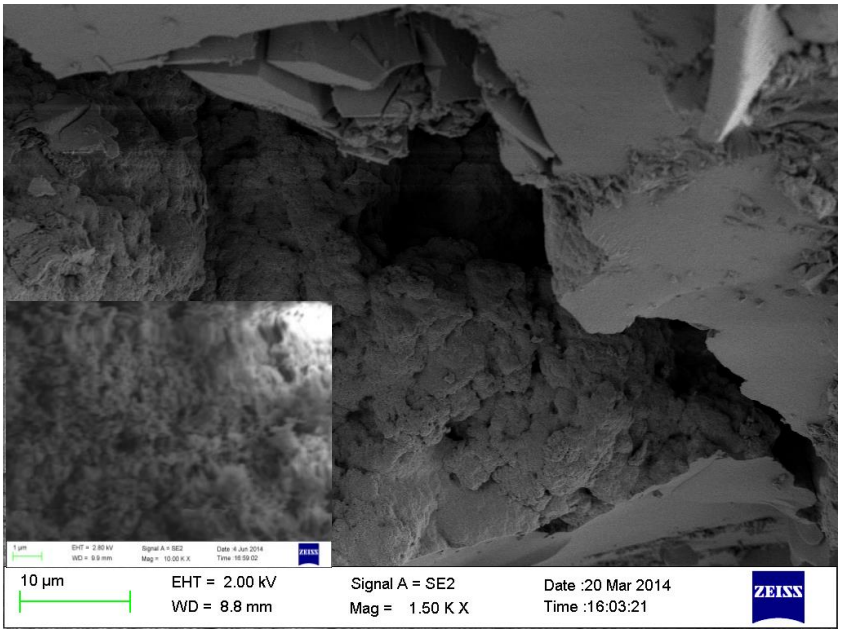

Figure C4.1: SEM image of zirconia aerogel, calcined at 523K.

Table C4.1: BET analysis of ZrO_2 aerogel at different calcination temperatures

BET Results	**ZrO_2-523K**	**ZrO_2-573K**	**ZrO_2-623K**
Surface Area (m^2/g)	251.84	229.26	193.12
Pore volume (cm^3/g)	0.17	0.14	0.12
Adsorption average pore width (nm)	2.65	2.36	2.49
Average Particle Size (nm)	23.82	26.17	31.07
Hysteresis Peak ($\frac{p}{p^o}$)	~0.50	~0.45	~0.45
Hysteresis Span ($\frac{p}{p^o}$)	0.40-0.65	0.40-0.53	0.40-0.55
Pore Distribution, 2-4nm (%)	71	84	85
Average Particle Size (nm)	23.82	26.17	31.07

Table C4.2: Comparison of TGA-DTA results with that of BET for ZrO_2 supports

Sample	T_c (K)	S_{BET} (m^2/g)	d_p (nm)	T_{ID} Range (K)	Residual Weight (%)	Interstitial Moisture Content (mole)
ZrO_2-523	523	251.84	23.82	300-700	80.06	1.70
ZrO_2-573	573	229.26	26.17	300-700	86.86	1.04
ZrO_2-623	623	193.12	31.07	300-700	86.90	1.03

T_{ID} = Intermolecular Dehydration Temperature

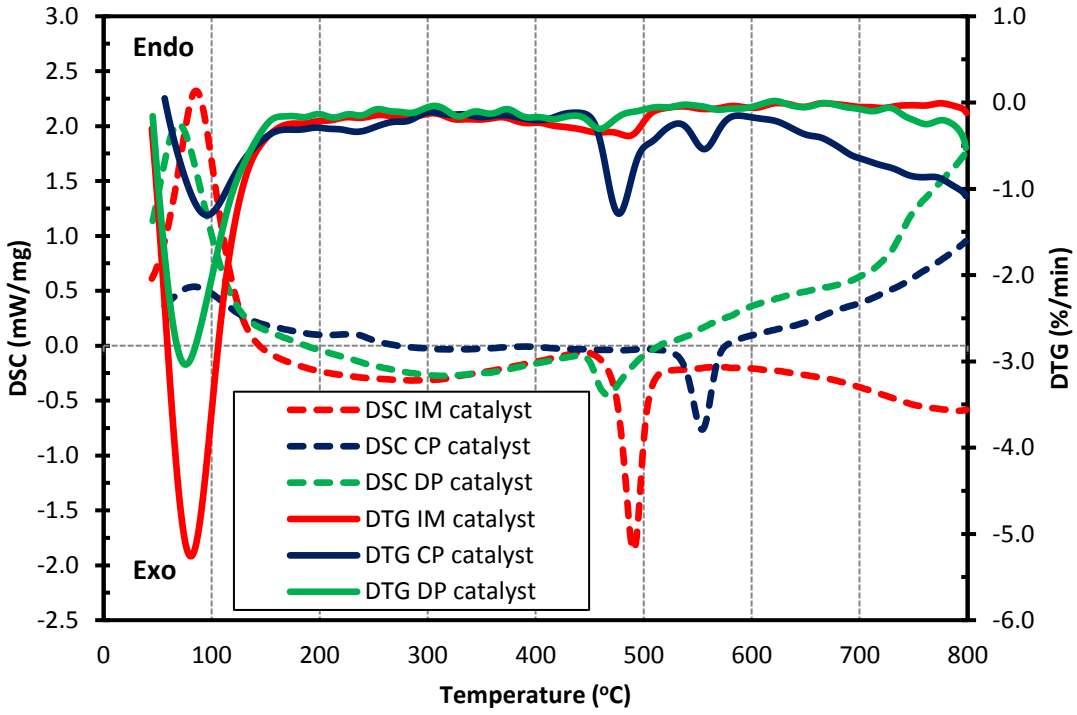

Figure C4.2: Comparison of Thermal Characterization of CuO/ZrO_2 catalyst with 30% Cu-loading at prepared via impregnation (IM), co-precipitation (CP) and deposition precipitation (DP)

Appendix D: Supporting Data for Chapter 6

Table D6.1: Average CO_2 uptake for LDHn and LDH-MEAn (n being the molar ratio of APTES to SDS)

Sample		LDH5	LDH2	LDH1	LDH-MEA5	LDH-MEA2	LDH-MEA1
55°C	1st Trial	0.76	0.37	0.63	1.96	1.07	1.32
	2nd Trial	0.88	0.42	0.55	0.94	0.65	0.93
	Average	**0.82**	**0.395**	**0.59**	**1.45**	**0.86**	**1.125**
80°C	1st Trial	0.52	0.2	0.37	0.76	0.32	0.46
	2nd Trial	0.56	0.2	0.26	0.63	0.12	0.34
	Average	**0.54**	**0.2**	**0.315**	**0.695**	**0.22**	**0.4**

Table D6.2: EDX results showing the elemental configuration for LDHn and LDH-MEAn (n being the molar ratio of APTES to SDS)

Element	Weight% (1mm)			Weight% (20µm)		
	LDH5	LDH2	LDH1	LDH5	LDH2	LDH1
C	61.00	62.86	61.39	51.35	40.90	58.69
O	29.62	28.35	29.56	26.74	35.52	18.42
Na	0.08	2.05	0.08	7.35	0.08	8.24
Mg	2.86	1.33	2.85	1.06	6.12	0.40
Al	0.95	0.38	0.95	0.27	2.15	0.17
Si	3.72	1.42	3.71	1.17	11.04	-
S	0.93	3.31	0.93	11.41	2.62	13.87
N	0.84	0.30	0.20	0.65	1.57	0.20
Total	**100.00**	**100.00**	**100.00**	**100.00**	**100.00**	**100.00**

(a)

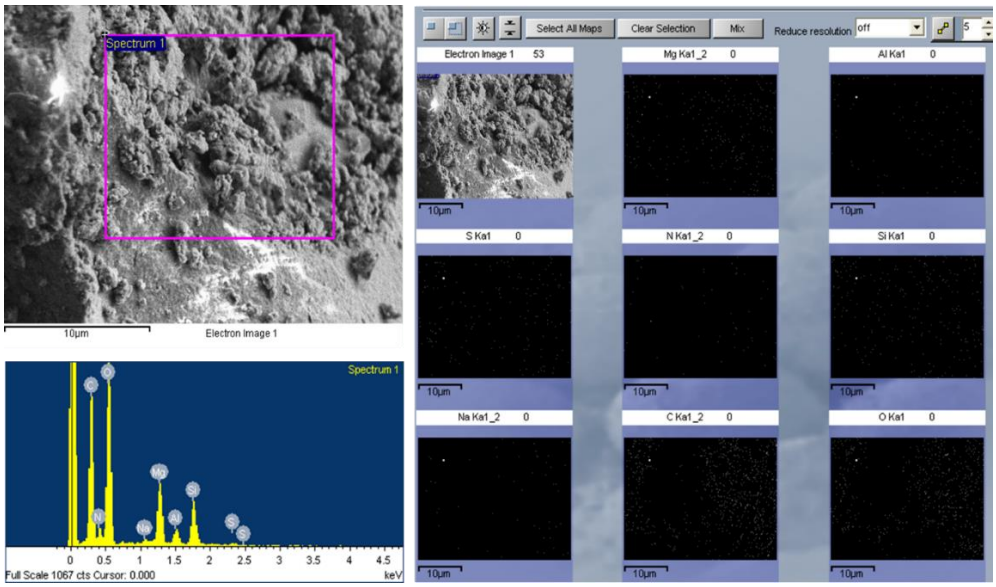

(b)

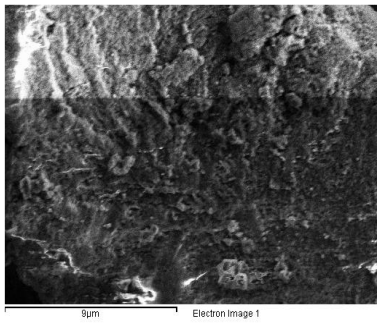
9µm
Electron Image 1

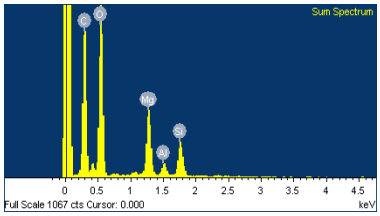
Sum Spectrum
0 0.5 1 1.5 2 2.5 3 3.5 4 4.5
Full Scale 1067 cts Cursor: 0.000
keV

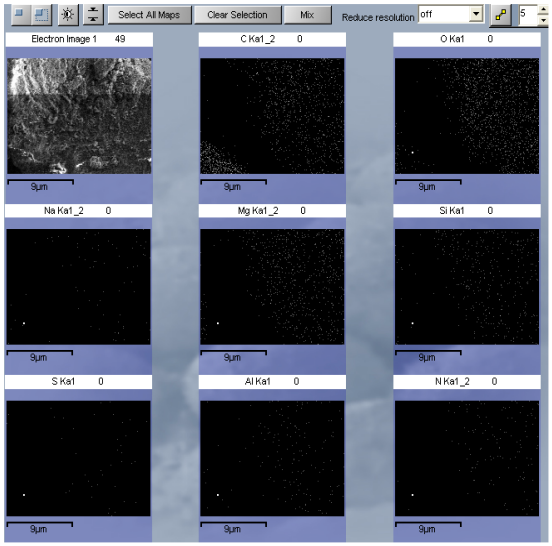
Select All Maps
Clear Selection
Mix
Reduce resolution
off
5
Electron Image 1 49
C Ka1_2 0
O Ka1 0
Na Ka1_2 0
Mg Ka1_2 0
Si Ka1 0
S Ka1 0
Al Ka1 0
N Ka1_2 0
9µm

(c)

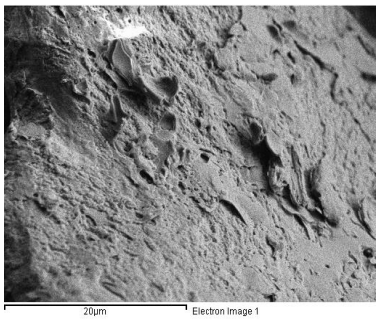
20µm
Electron Image 1

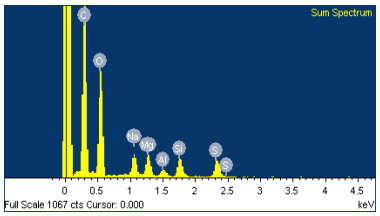
Sum Spectrum
0 0.5 1 1.5 2 2.5 3 3.5 4 4.5
Full Scale 1067 cts Cursor: 0.000
keV

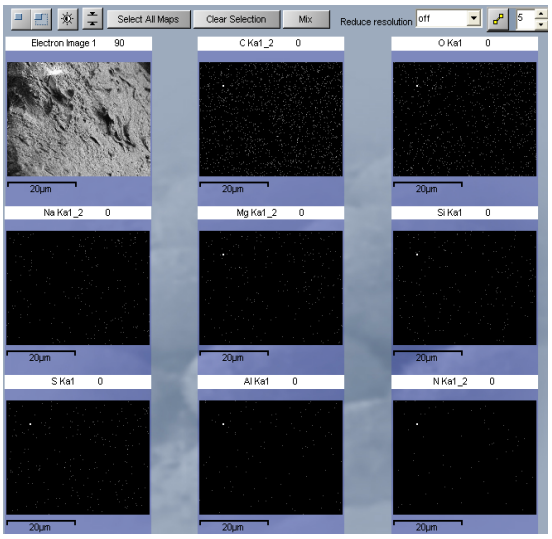
Select All Maps
Clear Selection
Mix
Reduce resolution
off
5
Electron Image 1 90
C Ka1_2 0
O Ka1 0
Na Ka1_2 0
Mg Ka1_2 0
Si Ka1 0
S Ka1 0
Al Ka1 0
N Ka1_2 0
20µm

(d)

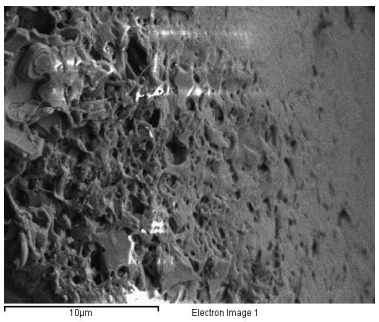
10µm
Electron Image 1

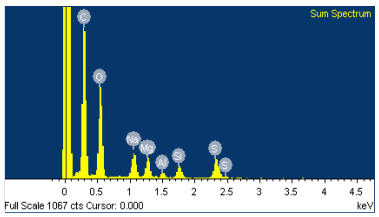
Sum Spectrum
0 0.5 1 1.5 2 2.5 3 3.5 4 4.5
Full Scale 1067 cts Cursor: 0.000
keV

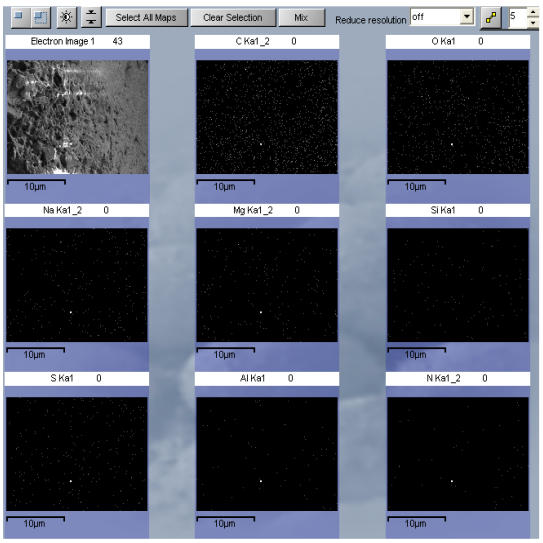
Select All Maps
Clear Selection
Mix
Reduce resolution
off
5
Electron Image 1 43
C Ka1_2 0
O Ka1 0
Na Ka1_2 0
Mg Ka1_2 0
Si Ka1 0
S Ka1 0
Al Ka1 0
N Ka1_2 0
10µm

(e)

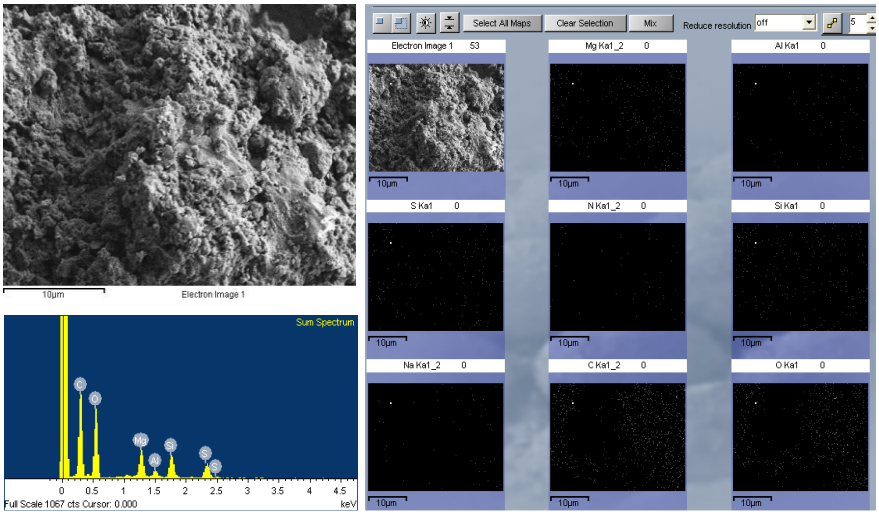

(f)

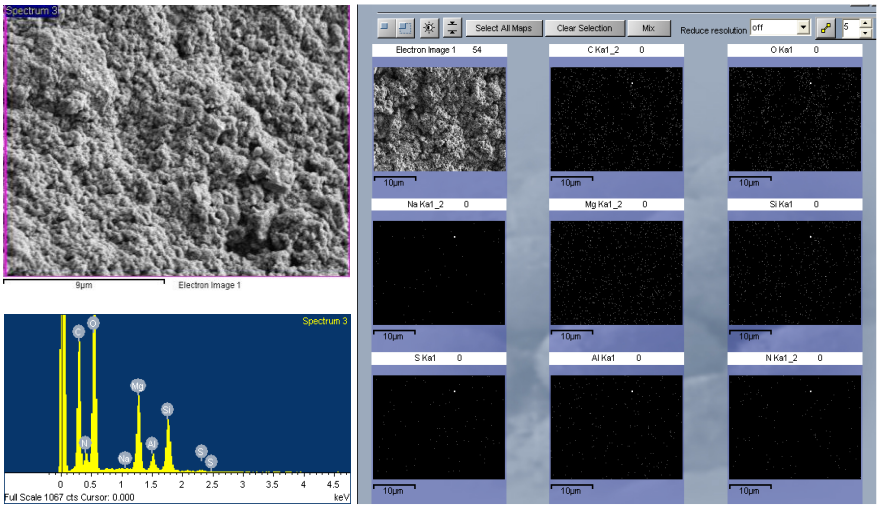

Figure D6.1: EDX elemental dispersion across the internal micro structures of the prepared adsorbents: (a) LDH5, (b) LDH-MEA5, (c) UB-LDH5, (d) UB-MEA5, (e) UH-LDH5, and (f) UH-MEA5.

Table D6.3: Amine loading of adsorbents containing monomeric amines presented in ascending order.

Sample	Support	Amine Loading (mmol/g)	Reference
ITQ-6/AP	ITQ-6 zeolite	1.26	(1)
MCM-41-G5	MCM-41	1.72	(2)
MgAl DS 0.2	LDH	1.91	(3)
SBA-15/AP2	SBA-15	2	(1)
MgAl DS 1	LDH	2.07	(3)
MgAl DS 0.5	LDH	2.13	(3)
MCM-41-G10	MCM-41	2.35	(2)
APS-loaded CNT	Carbon nanotube	2.44	(4)
APS-MCM-48	MCM-48	2.45	(5)
APTMS-DS	Layered organosilica	2.56	(6)
MgAl MEA 0.2	LDH	2.59	(3)
APS/SBA(III)	SBA-15	2.61	(7)
SBA-15/APS	SBA-15	2.72	(8)
SBA-12/APS	SBA-12	2.76	(8)
1N-APS-SDS-0.4	AMS	2.88	(2)
1N-APS-SDS-0.5	AMS	2.93	(2)
MCM-41/APS	MCM-41	3	(8)
MgAl MEA 0.5	LDH	3.35	(3)
ex-AMS	AMS	3.4	(9)
MgAl MEA 1	LDH	3.62	(3)

APS = aminopropyltriethoxysilane
AMS = anionic surfactant-mediated mesoporous silica
LDH = layered double hydroxide
MEA = monoethanolamine
SDS = sodium dodecyl sulfate

Table D6.4: BET results of LDH samples prepared by conventional co-precipitation (conv), ultrasonic mediated (US) and Hydrothermal (HPH) routes

Sample	SBET	VTotal	Vmicro	Average Pore Width	%Micro
	(m2/g)	(cm^3/g)	(cm^3/g)	(nm)	(%)
Conv	25.03	0.0161	0.0008	2.57	4.97
US	171.20	0.5528	0.0229	12.92	4.14
HPH	311.18	1.4005	0.0023	18.00	0.16

Table D6.5: Thermal degradation of amine modified samples prepared via conventional (LDH-MEAn) and ultrasonic irradiation route (UB-MEAn and UH-MEAn)

Preparation Route	APTES/SDS mole ratio, n	Sample Name	Weight Loss (%)			
			T<150°C	150< T<750°C	750°C< T	Total
Conventional	5	LDH-MEA5	10.03	38.97	4.00	**53.00**
	2	LDH-MEA2	9.79	42.08	3.83	**55.70**
	1	LDH-MEA1	11.17	46.14	6.40	**63.71**
Ultrasonic Bath	5	UB-MEA5	11.38	31.46	9.18	**52.02**
	2	UB-MEA2	10.64	32.98	2.48	**46.10**
	1	UB-MEA1	-	-	-	-
Ultrasonic Horn	5	UH-MEA5	11.07	38.02	3.20	**52.29**
	2	UH-MEA2	-	-	-	-
	1	UH-MEA1	-	-	-	-

Reference

1. Ostwal M, Singh RP, Dec SF, Lusk MT, Way JD. 3-Aminopropyltriethoxysilane functionalized inorganic membranes for high temperature CO2/N2 separation. Journal of Membrane Science. 2011 3/1/;369(1–2):139-47.
2. Cui S, Cheng W, Shen X, Fan M, Russell A, Wu Z, et al. Mesoporous amine-modified SiO2 aerogel: a potential CO2 sorbent. Energy & Environmental Science. 2011;4(6):2070-4.
3. Wang J, Stevens LA, Drage TC, Snape CE, Wood J. Preparation and CO2 adsorption of amine modified layered double hydroxide via anionic surfactant-mediated route. Chemical Engineering Journal. 2012;181-182:267-75.
4. Hiyoshi N, Yogo K, Yashima T. Adsorption characteristics of carbon dioxide on organically functionalized SBA-15. Microporous and Mesoporous Materials. 2005 9/15/;84(1–3):357-65.
5. Huang HY, Yang RT, Chinn D, Munson CL. Amine-grafted MCM-48 and silica xerogel as superior sorbents for acidic gas removal from natural gas. Industrial and Engineering Chemistry Research. 2003;42(12):2427-33.
6. Kim S-N, Son W-J, Choi J-S, Ahn W-S. CO2 adsorption using amine-functionalized mesoporous silica prepared via anionic surfactant-mediated synthesis. Microporous and Mesoporous Materials. 2008 11/1/;115(3):497-503.
7. Kim S, Ida J, Guliants VV, Lin JYS. Tailoring pore properties of MCM-48 silica for selective adsorption of CO 2. Journal of Physical Chemistry B. 2005;109(13):6287-93.
8. Sayari A, Belmabkhout Y, Serna-Guerrero R. Flue gas treatment via CO2 adsorption. Chemical Engineering Journal. 2011 7/15/;171(3):760-74.
9. Nik OG, Nohair B, Kaliaguine S. Aminosilanes grafting on FAU/EMT zeolite: Effect on CO2 adsorptive properties. Microporous and Mesoporous Materials. 2011 8//;143(1):221-9.

Appendix E: Supporting Data for Chapter 8

Table E8.1: EDX results showing the elemental configuration for synthesised LDH via conventional, ultrasonic and hydrothermal route

Element	Weight (%)		
	Conv	US	HPH
C	55.42	51.16	13.69
N	0.70	3.11	2.55
O	28.86	28.44	44.03
Mg	1.14	6.10	13.92
Al	0.29	1.57	6.26
Si	1.26	5.16	18.04
S	12.32	4.46	1.51
Total	**100.00**	**100.00**	**100.00**

Table E8.2: XPS results comparing surface elemental content of LDH prepared via conventional, ultrasonic and hydrothermal route

Spectrum	Position BE (eV)			Atomic Concentration (%)		
	Conv	US	HPH	Conv	US	HPH
O 1s	529.00	529.10	529.85	31.71	23.67	57.68
N 1s	396.90	396.65	397.90	6.21	5.70	1.79
C 1s	282.20	282.35	282.40	50.77	60.66	15.20
S 2p	166.10	166.00	1486.69	0.60	1.19	0.00
Al 2p	71.70	71.85	72.20	1.72	1.51	6.30
Mg 2p	47.20	46.95	48.35	5.36	2.80	7.53
Si 2p	99.15	99.30	100.70	3.63	4.47	11.50
				100.00	**100.00**	**100.00**

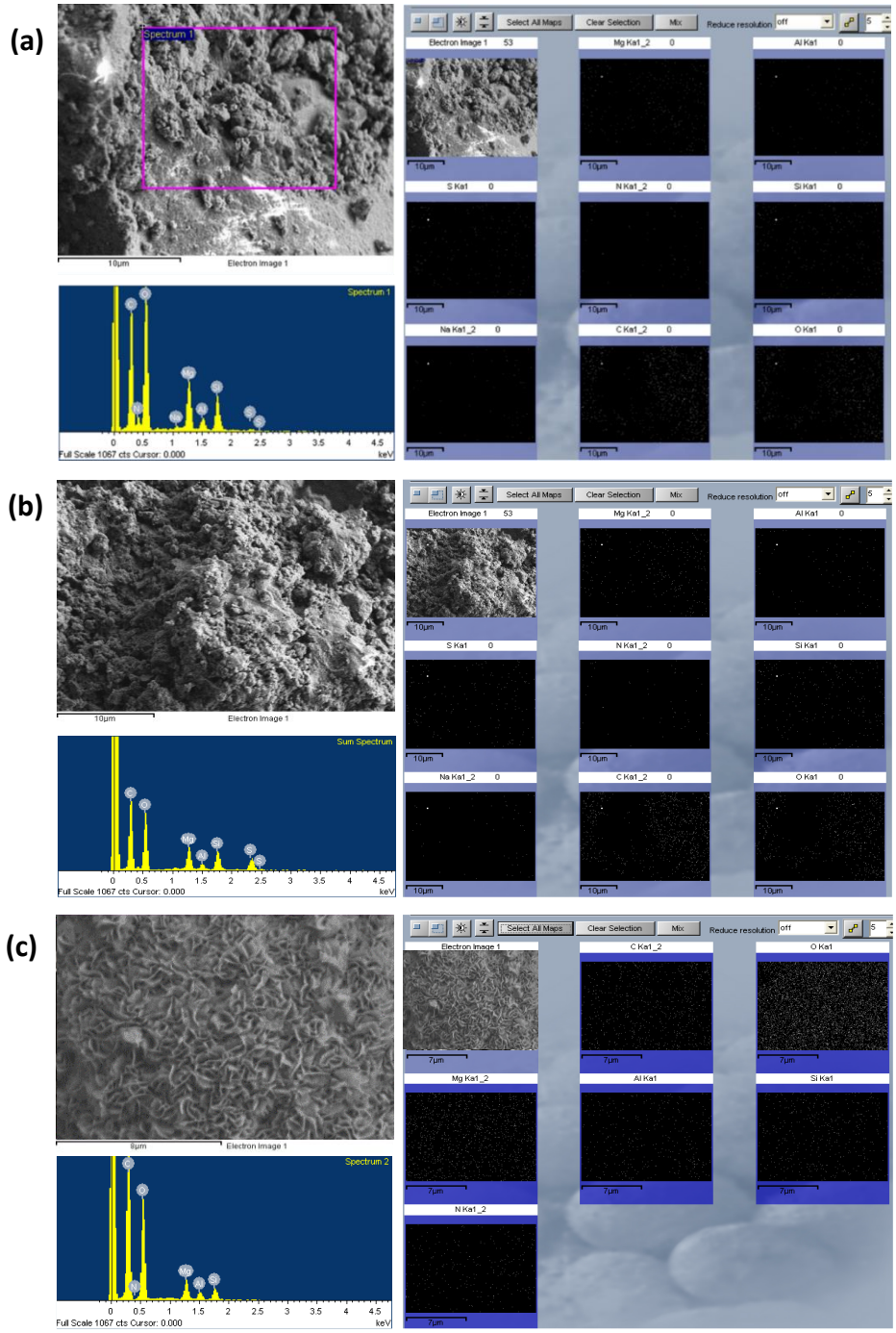

Figure E8.1: EDX elemental dispersion across the internal micro structures of the prepared adsorbents: (a) Conv-LDH, (b) US-LDH and (c) HPH-LDH

Table E8.3: Amine loading of adsorbents containing monomeric amines presented in ascending order.

Sample	Support	Amine Loading (mmol/g)	Reference
LDH5	LDH	0.46	(1)
ITQ-6/AP	ITQ-6 zeolite	1.26	(2)
MCM-41-G5	MCM-41	1.72	(3)
MgAl DS 0.2	LDH	1.91	(4)
SBA-15/AP2	SBA-15	2	(2)
MgAl DS 1	LDH	2.07	(4)
MgAl DS 0.5	LDH	2.13	(4)
UH-LDH5	LDH	2.22	(1)
MCM-41-G10	MCM-41	2.35	(3)
APS-loaded CNT	Carbon nanotube	2.44	(5)
APS-MCM-48	MCM-48	2.45	(6)
APTMS-DS	Layered organosilica	2.56	(7)
MgAl MEA 0.2	LDH	2.59	(4)
APS/SBA(III)	SBA-15	2.61	(8)
SBA-15/APS	SBA-15	2.72	(9)
SBA-12/APS	SBA-12	2.76	(9)
1N-APS-SDS-0.4	AMS	2.88	(3)
1N-APS-SDS-0.5	AMS	2.93	(3)
MCM-41/APS	MCM-41	3	(9)
MgAl MEA 0.5	LDH	3.35	(4)
ex-AMS	AMS	3.4	(10)
MgAl MEA 1	LDH	3.62	(4)
LDH-MEA5	LDH	4.71	(1)
UH-LDH5	LDH	5.24	(1)

APS = aminopropyltriethoxysilane
AMS = anionic surfactant-mediated mesoporous silica
LDH = layered double hydroxide
MEA = monoethanolamine
SDS = sodium dodecyl sulfate

Table E8.4: Thermal degradation of prepared LDHs and amine modified LDHs prepared via conventional (Conv-LDH and Conv-MEA), ultrasonic irradiation (US-LDH and US-MEA), ultrasonic-assisted hydrothermal route (HPH-LDH and HPH-MEA)

Preparation Route	Sample Name	Weight Loss (%)			
		T<150°C	150< T<750°C	750°C< T	Total
LDH					
Conventional	Conv-LDH	8.35	56.13	4.50	**68.98**
Ultrasonic	US-LDH	5.17	41.14	21.81	**68.12**
Hydrothermal	HPD-LDH	3.41	6.20	0.95	**10.56**
LDH-MEA					
Conventional	Conv-MEA	10.03	38.97	4.00	**53.00**
Ultrasonic	UH-MEA	11.07	38.02	3.20	**52.29**
Hydrothermal	HPH-MEA	-	35.72	2.45	**38.17**

Table E8.5: Average CO_2 uptake and cyclic sorption capacity of prepared LDH and amine functionalized LDH samples

Sample	CO_2 Uptake (mmol/g)		Average CO_2 Uptake (mmol/g)	Cyclic Sorption Capacity (mmol/g)			Cyclic Efficiency[b] (%)
	1st Trial	2nd Trial		1st Cycle	Q_d[a]	2nd Cycle	
Conv-LDH	0.76	0.88	0.82				
Conv-MEA	1.96	0.94	1.45	1.26	1.08	0.75	59.52 %
US-LDH	0.70	0.61	0.66				
US-MEA	1.42	1.32	1.37	1.44	1.12	1.10	76.39 %
HPH-LDH	0.89	0.86	0.88				
HPH-MEA	3.96	3.54	3.75	3.96	3.68	2.09	52.78 %

[a] amount of CO_2 regenerated by thermally-assisted desorption in N_2 atmosphere

[b] Cyclic efficiency = $\frac{2^{nd}\text{Cycle}}{1^{st}\text{Cycle}} \times 100\%$

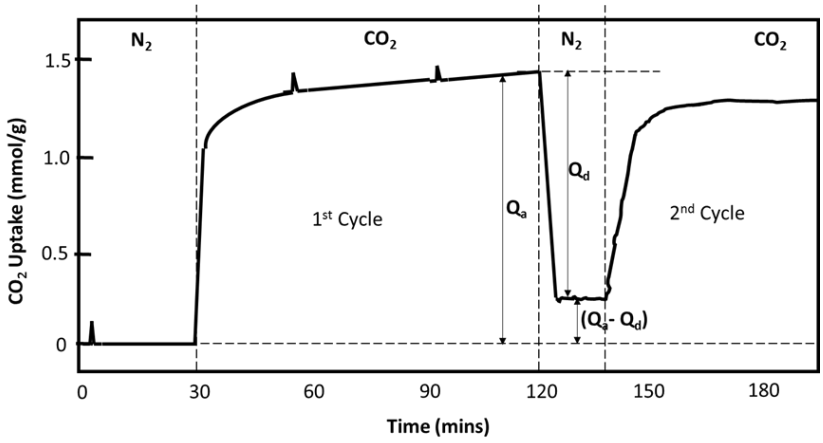

Sample	Cyclic Adsorption Capacity (mmol/g)		$RE^a = \frac{Q_d}{Q_a} \times 100\%$
	1st Cycle	2nd Cycle	
Conv-MEA	1.26	0.75	86 %
US-MEA	1.44	1.10	78 %
HPH-MEA	3.96	2.09	93 %

[a] Regeneration efficiency

Figure E8.2: Cyclic adsorption capacity of amine functionalized LDH prepared via different routes

Reference

1. Ezeh CI, Huang X, Yang X, Sun C-g, Wang J. Sonochemical surface functionalization of exfoliated LDH: Effect on textural properties, CO2 adsorption, cyclic regeneration capacities and subsequent gas uptake for simultaneous methanol synthesis. Ultrasonics Sonochemistry. 2017;39:330-43.
2. Ostwal M, Singh RP, Dec SF, Lusk MT, Way JD. 3-Aminopropyltriethoxysilane functionalized inorganic membranes for high temperature CO2/N2 separation. Journal of Membrane Science. 2011;369(1–2):139-47.
3. Cui S, Cheng W, Shen X, Fan M, Russell A, Wu Z, et al. Mesoporous amine-modified SiO2 aerogel: a potential CO2 sorbent. Energy & Environmental Science. 2011;4(6):2070-4.
4. Wang J, Stevens LA, Drage TC, Snape CE, Wood J. Preparation and CO2 adsorption of amine modified layered double hydroxide via anionic surfactant-mediated route. Chemical Engineering Journal. 2012;181-182:267-75.
5. Hiyoshi N, Yogo K, Yashima T. Adsorption characteristics of carbon dioxide on organically functionalized SBA-15. Microporous and Mesoporous Materials. 2005;84(1–3):357-65.
6. Huang HY, Yang RT, Chinn D, Munson CL. Amine-grafted MCM-48 and silica xerogel as superior sorbents for acidic gas removal from natural gas. Industrial and Engineering Chemistry Research. 2003;42(12):2427-33.
7. Kim S-N, Son W-J, Choi J-S, Ahn W-S. CO2 adsorption using amine-functionalized mesoporous silica prepared via anionic surfactant-mediated synthesis. Microporous and Mesoporous Materials. 2008;115(3):497-503.
8. Kim S, Ida J, Guliants VV, Lin JYS. Tailoring pore properties of MCM-48 silica for selective adsorption of CO 2. Journal of Physical Chemistry B. 2005;109(13):6287-93.
9. Sayari A, Belmabkhout Y, Serna-Guerrero R. Flue gas treatment via CO2 adsorption. Chemical Engineering Journal. 2011;171(3):760-74.
10. Nik OG, Nohair B, Kaliaguine S. Aminosilanes grafting on FAU/EMT zeolite: Effect on CO2 adsorptive properties. Microporous and Mesoporous Materials. 2011;143(1):221-9.

Appendix F: Copies of Published Articles

Ultrasonics - Sonochemistry 39 (2017) 330–343

Contents lists available at ScienceDirect

Ultrasonics - Sonochemistry

journal homepage: www.elsevier.com/locate/ultson

Sonochemical surface functionalization of exfoliated LDH: Effect on textural properties, CO_2 adsorption, cyclic regeneration capacities and subsequent gas uptake for simultaneous methanol synthesis

Collins I. Ezeh[a], Xiani Huang[a], Xiaogang Yang[a,*], Cheng-gong Sun[b,*], Jiawei Wang[c]

[a] Department of Mechanical, Materials and Manufacturing Engineering, University of Nottingham Ningbo, University Park, Ningbo 315100, PR China
[b] Department of Chemical and Environmental Engineering, University of Nottingham, University Park, Nottingham NG7 2RD, UK
[c] Chemical Engineering & Applied Chemistry, School of Engineering and Applied Science, Aston University, Birmingham B4 7ET, UK

ARTICLE INFO

Keywords:
CO_2 capture
Layered double hydroxide
Ultrasound
Adsorption
Regeneration

ABSTRACT

To improve CO_2 adsorption, amine modified Layered double hydroxide (LDH) were prepared via a two stage process, SDS/APTS intercalation was supported by ultrasonic irradiation and then followed by MEA extraction. The prepared samples were characterised using Scanning electron microscope-Energy dispersive X-ray spectroscopy (SEM-EDX), X-ray Photoelectron Spectroscopy (XPS), X-ray diffraction (XRD), Temperature Programmed Desorption (TPD), Brunauer-Emmett-Teller (BET), and Thermogravimetric analysis (TGA), respectively. The characterisation results were compared with those obtained using the conventional preparation method with consideration to the effect of sonochemical functionalization on textural properties, adsorption capacity, regeneration and lifetime of the LDH adsorbent. It is found that LDHs prepared by sonochemical modification had improved pore structure and CO_2 adsorption capacity, depending on sonic intensity. This is attributed to the enhanced deprotonation of activated amino functional groups via the sonochemical process. Subsequently, this improved the amine loading and effective amine efficiency by 60% of the conventional. In addition, the sonochemical process improved the thermal stability of the adsorbent and also, reduced the irreversible CO_2 uptake, CUirrev, from 0.18 mmol/g to 0.03 mmol/g. Subsequently, improving the lifetime and ease of regenerating the adsorbent respectively. This is authenticated by subjecting the prepared adsorbents to series of thermal swing adsorption (TSA) cycles until its adsorption capacity goes below 60% of the original CO_2 uptake. While the conventional adsorbent underwent a 10 TSA cycles before breaking down, the sonochemically functionalized LDH went further than 30 TSA cycles.

1. Introduction

Carbon dioxide adsorption is viewed as one of the promising methods in Carbon Capture and Storage (CCS) technology [1,2]. It has been widely accepted that an estimated 30–50% energy requirement reduction can be obtained when compared to absorption by amine solvents [3,4]. However, numerous factors must be considered for achieving this optimum performance as pointed out by Drage et al. [4]. Extensive reviews on materials used for CO_2 adsorption have been done by many researchers. These materials include amine polymers [5,6], immobilized amines [7,8], carbonaceous materials [9–11], Layered double hydroxides (LDHs) [2,12,13], zeolites [14–16] and organic-inorganic hybrids [17–19]. Owing to its comparably high adsorption capacity and numerous catalytic applications [13,20], the LDHs has been broadly investigated and considered to be one of the most promising flexible adsorbents [21]. In addition, its ionic inter-layered structural configuration provides the material with relatively high contact surface area and active basic sites to serve as a catalyst (or support) [20]. However, the material is challenged by its low CO_2 uptake, regeneration capacity and thermo-stability [21,22].

The low adsorption capacity of LDH is partly attributed to the poor textural characteristics [23,24] and low amine loading as reported in previous studies [2]. Adopted methods to improve these features involved the use of anionic surfactants and organoalkoxysilane amines which served the purpose of widening the interlayer gallery of the LDHs to bolster its exfoliation process [12] while simultaneously increasing the amine content [25]. Frequently used surfactants are sodium dodecyl sulphate (SDS) [2,26] and sodium dodecyl sulphonate [27], while the organoalkoxysilanes includes N-trimethoxysilylpropyl-N,N,N-trimethylammonium chloride [28], (3-aminopropyl)-triethoxysilane (APTS)

* Corresponding authors.
E-mail addresses: Xiaogang.Yang@nottingham.edu.cn (X. Yang), cheng-gong.sun@nottingham.ac.uk (C.-g. Sun).

http://dx.doi.org/10.1016/j.ultsonch.2017.04.041
Received 24 January 2017; Received in revised form 27 April 2017; Accepted 27 April 2017
Available online 03 May 2017
1350-4177/

[2,27,29] and (3-aminopropyl)-trimethoxysilane (ATMS) [26]. Nonetheless, reported amine loading and subsequent adsorption capacity of the adsorbent is not satisfactory. This was attributed to the poor pore structure of the adsorbent [24]. To further enhance the porosity and textural properties of the adsorbent, sonic irradiation has been applied in chemical synthesis of the adsorbent. Ultrasonic technology has been observed to rapidly promote inorganic and organic reactions without weakening the final material properties [23]. Furthermore, this technology improves the porosity and surface area of the synthesised material in addition to increasing metallic dispersion across the material [13]. However, in its industrial applicability, the prepared adsorbent should be able to withstand the thermal atmosphere during adsorption. Review of sonochemical route reports that ultrasonic irradiation can lead to detrimental acoustic cavitation [30] which can result to breakdown of the material. This can be partly due to the sonic intensity. Another crucial feature of LDH for industrial application is the lifetime and ease of regenerating the adsorbent. The ease of regeneration will reduce the energy required for CO_2 recovery; hence, improving the overall capture efficiency. Moreover, the adsorbents lifetime will define the rate of replacing the adsorbent, consecutively affecting the process economics.

In this work, we have understudied the contribution of the sonochemical preparation of functionalized LDH to its industrial applicability with regards to its textural characteristics, thermal strength, adsorption and cyclic regeneration capacity, as well as its impact for further gaseous adsorption. The LDH adsorbents were synthesised via anionic surfactant interaction and amine extraction through ultrasonic modulation. The adopted amine used for functionalization of the LDH is monoethanolamine (MEA). The obtained LDHs were characterised using Scanning Electron Microscope (SEM), Energy Dispersion X-ray Spectroscopy (EDX), Brunauer-Emmett-Teller (BET), Thermal Gravimetric Analyzer (TGA), Temperature-Programmed Desorption (TPD), X-ray Photoelectron Spectroscopy (XPS) and X-ray Diffraction (XRD). With consideration to the energy demand for CO_2 recovery, transportation and storage, the thermal swing adsorption cycle (TSA) was favoured against the pressure swing adsorption (PSA) to study the cyclic regeneration of the adsorbent [5]. To this regard, the regeneration of the adsorbent was carried out isothermally at ambient pressure using N_2 as the stripping gas. The adsorbents lifetime was also examined over numerous TSA cycles till its CO_2 uptake is 60% of the original sorption capacity.

2. Experimental

2.1. Materials

The LDHs were prepared via different route: co-precipitation and ultrasonic mediated means. Subsequently, MEA extractions of these LDHs were carried out to produce the amine modified LDHs. All reagents used for material synthesis were purchased from SinoPharm Chemical Reagents Co. Ltd. The CO_2 and N_2 gases used for characterization and adsorption measurements are 99.99% pure and were supplied by Linde Group, China.

2.2. Sample synthesis

For *MgAl LDH,* 200 ml solution containing APTS (≥98%) and SDS (≥86%) (molar ratio: 5:1) respectively dissolved in a mixture of 50 ml C_2H_5OH (≥99.7%) and 150 ml distilled water was stirred for about 30 min at a temperature of 60 °C until the pH stabilized at about 10.3. This solution was then reacted with $Mg(NO_3)_2{\cdot}6H_2O$ (≥98%) and $Al(NO_3)_3{\cdot}9H_2O$ (≥99%) (molar ratio: 3:1, dissolved in 100 ml of distilled water) solution by adding the latter dropwise while maintaining the temperature of the former at 60 °C. pH of the mixture was regulated towards 10 by adding 4 M NaOH (≥96%) solution. The substrate with a molar ratio of Mg:Al:APTS:SDS = 3:1:5:1 was then aged for 20hr with the temperature and stirring maintained. The precipitates were filtered, washed with distilled water and then dried in a vacuum oven (500 mbar at 70 °C) overnight. This sample is labelled as LDH5. Varying the amount of SDS, two other samples were produced with mole ratios of Mg:Al:APTS:SDS = 3:1:5:2.5 and 3:1:5:5 labelled as LDH2 and LDH1 respectively. Using the same chemical composition and process, a set of new samples were prepared using sonicated mixing either by ultrasonic horns (high intensity sonication, 600 W) or bath (low intensity sonication, 150 W). These samples are labelled as UH-LDHn and UB-LDHn respectively, n being the stoichiometric ratio of APTS to SDS.

For *MgAl LDH-MEA,* in the preparation of the amine modified LDH, the SDS surfactant were removed via MEA extraction as applied by Zheng et al. [31]. 0.5 g of LDH5 sample was dispersed in a solution of 100 ml C_2H_5OH (≥99.7%) containing 20 g MEA (≥99%). The mixture was then refluxed for 20 h at a temperature of 90 °C. After which the samples were filtered, washed with ethanol and dried in a vacuum oven overnight. These samples are labelled LDH-MEA5, LDH-MEA2 and LDH-MEA1 respectively. Using an ultrasonic bath, the procedure was repeated for the synthesised UB-LDHn samples. Synthesised UB-LDHn samples were similarly dispersed in a solution of C_2H_5OH and MEA; and then refluxed for 20 h while using the ultrasonic bath filled with distilled water at a temperature of 90 °C. The obtained samples are labelled as UB-MEAn. In the same procedure, UH-MEAn samples were prepared. During reflux, ultrasonic horn was used rather than the bath.

2.3. Characterization

2.3.1. Scanning electron microscopy (SEM) – Energy dispersive X-ray spectroscopy (EDX) analysis

The surface morphology of the prepared materials were studied with a Zeiss ΣIGMA™ Field Emission SEM. With the aid of an Oxford Instrument INCAx-act PentaFET® Precision EDX, the EDX spectra for the LDHs were obtained. This was also used to compute the amine content present in the adsorbents

2.3.2. X-ray diffraction (XRD and X-ray photoelectron spectroscopy (XPS)) analysis

XRD patterns were studied using a Bruker-AXS D8 advance powder diffractometer with a scanning range of $10^\circ \le 2\theta \le 90^\circ$. The basal spacing was calculated with Bragg's Law using the d_{003} peak from the diffraction pattern. X-ray Photoelectron Spectroscopy (XPS) data of the adsorbent was obtained using Kratos X-ray Photoelectron Spectrometer – Axis Ultra DLD with a 96 W monochromatic Al Kα X-ray source (1486.69 eV) at a photoelectron take-off angle of 45°. Wide scans were performed from 1100 eV to 0 eV with a dwell time of 150 ms and steps of 1 eV. Narrow scans were performed with steps of 0.05 eV with dwell time of 600 ms. The binding energy (BE) was calibrated by using the C 1 s peak at 284.6 eV as a reference

2.3.3. Nitrogen adsorption-desorption measurement

The textural properties of the prepared adsorbents were studied by Nitrogen physisorption analysis at −196 °C using the Micrometrics ASAP 2020 Surface Area and Porosity Analyser. Prior to this analysis, samples were degassed at a temperature of 105 °C for 4hr. The BET (Brunauer, Emmett and Teller) model was used to determine the surface area (S_{BET}) of the samples. The total pore volumes (V_{Total}) were computed from the amount of nitrogen adsorbed at relative pressure (P/P_o) of 0.99 and the average pore volumes from $4V_{Total}/S_{BET}$. The pore size distribution was calculated using the BJH (Barrett, Joyner and Halenda) model. The t-plot method was used to calculate the micopore volume (V_{micro})

2.3.4. CO_2 uptake measurement

CO_2 adsorption was measured by a Netzsch STA 449 F3 Jupiter thermo-gravimetric analyser (TGA). Approximately 5–10 mg of each sample was heated from 25 to 105 °C at 20 °C/min under N_2. The

sample was held at 105 °C for 30 min and then cooled to the desired adsorption temperature at a rate of 10 °C/min. The gas input was switched from N_2 to CO_2 and held isothermally for 90 min. The experimented adsorption temperatures were 55 °C and 80 °C (reported optimum adsorption temperature for most amine functionalised adsorbents [32]). The CO_2 adsorption capacity was determined from the weight change of the samples in CO_2 atmosphere. Effects of the change in gas density and viscosity were corrected by measuring the response to an empty alumina crucible using the same method

2.3.5. Adsorbent regeneration via thermal swing adsorption cycles

A thermal swing adsorption-desorption programme in the presence of N_2 was conducted using the Netzsch STA 449 F3 Jupiter thermogravimetric analyser. This is to determine the lifetime adsorption capacity of the adsorbent. After the CO_2 uptake measurement, the adsorbent was heated to 105 °C at a rate of 20 °C/min in a N_2 atmosphere with a constant flow rate of 20 ml/min and held isothermally for 30 min. After desorption, the adsorption cycle was repeated several times. The experimented adsorption temperature is 55 °C. Adsorption capacities were computed based on the mass of the adsorbent

2.3.6. Thermal stability measurement

The stability of the as synthesised LDH samples in air was determined using the Netzsch STA 449 F3 Jupiter thermogavimetric analyser. About 5–10 mg of sample was loaded into an alumina crucible, and the decomposition was monitored by increasing temperature from 25 to 1000 °C with a heating rate of 10 °C/min and under a flow of air (50 ml/min)

2.3.7. Temperature-programmed desorption (TPD)

CO_2-TPD analysis was conducted using AutoChem II 2920. The TPD of CO_2-measurements were implemented to analyze the acidity and basicity of the catalysts. 0.1 g of the adsorbent was first placed in the reactor and treated at 350 °C for 2 h in N2. During desorption, a thermal conductivity detector (TCD) was employed to record the TPD profiles from 100 to 800 °C with a heating rate of 10 °C/min.

3. Results and discussion

Fig. 1 shows the SEM images of prepared LDHs. At low amount of SDS (Mole ratio, n = 5), the layered hydroxide exhibits irregular shapes and is highly porous and permeable with little or no agglomeration on the surface of the sample. As the addition of SDS increases, APTS/SDS mole ratio decreases, accompanied by significant changes of the surface of the adsorbent with remarkably increased particle agglomeration. It can be seen from the figure that the LDH2 sample clearly forms a flake-like shell over an irregular dense shaped core. Further increase of SDS results in the flake-like shell becoming curled up as can be seen from the sample of LDH1. This may be explained by the formation of shell-core structure caused by the sequential reduction of two different metallic ions [33], resulting from difference in the reduction potentials of Mg^{2+} and Al^{3+} ions. It could be said that the excess Mg^{2+} ions are oxidized preferably to the Al^{3+} ions, resulting in the formation of Mg-core/Al-shell particles. The increased particle aggregation and subsequent surface restructuring was due to the physiochemical property of SDS. Due to its mean aggregation number of 62, SDS are able to form aggregates at high concentrations [34]. Comparing the inter-layer spacing between the flake-shells for different samples, LDH2 seems to be more spaced due to an irregular layering of flakes. Unlike LDH2, LDH1 was observed to have a lower interlayer spacing due to the folding of the flaky layers while undergoing intra-layer interactions. The amine modified LDHs show similar surface structures irrespective of the variation in SDS amount. However, they exhibited more surface granular agglomeration, as seen from Fig. 2. It is interesting to note here that the flaky-shells of the LDH2 and LDH1 were no longer visible after applying MEA extraction. The samples of LDH-MEA2 and LDH-MEA1 showed some coated edges on the surface of the particles while this was not found in the sample of LDH-MEA5. Fig. 3 shows the SEM image of LDH prepared using ultrasonic irradiation at APTS/SDS mole ratio of 5 (UH-LDH5) in comparison to the conventional method. The surface of the sonicated LDH shows an evenly distributed undulated surface sites (fig. 3b) when compared to that of the conventional (Fig. 3a). This stresses the impact of the sonication on the morphology, and probably, on the physical properties of the material [33] as shown in the Table 1. Comparing the BET results of the conventional and sonochemically modified LDHs, it is observed that there is a significant difference in the textural properties of LDHs. S_{BET} and V_{Total} increased from 25.03 m^2/g and 0.02 cm^3/g for the conventional route to 171.20 m^2/g and 0.5528 cm^3/g respectively from the sonochemical process. However, the percentage of micropores to the total pore volume showed a decrease in value.

In order to fundamentally reveal the effect of addition of SDS on the internal structures of the LDHs and modified LDHs, the X-ray diffraction (XRD) was also used to characterise the prepared samples. The XRD pattern for LDH samples are shown in Fig. 4. A rough look from the figure indicates that all samples exhibit similar patterns. However, a careful observation reveals that the intensity of the reflections at the peaks differs for each sample. A notable peak appears at $2\theta = 60^{\circ}$. The appearance of this peak is as a result of overlapping of reflections from structural configurations of (1 1 3) and (1 1 0). It has been observed from the test that an increase in SDS (decrease in n) results in a decrease in the non-basal reflections. Reflections at (1 1 0) are common for the non-modified LDHs with large interlayer spacing [33,35]. Hence, it can be stipulated that the increase in SDS will result in the reduction of large interlayer spacing [2], supported by the SEM images of the LDHs. Another insignificantly notable variation in peaks was observed to occur at $15^{\circ} \leq 2\theta \leq 25^{\circ}$. Within this range, the reflection is likely associated with the lattice (0 0 1 8) [36]. It was also noticed that the increase in surfactant results in an increase in the reflection sharpness and intensity. This clearly indicates that the crystallinity of the sample increases for the LDH modification with SDS-APTS intercalation. However, the non-basal reflections at (0 1 2) seem to be preserved, indicating that the layered structures were unaffected by the change in surfactant amount. These trends were also observed in the sonochemically modified LDHs (Figs. 5–8). Figs. 5 and 6 show the XRD patterns for the sonicated LDH samples using low and high intensity sonications respectively. The patterns show similar trends to those of non-sonicated LDHn. It can be conjectured with a certain reservation that the adoption of sonication has no remarkable impact on the structure of the LDHn. However, a slight increase in the peak of (1 1 0) reflection was noticed for both ultrasonic modulated LDH. The use of MEA extraction for all prepared samples also demonstrates less influence on the structure of the adsorbents. The results of non-basal XRD peaks (0 0 1 8), (0 1 2) and (1 1 0) shown in Figs. 7 and 8 clearly indicates that the structure of the adsorbents is less affected by using MEA extraction.

3.1. Effect of amine modification on the prepared LDH on CO_2 adsorption capacity

For evaluating the effect of amine modification on CO_2 adsorption capacity, the characterisation of CO_2 adsorption process using the TGA is divided into three phases: (1) pre-heating of the sample from room temperature to 105 °C for 30 min under N_2 atmosphere for the removal of absorbed water molecules; (2) under the same N_2 atmosphere, the sample was then cooled to the desired temperature for adsorption; and (3) switching the gas from N_2 to CO_2 for isothermal CO_2 adsorption. In the third phase, the CO_2 adsorbed by the sample is measured from the weight gained by the sample. An illustration of this process is shown in Fig. 9(a).

Fig. 10 shows the CO_2 adsorption capacities for those samples of (a) LDHn and (b) LDH-MEAn (with n being the molar ratio of APTS to SDS).

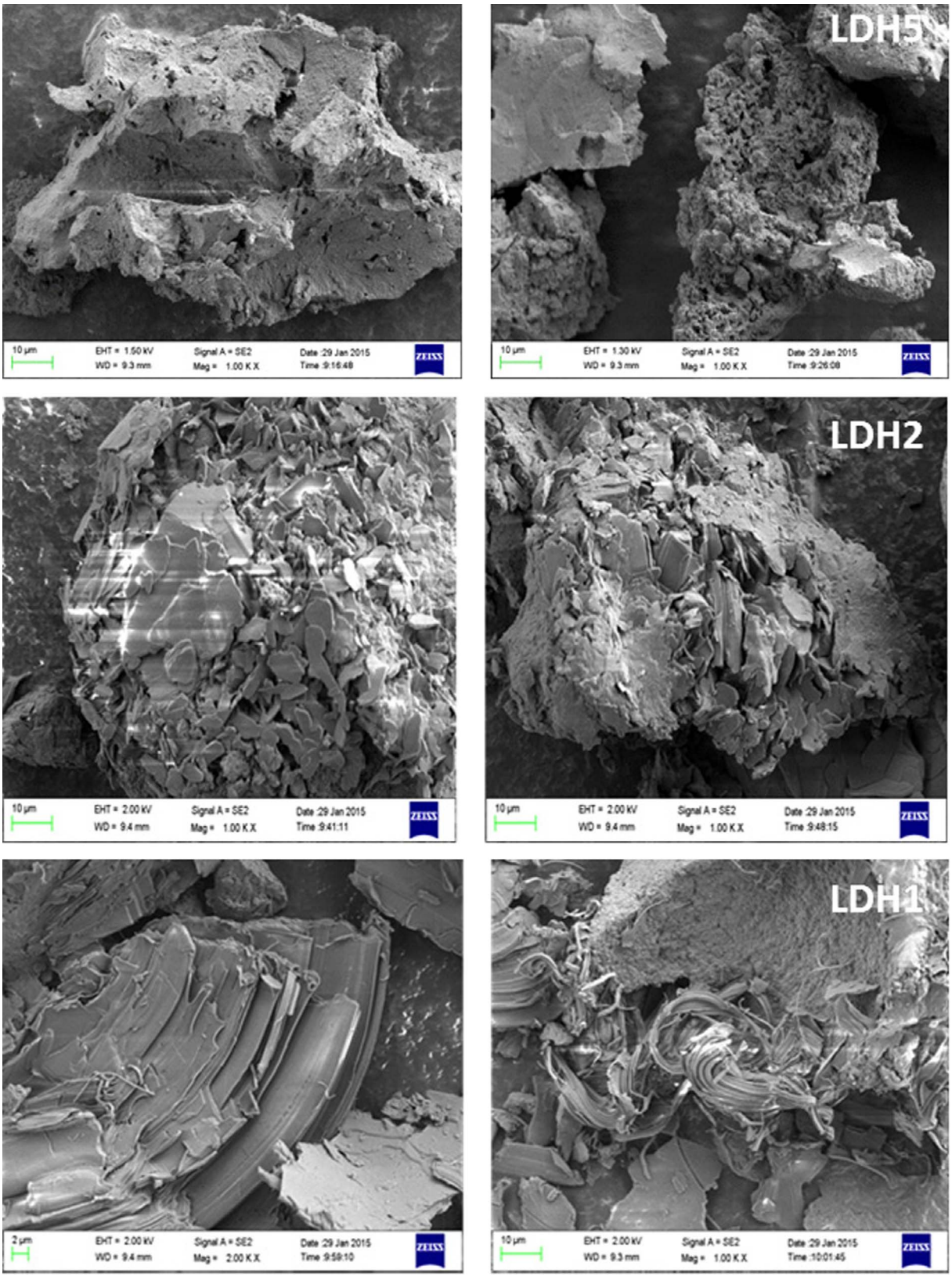

Fig. 1. SEM Images of prepared LDHs with variation in Surfactant, SDS.

The adsorption experiments were carried out twice (Supplementary document, Table S1) and the data of the averaged weight gained from CO_2 adsorption were used in generating the figure. It was observed from the obtained data that as SDS increases (indicated by the decrease in mole ratio from 5 to 1) at 55 °C, the CO_2 uptake decreases from 0.82 to 0.59 mmol/g. This is consistent with finding reported in previous study but with lower CO_2 adsorption capacities 0.58 to 0.12 mmol/g (2). The decrease in adsorption capacity is attributed to the protonation of amino groups by the surfactant's anions given the increased addition of SDS, thus preventing CO_2 adsorption on these sites. The same trend

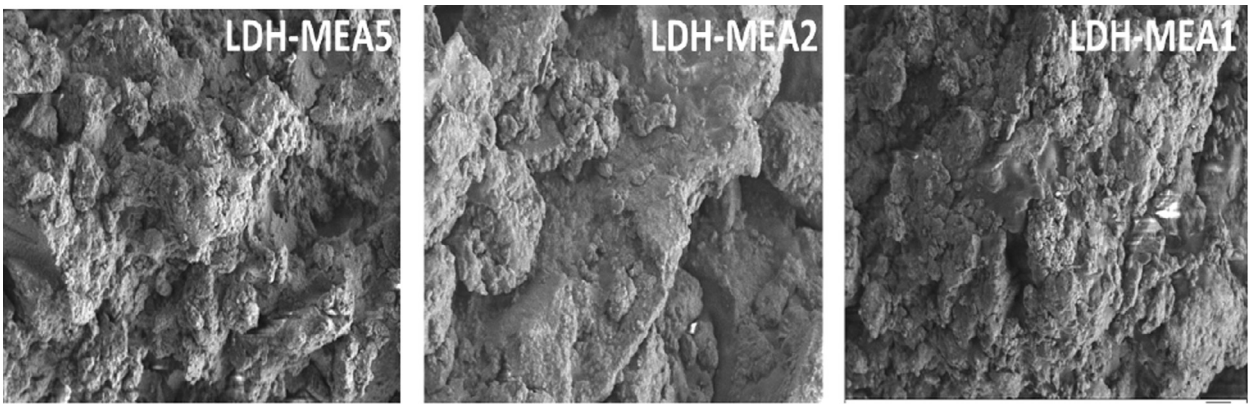

Fig. 2. SEM images of LDH-MEAn at various APTS/SDS mole ratios (n = 5, 2 and 1).

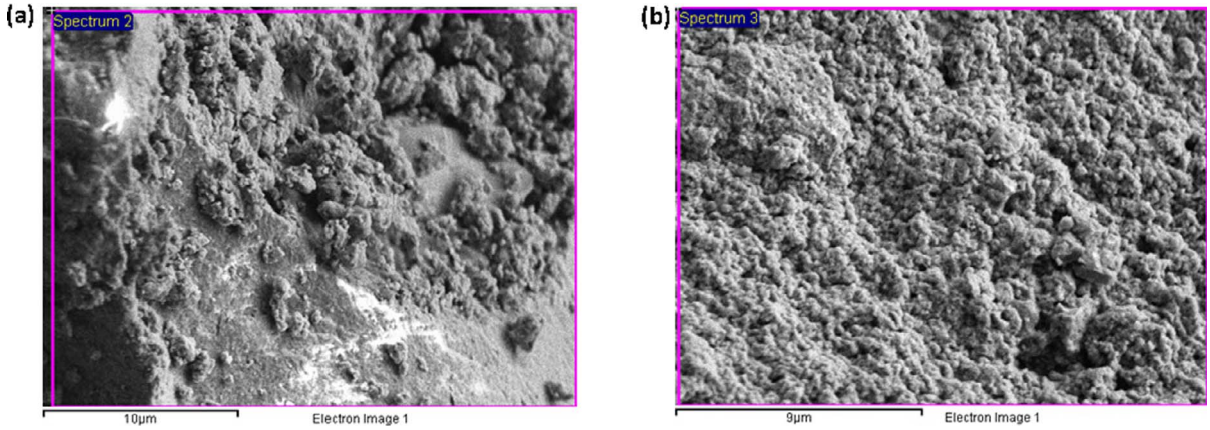

Fig. 3. Comparison of surface texture of LDH prepared via (a) conventional, and (b) ultrasonic irradiation routes, at APTS/SDS mole ratio = 5 using ultrasonic horn (UH-LDH5).

Table 1
Pore structure of modified LDHs, gas uptake and recoverable adsorbed CO_2.

Sample	Gas Uptake (mmol/g)		mmol N_2 mmol CO_2	CU_{rev}	CU_{irrev}	% of CU_{irrev}	S_{BET} (m^2/g)	Average Pore Width (nm)	V_{Total} (cm^3/g)	V_{micro} (cm^3/g)
	CO_2	N_2								
LDH-MEA5	1.45	0.23	0.16	1.27	0.18	12.64	25.03	2.57	0.0161	0.0008
UB-MEA5	0.54	0.14	0.25	0.51	0.03	6.39	–	–	–	–
UH-MEA5	1.37	0.43	0.31	1.33	0.03	2.43	171.20	12.92	0.5528	0.0229

was also observed at 80 °C but with a decreased adsorption capacity of about 35–50% of that at 55 °C.

After adoption of MEA extraction, the CO_2 uptake by the LDH-MEAn samples at 55 °C increased by about 75–90% based on the LDHn samples. This is partly due to the increased amine loading, facilitating the extraction of the surfactant and consequently making the amino groups available for CO_2 adsorption. This trend was also found at 80 °C with an increase of about 10–30% in the CO_2 adsorption capacity of the LDH-MEAs. This significant change in adsorption performance can be explained by the CO_2 adsorption profile of APTS at varying temperature which tends to achieve the maximum in the range of the temperature of 60 to70 °C (2). This trend was also observed in the sonicated LDHs. After amine modification, the adsorption capacity at 55 °C of the UB-LDH5 increased from 0.48 to 0.54 mmol/g, while UH-LDH increased from 0.66 to 1.37 mmol/g (Table 2). This increase can be attributed to the exfoliation of the surfactant and simultaneous increase in the amine loading by the MEA extraction process. In this regard, the interacted amino groups with the negative head-groups of the surfactant are deprotonated, which are now free to react with CO_2. This can be validated by the increase in amine loading after MEA extraction as shown in Table 2.

Using the EDX spectroscopy, inspection tests were carried out for each LDH and the tabulated results (Table 2) show the average composition of the samples. The EDX results show the elemental configuration and dispersion across the internal micro structures of the prepared samples (Supplementary documents, Fig. S1). From the obtained elemental analysis, the molecular formula of the grafted organic species, SDS and APTS, was computed using the general chemical formula for all amine modified LDH, $[Mg_3Al(OH)_m]_x{}^+.[C_{12}H_{25}SO_4]_y{}^-.[C_nH_{2.5n+0.5}SiNO_3]_z$ (5). From the table, it is observed that the amount of sulphur reduced after MEA extraction resulting to a corresponding increase in nitrogen content. This shows that the extraction process was effective (c.a. 97–99% of SDS was removed) across all preparation route; hence, increasing the adsorption capacity after MEA extraction (see Table 3).

3.2. Effect of ultrasonic modulation on CO_2 adsorption capacity

The effect of ultrasonic modulation was also studied in the preparation process. The stirring process was sonicated by applying either ultrasonic horn or ultrasonic bath. Table 4 shows the CO_2 uptake by LDHs produced using ultrasonic irradiation with ultrasonic horn and

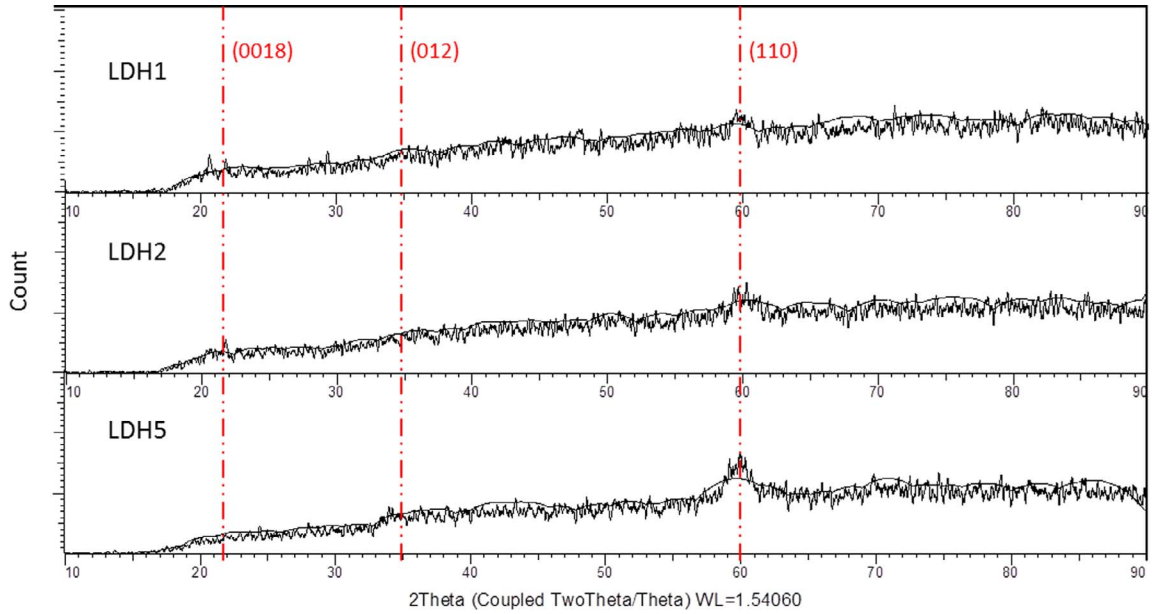

Fig. 4. XRD patterns for LDHn (n = 1, 2 and 5) samples.

bath at temperatures of 55 °C and 80 °C. The results show a reduction in CO_2 uptake at both temperatures when compared to the conventional co-precipitation route as shown in Fig. 11. It should be noted here that the result is yet to be validated with an optimum sonication condition for this material. This is subject to further research. However, the decrease in CO_2 adsorption by the sonicated sample can be explained by the enhanced chemical reaction facilitated by accelerated inter-particle collision within the local hot spot of the collapsing bubbles that are generated by the sonication [33]. Consequently, the available amino groups are readily bonded to the anionic surfactants, resulting to limited amino group active site for CO_2 adsorption. Sonication aids in rearranging reactions with a bias towards reaction mechanisms that yields molecules not necessarily obtained from purely thermal or light induced reactions [35] or by adjusted physicochemical parameters [33]. Adequate studies must be carried out to discern the optimal ultrasonic power output for any preparation process. This importance can be illustrated by the use of mild sonication using ultrasonic bath rather than intense sonication from the ultrasonic horn. With the limited results obtained from the ultrasonic bath, it was observed that at a temperature of 80 °C, the CO_2 adsorbed at APTS/SDS mole ratio of 5, 2 and 1 are 0.74, 0.81 and 0.61 mmol/g, respectively, which is remarkably higher than that obtainable from the conventional LDHs (0.54, 0.20 and 0.315 mmol/g, respectively) and LDH-MEAs (0.695, 0.22 and 0.40 mmol/g, respectively). This clearly demonstrated that the preparation method can be optimised for favourable adsorbent synthesis using the controlled sonication.

At the given desirable temperature of 55 °C, a comparison of the CO_2 uptake profile by the conventional and ultrasonic irradiation (both

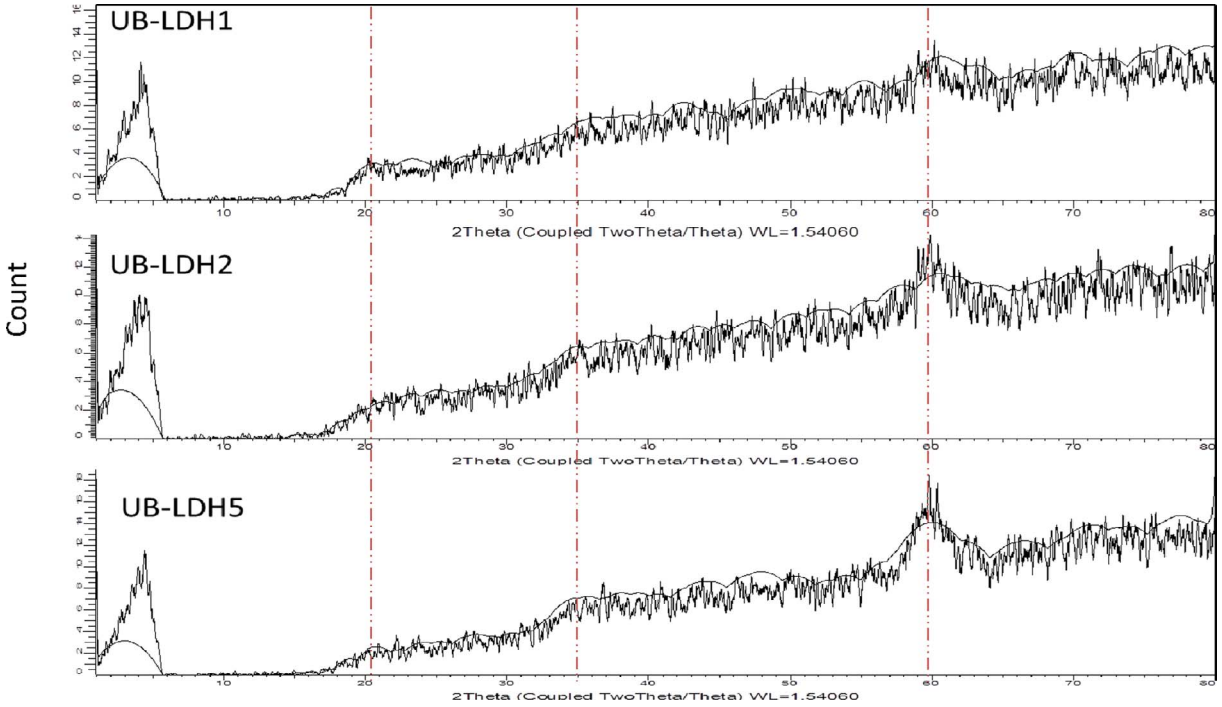

Fig. 5. XRD patterns for UB-LDHn (n = 1, 2 and 5) samples.

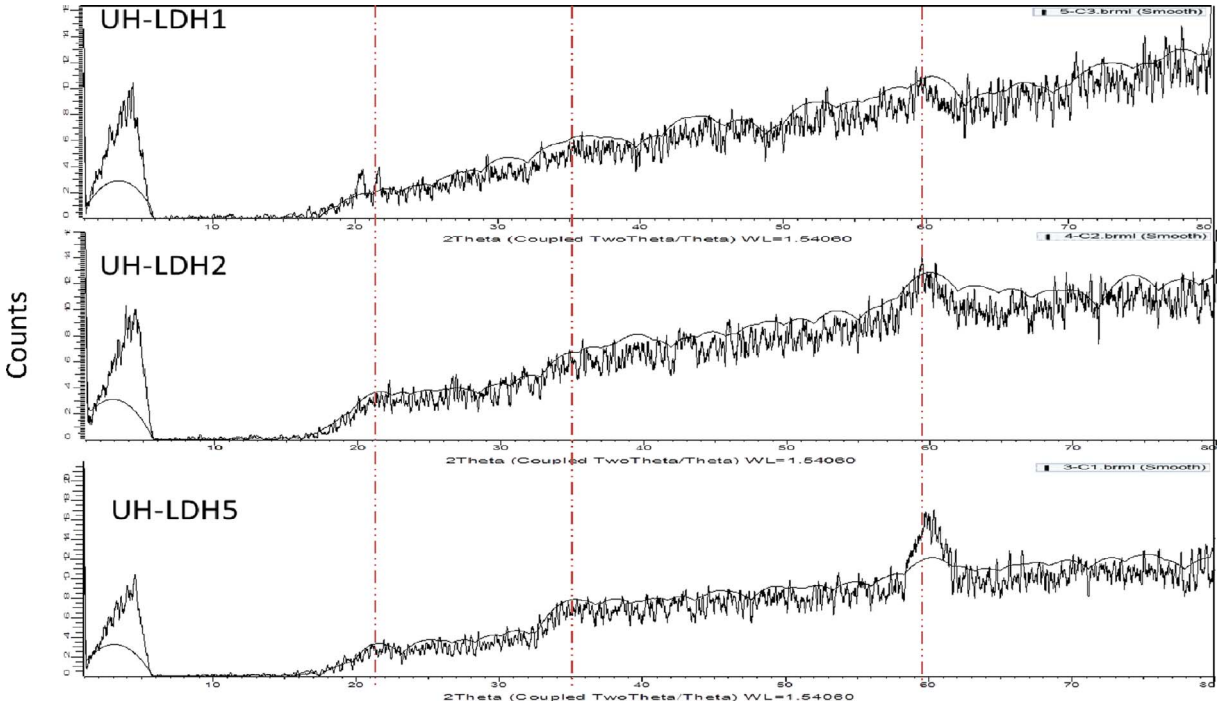

Fig. 6. XRD patterns for UH-LDHn (n = 1, 2 and 5) samples.

horn and bath) for APTS/SDS mole ratio of 5 is shown in Fig. 12. In comparison to the conventional LDH5, the sonochemically prepared adsorbents, UB-LDH5 and UH-LDH5 exhibit a lower CO_2 uptake of 0.44 and 0.66 mmol/g respectively despite the high amine loading of 1.21 and 2.22 mmol/g when compared to the 0.46 mmol/g of the conventional with a CO_2 uptake of 0.82 mmol/g (see Table 2). This can be attributed to the enhanced protonation of the amino groups by the negative head of the surfactant caused by the ultrasonic irradiation irrespective of the high surfactant content in LDH5 (depicted by the high SDS/APTS ratio), which still possesses more active amino groups for CO_2 uptake. This is supported by the XPS result presented in Fig. 13. XPS was conducted to investigate the content of the amino functional group on the adsorbent surface. Two bands of N 1s spectrum of LDH were observed at *ca.* 397 eV (Peak 1) and 401 eV (Peak 2) binding energies. These are assigned to free amine and protonated/H-bonded amines respectively [37,38]. The spectrum shows the sonochemically prepared LDH to have less concentration of free amines, depicted by peak 1 (Fig. 13b) when compared to that of the conventional (Fig. 13a). Consequently, it reveals that there are limited amino group active sites readily available for CO_2 adsorption for UH-LDH. In addition, it is also relevant to note that the amine loading increased with sonication intensity. This is subject to further research for optimizing adsorbent performance. However, after amine modification, the amine loading of LDH-MEA5, UB-MEA5 and UH-MEA5 increased to 4.71, 5.26 and 5.24 mmol/g respectively with a corresponding increase in CO_2 uptake to 1.45, 0.54 and 1.37 mmol/g respectively. As reported by Wang et al.

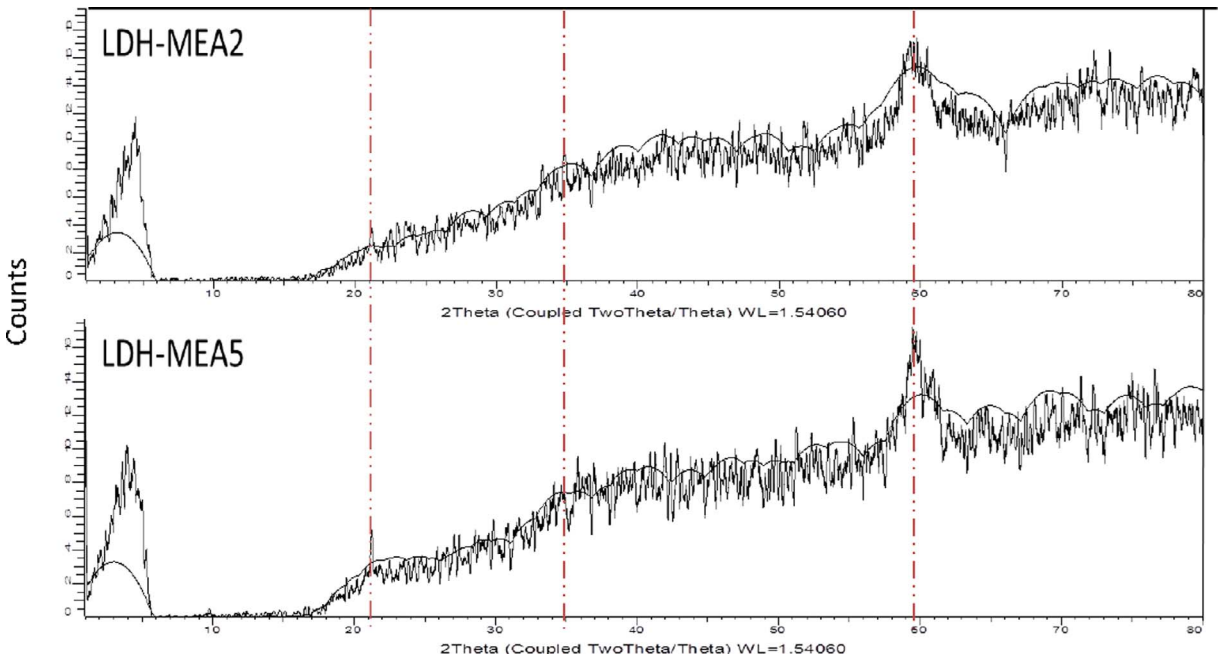

Fig. 7. XRD patterns for LDH-MEAn (n = 2 and 5) samples.

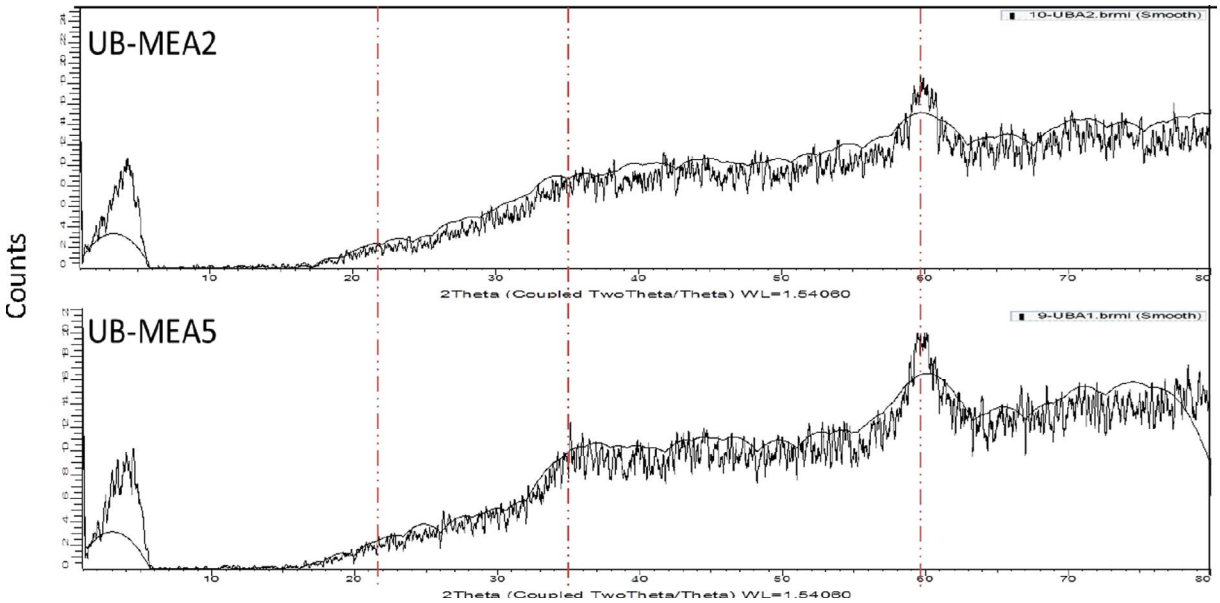

Fig. 8. XRD patterns for UB-MEAn (n = 2 and 5) samples.

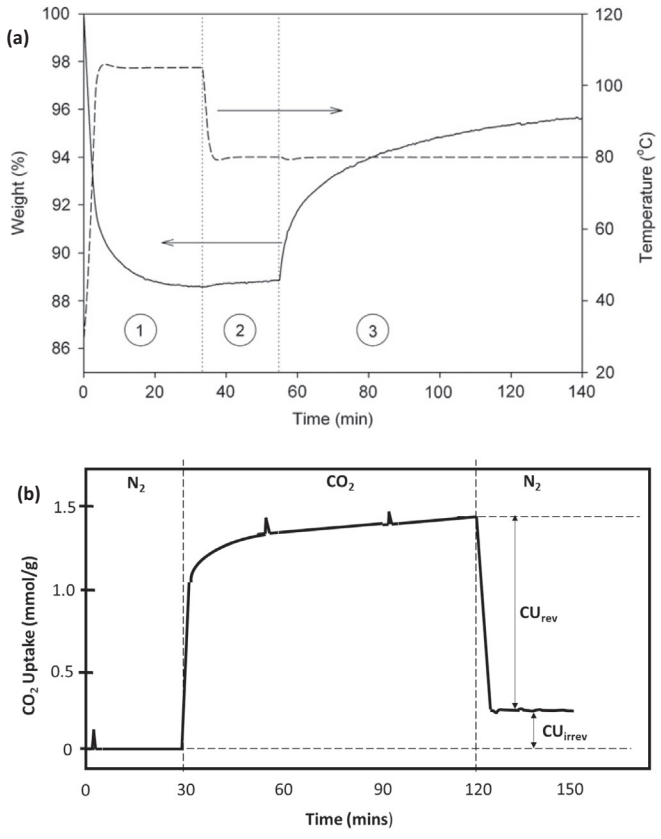

Fig. 9. Example of (a) TGA curve for CO_2 adsorption, (b) recoverable CO_2 uptake using TSA at 105 °C in N_2 atmosphere.

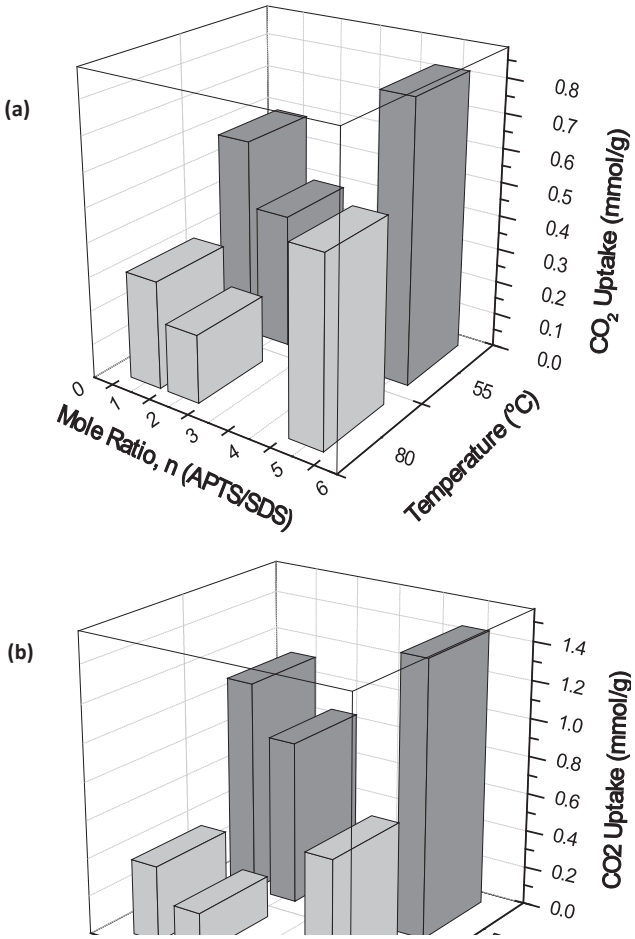

Fig. 10. CO_2 Uptake for (a) LDHn and (b) LDH-MEAn (with n being the molar ratio of APTS to SDS).

[2], the average amine loading for monomeric amines grafted adsorbents is 3–4 mmol/g (See supporting document, S3). However, in this study, it is shown that this can be further improved via ultrasonic irradiation. The incremental change in amine loading is part due to the exfoliation of the surfactant. Nonetheless, the percentage of surfactants removed decreased insignificantly according to the trend conventional > UB > UH. Subsequently, this has an impact on the effective amine loading and effective amine efficiency. In this study, the effective amine efficiency was calculated as the amount of CO_2 uptake resulting from the additional amine loading after LDH functionalization with MEA. UH-MEA5 showed the highest effective amine efficiency of 0.24 compared to 0.15 of LDH-MEA5. This elaborates the importance of sonication in deprotonating protonated and/or probably dispersing the amino groups during MEA extraction, making these groups available as

Table 2
EDX elemental analysis and CO_2 uptake of prepared LDH and calculation results for the molecular formulas, removed SDS and effective amine efficiency.

Sample	N (wt%)	C (wt%)	S (wt%)	Molecular formula (mmol/g)[a]	SDS/APTS	Amine Loading (mmol/g)	CO_2 Adsorbed (mmol/g)	SDS removed (%)	Effective amine loading (mmol/g)[b]	Effective Amine Efficiency[c]
LDH5	0.65	51.35	11.41	$[C_{12}H_{25}SO_4]_{3.57}\cdot[C_{0.01}H_{0.52}SiNO_3]_{0.46}$	7.68	0.46	0.82			
LDH-MEA5	6.60	26.60	1.05	$[C_{12}H_{25}SO_4]_{0.33}\cdot[C_{3.87}H_{10.17}SiNO_3]_{4.71}$	0.07	4.71	1.45	99.09	4.25	0.15
UB-LDH5	1.69	47.78	8.22	$[C_{12}H_{25}SO_4]_{2.57}\cdot[C_{7.45}H_{19.12}SiNO_3]_{1.21}$	2.13	1.21	0.48			
UB-MEA5	7.37	25.38	0.64	$[C_{12}H_{25}SO_4]_{0.20}\cdot[C_{3.56}H_{9.40}SiNO_3]_{5.26}$	0.04	5.26	0.54	98.21	4.06	0.02
UH-LDH5	3.11	51.16	11.08	$[C_{12}H_{25}SO_4]_{3.46}\cdot[C_{0.49}H_{1.72}SiNO_3]_{2.22}$	1.56	2.22	0.66			
UH-MEA5	7.34	30.64	0.60	$[C_{12}H_{25}SO_4]_{0.19}\cdot[C_{4.44}H_{11.60}SiNO_3]_{5.24}$	0.04	5.24	1.37	97.71	3.02	0.24

[a] All Nitrogen, Carbon and Sulphur elements in the grafted LDHs were attributed to come from organic compounds used for intercalation.
[b] Effective amine loading = Difference in amine loading before and after LDH modification.
[c] Effective Amine Efficiency = Difference in CO_2 adsorbed before and after LDH modification/effective amine loading.

active sites for CO_2 adsorption by about 60%.

3.4. Effect of the preparation routes on thermal stability of the amine modified LDHn

Using the TGA, the thermal stability of the prepared samples was determined from room temperature of about 20 °C to 1000 °C at a variation rate of 10 °C/min. The TGA profiles, as shown in Fig. 14, indicate that the samples disintegrate within three temperature phases: T < ~150 °C, ~150 < T < ~ 750 °C and ~750 °C < T. However, the second stage of disintegration for LDHn shows an uneven weight loss as compared to the regular weight loss for LDH-MEAn. The first stage of weight loss (T < ~150 °C) is attributed to the loss of interstitial water molecules. While for the second phase (~150 < T < ~750 °C), the decomposition can be ascribed to the dehydroxylation and breakdown of the organic alkyl chain of the LDH. The observed irregular decomposition curve in this stage may implicate the occurrence of an uneven bonding structure, resulting to multi-stage dehydroxylation processes. The final weight loss (~750 °C < T) results from the decomposition of the sulphate species residuum.

Table 4 shows the tabulated results of the weight loss (%) of LDHn samples prepared using conventional and the ultrasonic routes. From the table, it can be seen that as the APTS/SDS mole ratio, n, reduces, the amount of interstitial moisture decreases. This has been observed in all preparation methods and could be explained by the additional presence of anionic surfactants that replace the water molecules. However, the ultrasonic route (UH) shows a less weight loss in the second and third stage (49–64%) compared with the UB-route (54–66%), which has a nearly same weight loss as that of the conventional method (54–66%). This can be further elaborated by the comparison of those curves in Fig. 14a–c, where the decomposition curves of LDH and UB-LDH are seen to be undulated while the decomposition curve of UH-LDH seems to be regular, likely attributed to the more uniform mixing in UH_LDH so that a more even bonding structure within the material can be obtained. This indicates that the adoption of the UH-route may be beneficial to the synthesis of a more stable material than the UB and the conventional method.

After introducing amine modification of the samples, the decomposition curves clearly show different behaviour compared with that of the untreated LDHs prepared by the different methods. The curves display a well-defined three phase decomposition steps unlike the untreated ones, as can be seen from Fig. 14(d–f). Within the same temperature range as that of the LDHs, the MEA-treated LDHs show higher moisture content than the unprocessed ones (See Supporting document, S5). This can be caused by the presence of leftover MEA molecules after the extraction process. However, the weight losses in the second and third phase reduce significantly, benefitting to production of a more stable material than the pure LDH. This can be explained by the reduced presence of the surfactant after the amine extraction.

In addition, it can be discerned that the sonochemically prepared samples (UB-MEA and UH-MEA) demonstrate a more thermally stable profile than the conventional ones, showing by the total weight loss of 46–52% as compared with 53–64% of the LDH-MEA samples. This demonstrates that the adoption of ultrasonic route may contribute to an accessible distribution of the surfactant during the preparation of the LDH. As a result, the surfactants are easily extracted during the MEA extraction process, thus enhancing the stability of prepared material.

3.4. Effect of the sonochemical functionalization on ease of regeneration, lifetime of the LDH adsorbent and subsequent gas uptake

After CO_2 adsorption, the adsorbents were subjected to a desorption process at a temperature of 105 °C for 30 min in N_2 atmosphere. This was used to compute the ease of recovering the adsorbed CO_2 within the given regeneration test time. The ease of regeneration will contribute to the overall capture efficiency over a period of time and

Table 3
Average CO_2 adsorption for prepared ultrasonic mediated LDHn samples.

Sample		UH-LDH5	UH-LDH2	UH-LDH1	UB-LDH5	UB-LDH2	UB-LDH1
55 °C	1st Trial	0.70	0.39	0.21	0.49	0.34	0.21
	2nd Trial	0.61	0.51	0.30	0.46	0.35	0.17
	Average	**0.655**	**0.45**	**0.255**	**0.475**	**0.345**	**0.19**
80 °C	1st Trial	0.21	0.09	0.13	0.74	0.81	0.61
	2nd Trial	0.28	0.15	0.24	–	–	–
	Average	**0.245**	**0.12**	**0.185**	**0.74**	**0.81**	**0.61**

will impact on the economics of the process. Fig. 9(b) shows an example of recoverable CO_2 uptake using TSA. The recoverable CO_2 uptake was denoted as CU_{rev}, while the retained CO_2 uptake as CU_{irrev}. The results (Table 1) show that the sonochemical functionalized LDHs, UB-MEA5 and UH-MEA5 has CU_{rev} of 0.51 and 1.33 mmol/g representing c.a. 93% and 98% of the CO_2 uptake. Compared with the CU_{rev} of the conventional modified LDH-MEA5, of 1.27 mmol/g (c.a. 87% of the adsorbed CO_2), the sonochemically prepared adsorbents showed a better performance for the capture of CO_2. Analysing the CU_{rev} for UH-MEA5 and LDH-MEA5, it is observed that despite the higher CO_2 uptake of LDH-MEA5, the amount of CO_2 recovered during desorption is lower than that of UH-MEA5.

The impact of the preparation route on the cyclic sorption capacity is presented in Fig. 14. The sorption capacity is calculated as a percentage of the original capacity of 1.45 and 1.37 mmol/g for LDH-MEA5 and UH-MEA5 respectively. These two adsorbents were considered given that they have close adsorption capacities and that UH-MEA5 was more stable than UB-MEA5. The TSA cycle was repeated several times, with a regeneration temperature of 105 °C until the sorption capacity reduced below 60% of the original capacity. For deployment of these adsorbents on a large scale, the greater the cyclic adsorption capacity, the lesser the replacement of the adsorbent and potentially more efficient the adsorbent will be. From Fig. 15, LDH-MEA5 showed an initial high cyclic adsorption capacity greater than 90% of the initial sorption capacity. However, its lifetime did not exceed the 11th cycle before degrading to a capacity less than 60% of the original sorption uptake. Degradation in cyclic adsorption capacity can be attributed to the secondary reaction occurring between the amino group and CO_2 as observed in Fig. 12(b). This is shown by the second ascent in CO_2 uptake after 48, 50 and 55 min of adsorption by LDH-MEA5, UB-MEA5 and UH-MEA5 respectively. Drage et al. [5] refuted the possibility of adsorbent volatilization or loss of reactive amino functional groups as the responsible factors for degradation in performance of amine grafted adsorbent. It was revealed that secondary reaction resulted in the formation of stable poly urea compounds deposited on the adsorbent. This corresponds to the 12.64%, 6.39% and 2.43% of CU_{irrev} for LDH-MEA5, UB-MEA5 and UH-MEA5 respectively (Table 1) elaborating the potential ease of formation of urea linkages in the conventional LDH adsorbent. These linkages pose a

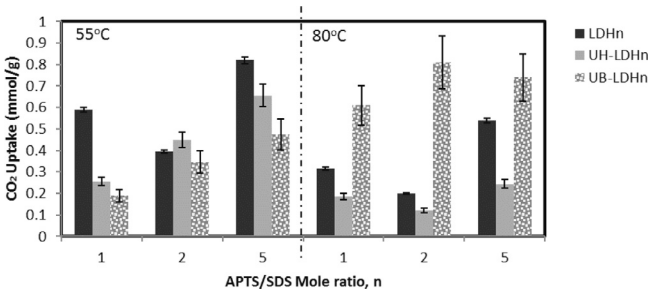

Fig. 11. Comparison of CO_2 uptake by samples prepared via conventional (LDHn) and ultrasonic irradiation route (UH-LDHn and UB-LDHn) at 55 °C and 80 °C.

deleterious effect on the reaction between CO_2 and the active amino functional groups. The destructive impact of this side reaction can be a contributor to the breakdown of LDH-MEA5 under numerous TSA cycles especially when the adsorption cycle is increased beyond 60 min. Unlike the LDH-MEA5, UH-MEA5 displayed a lower initial cyclic adsorption capacity (averaging about 80%) but seemed to oscillate about this capacity for more than 30 TSA cycles (trice the lifetime of LDH-MEA5).

These hypotheses can be supported by CO_2-TPD profile on the functionalised LDH is shown in Fig. 16. The desorption of CO_2 occurs at overlapping peaks of 270 °C (α) and 363 °C (β), 474 °C (γ) and 569 °C (δ) (Fig. 16a). The α-peak has been assigned to CO_2 desorption from bicarbonates formed on OH- groups and tends to occur at low temperatures, whereas the β-peak occurs at intermediate temperatures and is characterised by desorption of CO2 from bidentate carbonates formed on metal-oxygen pairs. At high temperatures, desorption is attributed to monodentate carbonates produced on low-coordination oxygen anions [23]. This is designated by the γ and δ-peaks (22). In this study, the low and intermediate energy states are the major contributors to CO2 uptake, predominated by the intermediate energy state. This is more pronounced in the ultrasonic irradiated adsorbents as shown in Fig. 16b where intermediate energy desorption of UH-MEA5 outweighs that of LDH-MEA5. Nonetheless, the reverse was observed at low energy desorption with LDH-MEA5 slightly desorbing more CO_2 than UH-MEA5. However, the overall desorption by the sonochemically

Table 4
Thermal degradation of samples prepared via conventional (LDHn) and ultrasonic irradiation route (UH-LDHn and UB-LDHn).

Preparation Route	APTS/SDS mole ratio, n	Sample Name	Weight Loss (%)			
			T < 150 °C	150 < T < 750 °C	750 °C < T	Total
Conventional	5	LDH5	10.43	43.63	11.24	65.30
	2	LDH2	8.35	56.13	6.50	70.98
	1	LDH1	2.73	46.02	20.30	69.05
Ultrasonic Bath	5	UB-LDH5	9.36	46.63	8.76	64.75
	2	UB-LDH2	5.67	54.82	10.02	70.51
	1	UB-LDH1	5.05	57.95	8.39	71.39
Ultrasonic Horn	5	UH-LDH5	9.04	44.74	12.39	66.17
	2	UH-LDH2	5.17	41.14	21.81	68.12
	1	UH-LDH1	3.77	36.32	13.46	53.55

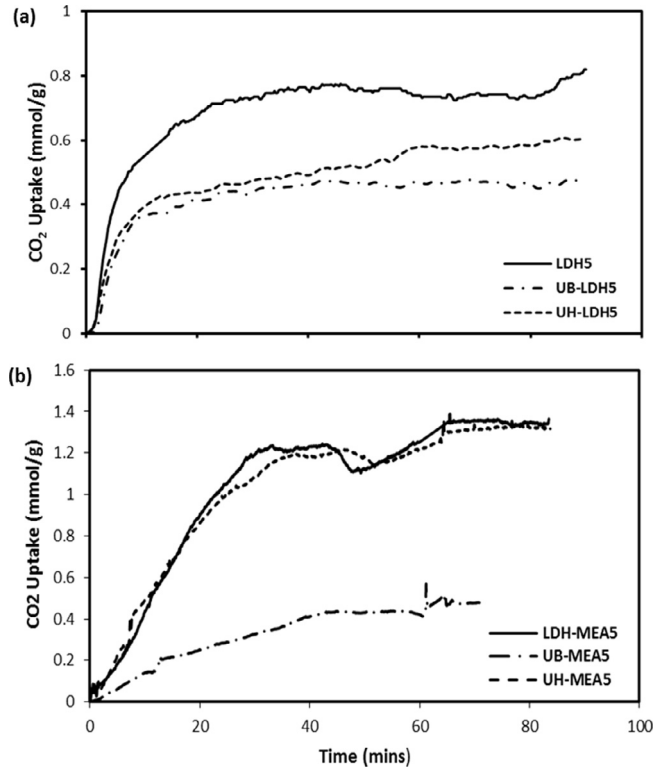

Fig. 12. Comparison of CO_2 uptake by samples prepared via conventional (LDHn) and ultrasonic irradiation route (ultrasonic horn, UH-LDHn and ultrasonic bath, UB-LDHn) with APTS/SDS mole ratio, n = 5 at 55 °C (a) prior MEA extraction, and (b) post MEA extraction.

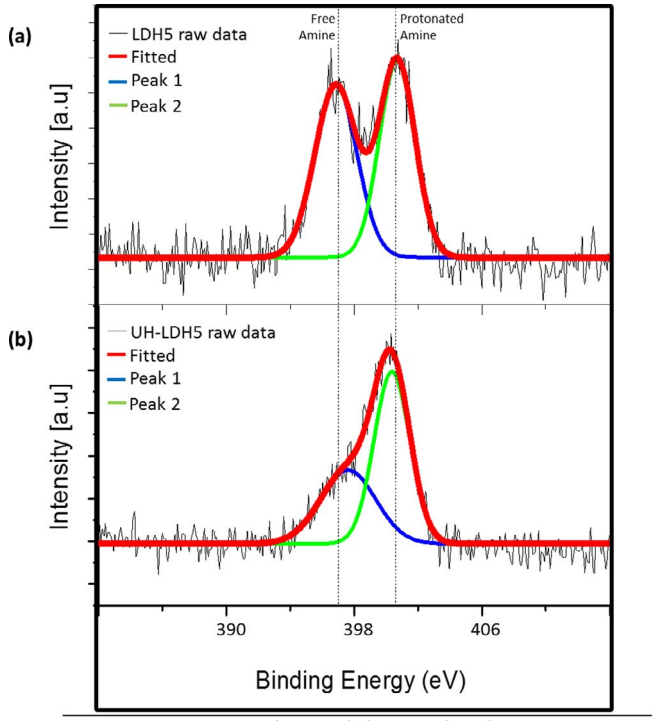

Preparation Route	Sample	Binding Energy (eV) Free Amine	Binding Energy (eV) Protonated Amine	Area (cps eV) Free Amine	Area (cps eV) Protonated Amine	Content (Free/Protonated)
Conventional	LDH5	396.7	400.8	660.0	606.4	1.1
Sonochemical	UH-LDH5	396.9	400.3	596.0	854.7	0.7

Fig. 13. N 1s XPS spectra for (a) LDH5 and (b) UH-LDH5.

prepared LDH within the time analysed showed a better performance than the conventional. In other words, it can be deduced that the performance of a conventionally synthesised LDH is dependent on its basicity while sonochemically synthesised LDHs will profit from low regeneration temperature gradients, especially in temperature-swing operations (see Fig. 15).

These findings were further compared to pseudo-first and pseudo-second order kinetic models:

Pseudo-first order:

$$Equation: \quad x = A_1(1-e^{-k_1 t}); \quad Differential\ form: \frac{dx}{dt} = k_1(A_1 - x)$$

Pseudo-second order:

$$Equation: \quad x = \frac{A_2^2 k_2 t}{A_2 k_2 t + 1}; \quad Differential\ form: \frac{dx}{dt} = k_2(A_2 - x)^2$$

where x and $A_{i,\ i=1,\ 2}$ represents the CO_2 uptake at a given time and equilibrium respectively for an ith order model, $k_{i,\ i=1,\ 2}$ is the ith order rate constant and t is the time of adsorption. The obtained experimental data are fitted to the models and selecting the one with the best fit. To determine the suitability of each model, an error function (Err) defined by Eq. (1) was applied:

$$Err\,(\%) = \sqrt{\frac{\sum\left[\frac{(x_{exp} - x_{mod})}{x_{exp}}\right]^2}{N-1}} \times 100 \tag{1}$$

where x_{exp} and x_{mod} are CO_2 uptake determined experimentally and computed using the model respectively and N is the total number of experimental points. It is reasonable to assume that the adsorption rate constant, k for both pseudo-first and -second order model is the same for each group of functionalized and non-functionalized adsorbents since they are both grafted with the same amino silane. The kinetic parameters are shown in Table 5 with the estimated standard errors and R^2 values. From the simulation results, it is observed that pseudo-second order model displayed a comparatively good fit with the value of equilibrium CO_2 uptake close to that of experimental data for the non-functionalized adsorbents. Hence, despite the effect of sonication on the adsorption capacity and textural properties of the adsorbent, the adsorption kinetics is more favoured by the second order rate function. This model explains adsorption process involving chemical reactions or at high amine loading as compared to pseudo-first order model which explains adsorption under low surface coverage. However, after amine extraction, UH-MEA5 experimental data was best fitted by the pseudo-first order model with a standard error of 0.20%. This explains the ease of recovering the CO_2 uptake as a result of the minimal chemisorption. Fig. 17 shows the fitting of the models with the experimental data for conventional (LDH5) and sonicated (UH-LDH5) non-functionalized adsorbents. Despite the pseudo second order being the better fit, the standard error tends to increase in the sonication route.

After CO_2 adsorption by the LDH adsorbent, the adsorbents were subjected to further isothermal adsorption in N_2 atmosphere at 50 ml/min for 20 min. This is to measure the additional gas uptake capacity of the adsorbent when considered as a catalytic support for hydrogenation of the adsorbed CO_2 to methanol. From the results (Table 1), it is observed that the ultrasonic mediated adsorbents (UB-MEA5 and UH-MEA5) showed a greater potential for additional gaseous uptake than the conventional LDH-MEA5. The amount of N_2 adsorbed per adsorbed CO_2 were 0.31, 0.25 and 0.16 mmol N_2/mmol CO_2 for UH-MEA5, UB-MEA5 and LDH-MEA5 respectively. This can be attributed to the high pore volume of the sonochemically produced adsorbents. Hence, proposing the sonochemical process as a viable catalyst preparation means for synthesising methanol via hydrogenation of CO_2.

4. Conclusions

The present study has shown that the LDHs with high CO_2

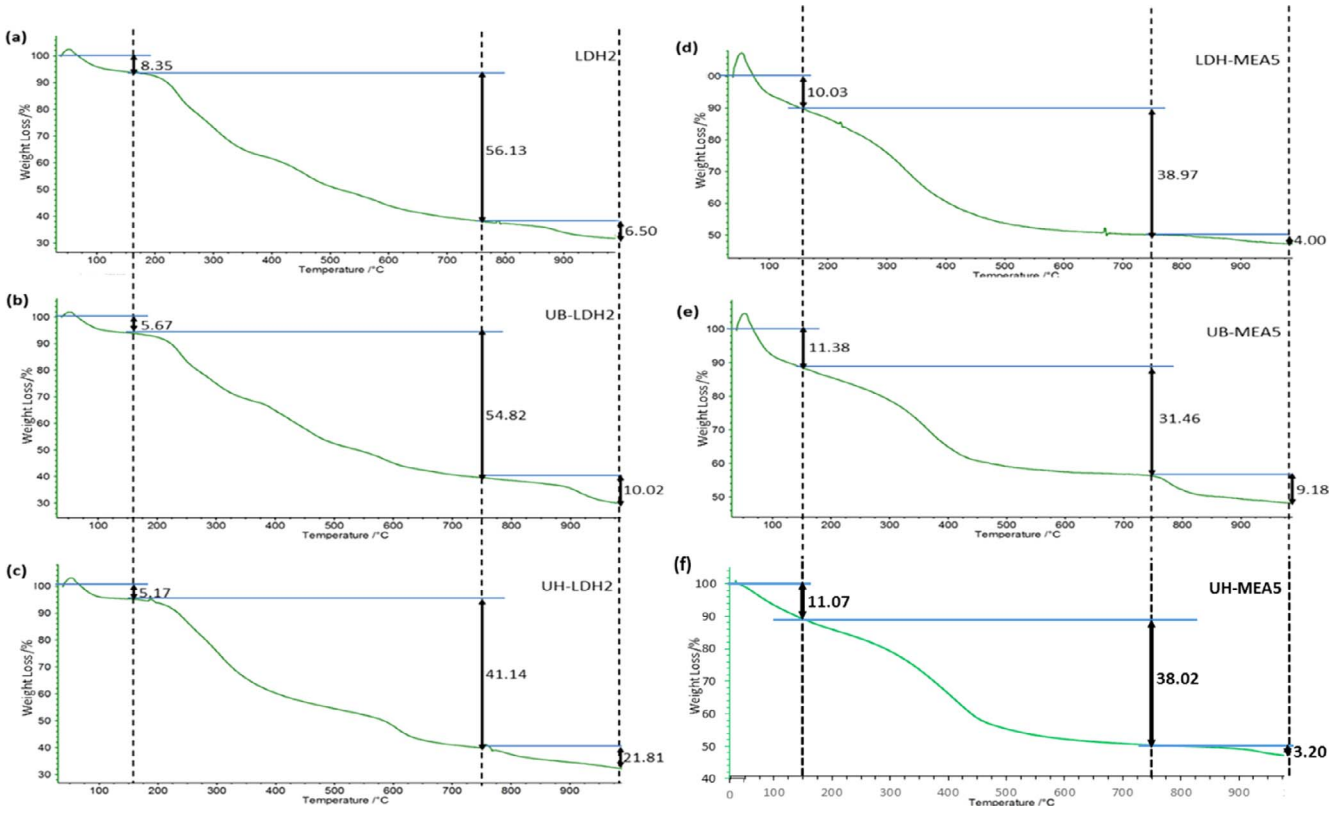

Fig. 14. TGA curves comparing thermal stabilities of LDHs prepared via conventional and ultrasonic irradiation: (a) LDH2, (b) UB-LDH2 and (c) UH-LDH2; as well as with amine modified LDHs: (d) LDH-MEA5 and (e) UB-MEA5 (f) UH-MEA5.

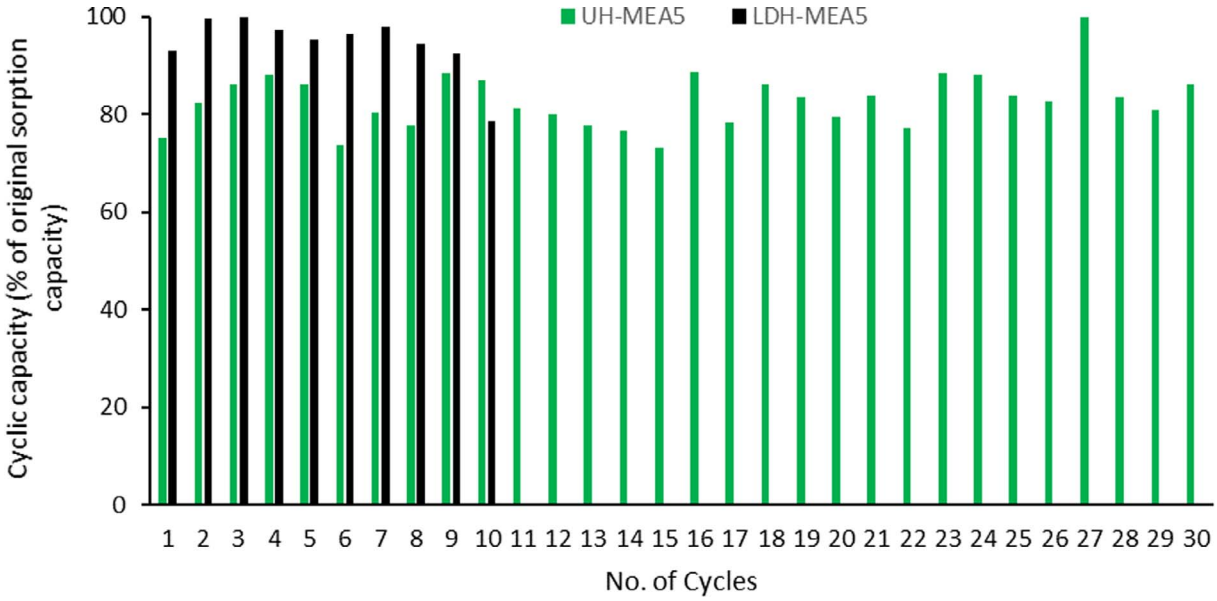

Fig. 15. TSA Cycles of LDH-MEA5 and UH-MEA5 at 55 °C (30 mins regeneration time at 105 °C in N_2 atmosphere) based on the initial adsorption capacity of 1.45 and 1.37 mmol/g respectively.

adsorption capacity can be synthesised via amine modification by means of anionic surfactant intercalation reinforced by ultrasonic irradiation. The use of sonochemical process in the synthesis step led to a more developed pore structure than that of the conventional process. However, this was dependent on sonication intensity. Despite the advancement in physical properties which is beneficial to the physical adsorption of CO_2, the further adoption of the sonochemical process for amine functionalization of the prepared LDH led to an improved amine loading and effective amine efficiency of the adsorbent. In addition, the recoverable CO_2 uptake of the sonochemically prepared adsorbent increased to 1.33 mmol/g as against 1.27 mmol/g of the conventional. In combination with the improved thermal stability of the adsorbent as a result of this process, the sonochemically functionalized LDH exhibited a greater ease of regeneration with a longer life span than the conventional LDH. Therefore, sonochemical route can be an effective preparation method for long-lasting recyclable layered double hydroxides for CO_2 adsorption.

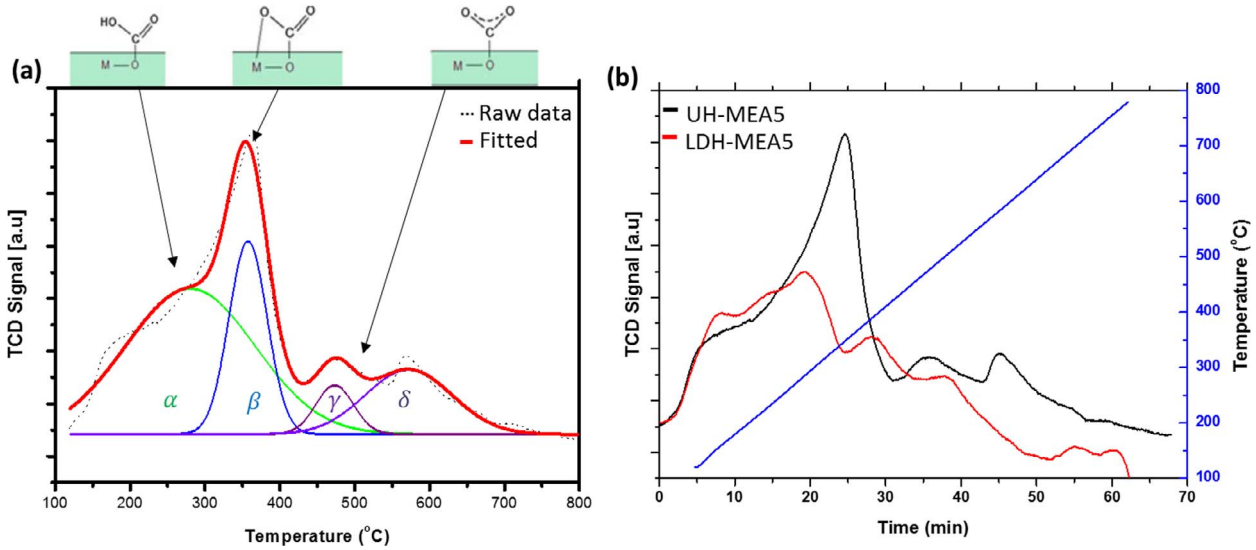

Fig. 16. CO_2-TPD of functionalised LDH (a) Deconvolution of the CO_2-TPD of UH-MEA5 and (b) Comparison of CO_2-TPD of UH-MEA5 and LDH-MEA5.

Table 5
CO_2 kinetic model parameters, R^2 and standard errors (%) for prepared LDHs and amine functionalized LDHs at 55 °C and APTS/SDS ratio, n of 5.

Samples	Pseudo 2nd Order		Err (%)	R^2	Pseudo 1st Order		Err (%)	R^2
	A_2	k_2			A_1	k_1		
LDH5	0.83	0.05	0.22	0.9483	0.76	0.06	0.23	0.9281
UB-LDH5	0.51		0.54	0.9609	0.46		0.38	0.9292
UH-LDH5	0.63		0.84	0.9629	0.56		0.74	0.9057
LDH-MEA5	1.35	0.04	0.16	0.8306	1.38	0.03	0.20	0.8177
UB-MEA5	0.51		0.13	0.8583	0.45		0.13	0.8361
UH-MEA5	1.67		0.55	0.8909	1.32		0.20	0.9226

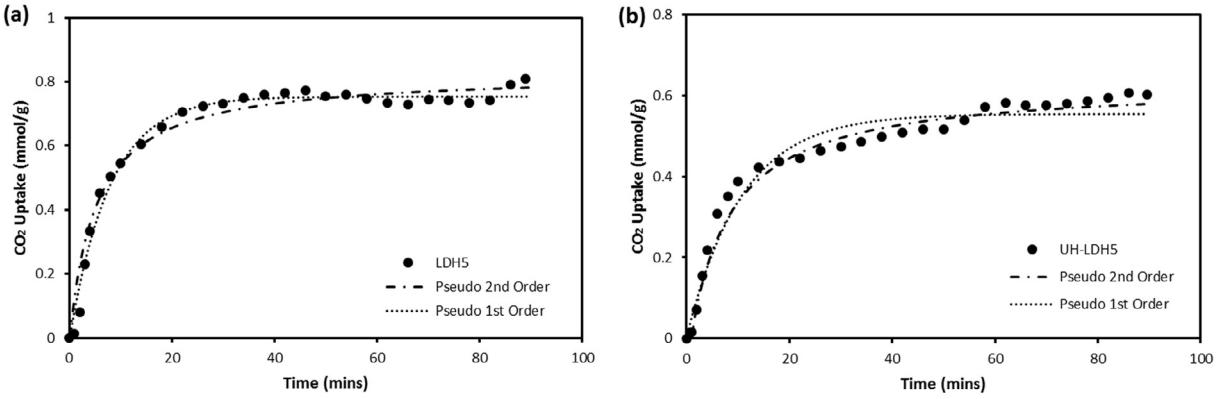

Fig. 17. Comparison of kinetic models with experimental results for CO_2 uptake on (a) LDH5 and (b) UH-LDH5.

Acknowledgements

This work was carried out at the International Doctoral Innovation Centre (IDIC). The authors would like to acknowledge the financial support through the grants of the Zhejiang Provincial Natural Science Foundation (Grant No. LY15B060001) and Ningbo Key Research Project 'A simultaneous removal of multi-pollutants from flue gas at power stations' (Grant No. 1012B10042), and from Ningbo Education Bureau, Ningbo Science and Technology Bureau, China's MoST and The University of Nottingham. The work is also partially supported by EPSRC (Grant no. EP/G037345/1).

Appendix A. Supplementary data

Supplementary data associated with this article can be found, in the online version, at http://dx.doi.org/10.1016/j.ultsonch.2017.04.041.

References

[1] J.D. Figueroa, T. Fout, S. Plasynski, H. McIlvried, R.D. Srivastava, Advances in CO_2 capture technology—The U.S. Department of Energy's Carbon Sequestration Program, Int. J. Greenhouse Gas Control 2 (1) (2008) 9–20.
[2] J. Wang, L.A. Stevens, T.C. Drage, C.E. Snape, J. Wood, Preparation and CO_2 adsorption of amine modified layered double hydroxide via anionic surfactant-mediated route, Chem. Eng. J. 181–182 (2012) 267–275.
[3] M.L. Gray, K.J. Champagne, D. Fauth, J.P. Baltrus, H. Pennline, Performance of immobilized tertiary amine solid sorbents for the capture of carbon dioxide, Int. J. Greenhouse Gas Control 2 (1) (2008) 3–8.
[4] T.C. Drage, C.E. Snape, L.A. Stevens, J. Wood, J. Wang, A.I. Cooper, et al., Materials

challenges for the development of solid sorbents for post-combustion carbon capture, J. Mater. Chem. 22 (7) (2012) 2815.
[5] T.C. Drage, A. Arenillas, K.M. Smith, C.E. Snape, Thermal stability of polyethylenimine based carbon dioxide adsorbents and its influence on selection of regeneration strategies, Microporous Mesoporous Mater. 116 (1–3) (2008) 504–512.
[6] X. Xu, C. Song, J.M. Andrésen, B.G. Miller, A.W. Scaroni, Preparation and characterization of novel CO_2 "molecular basket" adsorbents based on polymer-modified mesoporous molecular sieve MCM-41, Microporous Mesoporous Mater. 62 (1–2) (2003) 29–45.
[7] J. Tanthana, S.S. Chuang, In situ infrared study of the role of PEG in stabilizing silica-supported amines for CO(2) capture, ChemSusChem. 3 (8) (2010) 957–964.
[8] R. Serna-Guerrero, E. Da'na, A. Sayari, New insights into the interactions of CO_2 with amine-functionalized silica, Ind. Eng. Chem. Res. 47 (23) (2008) 9406–9412.
[9] D. Saha, S. Deng, Adsorption equilibrium and kinetics of CO_2, CH_4, N_2O, and NH_3 on ordered mesoporous carbon, J. Colloid Interface Sci. 345 (2) (2010) 402–409.
[10] M. Cinke, J. Li, C.W. Bauschlicher, A. Ricca, M. Meyyappan, CO_2 adsorption in single-walled carbon nanotubes, Chem. Phys. Lett. 376 (5–6) (2003) 761–766.
[11] A. Arenillas, K.M. Smith, T.C. Drage, C.E. Snape, CO_2 capture using some fly ash-derived carbon materials, Fuel 84 (17) (2005) 2204–2210.
[12] A.-Y. Park, H. Kwon, A.J. Woo, S.-J. Kim, Layered double hydroxide surface modified with (3-Aminopropyl)triethoxysilane by covalent bonding, Adv. Mater. 17 (1) (2005) 106–109.
[13] M. Szabados, R. Mészáros, S. Erdei, Z. Kónya, Á. Kukovecz, P. Sipos, et al., Ultrasonically-enhanced mechanochemical synthesis of CaAl-layered double hydroxides intercalated by a variety of inorganic anions, Ultrason. Sonochem. 31 (2016) 409–416.
[14] R. Hernandez-Huesca, L. Dıaz, G. Aguilar-Armenta, Adsorption equilibria and kinetics of CO_2, CH_4 and N_2 in natural zeolites, Sep. Purif. Technol. 15 (1999) 163–173.
[15] R.V. Siriwardane, M.-S. Shen, E.P. Fisher, Adsorption of CO_2 on zeolites at moderate temperatures, Energy Fuels 19 (2005) 1153–1159.
[16] K.S. Walton, M.B. Abney, Le.Van M. Douglas, CO_2 adsorption in Y and X zeolites modified by alkali metal cation exchange, Microporous Mesoporous Mater. 91 (1–3) (2006) 78–84.
[17] Y.-S. Bae, O.K. Farha, J.T. Hupp, R.Q. Snurr, Enhancement of CO_2/N_2 selectivity in a metal-organic framework by cavity modification, J. Mater. Chem. 19 (15) (2009) 2131.
[18] D.-A. Yang, H.-Y. Cho, J. Kim, S.-T. Yang, W.-S. Ahn, CO_2 capture and conversion using Mg-MOF-74 prepared by a sonochemical method, Energy Environ. Sci. 5 (4) (2012) 6465.
[19] K. Yamamoto, Y. Sakata, Y. Nohara, Y. Takahashi, T. Tatsumi, Organic-inorganic hybrid zeolites containing organic frameworks, Science 300 (2003) 470–472.
[20] F. Cavani, F. Trifirò, A. Vaccari, Hydrotalcite-type anionic clays: Preparation, properties and applications, Catal. Today 11 (2) (1991) 173–301.
[21] Q. Wang, J. Luo, Z. Zhong, A. Borgna, CO_2 capture by solid adsorbents and their applications: current status and new trends, Energy Environ. Sci. 4 (1) (2011) 42.
[22] D.I. Ferrer, Supported Layered Double Hydroxides as CO_2 Adsorbents for Sorption-Enhanced H2 Production, Springer International Publishing Switzerland, Imperial College, London, United Kingdom, 2016.
[23] S. Zhao, H. Yi, X. Tang, F. Gao, Q. Yu, Y. Zhou, et al., Enhancement effects of ultrasound assisted in the synthesis of NiAl hydrotalcite for carbonyl sulfide removal, Ultrason. Sonochem. 32 (2016) 336–342.
[24] M.P. Bernardo, F.K.V. Moreira, L.A. Colnago, C. Ribeiro, Physico-chemical assessment of [Mg-Al-PO4]-LDHs obtained by structural reconstruction in high concentration of phosphate, Colloids Surf., A 497 (2016) 53–62.
[25] S.D. Kenarsari, D. Yang, G. Jiang, S. Zhang, J. Wang, A.G. Russell, et al., Review of recent advances in carbon dioxide separation and capture, RSC Adv. 3 (45) (2013) 22739.
[26] K. Yao, Y. Imai, L. Shi, A. Dong, Y. Adachi, K. Nishikubo, et al., The functional layered organosilica materials prepared with anion surfactant templates, J. Colloid Interface Sci. 285 (1) (2005) 259–266.
[27] Q. Tao, H. He, R.L. Frost, P. Yuan, J. Zhu, Nanomaterials based upon silylated layered double hydroxides, Appl. Surf. Sci. 255 (7) (2009) 4334–4340.
[28] S. Che, A.E. Garcia-Bennett, T. Yokoi, K. Sakamoto, H. Kunieda, O. Terasaki, et al., A novel anionic surfactant templating route for synthesizing mesoporous silica with unique structure, Nat. Mater. 2 (12) (2003) 801–805.
[29] T. Yokoi, H. Yoshitake, T. Tatsumi, Synthesis of anionic-surfactant-templated mesoporous silica using organoalkoxysilane-containing amino groups, Chem. Mater. 15 (24) (2003) 4536–4538.
[30] H. Xu, B.W. Zeiger, K.S. Suslick, Sonochemical synthesis of nanomaterials, Chem. Soc. Rev. 42 (2013) 2555–2567.
[31] H. Zheng, C. Gao, S. Che, Amino and quaternary ammonium group functionalized mesoporous silica: An efficient ion-exchange method to remove anionic surfactant from AMS, Microporous Mesoporous Mater. 116 (1–3) (2008) 299–307.
[32] X. Zhao, X. Hu, G. Hu, R. Bai, W. Dai, M. Fan, et al., Enhancement of CO_2 adsorption and amine efficiency of titania modified by moderate loading of diethylenetriamine, Journal of Material Chemistry A. 1 (2013) 6208–6215.
[33] H. Xu, B.W. Zeiger, K.S. Suslick, Sonochemical synthesis of nanomaterials, Chem. Soc. Rev. 42 (7) (2013) 2555–2567.
[34] C.R. Hickenboth, J.S. Moore, S.R. White, N.R. Sottos, J. Baudry, S.R. Wilson, Biasing Reaction Pathways with Mechanical Force, Nature 446 (2007) 423.
[35] M. Herrero, F.M. Labajos, V. Rives, Size control and optimisation of intercalated layered double hydroxides, Appl. Clay Sci. 42 (2009) 510–518.
[36] F. Wypych, A. Bail, M. Halma, S. Nakagaki, Immobilization of iron(III) porphyrins on exfoliated MgAl layered double hydroxide, grafted with (3-aminopropyl) triethoxysilane, J. Catal. 234 (2) (2005) 431–437.
[37] Y. Kong, X. Shen, S. Cui, M. Fan, Development of monolithic adsorbent via polymeric sol-gel process for low-concentration CO_2 capture, Appl. Energy 147 (2015) 308–317.
[38] Y. Kong, G. Jiang, Y. Wu, S. Cui, X. Shen, Amine hybrid aerogel for high-efficiency CO_2 capture: effect of amine loading and CO_2 concentration, Chem. Eng. J. 306 (2016) 362–368.

Ultrasonics - Sonochemistry 40 (2018) 341–352

Contents lists available at ScienceDirect

Ultrasonics - Sonochemistry

journal homepage: www.elsevier.com/locate/ultson

Ultrasonic and hydrothermal mediated synthesis routes for functionalized Mg-Al LDH: Comparison study on surface morphology, basic site strength, cyclic sorption efficiency and effectiveness

Collins I. Ezeh[a], Marco Tomatis[a], Xiaogang Yang[a,*], Jun He[a], Chenggong Sun[b,*]

[a] Department of Mechanical, Materials and Manufacturing Engineering, University of Nottingham Ningbo, University Park, Ningbo 315100, PR China
[b] Faculty of Engineering, University of Nottingham, University Park, Nottingham NG7 2RD, UK

ARTICLE INFO

Keywords:
CO_2 adsorption
Layered double hydroxide
Ultrasound
Hydrothermal
Regeneration

ABSTRACT

Amine functionalized layered double hydroxide (LDHs) adsorbents prepared using three different routes: co-precipitation, sono-chemical and ultrasonic-assisted high pressure hydrothermal. The prepared adsorbent samples were characterized using X-ray diffraction (XRD), X-ray Photoelectron Spectroscopy (XPS), Scanning electron microscope-Energy dispersive X-ray spectroscopy (SEM-EDX), Temperature Programmed Desorption (TPD), Brunauer-Emmett-Teller (BET), and Thermogravimetric analysis (TGA), respectively. The performance of the prepared adsorbents was tested in a controlled thermal-swing adsorption process to measure its adsorption capacity, regeneration and cyclic efficiencies subsequently. The characterisation results were compared with those obtained using the conventional preparation routes but taking into account of the impact of sonochemical and hydrothermal pre-treatment on textural properties, adsorption capacity, regeneration and cyclic efficiencies. Textural results depicts a surge in surface area of the adsorbent synthesised by hydrothermal route (311 m^2/g) from 25 to 171 m^2/g for conventional and ultrasonic routes respectively. Additionally, it has been revealed from the present study that adsorbents prepared using ultrasonic-assisted hydrothermal route exhibit a better CO_2 uptake capacity than that prepared using sonochemical and conventional routes. Thus, the ultrasonic-assisted hydrothermal treatment can effectively promote the adsorption capacity of the adsorbent. This is probably due to the decrease of moderate (M-O) and weak (OH^- groups) basic sites with subsequent surge in the number of strong basic sites (O^{2-}) resulting from the hydrothermal process. Moreover, the cyclic adsorption efficiency of the ultrasonic mediated process was found to be 76% compared with 60% for conventional and 53% for hydrothermal routes, respectively. According to the kinetic model analysis, adsorption mechanism is mostly dominated by physisorption before amine modification and by chemisorption after the modification process.

1. Introduction

Adsorption of carbon dioxide (CO_2) is perceived as the most suitable CO_2 separation method for Carbon Capture and Storage (CCS) technology [1,2]. Extensive studies on various adsorbents used for CO_2 uptake has been carried out over the years. Layered double Hydroxides (LDHs) provided comparatively high uptake capacity with numerous catalytic applications [3,4]. Additionally, its ionic inter-layered configuration enhances the number of basic sites and provides high contact surface area [4]. LDHs are anionic clay minerals also known as mixed-metal layered hydroxides or hydrotalcites-like compounds. They possess two dimensional structure of layers shaped by trivalent and divalent cations parted by water and anions molecules (see Fig. 1) with a general formula:

$$(M^{2+}_{1-x}M^{3+}_{x}(OH)_2)^{x+}(A^{m-}_{x/m}\cdot nH_2O)^{x-}$$

where M^{2+} and M^{3+} are divalent and trivalent cations respectively, A^{m-} is a compensating anionic charge, x is the partial substitution of M^{2+} and M^{3+}, usually within a M^{2+}/M^{3+} ratio of 2 and 5 [4–6].

LDHs are basically synthesised via co-precipitation of solutions containing M^{2+} and M^{3+} metal salts in a preferred interlayer anion [6,7]. This synthesis method can be conducted at high or low supersaturation environments. In low supersaturation condition, the metal solutions are added concurrently to the solution containing the alkali; whereas the metal (at a given M^{2+}/M^{3+} ratio) mixture is added to the alkali and anion precursor solution for high supersaturation conditions. The former tends to produce more crystalline structures because of the increased rate of nucleation over crystallization [6]. Besides this method, other means of synthesizing LDH are sol-gel and urea

* Corresponding authors.
E-mail addresses: Xiaogang.Yang@nottingham.edu.cn (X. Yang), cheng-gong.sun@nottingham.ac.uk (C. Sun).

http://dx.doi.org/10.1016/j.ultsonch.2017.07.013
Received 13 June 2017; Received in revised form 6 July 2017; Accepted 6 July 2017
Available online 20 July 2017
1350-4177/

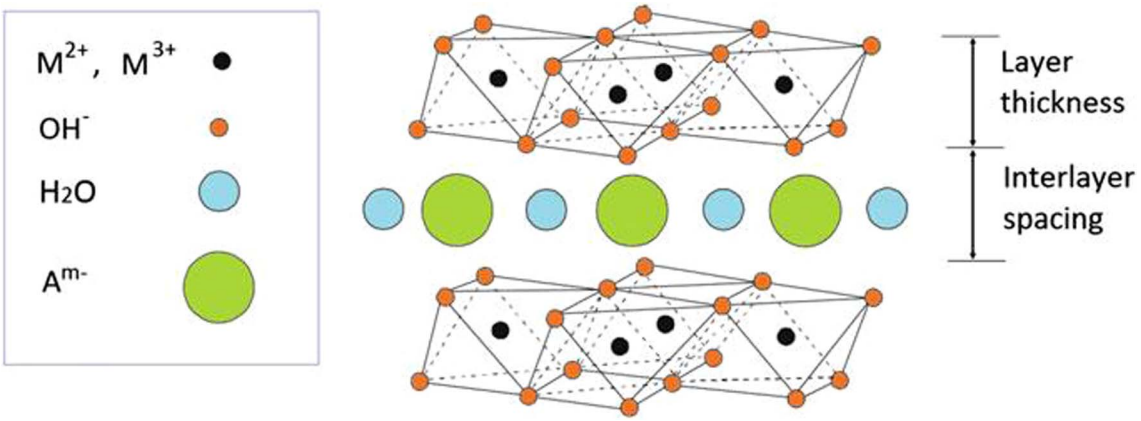

Fig. 1. Structural configuration of layered double hydroxides ([5]-permission obtained).

techniques [7,8].

A key property of this material for the purpose of CO_2 adsorption and other catalytic reactions is its basic property. Owing to the occurrence of interlayered anions and water molecules in the structure, LDH behave as solid bases. Wide ranges of basic strength can be obtained depending on the treatment route and metallic composition. This is primarily attributed to the nature and deposition of the divalent and trivalent cations on the material. With this property, CO_2 has enough acidic strength to bond with the weak basic sites of LDH. However, with an improved basic strength, CO_2 is chemisorbed weakly onto the low basic sites and surface hydroxyl groups of LDH to form bicarbonates and strongly onto the strong basic sites and free lattice oxygen (O^{2-}) to form mono-dentate carbonates. Adsorption on medium basic sites are on acid-base (metal-oxygen) pairs like Mg^{2+}-O^{2-} or Al^{3+}-O^{2-} forming tri-dentates or bi-dentates. The use of temperature-programmed desorption monitored by infrared spectroscopy are shown in Fig. 2 according to the work [9].

The strength of these basic sites determine the adsorption and regeneration capacity of the adsorbent. Most research studies, to the best our knowledge, have emphasised the effect of metallic composition on this property. However, it is observed from this study that the preparation route plays a key role in the basic strength of this material. Subsequently, this affects the adsorption and regeneration capacities, as well as the life span of the material [10]. In addition, the intimate contact between the metallic contents of the LDHs enhances the physico-chemical properties of these materials making it suitable precursors for the synthesis of mixed oxides for hydrogenation and dehydrogenation reactions [6,11]. Metallic contact can be improved upon by boosting the deposition and dispersion of the cations on the adsorbent. This can be achieved by adopting several preparation routes [3,12–14].

In this work, the impact of ultrasonic irradiation and ultrasonic-assisted hydrothermal synthesis conditions on the basicity, adsorption, regeneration and cyclic efficiencies were investigated. This is a follow-up study to recent work [10]. This method has shown to produce materials with well-ordered formation [15]. The prepared samples were characterized using Scanning Electron Microscope (SEM), Energy Dispersion X-ray Spectroscopy (EDX), Brunauer-Emmett-Teller (BET), Thermal Gravimetric Analyzer (TGA), Temperature-Programmed Desorption (TPD), X-ray Photoelectron Spectroscopy (XPS) and X-ray Diffraction (XRD).

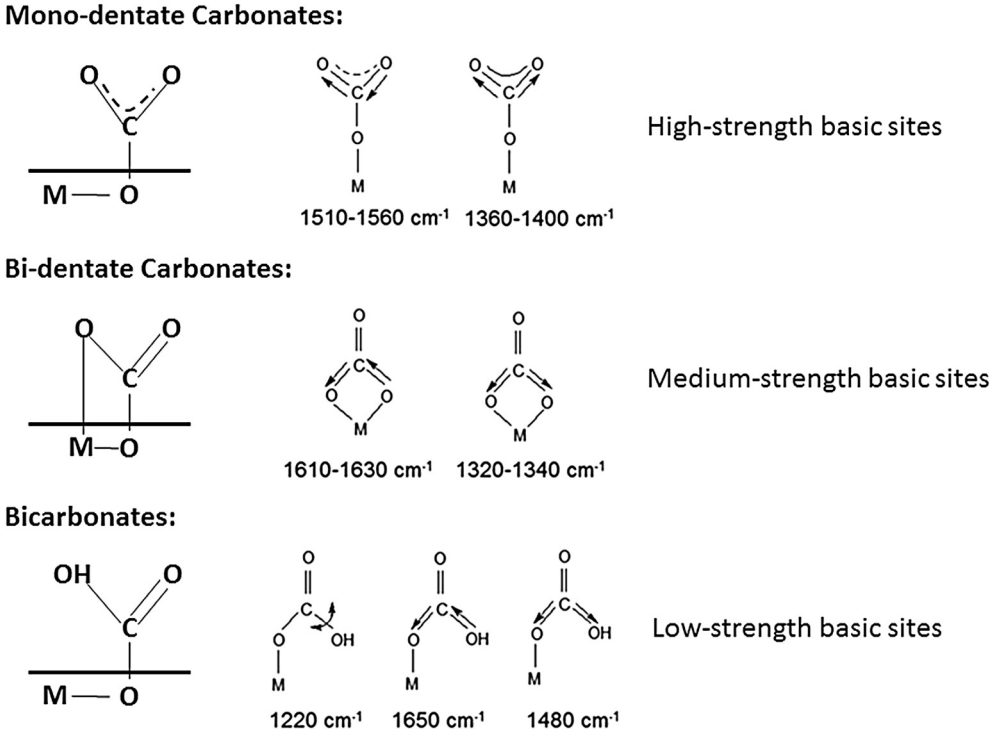

Fig. 2. Infrared bands of adsorbed CO_2 on LDH surface ([9]-Permission obtained).

2. Experimental

2.1. Material preparation

Different preparation methods were used in preparing the layered double hydroxides (LDHs) using the standard method from previous study [10]: conventional co-precipitation, ultrasonic mediated and ultrasonic-assisted hydrothermal. Subsequently, MEA extractions of these LDHs were carried out to produce the amine modified LDHs. All chemicals used for experimentation were acquired from SinoPharm Chemical Reagents Co. Ltd.

2.2. Sample synthesis

For *MgAl LDH,* 200 ml solution containing APTS (≥98%) and SDS (≥86%) (molar ratio: 5:1) respectively dissolved in a mixture of 50 ml C_2H_5OH (≥99.7%) and 150 ml distilled water was stirred for about 30 min at a temperature of 60 °C until the pH stabilized at about 10.3. This solution was then reacted with $Mg(NO_3)_2{\cdot}6H_2O$ (≥98%) and $Al(NO_3)_3{\cdot}9H_2O$ (≥99%) (molar ratio: 3:1, dissolved in 100 ml of distilled water) solution by adding the latter dropwise while maintaining the temperature of the former at 60 °C. The mixture pH was regulated towards 10 using 4 M NaOH (≥96%) solution. The substrate (molar ratio of Mg:Al:APTS:SDS = 3:1:5:1) was then aged for 20 h with the constant stirring at the maintained temperature. The filtered precipitates were then washed with ionised water before being vacuum dried (500 mbar at 70 °C) overnight. This sample is labelled as Conv-LDH. Using the same chemical composition and process, a set of new samples were prepared using sonicated mixing by ultrasonic horns (high intensity sonication, 600 W) [10]. This sample is labelled as US-LDH.

For ultrasonic-assisted hydrothermal synthesised samples, HPH-LDH, 32 ml solution containing APTS (≥98%) and SDS (≥86%) (APTS:SDS molar ratio: 5) was reacted with $Mg(NO_3)_2{\cdot}6H_2O$ (≥98%) and $Al(NO_3)_3{\cdot}9H_2O$ (≥99%) (Mg:Al molar ratio: 3, dissolved in 16 ml of distilled water) solution. The latter was added dropwise while maintaining the temperature of the former at 60 °C and sonicating with ultrasonic horn. The substrate (molar ratio of Mg:Al:APTS:SDS = 3:1:5:1) was moved to the hydrothermal reactor. After being vented with pure N_2 gas (99.99%) for 15 min in order to remove all of the oxygen before the reaction, the reactor was sealed and heated to a temperature of 450 °C with a ramp of 2 °C/min and then held for 15 min. After reaction, the solution was aged for 12 h. The precipitates were filtered, washed with distilled water and then dried in a vacuum oven (500 mbar at 70 °C) for 7 h.

For *MgAl LDH-MEA,* the prepared LDHs were functionalised via MEA extraction. 0.5 g of LDH sample was dispersed in a solution of 100 ml C_2H_5OH (≥99.7%) containing 20 g MEA (≥99%). The mixture was then refluxed for 20 h at a temperature of 90 °C. After which the samples were filtered, washed with ethanol and dried in a vacuum oven overnight. These samples are labelled Conv-MEA. Using an ultrasonic horn, the procedure was repeated for the synthesised US-LDHn samples. The obtained samples are labelled US-MEA. Similarly, this was repeated for the HPH-LDH samples and labelled as HPH-MEA.

2.3. Characterisation

2.3.1. Nitrogen adsorption-desorption analysis

The textural characteristics of the prepared catalysts were studied by Nitrogen physisorption analysis at −196 °C using the Micrometrics ASAP 2020 Surface Area and Porosity Analyser. Prior to this analysis, samples were degassed at a temperature of 105 °C for 4 h. The surface area (S_{BET}) of the samples was determined using the BET (Brunauer, Emmett and Teller) model. The total pore volumes (V_{Total}) were computed from the amount of nitrogen adsorbed at relative pressure (P/P_o) of 0.99 and the average pore volumes from $4V_{Total}/S_{BET}$. The pore size distribution was calculated using the BJH (Barrett, Joyner and Halenda) model. The t-plot method was used to calculate the micopore volume (V_{micro}).

2.3.2. Scanning electron microscope-energy dispersive X-ray spectroscopy (SEM-EDX)

The surface composition and structure of the prepared materials were studied with a Zeiss ΣIGMA™ Field Emission SEM and an Oxford Instrument INCAx-act PentaFET® Precision EDX. The EDX spectra for the LDHs were obtained. This was also used to compute the amine content present in the adsorbents

2.3.3. X-ray diffraction (XRD) and X-ray photoelectron spectroscopy (XPS) analysis

XRD patterns were studied using a Bruker-AXS D8 advance powder diffractometer with a scanning range of $10^\circ \le 2\theta \le 90^\circ$. X-ray Photoelectron Spectroscopy (XPS) data of the adsorbent was obtained using Kratos X-ray Photoelectron Spectrometer – Axis Ultra DLD with a 96 W monochromatic Al Kα X-ray source (1486.69 eV) at a photoelectron take-off angle of 45°. Narrow scans were conducted at steps of 0.05 eV with dwell time of 600 ms whereas wide scans were conducted from 1100 eV to 0 eV with 150 ms dwell time and at 1 eV steps. The C 1 s peak at 284.6 eV was used as the reference for standardizing the binding energy.

2.3.4. Temperature-programmed desorption (TPD)

CO_2-TPD analysis was conducted using AutoChem II 2920. The TPD of CO_2 measurements were conducted to evaluate the basicity of the catalysts. 0.1 g of the adsorbent was treated in the reactor in N_2 atmosphere at a temperature of 350 °C for 2 h. A thermal conductivity detector (TCD) was adopted to analyze desorption trends from 100 to 800 °C at a heating rate of 10 °C/min.

2.3.5. Thermo-gravimetric analysis

Thermal stability and CO_2 uptake measurements were conducted using the Netzsch STA 449 F3 Jupiter thermogravimetric analyser (TGA).

Thermal Stability Measurement. The stability of the as-synthesised LDH samples in air was determined. 0.4 cm^3 alumina crucible was loaded with 5–10 mg of sample and the thermal decomposition examined from 25 to 1000 °C, ramped 10 °C/min and under air flow (50 ml/min).

CO_2 Uptake Measurement. Approximately 5–10 mg of the synthesised sample was heated from 25 to 105 °C at 20 °C/min under N_2 at a flow rate of 50 ml/min; and then held isothermally for 30 min before being cooled to the required adsorption temperature at a rate of 10 °C/min. The gas was switched from N_2 to CO_2 and held isothermally for 90 min at a flow rate of 20 ml/min. The experimental adsorption temperature is 55 °C. The CO_2 adsorption capacity was calculated from the weight difference of the samples in CO_2 atmosphere. The uptake profile was measured against an empty alumina crucible using the same method so as to correct the impact of change in gas density and viscosity.

Thermally Assisted Regeneration of Adsorbent. Regeneration efficiency of the functionalized samples were analysed by thermal-assisted regeneration using nitrogen as a sweep gas. Two cycles of the CO_2 uptake measurement was repeated in this case. In between the cycles, the adsorbents were thermally desorbed at 105 °C in a stream of N_2 at a flow rate of 50 ml/min for 10 min. The amount adsorbed (Q_a) and desorbed (Q_d) were deduced by the change in weight of the samples. The regeneration efficiency (RE) was thus estimated based on Eq. (1):

$$RE = \frac{Q_d}{Q_a} \times 100\% \quad (1)$$

3. Theoretical

To predict kinetic behaviour, the experimental results were

simulated assuming pseudo-first, pseudo-second order and double-exponential kinetic models [16]. The double exponential model was considered because of its feasibility to explain the surface heterogeneity of the adsorbent accounting for two different adsorption sites. Additionally, it can partially elaborate the kinetic mechanisms associated with both pseudo-first and second order reactions. This mechanism can be categorised into a controlled slow phase intra-particle diffusion and a controlled fast phase surface reaction [17].

Pseudo-first order model:

$$x = x_e(1-e^{-k_f t}) \tag{2}$$

Pseudo-second order model:

$$x = \frac{x_e^2 k_s t}{1 + x_e k_s t} \tag{3}$$

Double exponential model:

$$x = x_e-(A_1 e^{-k_1 t} + A_2 e^{-k_2 t}) \tag{4}$$

where x and x_e represents the CO_2 uptake at a given time and equilibrium respectively, k_f and k_s are the first and second order rate constants respectively, A_i and k_i, $i = 1,2$ are pre-exponential factors and rate constants for the two adsorption sites respectively, and t is the time of adsorption. The obtained experimental data are fitted to the models and selecting the one with the best fit.

To determine the suitability of each model, an error function (Err) defined by Eq. (5) was applied:

$$Err(\%) = \sqrt{\frac{\sum_{j=1}^{N}\left[\frac{x_{j,\exp} - x_{j,\mathrm{mod}}}{x_{j,\exp}}\right]^2}{N-1}} \times 100 \tag{5}$$

where x_{exp} and x_{mod} are CO_2 uptake determined experimentally and computed using the model respectively and N is the total number of experimental points. It is reasonable to assume that the adsorption rate constant, k for both pseudo-first and -second order model is the same for each group of functionalized and non-functionalized adsorbents since they are both grafted with the same amino silane. However, this was not assumed in this study. The effect of preparation route on the rate constant was rather studied

4. Discussion of results

4.1. Impact of preparation route on textural properties and surface morphology

From Table 1, S_{BET} of Conv-LDH is *ca.* 25 m^2/g which showed an increase to 171.20 and 311.18 m^2/g for US-LDH and HPH-LDH respectively. In the same trend, the total pore volume showed a tremendous increase, indicating that the sonication and hydrothermal preparation methods enhances the porosity of the sample as well as the surface area when compared to other studies (see Table 2). However, these methods tend to reduce the micropores in the sample with the hydrothermal route exhibiting the least microporous percentile. This depicts that the sample is a mesoporous/macroporous material with minor microporous features. The features of these pores can be seen from Fig. 3. All three samples contained approximately the same volume ratio of mesopores to macropores. However, the Conv-LDH is observed to have a higher percentile of low range mesopores (2–10 nm) contributing to 55% of the total pore volume as compared to 10% and 15% for US-LDH and HPH-LDH respectively. The high range mesopores (10–50 nm) accounted for about 50% of the total pore volume of the US-LDH and HPH-LDH samples compared to *ca.* 7% in Conv-LDH. This can be further illustrated by the inserted image of Fig. 3 displaying the pore size distribution in terms of total volume percentages.

Table 1
Texture properties of the samples.

Sample	S_{BET} (m^2/g)	Particle Size (nm)	V_{Total} (cm^3/g)	V_{micro} (cm^3/g)	Average Pore Width (nm)	%Micro* (%)
Conv-LDH	25.03	239.67	0.0161	0.0008	2.57	4.97
US-LDH	171.20	35.05	0.5528	0.0229	12.92	4.14
HPH-LDH	311.18	19.28	1.4005	0.0023	18.00	0.16

*%Micro = V_{micro}/V_{Total}.

Table 2
Comparison of S_{BET} for different LDH adsorbent via different preparation routes.

Sample*	Preparation Method	SBET (m^2/g)	Reference
LDH	Commercial	2.90	[18]
CO_3-LDH	Commercial	18.90	[19]
Conv-LDH	Co-precipitation	10.50	[20]
Conv-LDH	Co-precipitation	44–70	[18]
Conv-LDH	Co-precipitation	69.78	[21]
Conv-LDH	Co-precipitation	25.03	Current work
c-LDH	Calcined Co-precipitation	84–123	[18]
c-CO_3-LDH	Calcined Solvothermal	165.07	[22]
US-LDH	Ultrasonic assisted	84.44	[21]
US-LDH	Ultrasonic assisted	171.20	Current work
r-LDH	Reconstructed	45–55	[18]
CO_3-LDH	Solvothermal	24.74	[22]
LDH	Silylated-Calcined	19.20	[23]
HPH-LDH	Hydrothermal	311.18	Current work

*LDH samples are Mg-Al LDH.

Fig. 4 shows the total absolute volume of the pores at various pore size. It depicts that the high range mesopores mostly contribute to the total pore volume of the samples and comprises of a higher pore distribution.

Fig. 5 shows the N_2 adsorption-desorption isotherms for Conv-LDH, US-LDH and HPH-LDH samples. The adsorbents show a type IV isotherm with H1 hysteresis loop characterized with the formation of a monolayer accompanied by multilayers occurring as a result of capillary condensation. This is a characteristic feature of mesoporous materials [24–26] validating the data represented in Table 1. These H1-hysteresis type materials are attributed to the formation of aggregates or compact uniform spheres as shown in the SEM images [26]. The hysteresis loop for the HPH-LDH was observed to be broader than that of US- and Conv-LDHs indicating the extent of capillary condensation in the samples. It is observed that the volume adsorbed by HPH-LDH is 3 folds that of US-LDH, which in turn is ~30 folds of the conventional LDH. This depicts an enhancement in the pore structure of the samples and is attributed to the enhancement of nucleation and precipitate growth resulting from improved dissolution and reaction process via sonication [20] and hydrothermal crystallization [27].

Considering the surface texture of the samples, Fig. 6 shows the images of surface morphology of the prepared LDH samples. It can be seen from the figure that Conv-LDH presents a boulder-shaped material with aggregated flaky plate-like surface. This may be explained by the formation of shell-core structure caused by the sequential reduction of two different metallic ions [10,28] resulted from the difference in the reduction potentials of Al^{3+} and Mg^{2+} ions. This is similar to the sonication route sample but without the plate-like surface. Surface of these samples displayed more pores attributable to high-speed jets or shock waves resulting from bubble collapse [28]. Unlike the conventionally and ultrasonically prepared samples, the hydrothermal LDHs were smaller and of spherical structure, hence increasing the effective surface area for adsorption.

4.2. Impact of preparation route on surface chemical content

To investigate the impact of different preparation routes on the

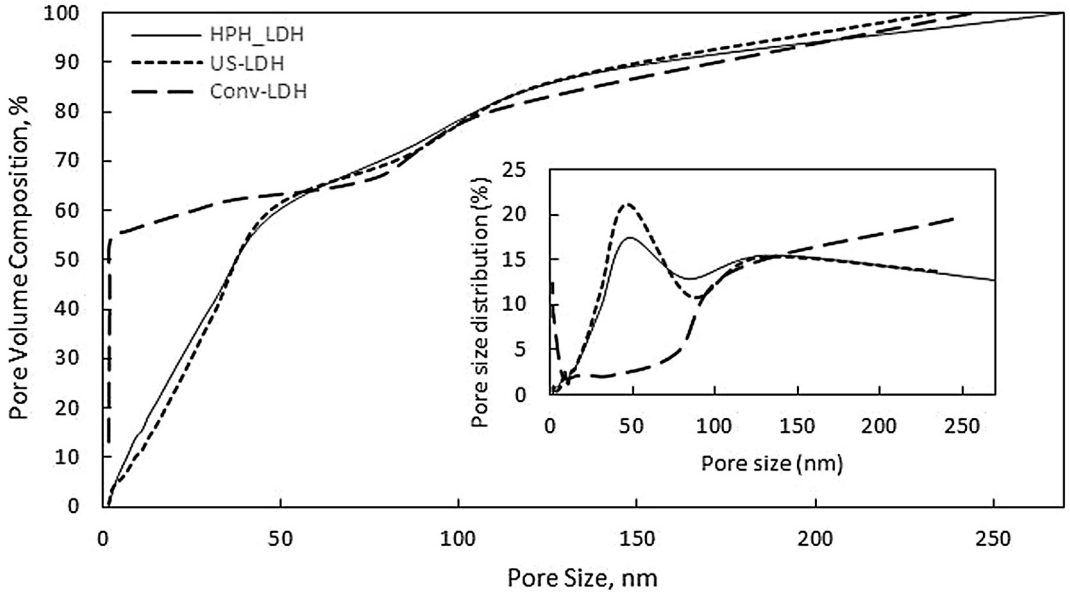

Fig. 3. Pore size distribution of Conv-, US- and HPH-LDH samples.

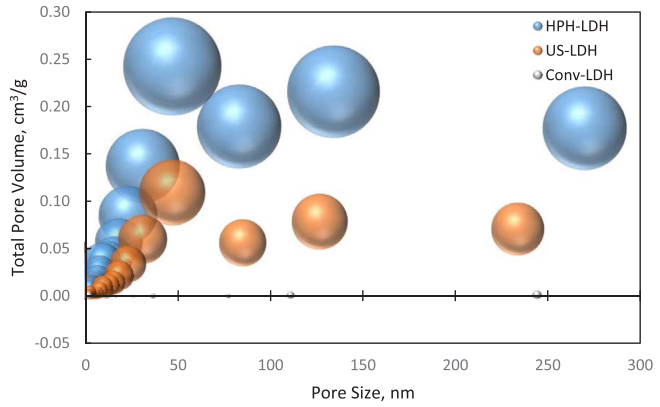

Fig. 4. Total pore volume of various pore sizes of Conv-, US- and HPH-LDH samples (bubble size indicates relative amount of pore size).

amine functional group and extent of oxidation on the surface of the adsorbent, XPS analysis was conducted. The N 1s and O 1s spectra are shown in Fig. 7 and the data are summarised in Table 3. The deconvolution of N 1s spectra has two peaks at *ca.* 396 (± 0.9) eV and 400 (± 0.9) eV respectively (Fig. 7a). These are assigned to free amine and protonated amines respectively [10,29]. The concentration of free amino group decreased for species prepared via ultrasonic and hydrothermal mediation. This reveals that despite the enhanced physical properties of the adsorbent, ultrasonic and hydrothermal process has a reduced amount of free amino active sites on the adsorbent. This can be explained by the enhanced protonation of the free amine groups. However, the amine loading (deduced by the total concentration of N atom) is highest in species prepared via ultrasonic irradiation and least in the hydrothermal process. This can be partially attributed to the efficient ejection of hydroxyl radicals from bubbles during cavitation, which readily hydrates the anions; hence bonding the anions within the interlayers of the adsorbent [30]. This can be supported by the high

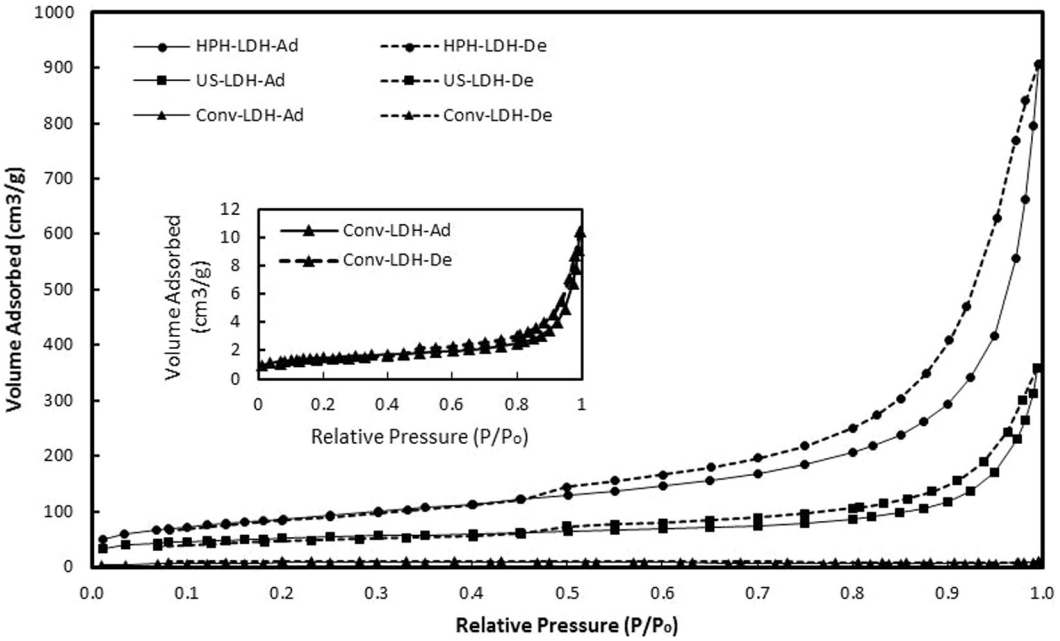

Fig. 5. Nitrogen adsorption-desorption isotherms for Conv-LDH, US-LDH and HPH-LDH samples (inserted image shows the enlarged isotherm for Conv-LDH).

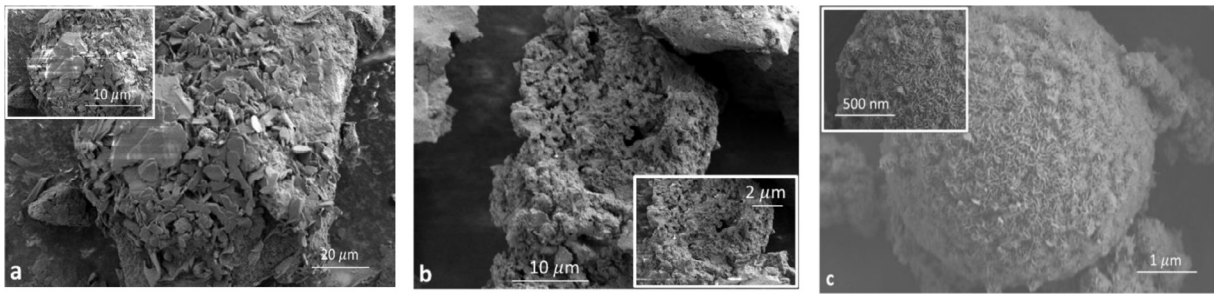

Fig. 6. SEM images of prepared LDHs (a) Conv-LDH, (b) US-LDH, and (c) HPH-LDH.

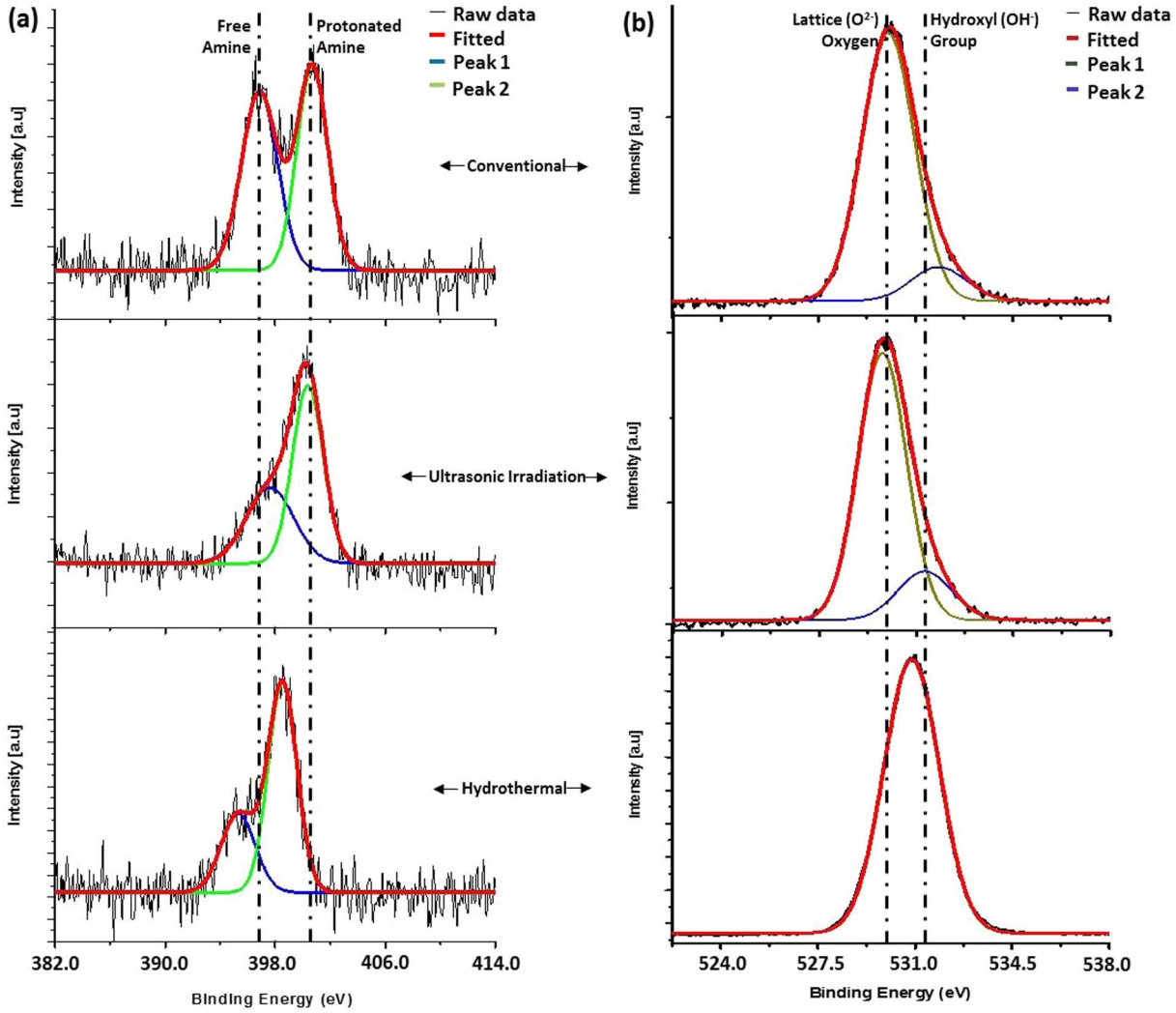

Fig. 7. XPS spectra of conventionally-, ultrasonically- and hydrothermally-prepared LDHs for (a) N 1s and (b) O 1s.

Table 3
Surface content and binding energy for N 1s and O 1s levels for LDH, US-LDH and HPH-LDH.

Preparation Route	Sample	N 1s Spectra					O 1s Spectra				
		Binding Energy (eV)		Area (cps eV)		Content $\left(\frac{Free}{Protonated}\right)$	Binding Energy (eV)		Area (cps eV)		Content $\left(\frac{OH^-}{O^{2-}}\right)$
		Free Amine	Protonated Amine	Free Amine	Protonated Amine		Lattice Oxygen (O^{2-})	Hydroxyl Group (OH^-)	Lattice Oxygen (O^{2-})	Hydroxyl Group (OH^-)	
Conventional	Conv-LDH	396.7	400.8	640.0	626.4	1.02	529.9	531.4	7633.2	1011.8	0.13
Ultrasonic	US-LDH	396.9	400.3	574.1	876.6	0.65	529.8	531.3	10109.2	2053.1	0.21
Hydrothermal	HPH-LDH	395.4	399.1	349.7	791.2	0.44	530.4	–	60510.2	–	–

content of hydroxyl group (OH^-) in samples synthesised via ultrasonic irradiation. Similar to the N 1s spectra, Fig. 7b shows the deconvolution of the O 1s spectra into two bands at 529.1 eV and 531.6 eV respectively. However, only the former band (with a 0.75 eV chemical shift) was observed in the hydrothermally prepared sample. The first band relates to lattice oxygen (O^{2-}), while the latter relates to adsorbed surface oxygen or hydroxyl groups (OH^-) [13,31]. The results summarised in Table 3 show that the ratio of hydroxyl group to lattice oxygen increased with ultrasonic irradiation but decreased with hydrothermal synthesis. This indicates that the surface concentration of the OH^- group is least for the hydrothermal process and greatest in the ultrasonic mediated process. This is consistent with findings from CO_2-TPD analysis. This can be ascribed to the boosted crystallization of the metal oxides due to enhanced transport properties of supercritical water, a characteristic of the hydrothermal process [32]. Supplementary documents (Tables S1 and S2) support this finding. This hypothesis is made visible with the aid of the EDX spectroscopy (see supplementary documents, Fig. S1), which shows the enhanced dispersion of the metals (Al^{3+} and Mg^{2+}) across the adsorbent. The high concentration of lattice oxygen in the hydrothermal route can be associated to the increased Mg content in the form of Mg-O-Mg groups or Mg^{2+}-O^{2-} ion pairs [33].

CO_2-TPD analysis was used to measure the surface basicity of the synthesised LDHs (Fig. 8). Surface basicity increases with increase in desorption temperature [6]. As shown in Fig. 8a, the desorption of CO_2 basically occurs at overlapping peaks of 270 °C (α) and 363 °C (β), 474 °C (γ) and 569 °C (δ). At low temperatures (< 400 °C), desorption of CO_2 is related to released CO_2 from bicarbonates formed on weak and medium basic sites [10]. These weak sites are characteristics of the Brønsted OH^- group which are observed to be more prominent in the conventional and ultrasonic mediated routes [6] (Fig. 8b). This corresponds with reported literatures validating that more weak and moderate basic sites are formed with the aid of ultrasonic irradiation [13]. Nonetheless, HPH-LDH desorbed CO_2 at intermediate/high temperature states (> 400 °C). These are strong basic sites and relate to bi-dentate and mono-dentate carbonates adsorbed on low coordinative unsaturated lattice oxygen (O^{2-}). This tends to agree with XPS and EDX results. A practical application of the basicity of this material vary from the recovery of CO_2 from flue gases at low basic strength (low temperature level) to higher basic strength (high temperature level) processes like sorption enhanced hydrogenation. The latter has the advantage of ease of regeneration at low temperature gradients [6].

To further understand the surface chemical content of the adsorbent, the amino functional group necessary for adsorption of CO_2 was quantified using EDX results (See supplementary data Table S1). Table 4 shows the elemental analysis of each prepared sample using the EDX results from Table S1. As shown in Table 4, the amine loading was more effective using ultrasonic mediated route with 2.22 mmol/g as against 1.82 and 0.46 mmol/g for ultrasonic-assisted hydrothermal and the conventional route respectively. However, after functionalization of the adsorbent, the amine loading increased to 4.71, 5.24 and 5.26 mmol/g for conventional, ultrasonic and ultrasonic-assisted hydrothermal synthesis respectively. This is observed to be a significant improvement compared to those results reported in literatures as documented in supplementary Table S3.

4.3. Impact of preparation route on structural configuration

Fig. 9 shows the XRD analysis of synthesised LDHs. Typical Mg-Al LDH exhibits three separate peak regions: (a) high angle region ($2\theta > 60^{\circ}$) consisting of *hk0* and *hkl* reflections attributed to the ordering within the metal hydroxide layers, (b) the mid-angle region ($30^{\circ}2\theta > 60^{\circ}$) attributed to non-basal reflection *0kl* whose locations are characteristic of the structural disorder and, (c) the low angle region ($2\theta > 60^{\circ}$) consisting of the *00l* and *h00* basal reflections characteristic of the size of intercalated anion [34]. These XRD reflections have been indexed according to the hexagonal lattice with rhombohedral symmetry (space group: R3m) [34–36]. A brief look from the figure indicates that the intensity of all reflections increased with the hydrothermal process. This is associated with an increase in interlayer water molecule and partial hydroxylation of double hydroxide sheets [37]. For the high angle region, peak at ($2\theta > 60^{\circ}$) containing overlapping reflections of (1 1 0) and (1 1 3) attributed to interlayer spacing indicates that the hydrothermal route increases interlayer spacing. This is reported to be associated with the presence of oxygen-containing functional groups [38], which is observed to be highest in the hydrothermal synthetic method due to high metallic deposition and dispersion. Hydrothermal route is considered an important synthetic method for the preparation of highly dispersed heterogeneous materials. This is due to its tendency to dissolve and recrystallize materials at high temperature and pressure [39]. The 200 lattice peak reflection explains the crystal size of the material and its intensity is dependent on chemical composition and molar (M^{2+}/M^{3+}) ratio [40]. Consequently, the strength of basic sites should vary with the peak intensity, thus validating the effect of deposition and dispersion of divalent and trivalent cations on basic strength. For the low and mid-angle region, the increase in peak intensities can be attributed to change in configuration of the interlayer nitrate from single flat-lying molecular layer to multiple layers and with different orientation [35,41]. To this effect, using the results of X-ray diffraction and polarized attenuated total reflection

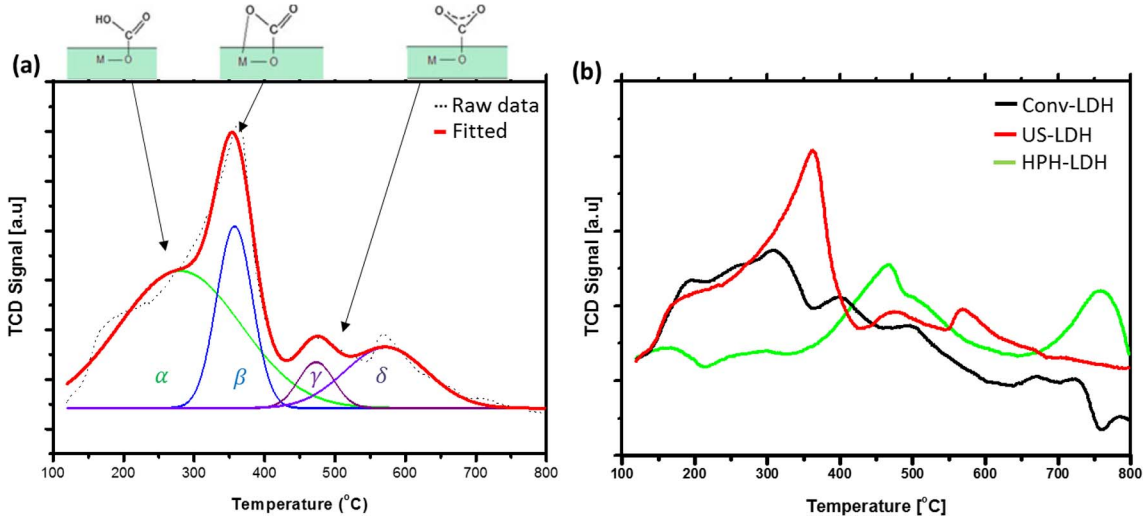

Fig. 8. CO_2-TPD of synthesised LDH (a) Deconvolution of the CO_2-TPD of UH-LDH and (b) Comparison of CO_2-TPD of Conv-LDH, US-LDH and HPH-LDH.

Table 4
EDX elemental analysis and CO2 uptake of prepared LDH and calculation results for the molecular formulas, removed SDS and effective amine efficiency.

Sample	N (wt%)	C (wt%)	S (wt%)	Molecular formula (mmol/g)[a]	SDS/APTS	Amine Loading (mmol/g)	CO_2 Adsorbed (mmol/g)	SDS removed (%)	Effective amine loading (mmol/g)[b]	Effective Amine Efficiency[c]
Conv-LDH	0.65	51.35	11.41	$[C_{12}H_{25}SO_4]_{3.57} - [C_{0.01}H_{0.52}SiNO_3]_{0.46}$	7.68	0.46	0.82			
Conv-MEA	6.60	26.60	1.05	$[C_{12}H_{25}SO_4]_{0.33} - [C_{3.87}H_{10.17}SiNO_3]_{4.71}$	0.07	4.71	1.45	99.09	4.25	0.15
US-LDH	3.11	51.16	11.08	$[C_{12}H_{25}SO_4]_{3.46} - [C_{0.49}H_{1.72}SiNO_3]_{2.22}$	1.56	2.22	0.66			
US-MEA	7.34	30.64	0.60	$[C_{12}H_{25}SO_4]_{0.19} - [C_{4.44}H_{11.60}SiNO_3]_{5.24}$	0.04	5.24	1.37	97.71	3.02	0.24
HPH-LDH	2.55	13.68	1.50	$[C_{12}H_{25}SO_4]_{0.47} - [C_{3.17}H_{8.43}SiNO_3]_{1.82}$	0.26	1.82	0.88			
HPH-MEA	7.36	9.27	0.82	$[C_{12}H_{25}SO_4]_{0.26} - [C_{0.88}H_{2.71}SiNO_3]_{5.26}$	0.05	5.26	3.75	81.06	3.44	0.83

[a] All Nitrogen, Carbon and Sulphur elements in the grafted LDHs were attributed to come from organic compounds used for intercalation.
[b] Effective amine loading = Difference in amine loading before and after LDH modification.
[c] Effective Amine Efficiency = Difference in CO_2 adsorbed before and after LDH modification/effective amine loading.

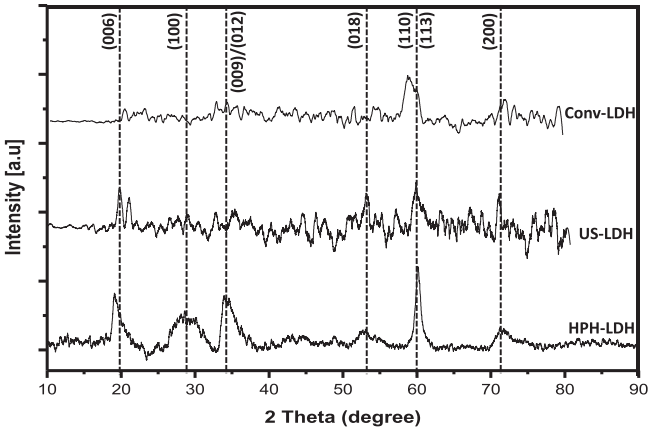

Fig. 9. X-ray diffraction patterns of synthesised Mg/Al LDHs via conventional co-precipitation (Conv-LDH), ultrasonic irradiation (US-LDH) and sonochemical-assisted hydrothermal route (HPH-LPH).

FTIR spectroscopy, Wang and Wang [41] explained that the change in orientation of interlayer nitrate anions is dependent on chemical composition of LDH. This corresponds with XPS and TPD results.

4.4. Impact of preparation route on thermal stability

The thermal stability of the prepared samples were obtained using Netzsch STA 449 F3 TGA from 25 °C to 1000 °C with a 10 °C/min ramp. Fig. 10 shows the TGA profiles for thermal disintegration of the prepared samples. Three distinct temperature phases were observed for material disintegration: T < ~ 150 °C, ~150 < T < ~ 750 °C and ~750 °C < T. The first phase of weight loss (T < ~ 150 °C) is attributed to the loss of interstitial water molecules. While for the second phase (~150 < T < ~ 750 °C), the decomposition can be ascribed to the dehydroxylation and breakdown of the organic alkyl chain of the LDH. The observed irregular decomposition curve in this stage may indicate the occurrence of an uneven bonding structure, resulting to multi-stage dehydroxylation processes. The final weight loss (~750 °C < T) results from the decomposition of the sulphate species residuum [10]. From Fig. 10a–c, it can be inferred that the thermal strength of HPH-LDH is higher than that of the conventional and ultrasonically prepared samples with a total weight loss of 68.98 amd 68.12% respectively, when compared to 10.56% of HPH-LDH as tabulated in Table S4 (supplementary document). For the first phase, the moisture content decreased significantly from 8.35 to 3.41% as the preparation process changed from conventional to hydrothermal. A more drastic reduction was experienced with the interstitial moisture content (second phase). This can be attributed to the enhanced bonding introduced by the hydrothermal process forming multi-layers as estimated from the XRD results. The third degradation phase infers that ultrasonic process is more likely to deposit more sulphate species, while the hydrothermal process is the least to do so. This is corresponds to the results obtained from XPS analysis (Table S2, supporting document). This indicates that the adoption of the hydrothermal-route may be beneficial to the synthesis of a more stable material than the ultrasonic and conventional method.

After introducing amine modification of the samples, the decomposition curves clearly show different behaviour compared with that of the untreated LDHs prepared by the same method. The curves display a well-defined three phase decomposition steps unlike the untreated ones, as can be seen from Fig. 10(d–f). Within the same temperature range as that of the LDHs, the MEA-treated LDHs showed higher moisture content than the unprocessed ones except for the hydrothermal samples. This can be caused by the presence of leftover MEA molecules after the extraction process, which may have been strongly bonded to the hydrothermal samples resulting to the increase in weight loss in the second and third phase. However, for the ultrasonic and conventional route, the weight losses in the second and third phase reduced significantly, benefitting to production of a more stable material than the pure LDH. This can be explained by the reduced presence of the surfactant after the amine extraction. Showing from the total weight loss, it can be concluded that the thermal strength of the hydrothermal samples (total weight loss: 38.17%) even after amine extraction is better than that of the conventional and ultrasonically prepared samples (total weight loss: 52–53%).

4.5. Impact of preparation route on effective amine efficiency, CO_2 uptake, regeneration efficiency and cyclic efficiency

The average CO_2 uptake for the various synthesis route is shown in Fig. 11. The results show a reduction in CO_2 uptake for the US-LDH when compared to the conventional, Conv-LDH. This corresponds to results from previous study [10]. However, an insignificant increase in CO_2 uptake was observed for the hydrothermally prepared sample, HPH-LDH. Despite the enhanced textural properties of HPH-LDH, the adsorption capacity of this adsorbent showed no appreciable improvement. However, after amine extraction, the amine loading of adsorbents increased for all considered routes. This is part due to the exfoliation of the surfactant (SDS) (shown in Table 4) which varied from *ca.* 99%, 98% and 81% in the conventional, ultrasonic and hydrothermal processes respectively. As a result, this impacted on the effective amine loading and efficiency of the adsorbent. The effective amine loading was computed as the difference in amine loading before and after amine extraction, whereas effective amine efficiency was computed as the ratio of the difference in CO_2 adsorbed before and after amine extraction to effective amine loading. HPH-MEA showed the highest effective amine efficiency of 0.83 compared to 0.24 and 0.15 for US-MEA and Conv-MEA respectively. This can be partly related to the improved deprotonation of protonated amino groups resulting from enhanced transport properties, characteristic of the hydrothermal process [32]. This expounds the impact of sonication and hydrothermal pre-

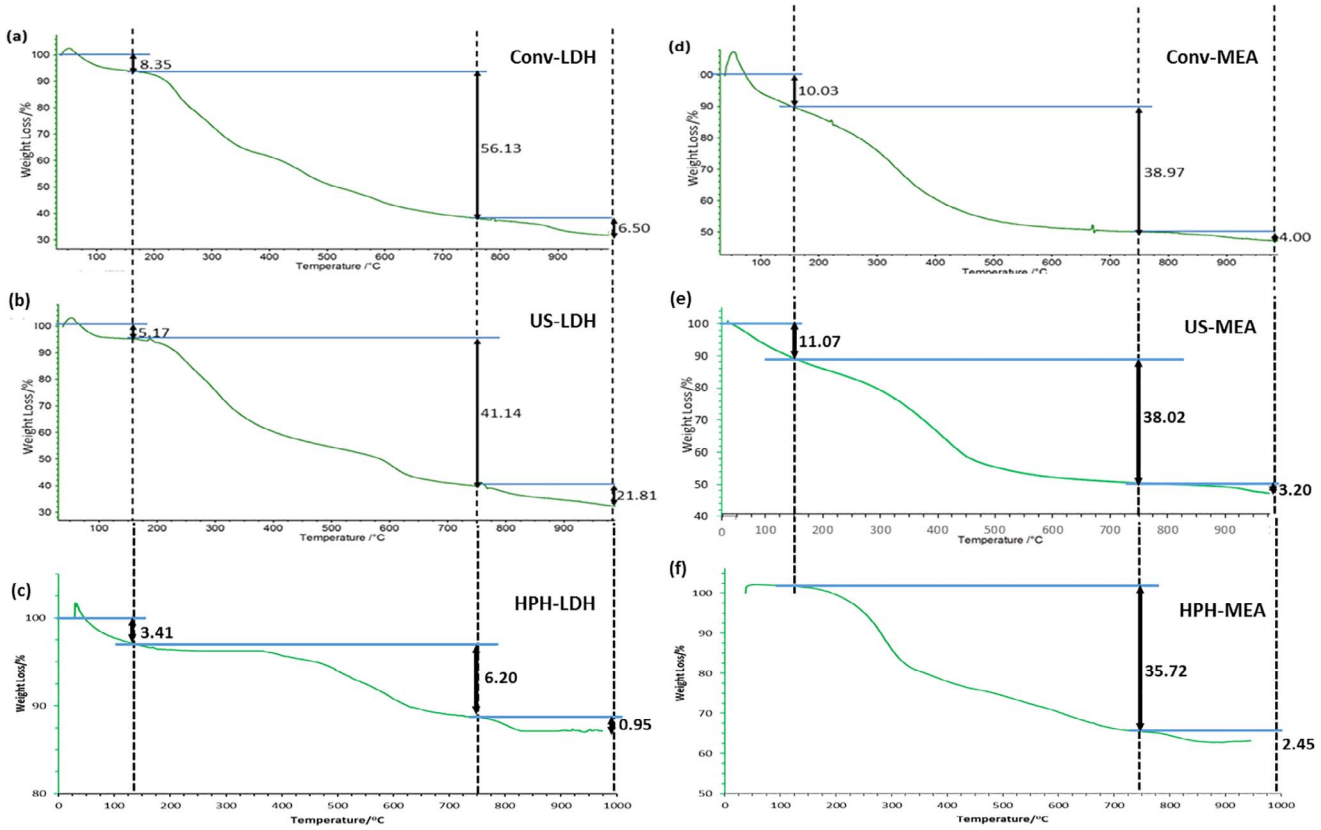

Fig. 10. TGA curves comparing thermal stabilities of LDHs prepared via conventional and ultrasonic irradiation: (a) Conv-LDH, (b) UH-LDH and (c) HPH-LDH; as well as with amine modified LDHs: (d) Conv-MEA (e) UH-MEA and (f) HPH-MEA.

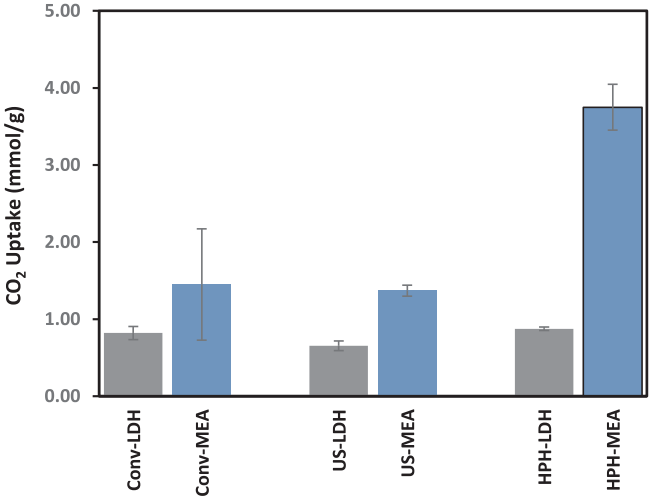

Fig. 11. Average CO_2 Uptake of LDH and amine-modified LDH prepared via the different routes.

treatment in deprotonating protonated and/or probable dispersion of amino sites during LDH-amine modification. Consequently, the adsorption capacity of HPH-LDH increases from 0.88 to 3.75 mmol/g when compared to the increase of Conv-LDH from 0.82 to 1.45 mmol/g (supplementary document, Table S5). This indicates that CO_2 uptake was stimulated more by chemisorption rather than physisorption. This can be attributed to the difference in basic strength of the prepared adsorbents.

Thermal swing regeneration in an atmosphere of N_2 was adopted for the regeneration of the amine modified adsorbent. A typical example of the regeneration profile is shown in Fig. S2 of supplementary document. In this figure, the effect of the preparation route on the cyclic sorption capacity of the adsorbent is presented. Amount of CO_2 desorbed was measured after the first adsorption cycle prior to the second adsorption process. Consecutively, the regeneration and cyclic efficiencies of the adsorbents were calculated (supplementary document, Table S5). From the tabulated results in the figure, it is observed that HPH-MEA has the highest regeneration efficiency of 93%. This is a significant change when compared to 78% and 86% regeneration efficiencies for US-MEA and Conv-MEA respectively. However, the cyclic efficiency (computed as the percentage ratio of CO_2 uptake from 2nd cycle to 1st cycle) of US-MEA is 76% compared to 60% and 53% for Conv-MEA and HPH-MEA respectively. Analysing the cyclic and regenerated efficiencies, it can be projected that the ultrasonic mediated synthesis route has an effective adsorption potential than the other two processes. It is observed that of the 78% regenerated active site, approx. 76% of this active site underwent the 2nd adsorption process. This is lesser in Conv-MEA and HPH-MEA respectively. The degradation in the cyclic adsorption efficiencies of these samples can be ascribed to the secondary reactions occurring between the amino group and CO_2 as elaborated in previous study [10]. This implies that the ultrasonic mediated route is more suitable for the synthesis of long term effective CO_2 LDH adsorbents. However, the hydrothermal process provides a significant change in sorption capacity of the adsorbent. Optimization of these two processes will contribute immensely to both sorption efficiency and effectiveness.

4.6. Comparison of kinetic models

From simulation results, the experimental kinetic uptake data for the samples synthesised from the different synthesis routes are summarised in Table 5. Comparative plots of these data using the kinetic models discussed in the previous section are shown in Fig. 12. The results show that the double exponential model produced the best fit for the experimental data (considering the R^2 values). This unlike the

Table 5
CO_2 kinetic model parameters, R^2 and standard errors (%) for prepared LDHs and amine functionalized LDHs at 55 °C and 1 atm.

Samples	Pseudo 1st Order		Err	R^2	Pseudo 2nd Order		Err	R^2	Double Exponential					Err	R^2
	x_e	k_f	(%)		x_e	k_s	(%)		x_e	A_1	A_2	k_1	k_2	(%)	
Conv-LDH	0.75	0.12	0.07	0.9766	0.83	0.23	0.34	0.9483	0.76	0.31	0.55	0.31	0.10	3.71	0.9815
US-LDH	0.55	0.09	0.37	0.9062	0.63	0.20	0.81	0.9631	0.85	0.47	0.45	0.01	0.23	9.24	0.9897
HPH-LDH	0.89	0.05	0.14	0.9356	1.14	0.04	0.38	0.9034	0.88	0.48	0.48	0.06	0.06	0.28	0.9421
Conv-MEA	1.33	0.13	0.10	0.8786	1.46	0.14	0.08	0.9711	1.41	0.75	0.67	0.05	0.69	0.41	0.9968
US-MEA	1.32	0.05	0.10	0.9826	1.67	0.03	0.28	0.9709	1.30	0.70	0.70	0.06	0.06	0.09	0.9861
HPH-MEA	3.52	0.35	2.06	0.8733	3.72	0.17	2.34	0.9155	3.58	1.63	2.04	0.14	1.07	2.01	0.9327

pseudo first and second order model, is explained to account for the heterogeneity of the adsorbent's surface [16]. In other words, it describes the adsorption mechanism to comprise of two different adsorption sites. Consequently, elucidating the occurrence of more than one reaction mechanism [42]. Therefore, the double exponential model can be explained to be of best fit of the three models because it possibly accounts for both chemisorption and physisorption of CO_2. Rate constants $k_{i=1,2}$ are the reaction rate coefficients for the respective adsorption mechanisms. The simulated results showed no particular variation of these parameter with the preparation route. The pre-exponential factors, $A_{i=1,2}$, indicate the weight coefficient that reflects the share of each adsorption mechanism [17]. From the tabulated results, it is observed that the second adsorption mechanism (indicated by i = 2) contributed a greater share towards CO_2 adsorption in Conv-LDH. This gradually reduced in US-LDH and was approximately evenly distributed between the two mechanisms in HPH-LDH.

Pseudo first and second order model also provided a relatively good fit for the experimental results. However, comparing to pseudo second order model, pseudo first order provided a better fit for both Conv-LDH and HPH-LDH experimental data. This model better explains low surface coverage adsorption [43] whereas the pseudo second order model accounts for adsorption by chemisorption or adsorption at high

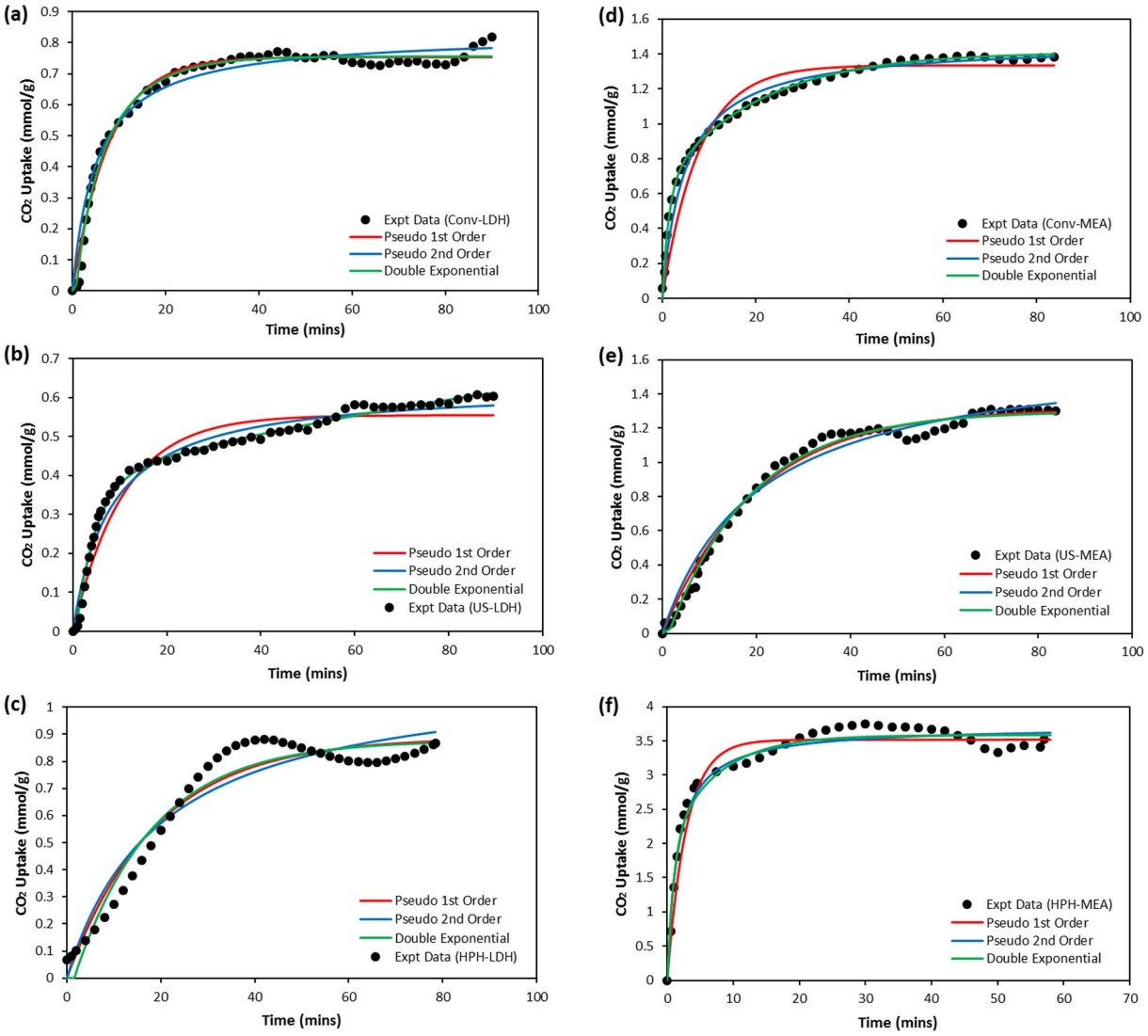

Fig. 12. Comparison of different kinetic models with experimental data generated for adsorption kinetics of CO_2 on (a) Conv-LDH, (b) US-LDH, (c) HPH-LDH, (d) Conv-MEA, (e) US-MEA and (f) HPH-MEA under and 55 °C and 1 atm.

adsorbate loadings [44]. Hence, it is logical to attribute the fitting of the second order model to US-LDH experimental data to the high amine loading. Considering the kinetic parameters, k_f and k_s, which depicts the time scale for the process to reach equilibrium [17]. Inverse of these parameters indicates the time required for the process to attain equilibrium. As shown in Table 5, the $k_{f,s}$ decreased in the following trend: conventional > ultrasonic > hydrothermal. This portrays that conventionally prepared LDH tends to attain equilibrium quicker than samples prepared from the other routes. Although pseudo first and second order models are associated with surface reaction control systems [17], the former was also derived by assuming film diffusion (FD) control [45] whereas the later simulates intra-particle diffusion (IPD)-driven kinetics of sorption for systems with both plane and spherical sorbent particles [46]. Consequently, it is likely to assume that IPD is more promoted in US-LDH.

After amine extraction, the double exponential model was also of best fit for the obtained experimental data. However, the reverse trend was observed for the share of each adsorption mechanisms. Summarised results (Table 5) show that both adsorption mechanism approximately contributed evenly in the adsorption process in Conv-MEA and US-MEA; but the second mechanism dominated in HPH-MEA. The nature of these mechanisms are undetermined in this study but can be seen to give an insight on the adsorption trend of each sample. Nonetheless, correlating these findings with characterization results, the first adsorption mechanism (indicated by i = 1) can be inferred to be associated with the physical textural properties of the adsorbent. Subsequently, the enhanced textural properties via ultrasonic and hydrothermal treatment resulted to the increase in the share of the first adsorption mechanism. However, after amine extraction, the second mechanism, assumed to be characterized by chemisorption, increased in share in the following trend: Conv-MEA < US-MEA < HPH-MEA. This can be attributed to the enhanced amine loading and effective amine efficiency.

5. Conclusion

A detailed comparison study of the impact of ultrasonic and hydrothermal pre-treatment on the basic strength, textural characteristics, effective amine efficiency, CO_2 adsorption and regeneration capacities of Mg-Al LDH has been conducted. In addition, the contribution of these preparation routes to the thermal stability and reaction kinetics was discussed. The results obtained using the kinetic models clearly indicate that prior to amine extraction, the adsorption of Mg-Al LDH adsorbent is mostly facilitated by physisorption while adsorption is mainly promoted by chemisorption after amine extraction. The conclusions reached as the result of the present study can be summarised:

(1) Characterization results show that the ultrasonic-assisted hydrothermal route immensely improves the porosity and surface morphology of the adsorbent. Furthermore, the surface chemical content was characterized with improved metal-ion distribution, hence increasing the basic strength of the adsorbent. This strongly contributes to the improved adsorption and regeneration capacities, as well as the thermal stability of the adsorbent.
(2) The reason that the ultrasonic-assisted hydrothermal treatment can effectively promote the adsorption capacity of the adsorbent can be partially attributed to the ascent in the amount of strong basic sites (O^{2-}) and subsequent decrease in both moderate (M-O) and weak (OH^- groups) basic sites resulting from the hydrothermal process.
(3) The cyclic adsorption efficiency of the sorbent materials from the sonochemical process is better than those from both hydrothermal and conventional preparation routes. The sonochemical route shows the potential for enhanced amine loading and cyclic efficiency, thus providing a more suitable and economical approach for synthesis of double layered hydroxides.

Acknowledgement

This study was conducted at the International Doctoral Innovation Centre (IDIC). The authors would like to acknowledge the financial support from National Natural Science Foundation of China (NSFC) (Grant No. 21576141) and Zhejiang Provincial Natural Science Foundation (Grant No. LY15B060001) and Ningbo Key Research Project 'Absorption/catalytic technologies for the simultaneous removal of multi-pollutants from flue gas at power stations' (Grant No. 1012B10042), and from Ningbo Science and Technology Bureau, The University of Nottingham, Ningbo Education Bureau and China's MoST. This work was also partly supported by the UK Engineering and Physical Sciences Research Council (Grant No. EP/G037345/1).

Appendix A. Supplementary data

Supplementary data associated with this article can be found, in the online version, at http://dx.doi.org/10.1016/j.ultsonch.2017.07.013.

References

[1] J. Wang, L.A. Stevens, T.C. Drage, C.E. Snape, J. Wood, Preparation and CO2 adsorption of amine modified layered double hydroxide via anionic surfactant-mediated route, Chem. Eng. J. 181–182 (2012) 267–275.
[2] J.D. Figueroa, T. Fout, S. Plasynski, H. McIlvried, R.D. Srivastava, Advances in CO2 capture technology—The U.S. Department of Energy's Carbon Sequestration Program, Int. J. Greenhouse Gas Control 2 (2008) 9–20.
[3] M. Szabados, R. Mészáros, S. Erdei, Z. Kónya, Á. Kukovecz, P. Sipos, I. Pálinkó, Ultrasonically-enhanced mechanochemical synthesis of CaAl-layered double hydroxides intercalated by a variety of inorganic anions, Ultrason. Sonochem. 31 (2016) 409–416.
[4] F. Cavani, F. Trifirò, A. Vaccari, Hydrotalcite-type anionic clays: Preparation, properties and applications, Catal. Today 11 (1991) 173–301.
[5] N.D. Hutson, B.C. Attwood, High temperature adsorption of CO2 on various hydrotalcite-like compounds, Adsorption 14 (2008) 781–789.
[6] D.I. Ferrer, Supported Layered Double Hydroxides as CO2 Adsorbents for Sorption-enhanced H2 Production, Chemical Engineering, Imperial College, London, United Kingdom, Springer International Publishing Switzerland, 2016, pp. 209.
[7] L.H. Chagas, G.S.G. De Carvalho, W.R. Do Carmo, R.A.S. San Gil, S.S.X. Chiaro, A.A. Leitão, R. Diniz, L.A. De Sena, C.A. Achete, MgCoAl and NiCoAl LDHs synthesized by the hydrothermal urea hydrolysis method: Structural characterization and thermal decomposition, Mater. Res. Bull. 64 (2015) 207–215.
[8] Y. Gao, Z. Zhang, J. Wu, X. Yi, A. Zheng, A. Umar, D. O'Hare, Q. Wang, Comprehensive investigation of CO2 adsorption on Mg-Al-CO3 LDH-derived mixed metal oxides, J. Mater. Chem. A 1 (2013) 12782–12790.
[9] J.I. Di Cosimo, V.K. Díez, M. Xu, E. Iglesia, C.R. Apesteguía, Structure and Surface and Catalytic Properties of Mg-Al Basic Oxides, J. Catal. 178 (1998) 499–510.
[10] C.I. Ezeh, X. Huang, X. Yang, C.-G. Sun, J. Wang, Sonochemical surface functionalization of exfoliated LDH: Effect on textural properties, CO2 adsorption, cyclic regeneration capacities and subsequent gas uptake for simultaneous methanol synthesis, Ultrason. Sonochem. 39 (2017) 330–343.
[11] D.P. Debecker, E.M. Gaigneaux, G. Busca, Exploring, tuning, and exploiting the basicity of hydrotalcites for applications in heterogeneous catalysis, Chemistry—A, Eur. J. 15 (2009) 3920–3935.
[12] Y. Mu, Y. Zhang, J. Fan, C. Guo, Effect of ultrasound pretreatment on the hydrothermal synthesis of SSZ-13 zeolite, Ultrason. Sonochem. 38 (2017) 430–436.
[13] S. Zhao, H. Yi, X. Tang, F. Gao, Q. Yu, Y. Zhou, J. Wang, Y. Huang, Z. Yang, Enhancement effects of ultrasound assisted in the synthesis of NiAl hydrotalcite for carbonyl sulfide removal, Ultrason. Sonochem. 32 (2016) 336–342.
[14] H.J. Jang, C.H. Lee, S. Kim, S.H. Kim, K.B. Lee, Hydrothermal synthesis of K2CO3-promoted hydrotalcite from hydroxide-form precursors for novel high-temperature CO2 sorbent, ACS Appl. Mater. Interfaces 6 (2014) 6914–6919.
[15] I. Khan, A.A.M. Ibrahim, M. Sohail, A. Qurashi, Sonochemical assisted synthesis of RGO/ZnO nanowire arrays for photoelectrochemical water splitting, Ultrason. Sonochem. 37 (2017) 669–675.
[16] S. Loganathan, M. Tikmani, A. Mishra, A.K. Ghoshal, Amine tethered pore-expanded MCM-41 for CO2 capture: Experimental, isotherm and kinetic modeling studies, Chem. Eng. J. 303 (2016) 89–99.
[17] K.L. Tan, B.H. Hameed, Insight into the adsorption kinetics models for the removal of contaminants from aqueous solutions, J. Taiwan Inst. Chem. Eng. 74 (2017) 25–48.
[18] M.P. Bernardo, F.K.V. Moreira, L.A. Colnago, C. Ribeiro, Physico-chemical assessment of [Mg-Al-PO4]-LDHs obtained by structural reconstruction in high concentration of phosphate, Colloids Surf., A 497 (2016) 53–62.
[19] A. Laskowska, M. Zaborski, G. Boiteux, O. Gain, A. Marzec, W. Maniukiewicz, Effects of unmodified layered double hydroxides MgAl-LDHs with various structures on the properties of filled carboxylated acrylonitrile–butadiene rubber XNBR, Eur. Polym. J. 60 (2014) 172–185.
[20] H.W. Olfs, L.O. Torres-Dorante, R. Eckelt, H. Kosslick, Comparison of different

synthesis routes for Mg–Al layered double hydroxides (LDH): Characterization of the structural phases and anion exchange properties, Appl. Clay Sci. 43 (2009) 459–464.
[21] L. Dong, C. Ge, P. Qin, Y. Chen, Q. Xu, Immobilization and catalytic properties of candida lipolytic lipase on surface of organic intercalated and modified MgAl-LDHs, Solid State Sci. 31 (2014) 8–15.
[22] B. Li, Y. Zhang, X. Zhou, Z. Liu, Q. Liu, X. Li, Different dye removal mechanisms between monodispersed and uniform hexagonal thin plate-like MgAl–CO32–LDH and its calcined product in efficient removal of Congo red from water, J. Alloys Compd. 673 (2016) 265–271.
[23] W. Lv, L. Yang, B. Fan, Y. Zhao, Y. Chen, N. Lu, R. Li, Silylated MgAl LDHs intercalated with MnO2 nanowires: Highly efficient catalysts for the solvent-free aerobic oxidation of ethylbenzene, Chem. Eng. J. 263 (2015) 309–316.
[24] H. Nina, A.R. Barron, BET Surface Area Analysis of Nanoparticles, Rice University, Houston TX, 2011.
[25] S. Brunauer, L.S. Deming, W.E. Deming, E. Teller, On a Theory of the van der Waals Adsorption of Gases, J. Am. Chem. Soc. 62 (1940) 1723–1732.
[26] K.S.W. Sing, D.H. Everett, R.A.W. Haul, L. Moscou, R.A. Pierotti, J. Rouquerol, T. Siemieniewska, Reporting Physisorption Data for Gas/Solid Systems with Special Reference to the Determination of Surface Area and Porosity, Pure Appl. Chem. 57 (1985) 603–619.
[27] T. Adschiri, Y. Hakuta, K. Arai, Hydrothermal synthesis of metal oxide fine particles at supercritical conditions, Ind. Eng. Chem. Res. 39 (2000) 4901–4907.
[28] H. Xu, B.W. Zeiger, K.S. Suslick, Sonochemical synthesis of nanomaterials, Chem. Soc. Rev. 42 (2013) 2555–2567.
[29] Y. Kong, G. Jiang, Y. Wu, S. Cui, X. Shen, Amine hybrid aerogel for high-efficiency CO2 capture: Effect of amine loading and CO2 concentration, Chem. Eng. J. 306 (2016) 362–368.
[30] R. Dolores, S. Raquel, G.-L. Adianez, Sonochemical synthesis of iron oxide nanoparticles loaded with folate and cisplatin: Effect of ultrasonic frequency, Ultrason. Sonochem. 23 (2015) 391–398.
[31] E. Genty, J. Brunet, C. Poupin, S. Casale, S. Capelle, P. Massiani, S. Siffert, R. Cousin, Co-Al mixed oxides prepared via LDH route using microwaves or ultrasound: Application for catalytic toluene total oxidation, Catalysts 5 (2015) 851–867.
[32] J. Otsu, Y. Oshima, New approaches to the preparation of metal or metal oxide particles on the surface of porous materials using supercritical water: development of supercritical water impregnation method, J. Supercrit. Fluids 33 (2005) 61–67.
[33] M. Manikandan, A.K. Venugopal, K. Prabu, R.K. Jha, R. Thirumalaiswamy, Role of surface synergistic effect on the performance of Ni-based hydrotalcite catalyst for highly efficient hydrogenation of furfural, J. Mol. Catal. A: Chem. 417 (2016) 153–162.
[34] N. Touisni, F. Charmantray, V. Helaine, C. Forano, L. Hecquet, C. Mousty, Optimized immobilization of transketolase from E. coli in MgAl-layered double hydroxides, Colloids Surf., B 112 (2013) 452–459.
[35] S.-L. Wang, C.H. Liu, M.K. Wang, Y.H. Chuang, P.N. Chiang, Arsenate adsorption by Mg/Al–NO3 layered double hydroxides with varying the Mg/Al ratio, Appl. Clay Sci. 43 (2009) 79–85.
[36] M. Bellotto, B. Rebours, O. Clause, J. Lynch, D. Bazin, E. Elkaïm, A Reexamination of Hydrotalcite Crystal Chemistry, J. Phys. Chem. 100 (1996) 8527–8534.
[37] H. Ji, W. Wu, F. Li, X. Yu, J. Fu, L. Jia, Enhanced adsorption of bromate from aqueous solutions on ordered mesoporous Mg-Al layered double hydroxides (LDHs), J. Hazard. Mater. 334 (2017) 212–222.
[38] S. Zhao, X. Meng, K. Zhu, F. Du, G. Chen, Y. Wei, Y. Gogotsi, Y. Gao, Li-ion uptake and increase in interlayer spacing of Nb4C3 MXene, Energy Storage Mater. 8 (2017) 42–48.
[39] H. Emadi, M. Salavati-Niasari, A. Sobhani, Synthesis of some transition metal (M: 25Mn, 27Co, 28Ni, 29Cu, 30Zn, 47Ag, 48Cd) sulfide nanostructures by hydrothermal method, Advances in Colloid and Interface Science, DOI: https://doi.org/10.1016/j.cis.2017.06.007.
[40] J.S. Valente, M. Sánchez-Cantú, E. Lima, F. Figueras, Method for large-scale production of multimetallic layered double hydroxides: formation mechanism discernment, Chem. Mater. 21 (2009) 5809–5818.
[41] S.-L. Wang, P.-C. Wang, In situ XRD and ATR-FTIR study on the molecular orientation of interlayer nitrate in Mg/Al-layered double hydroxides in water, Colloids Surf., A 292 (2007) 131–138.
[42] L. Sciascia, M.L. Turco Liveri, M. Merli, Kinetic and equilibrium studies for the adsorption of acid nucleic bases onto K10 montmorillonite, Appl. Clay Sci. 53 (2011) 657–668.
[43] R. Serna-Guerrero, A. Sayari, Modeling adsorption of CO2 on amine-functionalized mesoporous silica. 2: Kinetics and breakthrough curves, Chem. Eng. J. 161 (2010) 182–190.
[44] J.M. Borah, J. Sarma, S. Mahiuddin, Adsorption comparison at the α-alumina/water interface: 3,4-Dihydroxybenzoic acid vs. catechol, Colloids Surf., A 387 (2011) 50–56.
[45] W. Plazinski, Applicability of the film-diffusion model for description of the adsorption kinetics at the solid/solution interfaces, Appl. Surf. Sci. 256 (2010) 5157–5163.
[46] W. Plazinski, J. Dziuba, W. Rudzinski, Modeling of sorption kinetics: the pseudo-second order equation and the sorbate intraparticle diffusivity, Adsorption 19 (2013) 1055–1064.

Correlating Ultrasonic Impulse and Addition of ZnO Promoter with CO_2 Conversion and Methanol Selectivity of CuO/ZrO_2 Catalysts

Collins I. Ezeh, Xiaogang Yang, Jun He, Colin Snape, Xiao Min Cheng

PII: S1350-4177(17)30517-5
DOI: https://doi.org/10.1016/j.ultsonch.2017.11.013
Reference: ULTSON 3950

To appear in: *Ultrasonics Sonochemistry*

Received Date: 2 August 2017
Revised Date: 7 November 2017
Accepted Date: 8 November 2017

Please cite this article as: C.I. Ezeh, X. Yang, J. He, C. Snape, X.M. Cheng, Correlating Ultrasonic Impulse and Addition of ZnO Promoter with CO_2 Conversion and Methanol Selectivity of CuO/ZrO_2 Catalysts, *Ultrasonics Sonochemistry* (2017), doi: https://doi.org/10.1016/j.ultsonch.2017.11.013

Correlating Ultrasonic Impulse and Addition of ZnO Promoter with CO_2 Conversion and Methanol Selectivity of CuO/ZrO_2 Catalysts

Collins I. Ezeh[a,c], Xiaogang Yang[b, c,*], Jun He[a,c,*], Colin Snape[d], Xiao Min Cheng[e]

[a]Department of Chemical and Environmental Engineering, University of Nottingham Ningbo China, University Park, Ningbo 315100. P.R. China

[b]Department of Mechanical, Materials and Manufacturing Engineering University of Nottingham Ningbo China, University Park, Ningbo 315100. P.R. China

[c]International Doctoral Innovation Centre, University of Nottingham Ningbo China University Park, Ningbo 315100. P.R. China

[d]Department of Chemical and Environmental Engineering University of Nottingham, University Park, Nottingham NG7 2RD, UK

[e]Department of Mechanical, Materials and Manufacturing Engineering Ningbo University of Technology, Jiangbei District, Ningbo, Zhejiang, 315211

Abstract

The thermal characteristics of Cu-based catalysts for CO_2 utilization towards the synthesis of methanol were analysed and discussed in this study. The preparation process were varied by adopting ultrasonic irradiation at various impulses for the co-precipitation route and also, by introducing ZnO promoters using the solid-state reaction route. Prepared catalysts were characterised using XRD, TPR, TPD, SEM, BET and TG-DTA-DSC. In addition, the CO_2 conversion and CH_3OH selectivity of these samples were assessed. Calcination of the catalysts facilitated the interaction of the Cu catalyst with the respective support bolstering the thermal stability of the catalysts. The characterisation analysis clearly reveals that the thermal performance of the catalysts was directly related to the sonication impulse and heating rate. Surface morphology and chemistry was enhanced with the aid of sonication and introduction of promoters. However, the impact of the promoter outweighs that of the sonication process. CO_2 conversion and methanol selectivity showed a significant improvement with a 270% increase in methanol yield.

Keywords: *Carbon dioxide, Thermal stability, Hydrogenation, Catalysts, Methanol synthesis.*

---

*Corresponding authors:

Tel: +86-574-88182419 E-mail: Xiaogang.Yang@nottingham.edu.cn (X. Yang)

Tel: +44-115-7484577 E-mail: jun.he@nottingham.edu.cn (J. He)

1 INTRODUCTION

Present research undertaking towards methanol synthesis has been aimed at developing catalysts with great catalytic activity. One notable catalyst for this purpose is the alumina (Al_2O_3) based catalyst with good yield of methanol. However, this catalyst is limited in performance due to its strong hydrophilic characteristics [1-3]. Other catalysts used are Cu-ZrO_2 based catalysts with high thermal stability and Cu dispersion. This is due to the role of ZrO_2 in enhancing catalyst stability and active sites [3, 4]. As a result, the catalytic capacity of this material was observed to increase. Further improvement with the dispersion of Cu in this material was achieved by the use of promoters like oxides of Mg [5-7], Mn [5, 7, 8], Ga [7] and Zn [9, 10].

Despite the composition of the catalyst, other means of promoting the performance of the catalyst is the adopted synthetic method and conditions [7, 11-13]. Common synthetic methods used for the preparation of these compounds are co-precipitation [3, 4, 11, 12, 14-20], sol gel [21, 22] and citrate thermal decomposition [7, 19, 20, 23]. Recently, new synthetic methods are being proposed. This includes solid-state chemical reactions [24] and solution combustion [25, 26]. Nonetheless, these methods produce materials with low surface area, which is a demerit for catalytic activity [27-31]. To this effect, incorporating ultrasonic irradiation has shown to improve surface area and chemistry [32, 33]. Sonication alters particle morphology and it depends on various factors like sonication time and frequency [34, 35]. In addition, it can be stipulated that particle morphology also depends on sonication impulse time [34, 36].

In this work, CuO-ZrO_2 composite oxide was synthesised via ultrasonic enhanced co-precipitation method with varying impulse time. In addition, the use of ZnO promoter was also used to study the promotional effect of ZnO on CuO-ZrO_2 catalyst. The structural and textural characteristics of these compounds were assessed to study the impact of ultrasonic impulse time and Zn^{2+} introduction on the catalysts morphology and surface chemistry. In addition, a catalytic performance test was conducted to evaluate methanol selectivity and CO_2 conversion of the prepared catalyst.

2 EXPERIMENTAL

2.1 Material Preparation

In this study, the catalysts were synthesised by the ultrasonic aided co-precipitation method. All chemicals used for experimentation were acquired from SinoPharm Chemical Reagents Co. Ltd.

2.2 Preparation of catalyst

Cu/ZrO_2

The catalyst was prepared by a reaction of 0.17 M mixed reaction of $Zr(NO_3)_4$ and $Cu(NO_3)_2$ (Cu-loading = 30%) and 0.1M NaOH solution while sustaining the pH at 7.0. Mixing was done with the aid of ultrasonic irradiation at different impulse time (continuous, 1, 4 and 8 seconds). These impulses are chosen to determine appreciable differences in surface morphology around the traditional continuous irradiation which has no impulse time (0 seconds). After which, the precipitates were filtered, washed, dried (383 K for 6 hr) and calcined (at temperature of 623 K for 4 hr). This sample is labelled as CZr.

$Cu/Zn/ZrO_2$

A mix of $Cu(NO_3)_2 \cdot 3H_2O$, $Zn(NO_3)_2 \cdot 6H_2O$ and $Zr(NO_3)_4 \cdot 5H_2O$ were blended in a Cu^{2+}:Zn^{2+}:Zr^{4+} molar ratio of 3:1:6. This mix was further blended with citric acid ligand, $C_6H_8O_7 \cdot H_2O$ in a molar ratio of 1:1.3 [24] . This was carried out for 30 minutes in an ultrasonic bath at room temperature until the reactants were transformed to a homogeneous muddy precursor. Afterwards, the catalyst was dried at 383 K for 6 hr before being calcined at a temperature of 623 K for 4 hr. This sample is labelled as CZZr-316. The effect of Zn^{2+} on the catalyst was studied by varying the composition of Zn^{2+} in the catalyst while keeping the composition of Cu^{2+} constant. Given that the suitable Cu-loading for optimum methanol synthesis through hydrogenation for the CZr catalyst is 30%, Cu^{2+} content was restricted to this value with the introduction of Zn. Subsequently, this will reduce the Zr^{4+} content. For this purpose, additional molar ratios, 3:3:4 and 3:6:1, were synthesised to sparsely investigate the share of Zn^{2+} over Zr^{4+} for the remaining 70% content of the catalyst. The additional samples are labelled as CZZr-334 and CZZr-361 respectively.

2.3 Catalyst Characterization

The generated precursors were analysed using the Scanning Electron Microscope (SEM), Brunauer-Emmett-Teller (BET), Temperature-Programmed Desorption (TPD), Temperature-Programmed Reduction (TPR), Thermal Gravimetric Analysis (TGA), X-ray Diffraction (XRD), Differential Scanning Calorimetry (DSC) and Differential Thermal Analysis (DTA).

The surface composition and structure of the catalysts were studied with a SEM. The porosity and surface area of the catalysts were obtained using BET method determined via N_2 adsorption/desorption isotherms at 77 K, using a Micrometrics ASAP 2020 Surface Area and Porosity Analyser. Here, 0.2-0.4 g of the samples was degassed under vacuum at 363K for ~4 hours before being dosed with N_2. The BET surface area was computed within the relative pressure range of 0.06-0.3 and the pore volume at a pre-determined relative pressure of 0.9948.

The TGA, DSC and DTA were performed using a NETZSCH STA-449-F3 Jupiter Thermal Analyser. 5-10 mg of the catalyst were weighed into the sample pan and was subjected to a decomposition temperature from 293-1073 K at a constant ramp of 10 and 20 K/min respectively under N_2.

XRD patterns were studied using a Bruker-AXS D8 advance powder diffractometer using Cu radiation with a scanning range of $10^o \leq 2\theta \leq 90^o$ at a step size of 0.010216^o. Average crystallite size was estimated using the Scherrer's formula:

Equation 1: Scherrer's Formula

$$d = \frac{0.9\lambda}{\beta \cos\theta}$$

where d is the crystallite size (nm), λ is the radiation wavelength (nm) = 1.5406 nm in this case, β is the full width at half maximum (radians) and θ is the Bragg's angle of the maximum intense peak (degrees) [37].

CO_2-TPD was conducted using AutoChem II 2920 to assess the basicity of the catalysts. First, the 50 mg of the catalyst was reduced at 573 K for 1 hr in a flow of H_2 at 30 ml/min. Subsequently, the catalyst was cooled to 323 K before being flushed with He for 0.5 hr at same temperature at 40 ml/min. The catalyst was then exposed to pure CO_2 for 1 hr at a flow rate of 30 ml/min before being flushed with He at 40 ml/min to remove all physisorbed

molecules. TPD measurement was conducted at temperature range of 323-1073 K with a heating rate of 10 K/min under the flow of He at 40 ml/min, and the CO_2 desorption monitored using a thermal conductivity detector (TCD).

H_2-TPD experiment was performed in the same equipment as CO_2-TPD. 50 mg of the catalyst was first reduced in situ at 573 K for 2 hr in mixed flow of H_2/He (10:90 vol%). After which, the catalyst was cooled down to 323 K and then saturated in 10% H_2/He for 1 hr, followed by purging with N_2 for 0.5 hr to remove any physisorbed molecules. H_2-TPD measurement was then performed to 1073 K with a heating rate of 5 K/min under N_2 atmosphere.

H_2 temperature program reduction (H_2-TPR) of catalysts (50 mg) was carried out in a U-tube quartz reactor using a Micromeritics ChemiSorb 2920 with a thermal conductivity detector (TCD). Before reduction, the sample was first degassed with He flow of 40 mL min−1 at 473 K for 60 min to remove physically adsorbed water and cooled down to the 333 K. Then the sample was reduced at a heating rate of 10 K min−1–1023 K with 50 mL min−1 of 5% H2/Ar mixture gas.

2.4 Catalyst Performance Evaluation

The performance of the catalysts towards methanol synthesis was assessed in a continuous flow fixed bed reactor. First, 0.5g of the catalyst was reduced at 623 K in H_2/N_2 (10/90 vol%) environment for 3 hr at atmospheric pressure before being cooled to room temperature. The reactant gas H_2/CO_2 (molar ratio = 3:1) under operating conditions of 3 MPa, 623 K and gas hourly space velocity (GHSV) of 3100 hr^{-1}. The effluent was analysed online using an Agilent gas chromatograph (GC) 7890A with the transfer line from the reactor to the GC preheated at 373 K to avoid condensation of effluent products. TCD was used to measure N_2, CO and CO_2 gases while organic compounds were studied using the flame ionization detector (FID). From this test, catalytic conversion and selectivity were computed using mass balance and resulting steady-state values (SSV). SSV was computed as an average of three tests over a period of 3 hr of continuous operation. CO_2 conversion (x_{CO2}), selectivity (s_i) and yield (y_i) (where i is the molecule of interest) were computed as follows:

Equation 2: CO_2 conversion computation

$$X_{CO_2} = \frac{n_{CH_3OH} + n_{CO}}{n^0_{CO_2}}$$

Equation 3: Methanol and carbon monoxide selectivity computation

$$S_{CH_3OH} = \frac{n_{CH_3OH}}{n_{CH_3OH} + n_{CO}}$$

$$S_{CO} = \frac{n_{CO}}{n_{CH_3OH} + n_{CO}}$$

Equation 4: Computation of yield for methanol

$$Y_{CH_3OH} = s_{CH_3OH} \times x_{CO_2}$$

3 RESULTS AND DISCUSSIONS

3.1 Variation of Surface Morphology on Ultrasonic Modulation and Metal Composition

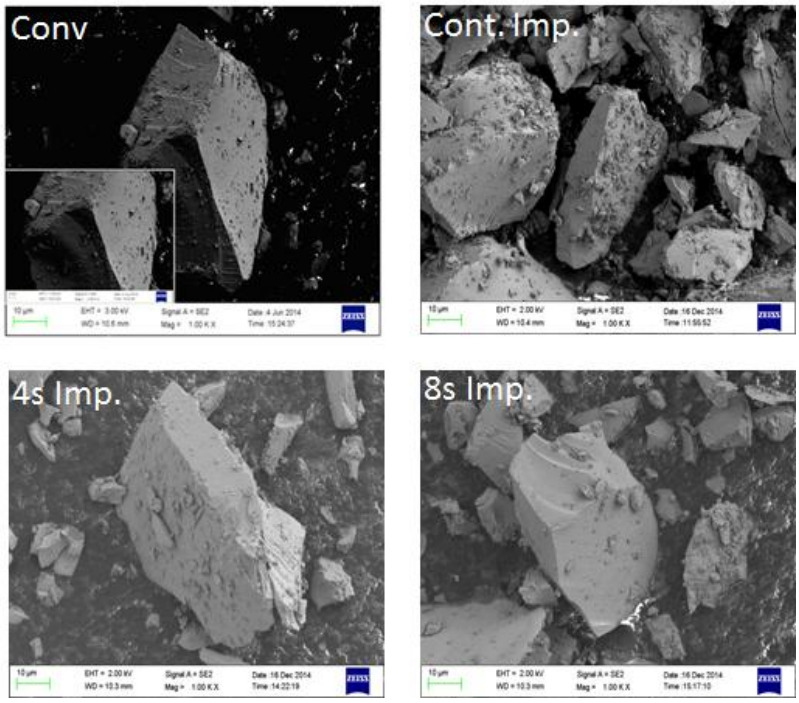

Figure 1: SEM Analysis of CZr prepared via Ultrasonic Modulation at different Impulse times (continuous impulse (Cont. Imp.), 4 sec and 8 sec) in comparison with conventional co-precipitation method (Conv)

The Cu/ZrO_2 catalysts prepared via normal co-precipitation and ultrasonic-assisted co-precipitation method are shown in Figure 1. SEM micrograph shows that the samples are of irregular shape with particle agglomeration. However, this is affected by the introduction of ultrasonic irradiation. Despite the similarity in particle boulder shape, agglomeration was observed to increase with decrease in impulse of ultrasonic irradiation. With no impulse (continuous impulse), agglomeration was attained its highest and least with 8 sec impulse, which was slightly similar to the conventional catalyst. This stresses the impact of ultrasonic irradiation on the morphology, and probably, on the physical properties of the material [38]. Figure 2 shows the surface morphology of the calcined CZZr catalysts. In each sample, possible cavities were observed all over the surface of the catalyst. This is attributed to the decomposition of formed citrates with an obvious caking of the particles [10]. The cavities and compactness or caking of the catalyst was detected to increase with increase in Cu/Zn ratio. This is similar to findings reported by Huang, Chen, Fei, Liu and Zhang [10].

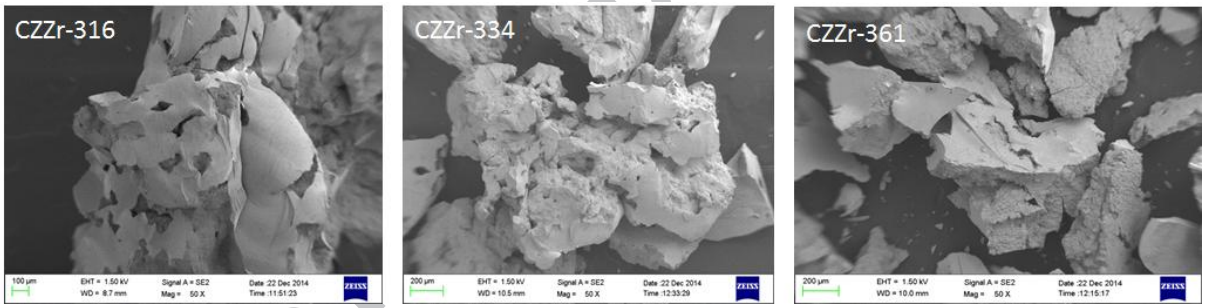

Figure 2: SEM images of prepared CZZr catalysts at varying compositions and continuous impulse ultrasonic irradiation (CZZr-xyz indicates catalyst with Cu^{2+}:Zn^{2+}:Zr^{4+} molar ratio = x:y:z)

The sorption isotherm obtained from the BET analysis for samples prepared with varying impulse time of ultrasonic irradiation was used to compute the surface area (S_{BET}), pore volume (V_P), and particle size (D_P). The results are tabulated in Table 1. The data indicates that an increase in surface area was obtained with decrease in impulse time. However, the particle size showed an appreciable decrease with decrease in pulse modulation. Moreover, there was an insignificant variation in V_p from 0.15 cm^3/g for the conventional CZr to 0.17 cm^3/g of the continuous-impulsed CZr. This can be attributed to the enhanced interaction as a result of continuous ultrasonic irradiation. This depicts an improvement in the pore structure of the samples and is attributed to the enhancement of nucleation and precipitate growth resulting from improved dissolution and reaction process via sonication [39, 40]. When

compared to the conventional samples (designated by conv), it was observed that at impulses greater than 1 s, sonication tends to have an adverse effect on the particle surface area. Nonetheless, with the introduction of Zn^{2+} metal ion into the composite oxide, the surface area and pore volume increased but varied inversely with increase in Cu^{2+}/Zn^{2+} ratio (Table 2). Although, not much difference was observed with pore volume. However, the particle diameter was detected to increase with Cu^{2+}/Zn^{2+} ratio. This can be associated with the additional interactions facilitated by the presence of the promoting metal ion. The observed trend corresponds with reported phenomenon and was explained that the variation in Cu/Zn ratio affects the crystal growth and particle agglomeration of the catalyst. This in turn alters the textural properties of the catalyst [10].

Table 1: BET results of CZr catalysts prepared at different ultrasonic impulse time

Structural Characteristics	8s Imp	4s Imp	1s Imp	Cont imp	Conv
BET Surface Area (m^2/g)	53.84	54.31	58.33	64.36	57.03
Pore Volume (cm^3/g)	0.15	0.14	0.14	0.17	0.15
Pore size (nm)	2.70	2.63	2.46	2.60	2.62
Average Particle Size (nm)	27.86	26.49	25.72	23.31	26.30

Table 2: BET and metallic composition analysis of CZZr catalysts prepared at different metallic composition

Sample	Metallic Composition (wt%)[a]			Cu^{2+}:Zn^{2+}	S_{BET} (m^2/g)	V_P (cm^3/g)	D_P (nm)
	Cu^{2+}	Zn^{2+}	Zr^{4+}				
CZZr-316	30.52	15.36	54.12	3.0	64.71	0.17	23.31
CZZr-334	32.19	31.37	36.44	1.0	68.52	0.20	21.36
CZZr-361	31.45	60.82	7.73	0.5	70.38	0.21	15.82

[a] computed by atomic emission spectroscopy (AES)

XRD pattern of the prepared samples are shown in Figure 3. Figure 3a shows the pattern for CZr catalysts at different ultrasonic modulation at constant Cu-loading of 30%. The pattern shows no difference in peak position. However, peak intensity was perceived to increase with ultrasonic irradiation at continuous impulse. This suggests that ultrasonic irradiation has limited impact in improving the crystallinity of the catalyst. The notable peaks observed were the tetragonal ZrO_2 (t-ZrO_2) at peak angles $2\theta = 62^o$, monoclinic ZrO_2 (m-ZrO_2) with peak angles $2\theta = 23^o$ and 28.2^o and Cu species with peak angles $2\theta = 35.6^o$ related to CuO and $2\theta = 42.8^o$ and 72^o related to Cu metal. Incorporating the metal Zn^{2+} to the CZr composite oxide, a

series of overlapping peaks were obtained. The presence of CuO was indicated with peaks at $2\theta = 32.4^o$, 35.4^o and 38.7^o. The 35.4^o peak overlapped with 36.3^o peak for ZnO. Other ZnO peaks are at $2\theta = 31.8^o$ and 34.5^o. Noticeably, as the Cu/Zn ratio decreases, the ZnO diffraction peaks increases as well relative to their individual CuO peak intensities. The diffraction peaks of ZrO_2 was also detected but as monoclinic at $2\theta = 23^o$ and 28.8^o and as tetragonal at $2\theta = 30.3^o$. It is observed that the m-ZrO_2 which was the more dominant ZrO_2 crystal increased in accordance with its normal composition in the composite oxide. The crystallite size of CuO crystal was computed using the Scherrer's equation as 16.64, 19.99 and 19.63 nm for CZZr-316, CZZr-334 and CZZr-361 respectively. This indicates that the presence of Zn^{2+} has an impact on the crystallinity and relative dispersion of Cu. Crystallinity of the catalyst is suggested to be highest at moderate composition of Zn^{2+}.

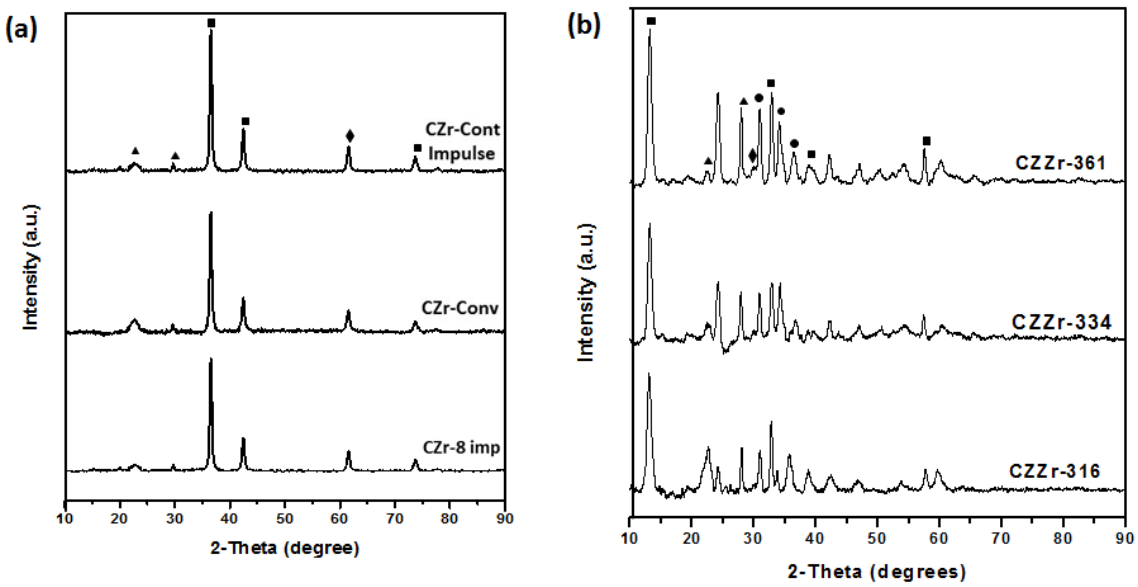

Figure 3: XRD pattern for (a) calcined CZr catalysts prepared with variation in ultrasonic impulse at Cu-loading of 30 wt%, and (b) CZZr catalyst prepared with difference in metallic composition. (□) CuO, (○) ZnO, (◊) t-ZrO_2 and (Δ) m- ZrO_2.

3.2 Thermal Characteristics

The thermal strength of the prepared catalysts with varying ultrasonic modulation is shown in Figure 4. It is detected that there are three decomposition steps in all cases. Although this varied with the level of ultrasonic impulse. As shown in the figure, the first decomposition step (of both weight loss and DTA plot) occurred at temperature less than 250 ^oC. This is associated with the loss of moisture and is identified by the lowest peak of the DTA plot. The

second decomposition step as a result of interstitial moisture loss is existed between 250 and maximum temperature of *ca.* 680 ^{o}C. Maximum temperature of the second decomposition peak varied with impulse of ultrasonic irradiation with continuous and 1 s impulse having the highest. Beyond this temperature is the loss of NO_3^- attached to the surface of the catalyst. This explains that the thermal stability of the catalyst was enhanced by ultrasonic modulation. Nonetheless, this is dependent on the intensity of the irradiation. With a continuous or near-continuous impulse, a more thermal stable material is obtained. In terms of energy required for the thermal breakdown of the catalyst, Figure 5 was obtained. This is the DSC analysis of the prepared catalysts within a temperature range of 0-800 ^{o}C. The result validates the thermal stability of samples prepared at continuous and 1 s impulse. This is observed from to the plot to be closest to the zero DSC line indicating a minimal energy differential per mass of the sample. In the profile, it is also noteworthy that the loss of NO_3^- was at a more extended temperature than that of the conventional and higher impulse samples.

Varying the heating rate, it is shown that a better thermal stability is achieved at 20 K/min as shown in Figure 6. The 20 K/min profile for both continuous and 1 sec impulse were observed to be have the minimal change in energy (closest to the zero line). In addition, it is also witnessed that at 20 K/min, the breakdown peaks of the catalysts (solid lines) occurred at higher temperatures than that of 10 K/min (broken lines). This suggests that for optimum industrial applicability, the material will be well suited at a thermal operation with heating rate at 20 K/min rather than 10 K/min. Since the thermal stability of this catalyst is directly proportional to Zr^{4+} content [3, 4], the thermal characteristics of CZZr was neglected.

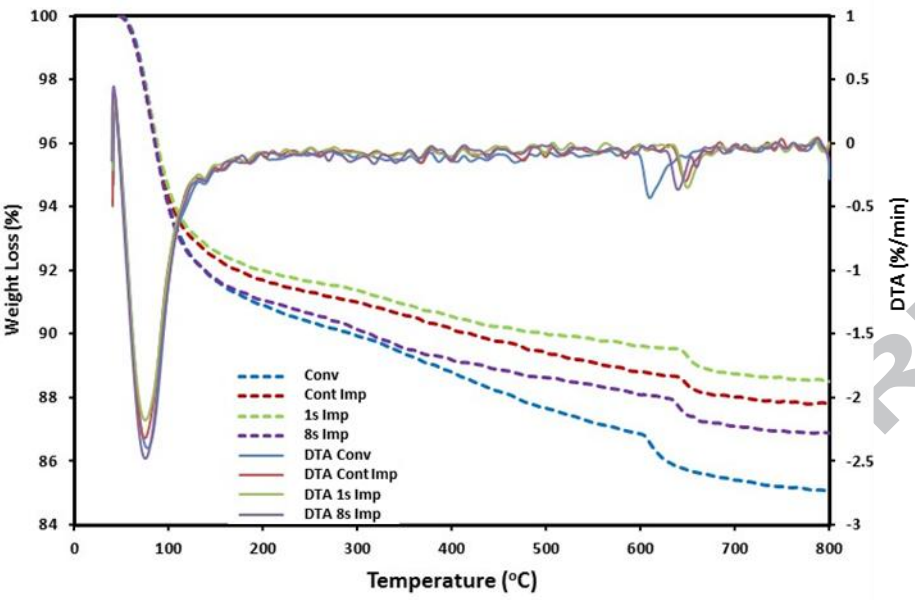

Figure 4: TGA-DTA profile for CZr catalysts

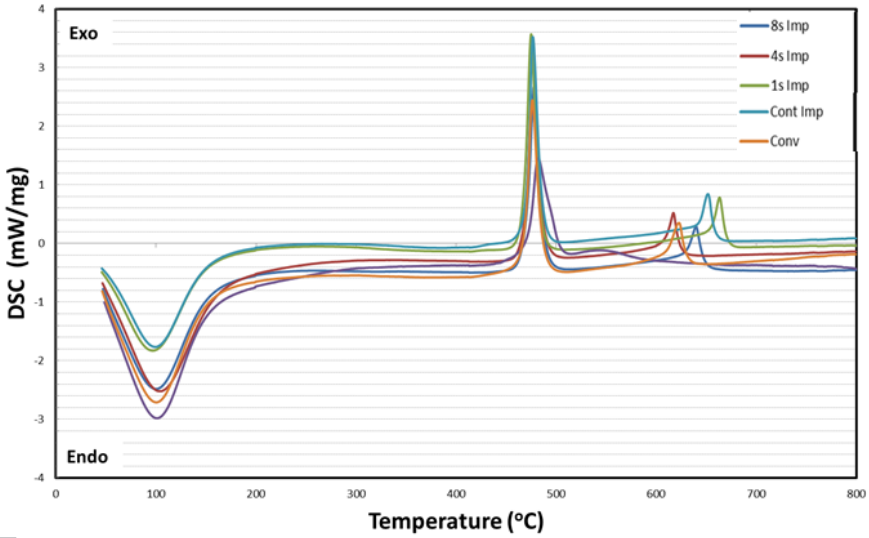

Figure 5: DSC profile for CZr catalysts at different ultrasonic impulse

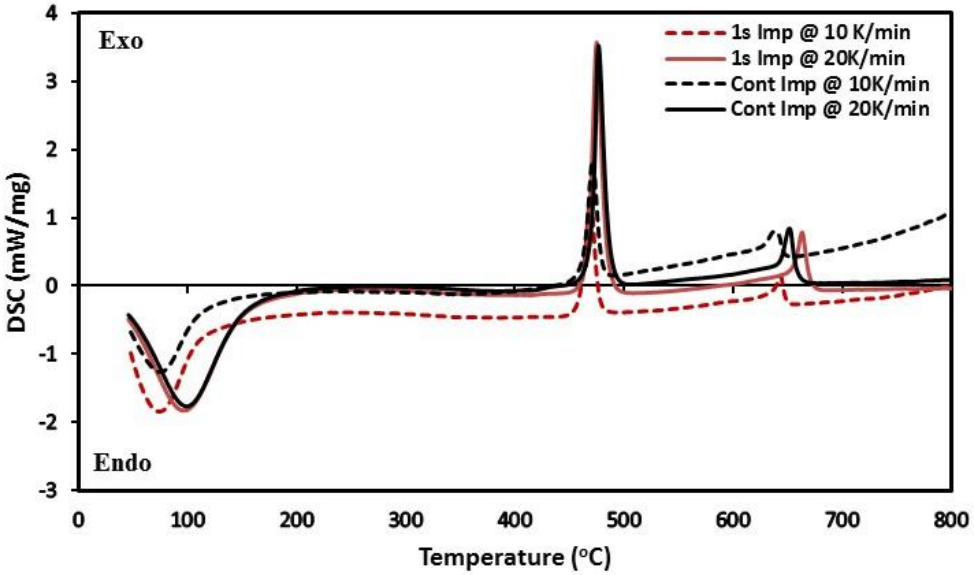

Figure 6: DSC analysis at different heating rate for CZr catalysts prepared with ultrasonic irradiation at 1s and continuous impulse

3.3 Reducibility of Catalysts

To understand the reducibility of the catalysts, H_2-TPR analysis was conducted. The results are as shown in Figure 7. Three classes of adsorption peaks were observed for the catalysts depending on the preparation method and composition of metal. In accordance with literature, the first peak (α) occurred at low temperature range (100-300 ^oC) and is attributed to the adsorption of atomic hydrogen highly dispersed Cu^{2+}. The second desorption peak (β) occurred at mid temperature range from 300-500 ^oC, assigned to the adsorption of hydrogen on moderately dispersed Cu^{2+} species. The final peak (γ) situated at temperature range 500-700 ^oC is associated with hydrogen adsorption by bulk Cu^{2+} species [41-44]. Figure 7a shows the profile for CZr reduction. Reducing the radiation impulse resulted to an increase in the intensity of α-peak and decrease in β-peak. High temperature adsorption of H_2 was not witnessed in this catalysts. This suggests that the increase in ultrasonic impact (designated by reduced impulse time) will aid in high Cu dispersion. The quantitative analysis of this effect is summarised in Table 3. Figure 7b shows the profile for CZZr at varying amount of Zn^{2+} ion. At low amount of zinc (CZZr-316), the α-peak was still detected alongside with the detection of a β'-peak, which can be explained to be due to difficulties in the reduction of some dispersed Cu [43]. However, both peaks tend to fade as the composition of Zn increased. This is associated with an increase in intensity, reduction in width and shift of β-

peak towards a higher temperature. A logical explanation can be given that the presence of Zn increases the dispersion of Cu species and makes it more accessible for potential dissociation of hydrogen molecule [10]. In this set of catalysts, the γ-peaks were observed and this tends to increase with increase in the amount of Zn. These results show that the amount of easily reducible well dispersed and bulk CuO increased with increase in Zn (Table 3). The result data also shows that the impact of introduction of Zn promoter outweighs the impact of ultrasonic modulation. For instance, comparing the total peak area of CZr at 1s impulse and CZZr-316 with that of the conventional catalyst, it is estimated that the difference between the former is a unit magnitude while the latter is of 6 fold magnitude difference.

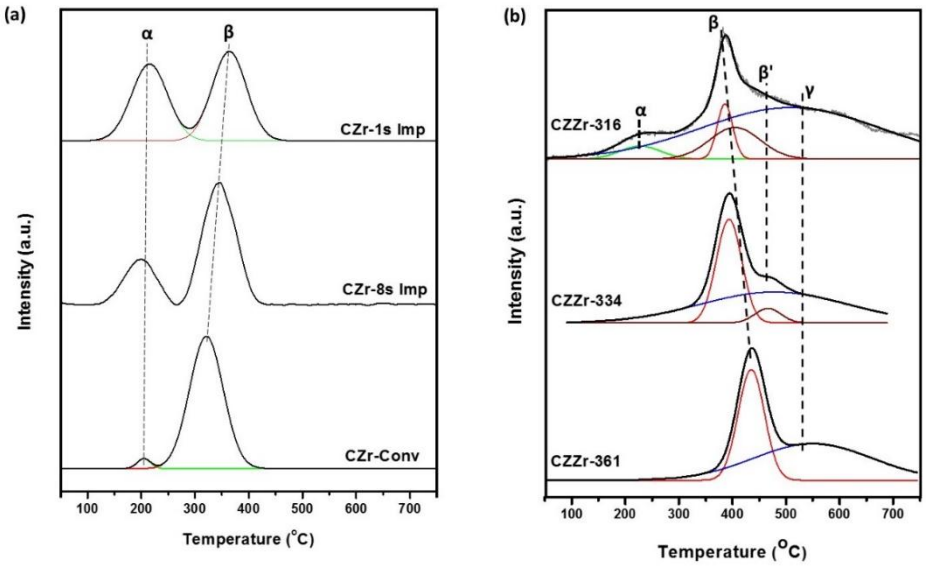

Figure 7: TPR profile of (a) CZr catalyst at various ultrasonic impulse, and (b) CZZr Catalyst at different metal composition

Table 3: Peak areas of H_2-TPD profiles of reduced CZr and CZZr catalysts

Sample	Peak Areas (a.u.)				Total Area (a.u.)
	α-peak	β-peak	β'-peak	γ-peak	
CZr-1s Impulse	2.74	3.04	-	-	5.78
CZr-8s Impulse	0.13	4.42	-	-	4.55
CZr-Conv	0.03	4.52	-	-	4.55
CZZr-316	3.32	11.61	15.89	1.84	32.66
CZZr-334	-	22.67	3.27	39.03	64.97
CZZr-361	-	28.98	-	42.39	71.37

3.4 H_2 Desorption

The H_2-TPD pattern for the pre-reduced catalysts was also studied (see **Error! Reference source not found.**8). The desorption profile spanned across a temperature range 50 – 800 ^oC and displayed several adsorption states of H-species on the catalysts. These peaks are classed into two categories, low (130 – 300 ^oC) and high (400 – 500 ^oC) temperature peaks designated as α and β peaks respectively [16, 43, 45]. Desorption at low and high temperature region is ascribed to the release of H-species adsorbed on surface Cu sites and on surface ZnO or ZrO_2 respectively. Figure 8a shows that as the impulse time reduces, the intensity of the peaks increased indicating that an increased impact in ultrasonic irradiation will boost the amount of surface Cu sites and available metal oxides. Hydrogen spillover phenomenon is suggested to facilitate the hydrogen adsorption process on ZnO and ZrO_2 sites [16, 45]. For the CZZr catalysts, two peaks were equally obtained within the reported temperature range. However, it was observed that both peaks had broader bands that the CZr catalysts. This is attributed to the presence of the Zn promoter which aids in increasing the amount of Cu active sites. CZZr-316 with the lowest composition of Zn showed the basic α and β peaks. But with an increase in Zn composition resulted to an increase in peak intensity with the detection of additional peaks, α' and β' peaks as shown in Figure 8b. The α'-peak can be attributed to both physical and chemical interactions between Cu and the metal oxides with an alteration in electron distribution, which will facilitate the adsorption of hydrogen [42]. The β' peak can be explained as a separated hydrogen adsorption on the individual ZnO and ZrO_2 surface sites. With further increase in Zn composition (CZZr-361), the intensity of the peaks was reduced. It may be suggested that above a specific metal composition, hydrogen adsorption will be deterred by the metals. Li, Mao, Yu and Guo [9] suggested that this interaction could be facilitated by the sintering effect [9], which in turn will result to reduction in surface area [10]. In conclusion, the best catalyst for the purpose of methanol synthesis via hydrogenation process is one with a better H_2 adsorption strength and good desorption of the dissociated hydrogen atom [46]. Emphasis for the selection of these catalysts should be based on the α-peak desorption profile because it is the hydrogen desorbed from this peak region that will be made available for the hydrogenation process [47].

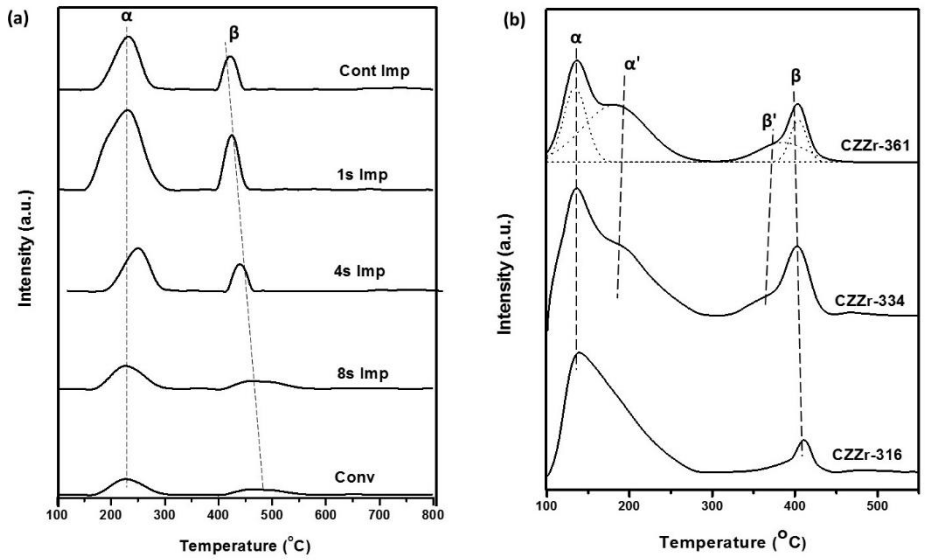

Figure 8: H_2-TPD profile for (a) reduced CZr at various ultrasonic impulse time, and (b) CZZr catalysts at different metal composition

3.5 Surface Basicity of Catalysts

The surface basicity of the catalysts were studied using the CO_2-TPD technique. The desorption profiles and data are shown in Figure 9 and Table 4 respectively. Generally, the basicity of metal oxides are categorized into three: weak, medium (or moderate) and strong basic strengths. In this study, these three zones are depicted at their corresponding temperature peaks ranging from 100-160 ^oC, 300-550 ^oC and > 600 ^oC respectively. Weak basic sites (α) are associated with the surface hydroxyl (OH^-) group; whereas the moderate basic sites (β) are related to metal-oxygen (M^{n+}-O^{2-}, where n+ is the valence of the metal) pair. The strong basic sites (γ) are attributed to the low coordination unsaturated oxygen (O^{2-}) and electronegative anions [43]. Figure 9a shows TPD profile for CZr catalysts at varying modulation impulse. As can be seen, peak intensities increased with increase in impact of ultrasonic modulation. Hence, ultrasonic irradiation has yet proven to improve the surface basicity of the catalyst. This can be attributed to the enhanced surface morphology of the catalyst hence making the basic sites accessible for CO_2 adsorption. Figure 9b portrays the CO_2 desorption profile for the CZZr catalysts prepared at different metal composition. Result data shows that a variation of metal composition has an impact on the surface basicity of the catalyst. As Cu/Zn ratio (also associated with the increase in Zr^{2+} content) increases, the intensity of α-peaks decreased but the β and γ-peaks showed an appreciable increase in intensity. The increase in moderate and strong basic sites can be attributed to the increase in

Zr^{4+} content since this metal is suggested to have a great synergetic effect on CO_2 desorption at moderate and strong basic sites when compared to Zn^{2+} [10]. Additionally, the γ-peak was observed to shift towards higher temperature with increase in Cu/Zn ratio. This is suggested to be due to the increased electron density of the strong basic sites, and can be attributed to the aggregation of saturated O^{2-} ions [43].

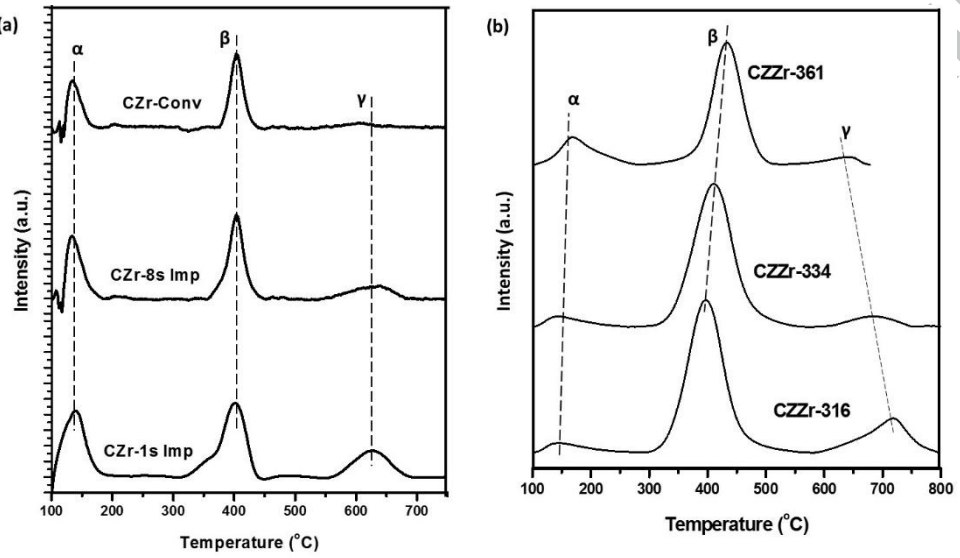

Figure 9: CO_2 desorption profile for (a) reduced CZr at various ultrasonic impulse time, and (b) CZZr catalysts at different metal composition

Table 4: Result data for CO_2 desorption profile for reduced CZr and CZZr catalysts

Sample	Weak Basic Site		Medium Basic Sites		Strong Basic Sites		Total (a.u.)
	Temp. (°C)	Peak Area (a.u.)	Temp. (°C)	Peak Area (a.u.)	Temp. (°C)	Peak Area (a.u.)	
CZr-Conv	148.00	3.53	400.00	8.67	620.00	0.06	12.26
CZr-8s Imp	147.00	4.31	399.00	9.31	632.00	1.35	14.97
CZr-4s Imp	147.00	4.99	400.00	8.48	630.00	2.49	15.96
CZr-1s Imp	148.00	5.84	400.00	11.43	625.00	5.43	22.70
CZr-Cont Imp	147.00	5.46	401.00	10.91	630.00	5.52	21.89
CZZr-361	148.00	6.53	412.00	30.23	658.00	0.86	37.62
CZZr-334	148.00	6.18	409.00	33.86	699.00	2.14	42.18

CZZr-316	160.00	5.30	400.00	39.71	717.00	10.82	55.83

3.6 Catalytic Performance for Methanol Synthesis

In this study, the catalytic performance was evaluated based on the catalytic selectivity and activity for CO_2 hydrogenation. The results are shown in Table 5. From the obtained results, it is observed that CO_2 conversion increased with increased impact of sonication. As the sonication impulse reduced from 8s to 1s, CO_2 conversion increased from 5.67% to 8.82%. This can be explained using the H_2-TPD data within the neighbourhood of the reaction temperature. The principle of H_2-TPD discloses the ease of hydrogen adsorption on Cu-sites. This is assumed to reflect the reducibility of the catalyst, hence showing readily available active Cu-sites for hydrogen dissociation. This will facilitate CO_2 conversion. Hence, the high CO_2 conversion capacity of this catalyst can be related tentatively to its high adsorption of hydrogen within the reaction temperature of 623 K (350 ^oC). Furthermore, it was observed that methanol selectivity was highest with the 1s impulse sample (50.72%) and least in CZr-8s impulse sample (47.83%). This can be attributed to various factors [48, 49]. Recent studies proposed that the surface basicity of the catalyst plays a key role in the catalytic selectivity. It is promulgated that CO_2 adsorbed at the strong basic sites favourably promotes methanol synthesis over RWGS [43, 45, 50]. The adsorbed CO_2 at this sites will hardly be reduced to CO. The results from CO_2-TPD shows that both intensity and contribution of strong basic sites is highest with the 1s impulse sample and least in the conventional CZr catalyst. With these parameters, the methanol yield was estimated with samples with frequent ultrasonic irradiation having the highest yields. Correlating the amount of CO_2 desorbed to the CO_2 conversion and methanol yield, a linear relationship was obtained for the former. This suggests that the amount of CO_2 converted is directly related to the amount adsorbed. Whereas, for methanol selectivity, a minimum is attained before it begins to ascend. This is as a result of the simultaneous occurrence of reverse water gas shift reaction with the production of CO (see Figure 10).

The presence of Zn in the catalyst is also considered to affect the conversion of CO_2 and selectivity of methanol. As the Cu/Zn ratio decreases from 3 to 0.5, the conversion of CO_2 showed an initial increase from 17.78% to 18.68% before descending to 17.08%. This corresponds to the H_2-TPD profile of these catalysts validating the effect of dissociative desorption of hydrogen on hydrogenation of CO_2. Moreover, the increase in Cu/Zn ratio was

associated with an increase in methanol selectivity. This is at par with the CO_2-TPD results for strong basic sites. Correlating the CO_2 desorption profile at this basic sites with the methanol selectivity and CO_2 conversion, it can be proposed that at a low Cu/Zn ratio (< 1), the methanol selectivity and CO_2 conversion displays a sharp reduction slope. But at higher Cu/Zn ratio (> 1), a low change gradient is observed for both selectivity and conversion of methanol and CO_2 respectively. This is diagrammatically illustrated in Figure 11.

Table 5.5: Catalytic performance of CZr and CZZr catalysts for methanol synthesis[‡]

Variation with ultrasonic impulse				
Sample	**X_{CO2} (%)**	**S_{CH3OH} (%)**	**S_{CO} (%)**	**Y_{CH3OH} (%)**
CZr-Conv	5.71	48.92	51.08	2.79
CZr-Cont Imp	8.43	50.31	49.69	4.24
CZr-1s Imp	8.82	50.72	49.28	4.47
CZr-4s Imp	6.36	49.16	50.84	3.13
CZr-8s Imp	5.67	47.83	52.17	2.71

Variation with metal composition				
Sample	**X_{CO2} (%)**	**S_{CH3OH} (%)**	**S_{CO} (%)**	**Y_{CH3OH} (%)**
CZZr-316	17.78	54.28	48.72	9.65
CZZr-334	18.68	53.57	46.43	10.01
CZZr-361	17.08	49.93	49.07	8.53

[‡] Reaction conditions: P = 3.0 MPa, T = 623 K, GHSV = 3100 hr^{-1}, CO_2:H_2 = 1:3. Experimental errors = ± 4.6 %

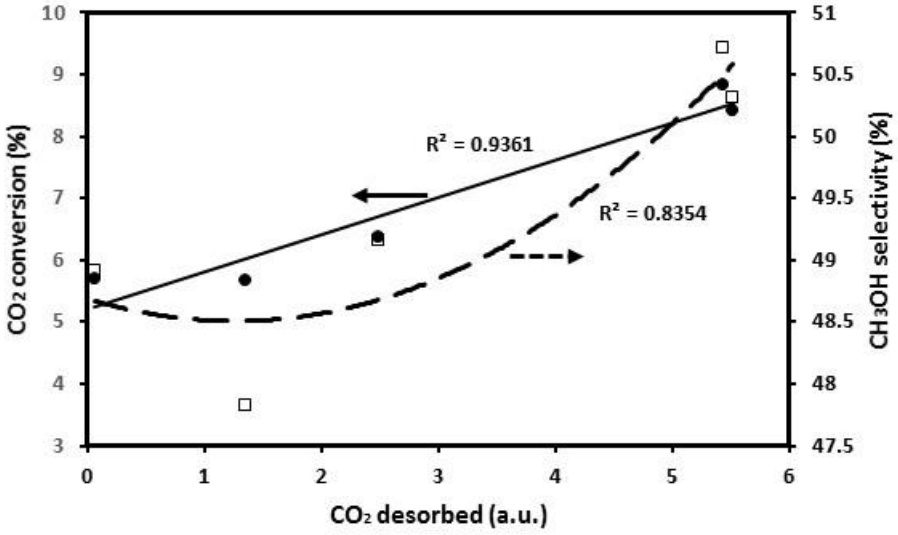

Figure 10: Correlation between CO_2-TPD data with CO_2 conversion and CH_3OH selectivity for CZr catalyst

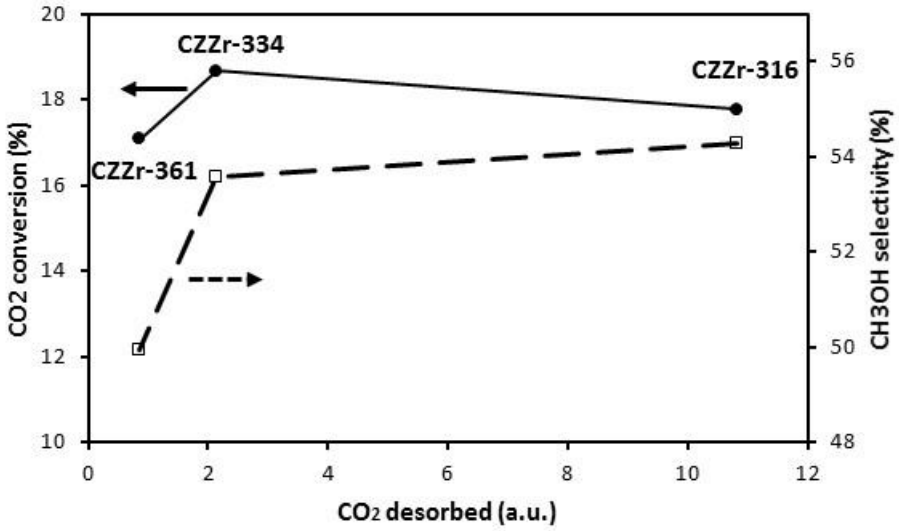

Figure 11: Correlation between CO_2-TPD data with CO_2 conversion and CH_3OH selectivity for CZZr catalyst

4 CONCLUSIONS

In the synthesis of methanol via hydrogenation process, one key contributor to the effectiveness of this process is the presence of a suitable catalyst. The most suitable and widely used catalyst is the Cu-based catalyst and its optimal performance is based partly on its thermal characteristics and surface morphology and chemistry. Subsequently, this is dependent on various factors including catalyst synthetic method, metal content and composition. In addition, its thermal strength is also dependent on the heating rate. The effect of these factors are summarised as follows based on the results of the current study:

1. The adoption of ultrasonic irradiation at different sonication impulse affects particle agglomeration, which in turn contributes to the surface morphology and chemistry of the Cu/ZrO_2 catalysts. Low sonication impulses displayed the best properties for the catalyst with improved surface area, particle size and porosity.
2. Metal promoter, ZnO had a greater impact on these properties with an optimum performance at moderate Zn content.
3. Based on the thermal tests, this study suggests that for optimum industrial applicability, the material will be well suited at a thermal operation with heating rate at 20 K/min rather than 10 K/min.

ACKNOWLEDGEMENT

This work was carried out at the International Doctoral Innovation Centre (IDIC). The authors would like to acknowledge the financial support through the grant of Ningbo Key Research Project 'Absorption/catalytic technologies for the simultaneous removal of multi-pollutants from flue gas at power stations' (Grant No. 1012B10042) and from Ningbo Education Bureau, Ningbo Science and Technology Bureau, China's MoST and The University of Nottingham. The work is also partially supported by EPSRC (Grant no. EP/G037345/1) and Ningbo Innovation Team Project on 'Indoor air pollution control technology' (Grant No. 2017C510001).

References

[1] K. Fujimoto, Y. Yu, Spillover effect on the stabilization of Cu-Zn catalyst for CO2 hydrogenation to methanol, Studies in Surface Science and Catalysis, 77 (1993) 393-396.

[2] F. Arena, K. Barbera, G. Italiano, G. Bonura, L. Spadaro, F. Frusteri, Synthesis, characterization and activity pattern of Cu–ZnO/ZrO_2 catalysts in the hydrogenation of carbon dioxide to methanol, Journal of Catalysis, 249 (2007) 185-194.

[3] C. Li, X. Yuan, K. Fujimoto, Development of highly stable catalyst for methanol synthesis from carbon dioxide, Applied Catalysis A: General, 469 (2014) 306-311.

[4] S. Natesakhawat, J.W. Lekse, J.P. Baltrus, P.R. Ohodnicki, B.H. Howard, X. Deng, C. Matranga, Active Sites and Structure–Activity Relationships of Copper-Based Catalysts for Carbon Dioxide Hydrogenation to Methanol, ACS Catalysis, 2 (2012) 1667-1676.

[5] J. Słoczyński, R. Grabowski, A. Kozłowska, P. Olszewski, M. Lachowska, J. Skrzypek, J. Stoch, Effect of Mg and Mn oxide additions on structural and adsorptive properties of Cu/ZnO/ZrO2 catalysts for the methanol synthesis from CO2, Applied Catalysis A: General, 249 (2003) 129-138.

[6] J. Słoczyński, R. Grabowski, A. Kozłowska, M. Lachowska, J. Skrzypek, Effect of additives and a preparation method on catalytic activity of Cu/ZnO/ZrO2 system in the

carbon dioxide hydrogenation to methanol, Studies in Surface Science and Catalysis, 153 (2004) 161-164.

[7] J. Słoczyński, R. Grabowski, P. Olszewski, A. Kozłowska, J. Stoch, M. Lachowska, J. Skrzypek, Effect of metal oxide additives on the activity and stability of Cu/ZnO/ZrO2 catalysts in the synthesis of methanol from CO2 and H2, Applied Catalysis A: General, 310 (2006) 127-137.

[8] M. Lachowska, J. Skrzypek, Methanol synthesis from carbon dioxide and hydrogen over Mn-promoted copper/zinc/zirconia catalysts, Reaction Kinetics and Catalysis Letters, 83 (2004) 269-273.

[9] L. Li, D. Mao, J. Yu, X. Guo, Highly selective hydrogenation of CO2 to methanol over CuO–ZnO–ZrO2 catalysts prepared by a surfactant-assisted co-precipitation method, Journal of Power Sources, 279 (2015) 394-404.

[10] C. Huang, S. Chen, X. Fei, D. Liu, Y. Zhang, Catalytic Hydrogenation of CO2 to Methanol: Study of Synergistic Effect on Adsorption Properties of CO2 and H2 in CuO/ZnO/ZrO2 System, Catalysts, 5 (2015) 1846.

[11] Y. Ma, Q. Sun, D. Wu, W.-H. Fan, Y.-L. Zhang, J.-F. Deng, A practical approach for the preparation of high activity Cu/ZnO/ZrO2 catalyst for methanol synthesis from CO2 hydrogenation, Applied Catalysis A: General, 171 (1998) 45-55.

[12] R. Raudaskoski, M.V. Niemelä, R.L. Keiski, The effect of ageing time on co-precipitated Cu/ZnO/ZrO2 catalysts used in methanol synthesis from CO2 and H2, Topics in Catalysis, 45 (2007) 57-60.

[13] E. Frei, A. Schaadt, T. Ludwig, H. Hillebrecht, I. Krossing, The Influence of the Precipitation/Ageing Temperature on a Cu/ZnO/ZrO2 Catalyst for Methanol Synthesis from H2 and CO2, ChemCatChem, 6 (2014) 1721-1730.

[14] M. Saito, T. Fujitani, M. Takeuchi, T. Watanabe, Development of copper/zinc oxide-based multicomponent catalysts for methanol synthesis from carbon dioxide and hydrogen, Applied Catalysis A: General, 138 (1996) 311-318.

[15] J. Słoczyński, R. Grabowski, A. Kozłowska, P. Olszewski, J. Stoch, J. Skrzypek, M. Lachowska, Catalytic activity of the M/(3ZnO·ZrO2) system (M = Cu, Ag, Au) in the hydrogenation of CO2 to methanol, Applied Catalysis A: General, 278 (2004) 11-23.

[16] F. Arena, G. Italiano, K. Barbera, S. Bordiga, G. Bonura, L. Spadaro, F. Frusteri, Solid-state interactions, adsorption sites and functionality of Cu-ZnO/ZrO2 catalysts in the CO2 hydrogenation to CH3OH, Applied Catalysis A: General, 350 (2008) 16-23.

[17] F. Arena, G. Italiano, K. Barbera, G. Bonura, L. Spadaro, F. Frusteri, Basic evidences for methanol-synthesis catalyst design, Catalysis Today, 143 (2009) 80-85.

[18] R. Raudaskoski, E. Turpeinen, R. Lenkkeri, E. Pongrácz, R.L. Keiski, Catalytic activation of CO2: Use of secondary CO2 for the production of synthesis gas and for methanol synthesis over copper-based zirconia-containing catalysts, Catalysis Today, 144 (2009) 318-323.

[19] F. Arena, G. Mezzatesta, G. Zafarana, G. Trunfio, F. Frusteri, L. Spadaro, Effects of oxide carriers on surface functionality and process performance of the Cu–ZnO system in the synthesis of methanol via CO2 hydrogenation, Journal of Catalysis, 300 (2013) 141-151.

[20] R. Ladera, F.J. Pérez-Alonso, J.M. González-Carballo, M. Ojeda, S. Rojas, J.L.G. Fierro, Catalytic valorization of CO2 via methanol synthesis with Ga-promoted Cu–ZnO–ZrO2 catalysts, Applied Catalysis B: Environmental, 142 (2013) 241-248.

[21] X. Liu, P. Ramírez de la Piscina, J. Toyir, N. Homs, CO2 reduction over Cu-ZnGaMO (M=Al, Zr) catalysts prepared by a sol-gel method: Unique performance for the RWGS reaction, Catalysis Today, DOI http://dx.doi.org/10.1016/j.cattod.2017.04.022(2017).

[22] S. Esposito, M. Turco, G. Bagnasco, C. Cammarano, P. Pernice, New insight into the preparation of copper/zirconia catalysts by sol–gel method, Applied Catalysis A: General, 403 (2011) 128-135.

[23] G. Bonura, M. Cordaro, C. Cannilla, F. Arena, F. Frusteri, The changing nature of the active site of Cu-Zn-Zr catalysts for the CO2 hydrogenation reaction to methanol, Applied Catalysis B: Environmental, 152 (2014) 152-161.

[24] X. Guo, D. Mao, G. Lu, S. Wang, G. Wu, CO_2 hydrogenation to methanol over $Cu/ZnO/ZrO_2$ catalysts prepared via a route of solid-state reaction, Catalysis Communications, 12 (2011) 1095-1098.

[25] X. Guo, D. Mao, G. Lu, S. Wang, G. Wu, Glycine–nitrate combustion synthesis of CuO–ZnO–ZrO2 catalysts for methanol synthesis from CO2 hydrogenation, Journal of Catalysis, 271 (2010) 178-185.

[26] X. Guo, D. Mao, S. Wang, G. Wu, G. Lu, Combustion synthesis of CuO–ZnO–ZrO2 catalysts for the hydrogenation of carbon dioxide to methanol, Catalysis Communications, 10 (2009) 1661-1664.

[27] F. Liao, Y. Huang, J. Ge, W. Zheng, K. Tedsree, P. Collier, X. Hong, S.C. Tsang, Morphology-Dependent Interactions of ZnO with Cu Nanoparticles at the Materials' Interface in Selective Hydrogenation of CO2 to CH3OH, Angewandte Chemie International Edition, 50 (2011) 2162-2165.

[28] M.-F. Luo, J.-M. Ma, J.-Q. Lu, Y.-P. Song, Y.-J. Wang, High-surface area CuO–CeO2 catalysts prepared by a surfactant-templated method for low-temperature CO oxidation, Journal of Catalysis, 246 (2007) 52-59.

[29] L. Qi, Q. Yu, Y. Dai, C. Tang, L. Liu, H. Zhang, F. Gao, L. Dong, Y. Chen, Influence of cerium precursors on the structure and reducibility of mesoporous CuO-CeO2 catalysts for CO oxidation, Applied Catalysis B: Environmental, 119 (2012) 308-320.

[30] Z. Wang, Z. Qu, X. Quan, Z. Li, H. Wang, R. Fan, Selective catalytic oxidation of ammonia to nitrogen over CuO-CeO2 mixed oxides prepared by surfactant-templated method, Applied Catalysis B: Environmental, 134 (2013) 153-166.

[31] X. Ma, X. Feng, X. He, H. Guo, L. Lv, J. Guo, H. Cao, T. Zhou, Mesoporous CuO/CeO2 bimetal oxides: One-pot synthesis, characterization and their application in catalytic destruction of 1,2-dichlorobenzene, Microporous and Mesoporous Materials, 158 (2012) 214-218.

[32] C.I. Ezeh, X. Huang, X. Yang, C.-g. Sun, J. Wang, Sonochemical surface functionalization of exfoliated LDH: Effect on textural properties, CO2 adsorption, cyclic regeneration capacities and subsequent gas uptake for simultaneous methanol synthesis, Ultrasonics Sonochemistry, 39 (2017) 330-343.

[33] C.I. Ezeh, M. Tomatis, X. Yang, J. He, C. Sun, Ultrasonic and hydrothermal mediated synthesis routes for functionalized Mg-Al LDH: Comparison study on surface morphology, basic site strength, cyclic sorption efficiency and effectiveness, Ultrasonics Sonochemistry, 40 (2018) 341-352.

[34] R. Lewis Clark, Y. Wu, Electrohydrodynamic Processing of Micro- and Nanometer Biological Materials, Biomaterials Fabrication and Processing Handbook, CRC Press2008, pp. 275-333.

[35] S. Pradhan, J. Hedberg, E. Blomberg, S. Wold, I. Odnevall Wallinder, Effect of sonication on particle dispersion, administered dose and metal release of non-functionalized, non-inert metal nanoparticles, Journal of Nanoparticle Research, 18 (2016) 285.

[36] A. Siddiqui, A. Alayoubi, Y. El-Malah, S. Nazzal, Modeling the effect of sonication parameters on size and dispersion temperature of solid lipid nanoparticles (SLNs) by response surface methodology (RSM), Pharmaceutical Development and Technology, 19 (2014) 342-346.

[37] A. Fathy, O. Elkady, A. Abu-Oqail, Synthesis and characterization of Cu–ZrO2 nanocomposite produced by thermochemical process, Journal of Alloys and Compounds, 719 (2017) 411-419.

[38] H. Xu, B.W. Zeiger, K.S. Suslick, Sonochemical synthesis of nanomaterials, Chemical Society reviews, 42 (2013) 2555-2567.

[39] C.I. Ezeh, M. Tomatis, X. Yang, J. He, C.-g. Sun, Ultrasonic and Hydrothermal Mediated Synthesis Routes for Functionalized Mg-Al LDH: Comparison Study on Surface Morphology, Basic Site Strength, Cyclic Sorption Efficiency and Effectiveness, Ultrasonics Sonochemistry, DOI https://doi.org/10.1016/j.ultsonch.2017.07.013.

[40] H.W. Olfs, L.O. Torres-Dorante, R. Eckelt, H. Kosslick, Comparison of different synthesis routes for Mg–Al layered double hydroxides (LDH): Characterization of the structural phases and anion exchange properties, Applied Clay Science, 43 (2009) 459-464.

[41] X. Dong, H.-B. Zhang, G.-D. Lin, Y.-Z. Yuan, K.R. Tsai, Highly Active CNT-Promoted Cu–ZnO–Al2O3 Catalyst for Methanol Synthesis from H2/CO/CO2, Catalysis Letters, 85 (2003) 237-246.

[42] J.A. Ahlers, J.A. Grasser, B.T. Loveless, D.S. Muggli, Room-temperature oxidation of reduced Cu/ZnO surfaces by lattice oxygen diffusion, Catalysis Letters, 114 (2007) 185-191.

[43] P. Gao, H. Yang, L. Zhang, C. Zhang, L. Zhong, H. Wang, W. Wei, Y. Sun, Fluorinated Cu/Zn/Al/Zr hydrotalcites derived nanocatalysts for CO2 hydrogenation to methanol, Journal of CO2 Utilization, 16 (2016) 32-41.

[44] H. Wilmer, T. Genger, O. Hinrichsen, The interaction of hydrogen with alumina-supported copper catalysts: a temperature-programmed adsorption/temperature-programmed desorption/isotopic exchange reaction study, Journal of Catalysis, 215 (2003) 188-198.

[45] X. Guo, D. Mao, G. Lu, S. Wang, G. Wu, The influence of La doping on the catalytic behavior of Cu/ZrO2 for methanol synthesis from CO2 hydrogenation, Journal of Molecular Catalysis A: Chemical, 345 (2011) 60-68.

[46] L. Zhang, Y. Zhang, S. Chen, Effect of promoter SiO2, TiO2 or SiO2-TiO2 on the performance of CuO-ZnO-Al2O3 catalyst for methanol synthesis from CO2 hydrogenation, Applied Catalysis A: General, 415–416 (2012) 118-123.

[47] H. Zhan, F. Li, P. Gao, N. Zhao, F. Xiao, W. Wei, L. Zhong, Y. Sun, Methanol synthesis from CO2 hydrogenation over La–M–Cu–Zn–O (M = Y, Ce, Mg, Zr) catalysts derived from perovskite-type precursors, Journal of Power Sources, 251 (2014) 113-121.

[48] R.d.l.P.P. Toyir J., Fierro J. L. G. and Homs N. , Catalytic Performace for CO_2 Conversion to Methanol of Gallium Promoted Copper based Catalysts: Influence of Metallic Precursors, Applied Catalysis B, 34 (2001) 255-266.

[49] C. Zhong, X. Guo, D. Mao, S. Wang, G. Wu, G. Lu, Effects of alkaline-earth oxides on the performance of a CuO-ZrO2 catalyst for methanol synthesis via CO2 hydrogenation, RSC Advances, 5 (2015) 52958-52965.

[50] P. Gao, F. Li, H. Zhan, N. Zhao, F. Xiao, W. Wei, L. Zhong, H. Wang, Y. Sun, Influence of Zr on the performance of Cu/Zn/Al/Zr catalysts via hydrotalcite-like precursors for CO2 hydrogenation to methanol, Journal of Catalysis, 298 (2013) 51-60.

Highlights

- Synthesis of CuO/ZrO_2 catalyst via ultrasonic-assisted co-precipitation route
- Surface area and porosity of catalyst improved by *ca.* 13% with sonication impulse
- Introducing Zn^{2+} (60 vol % max.) boosted the surface area by *ca.* 23% max
- Addition of Zn^{2+} promoter via solid state reaction route enhanced methanol yield by over 250%